Van Yuzuncu Yil University
Science Research and
Application Center

GLOBAL SUMMIT ON ADVANCED MATERIALS & SUSTAINABLE ENERGY

(*G-AMSE22*)

VAN, TURKEY
OCTOBER 03–04
2022

Theme: Sustainable living for “Lake Van”

CONFERENCE PROCEEDINGS

G-AMSE22

The Proceedings of Global Summit on Advanced Materials and Sustainable Energy October 3-4, 2022, Van Yuzuncu Yil University, Van, Turkey.

Edited by
Dr. Yuksel AKINAY

Copyright
Van Yuzuncu Yil University
ISBN 978-975-7616-84-9

Van, Turkey
http://g-amse2022.yyu.edu.tr/
g-amse22@yyu.edu.tr

Information for the Participants

Welcome to Van City

Van is a city in Eastern Turkey, with unique quirks, one of which is the rare breed of cats that, interestingly, inhabit around Lake Van. Van cats have curious different-colored eyes – one, amber and one, blue – and more curiously, a fondness for swimming in the vast Lake Van. Apart from exotic cats, Van prides in its deep-rooted history that goes as far back as 5,000 BC. Different civilizations and kingdoms shaped Van's history – Urartian, Armenian, Byzantine, Seljuk and Ottoman. Each of these eras left remarkable structures such as the Van Fortress (Urartian) and the Holy Cross Church (Armenian). Nature has also blessed the town of Van, with a lake that is the largest body of water in Turkey.

Conference Venue

The Conference will be held at the Van Yuzuncu Yil University Campus. Van Yuzuncu Yil University was founded on July 20, 1982. However, the attempts to create a university in the east region of Turkey had started much earlier. Atatürk, the president of republic of that period, sent Mustafa Necati, of The Ministry of Education, to examine on-site the situation in Van in 1927. Mustafa Necati found in favour of the foundation of a university in Van. Ferit Nur, the teacher, was sent to Van and was asked to transform the present middle school into a high school and to form the kernel of the planned university. Atatürk said, "We must go into action to constitute a modern city of culture with a primary school and finally a university in the most beautiful places on the coasts of The Lake Van for the east region" and with this aim, he sent Saffet Arıkan, The Ministry of Education of that period, to Van for land determination. Van Yüzüncü Yıl University, with its 17 faculties, 5 institutes, 4 vocational schools, 9 vocational schools, 1 conservatory, 43 practice and research centers, is located 15 km from the city center and around Lake Van.

Conference Sessions

The conference Welcome Reception will be held at the Engineering Faculty on Monday morning (Oct. 3h, 2022), and all technical sessions and networking events will follow on Monday through Tuesday. In addition, zoom links will be provided for the remote presenters and participants who have decided to telecommute.

Conference Chair
Yuksel AKINAY

Conference Chairs

Hamdullah SEVLI	Rector of Van Yuzuncu Yil University, Honorary Chair
Yuksel AKINAY	Manager of Science and Research Center of Van Yuzuncu Yil University, General Chair
Tayfun CETIN	Hakkari University, General Co-Chair & Technical Program Chair
Gul GORMEZ	Vice-Manager of Science and Research Center of Van Yuzuncu Yil University, General Co-Chair

Organizing Committee

Sedat YAYLA	Vice Rector of Van Yuzuncu Yil University (TURKIYE)
Hilal CELIK KAZICI	Coordinator of Scientific Research Projects Department of Van Yuzuncu Yil University
Yuksel AKINAY	Manager of Science and Research Center of Van Yuzuncu Yil University
Gul GORMEZ	Vice-Manager of Science and Research Center of Van Yuzuncu Yil University
Tayfun CETIN	Yuksekova Vocational High School, Hakkari University
Volkan TASDEMIR	Science and Research Center of Van Yuzuncu Yil University

International Scientific Committee

Ajay Kumar MISHRA	Univeristy of South Africa, South Africa
Filipe AMARAL	Escola Superior de Tecnologia da Saúde de Coimbra, Portogal
Gil GONÇALVES	University of Aveiro, Portugal
Jayanta MUKHOPADHYAY	CSIR-Central Glass & Ceramic Research Institute, India
Jarem Raul GARCIA	Universidade Estadual de Ponta Grossa, Brazil
Madhumita MUKHOPADHYAY	Maulana Abul Kalam Azad University of Technology, India
Mehmet GULCAN	Van Yuzuncu Yil University, Turkiye
Mehrdad SHAHBAZ	Urmia University, Iran
Mojtaba JAFARIAN	Islamic Azad University, Iran
Musa TÜRKER	Yildiz Technical University, Turkiye
Nahit AKTAS	Manas University, Kyrgyzstan
Petr KRATOCHVÍL	University of Chemistry and Technology in Prague, Czech Republic
Sabu THOMAS	University of Mahatma Gandhi, India
Selcuk GUMUS	Bartin University, Turkiye
Semiha DEDE	Van Yuzuncu Yil University, Turkiye
Semra DEMİR	Van Yuzuncu Yil University, Turkiye
Sílvio C. de OLIVEIRA	Universidade Federal de Mato Grosso do Sul, Brazil

Investigation of Halloysite Clay as a Binder in Porcelain Tile Compositions

N. Başaran[1*], E. Boztepe[1], A. Karakaya[1], S. Aksan[1], N. Tamsü Selli[1]

N. Başaran[1], E. Boztepe[1], A. Karakaya[1], S. Aksan[1], N. Tamsü Selli[1]*

[1]Department of Materials Science and Engineering, Gebze Technical University, Kocaeli 41400, Turkey

Mail: *nengin@gtu.edu.tr*

This study aims to determine whether halloysite clay, which has a tubular microstructure, can be used as an alternative binder in porcelain tiles by the change in green strength and cooked strength values. In the study, halloysite clay was doped at the rates of 0.1, 0.3, 0.6, and 1.0% by weight. First, the green strength of the doped samples was determined. The prepared samples were fired at 1220 degrees for 37 minutes. Phase analyzes (XRD) and microstructure analyzes (SEM/EDX) of these samples were also performed, and the fired strength results were compared. It was observed that the green strength value of the sample with 0.3% halloysite clay added increased 2.5 times compared to the standard. When the strength of the fired samples was examined, it was observed that the tubular structure of the halloysite deteriorated at high temperatures. Due to this effect, the fired tile strength value did not change. When evaluated from this point of view, the obtained results reveal that halloysite clay can be used as a green strength increasing binder.

Keywords: Halloysite, porcelain tiles, binders, green strength, fired strength.

1. Introduction

Today, developing technology increases the demands on the materials we use and increases the expectations for different properties from these materials. In order to meet these demands, gaining various properties to materials has become the focus of research. There is a continuous increase in the production of ceramic materials used in various fields around the world. Turkey, of the coating element consisting of ceramic material (floor tiles, wall tiles, porcelain tiles, and decor products), was considered to produce around 400 million. m2/year ninth world production capacity ranked third in Europe. Ceramic tile production is increasing rapidly around the world. Due to its remarkable mechanical properties, the demand for porcelain tiles is also increasing considerably. The main standard requirement for a porcelain tile is very low water absorption (it should be < 0.5% according to ISO 13006) (Biasini et al. 2002) Porcelain tile bodies are composed of 30-40% clay mixture, 40-50% feldspar, and 10-15% quartz. Quartz and quartzites have a structural function. All components must have low concentrations of coloring oxides (Fe2O3 and TiO2) to avoid contamination of the natural body color (Zanelli et al. 2003). While clays facilitate shaping and increase the wet and dry strength of the products, feldspars used as a smelter provide the sintering of the bodies and give the porcelain bodies the desired low porosity microstructure. In recent years, rather large (1m X 3m, etc.) tile productions have been added to innovative works such as applying functional coatings (photocatalytic coatings, hydrophobic coatings, antislip surfaces, etc.) to tile surfaces. For wall tiles to take their place in spaces with more aesthetic designs, the production of large-sized thin tiles has become quite common. By producing standard tiles from 11mm section thickness to 6mm section thickness, a product has a weight reduction of approximately 45%. Thin wall tiles with a section thickness of 6mm are generally preferred in large and rectangular sizes. These dimensions are generally preferred in (33 cm X 100 cm) and

(30 cm X 90 cm) sizes. The large and rectangular dimensions cause critical measures regarding deformation and strength in the production of traditional ceramic materials. Companies can produce these products by making different shaping investments to produce wall tiles in this thinness and in these sizes. However, the height of the press molds is intervened to make these products with the dry pressing method available in the enterprises. Therefore, to make these products with the existing production technique without making any extra investment, adding a binder that increases the green strength is necessary. Halloysite clay was used as an alternative binder composition in this study. Halloysite clay is clay with the formula Al2Si2O5(OH)4.2H2O, which naturally contains nano-sized tubes (Saif, Maghrour Zefreh, and Torok 2018). Fig. 1 shows the halloysite clay and kaolinite clay microstructure, which have a similar mineral structure. Halloysite nanotubes are often used in the literature to form a template. (Klimkiewicz and Drąg 2004).

Halloysites are generally used to form polymer nanocomposites. (Shi et al. 2007) compared the thermal, electrical, and dimensional stability performances of bulk polymers and halloysites with modification agents reinforced polymers. Generally, studies in the literature are on using halloysite minerals in polymer matrices (Huang et al. 2016). Halloysite was chosen for this project because of the rod-like structures indicated in Figures 1 (a) and (b). These rod-like structures are added to the slurry for their green strength to resist crack propagation.

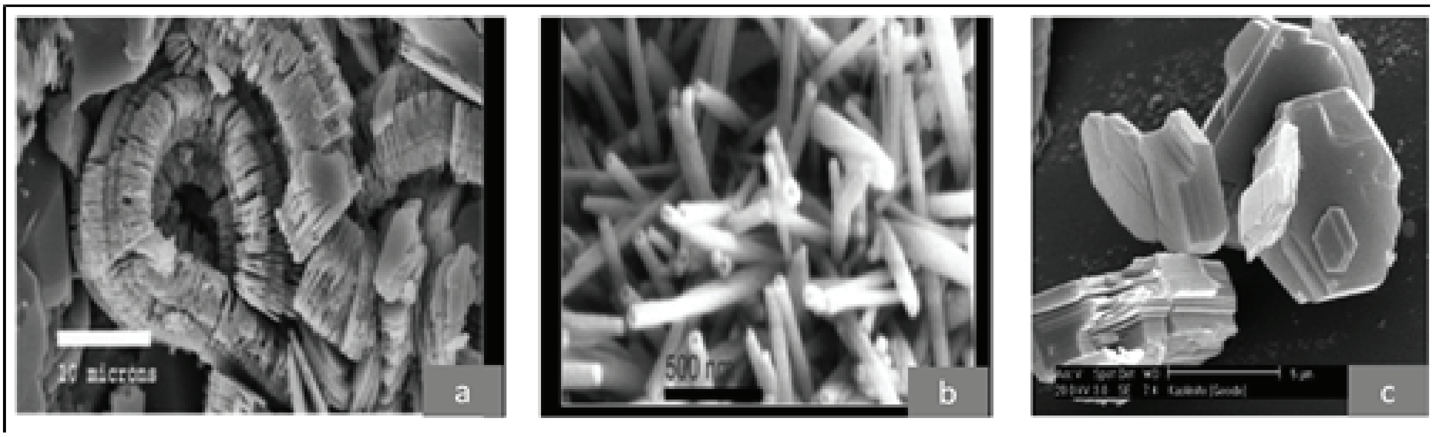

Figure 1. a) and b) *Microstructure of halloysite clay c) Microstructure of kaolinite (Saif, Maghrour Zefreh, and Torok 2018)*

2. Material and Methods

2.1. Preparation of the compositions

Firstly halloysite raw material (Esan Industrial Raw Materials, Turkey) was prepared to add the standard porcelain tile composition. Chemical characterization was carried out by means of wavelength dispersive X-ray fluorescence spectrometry (XRF), using Philips Model PW 2400 XRF Instrument fitted with an Rh white florescent tube. The sample was prepared as fused beads using a Philips PERL'X3 instrument. Chemical analysis of the halloysite clay (denoted as HAL) and standard porcelain tile body composition (denoted as STD) are given in Table1.

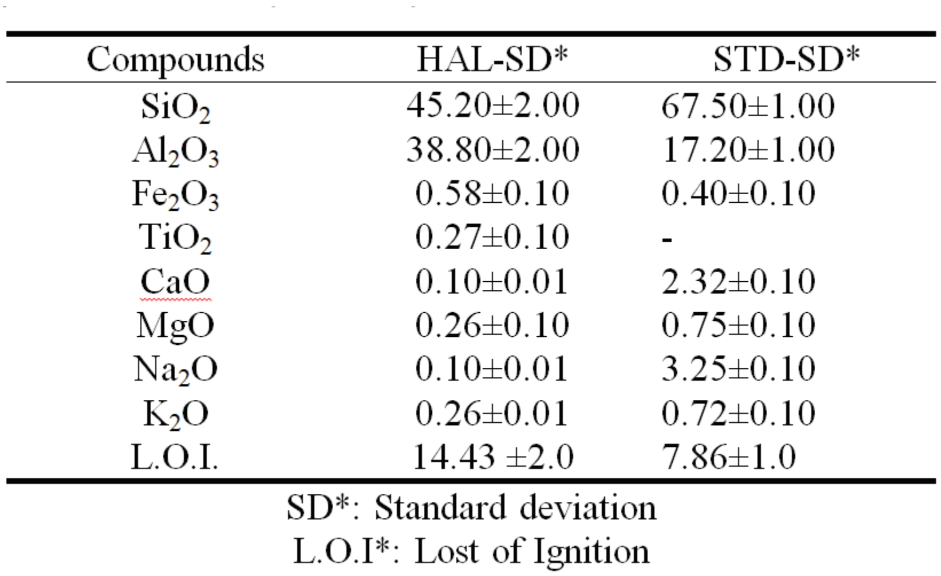

Compounds	HAL-SD*	STD-SD*
SiO_2	45.20±2.00	67.50±1.00
Al_2O_3	38.80±2.00	17.20±1.00
Fe_2O_3	0.58±0.10	0.40±0.10
TiO_2	0.27±0.10	-
CaO	0.10±0.01	2.32±0.10
MgO	0.26±0.10	0.75±0.10
Na_2O	0.10±0.01	3.25±0.10
K_2O	0.26±0.01	0.72±0.10
L.O.I.	14.43 ±2.0	7.86±1.0

SD*: Standard deviation
L.O.I*: Lost of Ignition

Table 1. *Chemical composition of halloysite clay (HAL) and standard wall tile body (STD)*

Halloysite firstly was wet-milled by a laboratory jar mill containing 60 wt.% solid and 1.0 wt.% deflocculant (sodium silicate), for 20 minutes. The slurry was sieved with an aperture of 45 microns. After the grinding process of the raw materials, the slurry dried at 100°C for 24 hours. For granulation of the dried powders, they were moistened by spraying water on them. Formed granules were passed through sieves with aperture sizes of 600 and 250 microns to collect between them.

The standard porcelain tile composition was prepared by weighing the raw materials appropriately to form the chemical analysis in Table 1. The raw materials were considered and then ground to 60 percent solids. 1% deflocculant (sodium silicate) was added. They were wet-milled by a laboratory jar mill for 20 minutes. The slurry was sieved with an aperture of 45 microns. The granulated halloysites were added to the obtained sludge at a weight ratio of 0.1, 0.3, 0.6 and 1.0%, then the sludge dried at 100°C for 24 hours. After drying, they were moistened by spraying water on them and granulated. Then, the test specimens were prepared from the granules of each composition. The weighed granules powders were put into the cavity of a steel die and shaped by applying a pressure of 30 MPa by using a hydraulic press. The rectangular-shaped samples were prepared for the mechanical study. The discs' dimensions were 31.5 mm in diameter, and rectangular bars were 75 mm × 7mm × 5 mm. Samples were fired at 1220°C for 40 minutes in laboratory furnace (Nabertherm Furnace). Sample numbers and details are summarized in Table 2.

Table 2. *Samples and details*

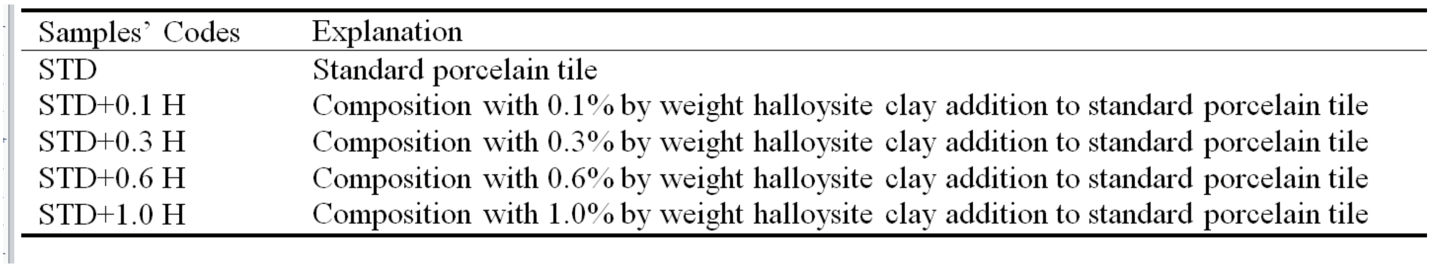

Samples' Codes	Explanation
STD	Standard porcelain tile
STD+0.1 H	Composition with 0.1% by weight halloysite clay addition to standard porcelain tile
STD+0.3 H	Composition with 0.3% by weight halloysite clay addition to standard porcelain tile
STD+0.6 H	Composition with 0.6% by weight halloysite clay addition to standard porcelain tile
STD+1.0 H	Composition with 1.0% by weight halloysite clay addition to standard porcelain tile

2.2. Technological properties of the samples

First, the samples' water absorption values check whether they provide the standard technological features that porcelain tiles should have. Water absorption value of the samples was determined by water saturation under vacuum and Archimedes' principle (ISO 10545-3) by using related equations (Eqs. (1)).

$$\%\text{Water absorption } (wa)=[(ww-wd)/wd]\,\text{x}100 \qquad (1)$$

where, wd, dry weight of the sample, ww, wet weight of the sample, wa, weight of solid suspended in water.

The colour values of the new compositions and standard composition were measured by a spectrometer (Minolta CR, 300 Colourmeter). The colorimeter operates on the CIELab method, which is utilized technique in the ceramic production to determine the whiteness and colour of the tiles by measuring three main parameters (Hunter parameters) L* (brightness) from absolute white L=100 to absolute black L=0, an (red–green), bn (yellow–blue) elaborated from the visible spectra. According to the standard wall tile sample (STD), the colour change value (Δ⌧) depend on the new compositions was measured with a spectrometer (Minolta CR, 300 Colourmeter). Δ⌧ value is below 0.5, which means that the colour variation can not be distinguished by the eye.

2.3. X-ray diffraction analysis

X⌧ray diffraction (XRD) method was applied to detect the crystalline phases formed in the microstructure of sintered samples. In the analyses, the samples were used in powder form. They were scanned at 2°/min speed in the range of 5⌧70° with CuK⌧ radiation, (⌧ = 0.154 nm), at 40 kV and 40 mA conditions using RIGAKU 2200 DMAX diffractometer.

2.4. Microstructural analysis

The microstructures of the samples were examined by scanning electron microscopy (SEM) analysis with the use of Philips XL30-SFEG-SEM equipped with energy dispersive X-Ray analysis (EDX). Firstly, the surface of the samples was made suitable for SEM analysis by grinding with a series of SiC abrasive papers and then polished using diamond paste. The polished surfaces were chemically etched in an aqueous solution containing 3% HF for about 1 min to reveal the crystalline structure, then the sample surfaces were coated with gold.

2.5. Mechanical properties of the samples

The flexural strength of green and sintered samples was measured by three-point bending test using an electronic universal tester (Model 5569, Instron Ltd.). Tests were carried out according to ASTM C1161-90 standard with a lower span of 50 mm and crosshead speed of 1 mm/min.

3. Results

3.1. Technological properties of the samples

This study, first, examined the technical properties of the standard porcelain tile represented in Table 3. Then, water absorption, and colour values of all the studied compositions were evaluated. The water absorption value of the standard porcelain tile is 0.03±0.0%, and the color values are L*:87.08, a*:0.25, and b* values 0.12.

Table 3. *Technological properties of the standard porcelain tile body (STD)*

Sample Code	Water Absorption (%)	Colour Value
STD	0.03±0.01	L*: 87.08 a*: 0.25 b*: 0.12

The technological properties of the new compositions are presented in Table 4. As can be seen here, the water absorption values of wall tiles are almost similar to the standard. No significant change was observed in the water absorption values of porcelain tiles after firing. Considering the color change of halloysite clay after firing, the color change values of all samples are below 0.5. When evaluated from this point of view, it did not cause a color change.

Table 4. *Technological properties of the new samples*

Sample Code	Water Absorption (%)	Colour Variation Value (ΔE)
STD+0.1 H	0.03±0.01	< 0.5
STD+0.3 H	0.04±0.01	< 0.5
STD+0.6 H	0.04±0.01	< 0.5
STD+1.0 H	0.04±0.01	< 0.5

3.2. Phases analyses of the samples

The phases of the halloysite clay used in the study were determined by XRD analysis (Fig. 2). Clay contains halloysite and quartz phases as main phases.

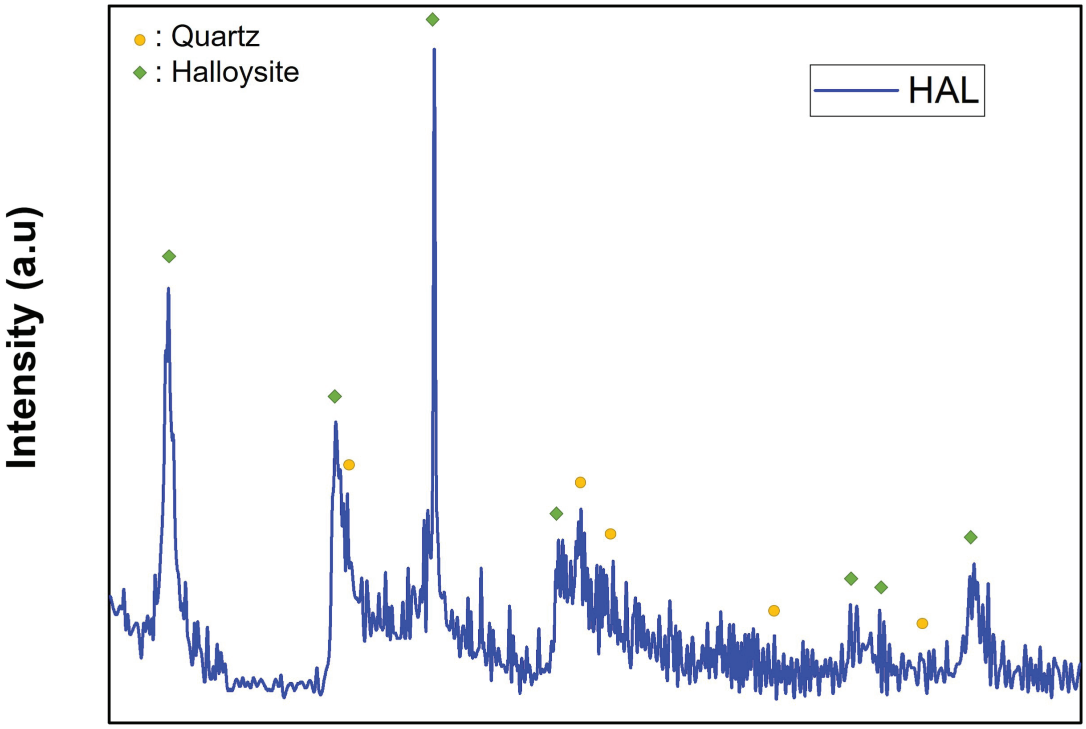

Figure 2. *XRD pattern of halloysite clay.*

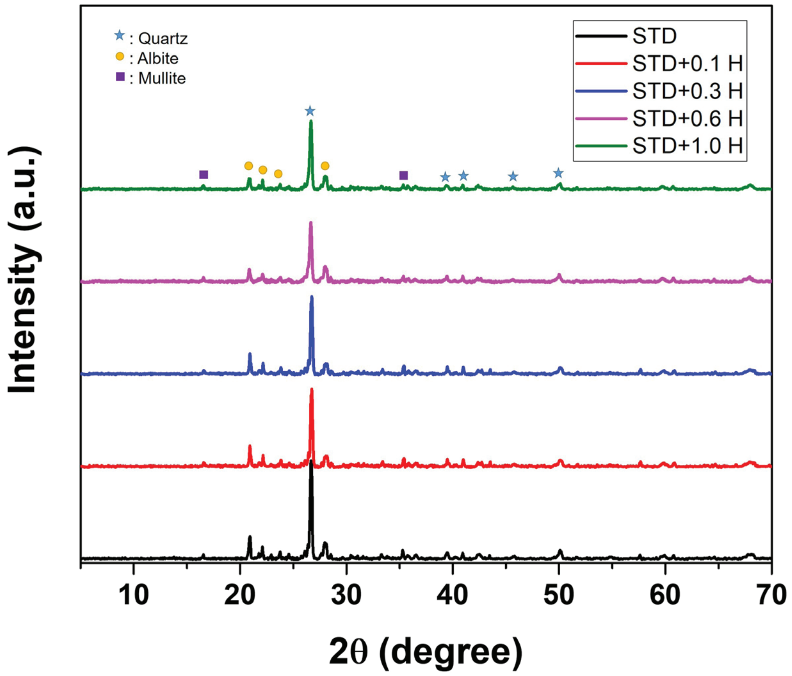

Figure 3. *XRD patterns of the samples.*

3.3. Microstructural properties of the samples

The microstructure image of the fired standard porcelain tile is given in Fig. 4. Rod-like crystals (region 1), angular crystals (region 2), and round crystals (region 3) draw attention to the microstructure. EDX results from these structures are also shown in Figure 3. According to the EDX results, it is clear that the rod-like crystals are mullite, the angular crystals are quartz, and the round crystals are anorthite (Wang et al. 2017; Mcfarlane et al. 2007; Tamsu Selli et al. 2021).

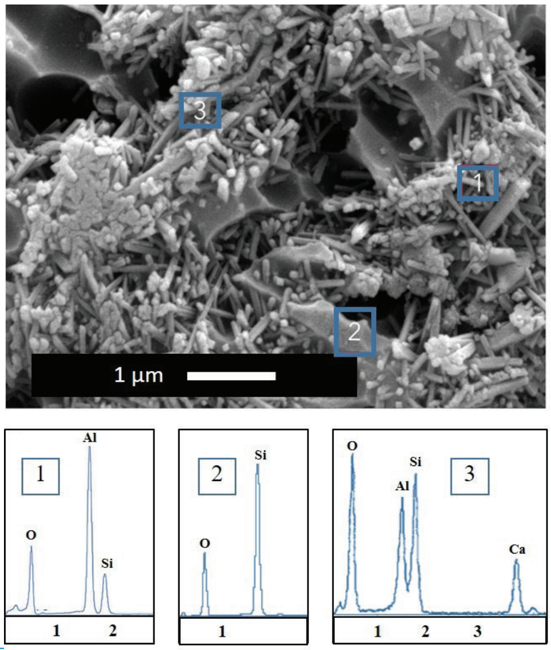

Figure 4. *Standard porcelain tile microstructure and EDX analysis*

Microstructural analyzes of halloysite added fired tiles were also carried out. The results are presented in Fig. 5. As seen in all microstructures, the phases formed in porcelain tiles are the same as the standard. There are anorthite, mullite, and quartz phases.

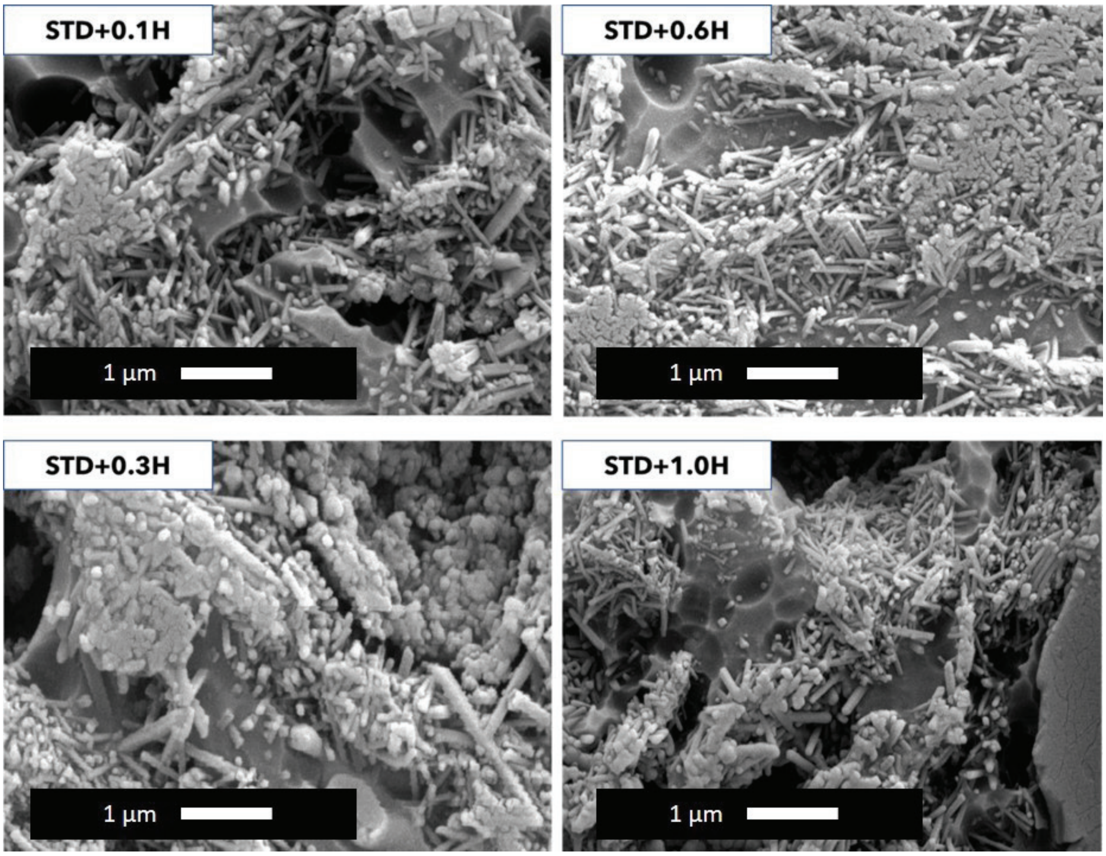

Figure 5. *Microstructures of the samples.*

3.4. Mechanical properties of the samples

Adding halloysite to porcelain tiles also determined the change in wet strength and fired strength (Table 5). The strength value, 0.36 MPa with the addition of halloysite clay to the porcelain tiles, increased to 0.91 MPa with the addition of 0.3% by weight halloysite. The increase in halloysite clay caused an increase in the green strength value. In the fired strength value, the addition of halloysite clay did not significantly affect the strength.

Sample Code	Green Strength (MPa)	Fired Strength (MPa)
STD	0.36±0.02	72.89±0.5
STD+0.1 H	0.47±0.02	72.85±0.5
STD+0.3 H	0.91±0.02	72.84±0.5
STD+0.6 H	0.75±0.02	72.83±0.5
STD+1.0 H	0.72±0.02	72.80±0.5

Table 5. *Mechanical properties of the new samples*

4. Discussion and Conclusion

In this study, halloysite was added to porcelain tiles in various proportions and its effects on porcelain tile green strength and fired strength were investigated. The addition of halloysite clay to standard porcelain tiles did not cause a significant change in technological properties such as water absorption, and colour values. When phase analysis was performed on the fired samples, phases similar to the phases formed in the standard body were obtained. These are quartz, mullite and anorthite phases. Considering the peak intensities, the intensities of the peaks are also very close to each other. Generally, halloysite clay additions support mullite formation (Raghdi et al. 2017) . However, no such effect was observed in its addition to porcelain tiles. Looking at the microstructures, rod-like mullite crystals, round anorthite crystals, and angular quartz crystals are dominant in all compositions. Microstructures also confirm the XRD results obtained.

The effects of halloysite clay addition on the raw and cooked strength of the samples were also examined. Especially in the addition of halloysite clay reached the maximum wet strength value with the addition of 0.3% by weight. With the addition of 0.6% and 1.0% halloysite clay by weight, this value decreased slightly (0.75 and 0.72 MPa), but these values are also considerably higher than the green strength value of the standard. Since halloysite clay contains tubular crystals by nature, it caused an increase in the green strength of the porcelain tile. The decrease in strength with the weight ratio reaching 0.6% and 1.0 may be because the halloysite clay is not dispersed homogeneously in the standard porcelain tile clay. Distributing such clays homogeneously in the added system is critical, significantly increasing green strength (Zhang et al. 2020).

The fired strength value of standard porcelain tile is 72.89 MPa. After adding halloysite clay, it was observed that there was no significant change in the fired strength of the porcelain tiles after firing. In addition, when we look at the XRD results, no different phase formation from the standard or no change in peak intensity was observed, and no different microstructural phase formation was observed. These results explain that halloysite clays decompose at porcelain tile firing temperature. Porcelain tiles were fired at 1220 degrees for 40 minutes. It can be concluded that this temperature and time disrupt the tubular structure in halloysite clay and therefore do not increase the firing strength. In the literature, there are deteriorations in halloysite clay with high temperatures (Wu, Zhang, and Zhou 2019).

This study investigated whether halloysite clay could be used as a binder to increase the raw strength in porcelain tiles. It has been observed that the use of halloysite clay at a rate of 0.3% by weight increases the raw strength of porcelain tiles approximately 2.5 times. It did not harm the firing strength. Therefore, it can be used as an alternative binder that will allow porcelain tiles to be produced thinner.

Acknowledgements

The authors want to express their gratitude to Mrs. Tugba Ucar Demir to supply the halloysite clay from Esan Industrial Raw Materials in Turkey.

References

Biasini, V, Michele, D., Stefano, G., Cesare, M., Raimondo, M., Generali, E., Davide, S., B. (2002). "Mechanical Properties of Porcelain Stoneware Tiles: The Effect of Glass-Ceramic

Systems." Key Engineering Materials - KEY ENG MAT 206–213 (January): 1799–1802. https://doi.org/10.4028/www.scientific.net/KEM.206-213.1799.

Huang, J., Tang, Z. H., Zhang X. H., Guo, B. C. (2016). "Chapter 21 - Halloysite Polymer Nanocomposites." In Nanosized Tubular Clay Minerals, edited by Peng Yuan, Antoine Thill, and Faïza B T - Developments in Clay Science Bergaya, 7:509–53. Elsevier. https://doi.org/https://doi.org/10.1016/B978-0-08-100293-3.00021-2.

Klimkiewicz, R., Edwarda, B. D. (2004). "Catalytic Activity of Carbonaceous Deposits in Zeolite from Halloysite in Alcohol Conversions." Journal of Physics and Chemistry of Solids 65 (2): 459–64. https://doi.org/https://doi.org/10.1016/j.jpcs.2003.09.017.

Mcfarlane, M., Stephan C., Kuhn, J., Cornelis, V., and Frank., E. (2007). "In Situ Rounding of Quartz Grains within an African Surface Weathering Profile in North West Ngamiland, Botswana." Zeitschrift Fur Geomorphologie 51 (September). https://doi.org/10.1127/0372-8854/2007/0051-0269.

Raghdi, A., Heraiz, M., Sahnoune, F., Nouari, S. (2017). "Mullite-Zirconia Composites Prepared from Halloysite Reaction Sintered with Boehmite and Zirconia." Applied Clay Science 146 (September): 70–80. https://doi.org/10.1016/j.clay.2017.05.037.

Saif, M. A., Zefreh, M. M., Torok, A. (2018). "Public Transport Accessibility: A Literature Review." Periodica Polytechnica Transportation Engineering 3 (February). https://doi.org/10.3311/PPtr.12072.

Shi, L., Yu, H. H., Yang, J., Tzumin, L. (2007). "Specific Drosophila Dscam Juxtamembrane Variants Control Dendritic Elaboration and Axonal Arborization." The Journal of Neuroscience : The Official Journal of the Society for Neuroscience 27 (July): 6723–28. https://doi.org/10.1523/JNEUROSCI.1517-07.2007.

Tamsu Selli, N., Aker, I. M., Basaran, N., Kabakci, E. (2021). "Influence of Calcined Halloysite on Technological & Mechanical Properties of Wall Tile Body." Journal of Asian Ceramic Societies 9 (3): 1331–44. https://doi.org/10.1080/21870764.2021.1974762.

Wang, H., Li, B., He, M., Hwang, J.Y. (2017). "Mullitization Characteristics and Sinterability of Kyanite in Ceramic Preparation," February, 251–59. https://doi.org/10.1007/978-3-319-51382-9_28.

Wu, H., Zhang, J., Zhou, Z. (2019). "Effect of Heat Treatment on Structure, Morphology and Surface Properties of Halloysite." IOP Conference Series: Materials Science and Engineering 678 (1): 12111. https://doi.org/10.1088/1757-899x/678/1/012111.

Zanelli, C., Dondi, M., Raimondo, M., Beccaluva, L., Vaccaro, C. (2003). "Phase Transformations Duringliquid Phase Sintering of Porcelain Stoneware Tiles: Apetrological Approach." International Conference on TheScience, Technology and Applications of Sintering.

Zhang, R., Hailong, H., Yang, L., Tan, J., Chen, W, Ying, C., Liu, Q., Fu, X., Hu, S., Wong, C.P. (2020). "Homogeneously Dispersed Composites of Hydroxyapatite Nanorods and Poly(Lactic Acid) and Their Mechanical Properties and Crystallization Behavior." Composites Part A: Applied Science and Manufacturing 132: 105841. https://doi.org/https://doi.org/10.1016/j.compositesa.2020.105841.

Poroz Grafen Kafesler (PGFs): Yüzey Alanı / Hidrojen Depolama İlişkisi Hakkında Hesaplamalı bir Durum Çalışması

Zeynel ÖZTÜRK[1, 2,*]

[1]*Cumhuriyet Universitesi, Mühendislik Fakültesi, Kimya Mühendisliği, Sivas*

[2]*Anadolu Inovasyon ArGe Ltd. Şti. Trabzon Teknokent, Trabzon*

Mail: *zeynelozturk@cumhuriyet.edu.tr, zeynelozturk61@yahoo.com*

Özet: Hidrojenin etkin depolanması için üzerinde çokça çalışmalar gerçekleştirilen adsorpsiyon prensibi ile çalışan yüzey etkileşimli depolama giderek önemini artırmaktadır. Malzeme esaslı yüzey etkileşimli depolama için öne çıkan kafes yapılı malzemelerden popüler olanlardan bir tanesi de Porous Grafen Kafesler (PGF; Porous Graphene Frameworks)'dir. Özellikle yapılarındaki olağan dışı büyüklükteki boşluklar sayesinde hidrojen ve benzeri gazların içerisinde depolanmasında oldukça başarılıdırlar. Bu çalışmada, farklı organik bağlayıcılarla üç farklı PGF yapı teorik olarak oluşturulmuş, geometri optimizasyonu gerçekleştirilmiş, yüzey alanı ve karakteristikleri belirlenmiş ve hidrojen depolama kapasiteleri hesaplanmıştır. Çalışmanın amacı hidrojen depolama kapasitesi ile yüzey karakteristiğinin, yüksek gözenekli yapılar için rutinden saptığının gösterilmesidir. Buna göre beklenenin aksine yüzey alanı değerleri azalmasına rağmen yapıların hidrojen depolama kapasitelerinin arttığı görülmüştür. Bunun sebebi yapıların içerisindeki devasa boşlukların sadece yüzeye tutunma değil, bu boşluklarda sıkıştırma ile depolamanın da gerçekleşmesi olduğu, yüzey alanı yerine boşluk hacminin buna benzer yapılar için daha iyi kıyaslanabilir bir veri olduğu anlaşılmıştır.

Anahtar Kelimeler; PGFs, Poroz Grafen Kafesler, Yüzey Alanı Karakteristiği, Hidrojen Depolama

1. Giriş

Hidrojen ekonomisi, hidrojenin yenilenebilir enerji kaynaklarından üretilerek uygun şekilde depolanıp taşınması ve yüksek verimli bir şekilde ihtiyaç duyulan yerde enerjiye dönüştürülmesi sistemi olarak tanımlanmaktadır [1]. Hidrojen ekonomisi, diğer adıyla hidrojen enerjisi sisteminin en önemli kısımlarından bir tanesi hidrojenin uygun şekilde depolanıp taşınmasıdır. Hidrojen enerjisi sisteminin özellikle mobil sistemlerdeki uygulamalarında, hidrojenin yerinde üretimi önem kazanmaktadır [2]. Yerinde hidrojen üretimi içinse hidrojenin makul boyutlardaki taşıyıcılarda depolanması ve yüksek geri alma oranlarında sisteme beslenebilmesi gerekmektedir. Bunun için hidrojen değişik şekillerde depolanmaktadır. En çok bilinen ve en yaygın hidrojen depolama şekli hidrojenin basınçlı kaplarda sıkıştırılarak depolanmasıdır [3]. Bu yöntem düşük depolama kapasitesi ve büyük konteyner hacmi ile alternatiflerin gelişmesinin önünü açmıştır. Üzerinde en çok çalışmalar yürütülen hidrojen depolama teknikleri, sıvılaştırılmış hidrojen [4] ve katı ortamlarda hidrojenin depolanmasıdır. Katı ortamlarda hidrojen depolanmasında depolayıcılar performanslarıyla ön plana çıkmaktadır. Kimyasal bağlanmayla hidrojeni depolayan metal hidrürler [5]ve yüzey etkileşimli, adsorpsiyon tekniğine dayanan diğer depolayıcılardır [6]–[8]. Adsorpsiyonla hidrojenin depolanması, depolanan hidrojenin neredeyse tamamının geri alınması, yüksek dolum/boşaltım döngüsü, hafif depolayıcılar gibi birçok üstün özelliklere sahiptir [9]. Zeolitler [10], Metal Organik Kafes (Metal Organic

Frameworks; MOFs) yapılı bileşikler [11], karbon bazlı depolayıcılar [12] hidrojen depolayıcıların en bilinenleridir.

Karbon bazlı hidrojen depolayıcılar zaman içerisinde aktif karbon [13], karbon nano-tüpler [14], grafen [15]ve modifiye edilmiş grafen yapılar [16] kullanılarak her geçen gün depolama performanslarını artırmışlardır. Poroz grafen kafesler (Porous Graphene Frameworks; PGFs), temelde grafen tabakaları arası açılarak tabakalar arası modifikasyonla ayrık kalmasının sağlandığı yapılardır [17]. Bu amaçla elde edilen yapılar genellikle mevcut teknoloji ve tekniklerle kolayca elde edilemeyecek periyodik yapılardır. Tylianakis ve arkadaşları [18] grafen tabakaları birbirlerine karbon nanotüplerle bağladıkları süper yapılar hidrojen depolama kapasitesi ve diğer birçok uygulamadaki mükemmel sonuçlara rağmen üretim konusunda oldukça sıkıntılıdır.

Hidrojen depolayıcılar için yaygın intiba, yüksek yüzey alanına sahip yapıların daha fazla hidrojen depolayabildiğidir. Mikro gözenekli hidrojen depolayıcı yapılar için aslında bu fenomen geçerlidir [19]. Ancak yüksek boşluklara sahip PGF gibi yapılar için durum farklılık göstermektedir. Malzeme içerisinde ana yapı arasındaki boşluklar o kadar büyük olabilir ki, bu boşluklarda sıkıştırılmış gaz depolama etkisi gözlemlenebilir [20]. Bundan dolayı yüzey alanı, gözenek boşlukları ile hidrojen depolama kapasitesi arasındaki ilişkinin irdelenmesi gerekmektedir. Bu çalışmada yüksek gözenek boşluklarına sahip birbirine benzer bağlayıcılar kullanılarak elde edilen üç farklı PGF yapılar elde edilmiş ve bu yapıların gözenek/yüzey alanı ve hidrojen depolama kapasiteleri arasındaki ilişki bir teorik durum çalışmasıyla irdelenmiştir.

2. Yürütüm Detayları

Çalışma boyunca kullanılacak olan malzemeler teorik olarak elde edilmiş, yüzey karakteristiği ve hidrojen depolama kapasiteleri hesaplanmıştır. Hesaplama/yürütüm detayları iki başlıkta sunulacaktır. Bunlar; “PGF’lerin oluşturulması ve geometri optimizasyonu” ve “Adsorpsiyon ve yüzey karakteristiği hesapları”dır.

2.1. PGF Oluşturulması ve Geometri Optimizasyonu

Yapılar oluşturulurken deneysel olarak yapılması mümkün tekniklerden esinlenilmiştir. Buna göre grafen tabakalar önce asitle etkileştirilerek aktif merkezler oluşturulabilmesi özelliğinden yararlanılarak karbon aktif merkzeler elde edilmiştir. Daha sonra bu merkezler Şekil 1’de gösterilen Benzene-1,3,5-tricarboxylic acid (BTC), 4,40,400- Benzene-1,3,5-triyltribenzoate (BTB) and 4,40,400-(benzene-1,3,5triyl-tris (benzene-4,1-diyl))tribenzoate (BBC) yapılarla birbirlerine bağlanmışlardır.

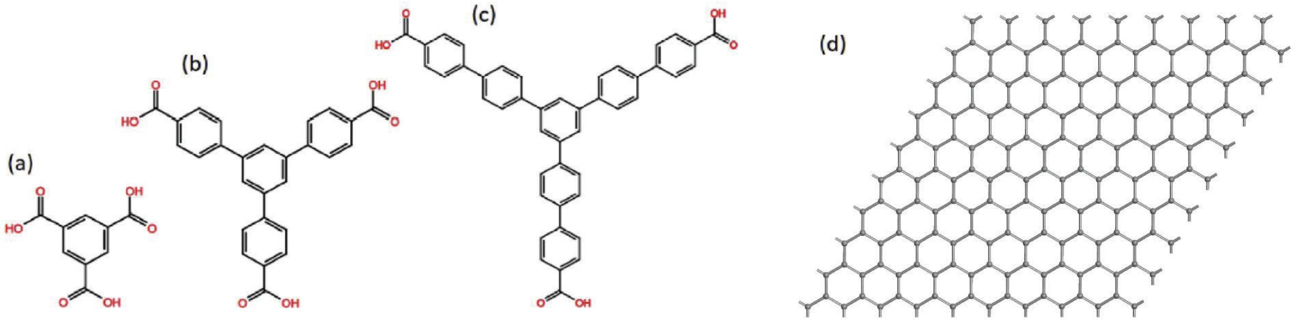

Şekil 1. Grafen tabakaları birbirine bağlamak için kullanılan (a) BTC, (b) BTB (c) BBC organik bağlayıcılarının ve (d) grafen tabakasının atomik yapıları.

Elde edilen yapıların gerçekte olması gerektiği haliyle elde edilebilmesi için geometri optimizasyonu yürütümleri gerçekleştirilmiştir. Bu yürütümler esas olarak yapının en düşük enerjili formda bulunması üzerine çalışmaktadır. Bunun için çokça uygulanan quasi-Newton [21] metodu ABNR [22]algoritması kullanılmıştır. Geometri optimizasyonu set edilen yakınsama değerine kadar devam eden iterasyonlardan oluşmaktadır ve bunu için belirli serbestlik derecesine göre atomların ve/veya grupların pozisyonlarını birim kafes içerisinde değiştirerek toplam enerji hesaplanmaktadır. Yakınsama değerleri toplam enerji değişimi için 10-4 kcal/mol, kuvvet için 0,005 kcal/mol/ Å ve yer değiştirme için 5*10-5 Å olarak kullanılmıştır.

2.2. Adsorpsiyon ve Yüzey Karakteristiği Hesapları

Adsorpsiyon çalışmaları, hidrojen ve azot adsorpsiyonu, Grand Canonical Monte Carlo (GCMC) [23]simülasyon algoritmaları yardımıyla hesaplanmıştır. Buna yöntem; hidrojen veya azot molekülleri oluşturulan yapı içerisinde rastgele dağıtılarak toplam entalpi hesaplanması ve bu moleküllerin pozisyonlarının değiştirilerek minimumum aranması prensibine göre çalışır. GCMC algoritması yapı içerisindeki atomlar arası etkileşimleri hesaba katmak için Force-Field parametreleri kullanılır. Lennard Jones (LJ) 12-6 parametreleri denilen ve aşağıdaki temel eşitliğe göre belirlenen atomlar arası itme/çekme kuvvetleri ile hesaplamalar gerçekleştirilir [24].

$$U_{ij} = 4\varepsilon_{ij}\left[\left(\frac{\sigma_{ij}}{r_{ij}}\right)^{12} - \left(\frac{\sigma_{ij}}{r_{ij}}\right)^{6}\right]$$

i ve j ikilileri için (seçili iki atom); U etkileşim enerjisi, ⍰ potansiyeller ve r uzaklık parametreleridir. LJ parametreleri kullanılarak oluşturulmuş en yaygın kullanıma sahip force-field Rappe ve arkadaşları [25] tarafından hazırlanan Universal Force Field (UFF)'dir. Ancak adsorpsiyon hesaplamalarının yapılacağı 77K gibi düşük sıcaklıklar için etkin değildir. Bundan dolayı düşük sıcaklık quntum etkilerinin de hesaba katıldığı yeni parametreler için UFF modifiye edilmiştir[24], [26], [27]. Daha sonra modifiye edilmiş UFF kullanılarak, 77K sıcaklık ve 1-10000 KPa basınç aralığında 20 dengeleme basıncı için azot ve hidrojen moleküllerinin birim hücrede bulunabileceği miktarlar hesaplanmı, diğer deyişle adsorpsiyon kapasiteleri veya izotermleri oluşturulmuştur. Hesaplamalar neticesinde elde edilen birim hücre için adsorplanan molekül sayıları birim hücre yoğunluk ve hacmi kullanılarak daha anlaşılır olan kütlece %, ml/g birimlerine dönüştürülmüştür.

Ayrıca atomların van der Waals (vdW) yarıçapları kullanılarak vdW yüzeyleri, çözücü vdW yarıçapları kullanılarak çözücü yüzey alanları görselleştirilmiş ve değerleri hesaplanmıştır. Şekil 2'de vdW ve çözücü yüzey alanlarının nasıl oluşturulduğu hakkında bir görsel verilmiştir [28].

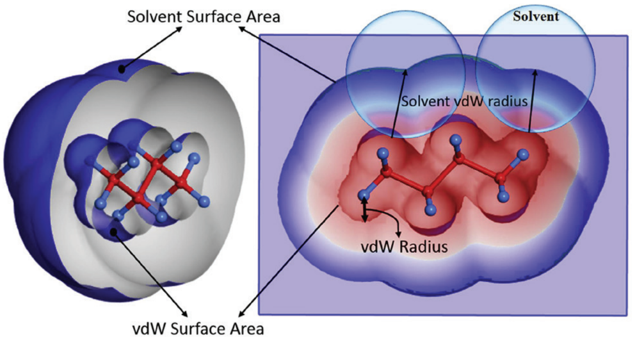

Şekil 2. Çözücü ve vdW yüzeylerinin nasıl oluştuğunun gösterimi.

Şekil 2'ye göre van der Waals yüzeyler ve vdW çözücü yüzey alanları birim hücreler için belirlenmiştir. Burada azot ve hidrojen için çözücü yüzey alanları hesaplanmıştır. Hesaplamalarda azot vdW yarı çapı 2,25 Å ve 1,2 Å olarak kullanılmıştır.

Son olarak adsorpsiyon izotermleri adsorpsiyon datası kullanılarak yüzey alanı ve por çapı alan hacim dağılımı hesaplamaları gerçekleştirilmiştir. L-curve ve eşleşme hata değerleri uygun olacak şekilde seçilerek kümülatif yüzey alanı, kümülatif por hacmi, por hacmi dağılımı (Por Volume Distribution; PVD; dV/dw) ve yüzey alanı dağılımı (Por Size Distribution; PSD; dS/dw) grafikleri elde edilmiştir. Son olarak, yüzey alanı, gözeneklilik ve por hacimleri ile hidrojen depolama arasındaki ilişkiyi irdeleyebilmek için, oluşturulan PGF'lerin 77 K ve 298 K sıcaklıklardaki hidrojen depolama kapasiteleri hesaplanıp grafiğe geçirilmiştir.

3. Sonuçlar

Elde edilen sonuçlar literatürle kıyaslanabilir ve daha anlaşılabilir olması adına daha bilinen birimlere çevrilerek hesaplamalar neticelendirilmiştir. Sonuç olarak oluşturulan PGF yapıların geometri optimiasyonları gerçekleştirilmiş ve azot-hidrojen adsorpsiyon izotermleri elde edilerek hesaplamalara tamamlanmıştır. Tüm sonuçlar iki alt başlık altında irdelenmiştir. Birincisi yapısal sonuçlar ve ikincisi yüzey karakteristiği ve hidrojen depolamadır.

3.1. Yapısal

Geometri optimizasyonu yürütümleri neticesinde yakınsama değerlerine erişen yapılar elde edilmiştir. Diğer deyişle oluşturulan yapıların geometrileri (kristal kafes yapıları) optimize edilmiştir. Bu yürütümler neticesinde elde edilen üç farklı yapı için geometri optimizasyonun takibi toplam enerji, birim hücre uzunluk ve açı değerlerinin optimizasyon adımlarındaki değişimi ile takip edilmiştir. Şekil 3'de BTC, BTB ve BBC kodlu PGF yapıların ilgili parametrelerinin optimizasyon adımlarındaki değişimi verilmiştir.

Grafen - BTC

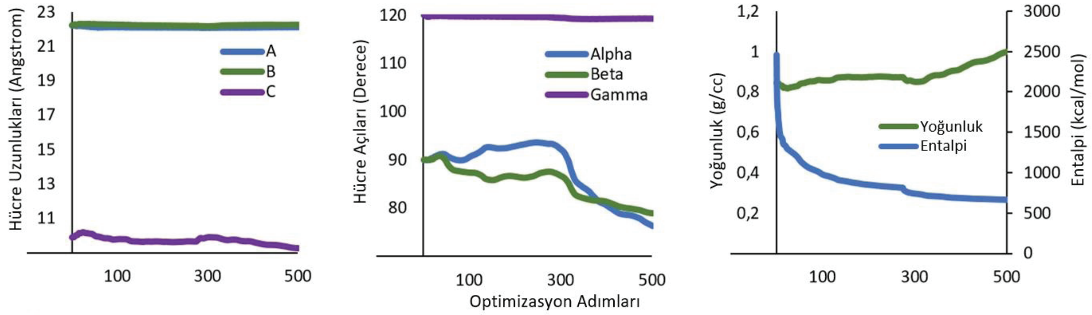

Grafen - BTB

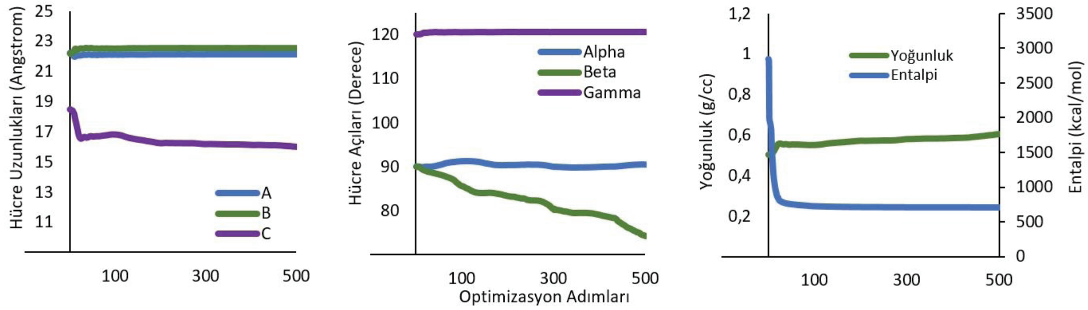

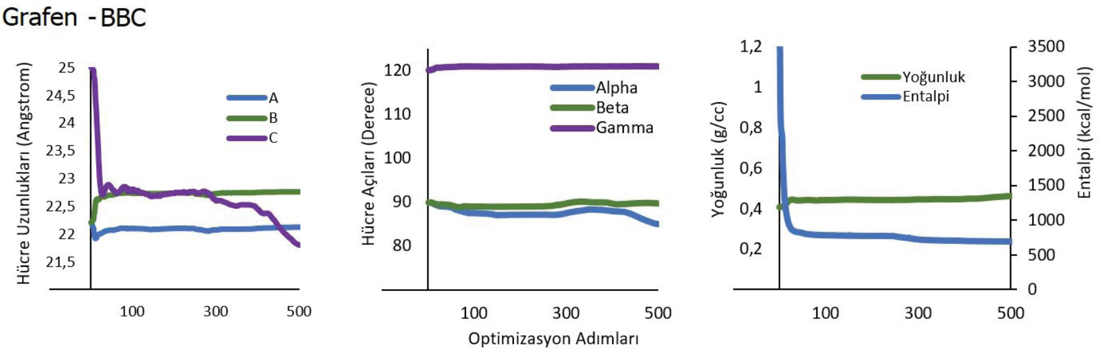

Şekil 3. Elde edilen yapıların geometri optimizasyonu adımlarındaki birim hücre parametrelerinin değişimi grafikleri.

Şekil 3'teki grafiklerde öncelikle enerji değişiminin yatay seyrettiği gözlemlenmiştir. Bu durum enerji minimizasyonu yani yakınsamanın gerçekleştirği, diğer deyişle geometrilerin optimize edildiği anlamına gelmektedir. Hücre parametrelerinden a, b ve c uzunlukları bu doğrultuda yenilenmiş, hücre açıları değiştirilmiş ve bunun neticesinde yoğunluk değişimleri gerçekleşmiştir. Elde edilen yeni hücre parametrelerine göre geometri optimizasyonu yapılmış PGF yapıların yoğunlukları BTC, BTB ve BBC kodlu yapılar için sırasıyla 0,99682, 060587 ve 0,46259 g/ml olarak bulunmuştur.

Geometri optimizasyonu gerçekleştirilmiş yapıların son görüntüleri Şekil 4'te verilmiştir. Üç boyutlu görselden anlaşılacağı ve grafen tabakalar arasında kullanılan bağlayıcıların moleküler yapıların farklılıklarından kaynaklı beklendiği üzere BBC yapısı en büyük grafen tabakası açıklığına sahipken, en düşük grafen tabakası arası açıklık BTC kodlu PGF için elde edilmiştir. Grafen tabakaları arası açıklıklar BTC, BTB ve BBC için sırasıyla 9,24, 16,02 ve 21,80 Å olarak ölçülmüştür.

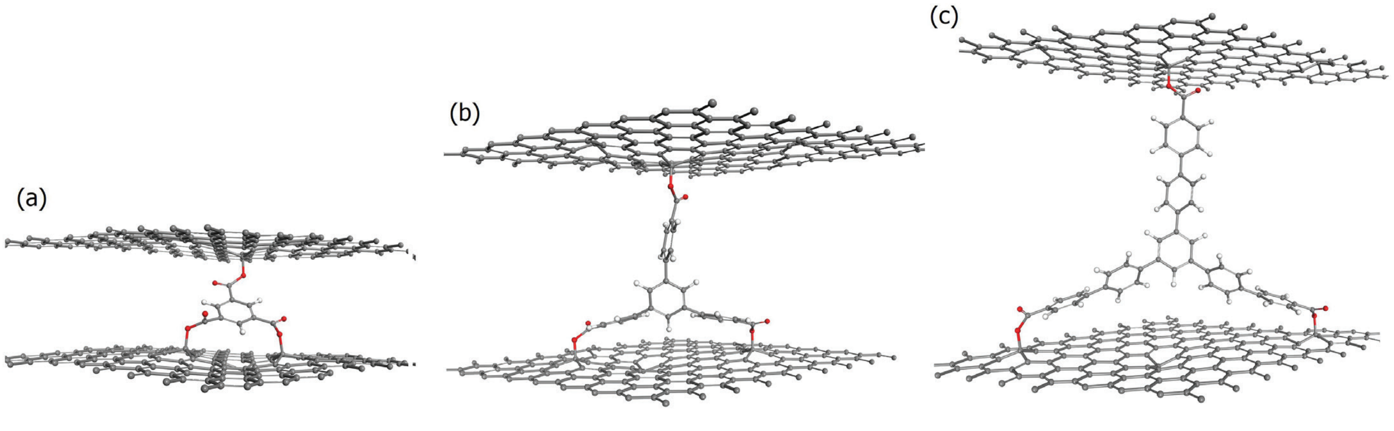

Şekil 4. Geometri optimizasyonu yapıldıktan sonra elde edilen yapıların üç boyutlu uzay gösterimleri (a) BTC, (b) BTB ve (c) BBC

3.2. Yüzey Karakteristiği ve Hidrojen Depolama

PGF yapıların birim hücrelerinin azot vdW yarı çapları kullanılarak oluşturulan çözücü yüzey alanları Şekil 5'te verilmiştir. Beklendiği üzere en yüksek birim hücre yüzey alanı BBC kodlu PGF yapı için oluşmuştur. Ancak düşük yoğunluğu nedeniyle, birim ağırlık başına hesaplanan yüzey alanı değerleri tüm PGF yapılar için birbirlerine yakın değerler olarak hesaplanmıştır.

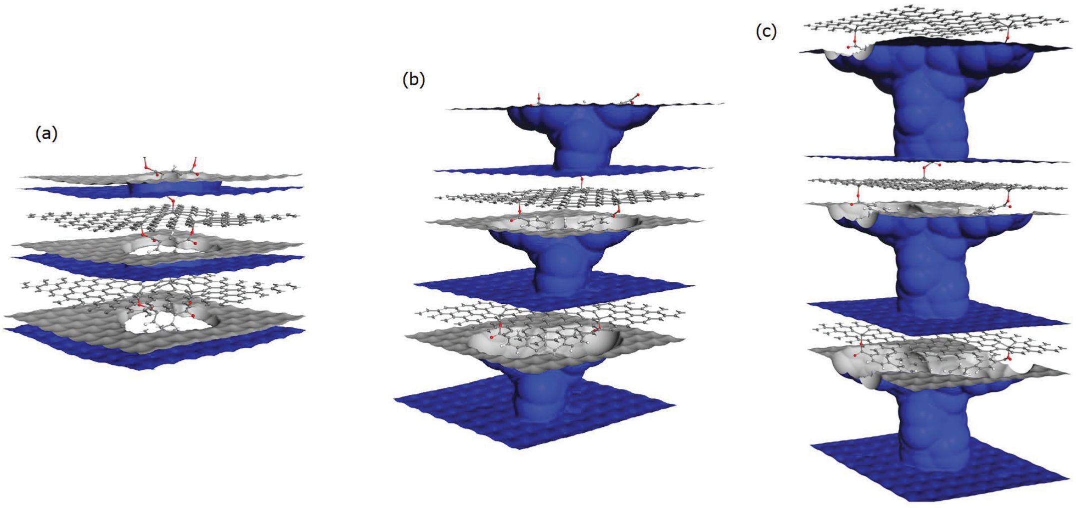

Şekil 5. (a) BTC, (b) BTB ve (c) BBC kodlu PGF yapıların birim hücrelerinde azot vdW yarıçapı kullanılarak oluşturulan yüzeyler.

Hesaplanan birim hücre yüzey alanları BTC, BTB ve BBC kodlu PGF'ler için sırasıyla 608,95, 1534,93 ve 1805,53 Å2'dir. Bu yüzey alanları ve birim hücrelerin yoğunlukları kullanılarak hesaplanan m^2/g cinsinden yüzey alanı değerleri aynı sıralamaya göre 1689,9, 1425,02 ve 891,39 m^2/g olduğu belirlenmiştir.

Şekil 6'da BBC kodlu PGF yapının (a) azot molekülü vdW yapı çapı kullanılarak oluşturulan yüzey alanı (mavi yüzeyler) ve yapının kendi atomlarının vdW yarıçapları kullanılarak oluşturulan yüzeyler (turkuaz) gösterilmiştir. Aynı şekilde (b) hidrojen vdW yarı çapı kullanılarak oluşturulan yüzey (kırmızı) ile azot azot molekülünün erişebileceği yüzeyler (mavi noktolar) gösterilmiştir. Buna göre yapıların kendi vdW yüzeyleri, hidrojenlerin ve azotların erişebileceği yüzeylerin farklı olduğu gösterilmiştir.

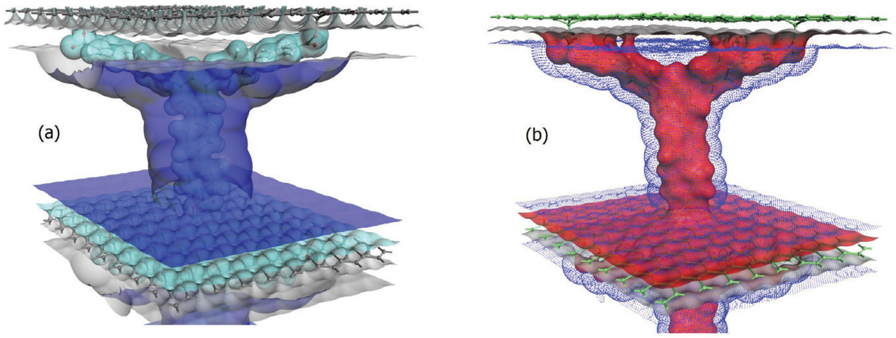

Şekil 6. BBC kodlu PGF'nin (a) gövde vdW yüzeyleri (turkuaz) ve azot vdW yarı çapına göre oluşturulmuş yüzeyleri (mavi), (b) hidrojenlerin erişebileceği yüzeyler (kırmızı) ve azotların erişebileceği yüzeyler (mavi nokta).

BBC kodlu PGF yapının vdWyüzeyleri (Şekil 6.a. turkuaz yüzey), 1,2 Å vdW yarıçapındaki çözücü, hidrojen için (Şekil 6.b. kırmızı yüzey) yüzey alanı ve 2,25 vdW yarıçapı çözücü (azot, Şekil 6.a. mavi yüzey) yüzey alanları sırasıyla 2012,15, 1912,15 ve 1805,53 Å2 olduğu hesaplanmıştır. Aynı yapının birim hücre gözenek boşlukları yine aynı sıraya göre 9012,15, 8876,75 ve 8056,78 Å3'tür.

GCMC ile elde edilen PGF yapıların birim hücrede depolanan azot miktarı verisi ml/g cinsinden farklı basınçlardaki değerler olarak, adsorpsiyon izotermi olarak Şekil 7'de verilmiştir. Bu hesaplamaya göre BBC kodlu PGF yapının diğerlerine göre daha fazla azot adsorpladığı çok net bir şekilde görülmektedir.

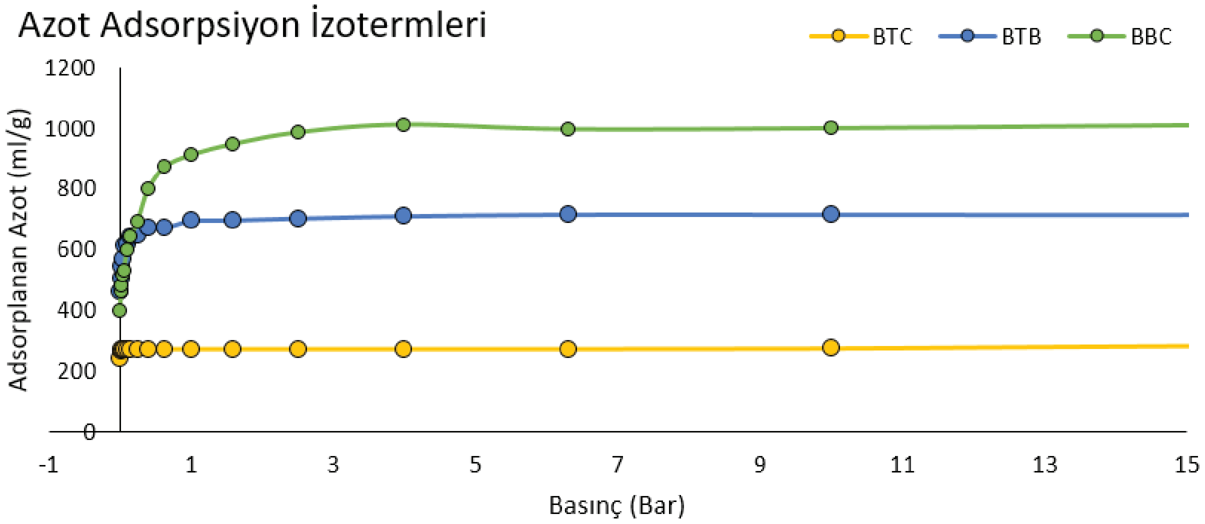

Şekil 7. PGF yapıların GCMC ile hesaplanan azot adsorpsiyonu izotermleri

Azot adsorpsiyonu izoterm verileri kullanılarak kümülatif por hacmi ve yüzey alanı verileri elde edilmiş ve Şekil 8'de grafiğe geçirilmiştir. Buna göre birim ağırlık başına toplam por hacmi en fazla olan yapı 1,42 ml/g ile BBC kodlu PGF'dir. Diğer yapılar BTC ve BTB sırasıyla 0,448 ve 0,9965 ml/g'dır. Birim ağırlıktaki toplam yüzey alanları ise BTC, BTB ve BBC için sırasıyla 1688,60, 1668,39 ve 1590,95 m2/g olarak hesaplanmıştır.

Şekil 8'de verilen por hacmi dağılımı beklendiği üzere yüzey alanı dağılımları ile benzerlik göstermektedir. BTC kodlu PGF için yaklaşık 6 Å çaplı gözeneklerin miktarı 0,25 ml/g ve az miktarda (yaklaşık 0,025 ml/g) yaklaşık 12 Å çaplı gözenekler bulunmaktadır. BTB ve BBC kodlu yapılar için yaklaşık 11 Å çaplı gözeneklerin daha fazla miktarda olduğu görülmektedir. Özellikle BBC kodlu yapının gözenek dağılımına bakıldığında farklı çaplarda gözenekliliğin olduğu görülmektedir.

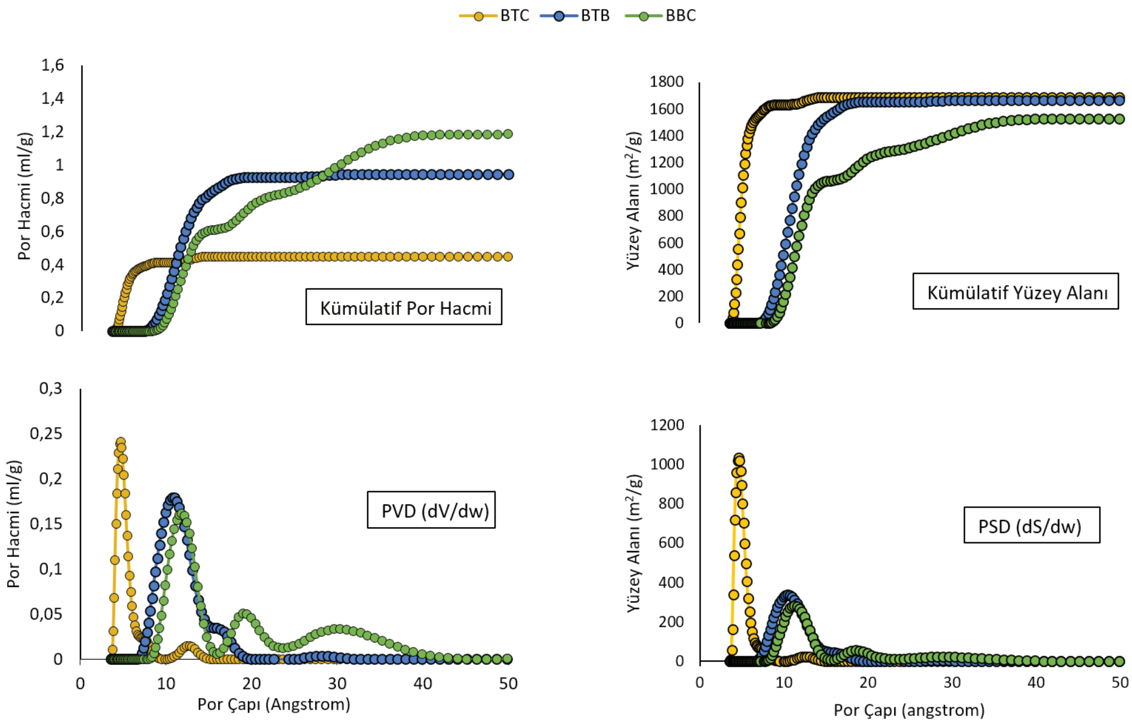

Şekil 8. Azot adsorpsiyonu verileri kullanılarak hesaplanan yüzey alanı ve gözenek hacimleri

Şekil 9'da hidrojen adsorpsiyonu izotermleri verilmiştir. Beklendiği üzere 77 K sıcaklıkta daha yüksek hidrojen depolama değeri görülmektedir. En fazla hidrojen depolama değeri kütlece yaklaşık % 20 ile BBC kodlu PGF yapı için hesaplanmıştır. Devamında sırasıyla BTB ve BTC için aynı sıcaklıkta yaklaşık kütlece % 15 ve kütlece % 8 civarında hidrojen depolandığı hesaplanmıştır. 298 K sıcaklık için yapılan yürütümler neticesinde yapılar arasında belirgin farklılık görülmemiştir.

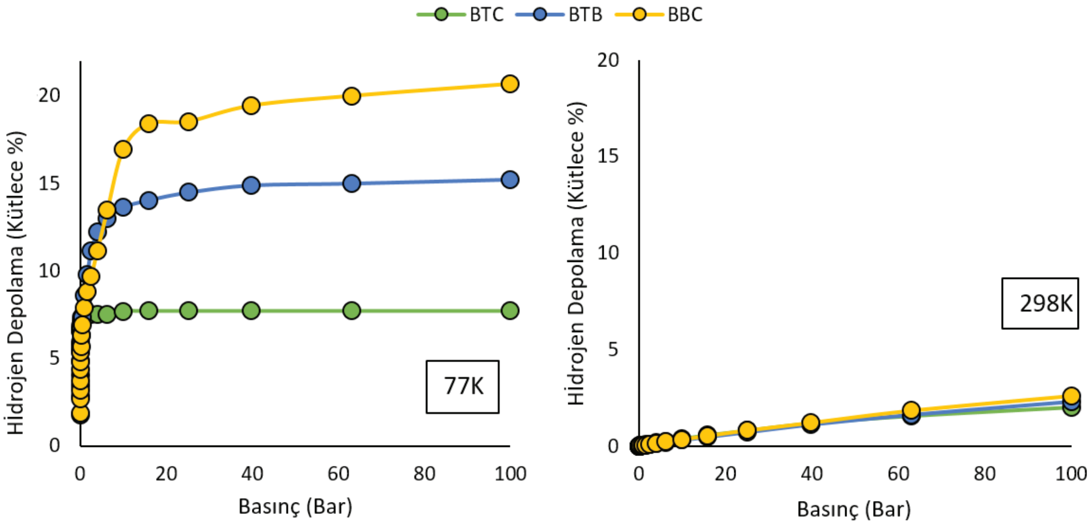

Şekil 9. Hidrojen adsorpsiyonu verileri kullanılarak oluşturulan hidrojen depolama izotermleri

4. Tartışma ve Sonuç

Tüm bulgular birlikte değerlendirildiğinde gözekliliğin hidrojen depolama üzerindeki etkisi ön plana çıkmaktadır. Öyle ki gözenekli adsorbanlar için hesaplanan m2/g cinsinden yüzey alanı büyük gözeklere sahip yapılar için çok doğru bir kıyas birimi olmaktan uzak görünmektedir. Genel intiba yüksek yüzey alanına sahip malzemelerin daha fazla hidrojen depolayacağı yönündedir. Wang ve Yang [29] yaptıkları çalışmada TC-EMC-1 ve TC-EMC-2 kodlu yapıların yüzey alanları sırasıyla 3798 ve 3512 m2/g, hidrojen depolama değerlerini ise aynı sıraya göre yaklaşık kütlece % 0,8 ve 0,7 olarak ölçmüşlerdir. Burada artan yüzey alanı hidrojen depolama performansında artış olarak görülmektedir. Benzer durum başka birçok çalışmada görülmektedir [28], [30], [31]. Ancak bu durum çok büyük gözenek hacmine sahip olmayan, genellikle mikro gözenekli yapılar için geçerlidir. Bu çalışmada irdelenen PGF ve benzeri yapılar henüz pratikte uygulanabilir/üretilebilir olmadığından sık rastlanılan yüzey alanı/hidrojen depolama kapasitesi incelemesi çalışmaları değillerdir. Dolayısı ile genel kanıdan sapan yapılar olarak karşımıza çıkmaktadır. Yine de gelişen teknoloji ile üretilip adından söz ettirir hale geleceklerdir. Böylece, hidrojen depolama kapasitesinden bahsedilirken birim ağırlık başına yüzey alanı (m2/g) cinsinden değil gözenek hacmi veya birim hücre yüzey alanı verileri ile değerlendirmek doğru olacaktır.

Yapıların içerisindeki boşluklarda/gözeneklerde depolanan hidrojenin yüzeye tutunan haricinde aynı zamanda kompresyonla da depolama özelliği gösterdiği anlaşılmaktadır. Öyle ki, Şekil 5 ve 6'da gösterilen mavi (kırmızı) yüzeyler hidrojenin yerleşeceği, diğer deyişle adsorplanacağı yüzeylerdir. Bundan sonra artan basınçla malzeme içerisine gönderilen gazlar, tutunan hidrojen tabakasının üzerine ikincil tabakalar ve devamında kompresyonla depolanan yerler olacağı aşikârdır.

Bu çalışmada elde edilen sonuç, standart hesaba göre daha düşük yüzey alanına sahip yapıların yüksek gözeneklilik ve düşük yoğunlukları sayesinde daha fazla hidrojen depolayabileceğidir. Diğer bir sonuç ise hidrojen depolama amacıyla hesaplamalar veya deneysel ölçümler yapılırken azot adsorpsiyonu izotermleri kullanılarak elde edilen yüzey alanı değerinin hedeflenen bilgiyi tam olarak temsil etmediğidir. Keza, Şekil 6'da gösterilen kırmızı yüzeyler (hidrojenlerin dolabileceği yüzeyler) ile mavi noktalı yüzeyler (azot moleküllerinin dolabileceği yüzeyler) arasında anlamlı farklılık vardır. Son olarak, mikro gözenekten büyük gözeneklere sahip yapılar grafen, modifiye edilmiş grafen ve çok özel şartlarda üretilen karbon yapılar, çok yüksek gözenekliliğe sahip MOF'lar için m2/g cinsinden yüzey alanı yerine kıyas parametresi olarak ya gaz depolama izotermleri ya da gözenek hacimlerini gösterir verilerin kullanılmasının daha doğru olacağı anlaşılmaktadır.

Referanslar

[1] G. W. Crabtree, M. S. Dresselhaus, and M. v. Buchanan, "The hydrogen economy," Physics Today. 2004. doi: 10.1063/1.1878333.

[2] J. O. Abe, A. P. I. Popoola, E. Ajenifuja, and O. M. Popoola, "Hydrogen energy, economy and storage: Review and recommendation," International Journal of Hydrogen Energy, vol. 44, no. 29, pp. 15072–15086, Jun. 2019, doi: 10.1016/J.IJHYDENE.2019.04.068.

[3] T. Q. Hua et al., "Technical assessment of compressed hydrogen storage tank systems for automotive applications," International Journal of Hydrogen Energy, 2011, doi: 10.1016/j.ijhydene.2010.11.090.

[4] A. Züttel, “Materials for hydrogen storage,” Materials Today, vol. 6, no. 9, pp. 24–33, Sep. 2003, doi: 10.1016/S1369-7021(03)00922-2.

[5] A. C. M. Oliveira and A. C. Pavão, “Theoretical study of hydrogen storage in metal hydrides,” Journal of Molecular Modeling, 2018, doi: 10.1007/s00894-018-3661-4.

[6] G. Turnes Palomino, M. R. Llop Carayol, and C. Otero Are?n, “Hydrogen adsorption on magnesium-exchanged zeolites,” Journal of Materials Chemistry, vol. 16, no. 28, p. 2884, Jul. 2006, doi: 10.1039/b607261e.

[7] F. D. Lamari and D. Levesque, “Hydrogen adsorption on functionalized graphene,” Carbon N Y, 2011, doi: 10.1016/j.carbon.2011.07.036.

[8] H. W. Langmi et al., “Hydrogen adsorption in zeolites A, X, Y and RHO,” Journal of Alloys and Compounds, vol. 356–357, pp. 710–715, Aug. 2003, doi: 10.1016/S0925-8388(03)00368-2.

[9] K. M. Thomas, “Hydrogen adsorption and storage on porous materials,” Catalysis Today, vol. 120, no. 3–4, pp. 389–398, Feb. 2007, doi: 10.1016/J.CATTOD.2006.09.015.

[10] Y. Li and R. T. Yang, “Hydrogen storage in low silica type X zeolites.,” J Phys Chem B, vol. 110, no. 34, pp. 17175–81, Aug. 2006, doi: 10.1021/jp0634508.

[11] Z. Ozturk, D. A. Kose, Z. S. Sahin, G. Ozkan, and A. Asan, “Novel 2D micro-porous Metal-Organic Framework for hydrogen storage,” International Journal of Hydrogen Energy, vol. 41, no. 28, 2016, doi: 10.1016/j.ijhydene.2016.05.170.

[12] L. Wang and R. T. Yang, “Hydrogen Storage on Carbon-Based Adsorbents and Storage at Ambient Temperature by Hydrogen Spillover,” Catalysis Reviews, vol. 52, no. 4, pp. 411–461, Oct. 2010, doi: 10.1080/01614940.2010.520265.

[13] G. Sethia and A. Sayari, “Activated carbon with optimum pore size distribution for hydrogen storage,” Carbon N Y, vol. 99, pp. 289–294, Apr. 2016, doi: 10.1016/j.carbon.2015.12.032.

[14] J. Lu, H. Xiao, and J. Cao, “Mechanism for high hydrogen storage capacity on metal-coated carbon nanotubes: A first principle analysis,” Journal of Solid State Chemistry, 2012, doi: 10.1016/j.jssc.2012.06.034.

[15] C. H. Chen et al., “Hydrogen storage performance in palladium-doped graphene/carbon composites,” International Journal of Hydrogen Energy, 2013, doi: 10.1016/j.ijhydene.2013.01.070.

[16] Z. Ozturk, C. Baykasoglu, and M. Kirca, “Sandwiched graphene-fullerene composite: A novel 3-D nanostructured material for hydrogen storage,” International Journal of Hydrogen Energy, vol. 41, no. 15, 2016, doi: 10.1016/j.ijhydene.2016.03.042.

[17] C. da Wu, T. H. Fang, and J. Y. Lo, “Effects of pressure, temperature, and geometric structure of pillared graphene on hydrogen storage capacity,” International Journal of Hydrogen Energy, 2012, doi: 10.1016/j.ijhydene.2012.07.040.

[18] G. K. Dimitrakakis, E. Tylianakis, and G. E. Froudakis, “Pillared graphene: a new 3-D network nanostructure for enhanced hydrogen storage,” Nano Letters, 2008, doi: 10.1021/nl801417w.

[19] J. Cai, L. Li, X. Lv, C. Yang, and X. Zhao, “Large surface area ordered porous carbons via nanocasting zeolite 10X and high performance for hydrogen storage application.,” ACS Appl Mater Interfaces, vol. 6, no. 1, pp. 167–75, Jan. 2014, doi: 10.1021/am403810j.

[20] Z. Öztürk, “Lithium decoration characteristics for hydrogen storage enhancement in novel periodic porous graphene frameworks,” International Journal of Hydrogen Energy, 2021, doi: 10.1016/j.ijhydene.2021.01.073.

[21] B. G. Pfrommer, M. Côté, S. G. Louie, and M. L. Cohen, “Relaxation of Crystals with the Quasi-Newton Method,” Journal of Computational Physics, 1997, doi: 10.1006/jcph.1996.5612.

[22] B. R. Brooks, R. E. Bruccoleri, B. D. Olafson, D. J. States, S. Swaminathan, and M. Karplus, “CHARMM: A program for macromolecular energy, minimization, and dynamics calculations,” Journal of Computational Chemistry, 1983, doi: 10.1002/jcc.540040211.

[23] D. J. Adams, “Grand canonical ensemble monte carlo for a lennard-jones fluid,” Molecular Physics, 1975, doi: 10.1080/00268977500100221.

[24] C. Baykasoglu, Z. Ozturk, M. Kirca, A. T. Celebi, A. Mugan, and A. C. To, “Effects of lithium doping on hydrogen storage properties of heat welded random CNT network structures,” International Journal of Hydrogen Energy, vol. 41, no. 19, 2016, doi: 10.1016/j.ijhydene.2015.11.182.

[25] A. K. Rappe, C. J. Casewit, K. S. Colwell, W. A. Goddard, and W. M. Skiff, “UFF, a full periodic table force field for molecular mechanics and molecular dynamics simulations,” J Am Chem Soc, vol. 114, no. 25, pp. 10024–10035, Dec. 1992, doi: 10.1021/ja00051a040.

[26] J. P. Bouanich, “Site-site Lennard-Jones potential parameters for N2, O2, H2, CO and CO2,” Journal of Quantitative Spectroscopy and Radiative Transfer, 1992, doi: 10.1016/0022-4073(92)90142-Q.

[27] N. Yu and A. A. Polycarpou, “Adhesive contact based on the Lennard-Jones potential: A correction to the value of the equilibrium distance as used in the potential,” Journal of Colloid and Interface Science, 2004, doi: 10.1016/j.jcis.2004.06.029.

[28] Z. Ozturk, “Hydrogen storage on lithium modified silica based CHAbazite type zeolite, A computational study,” International Journal of Hydrogen Energy, vol. 43, no. 49, 2018, doi: 10.1016/j.ijhydene.2018.10.056.

[29] L. Wang and R. T. Yang, “Molecular hydrogen and spiltover hydrogen storage on high surface area carbon sorbents,” Carbon N Y, vol. 50, no. 9, pp. 3134–3140, Aug. 2012, doi: 10.1016/J.CARBON.2011.09.049.

[30] Z. Ozturk, “The effect of surface area and dopant percentage on hydrogen storage of Pt@ac loaded activated carbon and Cu-BTC composites,” International Journal of Renewable Energy Research, vol. 6, no. 3, 2016.

[31] Z. Ozturk, D. A. Kose, A. Asan, B. Ozturk, O. Andac, and G. Ozkan, “Hydrogen storage properties of mono- and bidentate MOF structured orotate complexes,” Journal of Materials Research, vol. 29, no. 02, pp. 215–220, Jan. 2014, doi: 10.1557/jmr.2013.357.

Synthesis and Characterization of Flexible Butadien Containing Resin for 3D SLA Printers

Emre AKIN1[*], Mustafa ÇAKIR[1], Boran BERBEROĞLU[1]

[1]*Marmara University, Turkeyn*

As well known, epoxy acrylate resins have been widely used in 3D SLA printers applications. Epoxy acrylate system consisted of bisphenol-A glycerolate diacrylate (epoxy acrylate resin) and 1,6-Hexanediol diacrylate (HDDA, reactive diluent resin) were used in this study. The weight ratio of epoxy acrylate and HDDA was determined as 1/1. The purpose of this study is to develop a novel epoxy acrylate system for 3D SLA printers and observe its properties. For this reason, a novel urethane acrylate was synthesized as reactive resin and was added into epoxy acrylate system with various weight percents. In order to obtain this novel urethane acrylate resin, hydroxyl terminated butadien oligomer was used as backbone of the chain while isophorone diisocyanate (IPDI) and 2-Hydroxyethyl methacrylate (HEMA) were used for synthesizing urethane acrylate functional groups. The addition of this novel reactive resin was carried out up to 1.5 %. Mechanical and physical tests were applied to the produced samples such as tensile, Shore-D hardness, abrasive and density tests. Considering of the results, substantial increases were observed in terms of tensile modulus. As expected, tensile strain values presented large decreases. Shore-D hardness and densities presented slight increases. Moreover, taber abrasive resistances of the produced novel samples presented considerable increases.

1.Introduction

Currently, ultraviolet (UV)-curable products have received great interest due to both technological advances and the increasing environmental pressure to decrease the emission of volatile organic compounds (VOC) [1,2]. In comparison with conventional solvent-based products, UV-curable products present the advantage of low VOC emission, rapid curing at ambient temperature, low energy consumption, high productivity and high degrees of cross-linking (cause to outstanding scratch, chemical resistance). Therefore, these products provide a wide range of economic and ecological benefits. UV-curable coatings usually contain four main components the oligomer, the reactive diluent, the photoinitiator and various additives. Epoxy acrylate (EA) is a common oligomer in UV-curable coatings, which is the most principal component for film formation [3,4]. There have been two kinds of epoxy acrylate oligomers that have been widely used. These are bisphenol diglycidyl ether and epoxy novolac based epoxy acrylate oligomers. As reactive diluents, hexanediol diacrylate (HDDA) and tripropylene glycol diacrylate (TPGDA) have been generally used in epoxy acrylate systems. These reactive diluents dissolve pure epoxy acrylate resin, adjust the viscosity and crosslinking density of epoxy acrylate systems [3,5].

In this study, a novel reactive diluent was used. This reactive diluent was polybutadien. This butadien chain was acrylated with isophorone diisocyanate (IPDI) and 2-Hydroxyethyl methacrylate (HEMA). IPDI is diisocyanate having aromatic rings. Therefore, this reactive diluent would have both flexible aliphatic groups due to flexible butadiens and have rigid aromatic groups due to IPDI monomers. It was expected that this novel acrylated polybutadien would gain new properties to conventional epoxy acrylate system. In this study, conventional epoxy acrylate system consisted of bisphenol-A glycerolate diacrylate (epoxy acrylate resin) and 1,6-Hexanediol diacrylate (HDDA, reactive diluent resin) were used. The weight ratio of epoxy acrylate and HDDA was determined as 1/1. The synthesized novel polybutadien reactive diluent resin was incorporated into this conventional epoxy acrylate system in various ratios. By using these novel reactive diluent novel, novel epoxy acrylate systems were obtained. The addition of this novel reactive resin was carried out up to 1.5 %. Mechanical and physical tests were applied to the produced samples such as tensile, shore-D hardness, abrasive and density tests. Considering of the results, substantial increases were observed in terms of tensile modulus. As expected, tensile strain values presented large decreases. Shore-D hardness and densities presented slight increases. Moreover, taber abrasive resistances of the produced novel samples presented considerable increases.

2.1 Materials

Bisphenol A glicerolate diacrylate (Bisphenol A based epoxy acrylate oligomer) and 1,6-Hexanediol diacrylate (HDDA) were purchased from Sigma-Aldrich. Isophorone diisocyanate (IPDI) was used as aromatic diisocyanate that purchased from Covestro, 2-Hydroxymethyl methacrylate (HEMA) was used to acrylate IPDI and this functional monomer terminated hydroxyl terminated liquid polybutadien. This commercial name of this polybutadien is Polyvest-HT that purchased from Evonik. Irgacure 819 was used as photoinitiator. Dibutyltin dilaurate (T12) was used as catalyst for synthesis of a novel acrylated polybutadien. Tetrahidrofuran (THF) was used as solvent.

2.2. Preparation of conventional epoxy acrylate system

Conventional epoxy acrylate system was prepared by using bisphenol A glicerolate diacrylate and 1,6-Hexanediol diacrylate (HDDA) reactive diluent resin. These components were used as 1/1 by weight. They were mechanically stirred in flask and homogeneo**us resin was obtained.**

2. Material and Methods

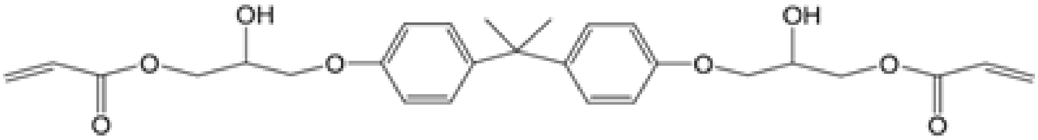

Figure 1. Bisphenol A diglycidyl ether based epoxy acrylate

These components were shown in Figure 1 and Figure 2.

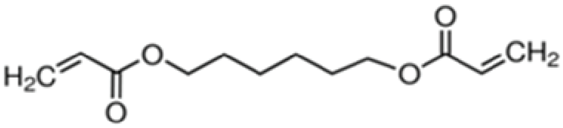

Figure 2. 1,6 Hexanediol diacrylate

ISBN: 978-975-7616-84-9

2.3. Synthesis of novel polybutadien reactive diluent resin

HEMA was added in a flask and THF was poured into the flask. HEMA in THF were magnetically stirred. After disolving, the diisocyanate (IPDI) was added into the flask drop by drop. Then, the tin catalyst (T12) was added and stirred magnetically at 60 oC in a nitrogen atmosphere for two hours. The diisocyanate was reacted with HEMA. The mole ratio was adjusted to 1/1. Therefore one isocyanate molecule of IPDI converted urethane group and a novel monomer was obtained. This novel monomer contained one isocyanate and acrylate functional groups as shown in Figure 3.

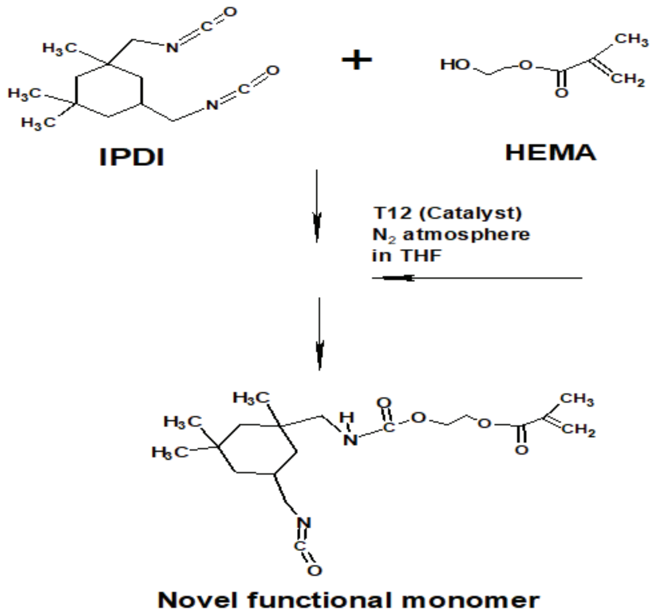

Figure 3. Synthesis of novel functional monomer

Then this novel monomer was reacted with hydroxyl terminated butadien (Polyvest-HT) in the flask. The mole ratio of the butadien was half of the synthesized novel monomer in Figure 3. Hence the butadien was terminated urethane acrylate groups. This structure was shown in Figure 4.

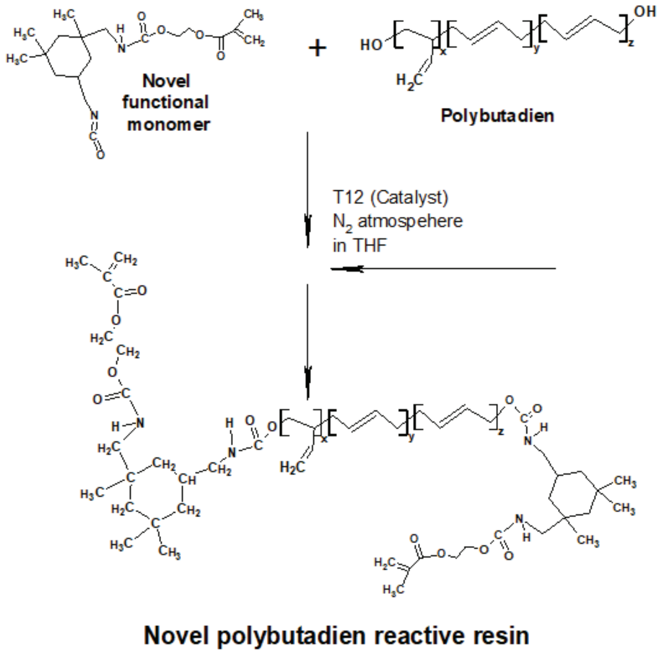

Figure 4. Synthesis of novel polybutadien reactive resin

2.4. Preparation of novel epoxy acrylate systems

The synthesized novel polybutadien reactive resin in Figure 4 was incorporated into conventional epoxy acrylate system in the range between 0%-1.5%. The novel reactive resin was mechanically stirred into conventional epoxy acrylate system and homogeneous solutions in various ratios were obtained. These resins were cured by SLA 3D printer and the novel products were prepared.

2.5. Measurements

Measurements were carried out for film and coating samples. Coating samples were used to characterize abrasion resistance. Film samples were used for the other tests. Fourier transform infrared spectroscopies (FT-IR) were conducted by Shimadzu 8303 FT-IR Spectrometer. The samples were characterized mechanically by standard tensile test in order to determine in terms of tensile strength, failure strain and young modulus according to ASTM D638. Tensile test was carried out by using a crosshead speed of 5 mm/min. Izod impact resistance was measured using unnotched samples according to ASTM D 4812-99 (ASTM D 256) using Zwick B5113.30 with hammer of 5.4J at a striking rate of 3.96 m/s. For each product, three replicated sample were prepared and measurements were taken. The average values of these samples was used for the calculations. Hardness of the samples was measured according to Shore D method. Coating samples were also produced for taber abrasion test besides film samples. Taber abrasion test were applied to the produced coating samples and weight loss was calculated. Density was measured according to archimed principle for film samples.

3. Results:

The FT-IR spectras of novel functional monomer and novel urethane acrylate terminated polybutadien reactive resin are given in Figures 5 and Figure 6. The absorption bands were given at around 3350, 1700 and 810 cm-1 relate to –NH stretching, C=O stretching and C=C twisting of acrylate,

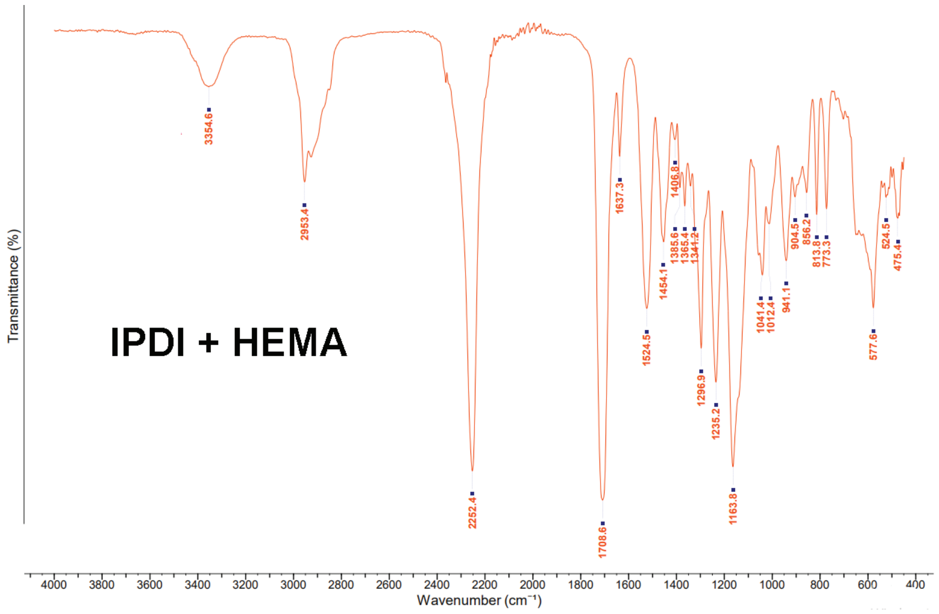

Figure 5. FTIR result of the novel monomer after the reaction of IPDI and HEMA

respectively.

From the IR spectra in Figure 6, the disappearance of the characteristic absorption band at 2250 cm-1 related to isocyanate group (-NCO) indicates the completion of the reaction (Bayramoglu, Kahraman, Kayaman-Apohan and Güngör, 2006). In additon this, the absorption bands at around 2850 and 2900 belonging to CH and CH2 bondings in Figure 6 became larger. These results confirmed the synthesizing of novel urethane acrylate terminated polybutadien reactive resin.

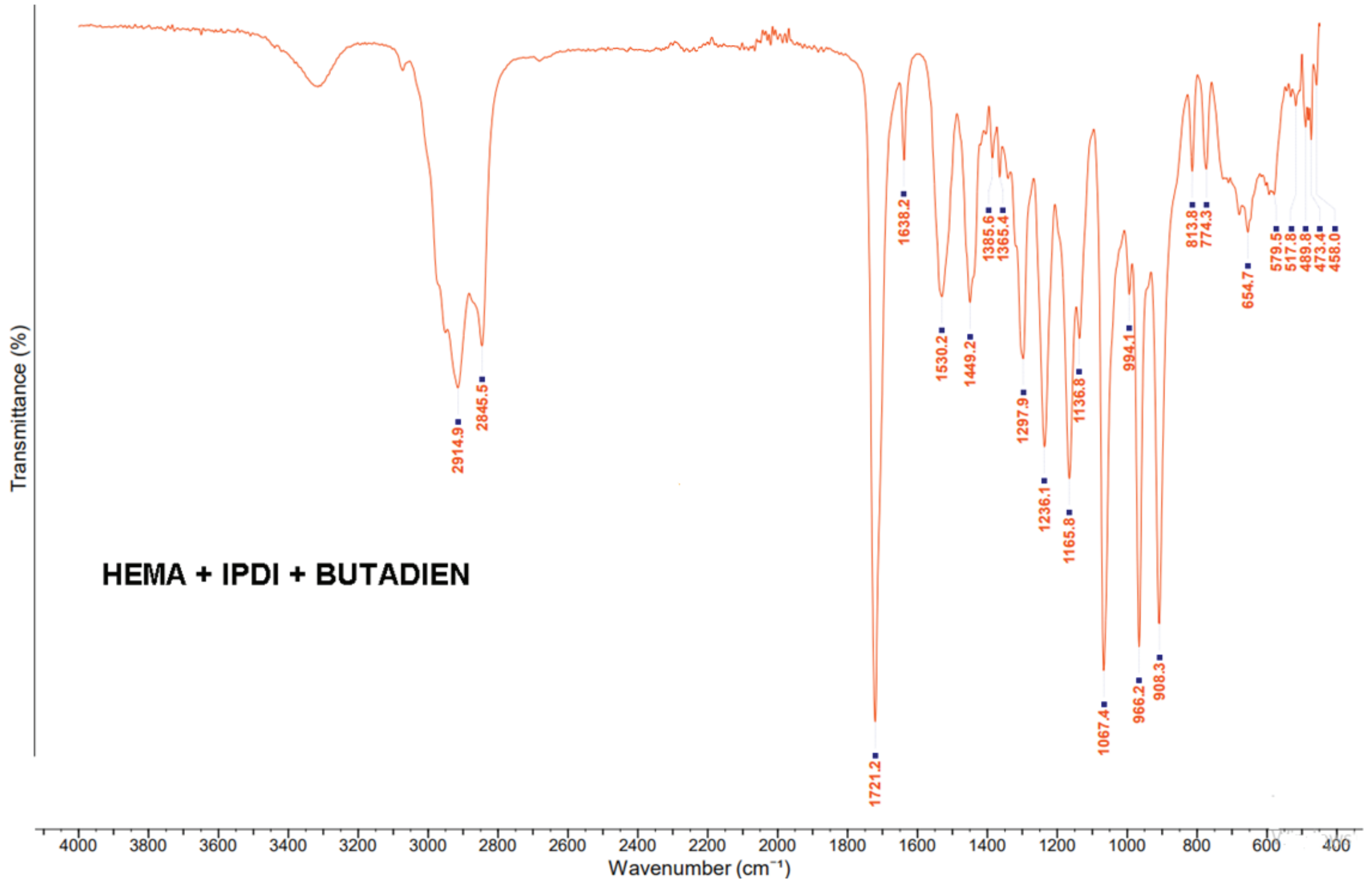

Figure 6. FTIR result of the novel polybutadien reactive resin after the reaction of novel monomer and polybutadien

Mechanical tests were performed to determine the overall effect of the synthesized novel polybutadien reactive resin samples on the performance of conventional epoxy acrylate system. This novel polybutadiene reactive resin was incorporated into conventional epoxy acrylate system up to 1.5% by weight. Mechanical properties of polybutadien containing samples showed

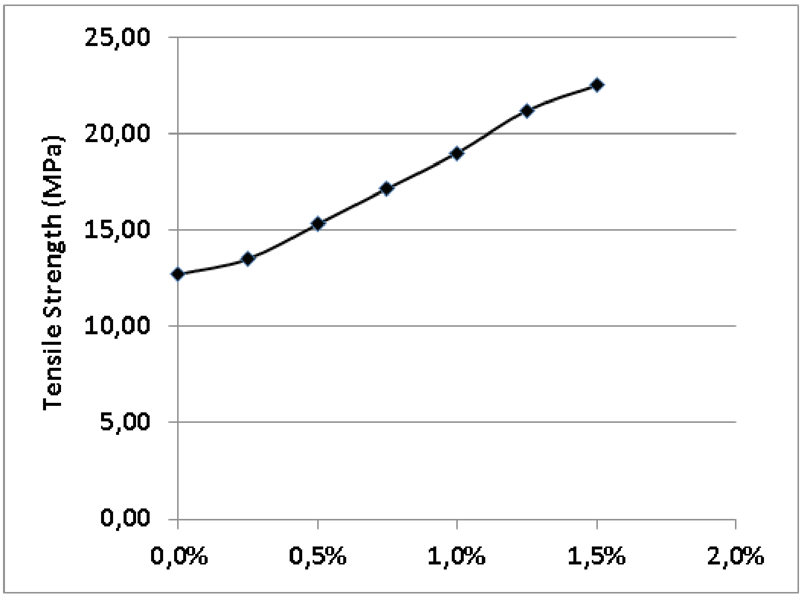

Figure 7. Tensile strength values of the novel polybutadien reactive resin

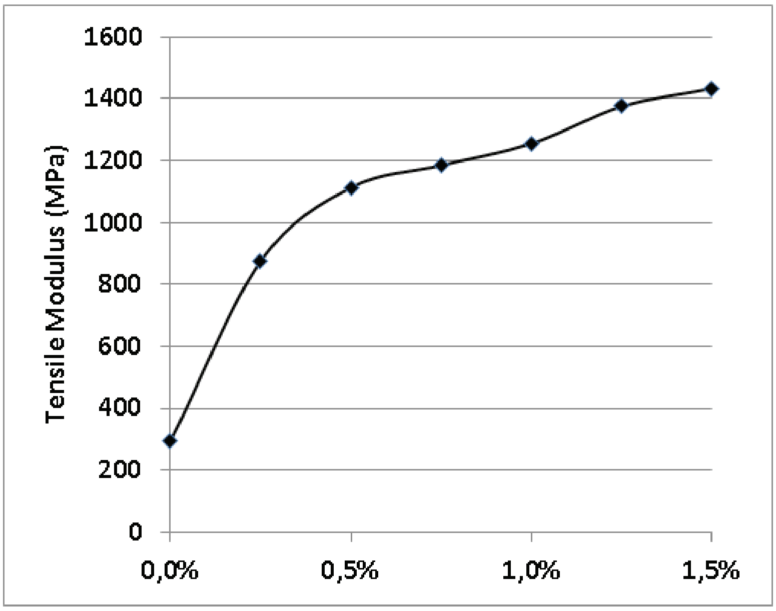

Figure 8. Tensile modulus values of the novel polybutadien reactive resin

that ultimate tensile strength and modulus increased up to 77% and 390%, respectively.

Moreover, impact resistance increased up to 27%. Novel polybutadien reactive resin containing samples exhibited maximum increase at 1% wt. It was thought that this situation could be derived from increasing of crosslinkings besides flexible structure of polybutadien. Hence, polybutadien is flexible polymer and have high amount of C=C bondings that can be crosslinked between polymer chains. Therefore impact resistance increased substantially at 1% wt. Figure 7, Figure

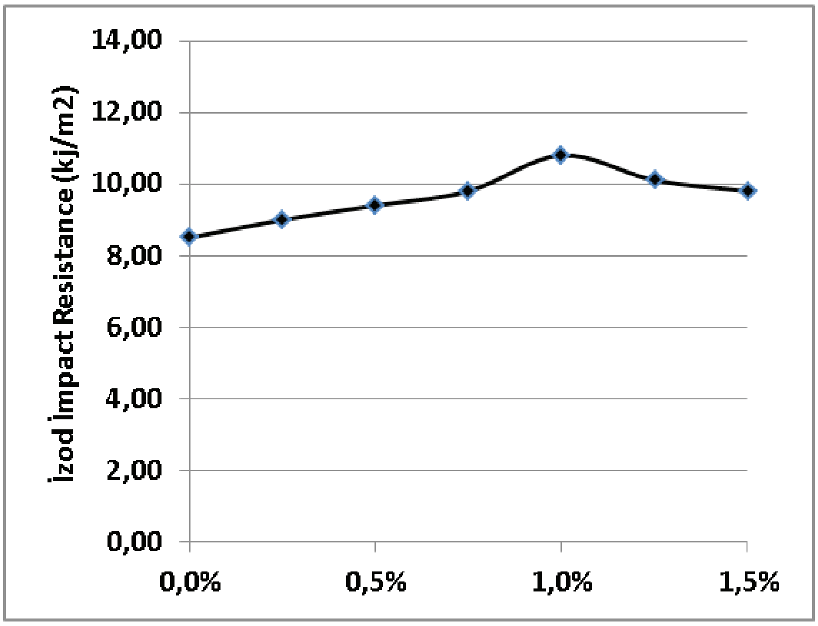

Figure 9. Izod impact resistance values of the novel polybutadien reactive resin

8 and Figure 9 showed the change of tensile strength, modulus and izod impact resistance values. These results were also given in Table 1.

Densities of the samples presented very close values each other. They showed increase trend slightly. The sample of 1.5% wt showed

Table 1. Mechanical properties of samples

Samples	Tensile Modulus (MPa)	Tensile Strength (MPa)	Izod Impact (kj/m^2)
%0	293	12,70	8,50
%0.25	875	13,50	9,00
%0.5	1113	15,30	9,40
%0.75	1185	17,15	9,80
%1	1255	19,00	10,80
%1.25	1375	21,20	10,1
%1.5	1433	22,50	9,8

Hence the weight loss decreased after taber abrasive test while the content of polybutadien increased in the conventional epoxy acrylate system.

Table 2. Density, taber abrasive resistance and hardness of samples

Samples	Density (g/cm^3)	Taber abrasive resistance (weight loss, gr)	Shore D hardness
%0	1,19	0,0011	63,6
%0.25	1,20	0,0011	64,3
%0.5	1,21	0,001	65,6
%0.75	1,21	0,0009	66,3
%1	1,22	0,0008	66,9
%1.25	1,22	0,0007	67,4
%1.5	1,22	0,0007	68,1

an increase of 2.5%. Taber abrasive resistance exhibited continuous increase trend up to 1.5 % wt. The increase trend of hardness and modulus also confirmed this situation. The sample of 1.5% wt showed a substantial increase of 36%.

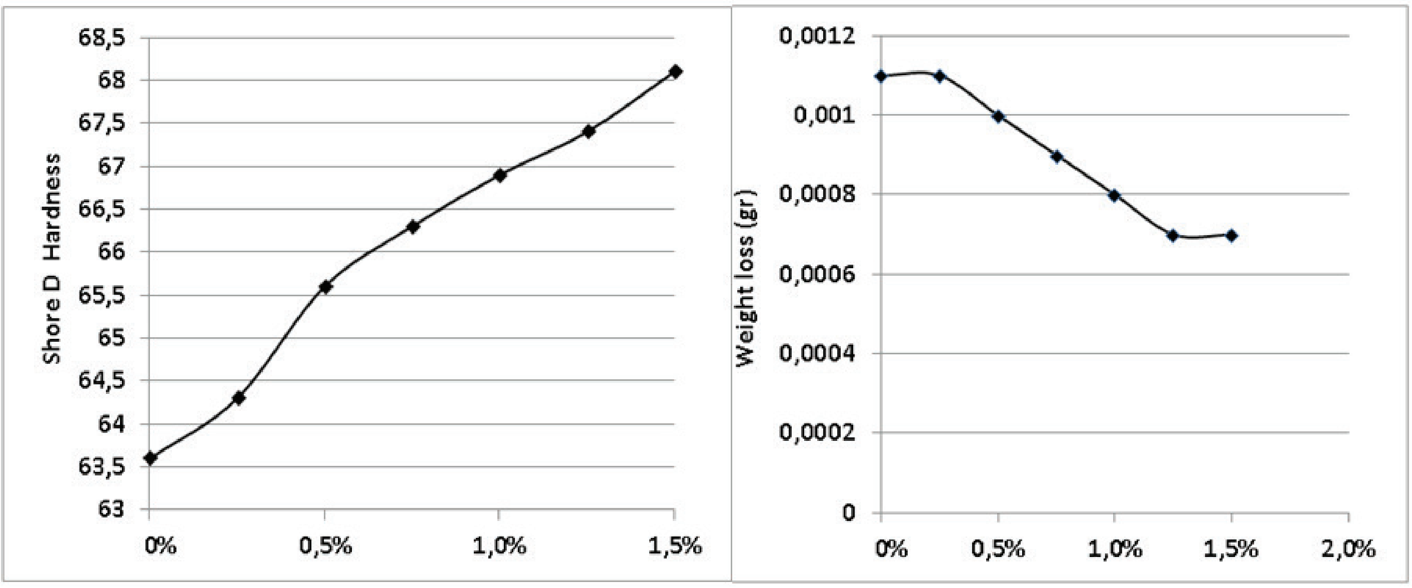

Figure 10. Shore D hardness and taber abrasive test results of the samples

The density, abrasive and hardness results of the samples were also given in Table 2.

The aromatic rigid groups and higher crosslinking amount could cause this situation. Hardness test was applied according to Shore D method. The hardness and abrasive test result trend of the samples were shown in Figure 10.

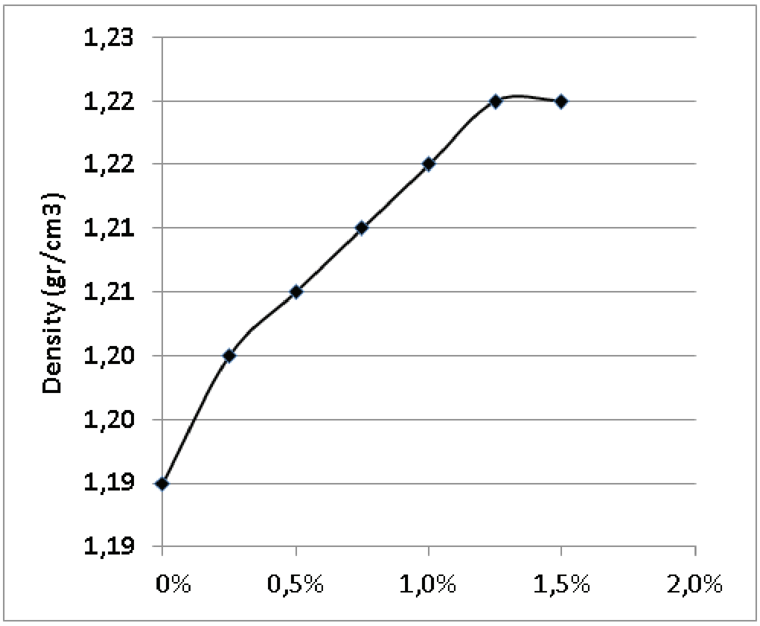

Figure 11. Densities of the samples

This method is generally applied for rigid plastics. The hardness trend of the samples showed continuous increase. The sample of 1.5% wt presented an increase of 7% as shown in Figure 11.

4. Discussion and Conclusion

In this study, novel epoxy acrylate systems were developed by synthesizing a novel butadiene reactive resin. This reactive resin was incorporated into conventional epoxy acrylate system in the range between 0%-1.5% by weight. This conventional epoxy acrylate system contained bisphenol A diglycidyl ether based epoxy acrylate and 1,6 hexanediol diacrylate. Tensile, izod impact, shore-D hardness, taber abrasive and density tests were applied to these produced samples. Considering of the results, novel butadiene reactive resin containing epoxy acrylate systems exhibited much more improved results compared to conventional epoxy acrylate system. It exhibited substantial increases in terms of tensile strength, modulus, izod impact resistance and hardness. Moreover, they presented more enhanced taber abrasive resistance. This synthesized novel polybutadien reactive resin containing epoxy acrylate systems can be used in applications that required higher mechanical and abrasive properties for epoxy acrylate systems of 3D SLA printers.

5. References

1. Aerykssen J.H., Khudyakov I.V. Industrial and Engineering Chemical Research., 9, 50:1523, 2010, DOI: 10.1021/ie101816b.
2. Bayramoglu G., Kahraman M.V, Kayaman-Apohan N., Güngör A. Progress in Organic Coatings, 57:1, 50-55, 2006.
3. Çakir M., Akin E. Journal of Applied Polymer Science, 2019, Doi: 10.1002/APP.47399.
4. Bongiovanni R., Malucelli G., Messori M., Pilati F., Priola A., Tonelli, C. Journal of Applied Polymer Science, 75, 651-659, 2000.
5. Davidson, R.S., Richard, E., Stephen, T. Susan, A.W., Polymer, 33, 14, 3031-3036, 1992.

Advanced Exergy Analysis of Goswami Power and Cooling Production Cycle

Leyla Khani[1*], Gülden G. Akkurt[2], Mousa Mohammadpourfard[1,2]

[1]Faculty of Chemical and Petroleum Engineering, University of Tabriz, Tabriz, Iran

[2]Department of Energy Systems Engineering, Izmir Institute of Technology, Izmir, Turkey

The declining trend of fossil fuel resources, the rise in their price, adverse environmental impacts, and greenhouse gas emissions have all intensified the effective use of available energy sources. Hence, new absorption refrigeration cycles like the Goswami cycle and novel system analysis methods such as advanced exergy analysis have gained much attention. The advantages of the Goswami cycle include the utilization of waste or low-temperature heat sources, stability, low noise, and availability. Also, advanced exergy analysis helps understand the interaction between system components by dividing the exergy destruction into endogenous/exogenous and avoidable/unavoidable parts. In this regard, an absorption refrigeration-power cogeneration Goswami cycle is studied from the conventional and advanced exergy viewpoint. First, mass and energy balance equations are written for each component at a steady state. Then, conventional exergy relations are applied to the system equipment to calculate its exergy destruction rate. After that, advanced exergy analysis is used to determine the avoidable part of exergy destruction and the percentage of exergy destruction caused by external factors and other components. The results show that endogenous exergy destruction rates for pump, boiler, and turbine are more than their exogenous ones. Moreover, endogenous exergy destruction for the whole system is much larger than the exogenous rate, i.e., the effect of the components' irreversibility is more significant than the deficiency of the cycle structure. Finally, total unavoidable endogenous exergy destruction is 37.2kW. Even if all cycle components are upgraded, the cycle exergy destruction will not be less than 37.2kW.

1.Introduction

Over the recent decades, there have been considerable concerns raised about greenhouse gas emissions, environmental pollution, and the unpredictability of the energy supply as a result of the over-dependence of human activities and development on fossil fuels [1]. Additionally, it is anticipated that between 2015 and 2040, the average annual growth rate of carbon dioxide emissions related to energy will be roughly 0.6% [2]. Hence, it is suggested that thermodynamic systems improvement, new cogeneration schemes, waste heat recovery, renewable energy resources utilization, and modified energy analysis methods are considered.

The absorption Goswami cycle is based on the Kalina cycle. It uses an ammonia-water mixture to generate power and refrigeration simultaneously [3]. The Goswami cycle has a wide range of scales and uses, such as bottoming cycles for recovering waste heat and producing electricity from renewable sources like solar or geothermal energy. Environmental friendliness, stability, increased efficiency, cheap cost, safety, and availability are further benefits of the Goswami cycle. [4].

Exergy measures the most useful amount of work and assesses energy systems from a thermodynamic perspective. The sources of inefficiency and irreversibility occurring in the energy conversion processes can be identified using conventional exergy analysis. Exergy destruction can result from a variety of processes, such as chemical reactions, heat transfer at a limited temperature difference, combining materials with various compositions or states, and unrestricted expansion and friction. A system's or component's exergy degradation is an inevitable result of practical and financial limitations in a particular stage of technological progress [5]. By dividing exergy destruction into avoidable and unavoidable portions and concentrating on the avoidable parts, advanced exergy analysis is useful for determining the system's true potential for thermodynamic improvements [6]. Additionally, in complex energy systems, each component's exergy destruction is influenced by both its own qualities and the inefficiencies of the other components. Because of this, it can be useful to divide total exergy destruction into endogenous and exogenous parts [7].

In this work, conventional and advanced exergy analysis methods are applied to the Goswami cycle to identify its efficiency, irreversibility, avoidable/unavoidable and endogenous/exogenous parts of exergy destruction, and possible real improvements to increase its efficiency and decrease exergy destruction.

2. Material and Methods

The schematic of the Goswami cycle is shown in Fig.1. As evident in this figure, the Goswami system receives heat in the superheater and boiler to generate power in the turbine and cooling in the refrigeration heat exchanger.

The following assumptions are applied for system modeling:

- The system operates under steady-state condition.
- The potential and kinetic energy and exergy changes are neglected.
- There is no pressure loss in connecting pipes.
- There is no heat loss to the ambient.

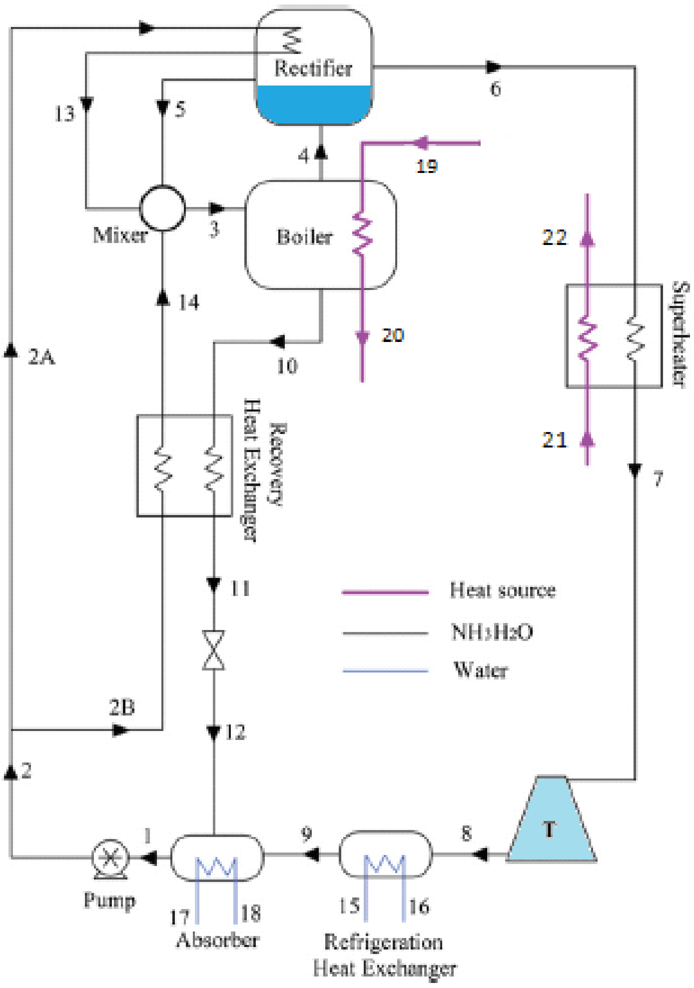

Fig.1 Schematic diagram of Goswami power and cooling cogeneration cycle

2.1. Conventional exergy analysis

Mass, ammonia concentration, and energy conservation laws for steady-state equipment are as follows [8]:

$$\sum_i \dot{m}_i - \sum_e \dot{m}_e = 0 \quad (1)$$

$$\sum_i \dot{m}_i x_i = \sum_e \dot{m}_e x_e \quad (2)$$

$$\dot{Q}_k - \dot{W}_k + \sum_i \dot{m}_i h_i - \sum_e \dot{m}_e h_e = 0 \quad (3)$$

The rate of exergy destruction in a control volume is calculated as below [8]:

$$\dot{E}_D = \sum_j \left(1 - \frac{T_0}{T_j}\right) \dot{Q}_j - \dot{W}_{cv} + \sum_i \dot{E}_i - \sum_e \dot{E}_e \quad (4)$$

2.2. Advanced exergy analysis

The total exergy destruction, calculated from Eq. (4), can be divided into [9]:

- Avoidable and unavoidable parts:

$$\dot{E}_{D,k} = \dot{E}_{D,k}^{AV} + \dot{E}_{D,k}^{UN}$$

- Endogenous and exogenous parts:

$$\dot{E}_{D,k} = \dot{E}_{D,k}^{EN} + \dot{E}_{D,k}^{EX}$$

Here, the thermodynamic cycle method is used to apply the advanced exergy analysis. Each component must follow certain basic assumptions so that the exergy destruction of components is equal to zero or the minimum, leading to a theoretical cycle [10]. In order to distinguish between endogenous and exogenous exergy destruction, hybrid cycles must be established. As a result, it is assumed that only the kth component is operating in the real state and that all other components are operating in the ideal state. When there are several components in the system, each component needs to have a corresponding hybrid cycle developed. Furthermore, these splitting methods can be combined to form the second-level splitting [9]:

$$\dot{E}_{D,k} = \dot{E}_{D,k}^{EN} + \dot{E}_{D,k}^{EX} + \dot{E}_{D,k}^{AV} + \dot{E}_{D,k}^{UN} \quad (5)$$

2.3. Overall performance analysis

Component exergy efficiency can be defined as follows:

$$\varepsilon_k = \frac{\dot{E}_{P,k}}{\dot{E}_{F,k}} = 1 - \frac{\dot{E}_{D,k}}{\dot{E}_{F,k}} \quad (6)$$

Energy and exergy efficiencies of the Goswami cycle are determined using the following equations:

$$\eta_1 = \frac{W + Q_c}{\sum Q_{in}} \quad (7)$$

$$\eta_2 = \frac{W_{net} + E_c}{E_{in}} \quad (8)$$

2.4. Input Data

Necessary input data for the real cycle are summarized in Table 1. To make the above cycle theoretical, the isentropic efficiencies of the turbine and pump are considered as 1, and the approach temperature for the heat exchangers is 5°C. Also, input values for determining unavoidable exergy destruction are listed in Table 2.

Table 1. Input data for the real cycle

Parameter	Value
η_t	0.85
η_p	0.8
$\Delta T_{Approach}$	15°C
T_{rec}	108°C
T_0	25°C
P_0	1bar
T_{boiler}	150°C
T_{sup}	20°C
T_{eva}	20°C
P_{high}	30bar
P_{low}	3.15°C
$\dot{m}_1$	1kg/s

Table 2. Input data for calculating unavoidable exergy destruction

Parameter	Value
$\eta^{UN}_{is,pump}$	0.95
$\eta^{UN}_{is,turbin}$	0.95
$T^{UN}_{min,rectifier}$	6°C
$T^{UN}_{min,heat}$	7°C
$T^{UN}_{min,sup erheter}$	11°C
$\Delta T_{Approach}$ (Real cycle)	15°C
$\Delta T_{Approach}$ (Theoretical cycle)	5°C
$T^{UN}_{min,evaperator}$	15°C
$T^{UN}_{min,boiler}$	6°C

3. Results

The real and theoretical cycles are compared in terms of the Goswami energy efficiency, exergy efficiency, net output power, and cooling capacity in Fig. 2. As obvious in this figure, the theoretical cycle has higher outputs and efficiencies because ideal operating conditions are assumed for the components leading to minimum irreversibility and maximum production in the cycle.

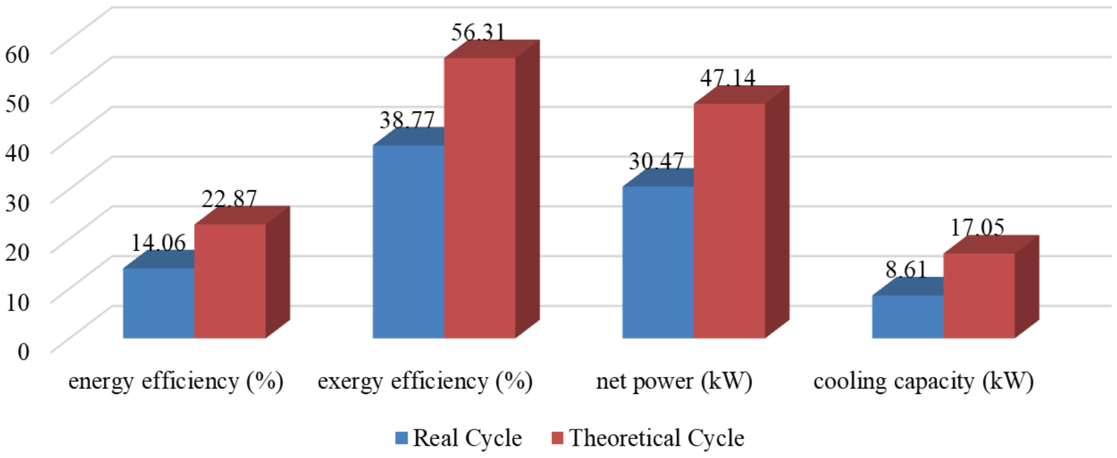

Fig. 2. Comparison of the real and theoretical cycle

The results of conventional exergy analysis for the real cycle are summarized in Table 3. The highest exergy destruction rate belongs to the boiler due to its significant temperature difference. Additionally, the overall exergy fuel rate to the cycle is 89 kW, of which 34.5 kW is converted to the products, and the rest is lost or destructed in the cycle components. Furthermore, the superheater is the most efficient equipment of the cycle, with 94.32% exergy efficiency. On the other hand, the improvement of the absorber should be prioritized because its exergy efficiency is the lowest.

Equipment	$\dot{E}_{F,k}$**(kW)**	$\dot{E}_{P,k}$**(kW)**	$\dot{E}_{D,k}$**(kW)**	ε_k (%)
Pump	3.965	3.186	0.779	80.35
Rectifier	16.953	8.725	8.228	51.47
Boiler	88.78	75.44	13.34	84.97
Recovery Heat Exchanger	74.14	62.93	12.21	84.88
Superheater	0.2151	0.2029	0.0122	94.33
Turbine	40.35	34.43	5.92	85.33
Absorber	14.77	2.10	12.67	14.24
Refrigeration Heat Exchanger	0.3542	0.0730	0.2812	20.62
Overall cycle	87.94	34.5	53.44	38.77

Table 3. Conventional exergy analysis results for the real cycle

The conventional exergy analysis results for the theoretical cycle are listed in Table 4. If this table is compared to Table 3, it is apparent that the exergy destruction in all components has decreased, and it is even zero for the pump and turbine. Hence, the exergy efficiency of the pump and turbine is 100%. Besides, the exergy efficiency of all components has increased. This leads to more exergy production rate for the Goswami cycle. In the theoretical cycle, the absorber has the highest exergy destruction ratio, 33.61%.

Table 4. Conventional exergy analysis results for the theoretical cycle

Equipment	$\dot{E}_{F,k}$(kW)	$\dot{E}_{P,k}$(kW)	$\dot{E}_{D,k}$(kW)	ε_k(%)
Pump	3.172	3.172	0	100
Rectifier	26.9	18.12	8.78	67.36
Boiler	88.16	81.06	7.09	91.94
Recovery Heat Exchanger	79.97	73.88	6.09	92.39
Superheater	1.543	1.498	0.045	97.08
Turbine	50.29	50.29	0	100
Absorber	16.94	4.30	12.64	25.42
Refrigeration Heat Exchanger	0.686	0.2034	0.4826	29.65
Overall cycle	89.62	50.51	35.11	56.31

In Table 5, the avoidable/unavoidable and endogenous/exogenous exergy destruction parts of each component and the overall cycle are written. The avoidable exergy destruction for the pump and refrigeration heat exchanger is larger than their unavoidable parts, so there is an excellent potential to improve the efficiency of these components and decrease their irreversibility. On the other hand, for other components, especially the rectifier and recovery heat exchanger, the unavoidable exergy destruction is greater. For the overall cycle, only 16.89 kW of its exergy destruction is avoidable. Furthermore, all the components have more endogenous exergy destruction rate than their exogenous ones, indicating that it is better to focus on upgrading these components and increasing their efficiencies. It will also lead to lower irreversibility in the overall cycle. It should be mentioned that the negative exogenous exergy destruction rate means as the inefficiency and irreversibility of other components of the cycle increases, the destruction of exergy in this component decreases and vice versa.

Table 5. Advanced exergy analysis results

Component	$\dot{E}_{D,k}$(kW)	$\dot{E}^{EN}_{D,k}$(kW)	$\dot{E}^{EX}_{D,k}$(kW)	$\dot{E}^{UN}_{D,k}$(kW)	$\dot{E}^{AV}_{D,k}$(kW)
Pump	0.779	0.779	0	0.1641	0.6151
Rectifier	8.228	8.461	-0.233	7.965	0.263
Boiler	13.34	10.61	2.73	8.497	4.843
Recovery Heat Exchanger	12.21	13.99	-1.78	9.551	2.659
Superheater	0.0122	0.01492	-0.0027	0.006162	0.006058
Turbine	5.92	4.267	1.648	3.834	2.081
Absorber	12.67	14.77	-2.1	6.435	6.235
Refrigeration Heat Exchanger	0.2812	0.5492	-0.268	0.09276	0.18844
Overall cycle	53.44	53.44132	-0.0057	36.545	16.89

Table 6 lists the second-level splitting results of the advanced exergy analysis. The positive exogenous avoidable exergy destruction rates of the rectifier, boiler, recovery heat exchanger, and superheater indicate that their thermodynamic performance is directly affected by the turbine, absorber, and refrigeration heat exchanger. The pump, turbine, and refrigeration heat exchanger can be the focus for improvement because their endogenous avoidable exergy destruction parts are more than their endogenous unavoidable ones. However, metallurgical limitations should be considered too. Moreover, even after applying all optimization and improvements to the Goswami cycle, its exergy destruction will not be less than 36.162 kW.

Table 6. Second-level splitting advanced exergy analysis results

Component	$\dot{E}^{EN,UN}_{D,k}$(kW)	$\dot{E}^{EN,AV}_{D,k}$(kW)	$\dot{E}^{EX,UN}_{D,k}$(kW)	$\dot{E}^{EX,AV}_{D,k}$(kW)
Pump	0.1641	0.6151	0	0
Rectifier	8.384	0.077	-0.419	0.186
Boiler	6.819	3.791	1.678	1.052
Recovery Heat Exchanger	11.75	2.24	-2.199	0.419
Superheater	0.007891	0.007029	-0.001729	0.000971
Turbine	1.358	2.909	2.476	-0.828
Absorber	8.514	6.255	-2.079	-0.02
Refrigeration Heat Exchanger	0.1656	0.3836	-0.07284	-0.195
Overall cycle	37.162	16.278	-0.62	0.615

4. Discussion and Conclusion

Advanced exergy analysis is applied to the Goswami absorption refrigeration and cooling production cycle. The results can be summarized as follows:

- The endogenous part of the exergy destruction rate for pump, boiler, and turbine is larger than the exogenous part.
- The endogenous part of the exergy destruction for the whole cycle is more than the exogenous one.
- The unavoidable exergy destruction rates for the pump and evaporator are higher than the avoidable ones.
- The unavoidable part of exergy destruction for the whole system is also higher than the avoidable part.
- If all components of the cycle are upgraded, the destruction of exergy will not be less than 37.2 kW.

References

1. IEA Energy Atlas n.d. http://energyatlas.iea.org/#!/tellmap/1378539487(accessed October 14, 2019)
2. Beaudin M, Zareipour H. Energy Solutions to Combat Global Warming. vol. 33. 2017.
3. YOGI GOSWAMI D. Solar Thermal Power Technology: Present Status and Ideas for the Future. Energy Sources 1998;20(2):137–45.
4. Tamm G, Goswami DY. Novel Combined Power and Cooling Thermodynamic Cycle for Low Temperature Heat Sources, Part II: Experimental Investigation 2003.
5. Szargut J., (2005), "Exergy method technical and ecological applications", WIT Press.
6. Tsatsaronis G, Park MH. On avoidable and unavoidable exergy destructions and investment costs in thermal systems. Energy Convers Manag. 2002;43:1259-1270.
7. Kelly S, Tsatsaronis G, Morosuk T. Advanced exergetic analysis: approaches for splitting the exergy destruction into endogenous and exogenous parts. Energy. 2009;34:384-391.
8. Bejan M, Tsatsaronis A, Moran G. Thermal Design and Optimization. John Wiley; 1996.
9. Morosuk T, Tsatsaronis G. A new approach to the exergy analysis of absorption refrigeration machines. Energy. 2008;33:890-907.
10. Chen J, Zheng X, Guo G, Luo X, Chen Y, Yang Z. A flexible and multi-functional organic Rankine cycle system: preliminary experimental study and advanced exergy analysis. Energy Convers Manag. 2019;187:339-355.

Performance of Graphite Matrix Composite with Phase Change for Small-Scale Li-Ion Package Under Square Wave Load

Mustafa Yusuf Yazıcı[*1,2]

[1]Samsun University, Türkiye

[2]University of Nottingham, UK

In this study, experimental observation is presented to evaluate the effect of the passive thermal management system of graphite matrix composite with phase change on the thermal/electrical behavior of li-ion package (3s2p) under dynamic load (square wave: Imax/Imin=16A/6.4A). Battery package was performed with two different configuration: free-air cooling case (reference case) and graphite matrix composite. The experimental results show that operating temperature is dimished by 34.7% and safe operating time is increased by 140% with the PCM/graphite matrix compared to reference case. Similarly, total discharge and energy capacity values is also enhanced 141% and 102%, respectively, with the PCM/graphite matrix in comparison reference case. Hence, proposed passive thermal management approach has considerable effect on the li-ion package.

1.Introduction

Electromobility is a global trend to avoid the threat of energy and climate crisis, and also severe environmental pollution such as air and noise leading environmental health risks. However, the battery is the key feature for spreading of electromobility including cars, bikes etc. Li-ion battery technology has the highest potential among other options with no-memory effect, high specific power, high specific energy density, long cycle life, high discharge voltage, low self-discharge rate and stable performance in the current era. Although the li-ion cell provides a considerable solution for electromobility, the operating conditions are subject to certain restrictions. One of the major hindrances is temperature-caused degradation. There are two main temperature concerns about li-ion batteries: unacceptable operating temperature, and low-temperature uniformity, which cause deteriorations on performance, safety and lifetime. The operating temperature of the li-ion battery needs to be kept within the narrow range of 15°C - 35°C. Besides, the maximum temperature difference between cells in the battery pack is desired to be less than 5 °C. Hence, battery thermal management systems (BTMS) is a critical role in addressing thermal safety, improving performance and extending lifetime (Liu et al., 2017; Arora, 2018; Zichen and Changqing, 2021).

BTMS through phase change material is an impressive way with good characteristics including high heat absorption capability in lesser volume, isothermally process, simple lightweight and also with noise-free and no-additional power to make reduced carbon footprint batteries for a green environment. Nevertheless, low thermal conductivity causes low heat transfer rates in the medium and leakage issues of PCM-based thermal management strategies for the type of paraffin are two main bottlenecks restricting the application of PCM-based technology. Graphite matrix is a promising approach with high porosity, high ratio heat transfer surface to volume, high thermal conductivity, chemically non-reactive nature, and also encapsulation medium to avoid these disadvantages. Therefore, graphite matrix provides abundant highly conductive thermal paths (Mills et al., 2006; Kang et al., 2019) and shape-stabilized encapsulation (12) for diffusing heat fast and leakage issues, respectively, for PCM medium.

The researches dramatically on graphite matrix/foam with PCM for battery thermal management are presented as follows: Mills et al. (2006) first reported (within the authors' knowledge) an expanded graphite matrix for battery cooling. They studied thermal conductivity, paraffin mass fraction, and latent heat of fusion of PCM/graphite matrix composite samples. They revealed the potential of the PCM composite for passive thermal management systems. Kızılel et al. (2008) investigated the effect of the PCM/graphite matrix thermal management systems over conventional active cooling systems. The results showed that the surface temperature of the cells was kept at lower temperatures when PCM was used. A numerical study was conducted to investigate the cooling performance of PCM/graphite matrix structure for a cylindrical battery pack by the same research group Kizilel et al. (2009). The PCM/graphite matrix helped the battery to achieve a more uniform distribution and to avoid the propagation of a thermal runaway from one cell to the entire pack. Somasundaram et al. (2012) carried out a numerical study by using a two-dimensional, transient mathematical model comprising conservation of charges, species, and energy for cylindrical li-ion battery under different discharge rates. The results showed that lower temperature measurements were observed with a PCM/graphite. The thermal performance of composite PCM-based BTMS was performed by Greco et al. (2015). They observed that the relation between latent heat and thermal conductivity was important. The authors also presented that the bulk density of the graphite-matrix was a critical parameter for optimizing the PCM/graphite matrix BTMS. Wilke et al. (2017) investigated the effect of the solid-liquid phase change composite (PCM/graphite matrix) on the thermal runaway for a single cell. Experimental results show that the use of PCM composite reduced the maximum temperature of adjacent cells by nearly 60 ˚C and prevented thermal runaway from propagating between the cells after nail penetration. Jiang et al. (2016) carried out an experimental and numerical study on composite PCM (EG/paraffin slurry)-based BTMS under constant current. The PCM was enhanced with EG and was packed in aluminium tubes to further enhance the thermal conductivity. The tube-shell battery module exhibited high efficiency of heat dissipation and the rise of temperature was reduced significantly, but the temperature difference across the whole battery pack was near 12 °C. A similar study (EG/paraffin slurry) was also carried out under constant current by Lv et al. (2016). Wu et al. (2016) studied the effect of a copper mesh-enhanced paraffin (PA)/expanded graphite (EG) composite for battery thermal management. The copper mesh acts as a skeleton to further enhance both thermal conductivity and strength. As a result, CM enhanced PA/EG plate (PCMP) presents much better heat dissipation performance and temperature uniformity under constant discharge rates. A heat pipe-assisted PCM/EG-based battery thermal management (BTM) system is investigated with constant discharge currents by same research group (Wu et al., 2017). Mallow et al. (2018) studied two enhancement materials including aluminium and graphite foams, and the enhancement materials saturated with PCM. The result indicated that the thermal charging enhancement of graphite foams is superior to that of aluminium foams. Ling et al. (2018) investigated the battery thermal performance using two different PCM expanded graphite composites (Expanded graphite-PCM and Expanded graphite-PCM-Fumed silica). It was observed that the maximum temperature of the battery was reduced and the temperature difference of the battery was reduced by 6 °C by using PCM/graphite composite. Similar study is performed by Wang et al. (2018) and Li et al. (2019). Li et al. (2018) extends the investigation with additional silica gel and Al-honeycomb (Al-Hc) components. It was declared by authors that composite PCM could improve the temperature uniformity and reducing the average temperature of the battery. He et al. (2019) developed CPCM by introducing a binary thermal conductive framework of EG/copper foam (CF) for BTMS. The results showed that the composite PCM-based battery pack with EG/CF (CPCM-EG/CF) achieves much better cooling and uniform temperature distribution than those without EG/CF or CF under constant discharge rates. Xin et al. (2022) performed a numerical study to investigate the effects on the maximum temperature and temperature uniformity of the battery module by parameters including composite phase change material thicknesses, expanded graphite mass fractions, coolant flow directions, coolant velocities and coolant temperatures. The results indicate that the mass fraction of expanded graphite has an optimal value of 12%, corresponding to the limitations of maximum temperature and temperature difference. Moreover, the counterflow flow direction scheme provides better thermal performance in comparison with the parallel flow direction. Akula and Balaji (2022) carried out both a numerical and an experimental study to illustrate the effect of proposed PCM-graphite composite slurry with fin on the thermal management of a battery at constant discharge rates (>2C-rate). Authors show considerable improvement in temperature regulation, thermal conductance, and thermal capacitance with the addition of 30% expanded graphite (EG) makes the heat sink with 130 fins better compared to the heat sink having 260 fins without EG.

From the cited literature, researchers have investigated experimentally/numerically the effect of graphite matrix with PCM on battery thermal management under constant discharge rates. However, there are scarce studies on the thermal behaviour of li-ion packages with PCM-based thermal management systems under dynamic discharge conditions. So, in this motivation, an experimental study is carried out to perform the graphite matrix composite with PCM under the dynamic discharge load for a small-scale li-ion battery pack. The effect of the melting phenomenon and porous media on the thermal performance of li-ion is also presented in detail. The time history temperature, transient thermal camera images and also voltage, discharge capacity, and energy capacity variations are utilized, respectively, to illustrate the thermal and electrochemical behaviour of the li-ion module (3s2p). Experimental results are given comparatively with a free-air cooling case to evaluate graphite matrix composite with PCM.

2. Material and Methods

2.1. Phase change composite Experimental setup and procedure

RT-35 (organic paraffin) supplied from brand of Rubitherm is utilized to store dissipated heat by li-ion battery pack. Paraffin is known to be an attractive material with its advantages including, high latent heat of fusion, chemical/physical/thermal stability, no phase segregation, good compatibility with other materials, non-reactivity and safe (Ahmed et al., 2022). The measured thermophysical properties of the paraffin and paraffin/graphite composite are presented in Table 1. Heat flow as a function of the temperature of pure paraffin and paraffin/graphite was measured by DSC analysis (Hitachi-DSC 7020).

Table 1. Thermo-physical properties of the pure paraffin and phase change composite

Thermo-physical property	Pure paraffin	Phase change composite
Melting temperature (°C)	37.2	36.1
Latent heat (kJ kg^{-1})	150	144
Thermal conductivity (W m^{-1} K^{-1})	0.2	7.2
Density (kg m^{-3}) (at 25 °C)	860	796

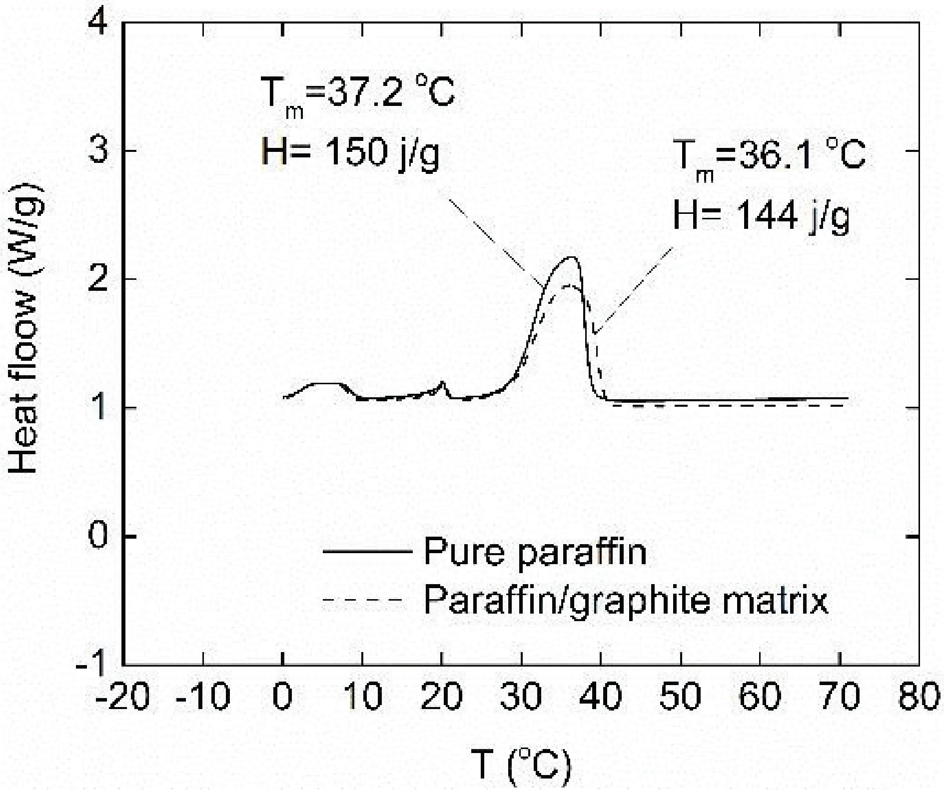

Figure 1. Heat flow-temperature variation for pure paraffin and paraffin/graphite

To build the graphite matrix, expanded graphite (EG) produced by heat treatment (rapid expansion and exfoliation of expandable graphite at 900-1000 °C - 60 seconds) was pressurized in an aluminium mould using Instron Universal Testing System (Instron 3382). A detailed description of the manufacturing process of expanded graphite is presented in the literature (Py et al., 2001: Mill et al., 2006). In this experimental study, expandable graphite with >%98 purity, 50 mesh, and 700 ml g-1 is provided by Asbury Carbon. Graphite matrix with a bulk density of 75 g L-1 and an overall dimension of 75mmx52mmx60mm (length width height) is made for small-scale battery pack configuration (3s2p). For graphite matrix composite with phase change material, the graphite matrix is submerged in a liquid paraffin bath (75°C) for about 4 hours to complete saturation. Liquid paraffin is impregnated to graphite matrix via surface tension and capillary forces (Py et al., 2001: Mill et al., 2006). The total amount of PCM in the graphite matrix composite with phase change is nearly 103 grams. The mass fraction of paraffin is about 92% in phase change composite. The porosity of the EG matrix is measured 85% by using PCM volume in the matrix. Impregnation encapsulation provides shape-stabilized PCMs (Zhang et al., 2021) to avoid PCM leakage from the matrix. The leakage test of graphite matrix composite with phase change sample is illustrated in Figure 2. The sample is put on the paper and heated at 75 °C for 150 minutes. PCM/graphite matrix keeps its form with a very low amount of leakage (< 0.42 gram) on the paper. The leakage mass percentage of the composite is 0.37 %. These low amounts of leakage can be explained by the melting of covered solid PCM on the surface.

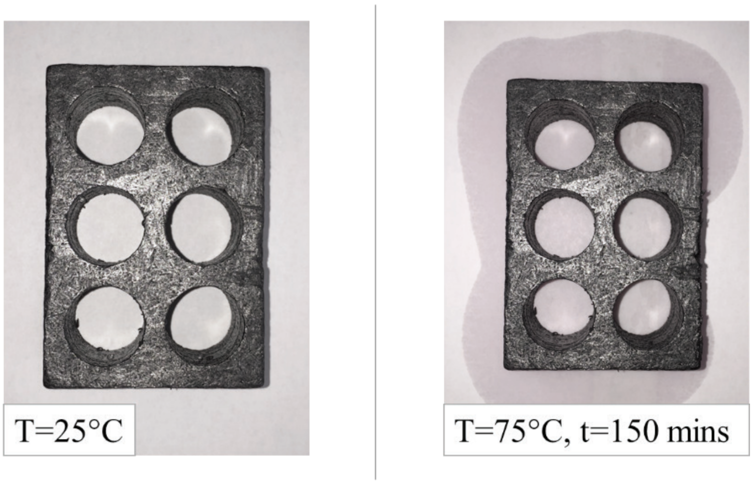

Figure 2. Leakage test: T=25°C (a), T=75°C(b)

Scanning electron microscope (SEM, Zeiss EVO LS10) images of the EG matrix and the graphite matrix composite with phase change are presented in Figure 3. EG matrix exhibits worm-like particles (Fig. 2a). The honeycomb-like network is built by the overlapping and intersecting of graphite flakes of the EG matrix (Fig. 2a) (Zou et al., 2020). It is also shown that there are some non-interlocking areas between EG layers. The morphology of the EG matrix saturated/coated with paraffin (PCM/graphite matrix) is illustrated in Figure 2b. It can be concluded that the EG layers adsorb most of the paraffin in their pores.

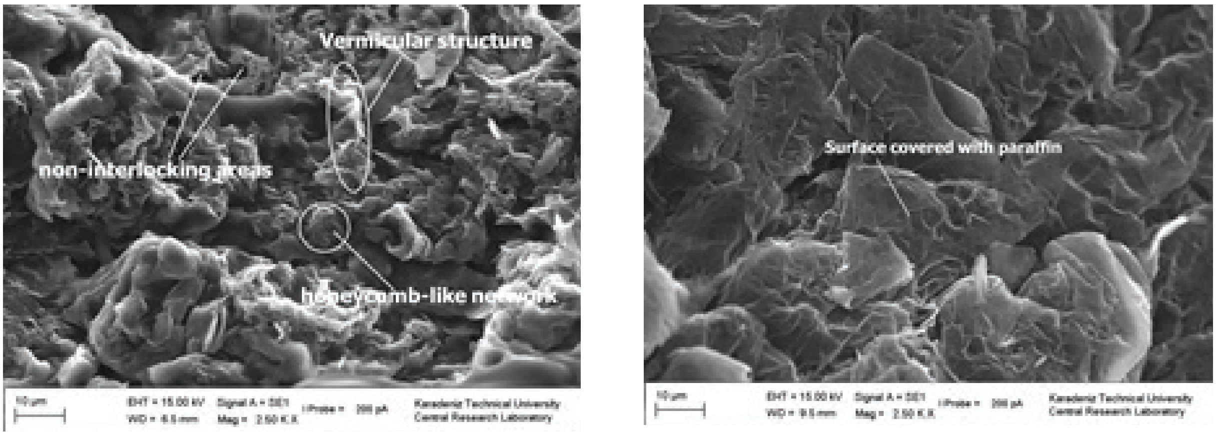

(a) (b)

Figure 3. SEM photographs: (a) the graphite matrix and (b) graphite matrix composite with phase change

2.1. Experimental setup and procedure

The experimental rig is shown in Figure 4. It consists of a test section, a DC load, a data logger, a PC, and a thermal camera.

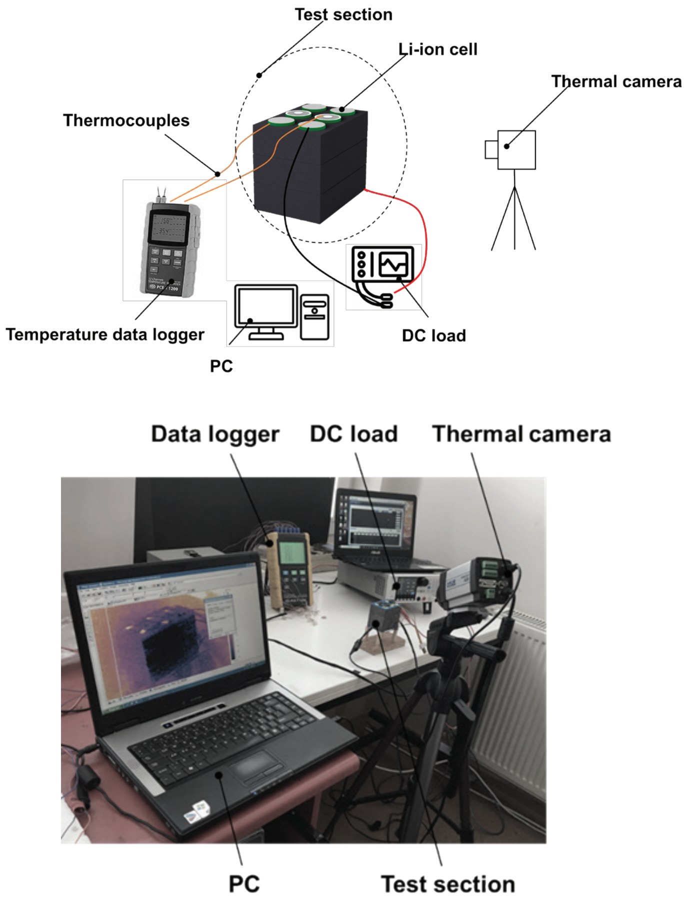

Figure 4. Experimental setup: (a) shematic view, (b) photograph

The test section is built to perform the effect of graphite matrix composite with phase change on the thermal management of small-scale battery package under dynamic load-square wave (Figure 5). Test section comprises li-ion cell (3s2p), nickel sheets for cell connection, terminals and thermal management system including PCM/graphite matrix and free-air cooling arrangements. For electric energy storage, a commercially available li-ion cell of Panasonic-Sanyo NCR 18650B was used to form battery pcakage (3s2p). The specifications of the battery module are summarized in Table 3.

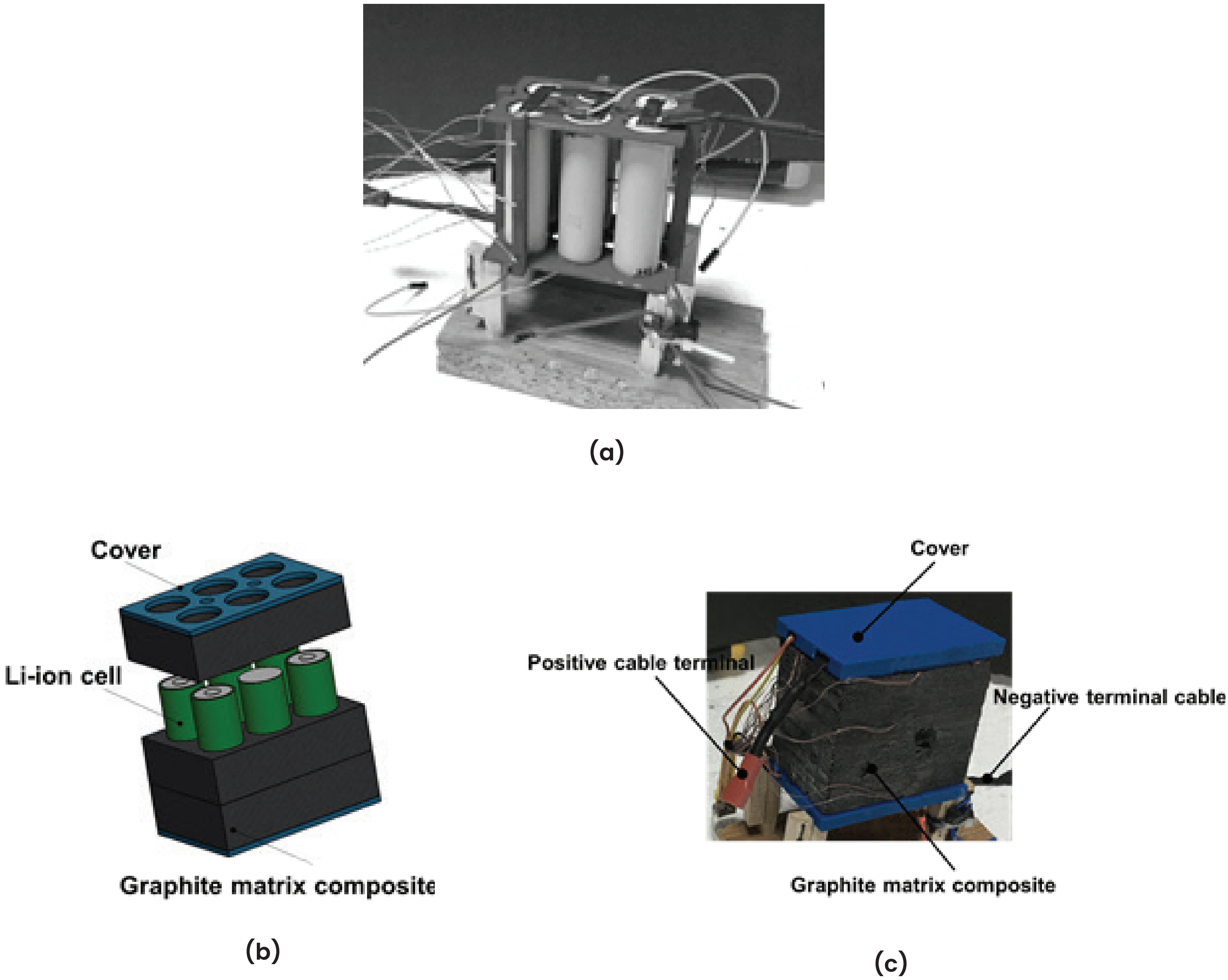

(a)

(b)

(c)

Figure 5. Test section: (a) free-air cooling case, (b) graphite matrix composite /shematic view, (c) phase graphite matrix composite /photograph

Specification	cell	module
Form factor	1s	3s2p
Capacity nominal (mA h)	3250	6500
Voltage nominal (V)	3.7V	11.1
Specific energy (W h kg^{-1})	243	258

Temperature measurements are the key evaluation criteria for the thermal performance of a thermal management system. Therefore, the time-dependent temperature history of the battery package is recorded with six T-type thermocouples (brand of OMEGA) with an accuracy of ±1°C (or 0.75% whichever greater). Transient temperature measurements were recorded via a data logger system (PCE-1200) by 5 s intervals Thermocouple positions/labels on the battery pack are presented in Figure 6. The thermal camera (Flir, A20 thermovision) was also used to support thermocouple measurements and also visualize the thermal image of PCM/graphite matrix and free-air cooling arrangements.

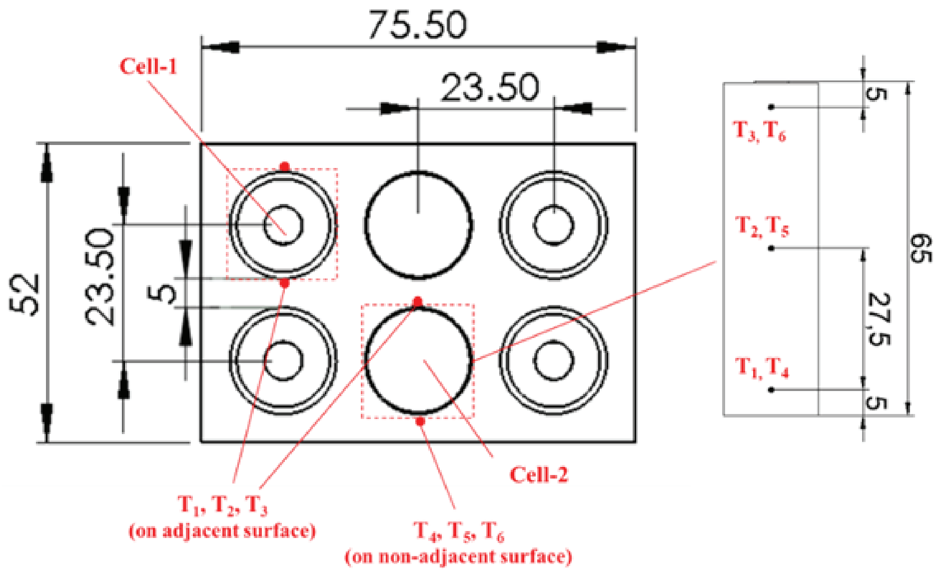

Figure 6. Temperature measurements locations/labels on the li-ion cell

To test the battery package under dynamic discharge load of the square wave, Chroma electronic DC load (CH-63004-150-60) , accuracy of current of ± 0.1 % F.S. (±0.06 amper). was used. The dynamic discharge current was set as Imaximum=16A (2.5C-rate) - t=16seconds and Iminimum=6.4A (1C-rate) - t=4seconds. The form of square wave is presented in Figure 7.

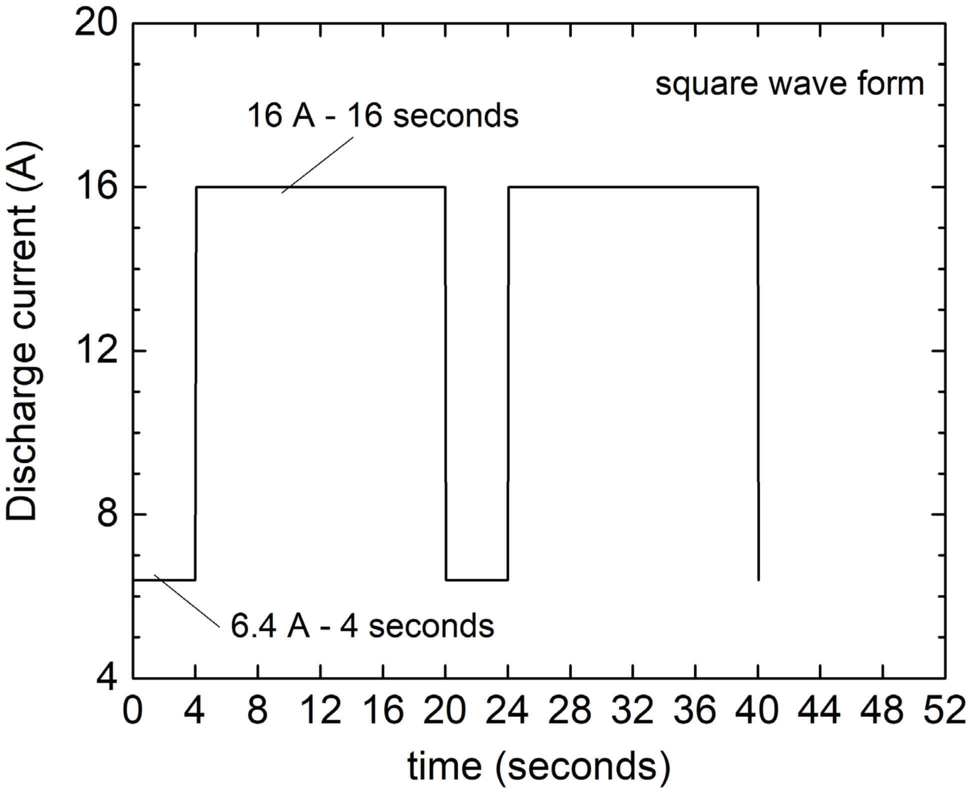

Figure 7. Square wave form

All the experiments were conducted in a conditioned room, where the ambient temperature is 25°C. Experiments were terminated by reaching the limit operating temperature (55°C) or cut-off voltage (2.5 V) value whichever comes first.

3. Results and Discussion

The performance of graphite matrix composite with phase chance compared to free-air cooling is experimentally investigated on a small-scale of 3s2p li-ion battery package's thermal and electrochemical behaviour under dynamic load. To illustrate the effect of graphite composite with phase change, transient temperature distributions are presented in Figures 8-9. Thermal camera images are also given for the initial and final stages of the experimental procedure. For the electrical performance of the battery pack under dynamic load, the voltage, discharge capacity and energy capacity variation are also shown in Figures 10-12.

Heat transportation in such a porous medium of graphite matrix composite has been considered conduction along highly conductive abundant thermal bridges (Mills et al., 2006; Kang et al., 2019). The advantage of highly conductive thermal bridges of the graphite matrix enhances the process of carrying and storing heat in the phase change phenomenon, which provides the usage of PCM in engineering applications. It should be noted that depending on pore sizes smaller than 10mm, the natural convection in such a porous medium is suppressed (Kang et al., 2019).

Transient temperature profiles of li-ion cell-1 and cell-2 for free-air cooling and graphite matrix composite are shown in Figure 8. For free-air cooling in Figure 8a and b, heat is not dissipated effectively on the surface of li-ion cell due to low thermal conductivity (0.025 W / m.K at 25°C) and also low natural convection heat transfer rates. Lower heat dissipation rates from the li-ion surface results in a higher operating temperature of 55 °C, which is critical, in a shorter time of 8.25 minutes. The hot spots are T1/cell-1 and T3/cell-2 for Cell-1 and Cell-2, respectively, because more heat is generated at positive/negative poles. It is shown in Figure 8a and b that the temperature increases almost linearly. Temperature rising rate is about 3.65 °C/minutes. The local temperature point recordings of Cell-2 are higher (4.8-9.4 °C) than Cell-1. This temperature difference between cells is associated with the thermal effect of the surrounding li-ion cell-2. It means cell-2 is under thermal load more than cell-1 depending on surrounding cells. In addition, temperature points of T1-3/cell-1 and T1-3/cell-2, which are positioned on opposing/adjacent surfaces facing each other, are higher than T4-6/cell-1 and T4-6/cell-2, respectively for each cell. This is the result of the thermal effect of opposing/adjacent surfaces to each other. It should be noted that heat loss from the outer/non-adjacent surfaces to the ambient is one of the reasons for this behaviour. So, these result in non-uniform temperature distribution on the battery pack, which causes adverse effect including unbalance of voltage between cells. From the Figures 8a and b, the maximum temperature difference (Tmaximum-Tminimum=T3/cell-2-T5/cell-1) on the battery pack is about 9.4 °C.

For the graphite matrix composite with phase change, the temperature rising rate is lower compared to free-air cooling in Figure 8c-d. With graphite matrix composite with phase change, a more uniform temperature distrubution is observed. This is the result of the highly conductive abundant thermal bridges, which provide effective heat dissipation from li-ion surface, and also thermal energy storage capability of PCM. Simultaneously, dissipated heat in graphite matrix composite with phase change is absorbed by paraffin in the form of sensible and latent heat. Temperature readings report variable temperature increase rates in different periods in Figure 8c and d. It is shown that a steep increase with a 2 °C/minutes in the first period (t<4 minutes) of discharging due to sensible heat storage. In the following period (4 minutes< t < 12 minutes), temperature measurements reach the melting range of RT-35, and then temperature rise slows down to 1.06 °C/minutes with a positive decrease due to phase transition, which provides high energy storage capacity. In the next period (t > 12 minutes), the rate of temperature rise goes up with a 1.71 °C/minutes, due to the completed phase transition phenomenon. To compare the graphite composite with free-air cooling case, temperature readings for T3/cell-2 are 35.6°C and 54.5°C, respectively, at t=8 minutes. Temperature non-uniformity (Tmaximum-Tminimum= T3/cell-2- T5/cell-1) is decreased up to 6.2 °C with graphite matrix composite with phase change. The outputs reveal that operating temperature (at t=8 minutes) and temperature difference (at the end of experiments) are about 34.7 % and 34 % lower for the graphite matrix composite with phase change in comparison to free-air cooling, respectively. Therefore, graphite matrix composite with phase change achieved a longer operating time in reliable operating temperatures. Figure 8c-d shows that safe operating time increases 19.83 minutes with an increase of 140 % for graphite matrix composite compared to free-air cooling case. It should be noted that the experiments are terminated after reaching the critical operating temperature (55 °C) for all configurations.

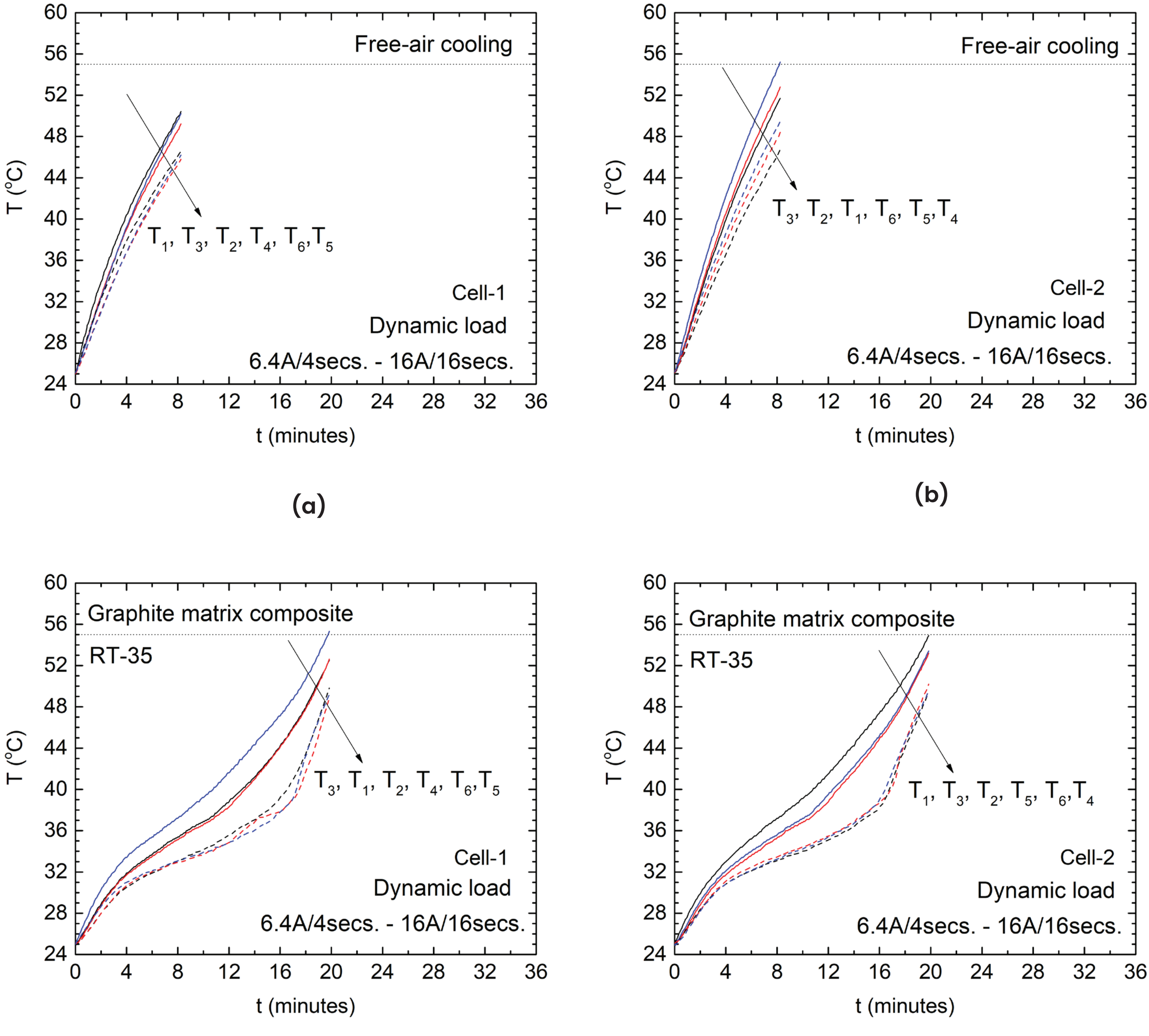

(a) (b)

(c) (d)

Figure 8. The time history of temperature along the li-ion cell surface: natural convection case (a, b), the PCM/graphite matrix (c,d)

Discharge capacity and energy capacity varitions are presented in Figure 9 and 10 to illustrate electrical performance of cooling strategies. It is shown in Figure 9 that discharge capacity variation did not decrease continously. This is the result of the load of square wave form. For the highest discharge current of 16 A/16seconds, voltage value decreased higher than the lowest discharge current of 6.4A/4seconds. For example (graphite matrix composite cooling), at the begining of the experiment, the voltage decreased from 12.5V to 11.448 V with the discharge current of 6.4A/4seconds, then, for the next stage with 16 A/16seconds, voltage value decreased 10.248 V suddenly. For following stage (6.4A/4seconds), the voltage value increases 11.261V suddenly in terms of discharge current, which has effect on ionic movement, and so voltage value. Discharge capacity values were recorded as 1.93 Ah and 4.65Ah for free-air cooling and graphite matrix composite with phase change, respectively at the end. So, utilized capacity was increased 141% for graphite matrix composite with phase change in comparison to free-air cooling. Depending on rapid increase in operating temperature, the discharge capacity is restricted for free-air cooling. Energy capacity variations are given in Figure 10. Similar curve profiles are observed in Figure 10 compared to Figure 9. But, energy capacity (Figure 10), which means power delivered for an hour by the battery, is increasing as expected. Figure 10a and b show that the consumed energy of the battery package is higher for the graphite matrix composite case in comparison with the free-air cooling case. In other words, more amount of work is performed by battery package with graphite matrix composite. This is the result of extended safe operating conditions, in which temperature is one of the key parameters. The reached total energy capacity is also presented comparatively in column chart format in Figure 11. The energy capacity delivers 37.3Wh and 18.5 Wh for graphite matrix composite with phase change and free-air cooling, respectively. This provides 102 % more power for an hour for graphite matrix composite case.

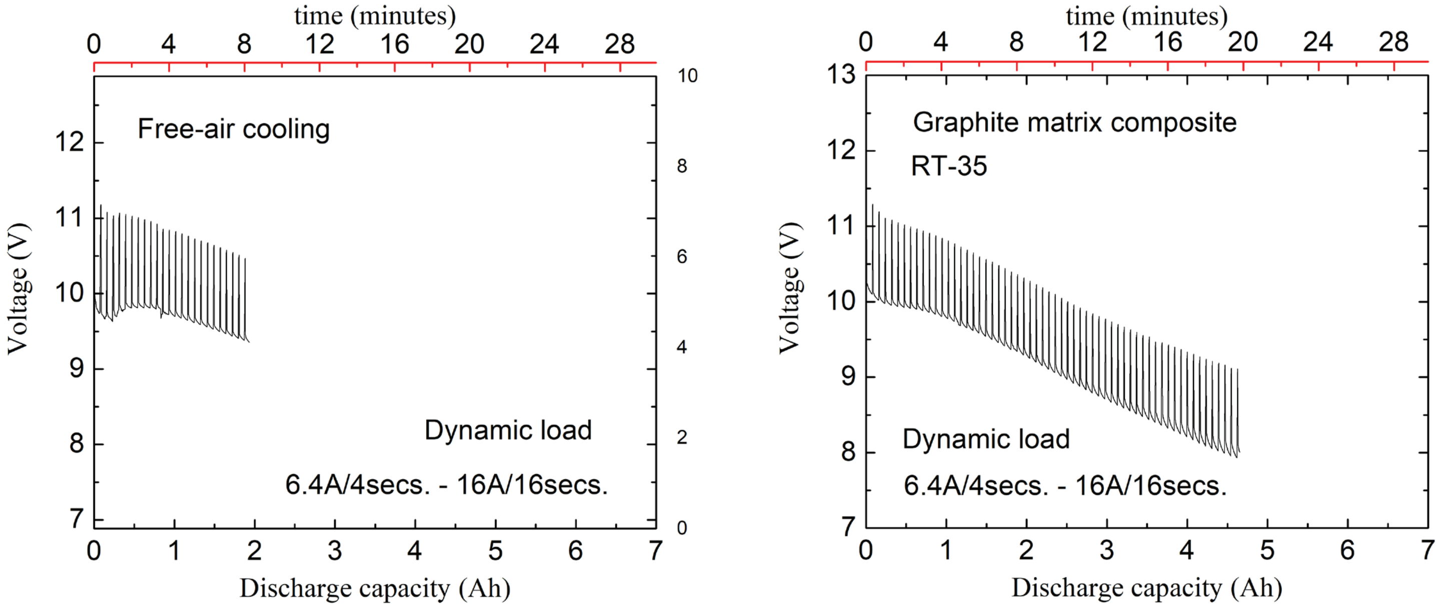

(a)

(b)

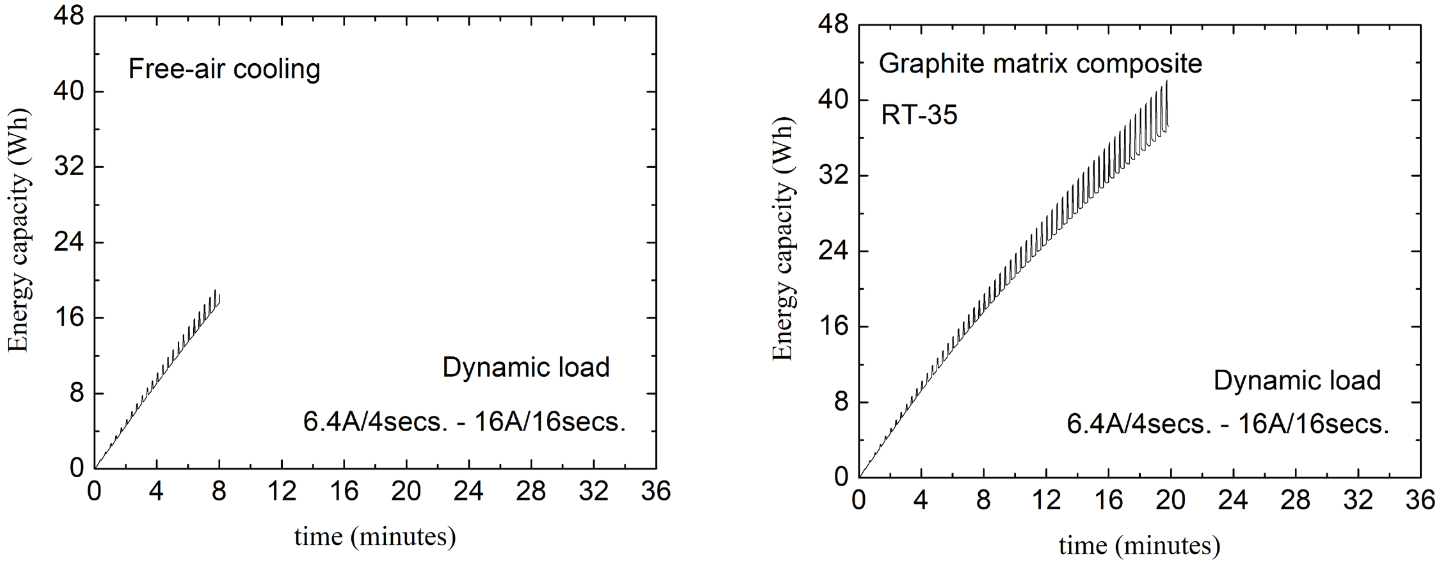

(c)

(d)

Figure 10. Energy capacity variation: free-air cooling (a), graphite matrix composite (b)

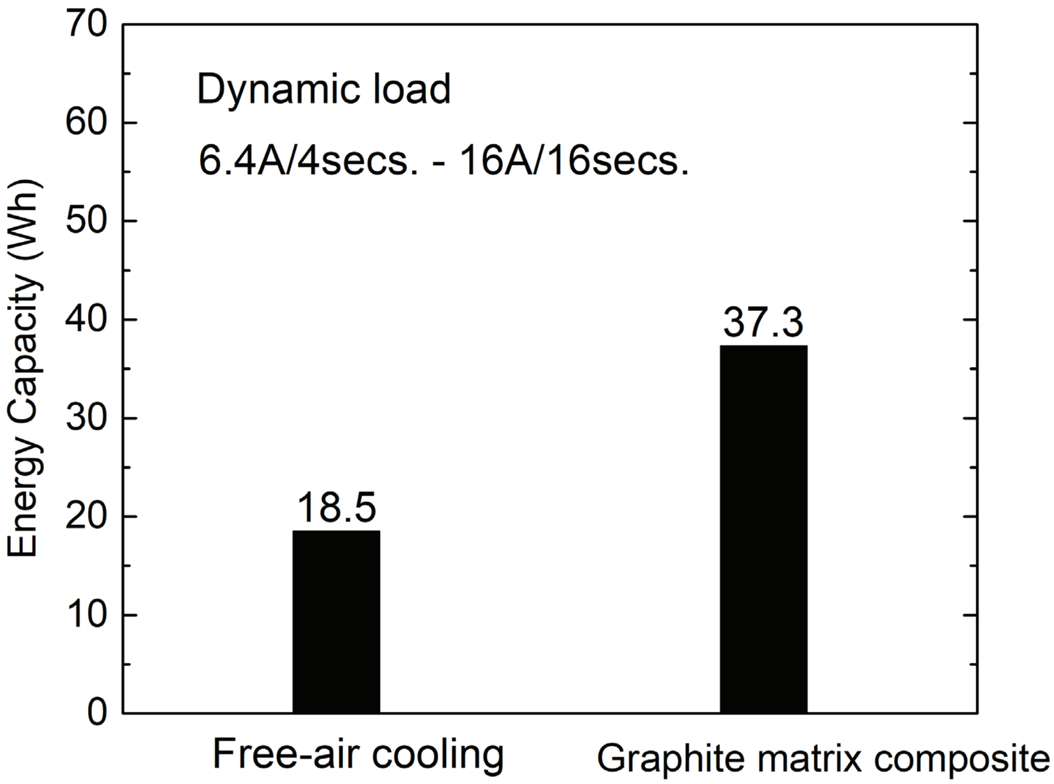

Figure 11. Total energy capacity values

4. Conclusion

In this experimental study, the effect of graphite matrix composite with phase change on the li-ion battery package thermal and electrical performance is investigated under square wave load form. The results show that the graphite matrix composite with phase change achieves considerable enhancement in thermal and electrical performance of small-scale battery package (3s2p) The main conclusions may be summarized as follows:

- For the graphite matrix composite with phase change, operating temperature and temperature gradient on the li-ion module is diminished by 34.7 % and 34 %, respectively, in comparison with free-air cooling.
- For the graphite matrix composite with phase change, the rate of temperature rising is decreased by about %70 in comparison with free-air cooling.
- For the PCM/graphite matrix, the safe operating time is enhanced 140 % compared to free-air cooling.
- For the PCM/graphite matrix, the utilized capacity, and energy capacity are increased by 141% and 102%, respectively, compared to free-air cooling.

References

Ahmed, S.F. et al., 2022. Integration of phase change materials in improving the performance of heating, cooling, and clean energy storage systems: An overview, Journal of Cleaner Production, 364, 132639.

Akula, R. and Balaji, C., 2022. Thermal management of 18650 Li-ion battery using novel fins–PCM–EG composite heat sinks, Applied Energy,316, 119048.

Arora, S., 2018, Selection of thermal management system for modular battery packs of electric vehicles: A review of existing and emerging Technologies, Journal of Power Sources, 400, 621-640.

Greco, A., Jiang, X., Cao, D., 2015. An investigation of lithium-ion battery thermal management using paraffin/porous-graphite-matrix composite. J. Power Sources, 278: 50–68.

He, J., Yang X, Zhang G, 2019. A phase change material with enhanced thermal conductivity and secondary heat dissipation capability by introducing a binary thermal conductive skeleton for battery thermal management. Applied Thermal Engineering, 148: 984-991.

Li, J., Huang, J., Cao, M., 2018. Properties enhancement of phase-change materials via silica and Al honeycomb panels for the thermal management of LiFeO4 batteries, Appl. Therm. Eng., 131, 660-668.

Jiang, G.W., Huang, J.H., Fu, Y.S., Cao, M., Liu, M.C, 2016. Thermal optimization of composite phase change material/expanded graphite for li-Ion battery thermal management. Thermal Engineering, 108: 1119-1125.

Kang, S, Choi, J.Y., Choi, S., 2019. Mechanism of heat transfer through porous media of inorganic intumescent coating in cone calorimeter testing. Polymers, 11(2): 1-16.
Kizilel, R., Lateef, A., Sabbah, R., Farid, M.M., Selman, J.R., Al-Hallaj, S., 2008. Passive control of temperature excursion and uniformity in high-energy Li-ion battery packs at high current and ambient temperature. Journal of

Power Sources, 183(1): 370-375.
Kizilel, R., Sabbah, R., Selman, J.R., Al-Hallaj, S., 2009. An alternative cooling system to enhance the safety of Li-ion battery packs. Journal of Power Sources, 194(2): 1105-1112.

Liu, H., Wei, Z., He, W., Zhao, J., 2017. Thermal issues about Li-ion batteries and recent progress in battery thermal management systems: A review. Energy Conversion and Management, 150: 304-330.

Lv, Y. et al., 2016. Experimental study on a novel battery thermal management technology based on low density polyethylene-enhanced composite phase change materials coupled with low fins, Applied Energy, 178, 15, 376-382.

Mallow, A., Abdelaziz, O., Graham, S., 2018. Thermal charging performance of enhanced phase change material composites for thermal battery design. Int. J. Thermal Science, 127: 19-28.

Mills, A., Farid, M., Selman, J.R., Al-Hallaj, S., 2006. Thermal conductivity enhancement of phase change materials using a graphite matrix. Thermal Engineering, 26(14-15): 1652-1661.

Py, X., Olives, R., Mauran, S., 2001. Paraffin/porous-graphite-matrix composite as a high and constant power thermal storage material. Int. J. Heat Mass Transfer, 44(14): 2727–2737.

Somasundaram, K., Birgersson, E., Mujumdar, A.S., 2012. Thermal–electrochemical model for passive thermal management of a spiral-wound lithium-ion battery. Journal of Power Sources, 203: 84-96.

Wang, W., Zhang, X., Xin, C., Rao, Z., 2018. An experimental study on thermal management of lithium ion battery packs using an improved passive method, Appl. Therm. Eng., 134, 163-170.

Wilke, S., Schweitzer, B., Khateeb, S., Al-Hallaj, S., 2017. Preventing thermal runaway propagation in lithium-ion battery packs using a phase change composite material: an experimental Study. J. Power Sources, 340: 51-59.

Wu, W., Yang, X., Zhang, G., Chena, K., Wang, S., 2017. Experimental investigation on the thermal performance of heat pipe-assisted phase change material-based battery thermal management system. Energy Conversion and Management, 138: 486-492.

Wu, W., Yang, X., Zhang, G., Ke, X., Wang, Z., 2016. An experimental study of thermal management system using copper mesh-enhanced composite phase change materials for power battery pack. Energy, 113: 909-916.

Xin, Q., Xiao, J., Yang, T., Zhang, H., Long, X., 2022. Thermal management of lithium-ion batteries under high ambient temperature and rapid discharging using composite PCM and liquid cooling, Applied Thermal Engineering, 210, 118230

Ling, Z., Wen, X., Zhang, Z., Fang, X., Gao, X., 2018. Thermal management performance of phase change materials with different thermal conductivities for Li-ion battery packs operated at low temperatures, Energy, 144, 977-983.

Zhang, S., Feng, D., Shi, L., Wang, L., Jin, Y., 2021. A review of phase change heat transfer in shape-stabilized phase change materials (ss-PCMs) based on porous supports for thermal energy storage. Renewable and Sustainable Energy Reviews, 135: 110127.

Zichen, W., Changqing, D., 2021. A comprehensive review on thermal management systems for power lithium-ion batteries. Renewable and Sustainable Energy Reviews, 139: 110685.

Zou, T., Liang, X., Wang, S., Gao, X., Zhang, Z., Fang, Y., 2020. Effect of expanded graphite size on performances of modified CaCl2·6H2O phase change material for cold energy storage. Microporous and Mesoporous Materials, 305, 110403.

Comparison of Corrosion and Antibacterial Properties of Silver Coatings on Ti6AL4V by Magnetron Sputtering

Emrah MELETLİOĞLU[1*],
Recep SADELER[1]

[1]Atatürk Üniversitesi, Mühendislik Fakültesi, Makine Mühendisliği Bölümü, 25242, Erzurum, Türkiye

Emrah MELETLİOĞLU, ORCID No: 0000-0002-6123-1609,

Recep SADELER, ORCID No: 0000-0001-5380-9733

**Sorumlu yazar e-posta: emrahmeletli@atauni.edu.tr*

Özet: Bu çalışmanın amacı, dental implant malzemesi olarak kullanılan Ti6Al4V alaşımının yüzeyine PVD (Magnetron Sputtering) yöntemi ile biriktirilen gümüş tabakasının korozyon davranışını ve antimikrobiyal etkisini belirlemektir. Kaplamalar, aynı kaplama koşulları altında farklı biriktirme süreleri kullanılarak elde edilmiştir. Kaplamaların kesit morfolojileri ise taramalı elektron mikroskobu (SEM) kullanılarak tespit edilmiştir. Kaplamaların fazları X-ışını difraksiyonu (XRD) kullanılarak tespit edilmiştir. PVD yöntemi ile kaplanmış ve işlemsiz Ti-6Al-4V numunelerin üzerinde korozyon deneyleri Kokubo'nun simüle edilmiş vücut sıvısı (SBF) pH 7.4 ve 36.5 °C çözeltisi içinde ve normal atmosfer şartlarında gerçekleştirilmiştir. Buna ek olarak, In vitro anti-bakteriyel etkinlik deneylerinde numunelerin yüzeylerine E. coli (Escherichia coli) ve S. aureus (Staphylococcus aureus) mikroorganizmaları sürülerek kaplamanın antibakteriyel özelliği araştırılmıştır. Antibakteriyel özelliklerini ölçmek için ise plaka sayma yöntemi kullanılmıştır. XRD sonuçlarına göre numunelerin yüzeylerindeki kaplama tabakaların homojenliği, SEM analiziyle elde edilen kesit morfolojileri ile de desteklenmiştir. Potansiyodinamik polarizasyon test sonuçları, gümüş kaplamadan sonra korozyon direncinin arttığını göstermektedir. In vitro anti-bakteriyel etkinlik deneyleri sonucunda, PVD ile kaplanmış numunelerde E. Coli ve S.Aureus mikroorganizmalarının tutunumu, kaplanmamış numuneye göre daha az çıkması, kaplamanın anti-bakteriyellik yönünden uygun olduğunu göstermiştir.

Anahtar Kelimeler: Ti6Al4V, Gümüş, DC Püskürtme, Korozyon, Antibakteriyel özellik

The aim of this study is to determine the corrosion behavior and antimicrobial effect of the silver layer deposited on the surface of the Ti6Al4V alloy, which is used as a dental implant material, by the PVD (Magnetron Sputtering) method. Coatings were obtained using different deposition times under the same coating conditions. The cross-sectional morphology of the coatings was determined using scanning electron microscopy (SEM). The phases of the coatings were determined using X-ray diffraction (XRD). Corrosion experiments on PVD-coated and untreated Ti-6Al-4V samples were carried out in Kokubo's simulated body fluid (SBF) pH 7.4 and 36.5 °C solution and under normal atmospheric conditions. In addition, the antibacterial properties of the coating were investigated by applying E. coli (Escherichia coli) and S. aureus (Staphylococcus aureus) microorganisms on the surfaces of the samples in in vitro antibacterial activity experiments. Plate counting method was used to measure its antibacterial properties. According to the XRD results, the homogeneity of the coating layers on the surfaces of the samples was also supported by the section morphologies obtained by SEM analysis. The potentiodynamic polarization test results show that corrosion resistance increases after silver plating. As a result of in vitro antibacterial activity tests, the adhesion of E. Coli and S. Aureus microorganisms in the PVD-coated samples and the less outgrowth of the uncoated samples showed that the coating was suitable in terms of antibacteriality.

Keywords: Ti6Al4V, Silver, DC Sputter, Corrosion, Antibacterial property

1. Giriş

Tıp endüstrisinde benzersiz mekanik özelliklere, korozyon ve yorulma direncinin yanı sıra biyouyumluluğa sahip biyomalzemelere ihtiyaç duyulmaktadır (Liu ve ark., 2019). Medikal endüstri alanında, saf titanyum (CP-Ti) alaşımları, düşük elastisite modülü, mükemmel mukavemet/ağırlık oranı, korozyona karşı üstün direnç, kolay imalat, vb. nedeniyle implant uygulamaları için kullanılır (Elias ve ark., 2008). Bununla birlikte, saf titanyumun (CP-Ti) en büyük dezavantajı, cilalama zorluğu, düşük mukavemeti ve zayıf aşınma direncidir. Bu veriler ışığında, Ti6Al4V alaşımı sahip olduğu mekanik ve biyouyumluluk özellikleri nedeniyle ilgi görmüştür. Yapılan çalışmalar, Ti6Al4V alaşımının daha iyi korozyon direnci ve yüksek mukavemette iyi sonuçlar verdiğine dikkat çekmektedir (Injeti ve ark., 2019). Ancak, tıbbi uygulamalardaki aktif araştırmalara rağmen, implantlar ve protezlerle ilgili enfeksiyon veya iltihaplanma sorunu hala devam etmektedir (Vasilev ve ark., 2009). İmplantlara bağlı bakteriyel enfeksiyonlar, implant veya protez yüzeyinde iltihaplanmaya neden olarak geri dönüşü olmayan implant kayıplarına neden olur (Yanovska ve ark., 2019). Bu ciddi duruma ek olarak korozyon da biyouyumluluğu ve mekanik özellikleri olumsuz etkileyebilir. Ağız içerisindeki ortam sürekli değişen pH değerlerinden dolayı korozif bir bölge olarak kabul edilir. (Licausia ve ark., 2013) Bundan dolayı, metalik implantlar vücut ortamına yerleştirildiklerinde korozyona uğrayabilmektedirler. Çiğneme esnasında metalik implantlarda, elektrokimyasal reaksiyonlar oluştuğunda iyon salınımı gerçekleşmektedir. Bu süreçte kullanılan implantların biyouyumluluğu azalıp, vücutta istenmeyen alerjik reaksiyonlara ve komplikasyonlara sebep olabilirler (Taddei vd. 2004). Bu yüzden yüzeye bakteri yapışmasını önlemek, implant enfeksiyonlarını daha da azaltmak ve korozyon gibi olumsuz etkilei gidermek için titanyum implantlarının antibakteriyel malzemelerle kaplanması gerekmektedir.

Titanyum implantların yüzeyi, bakteri yapışmasını önlemek ve implant enfeksiyonlarını azaltmak için çeşitli antibakteriyel malzemelerle (Ag, Cu, Zn vb.) kaplanır (Franci ve ark., 2015). Bu malzemeler içinden gümüş, çok çeşitli antibakteriyel özellikleri nedeniyle bir adım daha öne çıkmaktadır. Gümüşün ilgi çekici özelliği geç antik çağlardan beri bilinmektedir. Ayrıca bu elementin insan vücudundaki düşük toksisitesinden dolayı, ameliyat sırasında ve sonrasında bakteri tutunmasını engellediği de varsayılmaktadır (Stuart ve ark., 2022). Gümüş partikülleri bakteri ve mikroorganizmaların hücre duvarı ve hücre zarından geçerek bu bakteri ve mikroorganizmaların DNA'sını inhibe eder (Taglietti ve ark., 2014). Sonuç olarak, biyomalzemeler söz konusu olduğunda, bu tip gümüş yüzey modifikasyonları, özellikle temas öldürme aktivitesi yoluyla bakteri kolonizasyonunu önleyebilir. Son zamanlarda, nanoyapılı bir filmde gümüşün, yara iyileşme periyodu esnasında mükemmel antibakteriyel yetenek sergilediği de görülmüştür (Mao ve ark., 2022). Yüzey modifikasyonu yoluyla antibakteriyel kaplamaların doğrudan uygulanması basit ve uygun maliyetli bir yaklaşımdır. Biyomalzemelerin korozyon direncini, mekanik ve aşınma özelliklerini geliştirmek için bazı yüzey işleme ve kaplama yöntemleri sıklıkla kullanılmaktadır (Ye ve ark., 2009). Özellikle DC magnetron püskürtme yöntemi, titanyum alaşımları için düzgün yüzey fizibilitesi, daha kısa biriktirme zaman aralıkları ve diğer yüzey modifikasyon yöntemlerine kıyasla nispeten daha düşük sıcaklıklarda gerçekleştirilebilmesi gibi avantajlara sahiptir. Literatürde farklı zaman aralıklarında magnetron püskürtme ile gümüş kaplanmış Ti6AL4V alaşımlarının korozyon ve antibakteriyel özelliklerini karşılaştıran çalışmalar azdır.

Bu araştırmanın temel amacı, Ti6Al4V alaşımları üzerindeki Ag tabakalarının korozyon ve antibakteriyel özellikleri üzerine PVD kaplama süresinin etkilerini incelemektir.

2. Materyal ve Yöntem

2.1.Materyal

13 mm kalınlığındaki Ti6Al4V alaşım numuneleri, 20 mm çapındaki silindirik bir çubuktan tel kesme ile kesilmiş ve kimyasal kompozisyonu Çizelge 1'de verilmiştir. Numunelerin mekanik parlatılması için 200'den 1600'e kadar farklı boyutlardaki SiC grit kağıtları kullanılmıştır. Bu çalışmada, numunelerin osteoblast aktivitesini artırmak için asit ile pürüzlendirme işlemi uygulanmıştır. Bu işlem için %60'lık H2SO4 çözeltisi, %10'luk HCl çözeltisi ve distile su, sırasıyla, 1:1:2 oranında karıştırılarak bir asit çözeltisi hazırlanmıştır. Asit ile pürüzlendirme işlemine tabi tutulacak numuneler sıcaklığı 100 ˚C olacak bu asit çözeltisine 20 dk boyunca daldırılmıştır. Daha sonra numuneler distile suda 10 dk boyunca ultrasonik titreştirici ile temizlenmiştir.

Çizelge 1. Ti6Al4V alaşımının kimyasal kompozisyonu

Element	Al	V	Fe	Ti	Other
Kompozisyon (%Ağırlık)	6	4.1	<0.30	Kalan	0.40

Çizelge 2. Gümüş Kaplamalar için deney şartları

Numune Adı	Kaplama Türü ve Süresi	Kaplama Şartları (DC)
Ti6Al4V	Ag Kaplama 30 Dk	İyonlaşma Gazı: Argon (99.999%) Target Açısı : 35 ° Target Uzaklığı 11.8 cm Basınç : 6,8x10^{-3} mTorr Sıcaklık: 20 °C Dönme Hızı: 3 rpm DC Gücü:100 W
Ti6Al4V	Ag Kaplama 45 Dk	
Ti6Al4V	Ag Kaplama 60 Dk	

Ti6Al4V alaşımlarının gümüş filmler ile PVD kaplama işlemi Üniversitemiz Doğu Anadolu Yüksek Teknoloji Araştırma ve Uygulama Merkezinde (DAYTAM) yer alan temiz odada yapılmıştır. Gümüş kaplamalar için püskürtme zamanları hariç sabit deney koşulları seçilmiş olup, kullanılan deney planları ise Çizelge 2'de verilmiştir. Kaplama işleminin hemen öncesinde numuneler, etil alkol içerisinde ultrasonik temizleme işlemine tabi tutulmuş, ardından PVD Sistemi içerisine yerleştirilmiştir.Kaplama kalınlığının üniform olması için tabna malzemeler 3 rpm hızında döndürülmüştür. PVD kaplamalarda Ag katı hedeflerden sıçratma yapılmış ve iyonlaşma gazı olarak sadece argon kullanılmıştır.Düşük gerilmeli, yoğun, tok ve üniform bir film yapısı elde etmek için taban malzemelere, darbeli doğru akım (pulsed-dc) verilmiş ve sistem içerisinde taban malzemeler yine 3 rpm hızında döndürülmüştür.

2.2. Kaplamaların Mikroyapı Analizleri

Numunelerin yüzey pürüzlülüğü değerleri, bir prob ucu mekanik profilometrisi (Kla Tencor Stylus Profile P7) kullanılarak değerleri ölçülmüştür Yüzey özelliklerini tanımlamak ve değerlendirmek için kaydedilen tüm ölçümler, her numunede 100x100 μm alanın analiz edilmesiyle elde edilmiştir. Kaplanan yüzeylerin morfolojileri taramalı elektron mikroskobu (Quanta FEG 250 taramalı elektron mikroskobu (SEM) kullanılmıştır. Ti6Al4V alaşımlarının, DC manyetik alanda sıçratma yöntemi ile büyütülen gümüş filmlerin kristalografik yönlenmelerin tespitinde, λ=1.5418 Ao (0,154 nm) dalga boyuna sahip Cu-Kα kaynaklı GNR explorer XRD (X ışını kırınım ölçer) cihazı kullanılmış olup, çalışma şartları olarak -111-168 derece tarama açısı aralığında, 1 derece/dak tarama hızında, 0.0001 derece tarama adımında ve max 60 kV, max 100 mA enerji değerlerinde analizler yapılmıştır.

2.3. Elektrokimyasal Korozyon Deneyleri

PVD yöntemi ile kaplanmış numuneler ve taban malzeme Ti-6Al-4V alaşımları üzerinde korozyon deneyleri Kokubo'nun simüle edilmiş vücut sıvısı (SBF) pH 7.4 ve 36.5 °C çözeltisi içinde (Kokubo & Takadama, 2006), normal atmosfer şartlarında ve Gamry Series G 750 potensiostat/galvanostat polarizasyon test cihazında gerçekleştirilmiştir. SBF'nin kimyasal bileşimi Çizelge 3'de verilmiştir. SBF hazırlamak için reaktif dereceli NaHC03, NaCl, KCl, K2HPO4 • MgCl2 • 6H2O, 3H2O, CaCl2 ve Na2SO4 distile suda çözüldü. Reaktiflerin çözünmesi sırasında sıcaklık ve pH değerleri de ayrıca kontrol edildi.

Kimyasal	1 L SBF için gerekli miktar
NaCl	8.035 g
$NaHCO_3$	0.355 g
KCl	0.225 g
$K_2HPO_4 \cdot 3H_2O$	0.231 g
$MgCl_2 \cdot 6H_2O$	0.311 g
1 kmol/m^3 HCl	39 ml
$CaCl_2$	0.292 g
Na_2SO_4	0.072 g
Tris ($(CH_2OH)_3CNH_2$)	6.118 g
1.0M-HCl	0–5 ml

Çizelge 3. Güncellenmiş Simüle Vücut Sıvısı Hazırlamak için kullanılan çözeltiler pH 7.40 (Kokubo & Takadama, 2006)

Polarizasyon ölçümleri; Ag/AgCl referans elektrot (RE), karşıt elektrot (CE) olarak platin tel ve çalışma elektrotu (WE) deney numunesi kullanılarak üç elektrot tekniğine göre 0.29 cm2 lik alanda yapılmıştır. Her test için yeni bir solüsyon kullanılmıştır. Numune açık devre potansiyeline (OCP) erişinceye kadar yaklaşık 60 dakika bekletilmiştir. Tafel deneylerinde başlangıç ve bitiş potansiyel değerleri açık devre potansiyeli (Eoc) olarak ölçülmüştür. Potansiyodinamik polarizasyon ölçümleri, 0,5 mV s-1'lik bir tarama hızında -2000 mV - Ocp +2000 mV - Ref'den tarama yapılarak gerçekleştirilmiştir.

2.4 Antibakteriyel Test

Bu çalışmada Ti6Al4V numunelerinin antibakteriyel özelliklerini ölçmek için plaka sayma yöntemi ile gerçekleştirilmiştir (Zhu ve ark., 2015, Patil ve ark., 2019). Test için iki bakteri türü, Escherichia coli ATCC25922 ve Staphylococcus aureus ATCC25923 kullanılmıştır. Bakterilerin donmuş tozları pH ¼ 7.2 olan bir kültür ortamında çözündürüldü ve 37 °C'de 24 saat yetiştirildi. Daha sonra bakteri süspansiyonu elde edildi. Daha sonra, her numunede mililitre başına ~4 x 108 koloni oluşturan birim (CFU/mL) yaklaşık konsantrasyona sahip 100 µL hacimde aşılanmış bir bakteri çözeltisi kullanıldı. Tüm numuneler, deneylerden yaklaşık 1 saat önce UV ışınlarıyla sterilize edilmiştir. Numuneler petri kabına yerleştirilmiş ve 37 °C'de 24 saatlik bir inkübasyon süresinden sonra, numune üzerinde canlı bakterilerin üremesiyle oluşturulan koloniler sayılarak optik görüntüler elde edilmiştir. Mililitre kültür çözeltisi başına koloni oluşturan birim (CFU) şu formülle hesaplandı:

CFU/mL = (Koloni sayısı/plakadaki kültür kapasitesi) × Seyreltme faktörü.

Seyreltme faktörü, seyreltme sonrası bakteri süspansiyonunun nihai hacminin, seyreltme öncesi bakteri süspansiyonu hacmine oranı olarak tanımlanmıştır.

3. Bulgular ve Tartışma

3.1. Mikroyapı analizleri

Farklı süreler için PVD işlemi görmüş Ti6Al4V ve Ti15Mo alaşımlarının XRD modellerindeki varyasyon Şekil 1'de gösterilmektedir. XRD sonuçlarına göre, Şekil 1 (a)'da gösterildiği gibi işlemsiz Ti6Al4V numunelerinin, tamamen α-Ti [96-900-8518] ve β-Ti [96-900-8555] fazlarından oluştuğu görülmektedir. Şekil 1(b)'de, her iki numune için çeşitli sürelerde (30, 45 ve 60 dakikalık) biriktirilen Ag+ filmlerin XRD grafikleri verilmiştir. XRD sonuçları, gümüş fazların [96-500-0219] (111) yönünde, ve paralel düzlemde (200), (202) ve (311) küçük katkılarla piklerin oluştuğunu göstermektedir. Gümüş tek kristalli kübik bir yapıya sahip olduğundan, nanoparçacık benzeri yapıların çoğunun, alt-tabakaya paralel kübik yüzlere sahip kristalitler aracılığıyla oluşturulduğu tahmin edilebilir (Andrade ve ark., 2015). Kaplama kalınlığı 1,6 µm'den fazla olduğunda, tepe noktasının yoğunluğundaki pik noktasında (111) güçlü bir azalma söz konusudur. Ayrıca kaplama kalınlığı arttıkça (200), (202) ve (311) piklerin kaybolduğu da görülmektedir. Film kalınlığı arttığında, bu kristalitlerin bir birleşimi olur, ancak aynı kristal düzlemlerinde etkileşmezler. Scherrer denklemine göre, bu çarpışmalı birleşme, kristalli bir katı için beklendiği gibi, özellikle [111] her yönde büyüyen kristalli büyük tanelere katkıda bulunur (Çomaklı ve ark., 2017). Ayrıca, Ag+ kaplanmış numunelerin geniş XPS spektrumlarında Vanadyum (V) elementine ait herhangi bir pik durumuna rastlanılmamıştır. V elementinin insan vücudundaki toksik etkisini önlemede bu durum son derece önemlidir (Subramanian ve ark., 2011).

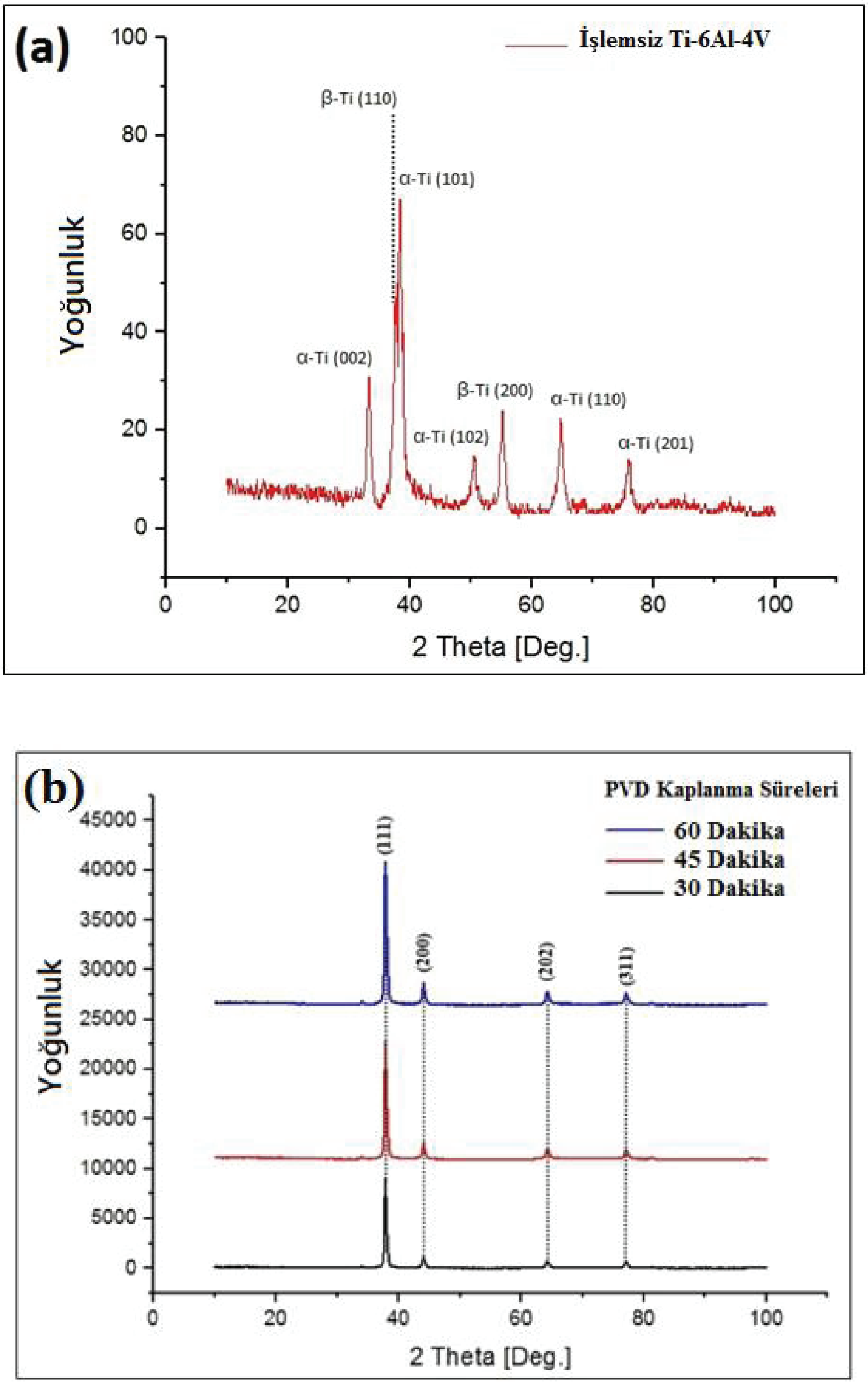

Şekil 1. XRD sonuçları: (a) İşlemsiz Ti6Al4V; (c) Gümüş Kaplı Ti6Al4V Numuneleri.

Ti6Al4V alaşımlarının yüzey pürüzlülük değerleri ve kaplama film kalınlıklarına ait değerler Çizelge 4'de gösterilmektedir.

Çizelge 4. Ti6Al4V alaşımlarının yüzey pürüzlülük ve film kalınlıklarına ait değerler

Numune	İşlem Parametreleri	Film Kalınlığı (µm)	Yüzey Pürüzlülüğü (µm)
Tİ6Al4V	İşlemsiz	-	0,310-0,321
	Aşındırılmış	-	2,010-2,124
	PVD 30 dk	1,00-1,10	0,212-0,224
	PVD 45 dk	1,58-1,62	0,243-0,255
	PVD 60 dk	1,92-2,07	0,276-0,289

İşlenmemiş numunelerin yüzey pürüzlülüğü Ra = 0.152 – 0.241 µm olarak bulunmuştur. Asitle aşındırma işleminden sonra yüzey pürüzlülük değerleri artmıştır. Yüzey pürüzlülüğünün artması osseointegrasyonu olumlu etkileyerek, implantın daha iyi tutunmasına neden olmaktadır. Asitle aşındırma işlemi sonrasında numunelerin yüzey pürüzlülük değeri Ra = ~2 µm olduğu tespit edilmiş olup, bu değer literatür çalışmalarıyla uyumludur (Chrcanovic ve ark., 2015). PVD kaplama işleminden sonra tüm numunelerin yüzey pürüzlülüğü düşük olmuştur. Ayrıca, daha ince tane boyutları nedeniyle tüm kaplamalar arasında 30 dakikalık kaplama süresi için en düşük yüzey pürüzlülüğü gözlemlenmiştir.

Üç farklı zaman aralığında kaplanan Ti6Al4V taban malzeme üzerine yüzey topografyası, kaplamalara kalınlıkları belirlenmesi için SEM kesit görüntüleri Şekil 2'de verilmiştir.

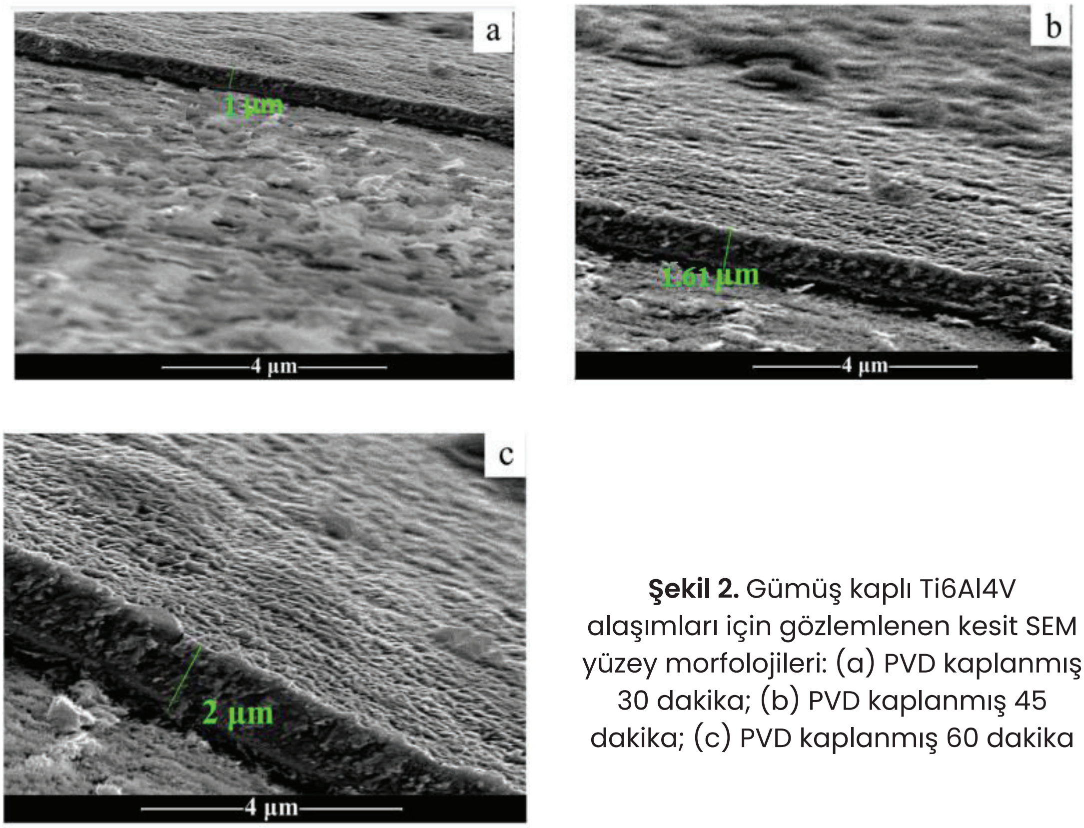

Şekil 2. Gümüş kaplı Ti6Al4V alaşımları için gözlemlenen kesit SEM yüzey morfolojileri: (a) PVD kaplanmış 30 dakika; (b) PVD kaplanmış 45 dakika; (c) PVD kaplanmış 60 dakika

Yüzey morfolojileri incelendiğinde, kaplama sürelerinin artmasıyla ince film kalınlık değerleri arttığı gözlemlenmiştir. Kaplama süresindeki artışlar, numunelerin yüzeyinde daha kompakt (sıkışmış, yoğun) morfolojik yapı oluşmasına neden olmuştur. Bu durum, daha uzun bir kaplama süresinin sonunda sıcaklıkta adatom hareketliliğini artıran bir artışa neden olduğu yüzey difüzyon etkisine atfedilebilir. Ayrıca, gümüş filmlerin nano sütunlu büyümesi, artan film kalınlığı ile bükülme eğilimindedir (Phaengam ve ark., 2021). PVD kaplama işlemi süresince numunelere sürekli gerilim uygulanması nedeniyle incelenen numunelerin tüm yüzey bölgelerinin homojen şekilde kaplandığı açık şekilde görülmektedir. Hedef malzemeden sıçratılan Ag+ iyonları numunelerin yüzeylerine yüksek hızlarda her yönden (tek yöne bağımlı olmadan) implante edilmiştir. Bu durum PVD kaplama işleminin temel prensibi ile uyumludur.

3.2. Elektrokimyasal Korozyon Deneyleri

Ti6Al4V alaşımları için kaydedilen polarizasyon eğrileri Şekil 3'de sunulmuştur.

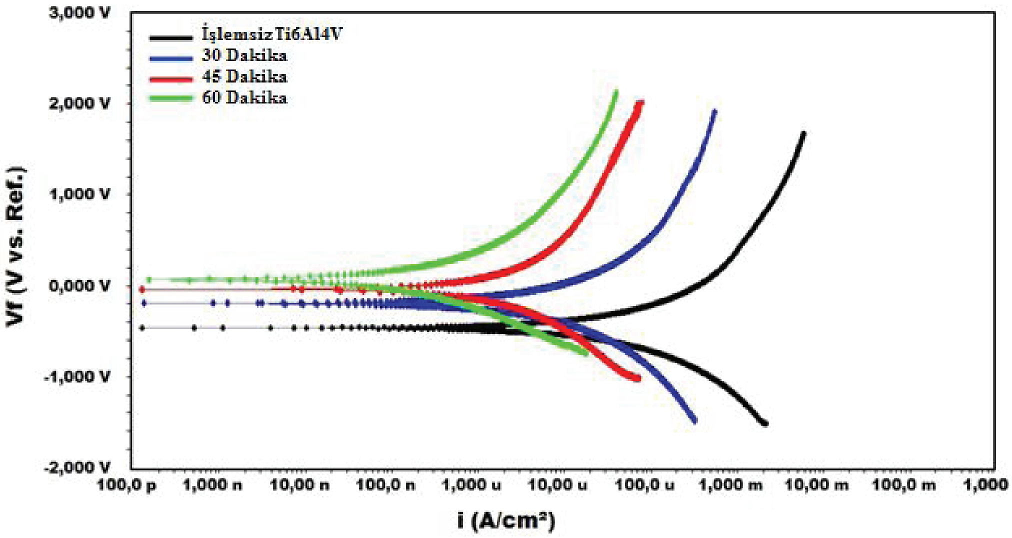

Şekil 3. İşlemsiz ve farklı sürelerde +Ag film kaplı Ti6Al4V numunelerine ait potansiyodinamik polarizasyon eğrileri

OCP değerlerine göre daha düşük bir değerden tarama yapılarak polarizasyon analizleri yapılmıştır. Korozyon potansiyeli (Ecorr), korozyon akım yoğunluğu (Icorr) ve korozyon hızı (mpy) gibi korozyon parametreleri Çizelge 5'te gösterilmiştir.

Çizelge 5. İşlemsiz ve farklı sürelerde +Ag film kaplı Ti6Al4V numunelerine ait korozyon testi sonuçları

İşlem Parametreleri	E_{corr}	I_{corr}	Korozyon Oranı (mpy)
İşlemsiz	-410 mV	$2x10^{-6}$ nA	0.209
PVD 30 dakika	-201 mV	$635x10^{-9}$ nA	0.041
PVD 45 dakika	-20 mV	$476x10^{-9}$ nA	0.055
PVD 60 dakika	62 mV	$205x10^{-9}$ nA	0.062

İşlem görmemiş Ti6Al4V numunelerinin korozyon potansiyeli (Ecorr) değeri -410 mV bulunmuştur. Polarizasyon eğrileri değerlendirildiğinde, +Ag film kaplı numunelerin korozyon özelliklerinde önemli bir gelişme görülmektedir. Gümüş film kaplamalı Ti6Al4V numuneleri için Ecorr değerleri sırasıyla -201 mV (30 dakika), -20 mV (45 dakika) ve 62 mV (60 dakika) olarak ölçülmüştür. Ti6Al4V numuneleri, yüzeylerinde doğal bir oksit tabakası ile iyi bir korozyon direncine sahiptir ve Ecorr değerinin gelişmesi, +Ag film kaplanmış numunelerin korozyon mukavemetindeki artışı göstermiştir. Bu durum + Ag film kaplamanın alaşımın çözünme hızını azalttığını ve daha kararlı bir pasif alana sahip olduğunu da göstermektedir.

Korozyon davranışını iyi anlamak için bir diğer önemli parametre de korozyon akım yoğunluğu (Icorr) değeridir. Gümüş film kaplamalı Ti15Mo numuneleri için İcorr değerleri sırasıyla 635x10-9 A/cm2 (30 dakika), 476x10-9 A/cm2 (45 dakika) ve 205x10-9 A/cm2 (60 dakika) olarak ölçülmüştür ki bu değer işlem görmemiş numuneye kıyasla (2,x10-6 A/cm2) daha düşüktür. Kaplama işleminden sonra, eğrilerin anodik kısmı daha düşük Icorr'a taşındı. Bu, anodik reaksiyonların kaplama işlemi ile sınırlandırıldığı ve titanyum için daha yüksek kimyasal stabilite ve koruma sağlandığı anlamına gelir (Hongxi ve ark., 2012). Ayrıca Icorr değerlerindeki +Ag film etkisi ile pozitif iyileşmesi bize göstermiştir ki kaplama kalınlığı arttıkça yüzeydeki oluşan gözeneklerinin çaplarının düşmesine neden olmaktadır. Kaplama kalınlığının uygun koşullarda artması ve numune üzerinde gözeneklerinin daha küçük olması taban malzemenin korozyon direncini arttırmaktadır (Yerokhin ve ark., 2000).

Korozyon testi sonrası numunelerin yüzey morfolojileri Şekil 4'de sunulmaktadır.

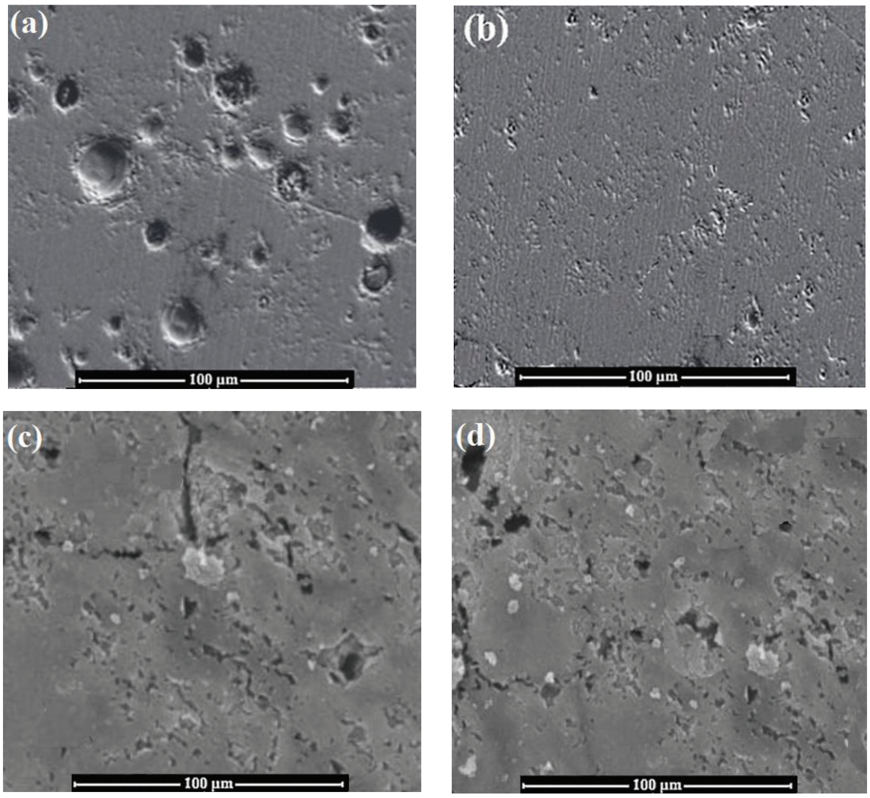

Şekil 4. Korozyon deneyi sonrası yüzey morfolojileri
(a) İşlemsiz Ti6Al4V;
(b) PVD 30 dakika;
(c) PVD 45 dakika ;
(c) PVD 60 dakika.

İşlem görmemiş Ti6Al4V (Şekil 4 (a)) numunelerde temel korozyon mekanizması lokalize korozyonun bir tipi olan çukurcuk şeklinde olduğu görülmüştür. Asitle pürüzlendirme işlemi ile birlikte +Ag film tabakasının oluşturduğu yapı titanyum malzemeleri üzerine yapılan kaplamalarda kaplama bütünlüğünün korunmasında yardımcı olmuştur. Gümüş film kaplamalı (30 dakika) Ti6Al4V (Şekil 4 (b)) numunesinin yüzeyi neredeyse hasarsızdı. Bu durumun korozyon testleri sırasında alaşım mikroyapısı üzerinde koruyucu ve caydırıcı pasif film (Ag oksit) ile ilişkili olduğu düşünülmektedir (Yetim 2016). Ancak gümüş film kaplamalı Ti6Al4V (Şekil 4 (c,d)) kaplama tabakasında derin çatlakların varlığı dikkat çekmektedir. Bu çatlaklar benzer çalışmalarda da tespit edilmiştir (Bakhsheshi-Rad ve ark., 2017). Ayrıca +Ag film kaplama (60 dakika) yüzeylerinde oksit tabakasının (beyaz renkli) varlığı görülmektedir. Bu çatlaklara nüfuz eden SBF, alt tabaka ile doğrudan temas haline geçerek korozyon sürecini hızlandırabilir.

3.3. Antibakteriyel Test Sonuçları

İşlem görmemiş ve +Ag film kaplı titanyum numunelerin antibakteriyel etkisini değerlendirmek için plaka sayma yöntemi kullanılmıştır. Her numunede bulunan bir dizi canlı bakteriyi gösteren optik fotoğraflar Şekil 5'de sunulmuştur.

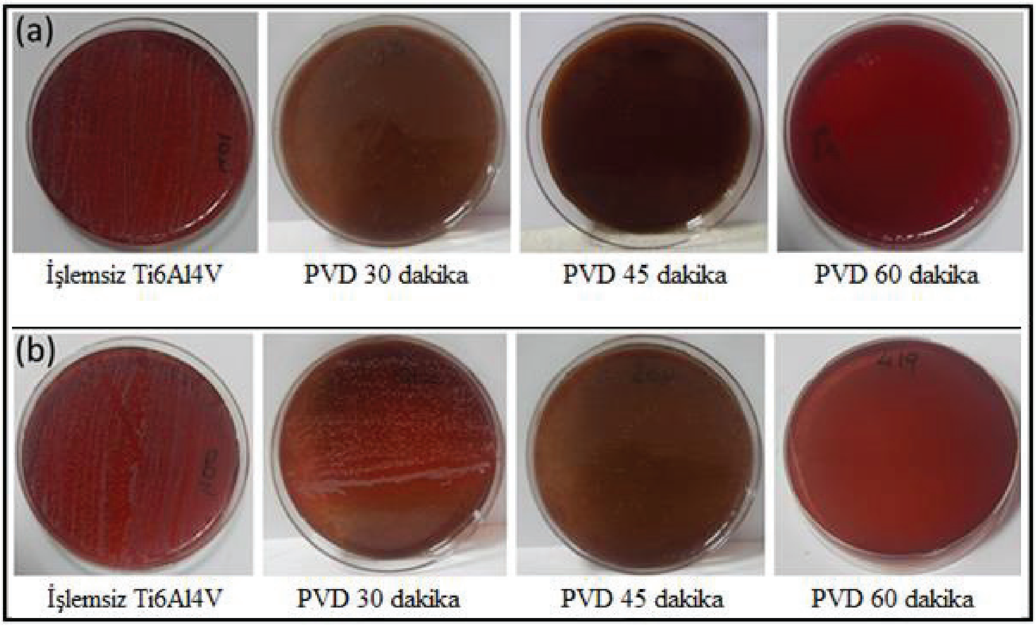

Şekil 5. Yüzey kolonizasyon sonuçları: (a) E. coli; (b) S. aureus; 24 saatlik sonuçlar

Bir koloni tek bir canlı bakteriden oluşmaktadır. Şekil 5 incelendiğinde işlem görmemiş titanyum numunelerinde bakteriyel film oluşumu gözlemlendiği görülmektedir. Bu durum, işlenmemiş titanyum yüzeyinde çok sayıda görünür bakteri olduğu anlamına gelir. Diğer taraftan, +Ag film kaplı titanyum numunesi yüzeylerinde, E. coli ve S. aureus bakterilerinin büyümesinde azalma görülmektedir. Antibakteriyel test sonuçlarına göre, PVD gümüş kaplama süresinin artmasıyla bakteri kolonileri giderek azaldığı tespit edilmiştir. İnkübasyon sırasında PVD gümüş kaplama (1µm) tabakasının bozulmasının gümüş iyonunun bakteriyel çözeltiye sızmasına izin vererek gerçekleşebileceği söylenebilir. Ancak artan film kalınlığı ile daha düzgün ve uyumlu kaplama elde edilmiş ve bunun sonucunda bakteriler titanyum yüzeyine ulaşamadığı için daha iyi antibakteriyel sonuçlar elde edilmiştir (Brobbey ve ark., 2019).

Her numune için hesaplanan CFU/mL değeri Şekil 6'da sunulmuştur.

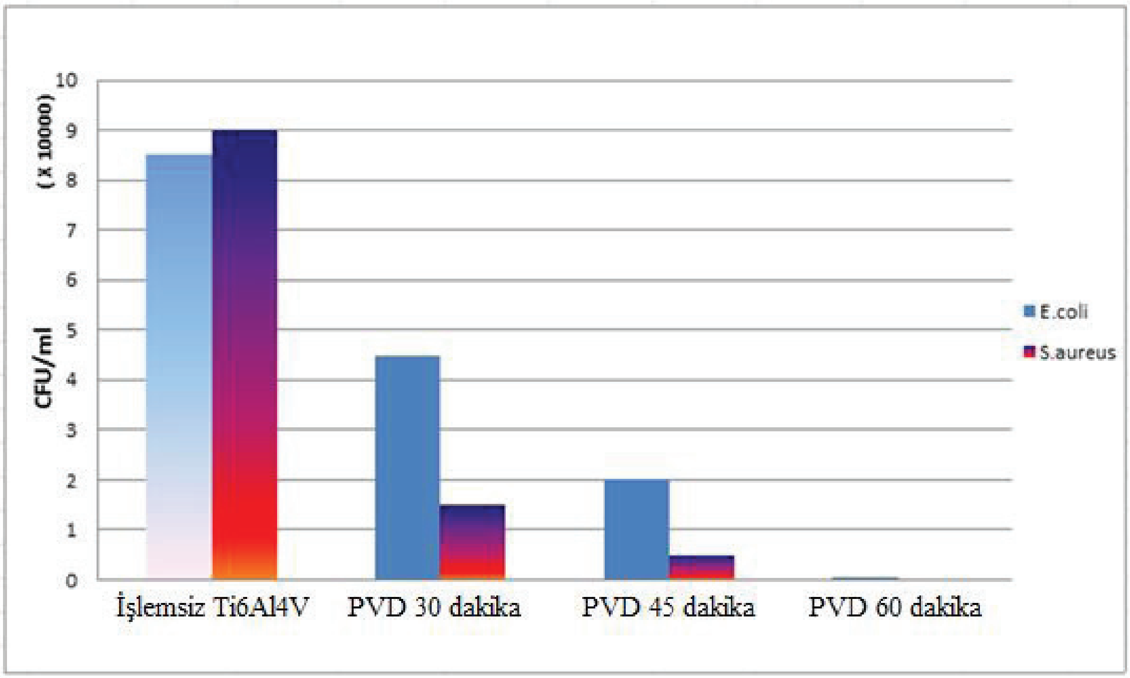

Şekil 6. Ti6Al4V yüzeyinin S. aureus ve E. coli'ye karşı antibakteriyel özelliğinin kantitatif sonuçları (CFU/mL cinsinden)

Şekil 6 incelendiğinde, işlem görmemiş titanyum numuneleri yüzeylerinde oldukça fazla koloni sayısı görülmektedir. Diğer taraftan, +Ag film kaplı titanyum numunelerinde ise bakteri kolonilerinin sayısının azaldığı görülmektedir. Şekil 4.28'e göre, gümüş kaplı Ti6Al4V yüzeyinin E. coli bakteri büyümesinin baskılama yeteneği S. aureus'tan daha az etkili olduğu görülmektedir. Bu durumun, Ag+ iyonunun reaksiyona girmesi için geniş bir yüzey alanı sağlayan S. aureus'un küresel formuyla ilişkili olduğu düşünülmektedir (Zhu ve ark., 2015). Antibakteriyel sonuçlara göre gümüşün iyi bir antibakteriyel özelliğe sahip olmasının arkasında iki ana neden vardır. Birinci neden, dış hücre duvarı ile temas eden, reaktif oksijen türleri yardımıyla oksidatif strese neden olan ve ardından hücre zarını tahrip eden Ag+ iyonunun rolüdür (Chernousova ve ark., 2013). Zarlar parçalandığında, gümüş iyonu sitoplazmaya girer ve hücre içi yapıları ortadan kaldırır. İkinci neden, gümüş kaplı Ti15Mo yüzeyinde bulunan bakteri hücreleri ve gümüş nanoparçacıkları arasındaki doğrudan fiziksel temastır. Bu doğrudan temas, bakterilerdeki hücre duvarlarının gerilmesine ve hasar görmesine neden olduğu düşünülmektedir.

Bu sonuçların analizi, PVD gümüş kaplı numunelerin bakteri üremesinde bir azalma sağladığı sonucuna varılmasını sağlar. PVD 60 dakikalık gümüş kaplanmış numunenin bakterisit etkisi, seyreltmede hiçbir bakteri kolonisinin bulunmaması özellikle ilginç sonuçlanmıştır. Tüm numuneler için antibakteriyel test koşulları aynı olduğundan, antimikrobiyal etkideki farklılıklar doğrudan Ag+'nın çevreye salınma süresine bağlanabilir. Ag+ iyon salımı film mikro yapısı, partikül boyutu, film kalınlığındaki dağılım, elektrolit erişiminin hedef açısı ve partikül çözünmesi parametrelerden etkilenir. Özellikle, yüzey oluşturan agregalarda zaman içinde gümüşün ayrılması, antibakteriyel etkinin nicel olarak tahmin edilmesi için son derece önemlidir. Bununla birlikte, E. coli ve S.aureus ile enfeksiyonun önlenmesi için Ag+ iyon salımının pozitif bir tepkisi tüm vakalarda kanıtlanmıştır, ancak 45 dakikanın üzerinde kaplamanın gösterdiği sitotoksik etkiler göz önüne alındığında (Mihailescu ve ark., 2016), gümüş dopingi bu eşiğin altında sınırlandırılmalıdır.

4. Sonuç

Bu çalışmada, dental implant yapımında kullanılan Ti6Al4V alaşımından hazırlanan numunelerin yüzeylerinde, gümüş hedef malzeme kullanılarak, PVD yöntemi ile farklı sürelerde kaplamalar elde edilmiştir. Buna göre;

- Kaplamasız numune yüzeylerinde α-Ti ve α-Ti faz pikleri görülürken, kaplama işleminden sonra numunelerde sadece Ag pikleri tespit edilmiştir. XRD sonuçlarına göre numunelerin yüzeylerindeki tabakaların homojenliği, SEM analiziyle elde edilen kesit morfolojileri ile de desteklenmiştir.Ayrıca, gümüş ile kaplanmış kaplanmamış numunelere kıyasla daha düşük yüzey pürüzlülüğüne sahiptir ve en düşük yüzey pürüzlülüğü değeri 30 dakika boyunca biriktirilen gümüşten elde edilmiştir.
- Potansiyodinamik polarizasyon test sonuçları, gümüş kaplamadan sonra korozyon direncinin arttığını göstermektedir. Bu durumun korozyon testleri sırasında alaşım mikroyapısı üzerinde koruyucu ve caydırıcı pasif film (Ag oksit) ile ilişkili olduğu düşünülmektedir. İşlem süresi arttıkça korozyon direnci arttığı, en iyi korozyon özelliklerinin 60 dakika gümüş film ile kaplanmış numune için elde edildiği görülmektedir. Ancak, SEM analizlerindeki 60 dakika gümüş film kaplama tabakasında derin çatlakların varlığı ve yüzeylerinde oksit tabakasının (beyaz renkli) oluşumlar dikkat çekmektedir. Bu çatlaklara nüfuz eden SBF, alt tabaka ile doğrudan temas haline geçerek korozyon sürecini hızlandırabilir.
- In vitro anti-bakteriyel etkinlik deneyleri sonucunda, PVD ile kaplanmış numunelerde E. Coli ve S.Aureus mikroorganizmalarının tutunumu, kaplanmamış numuneye göre daha az çıkmıştır. Bu durum, PVD yöntemi ile elde edilen kaplamaların bakteri tutunumunu azaltması, dolayısıyla anti-bakteriyellik yönünden uygun olduğunu göstermiştir. Ancak, 45 dakikanın üzerinde kaplamanın yapısı, partikül boyutu, film kalınlığındaki dağılım, elektrolit erişiminin hedef açısı ve partikül çözünmesi parametreler ve sitotoksik etkiler göz önüne alındığında, kaplama süresi bu eşiğin altında sınırlandırılmalıdır.

Teşekkür

Bu çalışma FDK-2019-7393 kodlu proje kapsamında Atatürk Üniversitesi BAP (Bilimsel Araştırma Projeleri) tarafından desteklenmiştir

Kaynakça

Andrade, J. E. D., Machado, R., Macêdo, M. A., & Cunha, F. G. C. (2013). AFM and XRD characterization of silver nanoparticles films deposited on the surface of DGEBA epoxy resin by ion sputtering. Polímeros, 23, 19-23. https://doi.org/10.1590/S0104-14282013005000009

Bakhsheshi-Rad, H. R., Hamzah, E., Ismail, A. F., Aziz, M., Kasiri-Asgarani, M., Akbari, E., ... & Hadisi, Z. (2017). Synthesis of a novel nanostructured zinc oxide/baghdadite coating on Mg alloy for biomedical application: In-vitro degradation behavior and antibacterial activities. Ceramics International, 43(17), 14842-14850. https://doi.org/10.1016/j.ceramint.2017.07.233

Brobbey, K. J., Haapanen, J., Mäkelä, J. M., Gunell, M., Eerola, E., Rosqvist, E., ... & Toivakka, M. (2019). Effect of plasma coating on antibacterial activity of silver nanoparticles. Thin Solid Films, 672, 75-82. https://doi.org/10.1016/j.tsf.2018.12.049

Chernousova, S., & Epple, M. (2013). Silver as antibacterial agent: ion, nanoparticle, and metal. Angewandte Chemie International Edition, 52(6), 1636-1653. https://doi.org/10.1002/anie.201205923

Çomakli, O., Yazici, M., Yetim, T., Yetim, A. F., & Çelik, A. (2017). The Effects of aging time on the structural and electrochemical properties of composite coatings on Cp-Ti substrate. Journal of Bionic Engineering, 14(3), 532-539. https://doi.org/10.1016/S1672-6529(16)60419-5

Elias, C. N., Lima, J. H. C., Valiev, R., & Meyers, M. A. (2008). Biomedical applications of titanium and its alloys. Jom, 60(3), 46-49. https://doi.org/10.1007/s11837-008-0031-1

Franci, G., Falanga, A., Galdiero, S., Palomba, L., Rai, M., Morelli, G., & Galdiero, M. (2015). Silver nanoparticles as potential antibacterial agents. Molecules, 20(5), 8856-8874. https://doi.org/10.3390/molecules20058856

Hongxi, L., Qian, X., Xiaowei, Z., Chuanqi, W., & Baoyin, T. (2012). Wear and corrosion behaviors of Ti6Al4V alloy biomedical materials by silver plasma immersion ion implantation process. Thin Solid Films, 521, 89-93. https://doi.org/10.1016/j.tsf.2012.02.046

Injeti, V. S. Y., Nune, K. C., Reyes, E., Yue, G., Li, S. J., & Misra, R. D. K. (2019). A comparative study on the tribological behavior of Ti-6Al-4V and Ti-24Nb-4Zr-8Sn alloys in simulated body fluid. Materials Technology, 34(5), 270-284. https://doi.org/10.1080/10667857.2018.1550138

Kokubo, T., & Takadama, H. (2006). How useful is SBF in predicting in vivo bone bioactivity?. Biomaterials, 27(15), 2907-2915. https://doi.org/10.1016/j.biomaterials.2006.01.017

Licausi, M. P., Muñoz, A. I., & Borrás, V. A. (2013). Influence of the fabrication process and fluoride content on the tribocorrosion behaviour of Ti6Al4V biomedical alloy in artificial saliva. Journal of the mechanical behavior of biomedical materials, 20, 137-148. https://doi.org/10.1016/j.jmbbm.2013.01.019

Liu, H., Yang, J., Zhao, X., Sheng, Y., Li, W., Chang, C. L., ... & Wang, X. (2019). Microstructure, mechanical properties and corrosion behaviors of biomedical Ti-Zr-Mo-xMn alloys for dental application. Corrosion Science, 161, 108195. https://doi.org/10.1016/j.corsci.2019.108195

Mao, C., Xiang, Y., Liu, X., Cui, Z., Yang, X., Yeung, K. W. K., ... & Wu, S. (2017). Photo-inspired antibacterial activity and wound healing acceleration by hydrogel embedded with Ag/Ag@ AgCl/ZnO nanostructures. ACS nano, 11(9), 9010-9021. https://pubs.acs.org/doi/abs/10.1021/acsnano.7b03513

Mihailescu, I. N., Bociaga, D., Socol, G., Stan, G. E., Chifiriuc, M. C., Bleotu, C., ... & Miculescu, F. (2016). Fabrication of antimicrobial silver-doped carbon structures by combinatorial pulsed laser deposition. International journal of pharmaceutics, 515(1-2), 592-606. https://doi.org/10.1016/j.ijpharm.2016.10.041

Patil, D., Wasson, M. K., Aravindan, S., Vivekanandan, P., & Rao, P. V. (2019). Antibacterial and cytocompatibility study of modified Ti6Al4V surfaces through thermal annealing. Materials Science and Engineering: C, 99, 1007-1020. https://doi.org/10.1016/j.msec.2019.02.058

Phae-ngam, W., Chananonnawathorn, C., Lertvanithphol, T., Samransuksamer, B., Horprathum, M., & Chaiyakun, T. (2021). Effect of deposition time on nanocolumnar TiZrN films grown by reactive magnetron co-sputtering with the OAD technique. Materials and Technology, 55(1), 65-70.

Stuart, B. W., Stan, G. E., Popa, A. C., Carrington, M. J., Zgura, I., Necsulescu, M., & Grant, D. M. (2022). New solutions for combatting implant bacterial infection based on silver nano-dispersed and gallium incorporated phosphate bioactive glass sputtered films: A preliminary study. Bioactive Materials, 8, 325-340. https://doi.org/10.1016/j.bioactmat.2021.05.055

Subramanian, B., Ananthakumar, R., & Jayachandran, M. (2011). Structural and tribological properties of DC reactive magnetron sputtered titanium/titanium nitride (Ti/TiN) multilayered coatings. Surface and Coatings Technology, 205(11), 3485-3492. https://doi.org/10.1016/j.surfcoat.2010.12.016

Taddei, E. B., Henriques, V. A. R., Silva, C. R. M., & Cairo, C. A. A. (2004). Production of new titanium alloy for orthopedic implants. Materials Science and Engineering: C, 24(5), 683-687. https://doi.org/10.1016/j.msec.2004.08.011

Taglietti, A., Arciola, C. R., D'Agostino, A., Dacarro, G., Montanaro, L., Campoccia, D., ... & Visai, L. (2014). Antibiofilm activity of a monolayer of silver nanoparticles anchored to an amino-silanized glass surface. Biomaterials, 35(6), 1779-1788. https://doi.org/10.1016/j.biomaterials.2013.11.047

Yanovska, A. A., Stanislavov, A. S., Sukhodub, L. B., Kuznetsov, V. N., Illiashenko, V. Y., Danilchenko, S. N., & Sukhodub, L. F. (2014). Silver-doped hydroxyapatite coatings formed on Ti–6Al–4V substrates and their characterization. Materials Science and Engineering: C, 36, 215-220. https://doi.org/10.1016/j.msec.2013.12.011

Vasilev, K., Cook, J., & Griesser, H. J. (2009). Antibacterial surfaces for biomedical devices. Expert review of medical devices, 6(5), 553-567. https://doi.org/10.1586/erd.09.36

Ye, S. H., Johnson Jr, C. A., Woolley, J. R., Oh, H. I., Gamble, L. J., Ishihara, K., & Wagner, W. R. (2009). Surface modification of a titanium alloy with a phospholipid polymer prepared by a plasma-induced grafting technique to improve surface thromboresistance. Colloids and Surfaces B: Biointerfaces, 74(1), 96-102. https://doi.org/10.1016/j.colsurfb.2009.06.032

Yerokhin, A. L., Nie, X., Leyland, A., & Matthews, A. (2000). Characterisation of oxide films produced by plasma electrolytic oxidation of a Ti–6Al–4V alloy. Surface and Coatings Technology, 130(2-3), 195-206. https://doi.org/10.1016/S0257-8972(00)00719-2

Yetim, T. (2016). Corrosion behavior of Ag-doped TiO2 coatings on commercially pure titanium in simulated body fluid solution. Journal of Bionic Engineering, 13(3), 397-405. https://doi.org/10.1016/S1672-6529(16)60311-6

Zhu, Y., Cao, H., Qiao, S., Wang, M., Gu, Y., Luo, H., ... & Lai, H. (2015). Hierarchical micro/nanostructured titanium with balanced actions to bacterial and mammalian cells for dental implants. International journal of nanomedicine, 10, 6659. https://doi.org/10.2147%2FIJN.S92110

Numerical Investigation of Thermal Performance of Diesel Engine Piston Coated with WC and ZrO_2

Bahadir Erman Yuce[1*] and **Serkan Ozel**[1]

[1]*Bitlis Eren University, Faculty of Engineering and Architecture, Mechanical Engineering Department, Turkey*

Abstract: In this study, the performance of thermal barrier coatings on an internal combustion diesel piston was investigated numerically with finite element analysis (FEA). A piston was modeled in three-dimensional, and the performance indicator of thermal barrier coatings was considered as piston surface temperature. The thickness value of the coating was 250μ and heat loads were performed. Firstly, a grid independence study was performed, and the optimum element number was selected without losing computational accuracy then the thermal performance of two different coating materials (WC and ZrO2) was investigated. The numerical results showed that thermal barrier-coated pistons have improved performance with lower surface temperature according to the bare piston..

1.Introduction

The efficient use of fuels is very important today due to the increasing energy demand and costs. In addition, the efficient use of fuels has critical importance in terms of reducing emission rates. Thermal losses in internal combustion engines are an engineering problem and directly affect efficiency. Similarly, thermal losses are an important problem in diesel engine pistons. These losses cause decreases in fuel efficiency and increases in emission rates [1,2].

To reduce thermal losses in diesel engine pistons, a coating process is carried out. The pistons are covered with a material with a lower thermal conductivity coefficient than the piston material and the amount of heat transferred from the combustion chamber to the piston is reduced. The coating on the piston is therefore also called the thermal barrier coating (TBC) [3]. TBC materials decrease the piston surface temperatures while insulating the heat transfer that occurred from the combustion reaction. This effect results to decrease heat transfer losses and increase the in-cylinder temperature [4,5].

Many experimental and numerical studies have been conducted on the thermal performance and effects of TBCs. Coated diesel engine piston [1,6–9] and cylinder [10] are also investigated as different applications. Wang et al. [1] investigated the effects of TBC material parameters like specific heat capacity, thermal conductivity, and porosity within reasonable ranges on engine combustion and emissions. Gok and Karabas [6] stated that they obtained a lower thermal conductivity value by doping LZ with Gd and Yb and coating them on a metal substrate by plasma spraying method to obtain single and double-layered TBCs. They simulated the thermal insulation and surface temperatures on the produced coating on a diesel engine piston with the finite element method. Gehlot and Tripathi [7] investigated the steady state thermal analysis of a diesel engine piston coated with a ceramic coating having holes on its surface. They compared the coating having no hole, a significant increase in the piston top surface temperature occurs with a coating having holes. They compared the coating which has holes with, having no holes then found a significant increase in the piston top surface temperature occurs with the coating having holes.

In this study, we investigated the effect of 250μ WC and ZrO2 coating on diesel engine piston thermal performance numerically under steady-state conditions. Piston surface temperature values are considered as performance criteria and results were compared with each other and an uncoated piston.

2. Material and Methods

2.1 Geometry and Modelling

A diesel engine piston was modeled in 3D and the dimensions of the model are shown in Figure 1. The model contains fundamental geometric characteristics of a diesel engine piston. Two different geometries were used as coated and uncoated pistons. The coated piston geometry has an extra body on the piston which represents 250μ coating materials.

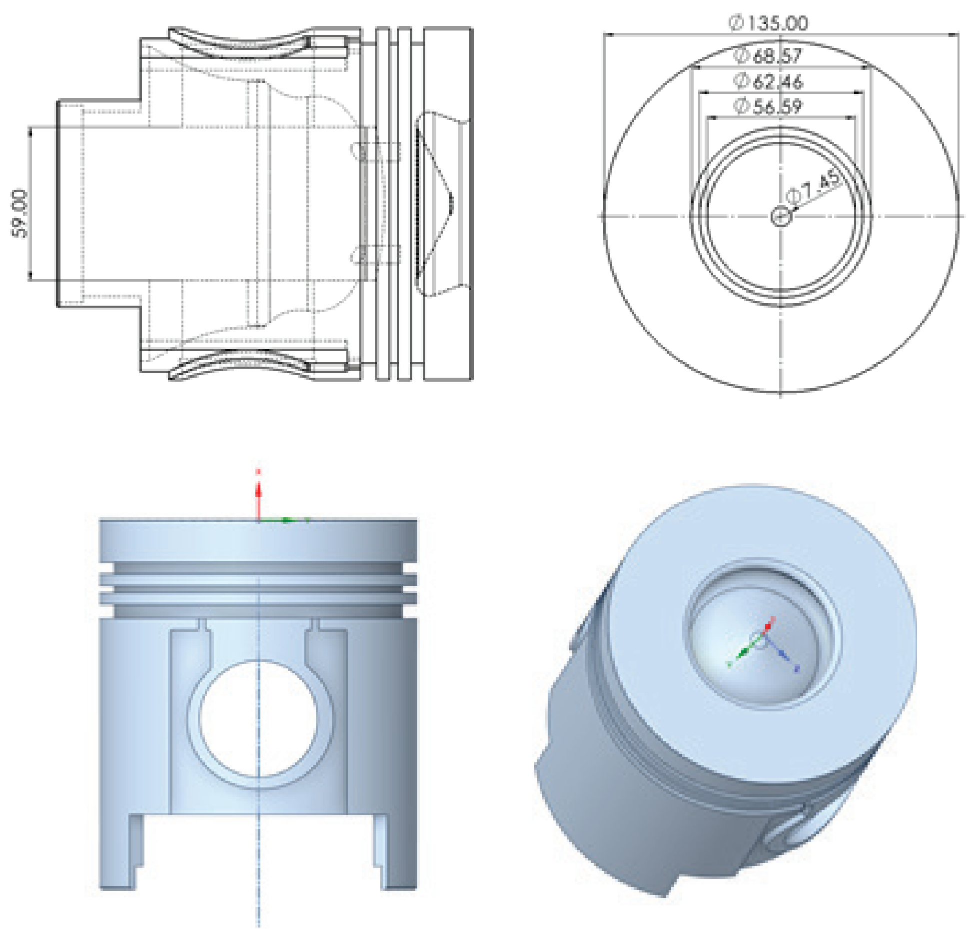

Figure 1 3D model and dimensions

2.2 Grid Independence

Grid independence study is critical for computational studies to show that the results are consistent and independent of the element numbers. It is also important to use computational sources efficiently. In this study, three different element numbers were tested to obtain grid independence; 992714, 1381668, and 1636620. A piston coated with ZrO2 is used for the grid independence study. The comparison of the results is shown in Figure 2. All grids have the same performance, so the grid has 992714 elements and is used for further simulations to decrease the computational cost.

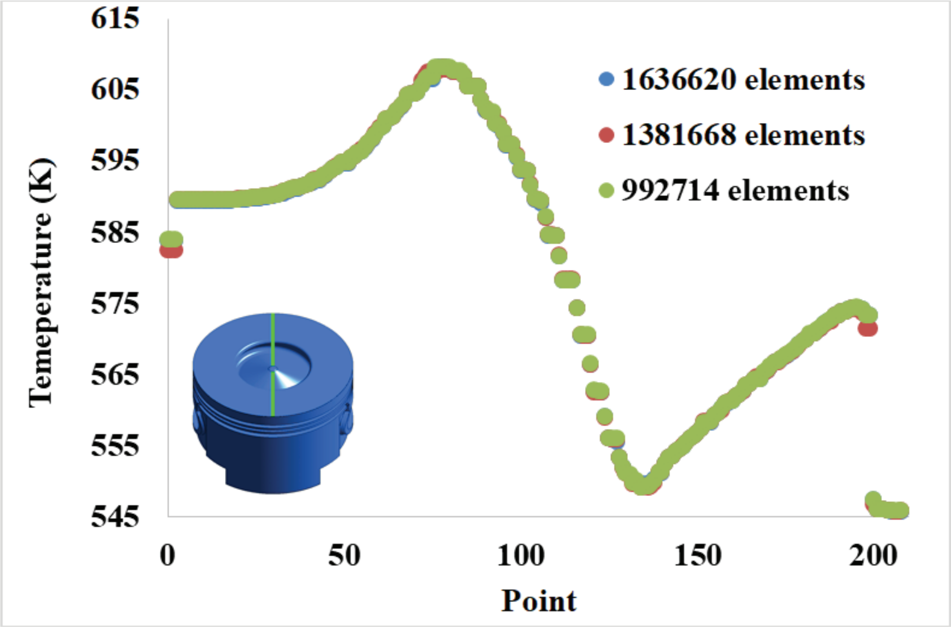

Figure 2 Comparison of different element numbers

2.3 Boundary Conditions

Three different diesel engine pistons were used. ZrO2 and WC were used for coating materials. Simulations are performed in steady-state conditions. The piston material is AlSi and the thermal conductivity coefficient of AlSi is 155 W/mK. The thermal conductivity coefficient of WC and ZrO2 were also set as 96 W/mK and 2.7 W/mK respectively.

Thermal loads on the piston surface are modeled as convection heat transfer and these surfaces are shown in Figure 3. The heat transfer coefficients and ambient temperatures are 800 W/m2K-600°C (Figure 3.a), 230 W/m^2K -300°C (Figure 3.b), 200 W/m^2K -160°C (Figure 3.c) and 1500 W/m^2K -110°C (Figure 4.a) [3].

ANSYS Fluent was used as the simulation program. Converge criteria were set as 10-15.

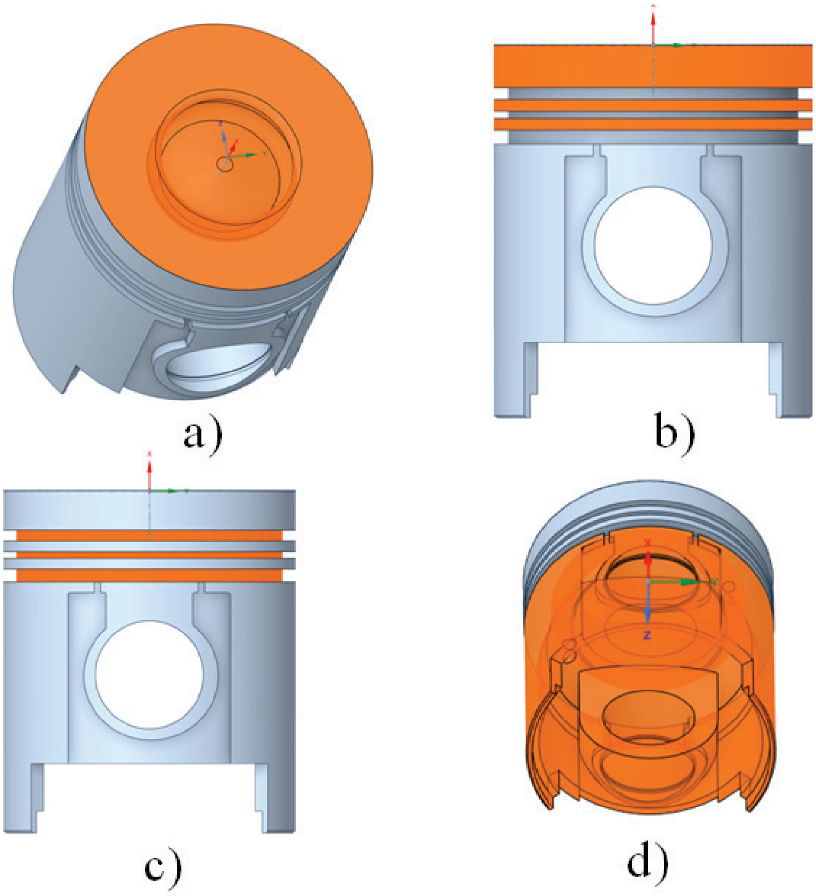

Figure 3 Surfaces in which convection boundary conditions are applied.

3. Results

In this study, the thermal loads affecting a diesel piston were investigated both on an uncoated piston and with two coated pistons. WC and ZrO2 were investigated as coating materials. These two coating materials have thermal conductivity coefficients of 95 and 2.7 W/mK that providing a wide comparison range to see the effect of the thermal conductivity coefficient in a 250μ coating.

The temperature distribution on the uncoated piston surface is shown in Figure 4. The maximum temperature on the piston is 319°C and the minimum temperature is 110°C as expected. The reason for this is that the lowest environmental temperature in the convective heat transfer boundary condition is defined in the bottom and interior of the piston. The piston combustion chamber surface temperature is not homogeneous and It can be seen clearly in Figure 4b which has a local color scale. The highest temperature in the piston combustion chamber is 319°C and the lowest temperature is 253°C. The highest temperature in the piston combustion chamber is in the middle point.

The temperature distribution over the piston surfaces coated with WC is shown in Figure 5. The maximum temperature on the piston is 319°C, and the minimum temperature is 110°C, as on the uncoated piston. The high thermal conductivity coefficient of the WC and the low coating thickness caused this result. The piston combustion chamber

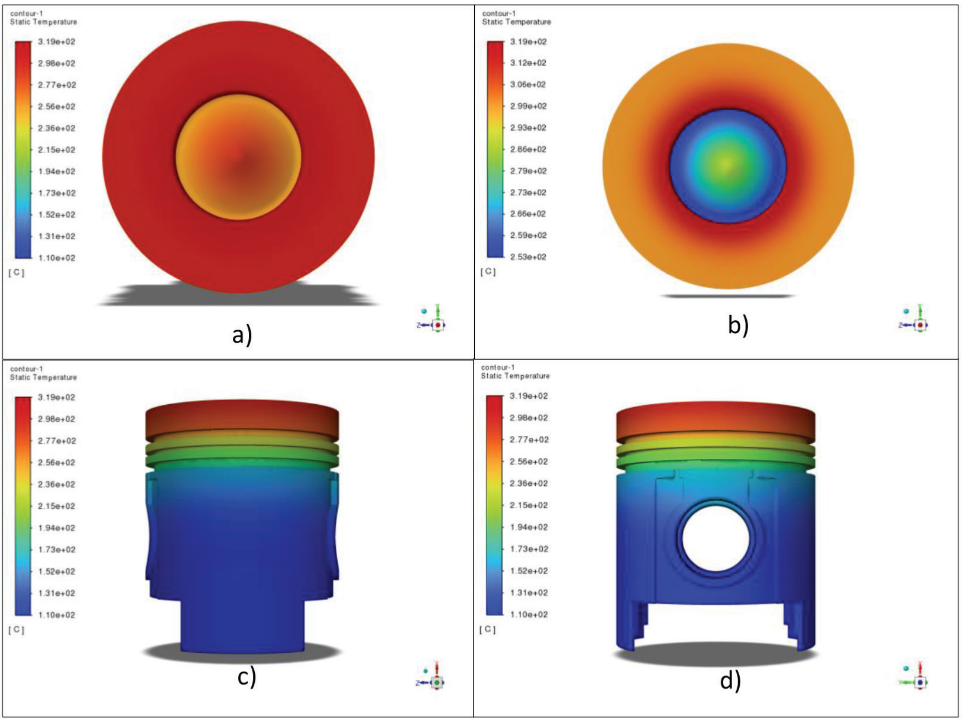

Şekil 4 Temperature distribution on the surfaces of the uncoated piston (a,c,d is colored with global temperature scale and, b is colored in local scale)

temperature distribution is also similar to the uncoated piston. The highest temperature in the combustion chamber is 319°C and the lowest temperature is 253°C. The place where the highest temperature is created in the combustion chamber is the middle part.

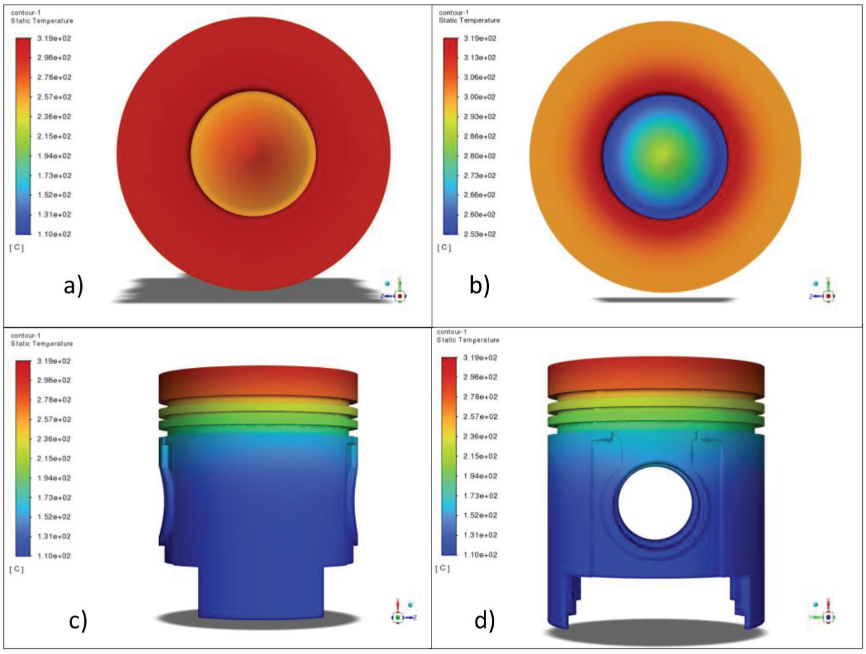

Şekil 5 Temperature distribution on the surfaces WC coated piston (a,c,d is colored with global temperature scale and, b is colored in local scale)

The temperature distribution on the surfaces of the piston coated with ZrO2 is shown in Figure 6. The maximum temperature on the piston surface is 336 ℃, and the minimum temperature is 110℃as in the other two pistons. The temperature distribution is different from the piston coated with the uncoated piston and WC due to the low thermal conductivity coefficient value of ZrO2. Higher temperature values were obtained on the surface.

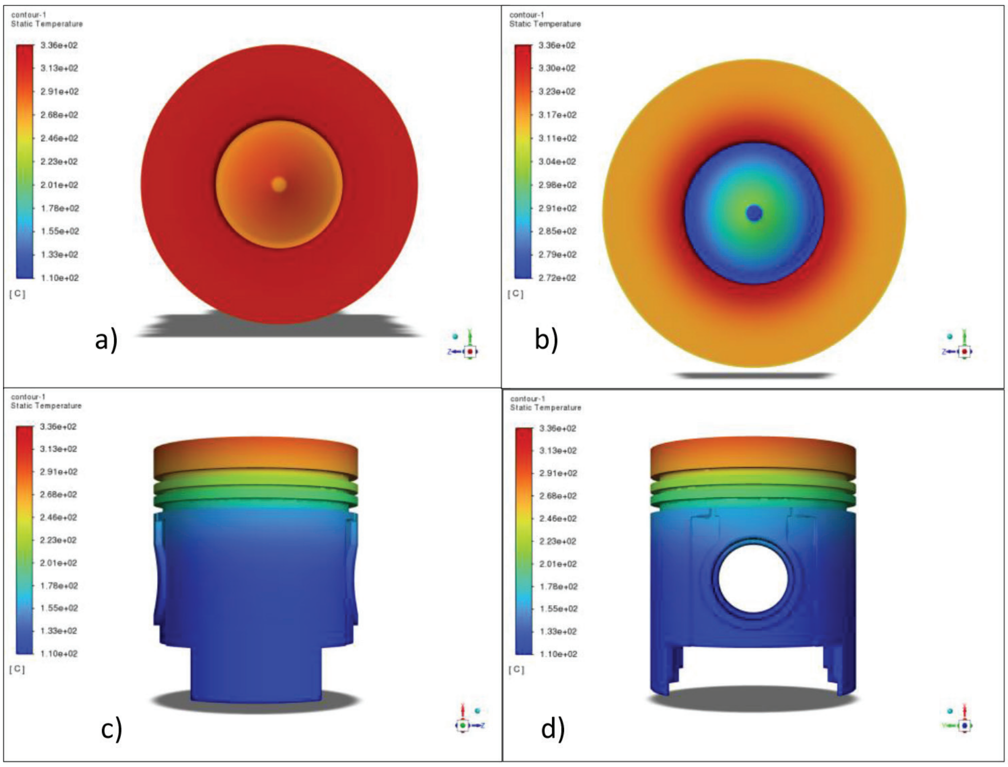

Şekil 6 Temperature distribution on the surfaces ZrO2 coated piston (a,c,d is colored with global temperature scale and, b is colored in local scale)

The surface temperature profiles of coated pistons and uncoated piston under the same thermal loads are given in Figure 7. It is seen that how the coating material with a low thermal conductivity coefficient decreases the thermal loads on the piston. The surface temperature values in the piston coated with ZrO2 are higher than the piston covered with WC and the uncoated piston. The temperature is maximum at the edge between the upper surface of the piston and the combustion chamber. The temperature distribution of the WC and the uncoated piston is similar except for minor differences in the steady state conditions. This is because the thermal conductivity coefficient of the WC is high and the coating thickness is low, as stated before.

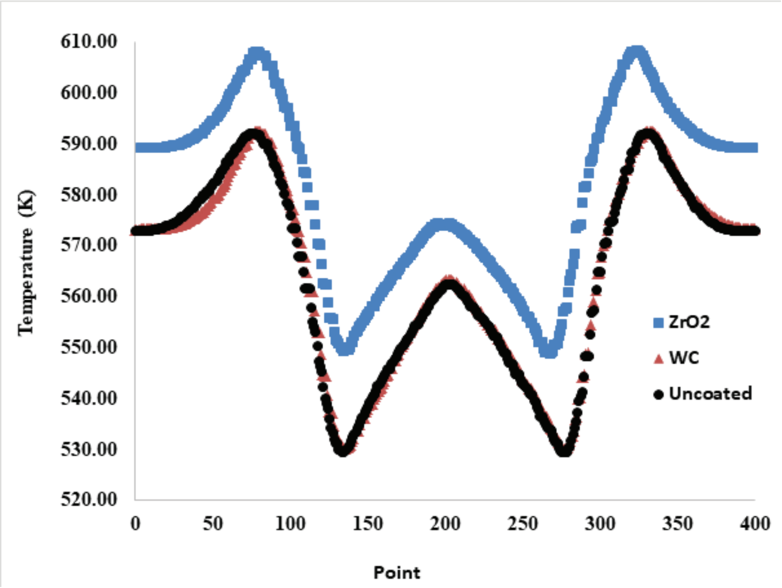

Figure 7 Temperature distributions on the top surface of the pistons

The surface temperature profile of the uncoated piston and the temperature profiles of the coated pistons' sub-surface are shown in Figure 8. The temperature profiles of the uncoated piston and the piston covered with WC are higher than the piston coated with ZrO2. In this case, it can be seen that the material with a low thermal conductivity coefficient creates a thermal barrier for the piston. The under-coating temperature of the WC-coated piston with a high thermal conductivity coefficient is higher than the coating surface temperature and has a similar temperature distribution to the uncoated piston.

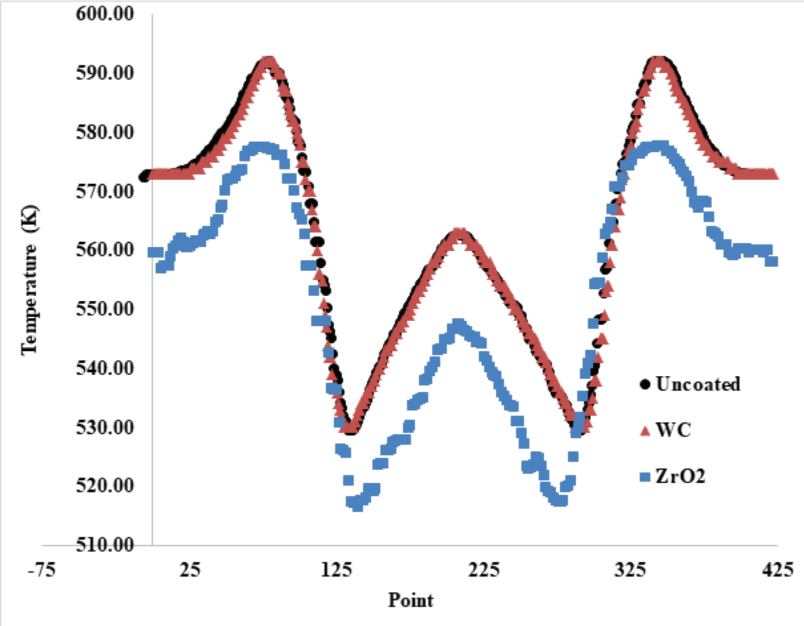

Figure 8. Temperature distributions on the sub-surface of the coating

4. Discussion and Conclusion

In this study, the temperature distributions of diesel engine pistons coated with 250µ WC and ZrO2 and in an uncoated piston were numerically investigated. The temperature distributions on the piston surfaces, and on the lower and upper surfaces of the coating layer, were calculated and compared.
According to the numerical results, ZrO2 is a better thermal barrier than WC due to its low thermal conductivity coefficient. It is more successful in reducing the transfer of heat generated by the combustion reaction to the piston. It is thought that this positive effect will be effective in reducing the thermal loads on the piston, as well as increasing the combustion temperature and reducing emissions and fuel consumption.
Although WC has a small heat transfer coefficient compared to the piston material, it has not been successful in reducing the temperature values on the piston under 250µ thick coating and steady regime conditions. The temperature profile of the piston covered with WC is nearly the same as the piston without coating.

References

1. Y. Wang, T. Ma, L. Liu, M. Yao, Numerical investigation of the effect of thermal barrier coating on combustion and emissions in a diesel engine, Appl. Therm. Eng. 186 (2021) 116497. https://doi.org/10.1016/j.applthermaleng.2020.116497.
2. N. Ramasamy, M.A. Kalam, M. Varman, Y.H. Teoh, Effect of Thermal Barrier Coating on the Performance and Emissions of Diesel Engine Operated with Conventional Diesel and Palm Oil Biodiesel, Coatings. 11 (2021) 692. https://doi.org/10.3390/coatings11060692.
3. E. Vural, Thermal Analysis of Al2O3, TiO2 and SiC Coatings Combustion of a Diesel Engine Piston 3D Finite Element Method, Int. J. Sci. Technol. Res. 1 (2015) 20–30.
4. T. Powell, R. O'Donnell, M. Hoffman, Z. Filipi, Impact of a Yttria-Stabilized Zirconia Thermal Barrier Coating on HCCI Engine Combustion, Emissions, and Efficiency, J. Eng. Gas Turbines Power. 139 (2017). https://doi.org/10.1115/1.4036577.
5. S. Aydin, C. Sayin, H. Aydin, Investigation of the usability of biodiesel obtained from residual frying oil in a diesel engine with thermal barrier coating, Appl. Therm. Eng. 80 (2015) 212–219. https://doi.org/10.1016/j.applthermaleng.2015.01.061.
6. M.G. Gok, M. Karabas, Production of Re doped La2Zr2O7 based TBCs and numerical analysis of their use on IC engine piston surface, Ceram. Int. 48 (2022) 11173–11180. https://doi.org/10.1016/j.ceramint.2021.12.337.
7. R. Gehlot, B. Tripathi, Thermal analysis of holes created on ceramic coating for diesel engine piston, Case Stud. Therm. Eng. 8 (2016) 291–299. https://doi.org/10.1016/j.csite.2016.08.008.
8. B. Dhinesh, Y. Maria Ambrose Raj, C. Kalaiselvan, R. KrishnaMoorthy, A numerical and experimental assessment of a coated diesel engine powered by high-performance nano biofuel, Energy Convers. Manag. 171 (2018) 815–824. https://doi.org/10.1016/j.enconman.2018.06.039.
9. P. Baldissera, C. Delprete, Finite Element Thermo-Structural Methodology for Investigating Diesel Engine Pistons with Thermal Barrier Coating, SAE Int. J. Engines. 12 (2018) 03-12-01–0006. https://doi.org/10.4271/03-12-01-0006.
10. X. Shen, X. Nie, H. Hu, Numerical Analysis of Thermal Distributions in Aluminum Engine Cylinders Influenced by Alumina Ceramic Coatings, Numer. Heat Transf. Part A Appl. 62 (2012) 463–478. https://doi.org/10.1080/10407782.2012.703095.

HİDRAZİN-BORANIN METANOLİZİ İÇİN RUTENYUM BAZLI KATALİZÖRLERİN GELİŞTİRİLMESİ VE TANIMLANMASI

DEVELOPMENT AND CHARACTERIZATION OF RUTHENIUM BASED CATALYST FOR HYDRAZINE-BORANE METANOLYSIS

Teoman KABADAYI, Mehmet TUNÇ

Van Yüzüncüyıl Üniversitesi Fen Fakültesi Kimya Bölümü, Van

ÖZET: Bu çalışmada, halloysite (HS) destekli Ru(0) nanokümeleri, sulu fazda rutenyum(III) tuzunun katı destek yüzeyine depolanması ve ardından NaBH4 kullanılarak indirgenmesiyle oluşturuldu. Hazırlanan Ru@HS katalizörünün hidrazin-boranın metanolizinden hidrojen üretiminde katalitik etkinlikleri test edildi ve Ru@HS katalizörünün etkin olduğu tespit edildi. Ru(0) nanokümelerinin hazırlanmasında izlenen deneysel yöntem; çözücü ve indirgeyici parametreleri kullanılarak işlemler gerçekleştirildi. Gerçekleştirilen işlemler sonucunda katalitik malzeme, indüktif olarak çiftleşmiş kütle spektroskopisi (ICP-MS), toz-X ışınları kırınımı (P-XRD) gibi tekniklerle karakterize edildi. HS kararlı Ru(0) nanokümelerinin katalitik etkinliği ile Ru@HS katalizörü varlığında hidrazin-boranın metanolizi tepkimesinin kinetiği; katalizör derişimine bağlı olarak incelendi.

ABSTRACT: In this study, Ru (0) nanoclusters supported by different solid support materials such as halloysite (HS), were prepared by storing ruthenium (III) salt in the aqueous phase on the solid support surface and then reducing it using NaBH4. The catalytic activity of the prepared Ru@ HS, catalyst in the hydrogen production from the methanolysis of hydrazine-borane was tested and it was determined that Ru@HS was catalyst foundto be active. The experimental method followed in the preparation of Ru(0) nanoclusters was carried out using the parameters of solvent and reductant. As a result of the processes carried out, catalytic material was characterized by techniques such as inductively coupled mass spectroscopy (ICP-MS), powder-X-ray diffraction (P-XRD). The catalytic activity of HS stabilized Ru (0) nanoclusters and the kinetics of the hydrazine-borane methanolysis reaction in the presence of Ru@HS catalyst were investigated depending on the catalyst concentrations .

1. GİRİŞ

Yenilenebilir temiz enerji kaynaklarından biri olarak değerlendirilen hidrojen, gerek yapısı gerekse kullanılabilir özelliği açısından bilim insanlarının dikkatini çekmeyi başarmıştır. Çünkü hidrojen enerjisi, günümüzde kullanılan birçok sonuçları bakımından temiz olmayan enerji kaynaklarının yerine, yenilenebilir, çevre dostu bir enerji taşıyıcısıdır ve hidrojen doğrudan yakıt hücresi ile beslenir. Hidrojen, en yakın rakibi olan metanın iki katı kadar bir enerji değerine sahiptir (Zuttel ve ark., 2008). Bu yüzyılın enerji talebinin büyük bir kısmını hidrojen bazlı yakıt hücresi teknolojisi ile yerine getirileceğine dair şüphe yoktur (Schlapbach ve ark., 2001).

Enerji geleceğinde, sürdürülebilir bir enerji modelinin sağlanabilmesi ve verimli bir hidrojen üretimi için hidrojenin, sağlıklı ve tehlikesiz bir şekilde depolanabilmesi ve dağıtım ağının oluşturulması zorunluluğu ortaya çıkmaktadır. Düşük basınçta hidrojenin büyük miktarlarda depolanması böyle bir hidrojen bazlı ekonominin kurulmasında önemli faktörlerden biridir. Özellikle, üzerinde kurulu enerji depolama için araçlar kompakt, hafif, güvenli ve uygun fiyatlı olması gerekir. Sıvı hidrojen, yüksek kütlesel ve hacimsel olarak hidrojen yoğunluğuna sahip olmasına rağmen, yerleşik depolama için birçok dezavantaj içermektedir. Sıkıştırılmış hidrojen gazının bir alternatifi olarak, 700 bar'lık yüksek basınçlı hidrojen depolama tankları, 300 mil menzil sürüş sağlayan bir araç geliştirilmiştir (FCTP., 2011). Hidrojen yoğunluğu açısından daha yüksek olan yüksek basınçlı sistemler, güvenlik ve aktarılabilirlik açısından endişeler içermektedir. Metal hidrürler, metal-organik kafes yapıları, hidrokarbonun hidrojene dönüşümü ve organik maddeler de dâhil olmak üzere diğer depolama malzemeleri ve yöntemleri de kapsamlı bir şekilde araştırılmıştır (Schlapbach ve Zuttel, 2001; Rosi ve ark., 2003; Deluga ve ark., 2004; Seayad ve Antonelli, 2004; Ferey, 2005; Wang ve ark., 2005; Orimo ve ark., 2007; Makowski ve ark., 2009; FCTP., 2011). Bununla birlikte, aday malzemelerinin birçoğunun hacimsel ve kütlece hidrojen kapasiteleri, taşıma basıncı ve sıcaklık gibi etkili olan faktörlerin, yan ürünlerin geri dönüşümü ve maliyeti gibi değişik gereksinimleri ve pratik gereklilikleri karşılayamamaktadır (FCTP., 2011). Kimyasal olarak depolanabilen hidrojenin fiziksel olarak depolanabilen hidrojenden daha güvenilir olması güzel bir alternatiftir (Eberle ve ark., 2009).

2. MATERYAL VE YÖNTEM

Rutenyum(III) klorür trihidrat (RuCl3.3H2O), halloysite (HS), hidrazin-boranın (N2H4BH3) sentezi için gerekli olan hidrazin-hemisülfat (N2H5)2.0.5 H2SO4), sodyum borhidrür (NaBH4) Merck ve Sigma gibi firmalardan ticari olarak temin edildi. Deiyonize su, musluk suyundan cihazla saflaştırıldı (Termo Scientific Barnsted Nanopure System). Tüm cam eşyalar ve teflon kaplı manyetik balıklar aseton ile temizlendi ve saf suyla yıkandıktan sonra 150 °C'ye kadar ayarlanmış fırında gece boyunca kurutulduktan sonra kullanıldı.

2.1. Yöntem

2.2.1. Hidrazin-boranın sentezi ve tanımlanması

Bu çalışmanın ilk aşamasında ilgili kaynakça kullanılarak (Moury ve ark., 2012) (Eşitlik 2) hidrazin-boran sentezi gerçekleştirilmiştir. Öncelikle ürünün kararlılığını arttırmak için hidrazin hemisülfat ve sodyum borhidrür vakumda kurutulduktan sonra kullanılmıştır. Ayrıca saflaştırma işlemleri yapılmıştır.

$$(N_2H_5)_2.SO_4 + 2NaBH_4 \xrightarrow[RT]{THF} 2N_2H_4BH_3 + Na_2SO_4 + 2H_2 \qquad (2)$$

2.2.2. Ru@HS nanokatalizörün hidrazin-boranın metanolizi tepkimesinde katalitik olarak etkinliğinin katalizör derişimine bağlı olarak incelenmesi

Katalizör miktarının, HB'nin metanolizi tepkimesindeki katalitik etkisini anlamak için, HB miktarı sabit tutularak farklı katalizör miktarları 50 mg, 75 mg, 100 mg, 125 mg olmak üzere katalitik etkinlikleri incelendi.
100 mg (3.9 mM) Ru@HS ceketli Schlenk kabı içerisine konuldu ve sistemin diğer girişinden sisteme azot gazı verilerek hava ile teması

kesildi, katalizörün üzerine 4 mL kuru metanol eklendi. Schlenk içerisinde mağnet konularak sirkülatörün sıcaklığı 25 °C'ye ve karıştırma hızı 600 rpm'e ayarlandı. Daha sonra Schlenk içerisine verilen azot gazı kesilerek, ağzı septumla hava almayacak şekilde kapatılarak karıştırıcının düğmesine basıldı. Muhtevanın üzerine 1 mL kuru metanolde çözünen 100 mM HB ilave edilerek açığa çıkan gazın büret içerisindeki suyu itmesi ile çıkan gaz hacmi zamana karşı gaz çıkışı tamamen sonlanana kadar not edildi. Diğer katalizör miktarları için de aynı prosedür uygulanarak katalitik etkinlikleri incelendi.

3.BULGULAR

ICP-MS analizi ile hazırladığımız bu katalitik malzemedeki Ru yoğunluğunun kütlece % 1.936 olduğu tespit edilmiştir.

Metal nanokümelerinin yüzeyde oluşumu sonucu destek malzemesinin kristal yapısının incelenmesi ve metal nanokümelerinin kristalliğinin tespiti için yapılan XRD analizine ait desen Şekil 3.1'de verilmiştir.

Şekilde görüldüğü gibi katı destek maddesinin ve katı destek maddesinin yüzeyine tutturulan rutenyuma ait pikler görülmektedir. Bu piklerin yapısına bakıldığında yüzeye tutturulan Ru(0) nanokümelerinin, katı destek maddesinin yapısını değiştirmediği anlaşılmaktadır. Bu durum bu çalışma için istenilen bir sonuçtur.

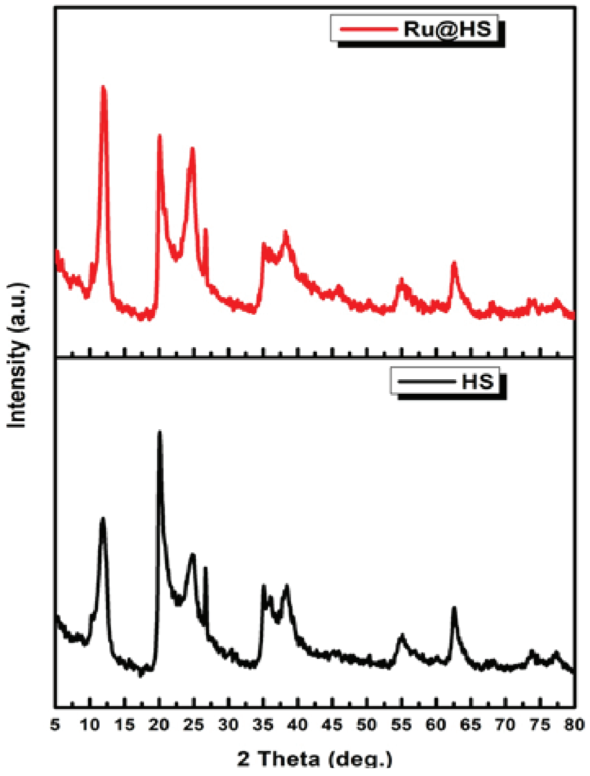

Şekil 3.1. Ru@HS nanokatalizörü ve HS'ye ait XRD desenleri.

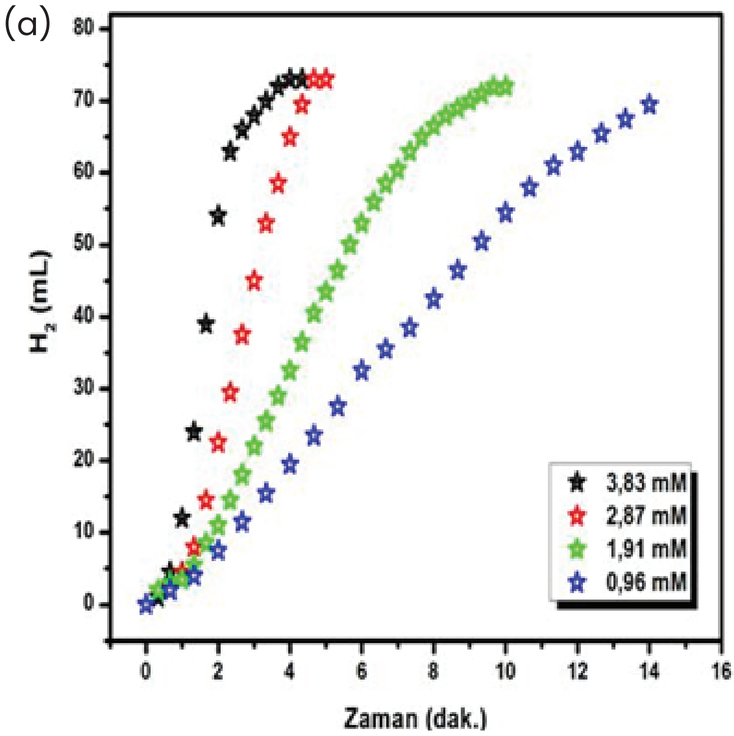

Şekil 3.2 (a) da görüldüğü gibi katalizör miktarı arttıkça zamana bağlı olarak açığa çıkan H gaz miktarının da arttığı görülmektedir. Bu durum bu çalışma için beklenen bir sonuçtur.

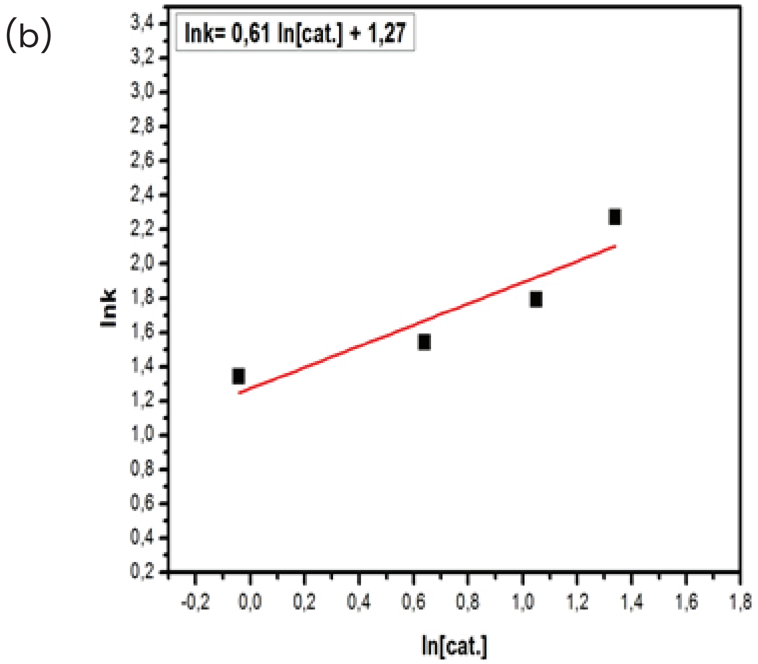

Şekil 3.2. Farklı derişimlerdeki Ru@HS ile katalizlenen hidrazin-boranın metanolizi tepkimesine ait (a) açığa çıkan gaz hacmine karşı zaman grafiği, (b) başlangıç hızlarının katalizör derişimine karşı logaritmik grafiği.

5. TARTIŞMA VE SONUÇ

Hidrazin-borandan metanoliz tepkimesi sonucunda hidrojen eldesi için yapılan çalışmalarda farklı yapıda katalizörlerin kullanıldığı bilinmektedir. Hidrazin-boran ve katalizör sistemlerinin, endüstri ve malzeme bilimi açısından önemli olması ve iyi bir katalizörün ölçütü sayılan katalizör etkinliği dikkate alınarak bu çalışmada ileri analitik analizler yapıldı. Tepkime sonunda kolay izole edilebilme, kolay sentezlenebilme, taşınabilirlik ve depo edilebilirlik gibi özellikler dikkate alındığında, bu çok önemli tepkime için yeni katalitik sistemlerin geliştirilmesi bu çalışmada hedeflenmiştir. Bu çalışmada, katalitik etkinliği iyi bilinen metal Ru(0) nanokümeleri hazırlanmış, analitik yöntemlerle hesaplanmış, hidrazin-boranın metanolizi tepkimesindeki katalitik etkinliği incelenmiştir.

Yapılan bu çalışmada; halloysite, katı destek malzemesi üzerine tutturulmuş metal nanokümeleri, çözelti fazında Ru(III) metal tuzunun destekleyici katı yüzeyine depolanması ve daha sonra NaBH4 ile indirgenmesiyle katalizör oluşturuldu. İncelenen bu Ru@HS nanokatalizörünün, hidrazin-boranın metanolizinde etkin olduğu deneysel sonuçlardan görülmüştür.

KAYNAKLAR

Deluga, G. A., Salge, J. R., Schmidt, L. D., Verykios, X. E., 2004. Renewable hydrogen from ethanol by autothermal reforming. Science, 303: 993-997.

Eberle, U., Felderhoff, M., Schuth, F., 2009. Chemical and physical solutions for hydrogen storage. Angewandte Chemie International Edition, 48: 6608–6630.

Ferey, G., 2005. Physical chemistry: Trapped gas. Nature, 436: 187–188.

FuelCell technologies program.(FTCP., 2011) http://www1.eere.energy.gov/hydrogenandfuelcells/mypp/ Erişim tarihi: 13.05.2021

Makowski, P., Thomas, A., Kuhn, P., Goettmann, F., 2009. Organic materials for hydrogen storageapplications: from physisorption on organic solids to chemisorption in organic molecules. Energy & Environmental Science journal, 2: 480-490.

Moury, R., Moussa, G., Demirci, U. B., Hannauer, J., Bernard, S., Petit, E., Lee, A., Miele, P., 2012. Hydrazine-borane: synthesis, characterization, and application prospects in chemical hydrogen storage. Physical Chemistry Chemical Physics, 14: 1768-1777.

Orimo, S., Nakamori, Y., Eliseo, J. R., Zuttel, A., Jensen, C. M., 2007. Complex hydrides for hydrogen storage. Chemical Reviews, 107: 4111-4132.

Rosi, N. L., Eckert, J., Eddaoudi, M., Vodak, D. T., Kim, J., Keeffe, M. O., Yaghi, O. M., 2003. Hydrogen storage in microporous metal-organic frameworks. Science, 300: 1127–1129.

Schlapbach, L., Züttel, A., 2001. Hydrogen-storage materials for mobile applications. Nature, 414: 353-358.

Seayad, A. M., Antonelli, D. M., 2004. Recent advances in hydrogen storage in metal-containing ınorganic nanostructures and related materials. Advanced Materials, 16: 765-777.

Züttel, A., Borgschulte, A., Schlapbach, L., 2008. Hydrogen as a future energy carrier weinheim. Wiley-VCH, 1: 978-3-527-30817-0.

Wang, Y. G., Shah, N., Huffman, G. P., 2005. Simultaneous production of hydrogen and carbon nanostructures by decomposition of propane and cyclohexane over alumina supported binary catalysts. Catalysis Today, 99: 359–364.

Effect of milling parameters on the microstructural features of nanopowders obtained by ball milling of Ti6Al4V scraps

Amirreza Alavizadeh, Mehrdad Shahbaz, Majid Kavanlouei

~~Van Yüzüncüyıl Üniversitesi Fen Fakültesi Kimya Bölümü, Van~~

Abstract: In this research, the Ti6Al4V scraps obtained from machining in were subjected to milling with a planetary ball mill to produce nanopowders. The effect of ball size and ball to powder ratio on the morphology, crystallite size, and phase composition of obtained powders were investigated. The structural and lattice features for powders were thoroughly characterized by different methods of X-ray Diffraction (XRD) peak analysis. The shape properties of particles were examined by analysis of scanning electron microscopy (SEM) images. The XRD analysis proved the formation of TiO nanoparticles with crystallite size ranging 50 to 150 nm. The synthesized nanoparticles, by mechanical alloying method, were heat treated and TiO2 nanoparticles were produced. The SEM microscopic observations, also, revealed nano sized particles after ball milling.

Keywords: Planetary ball milling, XRD, Ti6Al4V, Scraps,

1. Introduction

Nanocrystalline materials (NMs) have attracted the attention of researchers due to their extraordinary physical, chemical and mechanical properties. To this end, extensive research has been conducted to produce NMs, evaluating their mechanical, thermal and magnetic properties. Titanium alloys, in particular (Ti-6Al-4V) show a high strength-to-weight ratio and excellent ductility and excellent corrosion resistance. For these reasons, they are widely used in the aerospace and automotive industries, marine environments and biological applications. Various production processes are used to produce different parts for different applications, which are almost finally shaped using the machining process. Finding a suitable method for recycling and reusing machining produced chips is of great economic, strategic and environmental importance. Researchers have proposed various methods to achieve this goal, including the use of severe plastic deformation (SPD) and milling methods [???]. One of the advantages of the milling method is its ability to be industrialized and its cheapness. During mechanical alloying, various phenomena are observed in powder particles, the most important of which are the increase in the density of crystalline defects, especially dislocations, and the increase in strain in powder particles and the mutual penetration of elements [1].

Mahboubi et al., in a research work in 2011, used mechanical milling method to produce nanocrystalline powder from machining chips Ti-6Al-4V. For this purpose, they used two methods, Planetary and Shaker. In the planetary method, 5 balls made of hardened carbon steel with a diameter of 20 mm in a ball to powder ratio (BPR) of ten to one were used. The results of scanning electron microscopy (SEM) and laser analysis of powder size showed that after 50 hours of milling, 80 μm agglomerated clusters containing 1 μm powder particles were obtained. The results of microhardness also showed an increase in hardness from 400 HV for primary chips to 536 HV for powders obtained after 50 hours of milling [2].

In a work done by Mahboubi et al. in 2010, the milling behavior of Ti6Al4V alloy machining chips in the presence of 10 %wt of Al2O3 nanopowders in a high-energy planetary mill was investigated. SEM, transmission electron microscopy (TEM), X-ray diffraction (XRD), laser powder size analysis, and microhardness were used for this purpose. The results showed that the presence of Al2O3 nanoparticles reduced the size of Ti-6Al-4V powder to 4 µm after 30 hours of milling, which was reported to be 8 µm without the presence of Al2O3 nanopowder after 50 hours of milling. It was also concluded that the presence of these nanoparticles improves the work hardening and thus increases the microhardness of the powder and composite produced [3].

In 2017 [4], Dikiji and Sotjoo investigated the effect of disc mill speed and time on the powder properties of Ti-6Al-4V alloy machining chips. The results showed that the size of the resulting flake powders increased by increasing the milling speed from 800 rpm to 1400 rpm at a fixed time of 4 minutes, and reduced by increasing the milling time from 4 minutes to 24 minutes at a constant milling speed of 1200 rpm. Results of XRD, showed no phase change due to change of these parameters of milling [4].

In other research works, the producing the powder from machined Ti-6Al-4V alloy chips using heat treatment in a hydrogen atmosphere [5], the production of titanium powder from machined chips, and then to use it for titanium-based Ti-Fe coating on the titanium base [6], using the planetary milling method to produce Ti-TiC composite from Ti machining chips [7], and comparing commercial Ti-6Al-4V powder with the milling powder of the alloy machining chips and also the compression behavior of the two powders [8], were studied in details.

The literatures review in the field of the present study shows that study on the milling simultaneously with the different size of balls and the phase change analysis of the resulting powder has not been done, yet. In the present study, the production of nanocrystalline powder from machining wastes of titanium implants (Ti-6Al-4V-ELI) was investigated using a planetary mechanical mill method with balls of different sizes. SEM, and XRD were used to examine the resulting powders. The results showed a reduction in powder and crystallite size at very low millimeter-scale milling times as well as significant phase changes.

2. Experimental procedures

In this study, chips produced during machining of Ti-6Al-4V-ELI medical implants were used. In order to remove the oil and impurities from the chips, the washing was done in three steps, including; 1. The chips were first washed with the water, 2. They were then immersed in Aston solution, and 3. Finally, after washing again with water, it was placed at room temperature for 20 minutes in an ultrasonic bath with a solution mixed of 2 %wt hydrochloric acid (HCl), 8 %wt sulfuric acid (H_2SO_4) and water, and finally was dried in an oven at 60 °C for 4 hours. Then the cleaned chips were carefully chopped in a cup before milling and after thorough cleaning. Chips milling operation was performed in a ball mill with a chamber made of high chrome steel. The bullet to powder ratio was considered to be 20:1. The milling process was performed using balls in mixed sizes of 14 mm and 10 mm at room temperature with air atmosphere at a constant speed of 450 rpm at 10 h (Table 1). The tests were performed according to the table below and other parameters were kept constant (Table 2).

Rotation speed	500
Vial material	Hardened Cr steel
Vial capacity (ml)	250
Ball material	Hardened Carbon steel
Diameter of balls (mm)	14 and 10 mm
Ball to powder ratio	10:1-15:1-20:1
Total powder mass	14 g

Table 1 Milling parameters

sample	B/P Ratio	B1(14mm)-B2(10mm) Wt.%	Final product	
1	10:1	25-75	powder	
3	15:1	25-75	powder	
6	20:1	25-75	powder	

Table 2 effetct of B/P ratio in constant ball condition (25(14mm)-75(10mm) Wt.%)

Structural and phase changes of powders during the milling process were studied by XRD, using a Brucker D8-Advanced machine and CuKα tube. The Williamson-Hall (WH) method was used to calculate the grain size (Eq. 1), as follows;

$$\beta cos\theta = \frac{K\lambda}{D} + 4\varepsilon sin\theta \tag{1}$$

where; β is the peak width at half height, λ is the X-ray wavelength, d is the grain size, θ is the Bragg angle and ε is the lattice strain. Scanning electron microscopy (SEM Leica Cambridge, Stereoscan S360) images were used to evaluate the size and morphology of the powders.

3. Results and discussion

Figure 1 shows the SEM image of primary chips used in this study which it is similar to conventional chips in the shape of a spring.

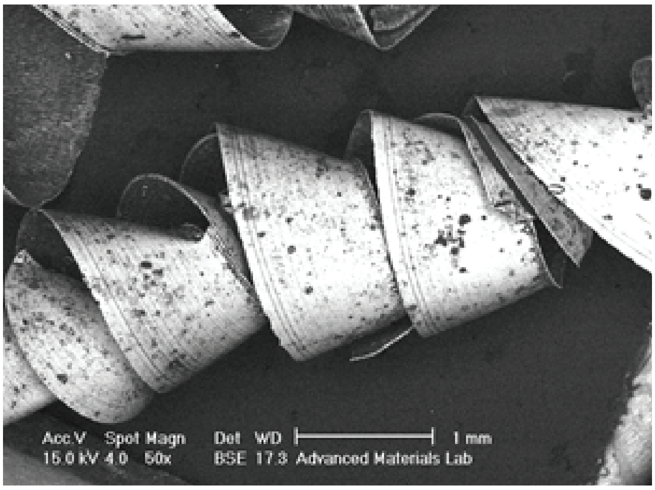

Figure 1. Scanning electron microscope image of primary chips.

Figure 2 shows the X-ray diffraction patterns of milling powders at different milling times. As can be seen, the XRD pattern from various sample consists of TiO main phase. By milling these chips, in addition to the TiO peaks (according to the scattering file No. 2961-900-96) two minor peaks related to iron (according to separation file No. 4905-720-96) can be seen. Iron impurities are probably due to the wear of steel balls and chambers. Also, the intensity of the peaks were changed, which indicates that the final product have various crystallite size and micro-strain.

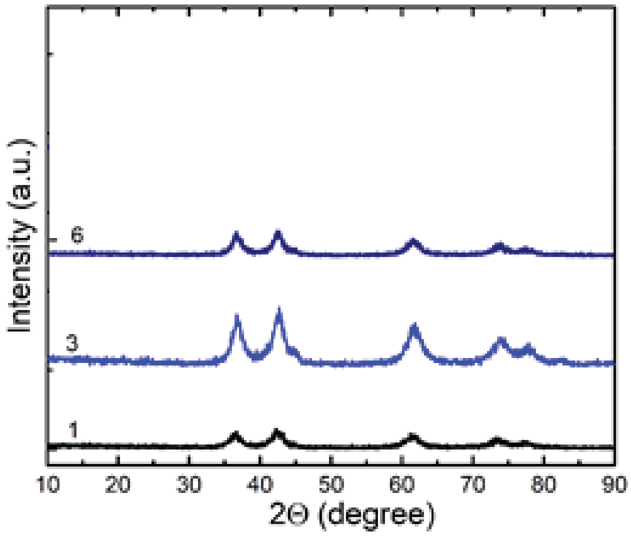

Figure 2 X-ray diffraction pattern of obtained powder.

There are some common methods to calculate the crystallite size and inhomogeneous lattice strain, resulted from defects and distortions of lattice by employing the diffraction patterns of X-ray, such as Debye Scherrer, modified Scherrer (Scherrer Plot), Williamson-Hall and Rietveld methods. The results of crystallite size based on Debye-Scherrer method, calculated for three main peaks of forged and raw samples and their average values are presented in table 3. But using this method in milling has limitations.

Table3. Quantitative results of W-H, D-S and Rietveld refinement using MAUD software.

	D-S method	WH method		Rietveld method				
sample	CS (A)	CS (A)	Strain %	CS (A)	Strain %	Wt.% TiO	Wt.% Fe	a_{TiO}(A)
1	47.35	64.46	0.69	64.57	0.0053	99.54	0.456	4.276
3	60.91	70.35	0.015	64.66	0.0034	99.469	0.53	4.271
6	53.27	56.8	0.00545	63.38	0.0043	99.27	0.72	4.276

The peak spreading in XRD reflections are not only affected by the crystallite size but also are influenced by the contribution of micro-strains in the lattice, which is not normally considered in the classical Scherrer equations. In Williamson-Hall method the peaks are regarded to be broadened by the contribution of two individual factors; strain and size, indicating as strain broadening and size broadening factors.

$$\beta \cos\theta = \frac{\kappa\lambda}{D} + 4\varepsilon \sin\theta \qquad (1)$$

The slope and intercept of the plot of θ cosθ versus sinθ give the lattice strain and CS, respectively, which are presented in fig 3 and table 3.

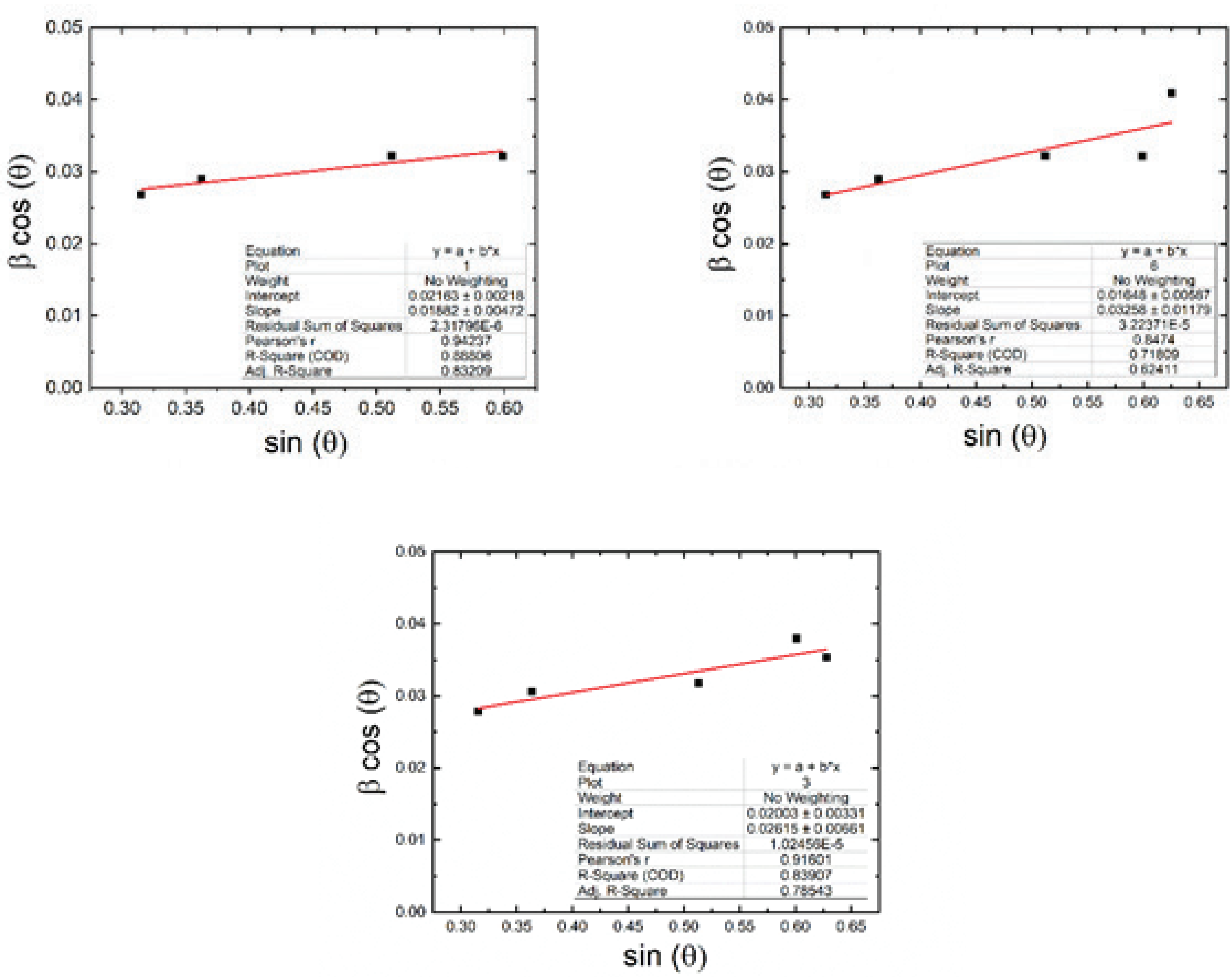

Figure 3 The graph of W-H for various sample 1,3 and 6.

Also, The XRD pattern of all powder sample are quantitatively analyzed using the Rietveld method and the corresponding fitted pattern (sample 3 for example) are illustrated in Figure 4. The quantitative results of the Rietveld refinement using Maud software are listed in Table 3. As shown in the figure below, there is a good agreement between the experimental data and the fitted graph, which indicates a suitable Rietveld analysis.

According to the data in the table, it can be seen that, by increasing B/P ratio, the peak intensity of iron increased. Also, the intensity of 6 sample decreased. It can be related to reducing the size of crystallite and increasing the lattice strain due to increasing energy of milling and impact frequency. Furthermore, it can be said that the milling process has also affected the position of the peaks (change lattice constant). In fact, in addition to the intensity and width of the peaks, the position of the peaks has also been affected by milling. This may be due to a change in the crystal lattice parameter due to the substitution of lattice atoms (Fe, Al or V) and the formation of a solid solution.

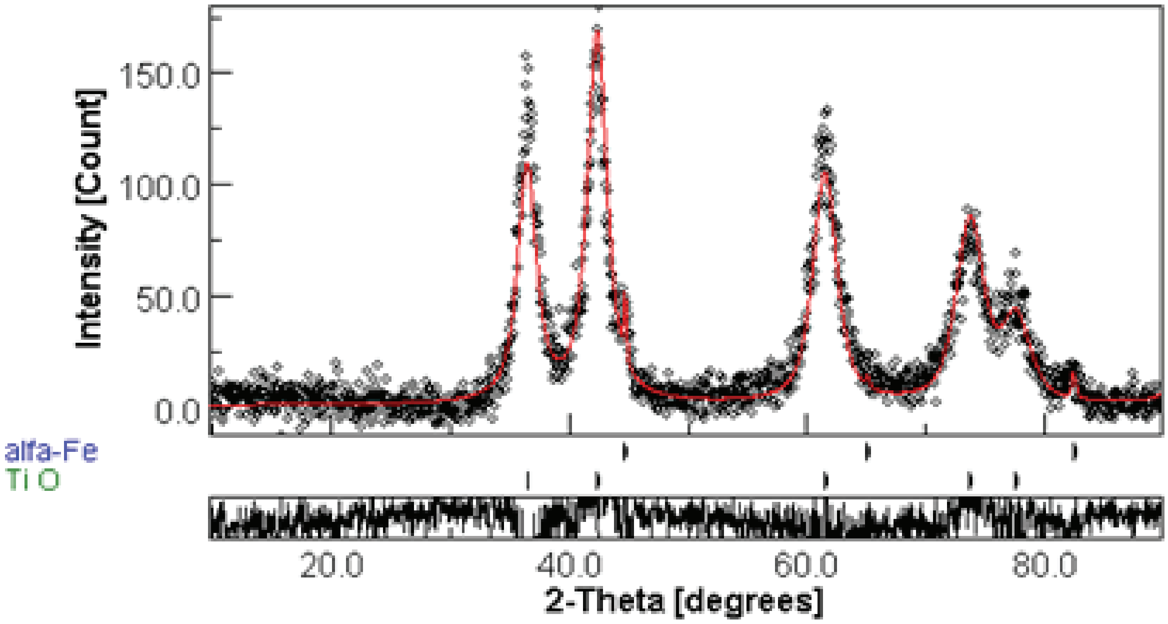

Figure 4 - The fitted XRD patterns of sample 3.

Generally, there are three main mechanisms for the morphological changes of particles in the mechanical milling process. 1) The mechanism of plastic deformation, 2) cold welding and c) fracture. In the first stage, the powder particles slide on each other due to the fracture and the mechanism of plastic deformation. In the second stage, the powder particles change their shape and a little elastic and plastic deformation and cold welding happens between them, and in the third stage, the powder particles are hardened and the processes of fracture and cold welding reach equilibrium.

In order to study the microstructural changes and morphology of the powders after milling in the planetary mill, SEM images were prepared from the powders, which are shown in Figure 5. Different distributions of fine-sized particles can be seen due to the high agglomeration capacity of these particles. As the B/P ratio increased to 20:1, the powder particles became almost spherical due to cold welding and breakage and severe plastic deformation (Figure 5(e,f)). After milling for up to 10 hours (B/P ratio 20:1), the particle size of the powder decreased and the powders became completely spherical. At this stage, however, fine powders began to agglomerate and form large agglomerates. In addition, the increase in the B/P ratio in sample 6 with the increase in grinding energy and impact frequency has led to the fact that most of the fracture mechanism is dominant in this sample and it has become finer.

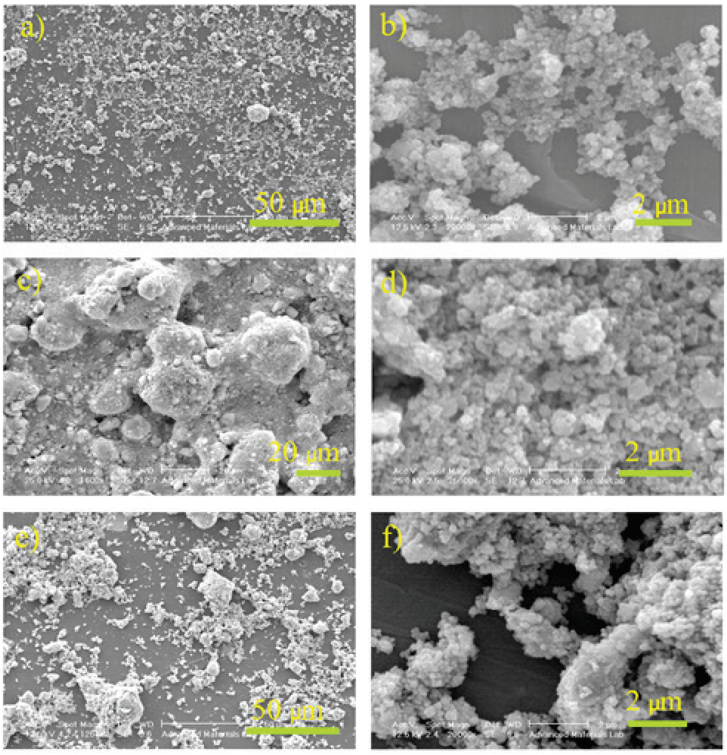

Figure 5 - SEM images of various powder samples 1,3 and 6.

Conclusion

Nanoparticle powder was successfully produced using mechanical milling as a cheap and industrial method of Ti6Al4V alloy scraps in a planetary ball mill, which has various applications in various industries such as paint, cosmetics, and optics. The results of phase analysis using Rietveld for powder sample using XRD test showed that the produced powder is single phase and only Fe impurity peak is observed in the system. The produced powders were studied using SEM, and the shape of the powders is spherical and the particle size distribution is different in different milling conditions. With the increase in the B/P ratio in the same milling conditions, the powders become finer, which is due to the increase in the collision frequency and milling energy, but the Fe impurity also increases.

References

1. Tamirisakandala S, Bhat R, Vedam BJJoME, Performance. Recent advances in the deformation processing of titanium alloys. 2003;12(6):661-73.

2. Boyer RRJMS, A E. An overview on the use of titanium in the aerospace industry. 1996;213(1-2):103-14.
3. Gonzalez J, Mirza-Rosca JJJoEC. Study of the corrosion behavior of titanium and some of its alloys for biomedical and dental implant applications. 1999;471(2):109-15.
4. McQuillan A, McQuillan M. Metallurgy of the Rarer Metals. 4: Titanium. London: Butterworths Sc. Pubh; 1956.
5. Wang RR, Fenton AJQi. Titanium for prosthodontic applications: a review of the literature. 1996;27(6).
6. Yetim A, Celik A, Alsaran AJS, Technology C. Improving tribological properties of Ti6Al4V alloy with duplex surface treatment. 2010;205(2):320-4.
7. Bruschi S, Bertolini R, Ghiotti AJTI. Coupling machining and heat treatment to enhance the wear behaviour of an additive manufactured Ti6Al4V titanium alloy. 2017;116:58-68.
8. Batalha G, Motyka M, Kubiak K, Sieniawski J, Ziaja W, Dos Santos D, et al. Editorial Board Contributors to Volume 2 Preface xv. 2014.

Aspir (*Carthamus Tinctorıus L.*) Bitkisinin Etanol ve Su Özütünün Antioksidan Kapasitesinin İncelenmesi

Investigation of Antioxidant Capacity of Ethanol and Water Extract of Safflower (*Carthamus Tinctorius L.*)

Tuğba Gür[1], İsmet Meydan[1], Canan Demir[1], Nuran Bazancir[1]*

[1]*Van Yüzüncü Yıl Üniversitesi, Sağlık Hizmetleri Meslek Yüksek Okulu, Türkiye*

Abstract: Safflower (Carthamus tinctorius L.), a member of the Asteraceae family spread over a wide area in the world, has an important place among medicinal aromatic plants due to its secondary metabolites with high antioxidant activity. In this study, Free Radical Removal (DPPH) analysis method was used to determine the antioxidant capacity of the ethanol and water extract of the safflower (Carthamus tinctorius L.) plant. BHA and BHT were used as positive controls. The experiment was performed at five different concentrations. As a result of the experiment, it was observed that the antioxidant capacity of Carthamus tinctorius L. plant increased depending on the increasing concentration of the ethanol extract. It was determined that it has the highest antioxidant capacity at 1000 mg/ml. As a result, it was determined that the ethanol extract of the safflower (Carthamus tinctorius L.) plant showed high antioxidant activity.

ÖZ

Dünyada geniş bir alana yayılmış Asteraceae familyasının bir üyesi olan aspir (Carthamus tinctorius L.) bitkisi, yüksek antioksidan aktiviteye sahip ikincil metabolitler içeriğinden dolayı tıbbi aromatik bitkiler arasında önemli bir yere sahiptir. Bu çalışmada, aspir (Carthamus tinctorius L.) bitkisinin etanol ve su ekstraktının antioksidan kapasitesini belirlemek için Serbest Radikal Giderme (DPPH) analiz yöntemi ile çalışılmıştır. Pozitif kontrol olarak BHA ve BHT kullanıldı. Deney beş ayrı konsantrasyonda yapıldı. Yapılan deney sonucunda Carthamus tinctorius L. bitkisinin etanol özütünün artan konsantrasyonuna bağlı olarak antioksidan kapasitesinin de artığı görüldü. 1000 mg/ml de en yüksek antioksidan kapasitesine sahip olduğu belirlenmiştir. Sonuç olarak aspir (Carthamus tinctorius L.) bitkisinin etanol eksraktının yüksek antioksidan aktivite gösterdiği belirlenmiştir.

1. Giriş

İnsan vücuduna alınan oksijenin kullanımı ve metabolizması sırasında agresif moleküller oluşur. Yapılarında eksik elektron bulunduran ve kararsız yapıdaki bu moleküllere serbest radikaller denir. Vücudumuz bu serbest radikalleri kontrol altında tutar ama bazen bu denge bozulunca çok sayıda serbest radikal oluşur (1). Reaktif oksijen türleri kısa ömürlü ve kararsız olmaları nedeniyle organizmalarda bulunan nükleik asitler, lipidler, karbonhidratlar ve proteinler gibi biyolojik moleküllerle kolayca reaksiyona girebilirler. Bunun sonucunda yaşlanma, kanserler, immün sistem hastalıkları, karaciğer hastalıkları gibi birçok hastalığın nedeni olarak gösterilmektedir (2-4). Dış ve iç etkiler sonucu meydana gelen zararlı moleküller olan serbest radikallere karşı koyan maddelere antioksidan denir (5). Serbest radikallerin tam tersi olarak yapılarında fazla elektron bulundururlar ve bu elektronlar vücudu serbest radikallerden korumak ve onları etkisizleştirmek için kullanırlar Antioksidanlar, bitkilerin, yapraklarında, tohumlarında, köklerinde, çiçeklerin de ve kabuklarında yoğun miktarda bulunmaktadır (6). Yapılan birçok araştırmalara göre fazla miktarda meyve ve sebze tüketilmesiyle, hastalıklara yakalanma olasılığının azaldığı, kalp-damar sistemi hastalıklarında, kanserlerde ve ölüm oranlarında önemli derecede azalmalar olduğu görülmüştür (7). Ayrıca insan vücudunda oluşan bu serbest radikallerden korunmak için doğal bitkilerin içerdikleri flavonoidler, antioksidan maddeler ve fenolik bileşiklerin etkili olduğu bilinmektedir (8).

Tıbbi bitkiler, polifenoller gibi ana sekonder metabolitleri sayesinde doğal antioksidanların kaynağıdır. Günümüzde antioksidanlar kanser, kardiyovasküler hastalıklar ve nörodejeneratif rahatsızlık risklerinin azaltılmasıyla ilişkilendirildiği için çok sayıda çalışmanın ana konusudur. Bu doğal antioksidanların kaynakları arasında Asteraceae familyasının bir üyesi olan aspir (Carthamus tinctorius L.) önemli aromatik ve tıbbi bitkilerden biridir (9). Yalancı safran, boyacı safranı ve Amerikan safranı gibi isimlerle de bilinen, bu bitki; geniş yapraklı, sarı, kırmızı, turuncu, beyaz ve krem renklerinde çiçeklere sahip ayrıca dikenli ve dikensiz tipleri bulunur. Anavatanı Arabistan Yarımadası olup İran, Hindistan ve Pakistan gibi ülkelere yayılmıştır (10). Türkiye'de Anadolu'da yabani olarak bulunmakta ve ayrıca ekimi yapılmaktadır. Ülkemizde, aspir (aslında aspir olmasına rağmen haspir olarak bilinmekte) çiçeği olarak bazı yemeklere renk vermek amacıyla kullanılmaktadır. Alternatif tedavide de kullanılan aspir halk arasında kalp ve damar hastalıkları riskini düşürmek amacıyla ve bağışıklığı güçlendirip, vücut direncini arttırmak için kullanılır (11-13).

Bu çalışma, Gaziantep yöresinden toplanan Carthamus tinctorius L. bitkisinin antioksidan kapasitesinin belirlenmesi amacı ile yürütülmüştür.

2. Materyal Ve Metot

2.1. Materyal

Yaptığımız DPPH söndürme aktivitesini gerçekleştirdiğimiz çalışmada, aspir (Carthamus tinctorius L.) bitkisinin çiçekleri materyal olarak kullanıldı. Aspir çiçekleri kurutularak toz haline getirildikten sonra deneyde kullanıldı.

2.2. Yöntem

2.2.1.DPHH radikal söndürme aktivitesi

DPPH metodu 1995 yılında ilk olarak Brand Williams ve arkadaşları tarafından kullanılmış 1998 yılında ise Sanchez ve arkadaşları tarafından geliştirerek kullanmışlardır. Şu an günümüzde yaygın olarak kullanılan iyi bir antioksidan analiz yöntemidir. (14). Çalışma konusu olan Carthamus tinctorius L. bitkisinin ekstratının DPHH söndürme aktivitesi hesaplandı. Bu işlemde pozitif kontrol olarak BHA ve BHT kullanıldı. Deney beş ayrı konsantrasyonda yapıldı. Farklı konsantrasyonda ekstraktın etkisini anlayabilmek için 1 mM DPPH metanol çözeltisi kullanılarak deney yapıldı. 1 mg/ml BHA ve aynı oranda ekstrakt çözeltileri 5 ayrı tüplerde farklı konsantrasyonlarda 50, 100, 250, 500 ve 1000 µg/ml olarak hazırlandı. Carthamus tinctorius L. etanol ekstraktı ve pozitif kontrol 3'er ml alınarak üzerlerine 1 mM DPPH çözeltisi ilave edildi. Tüpler içerisinde oluşan karışımlar 30 dk karanlıkta ve oda sıcaklığında inkübüsyona bırakıldı. Bu süre sonunda 517 nm'de absorbans değerleri okundu.

3. Bulgular

Bu çalışmada farklı konsantrasyonlar ile DPPH radikal söndürme aktivitesi arasındaki korelasyon katsayısı %99 olarak bulundu (Şekil 1). Carthamus tinctorius L. bitkisinin 50, 100, 250, 500 ve 1000 mg/ml konsantrasyonlarda hazırlanan etanol ve su eksraktının miktarı arttıkça antioksidan kapasitesinin arttığı görüldü (Şekil 2).

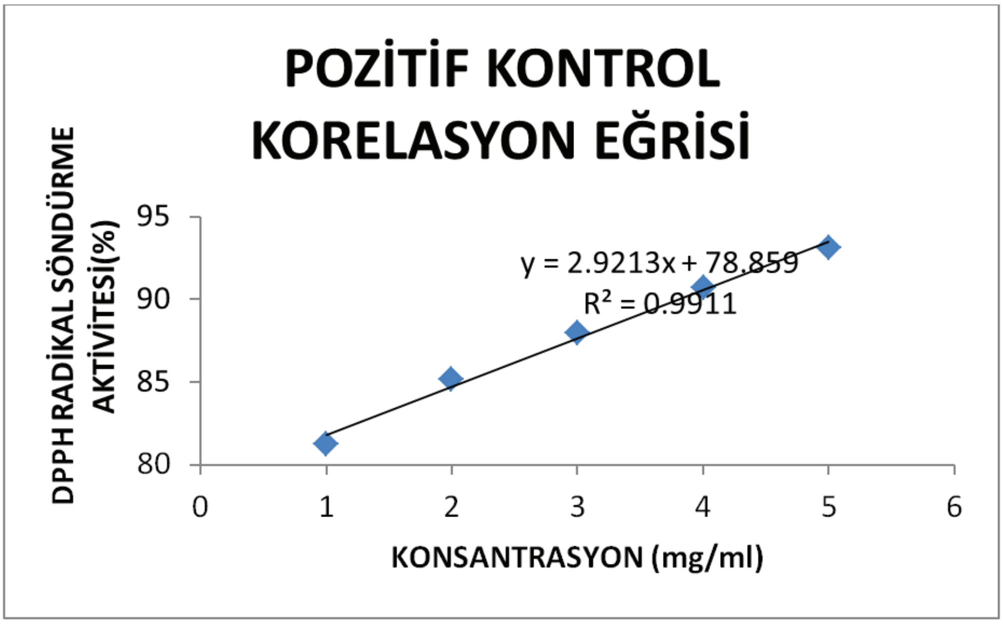

Şekil 1. Pozitif Kontrol Korelasyon Eğrisi

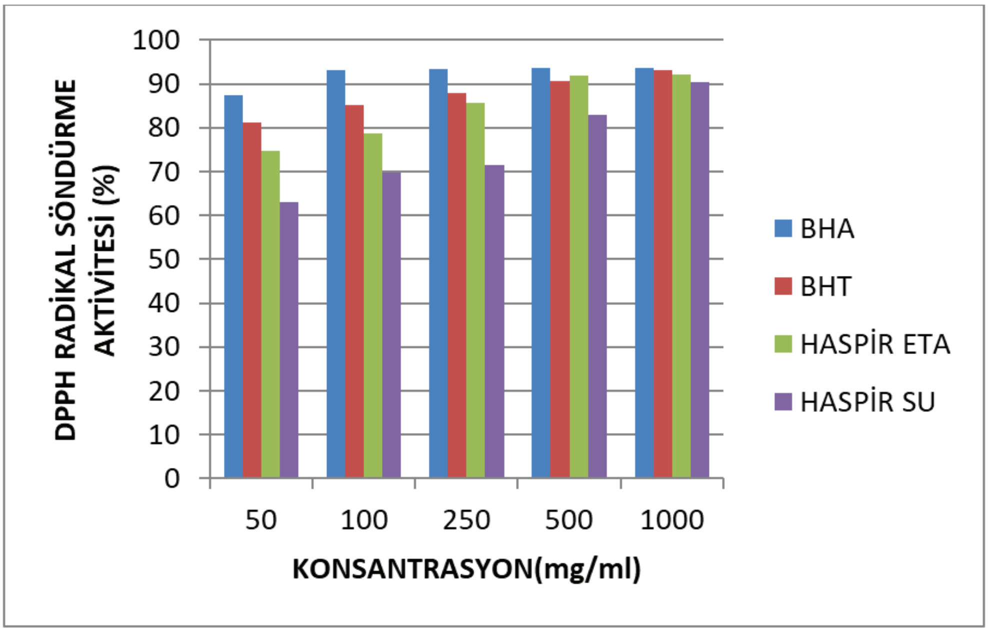

Şekil 2. DPPH analizi sonucunda aspir bitkisinin radikal giderme aktivitesi

4. Tartışma ve Sonuç

Bitki ve baharatların doğal antioksidan kaynaklar olarak kullanımlarını inceleyen çalışmalar son zamanlarda önem kazanmaktadır (15). Bitki uçucu yağ ve bileşenlerinin farmakolojik özellikleri incelenerek tıp, kozmetik ve endüstriyel alanlarda kullanılabilme imkânlarının geniş bir alana yayıldığı görülmektedir (16). Sentetik antioksidan ve koruyucuların yerine kullanılabilecek, özellikle bitkisel materyallerden doğal antioksidan ve antimikrobiyal maddelerin eldesine yoğun bir ilgi vardır. Bu konuda yapılan araştırmalar bitkisel materyallerin güçlü antioksidan ve antimikrobiyal aktiviteye sahip ikincil metabolitler adı verilen çok sayıda fitokimyasal bileşik içerdiğini belirtmektedir (3).

Metabolik olaylar sonucu insan vücudu içinde bazı reaktif oksijen türleri (süperoksit-O2-, hidroksil-OH- , hidrojen peroksit-H2O2, singlet oksijen-1O2) meydana gelmektedir (17). Araştırıcılar bu reaktif oksijen türlerinin; hipertansiyon, kalp yetersizliği, Alzheimer, diyabet, sağırlık, optik sinir dejenerasyonu gibi hastalıklara sebep olduğunu bildirmişlerdir (18,19). Vücutta bulunan antioksidan sistemler bahsi geçen hastalıkların oluşmasını engeller ve serbest radikallerin oluşmasına karşı koruyucu görev yapar. Özellikle sebze ve meyvelerde yoğun olarak bulunan antioksidan özelliğe sahip vitaminler (A, C, E), karotenoidler ve fenolik bileşikler insan beslenmesinde önemli yer tutmaktadırlar. Doğal kaynaklardan antioksidan üretimi ve kullanımı önem kazandığından, antioksidan bileşikler bakımından zengin gıdalara ilgi giderek artmaktadır. Aspir bitkisinin de çiçek, yaprak ve gövde kısımları; glutatyon, A, C, E vitaminleri ve β-karoten bakımından oldukça zengindir (20). Dünya'da 25 yabani türü olan Carthamus cinsinin ülkemizde 8 türü bulunmaktadır (21). Ana vatanı Arap Yarımadası olan aspir (Carthamus tinctorius), dünya çapında geniş bir yayılım göstermektedir. Aspirin en önemli özelliği tohumundan elde edilen yağın içeriğinin oldukça zengin olmasından kaynaklanmaktadır. Aspir yağı oleik asit (omega9) ve insanlar için esansiyel yağ asidi olan linoleik asit bakımından zengindir. Ayrıca insan sağlığı açısından önemi ise yüksek α-tokoferol içeriğidir (22). Aspir yağının bu özelliği, kandaki kolesterol seviyesini düşürmeye yardımcı olmaktadır.

Kuşoğlu (2015), Aspirin farklı kısımlarının (yaprak, tohum ve çiçek) toplam fenolik ve flavonoit içeriğini, DPPH, ABTS radikali giderme ve indirgeyici güç aktivitesini, OH-, H2O2 ve süperoksit radikali giderme aktivitesini incelemiştir. En yüksek fenolik madde içeriğinin yaprak ekstresinde, en yüksek flavanoit içeriğinin ise çiçek ve yaprak ekstresinden elde edildiğini bildirmiştir. Çiçek ekstresinin DPPH radikali giderme aktivitesinin standarttan da yüksek olduğunu, en yüksek ABTS radikali giderme aktivitesinin ise yaprak ekstresinin gösterdiğini belirlemiştir. İndirgeyici güç tayininde; yaprak ve çiçek ekstresinin, standart olarak kullanılan α-tokoferolden daha yüksek aktiviteye sahip olduğunu saptamıştır (23).

Yapılan bir çalışmada farklı tuz konsantrasyonları uygulanan aspir fidelerinden elde edilen ekstrelerin DPPH serbest radikali giderim aktiviteleri altı farklı konsantrasyonda (10, 25, 50, 100, 250, 500 µg ml-1) test edildi. Kontrol ve NaCl uygulama gruplarının tamamında konsantrasyon (10, 25, 50, 100, 250, 500 µg ml-1) arttıkça antioksidan aktivitenin de düzenli olarak arttığı belirlendi. (24).

Kırca ve arkadaşları tarafından yapılan çalışmada antioksidan aktivite belirleme yöntemlerinden biri olan DPPH yöntemini kullanmış ve Sarı Kantaron (Hypericum bupleuroides) ve Karaçalı (Paliurs spina-christi) bitkilerinin doğal antioksidan kaynağı olarak ümit verici bitki olduklarını bildirmişlerdir (25). Yine benzer şekilde Fathi ve ark., tarafından 2013 yılında Hypericum perforatum türü üzerine yapılan bir çalışmada DPPH aktivitesi 96,0±3,7 mg/mL, Toplam Polifenol içeriği 505,7±18 mg GAE/ g numune Toplam Flavanoid miktarı da 28,8±1,6 mg Quercetin/g numune olarak bildirilmiştir (26).

Bu çalışmada Carthamus tinctorius L. bitkisinin artan konsantrasyonuna bağlı olarak antioksidan kapasitesinin arttığı görülmektedir. 1000 mg/ml konsantrasyonda en yüksek antioksidan kapasitesine sahip olduğu belirlenmiştir. Bu konsantrasyonda pozitif kontroller ile kıyaslandığında elde edilen sonuçlar kayda değer olduğu fark edilmektedir. Serbest radikallerin neden olduğu birçok hastalığa karşı etkili olabilecek iyi bir antioksidan olduğu düşünülmektedir. Bununla ilgili daha fazla ve detaylı (in vivo ve in vitro) çalışmaların yapılmasına ihtiyaç vardır. Bu çalışma, çevre dostu olan yeşil sentez çalışmalarına bir ön bilgi niteliği taşımaktadır.

Kaynaklar

1. Kopani, M., Celec, P., Danisovic, L., Michalka, P., Biró, C.,. Oxidative stress and electron spin resonance. Clinica Chimica Acta, 364: 61-66, 2006.
2. Halliwell, B., Gutteridge, J.M.C., “A Role of free radicals and catalytic metal ions in human disease: An overview.” In: Methods in Enzymology, 186, 1-85, 1990
3. Young, I. S., Woodside, J. V., “Antioxidants in Health and Disease”. Journal of Clinical Pathology, 54: 176-186, 2001
4. Serteser, A., Gök, V., “Doğal Antioksidanların Biyoyararlılığı”. 3. Gıda Mühendisliği Kongresi. 2-4 Ekim, Sayfa: 83-98, Ankara, 2003.
5. Chen, Z. ve Zhong, C., Alzheimer hastalığında oksidatif stres. Sinir Bilim Bülteni , 30 (2), 271–281, 2014.
6. Katarzyna, M., Anna S., Zielinska-Blizniewska H., Ireneusz M.,. An evaluation of the antioxidant and anticancer properties of complex compounds of copper (ıı), platinum (ıı), palladium (ıı) and ruthenium (ııı) for use in cancer therapy. Mini Rev Med Chem. 18(16):1373-1381, 2018.
7. Somogyi, A, Rosta K, Pusztai P, Tulassay Z, Nagy G.,. Antioxidant measurements. Physiol Meas. Apr;28 (4):R41-55, 2007.
8. Kahkönen, M. P., Hopia, A. I., Vuorela, H. J., Rauha, J. P., Pihlaja, K., Kujala, T., S. Heinonen, M., “Antioxidant activity of plant extracts containing phenolic compounds”. Journal of Agricultural and Food Chemistry, 47: 3954-3962, 1999
9. Sun LP, Shi FF, Zhang WW, Zhang ZH, Wang K. Antioxidant and Anti-Inflammatory Activities of Safflower (Carthamus tinctorius L.) Honey Extract. Foods. Aug 2;9(8):1039, 2020. doi: 10.3390/foods9081039. PMID: 32748813;
10. Khémiri I, Essghaier B, Sadfi-Zouaoui N, Bitri L. Antioxidant and Antimicrobial Potentials of Seed Oil from Carthamus tinctorius L. in the Management of Skin Injuries. Oxid Med Cell Longev. Nov 4;2020:4103418, 2020.
11. Bacchetti T, Morresi C, Bellachioma L, Ferretti G. Antioxidant and Pro-Oxidant Properties of Carthamus Tinctorius, Hydroxy Safflor Yellow A, and Safflor Yellow A. Antioxidants (Basel). Jan 29;9(2):119, 2020.

12. Han SY, Li HX, Bai CC, Wang L, Tu PF. Component analysis and free radical-scavenging potential of Panax notoginseng and Carthamus tinctorius extracts. Chem Biodivers. 2010.
13. Aspir (Carthamus tinctorius L.) Çiçek Gelişimi Sırasında Fenolik Bileşiminde ve Antioksidan Aktivitesindeki DeğişimNidhal Salem, Kamel Msaada, Ghaith Hamdaoui, Ferid Limam ve Brahim Marzouk Tarım ve Gıda Kimyası Dergisi, 59 (9), 2011
14. Ali S.S., Kasoju N., Luthra A., Singh A., Sharanabasava H., Sahu A., Bora U., Indian Medicinal herbs as sources of antioxidants. Science Direct, Food Research, 41:1-15, 2008.
15. Tomaino, A., Cimino, F., Zimbalatti, V., Venuti, V., Sulfaro, V., De Pasquale, A. and Saija, A., Influence of heating on antioxidant activity and the chemical comparision of some spice essential oils. Food Chemistry, 89, 549-554, 2005.
16. Kırbağ, S. ve Bağcı, E., Picea abies (L.) Karst. ve Picea orientalis (L.) Link uçucu yağlarının antimikrobiyal aktivitesi üzerine bir araştırma, Journal of Qafqaz University, III (I), 183-190, 2000
17. Wallace, D., Mitochondrial DNA in Aging and Disease, Scientific American, 277(2): 40-47, 1997,
18. Demircan, G., Dıraman, E., Demircan, S., Kalp Hastalıklarında Oksidatif Stresin Rolü. Türk Kardiyoloji Derneği, 33(8): 488-492, 2005
19. Özdemir, F. A., Aymelek, F., Karataş, F., Aspir Bitkisinde Redükte, Okside Glutatyon ile A, C, E Vitamini ve β-karoten Miktarlarının Araştırılması, Fırat Üniversitesi Fen Bilimleri Dergisi, 23: 65-71, 2011,
20. Babaoğlu, M., Dünya'da ve Türkiye'de aspir bitkisinin tarihi, kullanım alanları ve önemi, Broşür, Trakya Tarımsal Araştırmalar Enstitüsü, Edirne, 2006,
21. Sujatha, M., Current Status and Future Prospects of In vitro Techniques and Biotechnology in Safflower Breeding, Sesame and Safflower Newsletter, 17: 9297, 2002,
22. Singh, V., Nimbkar, N., Safflower (Carthamus tinctorius L.), Chapter, 6: 167194, 2006,
23. Kuşoğlu, E., Aspir (Carthamus tinctorius L.) Bitkisinin Fenolik Bileşiklerinin Ve Antioksidan Aktivitesinin Tayini,Yüksek Lisans Tezi, İstanbul Aydın Üniversitesi Fen Bilimleri Enstitüsü, Gıda Mühendisliği Anabilim Dalı, İstanbul, 73s, 2015,
24. Keleş, B. İn vitro kültür koşulları ve tuzluluk (NaCl) stresi altında çimlendirilen aspir (Carthamus tinctorius L.) bitkisinde meydana gelen morfolojik, fizyolojik ve biyokimyasal değişimler (Master's thesis, Batman Üniversitesi Fen Bilimleri Enstitüsü), 2019
25. Kırca, A., Bilişli, A., Demirel, N.N., Turhan, H. ve Arslan, E., Çanakkale florasındaki bazı tıbbi ve aromatik bitkilerin antioksidan ve antimikrobiyal aktiviteleri. TÜBİTAK Proje No: 104 0 292. Çanakkale, 2007.
26. Fathi, H., Ebrahimzadeh,M.A., Antioxidant and free radical scavenging activities of Hypericum perforatum L. Int. J. Forest, Soil and Erosion. 20133(2):68-72, 2013. ISSN 2251-6387.

Experimental Investigation of Heat Transfer and Pressure Drop Characteristics of a Rectangular Narrow Channel Type Heat-Exchanger with Rectangular Staggered Fins

Şafak ÜRKMEZ[1]*, Assoc. Prof. Zafer GEMİCİ[1]

[1]*Yildiz Technical University, Turkey*

Abstract: In this paper, a new rectangular narrow heat-exchanger was investigated, and experiments were carried out to determine its heat transfer and pressure drop performance. Rectangular pin fins are placed on the bottom surface of the channel to increase the heat transfer. On the other hand, in order to reduce the hydraulic resistance of these pin fins, a distance called tip clearance is left between the fin tips and the upper surface of the rectangular channel. Different Reynolds numbers and heat supply position were examined to see the performance of the geometry. Heat fluxes were applied to only the upper surface and only the lower surface. According to the results, as the Reynolds number increases the Nusselt number increases but and friction factor decreases. While the tip clearance causes the heat transfer coefficient to increase in low Reynolds numbers somewhat, on the other hand, it loose positive effect with increasing Reynolds numbers.

Keywords: Heat-exchanger, clearance, heat transfer, pressure drop.

1.Introduction

Heat exchangers are widely used in different areas of our life, for example; for cooling batteries, electronic circuits, motors, household appliances, etc. Some of them use air as a coolant, while others use water, they have different geometries and scales. In this paper water is used as a coolant in experiments to cool down the flat electric heaters, by using miniature rectangular fins having a tip clearance with the other surface of the heat exchanger channel. On the other hand, the cooling of equipment with high heat flux such as batteries and electronic cards becomes more and more important with each passing day. Because the equipment is getting smaller and producing more heat per unit area. Therefore, it is necessary to develop higher performance heat exchangers. Due to this need, more and more researchers have been working on this subject every day. In this study, a finned heat exchanger, which can be placed on the surface of the heat generating battery or electronic card, in the form of a narrow channel, which can form a sandwich like structure, is designed. Experimental studies were carried out on the said heat exchanger.

Şara et al. (2003) used staggered pin fins with a clearance in a rectangular duct. In this study, air was used as a working fluid and fins were in square shape. They showed that staggered arrangement is better than inline arrangement in heat transfer, but inline arrangement is better in pressure drop or friction factor. Also, they have concluded that average Nusselt number and friction factor increased with decreasing clearance ratio [1]. Zhao et al. (2016)also studied on a rectangular channel and tried 5 different shaped pin fins. They compared these fins with their friction factors [2].

Peles et al. (2005) showed that with increasing Reynolds number, thermal resistance increases, so in this paper just small Reynolds numbers were focused. Because thermal resistance is a criterion to measure heat exchanger's efficiency [3].

Vatanparast et al. (2020), used numerical techniques for rectangular staggered fin pins to compare entropy generation according to Reynolds number (50-75-100). They found that with increasing Reynolds numbers entropy generation increases. Additionally, total entropy generation increases with increasing width of fins [4].

Tanda et al. (2001) examined the heat transfer and pressure drop in a rectangular channel using air as a working fluid and diamond shaped fins as an extended surface. In same conditions, Nusselt number of the staggered arrangement is always higher than the in-line arrangement of fins, and pressure drop is higher in staggered arrangement. The best thermal performance was obtained with low-intermediate degrees of fin density. Also, thermal performance of diamond-shaped elements showed that heat transfer rate by a factor of up to 4.4 for equal mass flow rate [5].

Dhumne and Farkade et al. (2013) examined pressure drop and heat transfer in perforated fins in staggered arrangement. They found that perforated fin has higher Nusselt number than solid fins, and with increasing fin number, heat transfer increases. Also in high Reynolds numbers, friction factor of perforated fins is slightly better than solid fins. Above 10000 Reynolds number, the flow with low Reynolds number shows more performance than higher Reynolds number in pin fins [6].

One of the other papers related to these topics is also mentioned here [7]. It is like previous articles, but it is concluded differently that performance efficiency of the in-line arrangement fins are a little bit higher than the staggered arrangement fins. Similar studies have been performed for the fluid material is air [8,9].

In addition, there are micro pin fin studies [10]. In these systems, different fluids are used such as water and water with nanofluids. Nanofluids increase the Nusselt number very much, but also increase the pressure drop drastically. Between 100-2000 Reynolds numbers, triangle geometry is the best with respect to their performance then square, hexagon and circle, respectively. Like the previous articles, it says staggered configuration is better at heat transfer but bad at pressure drop with respect to in-line configuration. Contrary to studies in which the Reynolds number is high and air is used as the working fluid, the authors say that in every cases, staggered geometries better than inline geometries around 4%.

In this experimental study, miniature rectangular pin fins having tip clearance, and staggered arrangement are used to cool the batteries were chosen to achieve high Nusselt numbers and low friction factor depending on Reynolds numbers. In literature, nearly nobody studied narrow channel with rectangular staggered fins having tip clearance, and fully developed flow in it. In this test system, water entrance part of the channel was made intentionally long so that the flow inside the channel can reach fully developed flow.

2. Material and Methods

2.1. Materials and test system

The system in which heat exchanger is tested consist of rectangular channel, tubes, pump, datalogger, energy supplier, computer, U-type manometer, flowmeter, and mini-chiller. The test apparatus can be seen in Figure-1.

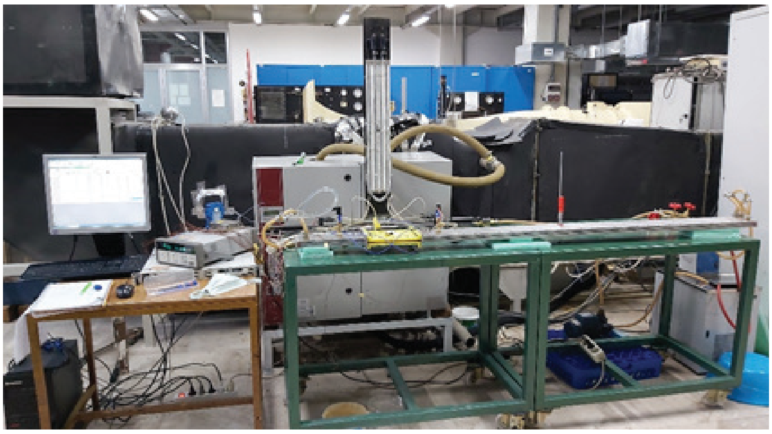

Figure 1: Experimental system

Water is used as a working fluid which flows through the system. Mini chiller sets the temperature of the water, and it keeps the temperature of water at 30°C. Pump takes the water from mini-chiller and is put beneath the mini-chiller consciously to create a low pressure and evacuate the water from mini-chiller to the pump. Pump flood the water to the system and supply the needed power and pressure. Then, water reaches the rectangular channel through the tubes. On this side of the tubes, there is a slide valve, and it adjusts the desired flow rate and Reynolds Number to the heat exchanger. This rectangular channel is intentionally long enough (1,5 m) to reach fully developed flow, this has nearly never tried in the literature. This long rectangular narrow channel is connected to the heat exchanger. Heat exchanger has 3 parts: fins and walls of the heat exchanger (made of copper, can be seen in figure 2), flat electric heaters (in figure 3 red parts) which are between the walls of the heat exchanger and Kestamide® (Cast Polyamide), outside of the heat exchanger which is Kestamide® (in figure 3 yellow parts).

Figure 2: Fins and walls of the heat exchanger

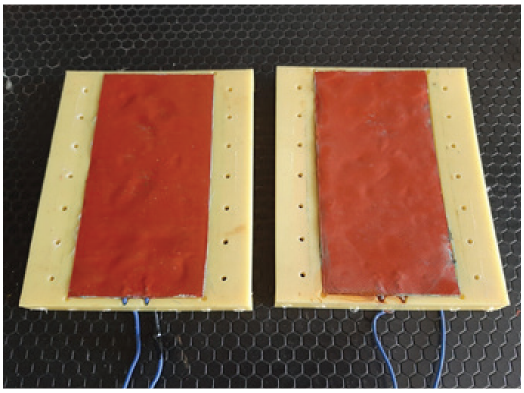

Figure 3: Flat heaters (red parts) and Kestamid® (yellow parts)

Water goes through the long rectangular channel, then the heat exchanger and after that reaches the short rectangular channel. This short channel is connected to a returning tube by means of a collector which has three ends attached on the channel. There is a flowmeter on the returning tube. Flowmeter measures the flow rate, but to increase the certainty of it, circulated water is weighed for a specified time, then mass flow rate is calculated. These manually measured data is used to find a correction constant for the flowmeter. After passing the flowmeter, water comes to the mini chiller where this cycle begins.

In this system, the electric heaters supply heat to circulated water in two ways: only from the upper surface and only from the lower surface. By adjusting the Reynolds numbers between 1000-4500 with a valve, it was investigated how these changes affect the heat transfer and pressure drop. Copper surface having fins placed bottom side of the heat exchanger and plain copper with no fins placed upper side of the heat exchanger. The heat exchanger and channels include 6 thermocouples and 2 resistance temperature detectors (RTDs). RTD measures temperature more precisely than thermocouple. 2 RTDs are used in entrance and exit of the heat exchanger which measure the entrance temperature and exit temperature of the water from the heat exchanger. Bottom and top of the heat exchanger contain thermocouples one for each, also the heat exchanger includes 4 thermocouples which are placed left and right side of the heat exchanger. The figure for thermocouple locations can be seen in Figure-4. In figure 4, right part is long channel which water enters, and left part is small channel which water exits. 15 and 14 numbers show RTDs, while 10, 11, 12, 16, 17, 18 numbers show thermocouples. 12 and 16 numbered thermocouples measure the temperature of the Kestamid® surfaces; 10, 11, 17 and 18 numbered thermocouples are located inside the wall of the heat exchanger (copper).

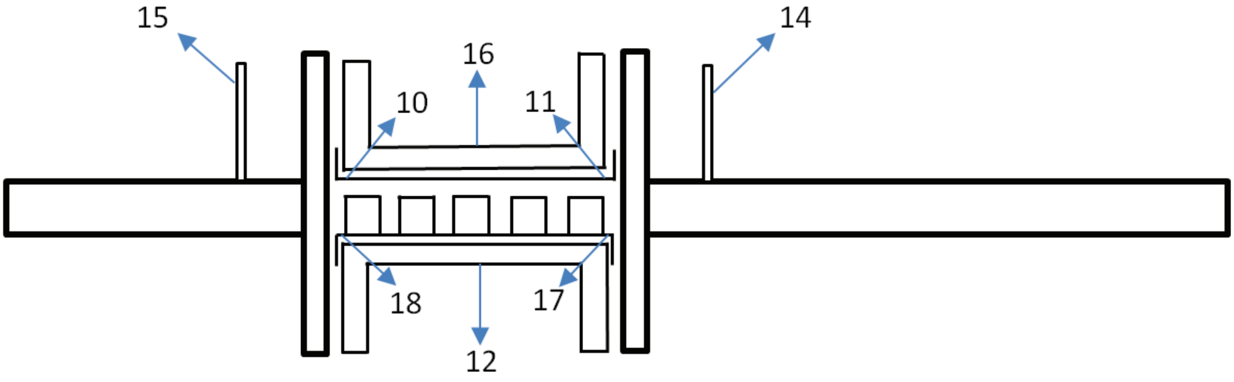

Figure 4: The Thermocouple Locations

There are two ports before and after the heat exchanger which are connected with tubes to the U-manometer for measuring the pressure drop through the channel with fins. For measuring the pressure drop precisely, with an acceptable length, water is used in the manometer whose ends are not open to the atmosphere. Instead, both ends of the manometer are connected to a collector having a pressure regulation valve on it. So, when static pressure exerted, water compresses the trapped air at the top of the water column of the manometer. The trapped air pressure equals to the static pressure of the flow, and the difference of the water columns gives us the pressure drops.

In this system, the channel is made of aluminium, inside of the heat exchanger made of copper and outside made of Kestamid®. Diameter of the tubes are 8 mm and cross-section of the channel is 5*100 mmxmm. All the thermocouples are connected to the datalogger which gathers data and transfers them to the computer.

Copper plates has an area of 200*100 mm x mm and equal to w and L respectively (figure 5). Height of the channel (h) is 5 mm and dimensions of the fin is 1*10*4 mm equal to t, l, H respectively (figure 6).

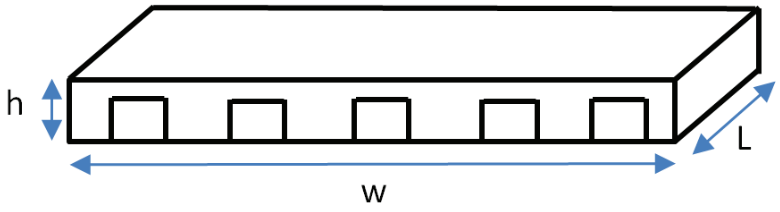

Figure 5: Dimensions of the copper plates

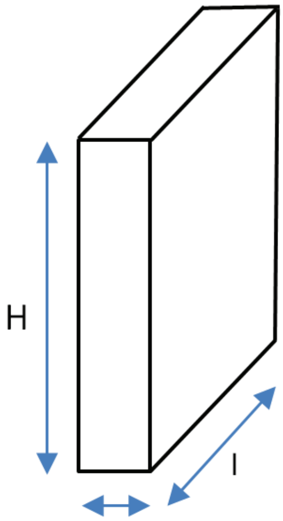

Figure 6: Dimensions of the fin

2.2. Methods

Thermocouples, RTDs and flowmeter have been calibrated to read the right values. To calibrate the flowmeter, mass flow rate was calculated at different Reynolds numbers by means of weighing the circulated water.

Nusselt number and friction factor are the dimensionless numbers used as appropriate means to compare heat transfer rate and pressure drop. Because of being unitless, it gives chance to compare different heat exchangers with different properties. In this paper, Nusselt number will be found by finding convection heat transfer coefficient and Nusselt-Reynolds graph will be found for comparing heat transfer. Friction factor-Reynolds graph will be found for comparing pressure drop, as well. Nusselt number:

$$Nu = \frac{h * D_h}{k} \tag{1}$$

To find Nusselt number, firstly convection heat transfer coefficient should be evaluated. Because there are two different heating modes of the system, these are heating from only top and heating from only bottom. Convection heat transfer coefficient should be determined for these two different conditions separately.

$$Q = Q_t + Q_b = \dot{m} * c_p * \Delta T \tag{2}$$

$$\Delta T = T_{in} - T_{out} \tag{3}$$

Heat transfer from the top surface to the water:

$$Q_t = A_t * \bar{h}_t * \Delta T_{lntop} \tag{4}$$

Where:

$$\Delta T_{lntop} = \frac{(T_{top} - T_{in}) - (T_{top} - T_{out})}{\ln\left(\frac{T_{top} - T_{in}}{T_{top} - T_{out}}\right)} \tag{5}$$

$$A_t = w * L \tag{6}$$

$\dot{m}$, c_p, T_{in}, T_{out} are the water properties, T_{in} and T_{out} are values of RTDs. T_{top} is average of thermocouples number 10 and 11.

Heat transfer from the bottom surface to the water:

$$Q_b = A_b * \bar{h}_b * \eta^* * \Delta T_{lnbot} \tag{7}$$

Where:

$$A_b = A_{fin} + A_{base} \tag{8}$$

$$A_{fin} = N_f * (2 * \left(H + {}^{t}/_{2}\right) * l + 2 * \left(H + {}^{t}/_{2}\right) * t) \tag{9}$$

$$A_{base} = w * L - N_f * t * l \tag{10}$$

$$\eta^* = 1 - \frac{A_{fin} * (1 - \eta)}{A_b} \tag{11}$$

$$\eta = \frac{\tanh\left(m * \left(H + \frac{t}{2}\right)\right)}{m * \left(H + \frac{t}{2}\right)} \tag{12}$$

$$m = \sqrt{\frac{\bar{h}_b * P}{k * A}} = \sqrt{\frac{\bar{h}_b * 2 * (l + t)}{k * l * t}} \tag{13}$$

$$\Delta T_{lnbot} = \frac{(T_{bot} - T_{in}) - (T_{bot} - T_{out})}{\ln\left(\frac{T_{bot} - T_{in}}{T_{bot} - T_{out}}\right)} \tag{14}$$

A_b is the bottom surface area of the heat-exchanger, N_f is the number of the fins, η is the fin efficiency, η^* is the overall fin efficiencies, T_{bot} is the average of thermocouples number 17 and 18. For both of the upper and bottom surfaces (this experimental study doesn't include):

$$Q = Q_b + Q_t \tag{15}$$

$$Q = A_t * \bar{h} * \Delta T_{lntop} + A_b * \bar{h} * \eta^* * \Delta T_{lnbot} \tag{16}$$

In these equations, only unknown parameter is convection heat transfer coefficient, so mean heat transfer coefficient will be found from these equations.

Friction factor will be calculated from the following equation:

$$f = \frac{2*\Delta P*D_h}{d*v^2*L} \tag{17}$$

3. Results

From equation 3, Q_t was obtained, then from equation 5, ΔT_{lntop} was obtained, after that equation 2 provides to calculate the h_t. Then, Nusselt numbers with respect to Reynolds numbers can be calculated. In second part of experiment, heat was given just from the bottom surface of the heat exchanger. Similar way can be followed but to find h_b, Excel was used to solve closed equations. In figure 7, values are obtained from these calculations and shown in this figure. In figure 8, more common way of expressing heat transfer using unitless numbers is shown, this is more common way in literature.

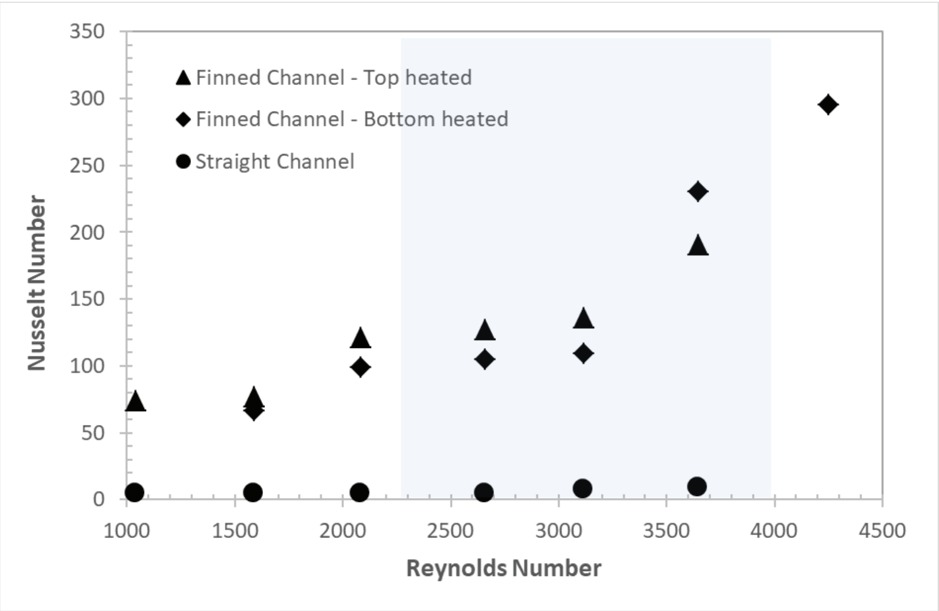

Figure 7: Nusselt number of the heat exchanger with respect to Reynolds number when only heated from the top surface, when only heated from the bottom surface and when it is a straight channel

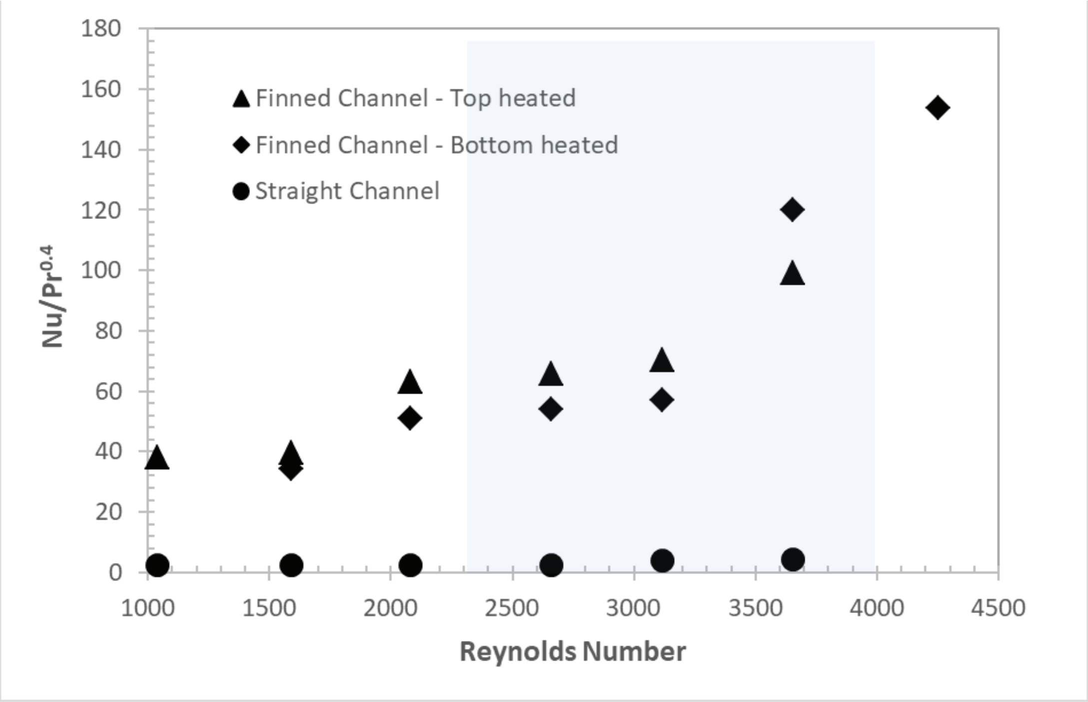

Figure 8: *Nu/Pr$^{0.4}$* Number with respect to Reynolds Number

From equation 17, friction factor was obtained with the help of ΔPbot which is read from the U-manometer and it can be seen in figure 9. Also in literature, to find heat transfer enhancement according to pressure drop, overall thermal performance factor (η) is defined [11] and can be seen in figure 10.

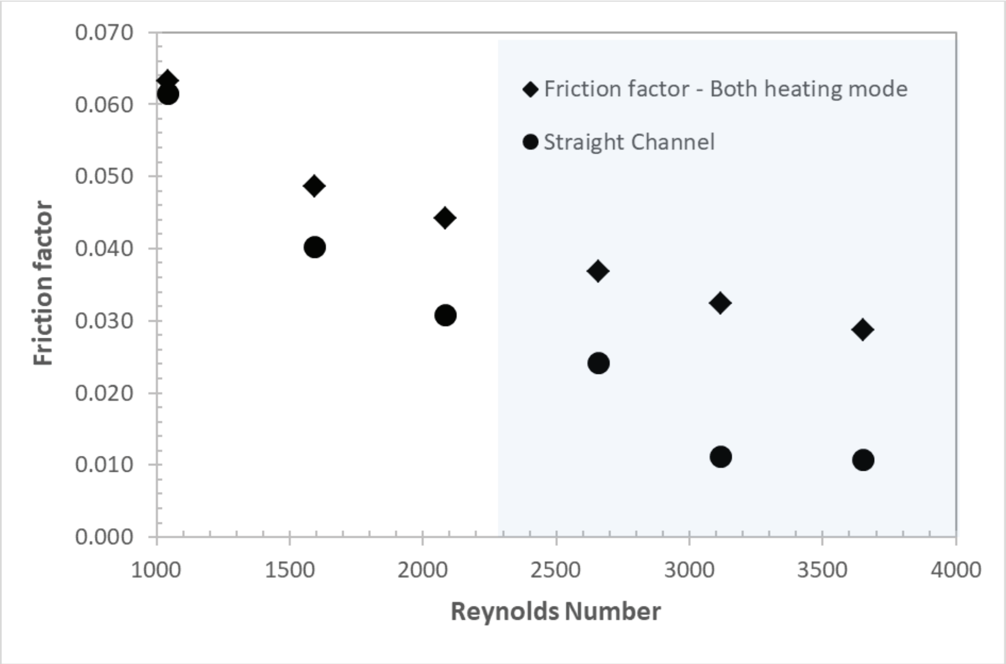

Figure 9: Friction factor of the heat exchanger with respect to Reynolds number when only heated from the top surface and bottom surface (which has the same values) and when it is a straight channel

$$\eta = \frac{\overline{Nu}/\overline{Nu_0}}{\left(f/f_0\right)^{1/3}} \tag{18}$$

Where $\overline{Nu_0}$ is Nusselt number of straight channel and f_0 is friction factor of straight channel, $\overline{h}$ and f average Nusselt number and friction factor of surface with fin.

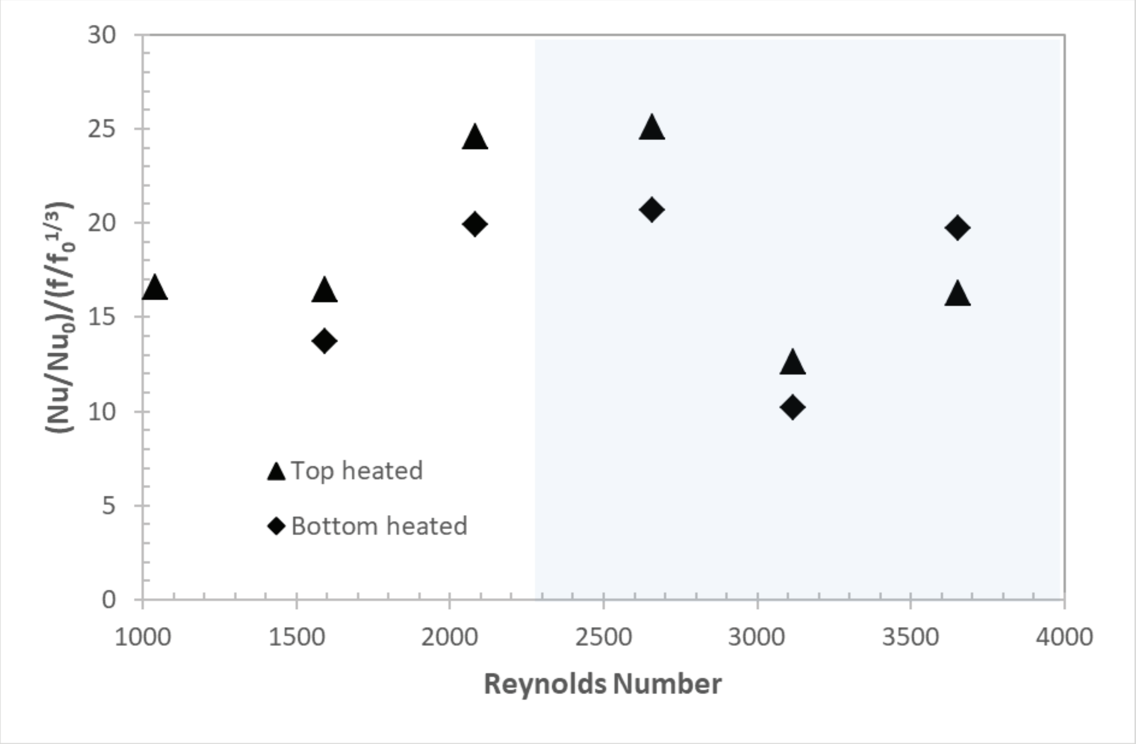

Figure 10: Overall thermal performance factor (η) with respect to Reynolds number

4. Discussion and Conclusion

As it can be seen from the figures, the flow in the system is changing from laminar to transition. Distribution of values are almost the same in figure 8 and figure 9. At laminar and transition flow region, top heated surface's Nusselt (or Nu/Pr0.4)numbers are slightly higher than the bottom heated surface's values but at the end of the transition region bottom heated surface get ahead of the top heated surface. It means that at laminar and transition region, mean heat transfer coefficient is almost identical for both top heated and bottom heated cases, while beyond laminar region, mean heat transfer coefficient of top heated case is much higher than the other case's one. The clearance between the fin tip and top surface causes additional turbulence between them and this increases the mean heat transfer coefficient for the top surface. On the other hand, at the end of the transition region bottom surface starts to get ahead of top region. So, because of bottom surface's high area with respect to bottom area, at the high Reynolds numbers bottom surface starts to get ahead of top surface. Also, these Nusselt numbers show that huge amount of heat with respect to straight channel can be taken from the source (it could be battery cell, electronic circuit, engine…).

Figure 10 shows that both heating modes have the same friction factor and therefore have same pressure drop. Also, straight channel has lower friction factor than both heating modes as expected. In figure 11, overall thermal performance factor (⊠) varies from 10 to 25, the highest values are near 2300 Reynolds numbers which is boundary of laminar flow. This factor also provides making comparison between this system and other arrangements

Acknowledgements

This project was supported by YTU Scientific Research Projects Coordination Unit ‘YTU BAP’.

References

[1] O.N Şara,
Performance analysis of rectangular ducts with staggered square pin fins,
Energy Conversion and Management,
Volume 44, Issue 11,
2003,
Pages 1787-1803

[2] Hongxia Zhao, Zhigang Liu, Chengwu Zhang, Ning Guan, Honghua Zhao,
Pressure drop and friction factor of a rectangular channel with staggered mini pin fins of different shapes,
Experimental Thermal and Fluid Science,
Volume 71,
2016,
Pages 57-69

[3] Yoav Peles, Ali Koşar, Chandan Mishra, Chih-Jung Kuo, Brandon Schneider,
Forced convective heat transfer across a pin fin micro heat sink,
International Journal of Heat and Mass Transfer,
Volume 48, Issue 17,
2005,
Pages 3615-3627

[4] Mohammad Amniyeh Vatanparast, Siamak Hossainpour, Alireza Keyhani-Asl, Sadra Forouzi,
Numerical investigation of total entropy generation in a rectangular channel with staggered semi-porous fins,
International Communications in Heat and Mass Transfer,
Volume 111,
2020,
104446,

[5] Giovanni Tanda,
Heat transfer and pressure drop in a rectangular channel with diamond-shaped elements,
International Journal of Heat and Mass Transfer,
Volume 44, Issue 18,
2001,
Pages 3529-3541

[6] Dhumne, Amol B., and Hemant S. Farkade. “Heat transfer analysis of cylindrical perforated fins in staggered arrangement.” International Journal of Innovative Technology and Exploring Engineering 2.5 (2013): 225-230.

[7] Ugur Akyol, Kadir Bilen,
Heat transfer and thermal performance analysis of a surface with hollow rectangular fins,
Applied Thermal Engineering,

Volume 26, Issues 2–3,
2006,
Pages 209-216

[8] Wang, Fengming, Jingzhou Zhang, and Suofang Wang. "Investigation on flow and heat transfer characteristics in rectangular channel with drop-shaped pin fins." Propulsion and power research 1.1 (2012): 64-70.

[9] Jeng, Tzer-Ming, and Sheng-Chung Tzeng. "Pressure drop and heat transfer of square pin-fin arrays in in-line and staggered arrangements." International Journal of Heat and Mass Transfer 50.11-12 (2007): 2364-2375.
[10] Arjun, Kozhikkatil Sunil, and Rakesh Kumar. "Optimization of micro pin-fin heat sink with staggered arrangement." Thermal Science 22.6 Part B (2018): 2919-2931.

[11] G. Liao, X. Wang, J. Li, F. Zhang, A numerical comparison of thermal performance of in-line pin-fins in a wedge duct with three kinds of coolant, Int. J. Heat Mass Transf. 77 (2014) 1033–1042. https://doi.org/10.1016/j.ijheatmasstransfer.2014.06.010.

Hydrogen and Electricity Production with Nuclear Power Plant and Solar Cells

Gurur Furkan SARILMAZ[1],
Candeniz SECKIN[1]
[1]*Marmara University, Istanbul, Turkey*
furkansarilmaz@marun.edu.tr, candeniz.seckin@marmara.edu.tr

Abstract: Today's world's biggest problem is energy. The answer to this problem comes from hydrogen. Producing zero-emission fuel with zero-emission methods is what the world needs. The electricity produced by renewable sources mostly fluctuates to compensate that a nuclear power plant will generate constant electricity production. The advantages of a Nuclear Hybrid Energy System continues, due to the nuclear power plant's safety regulations, there will be plenty of space to install Solar cells. In NHES the renewable power plants and nuclear power plants are competing with each other. The excess electricity or when the electricity demand is less than the hydrogen demand, the electricity will be converted to hydrogen via electrolysis. The most important part of this study is every component of the study is available and technologically ready..

1. Introduction

Energy demand increases as the global population and economy expand and more people move to urban locations [1]. Fossil fuels, which are limited by their geographic availability and ease of extraction and are exhausted, make up the majority of the energy used for electricity today. Constant use of energy derived from hydrocarbons resulted in enormous increases in atmospheric CO2 and greenhouse gases, which have been connected to global warming [2]. The future of the globe depends on the availability of sustainable and renewable energy sources in order to reduce global warming and maintain a clean environment [3]. It can be challenging to reach a large-scale, cost-effective production of power from renewable energy sources. In fact, one of these energy sources' most obvious traits is how varied and irregular they are. Technical solutions that are effective and scaled up must be used to address these difficulties. In order to address the volatility and discontinuity of renewable energy sources, large-scale storage systems have been developed and crafted to meet market demand [4]. Storage devices can separate supply from demand by transmitting generated energy over a range of time scales [5]. Due to their capacity for storing and transmitting energy as well as their affordability, hydrogen-based energy storage devices are growing in popularity for large-scale energy storage [6]. Despite the fact that some academics support hydrogen as an energy carrier for the previously mentioned reasons, most recent studies have found that a completely hydrogen dependent economy is still debatable and out of reach, especially now that it has started to show promise [7]. Whatever the obstacles, the production of clean hydrogen is increasing to lower CO2 emissions and supply the world's energy needs [8].

Hydrogen can be created by the use of some energy sources, including coal, natural gas, nuclear, biomass, solar, and wind. To meet the majority of the world's current hydrogen demand, fossil fuels like natural gas, oil, and coal are still used because they are the most economical source at the moment, with production costs ranging from \$2 to \$4 per kilogram [9].

Only a few of the methods for simultaneously producing heat and electricity in addition to hydrogen from water in the same nuclear power reactor have been documented in the literature [10]. These methods include traditional water electrolysis, steam reforming, high-temperature steam electrolysis, hybrid, and thermochemical cycles. Given that it can generate both hydrogen and inexpensive power simultaneously [11], the nuclear hybrid energy system (NHES) is one of the most alluring technologies.

Creating hydrogen and electricity are the main topics of this study. Location affects and varies the needs for hydrogen and electricity greatly. As a clear illustration, Bayburt, a small area with fewer residents, has a lower energy demand than Istanbul, a larger city. Furthermore, clean energy sources must take the place of fossil-based energy sources in order to meet global energy demands while reducing greenhouse gas emissions.

In conclusion, this paper offers details on nuclear-renewable clean hydrogen hybrid systems, with an emphasis on the electrolysis hydrogen production process. LabVIEW is used to integrate the electrolysis and pressurized water reactor-type small modular reactor (SMR) in order to collect data, and System Adviser Model is used to simulate a PV (photovoltaic) plant. By integrating hourly data from SAM into LabVIEW and displaying potential outcomes, it is possible to determine the amount of hydrogen in kg and electricity in kWh.

2. Material and Methods

2.1. PWR-type SMR

In this study, it was recommended to build a nuclear power facility that used pressurized water reactor light water technology. Over 250 PWRs are used for power generating, making it the most prevalent. Water serves as a moderator and a coolant in PWRs. Under high pressure and with the help of atomic fission energy, the primary coolant (water) is injected into the reactor core. The steam generator uses the heated water to transport its thermal energy to a secondary circuit, where steam is produced and transmitted through turbines to turn an electric generator, producing electricity. The primary circuit in major power plants is composed of a reactor pressure vessel (RPV), steam generators, pumps, and pressurizer, together with any connecting pipes [12].

The bulk of contemporary designs for compact modular reactors have an integrated layout. The main coolant system parts, such as the pumps, pressurizers, and steam generators, are housed inside integrated reactors of the RPV. The integrated solution reduces the dimensions of the nuclear power plant (NPP), eliminates some external pipes and components, and adopts a compact containment.

A PWR prototype as a typical small PWR, the Small Modular Nuclear Reactor is used in this study. The components and design of PWR-type SMR have been tested for Technology Readiness Level (TRL) and this type of SMR will soon be offered commercially. Additionally, this reactor doesn't require reactor coolant pumps because it has a pressurizer and may operate with natural circulation primary flow.

The steam generator for the prototypical PWR-type SMR is a helical-coil heat exchanger that is located in the annular space between the hot leg riser and the interior wall of the reactor vessel. Feedwater enters the tubes from the bottom, and slightly superheated steam exits from the top. Each reactor is housed in its own high-pressure containment vessel, which is submerged in a stainless steel-coated concrete pool. Installed inside the reactor is a modest 45 MW conventional steam turbine generator set made to operate under prototypical SMR steam generator outlet circumstances. To stop erosion in the final turbine stages, as in every PWR plant, the moisture separator and subsequently the re-heater must be taken into account.

Table 1: Parameters of PWR SMR similar to [13].

Parameters	
Live steam flow	71.3 kg/s
Turbine inlet temperature	528 K
Turbine inlet pressure	31 Bar
Condenser pressure	0.063 Bar
Exit steam quality	80,60%
Nuclear heat input	~160 MW
Total heat input	~160 MW
Net electric power	~45 MW
Net electric efficiency	28,14%

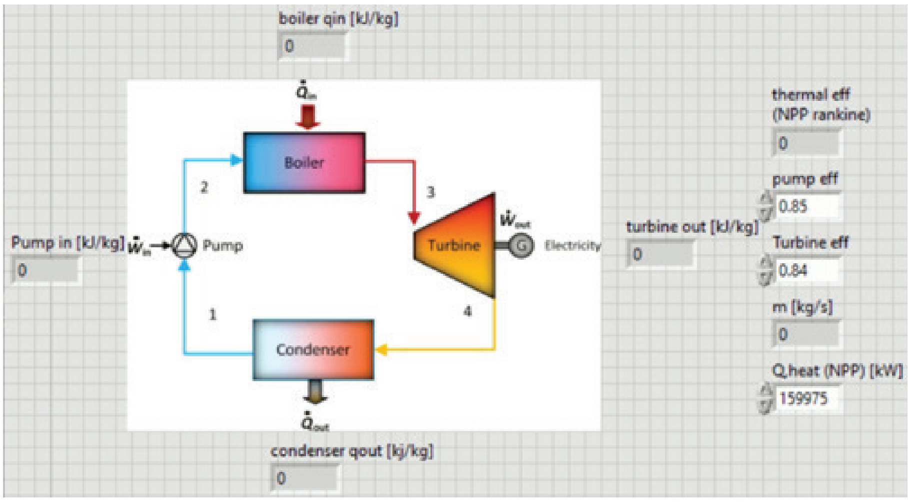

boiler qin [kJ/kg] 0

thermal eff (NPP rankine) 0

pump eff 0.85

Pump in [kJ/kg] 0

turbine out [kJ/kg] 0

Turbine eff 0.84

m [kg/s] 0

Q,heat (NPP) [kW] 159975

condenser qout [kj/kg] 0

Figure 1: An energy conversion cycle of the Rankine type for a PWR type SMR is modelled using LabVIEW at the system level.

2.2. Photovoltaic (PV) Solar Power

The substrate portion in the crystal solar cell is doped with either p-type (e.g. boron, gallium) or n-type materials (phosphorus, arsenic). On the surface of the cell, if the bulk structure is p-doped, n-type, if n-type doped, a p-n junction is formed in the structure and with p-type elements. The aim here is that the light falling on the photovoltaic cell creates a photocurrent by activating the charge carriers from the doping ions through the light in the bulk structure. These charge carriers travel through the solar cell to the metal contacts on the structure, and from there they are carried out by electrical circuits that carry the electricity out of the module via metal wires. In this way, electricity production is achieved.

One of the most cost-effective solar to hydrogen technologies being explored on both the electrolysis and solar portions uses a PV system for energy generation in conjunction with a low-temperature electrolyser. Beginning in the early 1970s, water electrolysis and a PV system were used to produce hydrogen. Given the ecological and financial concerns, using a PV current source that results from directly converting solar energy into electricity could be the most cost-effective way to produce solar hydrogen. The idea of converting solar energy into hydrogen using solar PV cells and the viability of using hydrogen as a clean fuel to replace liquid and gaseous fossil fuels were developed [12].

The efficiency of the solar hydrogen production plant would be around 18% if the efficiency of PV cells and the electrolyze system were assumed to be 20% and 80%, respectively [14].

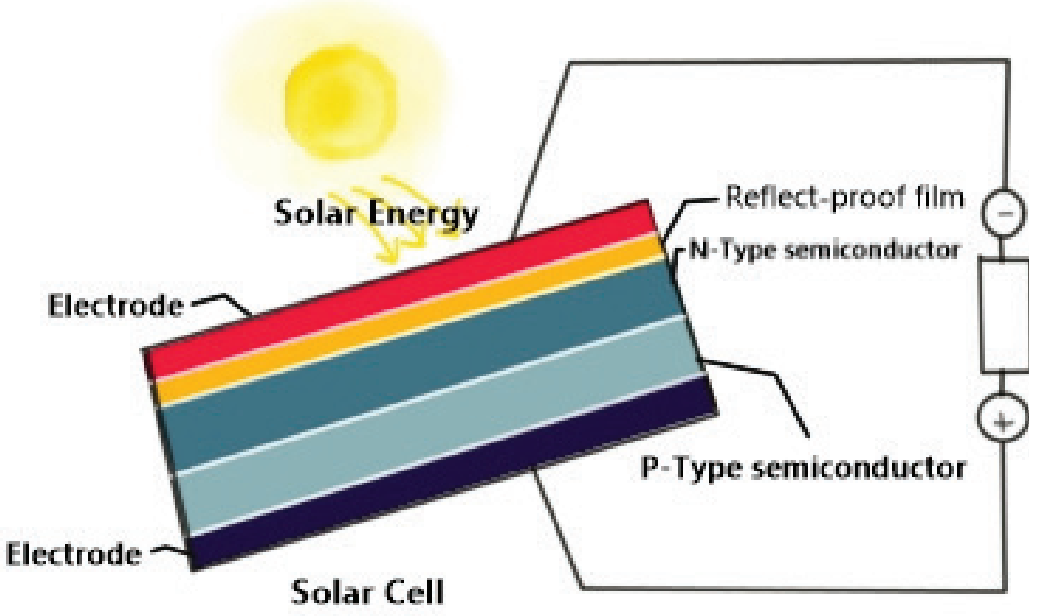

Figure 2: PV panel working mechanism.

Table 2: Parameters of PV system

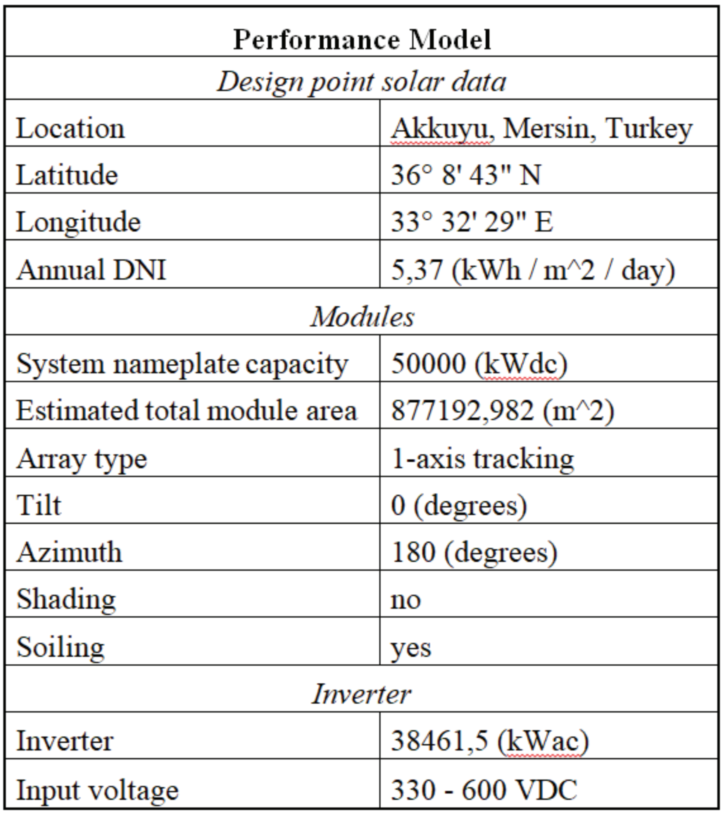

Performance Model	
Design point solar data	
Location	Akkuyu, Mersin, Turkey
Latitude	36° 8' 43" N
Longitude	33° 32' 29" E
Annual DNI	5,37 (kWh / m^2 / day)
Modules	
System nameplate capacity	50000 (kWdc)
Estimated total module area	877192,982 (m^2)
Array type	1-axis tracking
Tilt	0 (degrees)
Azimuth	180 (degrees)
Shading	no
Soiling	yes
Inverter	
Inverter	38461,5 (kWac)
Input voltage	330 - 600 VDC

2.3. Traditional Electrolysis Method

The only inputs needed for the electrolysis process are water (at room temperature) and electrical power, making traditional water electrolysis the most commercially and globally accessible of the three electrolysis methods taken into consideration for the hypothesized hydrogen economy. The high cost of solar electricity is the main obstacle to large-scale electrolytic solar-to-hydrogen conversion. Solar-to-hydrogen systems can operate without a grid by using a ground-based or roof-mounted PV system to generate the necessary electrical power, which lowers the cost of solar hydrogen [15].

In the traditional water-based hydrogen synthesis process, two non-electrochemical electrodes are separated from one another by a diaphragm and immersed in a liquid alkaline electrolyte (KOH or NaOH) [16]. The diaphragm allows water molecules and hydroxide ions (OH) to pass through it, separating the resultant gasses [17]. The traditional electrolysis is a commonly used and commercially available electrolyser, and the electrolyte can be recycled. Pressure range for aqueous alkaline electrolyte is 1 to 200 bar. Pressurized electrolysis is more efficient than air electrolysis, but the product purity is poorer. The most significant benefit of pressured electrolysis over atmospheric electrolysis is compressed hydrogen production. It was proposed using highly active nanostructured palladium-ceria electrocatalysts to generate H2 in the traditional electrolysis mechanism [17].

Anode:

$4OH^{-} \rightarrow O_2 + 2H_2 + 4e^{-}$ … (1)

Cathode:

$2H_2O + 2e^{-} \rightarrow H_2 + 2OH-$ … (2)

Experimental studies showed that, at a given pressure, the theoretical cell potential increases with increasing pressure at constant temperature but decreases with increasing temperature at a given pressure. The electrical power needed for the electrolyser and the electrolyte pumping is included in the overall electrical power that the solar cells should be able to supply. Additionally, the voltage and current requirements for this process should be taken into account because the rate of hydrogen production correlates to a specific current, which should be given at a voltage greater than the theoretical minimum value.

The working temperature of the electrolyser is assumed to be 80ºC when traditional (alkaline) electrolysis is combined with a photovoltaic module for solar hydrogen production [17].

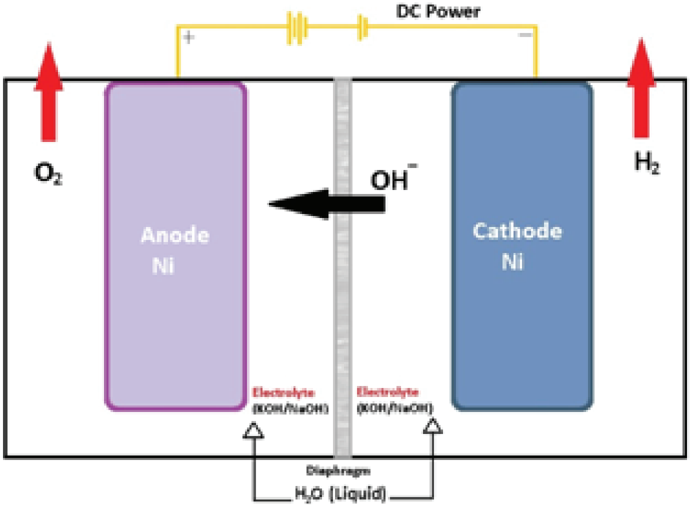

Figure 3: Alkaline electrolysis working mechanism.

2.4. Nuclear Hybrid Energy System

The subsystems listed below make up the NHES seen in Fig. 3. We use NPP and PV to make heat and electricity, and we employ those energies to electrolyze water to create hydrogen. In order to produce electricity, NPP has its own version of the Rankine cycle. Since one of them is anticipated to produce electricity when the other is shut down, NPP and CSP are not completely integrated. The regulation forbids them from being completely integrated in terms of safety; therefore NPP must adhere to the license conditions established by the regulator. Therefore, any problems with PV cannot compromise the security of NPP.

Location has a big impact on how much electricity is produced with PV. For NPP, there is no differentiation. It could be claimed that PV systems would not work well in places that don't get enough sunlight. Therefore, it is believed that when the position changes, the PV outputs will also change. It should not be forgotten that PV includes several inputs, such as the number of panels, which are related to outcomes. It is possible to get the same outcomes with fewer panels in an area with more sunlight than it is with more panels in an area with less sunlight.

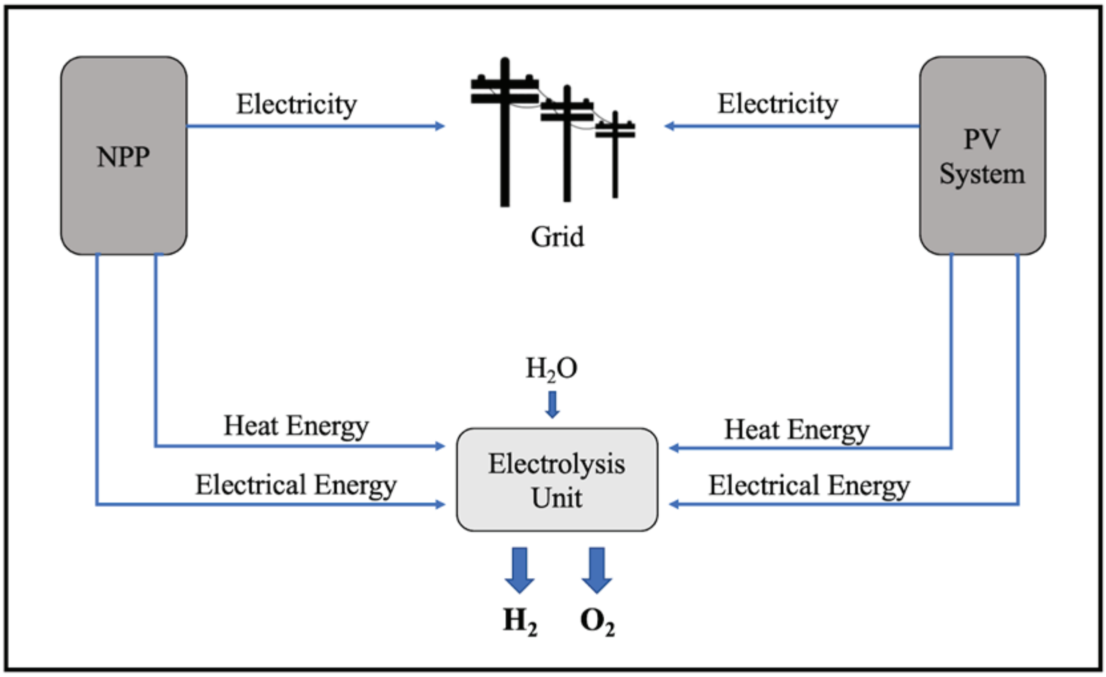

Figure 4: Nuclear Hybrid Energy System including NPP and PV System.

Producing 1 kg-H2 in the alkaline electrolysis, 26.33 MJ heat energy and 180.34 MJ electric energy must be provided as shown in the Fig. 5. Here, an electric heater is utilized to obtain the needed temperature from the PV system in order to supply heat energy. The required temperature is achieved via adjusting the mass flow on the NPP side.

NPP and PV energy are used to produce electricity and hydrogen. For the purpose of producing hydrogen, the amount of power from NPP and/or PV is expressed as a percentage. Additionally, by specifying a date range, the LabVIEW code allows for the calculation and individual presentation of the power and hydrogen production amounts on the graph.
By indicating hours or dates, the total amounts of hydrogen and electricity produced by NPP and PV are shown, allowing us to understand how production levels fluctuate over time.

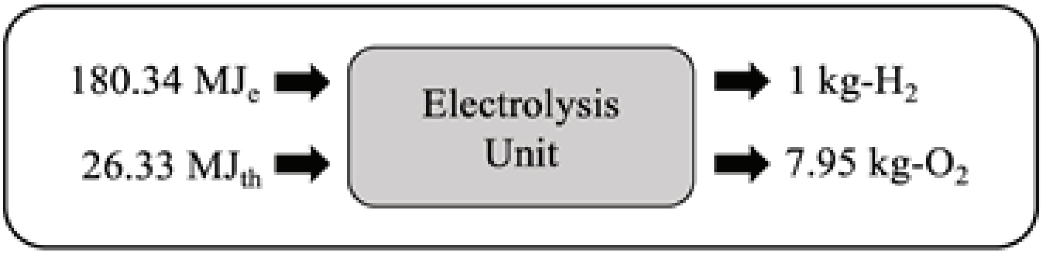

Figure 5: Hydrogen production via Alkaline Electrolysis

3. Results and Discussion

The percentage numbers in Table 3 show how much of the energy source is used to produce hydrogen. The first day of each season is included in the tables as a model for all seasons; the statistical variance of observed meteorological variables is taken into consideration and acknowledged as a constraint. The samples given here serve to illustrate how much electricity and hydrogen are produced. The tables also show how the volume of output varies according to the season. This work examines four key circumstances for each season.

The results can be acquired by specifying the date range (per the appropriate yearly season) and power percentage of the sources using the LabVIEW code that has been written. The amount of energy and hydrogen produced by the NPP is different, even though its power remains constant. In terms of renewable energy, the PV system is very reliant on the weather, including temperature, cloudiness, daylight hours, and so on. As a result, the NHES experiences power fluctuations.

Table 3: Productions of electricity and hydrogen for three distinct NPP and PV % contributions on any given day.

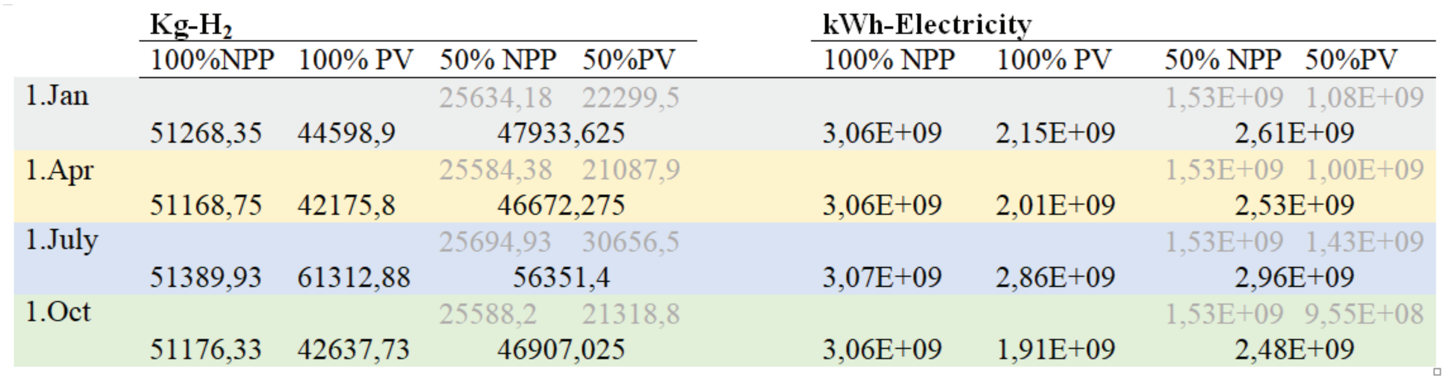

	Kg-H_2				kWh-Electricity			
	100%NPP	100% PV	50% NPP	50%PV	100% NPP	100% PV	50% NPP	50%PV
1.Jan			25634,18	22299,5			1,53E+09	1,08E+09
	51268,35	44598,9	47933,625		3,06E+09	2,15E+09	2,61E+09	
1.Apr			25584,38	21087,9			1,53E+09	1,00E+09
	51168,75	42175,8	46672,275		3,06E+09	2,01E+09	2,53E+09	
1.July			25694,93	30656,5			1,53E+09	1,43E+09
	51389,93	61312,88	56351,4		3,07E+09	2,86E+09	2,96E+09	
1.Oct			25588,2	21318,8			1,53E+09	9,55E+08
	51176,33	42637,73	46907,025		3,06E+09	1,91E+09	2,48E+09	

The production amounts of electricity and hydrogen are displayed in Table 3 for particular days. When carefully examining the tables. The reduction in daylight on July 1st might be proven as the cause of this predicament. There are numerous unknown parameters dependent on the weather conditions. The power of the PV is greatly influenced by the reduction in the amount of hydrogen produced by PV on October 1st, as well as other weather-related factors. For instance, the amount of dust in the air, the concentration of different gasses in the atmosphere, the angle of the sun at a certain time of year and location, or the butterfly effect. There are still a few unanswered questions, but these should be handled in greater detail in a subsequent investigation. PV simulation does not offer that kind of information.

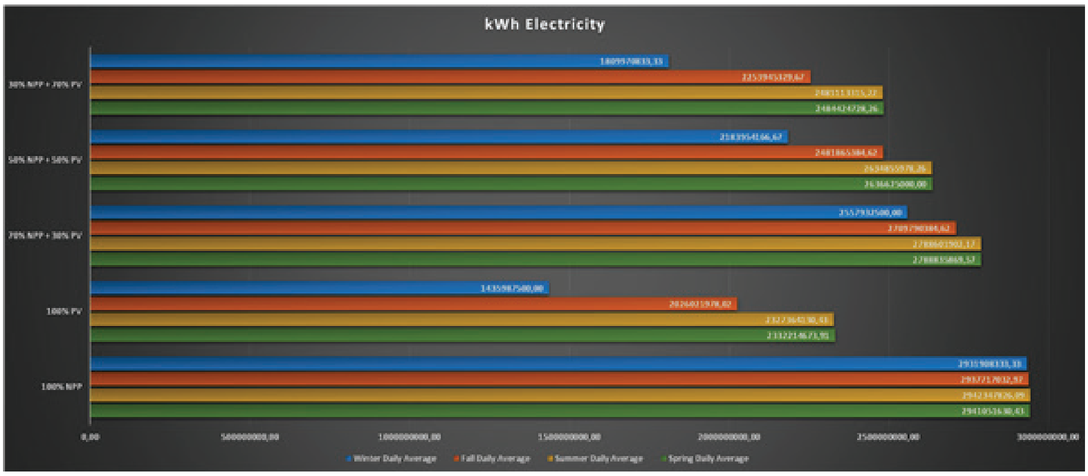

Figure 6: Every season's daily averages of electricity production with different percentages.

The amount of electricity produced decreases in the fall and winter, as shown in Fig. 6. PV as a result of the reduction in solar energy. From the data collected this is clearly can be seen that producing only PV is an unstable method and NPP is quite constant. As soon as we check the hybrid system even without full power there is a significant amount of production. Except the winter season the electrical energy that produced is quite constant and high therefore from the created scenarios we may turn our energy to hydrogen.

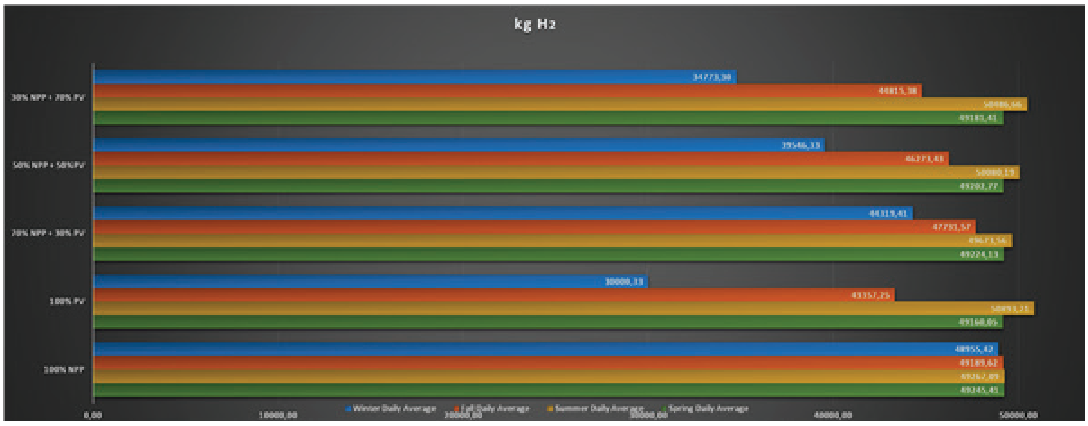

Figure 7: Every season's daily averages of hydrogen production with different percentages.

It can be observed in Fig. 7 that although the percentage rates of the sources are different, the average daily hydrogen production quantities for the spring are virtually comparable. Again it is evident from the data gathered that producing simply PV is an unstable method while NPP is rather constant. As soon as we verify the hybrid system, production is still rather high even when not operating at full capacity. But during the summer, more hydrogen is produced as a result of the extra energy that PV provides. The amount of hydrogen generated with 100 percent NPP electricity is less when compared to daily average levels in the winter. Because the PV loses electricity throughout the winter, this is the cause.

4. Conclusion

This study is planning to create a new hybrid energy trend without losing time. With only focusing to traditional methods, also known as technologically ready which has 9 levels out of 9 from technologically readiness level (TRL). Due to the safety regulations of NPP, the plant's bare area will be evaluated as PV field. Having 2 power plants in the same area will cause high production on the grid and over producing. To be able to avoid this unwanted situation, again a TRL 9 plant has been used which is traditional water electrolysis method, alkaline electrolysis. In this way completely carbon free, efficient and promising NHES is designed. With the different scenarios at different dates and different power dividing, possibilities of NHES have shown.

Nuclear energy and the hydrogen it produces can be argued to be rational known electricity sources and energy carriers that have the ability to support global energy demand while transitioning to a larger scale lower carbon economy, respectively. Producing hydrogen simultaneously from nuclear and renewable energy sources is therefore one of the most important engineering issues of the present. Since they meet anticipated thermal and electrical energy needs, hybridization of the nuclear and renewable industries will be a critical problem for reducing greenhouse gas emissions and moving toward a low-carbon future in the long run. In order to counter climate change, nuclear and renewable technologies will be important for producing "clean energy" needed for total electrification in a variety of industries, including automobiles, public transport, construction-related vehicles, home heating, and a spectrum of thermally-driven industries. The amounts of hydrogen and electricity produced via a PWR type SMR and PV are detailed in this research. Furthermore, the constant volume of hydrogen and electricity may not be significant. However, it is important that NHES is technologically ready and with the created trend it can be seen as a necessary hybrid system.

References:

[1] Van Ruijven, B. J., De Cian, E., & Sue Wing, I. (2019). Amplification of future energy demand growth due to climate change. Nature Communications, 10(1). doi:10.1038/s41467-019-10399-3.

[2] Gillingham, Kenneth, and James H. Stock. 2018. "The Cost of Reducing Greenhouse Gas Emissions." Journal of Economic Perspectives, 32 (4): 53-72. DOI: 10.1257/jep.32.4.53.

[3] Field, R. A., & Derwent, R. G. (2021). Global warming consequences of replacing natural gas with hydrogen in the domestic energy sectors of future low-carbon economies in the United Kingdom and the United States of America. International Journal of Hydrogen Energy, 46(58), 30190–30203. doi:10.1016/j.ijhydene.2021.06.120.

[4] Poullikkas, A. (2013). A comparative overview of large-scale battery systems for electricity storage. Renewable and Sustainable Energy Reviews, 27, 778–788. doi:10.1016/j.rser.2013.07.017.

[5] Bussar, C., Stöcker, P., Cai, Z., Moraes Jr., L., Magnor, D., Wiernes, P., … Sauer, D. U. (2016). Large-scale integration of renewable energies and impact on storage demand in a European renewable power system of 2050—Sensitivity study. Journal of Energy Storage, 6, 1–10. doi:10.1016/j.est.2016.02.004.

[6] Hannan, M. A., Hoque, M. M., Mohamed, A., & Ayob, A. (2017). Review of energy storage systems for electric vehicle applications:

Issues and challenges. Renewable and Sustainable Energy Reviews, 69, 771–789. doi:10.1016/j.rser.2016.11.171.

[7] Ball, M., & Weeda, M. (2015). The hydrogen economy – Vision or reality? 1 1This paper is also published as Chapter 11 "The hydrogen economy – vision or reality?" in Compendium of Hydrogen Energy Volume 4: Hydrogen Use, Safety and the Hydrogen Economy, Edited by Michael Ball, Angelo Basile and T. Nejat Veziroglu, published by Elsevier in 2015, ISBN: 978-1-78242-364-5. For further details see: http://www.elsevier.com/books/compendium-of-hydrogen-energy/ball/978-1-78242-364-5. International Journal of Hydrogen Energy, 40(25), 7903–7919. doi:10.1016/j.ijhydene.2015.04.032.

[8] Sharma, S., & Ghoshal, S. K. (2015). Hydrogen the future transportation fuel: From production to applications. Renewable and Sustainable Energy Reviews, 43, 1151–1158. doi:10.1016/j.rser.2014.11.093.

[9] Centi, G., Iaquaniello, G., & Perathoner, S. (2011). Can We Afford to Waste Carbon Dioxide? Carbon Dioxide as a Valuable Source of Carbon for the Production of Light Olefins. ChemSusChem, 4(9), 1265–1273. doi:10.1002/cssc.201100313.

[10] Wang, Z., Roberts, R. R., Naterer, G. F., & Gabriel, K. S. (2012). Comparison of thermochemical, electrolytic, photoelectrolytic and photochemical solar-to-hydrogen production technologies. International Journal of Hydrogen Energy, 37(21), 16287–16301. doi:10.1016/j.ijhydene.2012.03.057.

[11] Dincer, I., & Acar, C. (2015). Review and evaluation of hydrogen production methods for better sustainability. International Journal of Hydrogen Energy, 40(34), 11094–11111. doi:10.1016/j.ijhydene.2014.12.035.

[12] Fukami, M. V. I., & Santecchia, A. (2000). CAREM project: Innovative small PWR. Progress in Nuclear Energy, 37(1-4), 265–270. doi:10.1016/s0149-1970(00)00057-3.

[13] D. Popov, A. Borissova, Innovative configuration of a hybrid nuclear-solar tower power plant, Energy, 2017, doi: 10.1016/j.energy.2017.02.147.

[14] Joshi, A. S., Dincer, I., & Reddy, B. V. (2011). Solar hydrogen production: A comparative performance assessment. International Journal of Hydrogen Energy, 36(17), 11246–11257. doi:10.1016/j.ijhydene.2010.11.122.

[15] Bhattacharyya R, Misra A, Sandeep KC. Photovoltaic solar energy conversion for hydrogen production by alkaline water electrolysis: conceptual design and analysis. Energ Conver Manage. 2017;133:1-13.

[16] Yeo, R. S., McBreen, J., Kissel, G., Kulesa, F., & Srinivasan, S. (1980). Perfluorosulphonic acid (Nafion) membrane as a separator for an advanced alkaline water electrolyser. Journal of Applied Electrochemistry, 10(6), 741–747. doi:10.1007/bf00611277 .

[17] Ganley, J. C. (2009). High temperature and pressure alkaline electrolysis. International Journal of Hydrogen Energy, 34(9), 3604–3611. doi:10.1016/j.ijhydene.2009.02.083.

Biogas Potential to be Obtained from Gaziantep Province Cattle

Murat Ozdemir[1], Cuma Karakus[1], Emrullah Kocaman[2]

[1]Iskenderun Technical University, Turkiyemuratozdemir02@gmail.com, cuma.karakus@iste.edu.tr

[2]Gaziantep University, Turkiye, ekocaman@gantep.edu.tr

Abstract: Biomass resources, which have the potential to significantly reduce the dependence on fossil fuels and carbon dioxide emissions, are one of the largest and most sustainable renewable energy sources in the world. In this study, the amount of biogas production from cattle for Gaziantep province, the amount of electrical energy and CO2 emission reduction that can be obtained by using the produced biogas were investigated. Within the scope of the study, biomass production data were obtained from TUIK for the years 2017-2021, depending on the numbers of Dairy cattle, Meat cattle, local cattle and young calves in Gaziantep. As a result of the analysis made in line with the data received, it has been seen that dairy cattle are more widespread in the region than other species. As a result of the analyzes made, it was seen that there is a potential of 66.856,20 m3/year biogas in Gaziantep and 212,99MWh/year electrical energy potential from the obtained biogas. In addition, it has been calculated that the CO2 emission reduction value is around 30%.

Özet: Fosil kaynaklı yakıtlara olan bağımlılığı ve karbondioksit salımı önemli ölçüde azaltacak potansiyele sahip olan biyokütle kaynakları, dünyadaki en geniş ve çoğu sürdürülebilir yenilenebilir enerji kaynaklarından biridir. Çalışmada Gaziantep ili için büyükbaş hayvanlardan biyogaz üretim miktarı, üretilen biyogazın kullanım ile elde edilebilecek elektrik enerjisi ve CO2 salım azaltım miktarı araştırılmıştır. Çalışma kapsamında 2017-2021 yıllarına ait Gaziantep ilinde bulunan süt sığırı, et sığırı, yerli sığır ve genç buzağıların sayılarına bağlı olarak biyokütle üretim verileri TUİK' ten alınmıştır. Alınan veriler doğrultusunda yapılan analiz sonucunda bölgede süt sığırcılığının diğer türlere göre daha geniş yayıldığı görülmüştür. Yapılan analiz sonucunda Gaziantep ilinde 66.856,20 m3/yıl biyogaz, elde edilen biyogazdan 212,99 MWh/yıl elektrik enerjisi potansiyeli olduğu görülmüştür. Ayrıca CO2 salım azaltım değerinin ise yaklaşık %30 civarında olduğu hesaplanmıştır.

1. Giriş

Dünyadaki ekonomik gelişimin temel taşı enerjidir. Enerjiye olan ihtiyaç her geçen gün artığından insan yaşamı için kaçılmaz olmaktadır. Enerjiye olan talep ve gereksinim artığından mevcut enerji bir süre sonra bu talepleri karşılayamayacaktır. Artan enerji ihtiyacı ile enerji alanında yeni enerji arayışları içerisine girilmesine neden olmaktadır (Yetiş vd. 2003; Asif, M. and Muneer T. 2007). Enerji kaynağı arayışında fosil yakıtlar gibi belirli bir süre sonra tükenebilen değil de sürekliliği olan, temiz ve tükenmeyen yenilenebilir enerji kaynaklarına yönelim artmıştır. Yenilenebilir enerji kaynakları güneş, rüzgâr, jeotermal, biyokütle gibi kaynaklardan oluşmaktadır. Biyokütle kaynakları, dünyadaki en geniş ve çoğu sürdürülebilir yenilenebilir enerji kaynağı potansiyelidir (WBA 2018). Yenilenebilir enerji kaynakları Türkiye Sınai Kalkınma Bankası A.Ş. (TSKB) 2022 yılı Ağustos ayı içerisinde yayınlamış olduğu enerji bültene göre

Türkiye'de elektrik üreten santrallerin %54,3 yenilenebilir enerji kaynaklarından elektrik üreten santraller oluşturduğu ifade edilmiştir (Hakyemez , 2022).

Literatürde yenilenebilir enerji kaynaklarından biyogaz ile ilgili yapılan birçok çalışmadan bazıları şunlardır:

Gençyılmaz ve Seçkinin (Gençyılmaz ve Seçkin, 2020) yapmış olduğu çalışmada Hollanda'da CO2 salımı üzerinde çalışmalar yapıldığını ve Çankırı ilinin biyogaz potansiyeli, elektrik üretimi ve CO2salımları üzerinde çalışma yapmıştır. Çankırı ilinde biyogaz üretiminden elektrik enerjisi sağlandığında ise CO2salımın %40 civarında olduğunu hesaplanmıştır.

Kaya (Kaya vd., (2015), yapmış olduğu çalışmada Osmaniye ilinde bulunan 67 tane büyükbaş hayvan çiftlikleri ve 3 adet tavuk çiftliği ziyaret ederek her biri için ayrı bir rapor oluşturmuştur. Raporunda küçükbaş hayvanlardan gübre elde edileceği günlerde dış ortamda bırakıldıklarından ihmal etmiştir. Oluşturulan rapor sonucuna göre hayvan çiftliklerinden biyogaz elde etmek için tesislerde atıkların nasıl depolandığı ve nasıl depolanması gerektiği, gezilen tesislerin hiçbirinde atılan atıkların hesaplanmadığı ve bunun için TUİK verilerini kullanıldığı, 823 kW kapasitesi bir tesis tasarımı, tesisin yerinin belirlenmesi ve tesis kurulum maliyetleri gibi konuları araştırmıştır.

Ay (Ay, 2020), yapmış olduğu çalışmada Kahramanmaraş ili için 5 farklı yöntem kullanarak gübre, biyogaz ve elektrik potansiyellerini hesaplamıştır. Bazı ilçelerin konutlarında 4 kişi olduğu hesabı yapılarak ilçede bulunan konutlar için üretilen elektrik enerjisinin yettiğinin araştırması yapılmıştır.

Gönbe (Gönbe, 2020), yapmış olduğu çalışmada Isparta ilinin büyükbaş hayvanları verilerini kullanarak Ligno paket modelleme sistemiyle tesis tasarımını araştırmıştır. Ligno modelin amaç fonksiyonu biyogaz tesislerinin ilk yatırım maliyetleri ve gübre taşıma maliyetlerinin minimizasyonudur. Bu modelleme çalışması sonucunda küçük çaplı olan aile tipi tesislerin enerji açısından ve verimlilik açısından yetersiz olduğunu, büyük çaplı olan tesislerin ise yatırımlarına yatırım şirketlerinin tercih etmediği tespit etmiştir. Gelişmiş ülkelerde ise biyogaz dönüşüm sistemleri, güneş, rüzgar, vb. gibi yenilenebilir enerji üretim yöntemleri ile birlikte değerlendirilmekte ve ciddi yatırımlar yapılmaktadır.

Nuralan Poyraz (Nuralan Poyraz, 2020), yapmış olduğu çalışmada Kayseri ilinde büyükbaş hayvan yetiştiriciliği en fazla yapıldığı mahallelerin biyogaz üretim potansiyeli, elektrik enerjisi ve elektrik enerjisinden elde edilecek CO2 salım miktarını 3 farkı durumda incelemiştir. 3 farklı durum incelendiğinde ise CO2 salınımının azaltılması için biyogaz tesislerinin kurulumunun mümkün olduğunca ham maddeye yakın olarak kurulmasının uygun olacağını belirtmiştir. Biyogaz tesislerinin ham maddeye uzak kurulmasında ham maddenin taşınması esnasında CO2 salımı artırıcı etkenler mevcut olduğu incelenmiştir.

Yapılacak çalışmada, Gaziantep ilinde bulunan hayvan sayıları ile elde edilebilecek biyogaz potansiyeli analizi yapılacaktır. Elde edilen biyogazın kombine ısı ve güç (Combined heat and power, CHP) motorunda elektrik enerjisine dönüştürülmesiyle CO2 salım hesaplaması yapılacaktır.

1.1 Biyokütle Tanımı

Biyokütle, yenilenebilir enerji kaynakları içerisinde yer almaktadır. Biyokütle her yerde bulunabilmektedir (Topal ve Arslan, 2008). Biyokütle aynı zamanda bir organik karbon olarak da kabul edilmektedir (Enerji ve Tabii Kaynaklar Bakanlığı, 2020). Bitkisel, hayvansal, evsel, endüstriyel, kanalizasyon ve gıda atıkları biyokütleyi oluşturmaktadır. Biyokütle kaynakları ile enerji elde etmek için çeşitli yöntemler bulunmaktadır. Biyokütleden en verimli bir şekilde enerji elde etmenin yolu oksijensiz ortamda fermantasyonudur (Sarıkaya, 2020). Biyokütlenin oksijensiz ortamda fermantasyonu sonucunda elde edilen ürünlerin biyokütlenin ham olarak kullanılmasına göre daha az küresel ısınmayı artıracak ürünler elde edilmektedir. Aynı zamanda biyokütleden elde edilen ürünlerden toprağı güçlendirecek verimli gübreler elde edilmektedir. Kullanılan gübreler tarımda önemli bir yere sahiptir (Yiğit,2020).

Çizelge 1. Biyogazın bileşenleri

Bileşenler	**İçerik (%)**
Metan (CH_4)	55 - 75
Karbondioksit (CO_2)	30 - 45
Hidrojen sülfür (H_2S)	1 - 2
Azot (N_2)	0 - 1
Hidrojen (H_2)	0 - 1
Karbon monoksit (CO)	Eser Miktarda
Oksijen (O_2)	Eser Miktarda

Biyokütlenin oksijensiz ortamda fermantasyonu sonucu biyogaz oluşmaktadır. Oluşan biyogaz bileşimi %55 - 75 metan (CH4) , %30 - 45 karbondioksit (CO2) ile az miktarda hidrojen sülfür, hidrojen, karbon monoksit ve azot içeren renksiz ve yanıcı bir gaz karışımıdır. Genel olarak biyogazın bileşenleri Çizelge 1'de görülmektedir (Öçal, 2013). Biyogaz üretimini sıcaklık, hidrolik bekleme süresi, organik yükleme hızı, pH, C/H oranı, mikroorganizma konsantrasyonu, karıştırma, ışık, iz elementler, gaz giderimi, inhibitörler ve atıkların ön arıtımı etkileyen etmenlerdir (Sabuncu, 2010). Elde edilen biyogazın enerji biçiminde kullanılıp kullanılmadığı içerisinde bulunan metan oranına bağlı olarak değişmektedir (Nuralan Poyraz, 2020). Biyogazın ısıl değerine bakıldığında içeriğinde bulunan metan yüzdesine göre ısıl değeri 17-25 MJ/m3 arasındadır. 1m3 biyogazın 4,70 kWh elektrik enerjisinin sağladığı ısıya eşittir (Buğutekin, 2007). Biyokütleden elde edilen biyogaz gaz yakıtlarının kullanıldığı alanlarda kullanılabilmektedir. Biyogazı kullanabilmek için özel tasarlanmış biyogaz yakma üniteleri veya bunlar için uyarlanmış tüketiciler olması gereklidir. Biyogazın yanmasını içinde bulunan metan CH4 gazından kaynaklanmaktadır. Metan gazının yanması için hava ile 1/7 oranında karışması gerekmektedir. Yanan biyogaz evlerin ısınmasında, ocakta yemek pişirmede, aydınlatma işlerinde kullanılabilmektedir. Biyogaz elektrik enerjisine çevrilerek elektrikle ilgili yapılabilecek işlerde kullanılabilmektedir. Biyogazı, benzinle çalışan motorlu araçlarda doğrudan ya da içeriğinde bulunan metan gazının saflaştırma işlemi yapılarak da kullanılabilmektedir. Dizel motorlu araçlarda kullanılabilmesi için motorinle belirli bir oranda karıştırmak gerekir. Biyokütlenin oksijensiz ortamda fermantasyonu sonucunda oluşan gübre tarlada kullanılabilmektedir (Kaya ve Öztürk, 2012).

2. Materyal ve Yöntem

Gaziantep ili 36o 28′ ve 38o 01′ doğu boylamları ile 36o 38′ ve 37o 32′ kuzey enlemleri arasında bulunmaktadır. İlin doğusunda Şanlıurfa, batısında Osmaniye ve Hatay, kuzeyinde Kahramanmaraş, güneyinde Suriye, kuzeydoğusunda Adıyaman ve güneybatısında Kilis illeri bulunmaktadır. 6222 km2'lik alanıyla Türkiye topraklarının yaklaşık olarak %1'lik bölümünü kapsamaktadır (Gaziantep valiliği, 2021).

Şekil 2. Gaziantep İlinin İlçelere Göre Haritası

Gaziantep ilinde son 18 yılda büyükbaş hayvan sayısının %410 oranında artması büyükbaş hayvancılığına olan ilginin artığını göstermektedir (Gaziantep Tarım ve Orman İl Müdürlüğü, 2021).

2.1 Yapılacak Bu Çalışma İle İlgili Kabuller

Biyogaz potansiyeli hesabında hayvanların bulundukları ilin konumu, beslenme şekilleri, yaşları ve türüne göre farklı biyogaz potansiyeline sahiptir. Yapılan çalışma kapsamında Gençyılmaz, Kaya ve Yağlının çalışmalarında almış olduğu değerler göz önünde bulundurulacaktır.(Gençyılmaz vd., 2020; Kaya ve Öztürk, 2012; Yağlı ve Koç, 2019)

Çizelge 2. Hayvan Türlerine Göre Elde Edilecek Veriler

Hayvan Türü	Hayvan Başına Ortalama Yaş Gübre Üretimi (M_{YG})	Toplanabilir Faydalı Gübre Oranı (T)	Yaş Gübredeki Katı Madde Oranı (KM)	KM içerisindeki Uçucu Katı Madde Oranı (UKM)	Metan Üretim (MO)
	Kg/gün-hayvan	%	%	%	Nm^3 CH$_4$/kg-UKM
Süt Sığırı	43,00	100	17,27	83,36	0,18
Et Sığırı	29,00	100	12,41	84,65	0,33
Yerli Sığır	29,00	50	17,27	83,36	0,33
Buzağı	2,48	100	3,71	44,23	0,33

Biyogaz potansiyelini hesaplamak için aşağıdaki Denklem 1 kullanılacaktır.

$$M_{YYM}=M_{YG}\times S\times 365 \tag{1}$$

Burada M_{YYM}; Toplam hayvanlardan günlük elde edilecek yaş gübre miktarı, M_{YG}; Hayvan başına ortalama yaş gübre miktarı ve S ise Toplam hayvan sayısı olarak verilmiştir. Hayvanların ahırlarda beslenme süreleri göz önüne alındığında yıllık toplam faydalanılabilir ortalama yaş gübre miktarı Denklem 2 kullanılarak hesap edilir

$$M_{YFYG} = M_{YYM} \times T \tag{2}$$

Burada M_{YFYG} = Hayvanlardan faydalanılabilecek olan yıllık ortalama yaş gübre miktarı ve T ise hayvanların üretmiş olduğu yaş gübreyi toplayabilme oranıdır (%). Faydalanılabilen yaş gübrelerdeki katı madde oranı Denklem 3 kullanılarak hesap edilir.

$$M_{KM}=M_{YFYG} \times KM \tag{3}$$

Burada M_{KM}; Yıllık hayvanlardan toplanabilir faydalı gübre içerisindeki kuru madde oranını verir ve KM ise hayvanlardaki yaş gübre içerisindeki kuru madde oranını vermektedir. Katı uçucu madde miktarı Denklem 4 kullanılarak hesap edilir.

$$M_{UKM}=M_{KM} \times UKM \tag{4}$$

Burada M_{UKM}; hayvanlardan yıllık toplanabilen ve faydalanılabilen gübre içerisindeki uçucu katı madde oranıdır (kg/yıl) ve UKM ise uçucu katı madde oranı (%) Metan üretim oranı ise Denklem 5 kullanılarak hesap edilir.

$$M_{METAN}=M_{UKM} \times MO \tag{5}$$

Burada M_{METAN}; hayvanlar tarafından üretilebilen ve toplanabilen gübreden elde edilen toplam yıllık metan miktarıdır ve MO ise 1 kg UKM' den üretilebilen metan miktarıdır. Metan içeriği %60 sahip biyogazın enerji değeri 22,7 MJ/Nm^3 ve hayvanlardan elde edilen yıllık toplam biyogazın enerji değeri 36MJ/Nm3. Metan gazından enerji üretimini Denklem 6 kullanılarak hesaplanabilir.

$$Q = M_{METAN} \times H_{METAN} \tag{6}$$

Burada, Q bir yılda üretilecek metanın enerji karşılığı (MJ/yıl) ve H_{METAN} metan gazının ısıl değeri olup 36 MJ/m3 olarak alınmıştır. Metan gazı bir kombine ısı ve güç (CHP) motorunda yakılarak elektrik üretilmesi sonucu elde edilecek elektrik miktarı Denklem 7 kullanılarak hesap edilir.

$$E = M_{METAN} \times \eta_e \times W \tag{7}$$

Burada, E CHP motorunun yıllık elektrik üretimi (MWhe/yıl), ηe CHP motorunun elektriksel verimi (%35 alınmıştır) ve W Metan gazının kWh olarak enerji değeri olup 10 kWh/m^3 olarak alınmıştır. 4 kişilik bir ailenin aylık ortalama elektrik gideri 230 kWh/ay olarak kabul edilmiştir (Elektrik Mühendisleri Odası, 2022).

Biyogaz üretimi sonucu oluşan CO_2 salım azaltımının belirlenmesinde;

Biyogaz potansiyelleri elektrik enerjisine dönüştürüldüğünde oluşan CO_2 salım azaltımı ayrı ayrı hesaplanır. Bu hesaplamalarda 1m3 biyogaz için 9,19 kg CO_2salımı (CO_2bio) ve biyogazdan üretilen elektrik (CO_2e) ise 0,8 değerleri kabul edilmiştir (Gençyılmaz vd. 2020).

3. Bulgular ve Tartışma

TUİK'ten alınan 2017-2021 yılları verilerine göre Gaziantep ilinde son yıla ait veriler Çizelge 3'de verilmiştir. Gaziantep ilinde daha öncesinde yapmış olduğum ziyaretler ve TUİK' ten alınan veriler doğrultusunda Süt sığırı, Et sığırı, yerli sığır ve genç buzağılardan elde edilecek biyogaz potansiyeli hesaplaması yapılacaktır.

Çizelge 3. Gaziantep İli 2017-2021 yıllarına ait hayvan türlerine göre sayıları

Hayvan Adı	Yıllara Göre Hayvan Sayıları				
	2017	2018	2019	2020	2021
Süt Sığırı	102968	121967	106774	92621	96752
Et Sığırı	43439	103431	59560	46068	57482
Yerli Sığır	886	999	976	764	766
Buzağı	44549	45482	60258	52216	45050
Toplam	**191842**	**271879**	**227568**	**191669**	**200050**

Gaziantep ili hayvan sayıları göz önüne alındığında 2018 yılına kadar hayvan sayılarında artış olduğu görülmektedir. 2021 yılını ise 2018 yılı ile kıyasladığımızda bir düşüş olduğu görülmektedir. 2021 yılı hayvan verilerinde bölgede süt sığırcığının daha yaygın olduğu görülmektedir. Yapılacak çalışmada ise 2021 yılına ait veriler kullanılarak hesabı gerçekleşecektir. 2021 yılına ait verilerine göre yıllık ortalama yaş gübre miktarı (kg/yıl), toplanabilir faydalı gübre oranı (%), Yaş gübre içindeki katı madde oranı (%) ve katı madde içerisindeki uçucu madde oranı (%) Çizelge 4' de verilmiştir.

Çizelge 4. Hayvan Türlerine Göre Elde Edilen Gübre Miktarları

Hayvan Türü	Hayvan Sayıları 2021	Hayvanlar tarafından bir yılda üretilebilecek toplam gübre	Toplanabilir Faydalı Gübre Miktarı (T)	Yaş Gübredeki Katı Madde (KM)	Uçucu Katı Madde Miktarı (UKM)
		ton/yıl	ton/yıl	ton/yıl	ton/yıl
Süt Sığırı	96752	1.518.522,64	1.518.522,64	262.248,86	218.610,65
Et Sığırı	57482	608.446,97	608.446,97	75.508,27	63.917,75
Yerli Sığır	766	8.108,11	4.054,06	700,14	583,63
Buzağı	45050	40.779,26	40.779,26	1.512,91	669,16
Toplam	**200.050**	**2.175.856,98**	**2.171.802,93**	**339.970,17**	**283.781,19**

Çizelge 4 incelendiğinde en yüksek değerlerin süt sığırcılığında olduğu görülmektedir. Hayvanlardan bir yılda üretilebilecek toplam gübre miktarı incelendiğinde süt sığırcılığında 1.518.522,64 ton/yıl gübre elde edileceği ve toplamda ise 2.175.856,98 ton/yıl gübre elde edilmektedir. Toplanabilir faydalı gübre miktarında ise süt sığırcılığında ise 1.518.522,64 ton/yıl gübre elde edileceği ve toplamda ise 2.171.802,93 ton/yıl gübre elde edilmektedir. Yaş gübredeki katı madde miktarına baktığımızda süt sığırcılığında 262.248,86 ton/yıl gübre ve toplamda ise 339.970,17 ton/yıl gübre elde edilmektedir. Yaş gübre içerisindeki uçucu katı madde miktarına bakıldığında ise süt sığırcılığında 218.610,65 ton/yıl gübre ve toplamda ise 283.781,19 ton/yıl gübre elde edilmektedir.Elde edilen bu veriler doğrultusunda Metan üretimi, elektrik üretimi ve ısı miktarı üretimi Çizelge 5'de belirtilmiştir.

Çizelge 5. Hayvan Türlerine Göre Metan, Elektrik ve Isı Miktarları

Hayvan Türü	Hayvan Sayıları 2021	Metan Üretim (m^3-CH_4/yıl)	Bir yılda üretilecek metanın enerji değeri (MJ/yıl)	Elektrik Enerjisi MWhe/yıl
Süt Sığırı	96.752	39.349,96	1.416,60	137,72
Et Sığırı	57.482	21.092,86	759,34	73,83
Yerli Sığır	766	192,60	6,93	0,67
Buzağı	45.050	220,82	7,95	0,77
Toplam	**200.050**	**60.856,20**	**2.190,82**	**212,99**

Çizelge 5 incelendiğinde üretilen toplam metan miktarının 60.856,20 m3-CH4/yıl elektrik enerjisinin ise 212,99 MWh/yıl olduğu hesaplanmıştır. Elde edilen elektrik enerjisiyle 77 tane 4 kişilik ailenin aylık elektrik enerji ihtiyacını karşılamaktadır. Elde edilen biyogazın CO2 salım değerleri Çizelge 6 da verilmiştir.

Çizelge 6. Gaziantep ili büyükbaş hayvanlardan elde edilen CO_2 salım değerleri

Hayvan Türü	Hayvan Sayıları 2021	Metan Üretim (m^3-CH_4/yıl)	1m³ biyogazın CO_2salımdeğerleri (CO_{2bio})	Biyogazdan üretilen elektrik miktarı (CO_{2e})
Süt Sığırı	96.752	39.349,96	361.625,74	110.179,77
Et Sığırı	57.482	21.092,86	193.843,36	59.060
Yerli Sığır	766	192,60	1.769,98	539,28
Buzağı	45.050	220,82	2.029,36	618,30
Toplam	**200.050**	**60.856,20**	**559.268,44**	**170.397,35**

Çizelge 6 incelendiğinde Gaziantep ili büyükbaş hayvanlarından elde edilen karbondioksit salım değerinin toplam 559.268,44 (CO2bio) olduğu ve biyogazdan üretilen elektrik enerjisi (CO2e) değeri ise toplam 170.397,35 (CO2e) olduğu görülmüştür. Hayvansal atıkların enerjisi elektrik enerjisinde kullanıldığında ise CO_2 salım değerinin yaklaşık %30 olduğu belirlenmiştir.

4. Sonuçlar

Yapılan çalışmada Gaziantep ilinde bulunan manda, sığır (yerli ırk), sığır (kültür melezi ırkı), sığır (kültür ırkı) hayvanlarının ilçe bazlı toplam sayıları alınarak elde edilebilecek biyogaz ve enerji hesabı yapılmıştır. Hesaplamalar ve analiz sonuçlarında elde edilen sonuçlar şunlardır:

- Gaziantep ilinde süt sığırcılığı yetiştiriciliği büyükbaş hayvanları içerisindeki oranı yaklaşık %48 olduğu hesaplanmıştır. Bu hesaplanan değer bize büyükbaş hayvan yetiştiriciliği içerisinde süt sığırcılığının önde geldiğini göstermektedir.

- Biyogaz potansiyeli en çok 39.349,96 m3 ile süt sığırda olduğu ve Gaziantep ilinin ise toplam 60.856,20 m3 olarak hesaplanmıştır.
- Elde edilen metan enerjisinin CHP motorunda çevrilmesiyle 212,99 MWh/yıl elektrik enerji elde edilmektedir.
- Elde edilen elektrik enerjisi sonucunda 4 kişilik 77 tane ailenin bir aylık elektrik enerji ihtiyacı karşılanmaktadır.
- Hayvansal atıklardan elde edilen enerjinin elektrik enerjisine dönüştürülmesi sonucunda CO2 salım değerinin yaklaşık %30 olduğu hesaplanmıştır.

Elde edilen sonuçlar incelendiğinde ise Gaziantep iline kurulacak biyogaz tesisi önerileri ise;

- Biyogaz tesisi kurularak bir sanayi şehrimizin CO2 salım değerlerinin azaltılabilir.
- Biyogazın üretilip kullanılmasıyla ekonomik kazanç ve istihdam sağlayabilir.
- Enerjide dışa bağımlılığı azaltmaya katkı sağlayabilir.
- Biyogaz tesisi kurulacağı zaman hayvan yetiştiriciliğinin özelliklede büyükbaş hayvan yetiştiriciliğin çok olduğu yerlere yakın olması kurulacak tesisin ham madde ihtiyacını azaltmaya yardımcı olacaktır.

5. Referanslar

Asif, M. and Muneer T., 2007. Energy supply, its demand and security issues for developed and emerging economies. Renewable and sustainable energy reviews, 11 (2007) 1388-1413.

Ay, Ö.F., (2020). Kahramanmaraş İlinin Teorik Biyogaz Potansiyelinin Farklı Modellerle Belirlenmesi. Kahramanmaraş Sütçü İmam Üniversitesi Fen Bilimleri Enstitüsü Yüksek Lisans Tezi. Kahramanmaraş

Buğutekin A., Atıklardan Biyogaz Üretiminin İncelenmesi, Doktora Tezi, Fen Bilimleri Enstitüsü, İstanbul, 2007, 177994.

Demir Yetiş, A. Gazigil, L. Yetiş, R. Ve Çelikezen, B. (2019). Hayvansal Atık Kaynaklı Biyogaz Potansiyeli: Bitlis Örneği. Academic Platform Journal Of EngineeringandScience 7-1, 74-78, 2019)"

Elektrik Mühendisleri Odası, (2021), 4 kişilik bir ailenin aylık elektrik faturası, https://www.emo.org.tr/genel/bizden_detay.php?kod=135116&tipi=2&sube= (Erişim tarihi 03.10.2022 00:44)

Enerji ve Tabii Kaynaklar Bakanlığı. https://enerji.gov.tr/bilgi-merkezi-enerji-biyokutle (erişim tarihi, 04.12.2020)

Gaziantep İl Müdürlüğü. Brifing - 2017 (Ocak - Aralık). Gıda Tarım Ve Hayvancılık Bakanlığı.

Gaziantep Tarım ve Orman İl Müdürlüğü, (2021), 2021 yılında yürütülen çalışmalar https://gaziantep.tarimorman.gov.tr/Belgeler/2022/Brifing_2021%20son%20pdf.pdf (Erişim tarihi, 03.10.2022 00:55)

Gaziantep valiliği, http://www.gaziantep.gov.tr/ilimiz-gaziantep (Erişim Tarihi: 25.01.2021 saat 11.38)

Gençyılmaz, O. ve Seçkin, G. Çankırı İl'inin Hayvansal Kaynaklı Biyogaz Potansiyelinin Belirlenmesi. International Journal of Life SciencesandBiotechnology, 2020. 3(3). p. 325-341.

Gönbe. Y. (2020). Karma Programlama Yöntemi Kullanılarak Isparta İli Merkezi Biyogaz Tesisleri Planlama Modelinin Geliştirilmesi. Isparta Uygulamalı Bilimler Üniversitesi

Lisansüstü Eğitim Enstitüsü. Isparta

Hakyemez, C. (2022, 19 Eylül). Aylık Enerji Bülteni TSKB Ekonomik Araştırmalar. Erişim tarihi: 30.09.2022, https://www.tskb.com.tr/uploads/file/enerji-bulteni-agustos-2022.pdf

Kaya, D. Ve Öztürk, H. (2012). Biyogaz Teknolojisi Üretim-Kullanım-Projeleme. Kocaeli: Umuttepe Yayınları

Kaya, D., Çoban, V., Çağman, S. ve Eyidoğan, M. 2015. Osmaniye İlindeki Hayvansal Biyogaz Ve Enerji Potansiyelinin Araştırmasına Yönelik Fizibilite Raporu. Karatepe Enerji Araştırma Geliştirme San. Ve Tic. Ltd. Şti. Kocaeli

Nuralan Poyraz. H, (2020). Kayseri İli İçin Hayvansal Atık Kaynaklı Biyogazdan Elektrik Enerjisi Üretim Potansiyelinin Ve Maliyetinin Araştırılması, Erciyes Üniversitesi Fen Bilimleri Enstitüsü Enerji Sistemleri Mühendisliği Anabilim Dalı, Kayseri, 3

ÖÇAL, F. (2013). Biyogaz Enerjisi Üretimi Ve Eskişehir İli İçin Uygulama, Yüksek Lisans Tezi. Makine Mühendisliği Anabilim Dalı

Sabuncu, Ö.C, (2010). Biyogaz Üretiminin Teknik, Ekonomik ve Çevresel Analizi. Hacettepe Üniversitesi Çevre Mühendisliği Anabilim Dalı Yüksek Lisans Tezi. Ankara, 42

Sarıkaya, F. (2020), Çoklu Besiyeri Anaerobik Çamur Çürütmenin Biyogaz Eldesine Etkisinin Belirlenmesi, Konya Teknik Üniversitesi Lisansüstü Eğitim Enstitüsü, Konya, 1

Topal, M. ve Arslan, E.I., 2008. Biyokütle Enerjisi ve Türkiye, VII. Ulusal temiz Enerji Sempozyumu, UTES'2008, İstanbul, 241-248

World Bioenergy Association. WBA Global Bioenergystatistics 2018, Summary Report; 5-10.

Yağlı H. ve Koç Y., 2019. Hayvan Gübresinden Biyogaz Üretim Potansiyelinin Belirlenmesi:Adana İli Örnek Hesaplama, Çukurova Üniversitesi Mühendislik Mimarlık Fakültesi Dergisi, 34(3) ss 35-48

Yiğit, D. (2020). Biyogaz / Biyometanizasyon Tesislerinin Çevre Kanunundaki Yeri, Kocaeli Üniversitesi Fen Bilimleri Enstitüsü Enerji Sistemleri Mühendisliği Anabilim Dalı, Kocaeli,

Türkiye’nin farklı bölgelerinde kara mürver (Sambucus Nigra) meyvesinde, bazı antioksidan aktiviteler ve polifenol oksidaz enziminin karşılaştırılması

Mesut Aydın[1], Halit Demir[2], Keziban Evliyaoğlu[3], Canan Demir[4]

[1]Van Yüzüncü Yıl Üniversitesi, Tıp Fakültesi, Gastroenteroloji AD. VAN-Türkiye

[2]Van Yüzüncü Yıl Üniversitesi, Fen Fakültesi, Kimya Bölümü, Biyokimya AD. VAN-Türkiye

[3]Orhan Okay Mesleki Teknik Anadolu Lisesi, Van

[4]Van Yüzüncü Yıl Üniversitesi, Sağlık Hizmetleri Meslek Yüksekokulu. VAN-Türkiye

Özet: Amaç: Bu çalışmada, Türkiye’nin farklı bölgelerinde kara mürver (Sambucus Nigra) meyvesinde, bazı antioksidan aktiviteler ve polifenol oksidaz enziminin karşılaştırılması amaçlandı.

Materyal ve yöntem: Süperoksit dismutaz, katalaz ve polifenol oksidaz enzim aktivitesi pektrofotometrik tayin edildi.

Bulgular: CAT, SOD ve PPO için grup ortalamaları arasındaki fark istatistik olarak anlamlı bulunmuştur ($p<0.05$). Bu sonuçlara göre Marmara bölgesinde yetişen kara mürver bitkisindeki CAT, SOD ve PPO düzeyi, İç Anadolu ve Karadeniz bölgesine gore anlamlı derecede yüksekti.

Sonuç: CAT, SOD ve PPO düzeyi, İç Anadolu ve Karadeniz bölgesine gore anlamlı derecede yüksek bulundu. Bu nedenle, kara mürver neyvesi insan sağlığı açısından tüketilebilir.

Anahtar kelimeler: Kara mürver, SOD, CAT, PPO

Objective: In this study, it was aimed to compare some antioxidant activities and polyphenol oxidase enzyme in black elderberry fruit in different regions of Turkey.

Materials and methods: Superoxide dismutase, catalase and polyphenol oxidase enzyme activities were determined pectrophotometrically.

Results: The difference between group means for CAT, SOD and PPO was statistically significant ($p<0.05$). According to these results, the levels of CAT, SOD and PPO in the black elderberry plant grown in the Marmara region were significantly higher than the Central Anatolia and Black Sea regions.

Conclusion: CAT, SOD and PPO levels were found to be significantly higher compared to Central Anatolia and Black Sea regions. Therefore, elderberry fruit can be consumed for human health.

Keywords: Black elderberry, SOD, CAT, PPO

Giriş:

Yapılan çalışmalarda kara mürverin çok sayıda hastalıkların önlenmesinde ve tedavisinde kulanıldığı bildirilmiştir. Literatürde yapılan çalışmalarda karamürver meyvesinin antibakteriyal, antitumoral, antifungal,obeziteye karşı, diüretük velaksativ aktivite,immun sisiteminin korunması ve uv radyasyonlara karşı vücudu koruduğu saptanmıştır (Bhattacharya et al., 2013;Folmer et al., 2014; Gray et al., 2000; Kashyap and DeFronzo, 2007; Netzel et al., 2005; Song et al., 2014), (Christensen et al., 2010; Chrubasik et al., 2008), (Hearst et al., 2010; Kinoshita et al., 2012; Kong, 2009; Krawitz et al., 2011), (Thole et al., 2006), (Ciocoiu et al., 2012; Frøkiær et al., 2012; Groza et al., 2010), (Chen et al., 2012; Jarzycka etal., 2013), (Beaux et al., 1999; Picon et al., 2010).

Polifenol oksidaz (PPO), E.C.(1.14.18.1), oksidoredüktaz sınıfına sahip bir enzimdir. Bu enzim aynı zamanda bakır ihtiva eden bir metaloenzimdir. En çok bulunduğu canlılar, hayvanlar, bitkiler, bakteriler ve mantarlardır (Yoruk and Marshall, 2003; .Kolcuoğlu, 2012).

Serbest radikaler veya reaktif oksijen raddikalleri, eşleşmemiş elektron çifti atamlardır. Reaktif oksijen radikaller artarsa artışı lipid peroksidasyon oluşur. Böyle bir durumda oksidatif stres meydana gelir. Serbest radikaller lipid peroksidasyonun son ürünü olan malondialdehidi (MDA) oluşturur. MDA aynı zamanda oksidatif stres düzeylerinden biridir. Reaktif oksijen radikali yükseldiğinde malondialdehit asit artar, bunun sonucunda oksidatif stres oluşur (Köse and Doğan, 1992; Gaweł ve ark., 2004).

Katalaz (CAT), antioksidant bir enzimdir. Toksit hidrojen peroksidin uzaklaştırmasında kulanılır, böbrek, serum, eritrosit, karaciğer, beyin, kalp, kas, mide ve birçok organelerde bulunan bir enzimdir. Katalaz, hidrojen peroksiti su ve oksijene dönüştürür (Matésve ark., 1999).

Süperoksit dismutaz (SOD), biyokimyasal reaksiyonlarda oksidatif stres olayının kontrolü için etkili bir antioksidantır. Antioksidantlar arasında en güçlü olanlardan biridir (McCord ve ark., 1971).

Bu çalışmada, Türkiye'nin farklı bölgelerinde kara mürver meyvesinde, bazı antioksidan aktiviteler ve polifenol oksidaz enziminin karşılaştırılması amaçlandı.

Materyal ve yöntem

Ekstrakt tamponun hazırlanması:

Mevsiminde toplanan kara mürver kullanılıncaya kadar -80°C'de bekletildi. Dondurulmuş olan kara mürver çekirdekleri çıkarıldı ve bir havanda iyice ezilerek parçalandı. Ezilen parçalar %1 PEG içeren 50 mM pH 7.0 fosfat tamponunda ilave edildi. Daha sonra tülbentten süzüldü 4°C'de 10.000 rpm'de 30 dakika santrifüj edildi (Aydemir,2003). Elde edilen süpernatandan süperoksit dismutaz, katalaz ve polifenol oksidaz enzim aktivitesi tayin edildi.

Katalaz enzim aktivitesi (CAT) tayini

Hidrojen peroksidin substrat olarak kullanılan bu çalışmada Aeibi yöntemine göre katalaz aktivitesi belirlendi. Aktivite şu şekilde yapıldı önce iki tüp alındı kör tüpüne 1.4 ml 30 mM'lık H2O2 ilave edilir ve üzerine 0.1 ml fosfat tamponu eklenir. Numune tübüne ise 1.4 ml 30 mM'lık H2O2 ilave edilir. Üzerine 0.1 ml enzim eklenerek vortexle karıştırıldı. 30 saniye aralıklarla iki defa 240 nm'de absorbanslar okundu ve böylece aktivite tayin edildi (Aeibi, 1984).

Süperoksit dismutaz (SOD) enzim aktivitesi tayini

SOD aktivitesi, Sun ve ark. (1988) tarafından önerilen yöntem kullanılarak tayin edilmiştir. SOD, oksidatif enerji üretimi sırasında oluşan toksik süperoksit radikallerinin($O_2•-$) hidrojen peroksit ve moleküler oksijene dismutasyonunu hızlandırır. Bu yöntem, ksantin ve ksantin oksidaz (XOD) kullanılarak oluşturulan süperoksit radikallerinin, nitro blue tetrazolium (N.B.T) ile meydana getirdiği mavi renkli formazan boyasının 560 nm dalga boyunda verdiği optik dansititenin (OD) okunması esasına dayanmaktadır. Örnekte bulunan SOD, süperoksit radikallerini ortamdan uzaklaştırarak formazan reaksiyonunu inhibe eder. SOD'nin bir ünitesi deneme koşulları altında N.B.T indirgenme hızının % 50 inhibisiyonudur.

Polifenol oksidaz (PPO) enzim aktivitesi tayini

Polifenol oksidaz enziminin aktivitesi spektrofotometrik olarak tayin edildi (Espin et al.,1995). Deneyin yapılışı, 100 mM substrat çözeltisi üzerine 10 mM MBTH çözeltisi ve 20 µl DMF içeren reaksiyon karışımı tampon çözelti eklenir ve 950 µl'ye tamamlanır daha sonra karışıma 50 µl bitki ekstraktı eklenir. Sonra 1 dakika boyunca belirtilen dalga boyunda absorbansdaki artış izlenmiş ve aktivite hesabı yapılmıştır. Bir ünite PPO aktivitesi; 1 ml reaksiyon karışımında bir dakikadaki 0,001 absorbans artışına neden olan enzim miktarı olarak, PFO'nun spesifik aktivitesi ise; 1 mg protein başına aktivite (ünite) olarak tanımlandı (Galeazzi and Sgarbieri,1981; Türkhan et al., 2018).

İstatistiksel analiz

Tanımlayıcı istatistikler Ortalama ve standart Sapma olarak ifade edildi. Normal dağılım koşulu olan durumlarda tek yönlü varyans analizi (ANOVA) kullanıldı. Normal dağılım koşulunun sağlanamadığı durumlarda Kruskal wallis testi kullanıldı. İstatistiksel anlamlılık düzeyi $p < 0,05$ olarak alınmış ve analizler için SPSS istatistiksel yazılım versiyonu 19.0 (SPSS Inc, Chicago, Ill, USA) paketi kullanılmıştır.

Tablo 1: Tanımlayıcı istatistikler ve karşılaştırma sonuçları

Biyokimyasal Parametreler		n	Mean±Std. Deviation	p
CAT	(U/L) İç Anadolu	10	5.8770±0.56888	0.001
	Karadeniz	10	10.8220±0.50179	
	Marmara	10	12.4980±0.26220	
SOD	(U/L) İç Anadolu	10	21.5010±1.28099	0.001
	Karadeniz	10	37.3810±1.03790	
	Marmara	10	48.8710±0.82585	
PPO (U/L)	İç Anadolu	10	2.0410±0.02132	0.001
	Karadeniz	10	3.8640±0.06867	
	Marmara	10	4.1480±0.10390	

Bulgular: CAT, SOD ve PPO için tanımlayıcı istatistikler ve karşılaştırma sonuçları Tablo 1'de verilmiştir. Tablo 1 incelendiğinde CAT, SOD ve PPO için grup ortalamaları arasındaki fark istatistik olarak anlamlı bulunmuştur ($p < 0,05$). Bu sonuçlara göre Marmara bölgesinde yetişen kara mürver bitkisindeki CAT, SOD ve PPO düzeyi, İç Anadolu ve Karadeniz bölgesine gore anlamlı derecede yüksektir (Şekil 1).

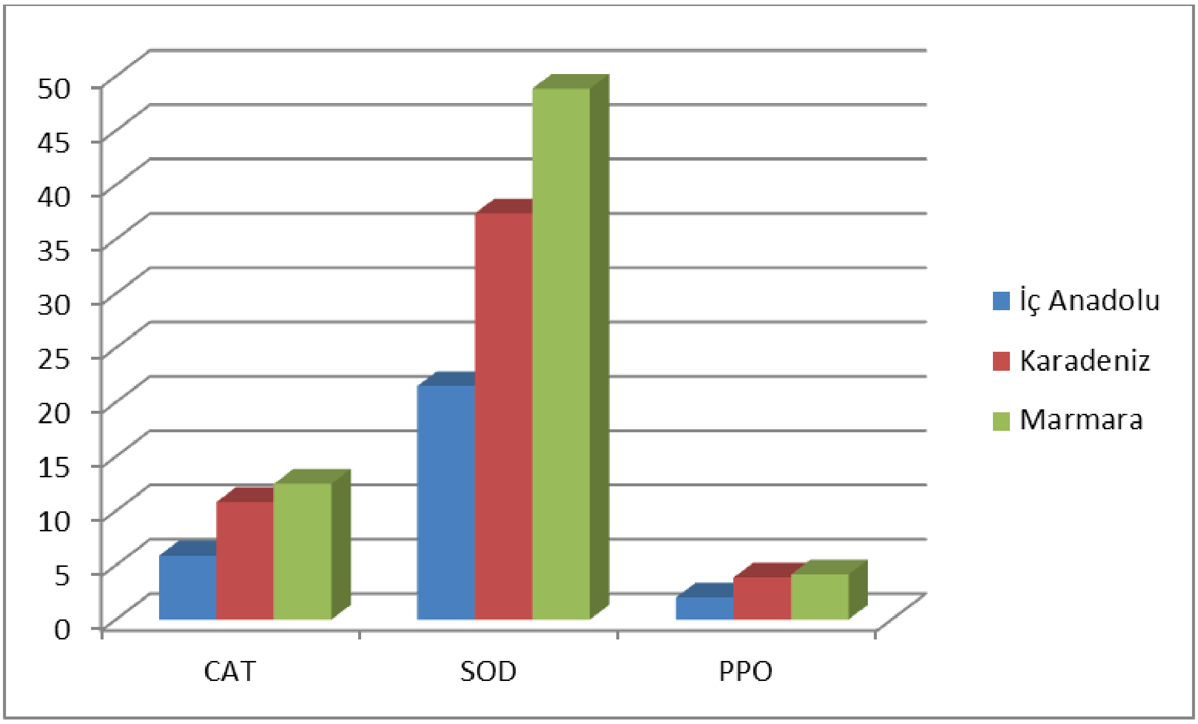

Sonuç ve Tartışma

Lipid peroksidasyonu serbest oksijen radikallerinin poliansatüre yağ asitlerinin yan zincirindeki metilenik karbonlardan hidrojen iyonu çıkarması ile başlar ve lipid radikali oluşur. Oluşan lipid peroksi radikalinin hemen yakınındaki ansatüre lipid molekülündeki hidrojen iyonu çıkarılmasıyla lipid hidroperoksit ve yeni bir lipid radikali meydana gelir (Sreejai and Jaya D, 2010). Reaktif oksijen radikaleri, romatoid artrit, diyabetes mellitus, ateroskleroz, hipertansiyon ve iskemi gibi kardiyovasküler hastalıklar gibi hastalıklarda artığı bildirilmiştir. Literatür araştırmalarında, böbrek, akciğer, karaciğer ve meme kanserleri gibi birçok kanser türünde oksidatif stresin yükseldiği tesbit edilmiştir.

Malondialdehid, olusan serbest oksijen radikallerinin iyi bir göstergesidir. Malondialdehitt'in artması, serbest oksijen radikallerinin etkisi ile artan lipid peroksidasyonunu gösterir. Lipid peroksidasyonu, organik yapılar ve membranların fonksiyonları üzerine çok zararlı etkilerine bağlı olarak, hücre ölümüne kadar ilerleyen farklılıklar oluşturur (Salman and Ashraf, 2013).

SOD oksijeni metabolize eden tüm hücrelerde ve oksijeninin zararlı etkilerine karşı önemli bir savuma bir sistemidir. SOD katalitik olarak aktivitesi çok yüksek olan bir enzimdir (Greenwald, 1990). Yüksek düzeylerdeki oksidatif strese aşırı miktarda SOD üretimine yol açar. Aynı zamanda, etkili bir koruma için yeterli SOD enzim sentezi gerekliliği vardır (Scandalios, 1993). SOD aktivitesi için tanımlayıcı istatistikler ve karşılaştırma sonuçları Tablo 1'de verilmiştir. Tablo 1 incelendiğinde CAT için grup ortalamaları arasındaki fark istatistik olarak anlamlı bulunmuştur ($p<0.05$). Bu sonuçlara göre Marmara bölgesinde yetişen kara mürver bitkisindeki SOD aktivitesi, İç Anadolu ve Karadeniz bölgesine gore anlamlı derecede yüksektir.

Katalaz tetramerik sert porfin proteindir. Katalaz, H_2O_2'nin bir mol H_2O ve yarım mol O2'ye dismutasyonunu katalizler. CAT, heme prostetik grubuna sahip 4 alt birimden meydana gelmektedir. Katalaz, hücreleri zararlı bileşiklerden korur. H_2O_2, katalaz ve glutatyon peroksidaz tarafından zehirsiz hale getirir(Matésve ark., 1999). CAT aktivitesi için tanımlayıcı istatistikler ve karşılaştırma sonuçları Tablo 1'de verilmiştir. Tablo 1 incelendiğinde CAT için grup ortalamaları arasındaki fark istatistik olarak anlamlı bulunmuştur ($p<0.05$). Bu sonuçlara göre Marmara bölgesinde yetişen kara mürver bitkisindeki CAT aktivitesi, İç Anadolu ve Karadeniz bölgesine gore anlamlı derecede yüksektir.

Enzimatik esmerleşme reaksiyonlarının azaltmak ya da esmerleşmeleri önlemek için polifenol oksidaz yararlanılır. Bu nedenle, enzim aktivitesine etkileyen parametrelerin bilinmesi gerekir. Böyle bir durumda gıda sektöründe, meyve ve sebzelerin ihracat ve saklanmasında önemli yararlar sağlar (Labuza et al., 1992). Meyve ve sebzelerde üzerinde etkli olan polifenol oksidaz enzimi katalizi sonucu eenzimatik kararma reaksiyonları oluşur. Böyle bir durumda sebze ve meyvenin hem tat ve görünüm hem de besin değeri azalmaktadır. Gıda bilimcileri PFO enziminin üzerinde özelikle enzimatik kararma olayı ile ilgilenmeye başlamışlardır. Bu kararmayı engelemek için birtakım inhibitörler kullanmışlardır (Cimen et al., 2007; Demir et al., 2012). Yapılan çalışmalarda kara mürverin yüksek polifenol iceriğine sahip olduğu bildirilmiştir (Olejnik A et al., 2016). PPO için tanımlayıcı istatistikler ve karşılaştırma sonuçları Tablo 1'de verilmiştir. Tablo 1 incelendiğinde PPO için grup ortalamaları arasındaki fark istatistik olarak anlamlı bulunmuştur ($p<0.05$). Bu sonuçlara göre Marmara bölgesinde yetişen kara mürver bitkisindeki PPO düzeyi, İç Anadolu ve Karadeniz bölgesine gore anlamlı derecede yüksektir. Bu durumun mühtemelen sebebi, iklimsel durum olabilir.

Sonuç olarak, CAT, SOD ve PPO düzeyi, İç Anadolu ve Karadeniz bölgesine gore anlamlı derecede yüksek bulundu. Bu nedenle, kara mürver neyvesi insan sağlığı açısından tüketilebilir.

Kara mürver ürünlerini literature uygun bir şekilde hazırlanmalı, sağlıkta ve eczacılıkta kulanıma yönelik çalışmalar daha fazla yapılmalıdır. Bu nedenle, antioksidan maddelere ilgiyi artıran, sağlığı geliştirici özelliklere sahip kara mürver ürünleri üretmeyi mümkün kılan ideal içerikli gıdalara sahip yeni hammaddeler planlanabilir.

Kaynaklar:

Aeibi, H., 1984. Catalase.(in) methods in enzymology. L. Packer(Editör), Academic Pres, Orlando. 105: 121-126.

Bhattacharya S, Christensen KB, Olsen LCB, Christensen LP, Grevsen K, Færgeman NJ, Kristiansen K, Young JF, Oksbjerg N (2013). Bioactive components from flowers of Sambucus nigra L. increase glucose uptake in primary porcine myotube cultures and reduce fat accumulation in Caenorhabditis elegans. J Agric Food Chem 61:11033– 11040.

Folmer F, Basavaraju U, Jaspars M, Hold G, El-Omar E, Dicato M, Diederich M (2014). Anticancer effects of bioactive berry compounds. Phytochemistry Reviews 13(1):295–322.

Gray AM, Abel-Wahab YHA, Flatt PR (2000). The traditional plant treatment, Sambucus nigra (elder), exhibits insulin-like and insulin-releasing actions in vitro. The Journal of Nutrition 113:15–20.

Kashyap SR, DeFronzo RA (2007). The insulin resistance syndrome: Physiological considerations. Diabetes and Vascular Disease Research, 4, 13–19. Fowler, M. J. (2010). Diagnosis, classification, and lifestyle treatment of diabetes. Clinical Diabetes 28:79–86.

Netzel M, Strass G, Herbst M, Dietrich H, Bitsch R, Bitsch I, Frank I (2005). The excretion and biological antioxidant activity of elderberry antioxidants in healthy humans. Food Res Int 38(8-9):905-910.

Song Y, Wu T, Yang Q, Chen X, Wang M, Wang Y, Peng X, Ou S (2014). Ferulic acid alleviates the symptoms of diabetes in obese rats. Journal of Functional Foods 9: 141–147.

Christensen K, Olsen L, Kotowska D, Bhattacharya S, Fretté XC, Færgeman N, Kristiansen K, Oksbjerg N, Christensen L (2010). Elderflowers (Sambucus nigra L.) have a significant impact on cellular mechanisms related to lipid storage and insulin resistance. Planta Medica 76(12): 1355-1355.

Chrubasik C, Maier T, Dawid C, Torda T, Schieber A, Hofmann T, Chrubasik S (2008). An observation study and quantification of the actives in a supplement with Sambucus nigra and Asparagus officinalis used for weight reduction. Phytoterapy Research 22:913–918.

Hearst C, McCollum G, Nelson D, Ballard LM, Millar BC, Goldsmith CE, Rooney PJ, Loughrey A, Moore JE, Rao JR (2010). Antibacterial activity of elder (Sambucus nigra L.) flower or berry against hospital pathogens. Journal of Medicinal Plants Research 4:1805–1809.

Kinoshita E, Hayashi K, Katayama H, Hayashi T, Obata A (2012). Anti-influenza virus effects of elderberry juice and its fractions. Bioscience, Biotechnology and Biochemistry 76:1633–1638.

Kong F (2009). Pilot clinical study on a proprietary elderberry extract: Efficacy in addressing influenza symptoms. Online Journal of Pharmacology and Pharmacokinetics 5:32–43.

Krawitz C, Mraheil MA, Stein M, Imirzalioglu C, Domann E, Pleschka S, Hain T (2011). Inhibitory activity of a standardized elderberry liquid extract against clinicallyrelevant human respiratory bacterial pathogens and influenza A and B viruses. BMC Complementary and Alternative Medicine 11:16.

Thole JM, Kraft TFB, Sueiro LA, Kang YH, Gills JJ, Cuendet M, Pezzuto JM, Seigler DS, Lila MA (2006). A comparative evaluation of the anticancer properties of European and American elderberry fruits. Journal of Medicinal Food 9:498–504

Ciocoiu M, Serban D, Bădescu L, Tutunaru D, Badulescu O, Bădescu M (2010). The effects of Sambucus nigra extract in experimental arterial hypertension. Annals of the Romanian Society for Cell Biology 15:87–92.

Frøkiær H, Henningsen L, Metzdorff SB, Weiss G, Roller M, Flanagan J, Fromentin E, Ibarra A (2012). Astragalus root and elderberry fruit extracts enhance the IFN-β stimulatory effects of Lactobacillus acidophilus inmurinederived dendritic cells. PLoS ONE 7.

Groza M, Ciocoiu M, Bădescu L, Bădulescu O, Bădescu M (2010). The effects of Sambucus nigra vegetal extracts on the immune system dysfunction in the diabetes mellitus. Annals of the Romanian Society for Cell Biology 15:241– 246.

Chen L, Hu JY, Wang SQ (2012). The role of antioxidants in photoprotection: A critical review. Journal ofthe American Academy of Dermatology 67:1013–1024.

Jarzycka A, Lewińska A, Gancarz R, Wilk KA (2013). Assessment of extracts of Helichrysum arenarium, Crataegus monogyna, Sambucus nigra in photoprotective UVA and UVB; photostability in cosmetic emulsions. Journal of Photochemistry and Photobiology B Biology 128:50–57.

Beaux D, Fleurentin J, Mortier F (1999). Effect of extracts of Orthosiphon stamineus Benth, Hieracium pilosella L., Sambucus L. and Arctostaphylos uva-ursi (L.) Spreng. in rats. Phytotherapy Research 13:222–225.

Picon PD, Picon RV, Costa AF, Sander GB, Amaral KM, Aboy AL, Henriques AT (2010). Randomized clinical trial of a phytotherapic compound containing Pimpinella anisum, Foeniculum vulgare, Sambucus nigra, and Cassia augustifoliafor chronic constipation. BMCComplementary and Alternative Medicine 10:17.

Olejnik A, Olkowicz M, Kowalska K, Rychlik J,Dembczyński R, Myszka K, Juzwa W, Białas W, Moyer MP (2016). Gastrointestinal digested Sambucus nigra L. fruit extract protects in vitro cultured human colon cells against oxidative stress. Food Chem 197(Pt A):648-657.

Yoruk R and Marshall MR, "Physicochemical properties and function of plant polyphenoloxidase:a review," Journal of Food Biochemistry, 27, 361–422, 2003.

Kolcuoğlu Y, "Purification and comparative characterization of monophenolase and diphenolase activities from a wild edible mushroom (macrolepiota gracilenta)," Process Biochemistry, 47, 2449–2454, 2012.

Espin JC , Morales M, Varon R, Tudela J, and Garcia-Canovas F, "A continuous spectrophotometric method for determining the monophenolase and diphenolase activities of apple polyphenol oxidase," Analytical Biochemistry, 43, 2807-2812, 1995.

Galeazzi MAM and Sgarbieri VCJ, "Substrate SpecificityandİnhibitionofPolyphenoloxidase from a Dwarf Variety of Banana (musa cavendishii, L.)," Journal Of Food Science, 46, 1404-1406, 1981.

Aydemir T, "Partial purification and characterization of polyphenol oxidase from artichoke (cynara scolymus L.) heads," Food Chemistry, 87, 59–67, 2004.

Türkhan A, Kaya ED, Yılmaz I. Partial purification and characterization of polyphenol oxidase enzyme from hawthorn (crataegus monogyna) fruit. Sakarya Unıversıty Journal of Scıence, 22 (3), 1048-1054, 2018.

Sun Y., Oberley L.W., Li Y., 1988. A simple method for clinical assay of superoxide dismutase. Clin. Chem., 34: 497-500.

Labuza TP, Lillemo JP, and Taoukis PS, "Inhibition of polyphenol oxidase by proteolytic enzymes," Fruit Processing, 2, 9-13, 1992.

Cimen, Ç., Demir, H., Gur, A. ve S. Kubilay, "Investigations of the inhibition kinetics of some drugs and chemicals on enzyme of polyphenol oxidase purified from Apricot's (Salak)", Biosciences, Biotechnology Research Asia. 4, 659-664 (2007).

Demir, H., Çimen, C., F.Ç. Çelikezen," Purification and characterization of polyphenol oxidase enzyme from Iğdır apricot (Prunus armeniaca L.)", Bitlis Eren University Journal of Science and Technology, ISSN 2146-7706 2, (2012), 22-26.

Köse, K. and Doğan, P.: Lipid Peroksidasyonu. Erciyes Tıp Dergisi. 1992; 340-350.

Gaweł S, Wardas M, Niedworok E, Wardas P. Dialdehyd malonowy (MDA) jako wskaźnik procesów peroksydacji lipidów w organizmie [Malondialdehyde (MDA) as a lipid peroxidation marker]. Wiad Lek. 2004;57(9-10):453455.

Salman, KA., Ashraf, S., 2013. Reactive oxygen species: A link between chronic inflammation and cancer. Asia-Pacific Journal of Molecular Biology and Biotechnology, 21(2): 42-49.

Matés, J. M., Pérez-Gómez, C., & De Castro, I. N., 1999. Antioxidant enzymes and human diseases. Clinical biochemistry, 32(8), 595-603.

McCord, J. M., Keele, B. B., & Fridovich, I., 1971. An enzyme-based theory of obligate anaerobiosis: the physiological function of superoxide dismutase. Proceedings of the National Academy of Sciences, 68(5), 1024-1027.

Sreejai R., Jaya D.S., 2010. Studies on the changes in lipid peroxidation and antioxidants in fishes exposed to hydrogen sulfide. Toxicol Int., 17: 71-77.

Greenwald R.A., 1990. Superoxide dismutase and catalase as therapeutic agents for human diseases. A critical review. Free Radic Biol Med., 8 (2): 201-209.

Schmidley J.W., 1990. Free radicals in central nervous system ischemia. Stroke, 21: 1086-90.

Does decreased antioxidant defense systems cauce cancer?

Halit Demir

Van Yuzuncu Yil University, Faculty of Science, Division of Biochemistry, Department of Chemistry, Van-Turkey.65100.

Abstract: In most of the studies, antioxidant defense systems are decreased in different cancer types. Cancer is the uncontrolled growth of cells. Changes appear in cells. Antioxidant defense systems may decrease as a result of the increase in free radicals. As a result, lipid peroxidation levels or oxidative stress generally increase. Oxidative stress is known to cause not only cancer but also diseases such as diabetes, aging, cardiovascular diseases, hypertension and rheumatoid arthritis.

In conclusion, antioxidant defense systems or decreased antioxidant activities may play an important role in the etiopathogenesis of cancer diseases.

Key words: Antoxidant enzymes, cancer, oxidative stress.

Introduction: Oxidative stress, which causes cellular damage, is a state of disruption of the balance between free radicals and antioxidants. Examples of free radicals include UV rays, drugs, fat oxidation, immune system reactions, radiation, stress, smoking and alcohol. Oxidative stress is a source of diseases. Disruption of circadian rhythm, chronic inflammation, infection, smoking, processed foods, drugs, sedentary lifestyle, psychological disorders, aging, hormonal imbalances are among the causes of oxidative stress. There is extensive research on oxidative stress (Gunes et al., 2020).

Oxidative stress is also caused by the overproduction of reactive oxygen species, which occurs in oxygen metabolism. ROS molecules are (free) radicals that contain oxygen and react with other molecules within a cell or tissue. Sometimes they can be of little benefit. However, their excess residues can damage the living organism (Tuncer G Seven et al., 2022).

In this study, the role of antioxidants in different types of cancer was investigated.

Discussion: Ectopic pregnancy is the most common life threatening emergency in early pregnancy. Although spontaneous resolution of ectopic pregnancy can occur, patients are at risk of tubal rupture and catastrophic haemorrhage.

The resulting free radicals lead to cardiovascular disease, cancer, diseases related to decreased blood circulation of the brain, diabetes, sudden renal failure, emphysema, bronchitis, lung diseases, alcoholic liver diseases, aging related tissue disorders and distupt the function of utern tubes (espacially slia) so that may be cause to many diseases. It has been proven in studies that high free oxygen radicals and lipid peroxidation have serious roles in the pathogenesis of diseases. In a study in bladder cancer, it was explained that patients showed a decrease in SOD, GST, GR and GSH levels, but an increase in XO levels (Gunes et al., 2020). SOD, CAT, GPx, PON1 and ARE activities are decreased in laryngeal cancer. In the same study, it was determined that MDA levels were high (Bozan et al., 2018). SOD, CAT and GSH levels decreased in prostate cancer. In the same study, it was determined that MDA levels were high. (Ahmed Amer et al., 2019). Oxidative stress index, total oxidant status and nitric oxide levels were found to be high in esophageal cancer patients (Sayır et al., 2019). Catalase activity was found to be low in patients with colon cancer (Gür et al., 2011). Decreased catalase activity detected in bladder cancer patients (Pirinççi et al., 2012). Decreased catalase activity was detected in patients with acute leukemia (Demir et al 2011). Catalase activity was found to be low in patients with lung cancer (Cobanoglu et al., 2010). While oxidative stress level increased in patients with lung cancer, antioxidant activities decreased. (Cobanoglu et al., 2011). The activity of catalase, an antioxidant, is decreased in patients with brain tumors (Arslan et al., 2011). Catalase activity was also decreased in patients with head and neck tumors (Tuncer G Seven et al., 2022).

Conclusion: Generally, studies measure the level of oxidative stress. We measure these measurements in the laboratory, because they are important markers. For example, it can be said that high amounts of reactive oxygen species are associated with cancer, cardiovascular and other diseases. Using these biomarkers, we can reveal the probability of people getting the disease.

We think that this change in antioxidant enzymes activitys may be related to the etiopathogenesis of the diffrent disease (especially, cancer and other diseases).

References:

Gunes M, Eryilmaz R, Aslan R, Taken K, Demir H, Demir C. Oxidant-antioxidant levels in patients with bladder tumours. Aging Male. 2020 Dec;23(5):1176-1181.

Engin A, Altan N. Effects of obstructive jaundice on the antioxidative capacity of human red blood cells. Hematologia. 2000;30(2):91–96.

Yardım-Akaydın S, Sepici A, Ozkan Y, et al. Oxidation € of uric acid in rheumatoid arthritis: is allontoin a marker of oxidative stress? Free Radic Res. 2004;38(6): 623–628.

Bozan N, Demir H, Gürsoy T, Özkan H, Düzenli U, Sarıkaya E, Turan M, Kiroglu AF, Çankaya H. Alterations in oxidative stress markers in laryngeal carcinoma patients.J Chin Med Assoc. 2018 Sep;81(9):811-815.

Ahmed Amar SA, Eryilmaz R, Demir H, Aykan S, Demir C. Determination of oxidative stress levels and some antioxidant enzyme activities in prostate cancer. Aging Male. 2019 Sep;22(3):198-206.

Sayır F, Şehitoğulları A, Demir H, Aslan M, Çobanoğlu U, Bilgin C. Turk Gogus Kalp Damar Cerrahisi Derg. 2019 Apr 24;27(2):206-21. Serum prolidase activity, total oxidant/antioxidant, and nitric oxide levels in patients with esophageal squamous cell carcinoma.

Gür T, Demir H, Kotan MÇ. Tumor markers and biochemical parameters in colon cancer patients before and after chemotherapy Asian Pac J Cancer Prev. 2011;12(11):3147-50.

Pirinççi N, Geçit I, Güneş M, Yüksel MB, Kaba M, Tanık S, Demir H, Aslan M. Serum adenosine deaminase, catalase and carbonic anhydrase activities in patients with bladder cancer. Clinics (Sao Paulo). 2012 Dec;67(12):1443-6.

Demir C, Demir H, Esen R, Atmaca M, Tagdemir E. Erythrocyte catalase and carbonic anhydrase activities in acute leukemias. Asian Pac J Cancer Prev. 2010;11(1):247-50.

.Cobanoglu U, Demir H, Duran M, Şehitogullari A, Mergan D, Demir C. Erythrocyte catalase and carbonic anhydrase activities in lung cancer. Asian Pac J Cancer Prev. 2010;11(5):1377-82.

Cobanoglu U, Demir H, Cebi A, Sayir F, Alp HH, Akan Z, Gur T, Bakan E. Lipid peroxidation, DNA damage and coenzyme Q10 in lung cancer patients--markers for risk assessment? Asian Pac J Cancer Prev. 2011;12(6):1399-403.

Arslan M, Demir H, Arslan H, Gokalp AS, Demir C. Trace elements, heavy metals and other biochemical parameters in malignant glioma patients. Asian Pac J Cancer Prev. 2011;12(2):447-51.

Tuncer G Seven, Demir H, Izmirli M, Cakir T, Yilmazer G, Demir C. Effect of radiotherapy on erythrocyte catalase, and carbonic anhydrase activities, serum levels of some trace elements and heavy metals (Zn, Cu, Pb, Cd, Mn, Fe, Mg and Co) in cancer patients. International Journal of Radiation Research; Tehran Vol. 20, Iss. 1, (Jan 2022): 97-102.

Conduction Mechanism in Ion Conducting Electrolyte & Mixed Conducting Electrodes for Electrochemical Device Application

Madhumita Mukhopadhyay[1*], **Satadal Paul**[2] and **Jayanta Mukhopadhyay**[3]

[1]Department of Materials Science & Technology, Maulana Abul Kalam Azad University of Technology (MAKAUT), West Bengal, 741249, India

[2]Department of Chemistry, Bangabasi Morning College, Kolkata-700099

Energy Materials & Devices Division, CSIR-Central Glass and Ceramic Research Institute, Kolkata – 700 032, India).

**Presenter: madhubanerji@gmail.com*

J. Mukhopadhyay: jmukhopadhyay75@gmail.com

Abstract: In the arena of material science, conducting materials irrespective of their origin being either polymeric or composite is of significant importance. Based on the synthesis process/ crystallization etc., the structure property correlation is highly affected and this tailoring enables the incorporation of novel properties in such functional materials. In this connection, understanding of conduction mechanism in terms of either electronic, ionic or mixed ionic and electronic (MIEC) is important. The present endeavour is initiated with the basic analyses of electronic conduction in terms of density of states and orbital coherence. The conceptualization of bound and free electron towards the density of states (DOS) enables the introduction of band gap which is the primary factor in the segmentation of metals, semi-conductors and insulators. This is correlated to the defect formation and propagation which is the primary requisite for ionic conduction mechanism. Concept and application of Mott Hubbard insulator is further exemplified in conjunction with crystal field stabilization energy associated with d-orbital splitting. Such electronic and MIEC mechanism is correlated with the application of electrochemical devices viz. fuel cell, sensors, lithium-ion battery etc. The generation and extension of triple phase boundary regions in either metal-ceramic composite (as hydrogen electrode) and/or multicomponent perovskite/ pyrochlore systems (as oxygen electrode) are well correlated with the electrochemical performance analyses of solid oxide cells. On a similar note, understanding of ionic conduction mechanism bears significance in the generation and functionality of electrolyte materials applicable in solid state devices. The tenable long term performance analyses and its correlation with conduction mechanism using tailoring at atomic level within the microstructure is discussed with details.

Reference:

- Introduction to ceramics, W. David Kingery, H. K. Bowen, Donald R. Uhlmann • 1976
- Material Science and Engineering. V. Raghavan (2000)
- M. Mukhopadhyay, J Mukhopadhyay, A Das Sharma and R.N. Basu", Solid State Ionics, 233, 20-31 (2013)
- M. Mukhopadhyay, J Mukhopadhyay, A Das Sharma and R.N. Basu", Int. Journal of Hydrogen Energy. 37, 2524-2534 (2012)
- K. Banerjee, J. Mukhopadhyay, S Bysakh and R.N. Basu Int. Journal Hydrogen Energy, 42, 4 (2017), 2327-2337
- K Banerjee, J Mukhopadhyay and R.N. Basu J. Power Sources, 328 (2016) 15-27

First order reversal curve method for characterization of magnetic materials

Basharat Want

Department of Physics, University of Kashmir , Srinagar, India

Abstract: The First Order Reversal Curves (FORC) method is a novel approach for investigating the magnetic materials. FORC method provides a way for evaluating the distribution of switching and interaction fields between magnetic particles, irreversible magnetization components and for differentiating between magnetic phases in composite materials that containing more than one magnetic phase. The FORC method will be presented and discussed. FORC diagrams of some rare-earth based spinal ferrites and hexaferrites will also be presented.

The theoretical description for polyindolic green conducting synthesis, assisted by cobalt (iii) oxyhydroxide

Volodymyr V. Tkach[*1], Marta V. Kushnir[1], Sílvio C. de Oliveira[2], Jarem Raul Garcia[3], Yana G. Ivanushko[4], Adriano O. da Silva[5], Petro I. Yagodynets´[1], Zholt O. Kormosh[6], Olga V. Luganska[7], José Inácio Ferrão da Paiva Martins[8], Eloi A. da Silva Filho[9]

[1]Chernivtsi National University, 58000, Kotsyubyns´ky Str. 2, Chernivtsi, Ukraine (E-mail: nightwatcher2401@gmail.com)

[2]Universidade Federal de Mato Grosso do Sul, Av. Sen. Felinto. Müller, 1555, C/P. 549, 79074-460, Campo Grande, MS, Brazil

[3]Universidade Estadual de Ponta Grossa, Campus de Uvaranas, Av. Gal. Carlos Cavalcanti, 4748, 84030-900, Ponta Grossa, PR, Brazil

[4]Bukovinian State Medical University, 58001, Teatralna Sq., 9, Chernivtsi, Ukraine,

[5]Campus Juruti, Universidade Federal do Oeste do Pará, 68170 – 000, Rua Veríssimo de Souza Andrade, s/n, Juruti, PA, Brazil,

[6]East Ukrainian National University, 43000, Voli Ave., 13, Lutsk, Ukraine, 7Zaporizhzhia National University, 69600, Zhukovsky Str. 66, Zaporizhzhia, Ukraine

[8]Faculdade de Engenharia da Universidade do Porto, Faculdade de Engenharia da Universidade do Porto, 4200-465, Rua Dr. Roberto Frias, s/n, Porto, Portugal

[9]Universidade Federal de Espírito Santo, Av. Fernando Ferrari, 514, 29075-910, Vitória, ES, Brasil

Indole (Fig. 1) is an aromatic system, consisted of a pyrrolic ring, condensed with a benzolic aromatic moiety. It is base of different important biologically active compounds [1], like also plant, animal and mushroom toxins.

The major part of these compounds possesses the indole fragment, substituted by donor substituents, which makes viable the hypothesis of the electropolymerization of these compounds. As polyindoles are already known, the presence of donor groups lowers the monomer polymerization potential, leading to the possibility of the conducting polymers from renewable natural fonts.

Either direct or indirect electropolymerization processes may be applicable to them. In this work, we describe the possibility of the use of Cobalt (III) oxyhydroxide in the electropolymerization processes of the natural indole derivatives.

Two mathematical models may be described for the use of CoO/CoO(OH) and CoO(OH)/CoO2 redox pairs. The analysis of both of the processes for galvanostatic and potentiostatic modes shows that the polymer composite may be efficiently synthetized. The steady-state is easy to obtain and maintain. As for the oscillatory behavior, its probability varies, depending on whether the monomer is ionic or not.

References:

1. N. A. S. Ali, B.A. Dar, V. Pradhan, M. Farooqui, Mini-Rev. Med. Chem., 13(2013), 1792.

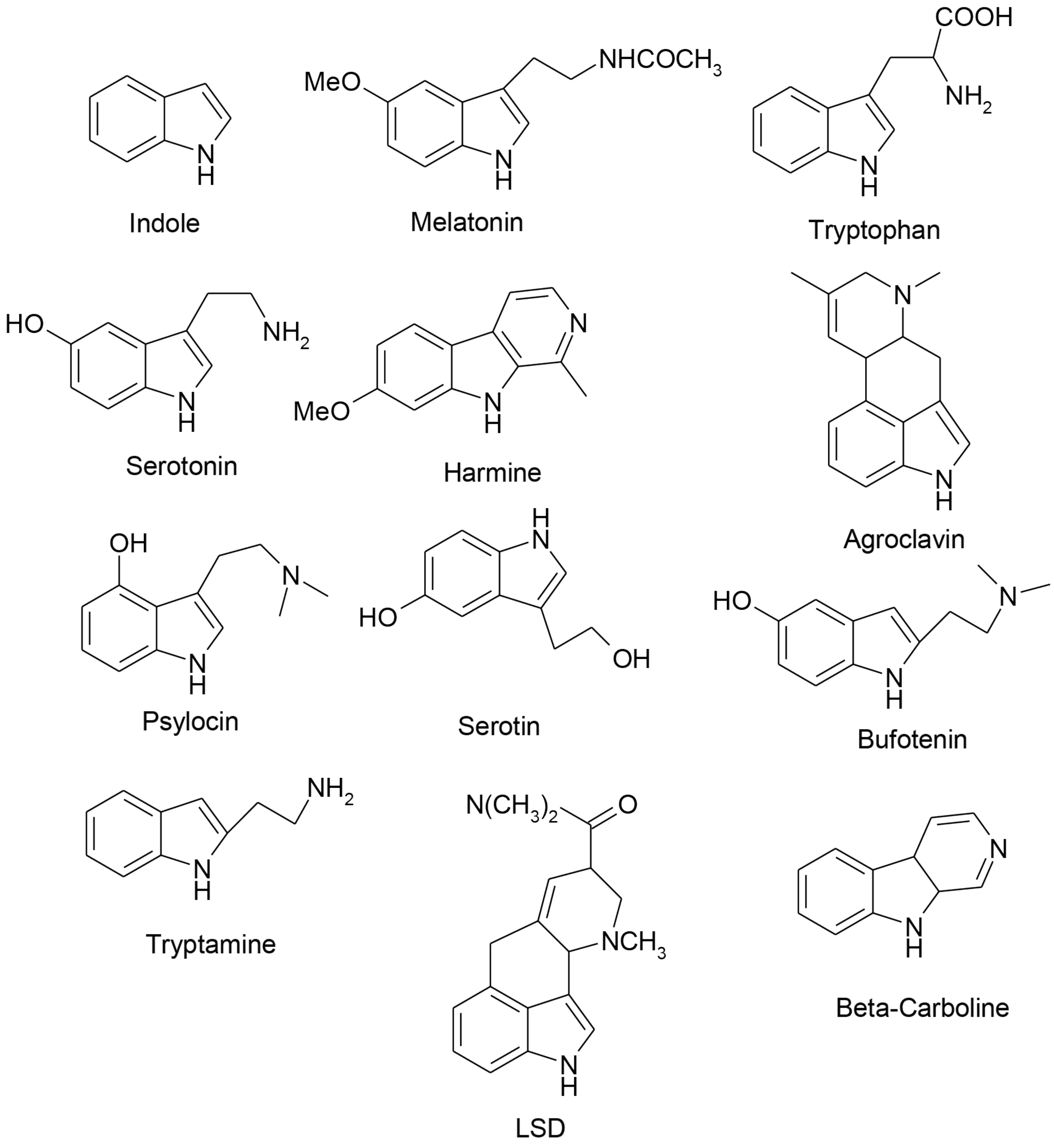

Fig. 1. Some important indole derivatives.

Facile synthesis of Nitrogen-doped reduced graphene oxide as cobalt support for oxygen reduction reaction and oxygen evolution reaction in alkaline media

Karim Kakaei[1]* and **Sheyda Rasouli**[1]

[1]*Department of Chemistry, Faculty of Science,*
University of Maragheh, P.O. Box. 55181-83111,
Maragheh ,Iran

Abstract: The development of functional catalysts for oxygen evolution reaction (OER) and oxygen reduction reaction (ORR) is highly desirable for rechargeable metal-air batteries and fuel cells.

In this work, reduced graphene oxide and nitrogen-doped reduced grapheme oxide (N-RGO) with a high nitrogen doping content are synthesized via electrochemical approach. RGO was synthesized using graphite rods as anode and cathode by electrochemical exfoliation method with a separation of 1 cm in H2SO4 (0.5 M). The N-doped graphene was also prepared by using two graphite electrods. Choline chloride crystals were used to exfoliate graphite dispersion electrolyte (0.5 M) and 1 M of urea as N-doping source in 100 ml of DI water. Electrochemical exfoliation was occured in both experiments by applying positive voltage (4 V) to the anode graphite electrode in room temperature. As the exfoliation was complete, the suspended product was collected with membrane filter and washed with deionized water. The third electrode has been fabricated by using Cobalt nitrate hexahydrate and obtaining N-RGO in presence of urea solution by hydrothermal method. Urea is used as the electrolyte for providing nitrogen source and reducing agent.

The bare RGO, NRGO, Co-NRGO electrocatalysts are very active for the oxygen reduction reaction (ORR), providing the best performance in terms of tafel slope and onset potential. But, the resulting Co/NRGO electrocatalyst shows outstanding electrocatalytic performance toward both ORR and OER.

The theoretical description for 4-4´-dihydroxydiphenyl and 4-4´-dihydroxyazobenzene electrochemical determination in agaricus xanthodermus mushroom over cobalt (iii) oxyhydroxide

Volodymyr V. Tkach[*1], **Marta V. Kushnir**[1], **Sílvio C. de Oliveira**[2], **Jarem Raul Garcia**[3], **Yana G. Ivanushko**[4], **Oksana P. Vitriak**[5], **Dina V. Fedorova**[5], **Petro I. Yagodynets´**[1], **Zholt O. Kormosh**[6], **Mykhailo M. Kucher**[6], **Olga V. Luganska**[7], **José Inácio Ferrão da Paiva Martins**[8], **Karina V. Palamarek**[9], **Konon L. Bagrii**[9] and **Tetyana V. Morozova**[10]

[1]Chernivtsi National University, 58000, Kotsyubyns´ky Str. 2, Chernivtsi, Ukraine (E-mail: nightwatcher2401@gmail.com)

[2]Universidade Federal de Mato Grosso do Sul, Av. Sen. Felinto. Müller, 1555, C/P. 549, 79074-460, Campo Grande, MS, Brazil

[3]Universidade Estadual de Ponta Grossa, Campus de Uvaranas, Av. Gal. Carlos Cavalcanti, 4748, 84030-900, Ponta Grossa, PR, Brazil

[4]Bukovinian State Medical University, 58001, Teatralna Sq., 9, Chernivtsi, Ukraine,

[5]Kyiv National University of Trade and Economics, 02156, Kyoto Str. 21, Kyiv, Ukraine

[6]East Ukrainian National University, 43000, Voli Ave., 13, Lutsk, Ukraine, 7Zaporizhzhia National University, 69600, Zhukovsky Str. 66, Zaporizhzhia, Ukraine

[8]Faculdade de Engenharia da Universidade do Porto, Faculdade de Engenharia da Universidade do Porto, 4200-465, Rua Dr. Roberto Frias, s/n, Porto, Portugal

[9]Chernivtsi Institute of Trade and Economics of Kyiv National University of Trade and Economics, 58012, Central Sq. 9, Chernivtsi, Ukraine

[10]National Transport University, 02000, M. Omelianovych-Pavlenko Str., 1, Kyiv, Ukraine

Agaricus is the most cultivated and consumed genus of mushrooms in Western and Northern Europe. Its principal and most known representants are button mushroom (*Agaricus bisporus*) and field mushroom (Agaricus campestris). Both of them are edible and are cultivated in the special farms.

Nevertheless, alongside with the edible species, this genus includes also some poisonous species. The most common of them is the so called yellow stainer (*Agaricus xanthodermus*). It may readily grow among the edible Agaricus mushrooms and even compart the same mycelium, so it is easy to be confounded with the button and field mushrooms. Of those who gather *Agaricus* mushrooms, the yellow stainer poisoning cases are nearly the half of the total of the mushroom intoxications. The yellow stainer may be discriminated among the rest of the *Agaricus* mushroom by color and a disgusting smell, which becomes even more intense on cooking. Either the color or the smell or the toxic effects of the mushroom for the most people are explained by the presence of the phenolic compounds in it. The most toxic of these phenolic compounds is the 4-4´-dihydroxyazobenzene, which in fact is responsible for the color of the mushroom. It was the first naturally found endogenous azo-dye: . In the mushroom pulp, the phenolic compounds act as antioxidants, detaining the

ISBN: 978-975-7616-84-9

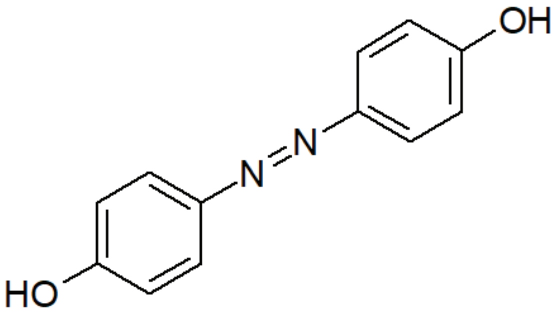

Fig. 1. 4-4´-dihydroxyazobenzene

metabolic oxidation processes. Nevertheless, containing a strongly accepting azo-group, this compound becomes much more acidic, while compared to the simplest phenol, and its ingestion may cause gastric problems. Moreover, the 4-4´-dihydroxyazobenzene has also a potential to be used as an industrial dye, being intentionally or unintentionally added into food. Thus, the development of the determination methods for 4-4´-dihydroxyazobenzene is really actual.

In this work, the electrochemical determination for two *Agaricus xanthodermus* phenolic compounds has been theoretically evaluated. Alongside with the azo-dye, the 4-4´-dihydroxyazobenzene is considered. For the case of anodic oxidation, the use of the cobalt (III) oxyhydroxide may be suggested. It is a p-type semiconductor, proposed by some researchers as an alternative to titanium dioxide, but with more flexible electrochemical behavior. Possessing trivalent cobalt, it may act either as an oxidant or as a reducent. Both redox pair may be applied to the phenolic compounds. Its electroanalytical behavior has been analyzed by either experimental or theoreticalmeans. For stability reasons, cobalt (III) oxyhydroxide may be used as a part of composite material with the conducting polymer, carbon material or a squaraine dye. Thus, the cobalt (III) oxyhydroxide acts as an active substance, and the conjugated material, as a mediator.

In neutral media, both of the compounds are oxidized to the correspondent quinonic forms. Either homo- or copolymerization scenarios are considered. In the last case, it may give a path to the appearance of an economic and green conducting polymer.

In this system, a squaraine dye or conducting polymer may be used as a cobalt(III) oxyhydroxide stabilizer and electron transfer mediator. It is shown that, contrarily to the great part of the systems with cobalt (III) oxyhydroxide, this system will behave in a more stable manner, providing an efficient diffusion-controlled process. On the other hand, the oscillatory and monotonic instabilities, although possible, are caused by the double electric layer influences of either chemical or electrochemical stage.

The theoretical description for hydroxyquinol and sesamol CoO(OH)-assisted electrochemical determination in tahini halva

Volodymyr V. Tkach[*1], Marta V. Kushnir[1], Sílvio C. de Oliveira[2], Jarem Raul Garcia[3], Yana G. Ivanushko[4], Oksana P. Vitriak[5], Viktoriia A. Gnitsevych[5], Petro I. Yagodynets´[1], Zholt O. Kormosh[6], Mykhailo M. Kucher[6], Olga V. Luganska[7], José Inácio Ferrão da Paiva Martins[8], Karina V. Palamarek[9], Konon L. Bagrii[9] and **Tetyana V. Morozova[10]**

[1]Chernivtsi National University, 58000, Kotsyubyns´ky Str. 2, Chernivtsi, Ukraine (E-mail: nightwatcher2401@gmail.com)

[2]Universidade Federal de Mato Grosso do Sul, Av. Sen. Felinto. Müller, 1555, C/P. 549, 79074-460, Campo Grande, MS, Brazil

[3]Universidade Estadual de Ponta Grossa, Campus de Uvaranas, Av. Gal. Carlos Cavalcanti, 4748, 84030-900, Ponta Grossa, PR, Brazil

[4]Bukovinian State Medical University, 58001, Teatralna Sq., 9, Chernivtsi, Ukraine,

[5]Kyiv National University of Trade and Economics, 02156, Kyoto Str. 21, Kyiv, Ukraine

[6]East Ukrainian National University, 43000, Voli Ave., 13, Lutsk, Ukraine, 7Zaporizhzhia National University, 69600, Zhukovsky Str. 66, Zaporizhzhia, Ukraine

[8]Faculdade de Engenharia da Universidade do Porto, Faculdade de Engenharia da Universidade do Porto, 4200-465, Rua Dr. Roberto Frias, s/n, Porto, Portugal

[9]Chernivtsi Institute of Trade and Economics of Kyiv National University of Trade and Economics, 58012, Central Sq. 9, Chernivtsi, Ukraine

[10]National Transport University, 02000, M. Omelianovych-Pavlenko Str., 1, Kyiv, Ukraine

Hydroxyquinol is one of the natural polyphenolic compounds [1 – 5], widely used as biomarkers and monomers for conducting polymers. Its natural occurrence is abundant and it is formed by fructose dehydratation (1):

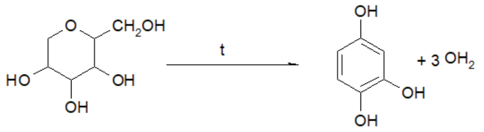

(1)

Sesamol is one of the hydroxyquinol cyclic eters. It gives its specific flavor and scent to Turkish delights like tahini halva, lokum, baklava etc. On the other hand, hydroxyquinol and its derivatives may also be pharmaceutical wastewater pollutants, like their isomers, as they may be toxic for aquatic organisms, reason why the development of an efficient method for its quantification is really actual.

Both hydroxyquinol and sesamol are phenolic compounds. So, they are electrochemically active. Phenolic and polyphenolic compounds are very popular objects for electroanalytics and are popular monomers for conducting polymers.

Nevertheless, their electroanalytic properties´ investigation has only begun, and a CoO(OH)-assisted electrochemical oxidation may confront the problems like:

- the indecision in the modifier mechanism of action;
- the compatibility of the modifier with the pharmaceutical tissue or biological

object (some modifiers, used in vitro may be non-compatible with in vivo sensing);

- the presence of electrochemical instabilities, accompanying both electrochemical synthesis of cobalt (III) oxyhydroxide [31], and electrochemical oxidation and electrooxidative polymerization of organic molecules.

So, the goal of this work is to describe an interesting electroanalytical process for hydroxyquinol and sesamol electrochemical determination on cobalt (III) oxyhydroxide has been described. As hydroxyquinol is 1,2 and 1,4-hydroquinonic derivative simultaneously, two low-molecular oxidation possibilities are foreseen. The polymerization scenario is not discarded.

The analysis of the correspondent mathematical model confirms that the oscillatory behavior is lower in neutral media and higher in the alkaline media. Either way, the electroanalytical process is diffusion-controlled, being efficient in a wide concentration range.

Electrosynthesis and characterization of new Cobalt-MOFs as an effective catalyst in C-X bond formation reactions

Rahman Karimi-Nami[1*] and **Vahid Khakyzadeh**[2]

[1]Department of Chemistry, Faculty of Science, University of Maragheh, P.O Box 55181-83111, Maragheh, Iran

Abstract: This study develops a highly efficient metal–organic framework (MOF) catalyst for the C-X bond formation reactions such as C-C or C-S and C-N bond formations. As an efficient cooperative catalyst for such kinds of reactions, Cobalt (Co)-MOF, displays great sustainability and efficiency. Metal–organic frameworks (MOFs) represent a rising class of porous crystalline materials with exceptional surface areas and uniformly dispersed metal ions. Such inherent properties make MOFs advanced materials for processes such as gas storage and separation, drug delivery, heterogeneous catalysis, and so on. Recently, we have designed a series of modified electrodes through MOFs with diverse pore shapes, sizes and compositions for targeted applications. Thus, it is probed to explore the potentials of MOFs as the new-type catalysts for C-X bond formation reactions. Notably, Co-MOFs on electrodes show significant development in these reactions in terms of time and energy throughout electrochemical processes. By means of the present study, we will synthesize Co-MOFs on Graphite electrodes by using anchoring diazonium salt and test the morphology and electrochemical behaviour of the electrode in our target reactions respectively.

Keywords: Electrosynthesis, MOFs, Co-MOF, C-X bond formation.

Investigation of RSW Hardness of Deep Drawing Steel Used in Shaping Vehicle Body Panels

Muhammed Elitaş[1*]

[1]*Bilecik Şeyh Edebali University, Turkey*

Abstract: In this study, resistance spot welding combinations were made on deep drawing steel with different welding current and electrode force parameters. Microhardness tests were carried out and theoretical hardness value was calculated using the equations found in the literature. As a result, microhardness value increased as the welding current and electrode force increased. Compared to the base material, the hardness value of the weld metal increased approximately 2 times. While a higher hardness value was found at the highest welding current and electrode force parameters compared to the theoretical value, lower values were obtained in other welding parameters.

Keywords: Deep drawing steel, resistance spot welding, micro hardness.

A Study on Analysis of Surface Roughness Variations of Nimax Mould Steel after Turning Operation

Rüstem Binali[1*] and **Mustafa Kuntoğlu**[2]

[1,] *Selcuk University, Turkey*

Abstract: Industrially important materials are attracting more attention in the last years with the development of machinery and artificial intelligence revolutions mostly due to costly and time-consuming production processes. One of them, a mould steel Nimax carries the combinations of several mechanical properties such as weldability, crack hardness, polishing, resistance to indentations etc. Despite this special material has a good machinability, there is insufficient literature study currently about its machining performance. In this direction, main purpose of this article is to analyze the impacts of basic machining inputs on the average roughness value. An experimental plan was composed using Taguchi design. Three levels of speed, feed and cutting depth were included into the experiments. According to the obtained findings from the experiments, feed was detected as the dominant variable with the contribution rate about 67.21 % and followed by cutting speed with the efficiency about 31.54 % based on analysis of variance. To achieve the best surface roughness value, first feed value (0.15 mm/rev), third speed value (60 m/min) and first cutting depth value (0.05 mm) should be selected according to Taguchi optimization. With this study, it is expected to make a contribution to the literature papers by showing the place of optimization and analysis methods for machinability improvement of industrial materials.

1. Introduction

Machining processes generally includes a relative movement that realized with the help of cutting tool and workpiece materials [1]. Such a motion directly produces high temperatures and pressures at the contact surfaces [2]. As a result of these developments, high plastic deformation is created at the contact zones. During this period, a new surface is formed constantly as a result of the removed chips. By the common impact of the pressure and temperature, really high coefficient of friction around the cutting zone cause tool wear [3]. The case is known as natural and on the other hand the acceleration of the wear progression is tried to slow down. The mechanical properties of the machined part, the heat treatment applied, the chemical composition directly affects wear mechanisms [4]. The necessity of wearing the cutting tool to form chips has prompted manufacturers and researchers to understand this formation. Deteriorations in the tool not only change the geometry and chemical structure of the tool, but also affect all other variables. Parameters such as chip type, cutting forces and consumed power, especially workpiece surface roughness and dimensional accuracy are involved into a dynamic change [5]. From all machining variables, roughness of the surface exists among the significant outcomes as it defines the quality of the material which will be the main topic of this study.

Surface roughness is a property measured from the material surface that indicates the quality of the surface according to the depth and height of peaks that deviate from a reference profile line [6]. Surface roughness is a variable of the exterior side of the manufactured part and it is desirable to have functional properties in order to fulfill various tasks such as friction properties, thermal conductivity, oil retention, and tolerance determination [7]. For these reasons, the surface roughness should be kept within a certain range and the process should be optimized in this direction [8]. Since surface roughness belongs to a machine element or manufactured part, it is considered the ultimate task for operators and workers. Surface roughness is detected by the assistance of roughness measurement devices. Measurements are made with the tips that can move freely on the vertical axis, called the probe, which is placed on the end of the holder supported by a body. This movable head makes linear movement on the surface with the help of the holder, which is put forward with the start of the measuring process. In the meantime, it detects the peaks and troughs in the surface profile. Because the roughness measuring probe has a very sensitive tip, it is very important to calibrate and measure carefully on the surface. Depending on the capacity of the roughness device, the travel length of the probe or the measurement length can be determined in different scales. Thus, the measurement length on the surface to be evaluated is selected from the determined standard values. Depending on the sensitivity of the roughness device, it is generally in a structure that can measure at the micrometer level. Since the number of peaks and pits in the profile and the excess of depth and heights in the profile spoil the profile, it is purposed to obtain the smallest possible roughness value. Bayraktar and Uzun evaluated the machinability of pre-hardened Toolox 44 and Nimax die steels on cutting force and surface roughness by using the milling method. As a result of their studies, according to the processed subsurface images, Nimax stated that a pit formed on the machined surface with the increase of feed [9]. Bostancı examined the workability of Nimax in his study. He used the milling method in his study and carried out on cutting force and surface roughness. As a result, it was stated that the cutting forces and surface roughness values that occurred during machining decreased with the increase in cutting speed [10].

The utilized material Nimax is a mould steel that is preferred in the injection and extrusion applications. As a consequence, there is a need for good surface quality for such parts. The main properties of this special steel are good machinability, weldability, polishing, resistance to indentations, impact and crack hardness and consistent features across large sections [11]. Despite these positive features, the machinability studies about this steel are not enough. Therefore, this paper aims to investigate the machinability of Nimax in terms of surface quality. In this direction, surface roughness was considered as the response parameter. For the experimental studies, turning operation was considered and basic turning parameters were handled as the machining parameters. The results obtained from the experiments were evaluated by three approaches: i) optimization, ii) statistical analysis, iii) graphical evaluation. The outcomes of this paper are expected to contribute to the literature papers by applying several scientific approaches to the industrial materials.

2. Material and Methods

This section addresses the details of materials and methods used in this study along with the measurement details of the response parameter i.e., surface roughness. Also, this section includes the experimental details such as experimental plan, handling and performing in the course of the paper.

2.1. Material properties

Nimax steel was used as the workpiece materials in the experiments. Nimax is a mould steel that carries many significant mechanical and physical properties such as good welding and polishing, texture building, resistance to indentations etc. The chemical ingredients of this special steel utilized are given in Table 1. The dimensions of the mould steel were utilized as 50 x 100 x 50 mm during the experiments. Cutting tools used have TiC coatings and CCMT 09T308-304 codes.

Table 1. *Chemical composition of Nimax plastic mold steel [12]*

Material	C	Si	Mn	Cr	Ni	Mo
Nimax	0.1	0.3	2.5	3	1	0.3

2.2. Experimental setup and tests

The experiments were performed on a lathe (De Lorenzo, Italy). It is needed to be said that a new cutting insert was utilized for each experiment. After completing all of the tests, the roughness data was handled while calculating each data for all of the experimental lines. Experimental setup of the study is demonstrated in Figure 1. In the experiments, three levels of feed, speed and cutting depth were used. During this period of time, depth of cut values were found at first and cutting speed ranges was defined and

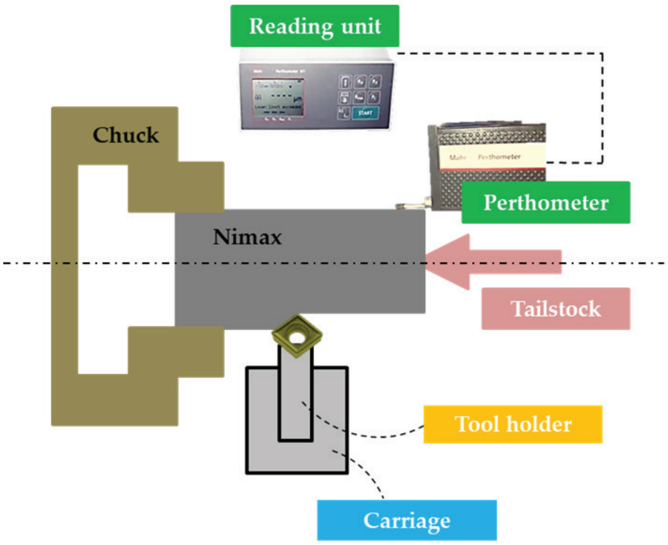

Figure 1. *Experimental setup*

lastly the feed rates were decided. Before making the experiments, comprehensive preliminary tests were performed according to the machine tool specifications, recommendations of manufacturers. As a consequence, 0.5 mm metal was removed to overcome the problematic cases which may come from the manufacturing procedure. Moreover, some challenging issues such as chatter and distorted chips were considered and these experiments were eliminated.

2.3. Experimental plan

Taguchi is widely preferred as it presents an approach for the modelling of the experimental plan and optimizing the design parameters for better results. It is fully accepted with the long past of the experimental studies in the field of machining [13,14]. Taguchi provides minimum economic burden, labor and the energy consumption as it shortens the outcomes and time [15]. Owing to the excessive outcomes of the used material, i.e., Nimax, this approach was addressed in order to achieve the sorted reasons. As a result, Table 2 was obtained which provides to make 9 experiments instead 27 experiments which reduce the time and material needs significantly.

Table 2. *Experimental results with Taguchi based orthogonal design*

Test No	f	d	Vc	Ra (µm)
1	0.15	0.05	30	2.33
2	0.15	0.1	40	1.24
3	0.15	0.15	60	1.1
4	0.3	0.1	40	3.94
5	0.3	0.15	60	3.66
6	0.3	0.05	30	5.59
7	0.45	0.05	60	2.32
8	0.45	0.1	30	4.32
9	0.45	0.15	40	2.2

2.4. Measurement of response parameter

Surface roughness is defined as the response parameter. For measuring the roughness index, average roughness value was selected. To determine the ultimate roughness value, five consecutive measurements were taken from each surface after experiments first. Then, the minimum and maximum values were eliminated and remained three values were averaged. Since the workpiece material fixed at the lathe, it is easy to take measurements after completing each test. The device was calibrated before making the measurements. For roughness measurement the perthometer device (Mahr, Germany) was used. The figure of the device can be seen in Figure 1 on the experimental setup image.

3. Results

This section concludes the evaluation of the experimental results of turning Nimax steel under the combination of the basic turning parameters. Therefore, optimization of these parameters, statistical analysis and graphical evaluation were carried out to complete a comprehensive discussion on this special steel.

3.1. Optimization of the results

Optimization is an approach to discover the group of the best design parameters for obtaining the desired range of the response parameters [16]. In the context of the machining operations, numerous input parameters can be considered as the design parameters such as tool geometry components, basic machining parameters, workpiece properties, cooling and lubricating regimes etc. and various quality criteria such as force, vibration, wear and roughness can be thought as response parameter [17]. In the concept of this paper, fundamental turning parameters are accepted as the design parameters and average surface roughness is considered as the response parameter. Taguchi based signal-to-noise ratios are the most influentive and simple method to solve the optimization problems which was addressed many times in the current literature. In this way, it is critical to determine which design methodology need to be considered for the optimization. This procedure includes only knowing about what is desired from the response. In the concept of this study, surface roughness is expected to be as much as small. Taguchi proposes three equations for the determination of the response parameters according to the expectations. In this study, the following equation (1) is used to obtain minimum surface roughness:

$$\text{Signal to Noise Ratios}_{\text{Smaller is the best}} = -10 * \log\left[\frac{1}{n} * \sum_{i=1}^{n} {y_i}^2\right] \tag{1}$$

where, “y” shows the quality indicator, i.e., surface roughness. “n” shows the number of repeating for each experimental line. “i“ illustrates the time of iteration among “n” trial number. Main effects plot for means of the graph demonstrates that high level of the cutting parameters demonstrate the lowest value is the desired value in the concept of this study. Therefore, high cutting speed (60 m/min), low feed rate (0.15 mm/rev) along with low cutting depth (0.05 mm) should be preferred for the minimization of the surface roughness according to Figure 2.

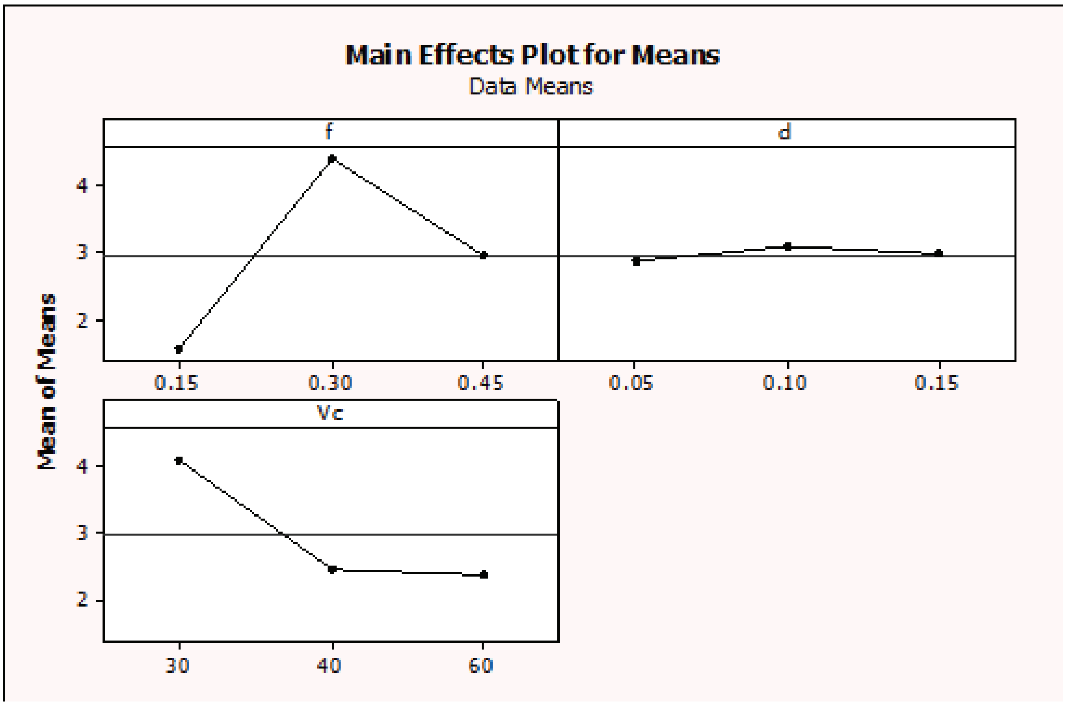

Figure 2. *Main effects plot according to means for surface roughness*

3.2. Graphical evaluation of the surface roughness

Graphical evaluations have many benefits such as obtaining the effects of intermediate values in the range of cutting parameters. Also, it is possible to observe the general trends of modelling parameters on the responses. The effects of basic turning parameters were discussed considering the average surface roughness as the machinability criteria. Surface roughness is among the valuable outcomes as it defines somehow the quality of the machined part [18-21]. Surface roughness can be represented by many parameters as determined in the current literature [22, 23]. Among other types, average surface roughness is the most addressed one due to its calculation logic [24, 25]. Average surface roughness is insensitive to instant variations which provide to achieve robust results [26]. Basically, through a long distance, average surface roughness calculates the deviation from the nominal line to determine the roughness. The equation (2) for this task can be defined by the following:

$$\mathrm{Ra} = \int_0^{T_n} \frac{|x|}{T_n}$$

where; "Ra" represents the average roughness "Tn" is the detected distance on the target surface and "x" defines the deviation from the nominal line through the surface. From the point of view of listed reasons, Figure 3 summarizes the impacts of parameters on the average roughness. First glance tells that cutting depth has no impact on the surface roughness deviation as the surface curve changes a little especially at Figure 3x. Since the cutting speed has lower impact, the influence of cutting depth is more visible on Figure 3z. However, it is highly difficult to comment on the effect which can be explained as at low cutting speed, low cutting depths create good surface roughness and vice versa. It can be easily said that higher cutting speeds always generate better roughness values which seen in Figure 2y and Figure 2z. Lastly, increasing of feed rate values up to some value make bad surface quality however roughness reduces after this point as can be seen in Figure 2x. It means it is possible to create good surface roughnesses by enhancing the feed rate which is attributed to the good machinability of Nimax.

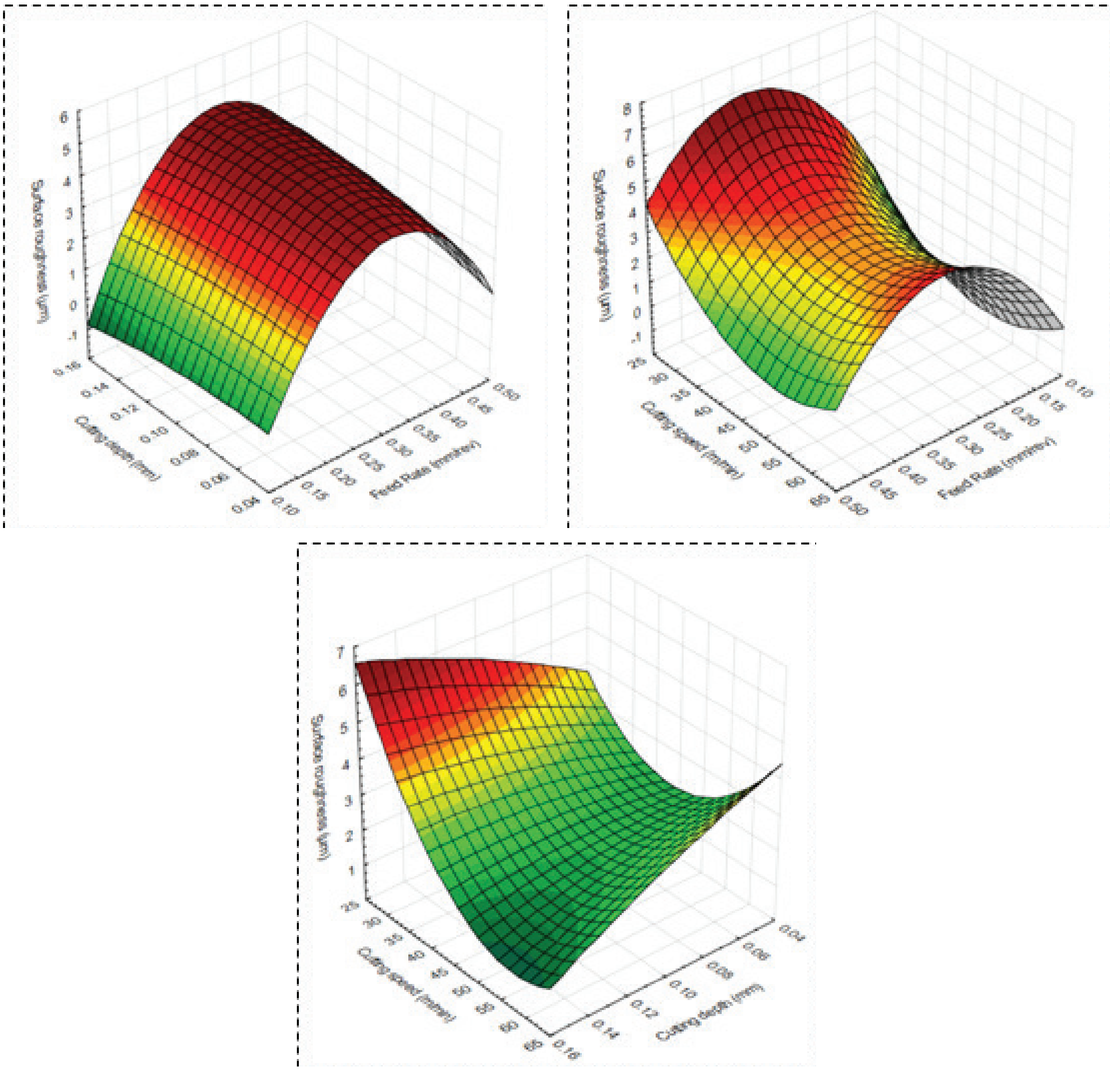

Figure 3. *The effects of cutting variables on surface roughness*

3.3. Statistical analysis of the surface roughness

ANOVA is a widely preferred method to evaluate the process parameters in terms of their effectiveness on the response parameters [27]. In any field of the research, this statistical approach is easy and comprehensive thanks to its various mathematical equations provide different point of views. Due to its complex nature and the interrelations between modelling parameters in machining, different levels of different inputs may change the relevant responses [28, 29]. This kind of information helps to the researchers and industries to understand the roots of cutting mechanism. Also, with the assistance of the statistical importance results in the experimental test period, it is possible to arrange the optimum range of basic cutting components.

Table 3 presents the several outcomes of the analysis of variance results belong to surface roughness during turning of the Nimax mould steel. This table includes three main influence indicators which are P, F and PC [30]. In the context of this study, the effects of cutting speed, feed rate and depth of cut on the surface roughness were identified. When looking at the percent contributions, it is clear that the feed rate is the dominant parameter on the surface roughness deviations. Both percent contribution value about 67.21 % and F value about 46.65 confirm this result. Compared to the effect of feed rate cutting speed has nearly half of this influence about 31.54 %. And as a remaining, cutting depth has minimal influence on the surface roughness which can be neglected.

Source	DOF	SS	F	P	Percent Contributions (%)
f	2	12.1002	46.65	0.021	67.21
d	2	0.0662	0.26	0.797	0.3
Vc	2	5.5928	21.56	0.044	31.54
Error	2	0.2594	-	-	1.4
Total	8	18.0186	-	-	100

Table 3. *Analysis results of the surface roughness*

4. Conclusion

Machining operations are special as per their place in the modern manufacturing technologies. Such processes require in depth analysis in terms of the effect of designing parameters. Most important reason for that is the machining process is applied as the final operation to produce the machine elements in the industrial practices. This study proposes an approach which can be an important example for the similar materials utilized in the metal industry as a raw material. The authors evaluated the surface roughness quality of the Nimax mould steel after making a series of turning experiments under dry machining. The following outcomes can be obtained from this comprehensive paper:

Statistical analysis demonstrated that feed is the dominant factor among three parameters with the effectiveness ratio of

67.21 %. This value is followed by the cutting speed with the contribution rate of 31.54 %. Accordingly, depth of cut has no importance on determining the roughness in turning of the Nimax steel. F value (46.65) and P value (0.021) confirms the dominance of the feed rate on the surface roughness.

The results reached with the Taguchi's signal to noise ratios indicated the optimal values of the cutting parameters for creating the minimized surface roughness. High level of cutting speed (60 m/min), low level of feed rate (0.15 mm/rev) and low level of cutting depth (0.05 mm) should be preferred for the minimization of the surface roughness in turning of the Nimax steel.

Graphical results show that depth of cut has a varied effect on the surface roughness especially at the boundary levels of feed rate and cutting speed. However, with the information of statistical results, influence of the cutting depth is neglected. Increasing feed rate increases the average surface roughness however at some point adverse effect reveals and surface roughness indicates decreasing trend. This can be accepted as Nimax has a good machinability. Seemingly, higher levels of cutting speed decrease the surface roughness.

For the future prospects, the authors highly recommend that the machinability of the Nimax steel can be tested under milling conditions. Plus, in addition to the dry environment, several cooling and lubricating regimes can be tried for better results in terms of machinability can be applied.

References

[1] C. Brecher, F. du Bois-Reymond, J. Nittinger, T. Breitbach, D. Do-Khac, M. Fey, S. Schmidt, Qualifying multi-technology machine tools for complex machining processes, CIRP Journal of Manufacturing Science and Technology, 13 (2016) 1-14.

[2] W. Zhang, X. Wang, S. Wang, H. Wu, C. Yang, Y. Hu, K. Fang, H. Jiang, Combined effects of machining-induced residual stress and external load on SCC initiation and early propagation of 316 stainless steel in high temperature high pressure water, Corrosion Science, 190 (2021) 109644.

[3] M. Sarıkaya, M.K. Gupta, I. Tomaz, D.Y. Pimenov, M. Kuntoğlu, N. Khanna, Ç.V. Yıldırım, G.M. Krolczyk, A state-of-the-art review on tool wear and surface integrity characteristics in machining of superalloys, CIRP Journal of Manufacturing Science and Technology, 35 (2021) 624-658.

[4] M.E. Korkmaz, M.K. Gupta, Z. Li, G.M. Krolczyk, M. Kuntoğlu, R. Binali, N. Yaşar, D.Y. Pimenov, Indirect monitoring of machining characteristics via advanced sensor systems: a critical review, The International Journal of Advanced Manufacturing Technology, (2022) 1-36.

[5] M. Kuntoğlu, O. Acar, M.K. Gupta, H. Sağlam, M. Sarikaya, K. Giasin, D.Y. Pimenov, Parametric optimization for cutting forces and material removal rate in the turning of AISI 5140, Machines, 9 (2021) 90.

[6] M. Sarıkaya, A. Güllü, Taguchi design and response surface methodology based analysis of machining parameters in CNC turning under MQL, Journal of Cleaner Production, 65 (2014) 604-616.

[7] A.M. Khorasani, M.R.S. Yazdi, M.S. Safizadeh, Analysis of machining parameters effects on surface roughness: a review, International

Journal of Computational Materials Science and Surface Engineering, 5 (2012) 68-84.

[8] R. Binali, M. Kuntoğlu, D.Y. Pimenov, Ü.A. Usca, M.K. Gupta, M.E. Korkmaz, Advance Monitoring of Hole Machining Operations via Intelligent Measurement Systems: A Critical Review and Future Trends, Measurement, (2022) 111757.

[9] Ş. Bayraktar, G. Uzun, Experimental study on machinability of pre-hardened Toolox 44 and Nimax mould steels, Journal of the Faculty of Engineering and Architecture of Gazi University, 36 (2021) 1939-1947.

[10] Z. Bostancı, Plastik kalıp çeliğinin (Nimax) işlenebilirliğinin incelenmesi, Fen Bilimleri Enstitüsü, Karabük Üniversitesi 2018.

[11] https://www.uddeholm.com/turkey/tr/products/uddeholm-nimax/, 2022.

[12] https://www.uddeholm.com/files/PB_Uddeholm_nimax_english.pdf, 2022.

[13] A.T. Abbas, A.E. Ragab, F. Benyahia, M.S. Soliman, Taguchi Robust Design for Optimizing Surface Roughness of Turned AISI 1045 Steel Considering the Tool Nose Radius and Coolant as Noise Factors, Advances in Materials Science and Engineering, 2018 (2018).

[14] M. Mia, P.R. Dey, M.S. Hossain, M.T. Arafat, M. Asaduzzaman, M.S. Ullah, S.T. Zobaer, Taguchi S/N based optimization of machining parameters for surface roughness, tool wear and material removal rate in hard turning under MQL cutting condition, Measurement, 122 (2018) 380-391.

[15] S. Debnath, M.M. Reddy, Q.S. Yi, Influence of cutting fluid conditions and cutting parameters on surface roughness and tool wear in turning process using Taguchi method, Measurement, 78 (2016) 111-119.

[16] G. Kant, K.S. Sangwan, Prediction and optimization of machining parameters for minimizing power consumption and surface roughness in machining, Journal of cleaner production, 83 (2014) 151-164.

[17] M. Kuntoğlu, A. Aslan, D.Y. Pimenov, Ü.A. Usca, E. Salur, M.K. Gupta, T. Mikolajczyk, K. Giasin, W. Kapłonek, S. Sharma, A review of indirect tool condition monitoring systems and decision-making methods in turning: Critical analysis and trends, Sensors, 21 (2020) 108.

[18] Ş. Karabulut, Optimization of surface roughness and cutting force during AA7039/Al2O3 metal matrix composites milling using neural networks and Taguchi method, Measurement, 66 (2015) 139-149.

[19] M. Kuntoğlu, A. Aslan, H. Sağlam, D.Y. Pimenov, K. Giasin, T. Mikolajczyk, Optimization and Analysis of Surface Roughness, Flank Wear and 5 Different Sensorial Data via Tool Condition Monitoring System in Turning of AISI 5140, Sensors, 20 (2020) 4377.

[20] R.A. Laghari, J. Li, Z. Xie, S.-q. Wang, Modeling and Optimization of Tool Wear and Surface Roughness in Turning of Al/SiCp Using Response Surface Methodology, 3D Research, 9 (2018) 46.

[21] M. Coşkun, İ. Çiftçi, H. Demir, AISI P20S Kalıp Çeliğinin İşlenebilirliğinin İncelenmesi, İmalat Teknolojileri ve Uygulamaları, 2 (2021) 1-9.

[22] E. Gadelmawla, M.M. Koura, T.M. Maksoud, I.M. Elewa, H. Soliman, Roughness parameters, Journal of materials processing Technology, 123 (2002) 133-145.

[23] H. Demir, H. Ulas, R. Binali, Investigation of the effects on surface roughness and tool wear in the toolox44 material. Technol, Appl. Sci, 13 (2018) 19-28.

[24] Y. Sahin, A.R. Motorcu, Surface roughness model for machining mild steel with coated carbide tool, Materials & design, 26 (2005) 321-326.

[25] J.P. Davim, V. Gaitonde, S. Karnik, Investigations into the effect of cutting conditions on surface roughness in turning of free machining steel by ANN models, Journal of materials processing technology, 205 (2008) 16-23.

[26] P. Benardos, G.-C. Vosniakos, Predicting surface roughness in machining: a review, International journal of machine tools and manufacture, 43 (2003) 833-844.

[27] M. Kuntoğlu, H. Sağlam, ANOVA and fuzzy rule based evaluation and estimation of flank wear, temperature and acoustic emission in turning, CIRP Journal of Manufacturing Science and Technology, 35 (2021) 589-603.

[28] M. Kuntoğlu, H. Sağlam, Investigation of signal behaviors for sensor fusion with tool condition monitoring system in turning, Measurement, 173 (2021) 108582.

[29] B. Rüstem, D. Halil, N. Süleyman, Y. Süleyman, An Investigation of Factors Affecting Machinability of Milling Toolox 44 Hot Work Tool Steel by Taguchi Method, International Conference on Engineering Technologies (ICENTE'20), 2020, pp. 317-321.

[30] I. Asiltürk, H. Akkuş, Determining the effect of cutting parameters on surface roughness in hard turning using the Taguchi method, Measurement, 44 (2011) 1697-1704.

Chloramine-T in an On-line Photo-production of Reagent Radicals for Fast and Sensitive Detection of Biological Thiols Using Highly Photoluminescent Carbon Quantum Dots

Habibollah Eskandari[1]*, **Fereshteh Khajavi**[1] and **Eslam Pourbasheer**[1]
[1]*University of Mohaghegh Ardabili, Iran*

Abstract: Cysteine (Cys), N-acetylcysteine (Acy) and glutathione (GSH) are some important biological and medical thiols. Therefore, sensitive and simple detection of the biothiols in biological and environmental samples, and supplements should be a valuable goal in bioanalytical chemistry [1]. In this research, a new simple solvothermal method was developed for synthesis of a new N-doped carbon quantum dots (N-CQDs) employing citric acid and 3, 4-diaminobenzoic acid. N-CQDs were characterized by EDX-mapping and EDX-spectroscopy, X-ray diffraction spectroscopy, high resolution transmission electron microscopy, FT-IR spectroscopy, X-ray photoelectron spectroscopy and field emission scanning electron microscopy. The photoluminescence studies showed that N-CQDs have a high quantum yield of 0.43. By employing the new N-CQDs, a novel turn off-on photoluminescence procedure with an interesting pathway was developed for simple trace detection of Cys, Acy and GSH. In a flow injection manifold, a mixture of chloramine-T, N-CQDs and the thiols (as individual) were irradiated by UV light and the photoluminescence signal was monitored as a time-trace. Under the UV-irradiation, the photoluminescence of N-CQDs was drastically decreased in presence of chloramine-T. When the biothiols were added to the mixture (due to their strong antioxidant and radical scavenging properties) a turn off-on method was born for assay of the biothiols through a competitive mechanism. The limit of detection for the biothiols was in sub-micromolar range. Also, the method showed satisfactory selectivity, repeatability and accuracy with a sample throughput of 70 h^{-1}.

Keywords: N-doped carbon quantum dots, Cysteine, N-Acetylcysteine, Glutathione, Chloramine-T, Photo-production of reagent radicals.

References:

[1] Y. Yin, B. Zhen, J. Sun, J. Ouyang, N. Na, Detection of glutathione, cysteine, and homocysteine by online derivatization-based electrospray mass spectrometry, Rapid Communications in Mass Spectrometry 36(11), 2022, e9291.

Using α-Fe2O3/Kaolin Nanocomposite as Heterogenous Fenton Catalyst for Malachite Green Decolorization

Zilan SİRP[1*], Ayse OZGUVEN[1] and **Dilara OZTURK[1]**

[1]*Van Yuzuncu Yil University, Faculty of Engineering, Department of Environmental Engineering, 65080, Van, TURKEY*

**Corresponding Author: zilansirp@yyu.edu.tr*

Abstract: In this study, the efficiency of α-Fe_2O_3/Kaolin nanocomposite on malachite green (MG) decolorization by heterogeneous fenton (HF) process was investigated. α-Fe_2O_3/Kaolin nanocomposite was synthesized via precipitation method and characterized by FTIR and SEM/EDX techniques. Operating parameters were pH (3-9), catalyst dose (0.25-1.7 g/L) and H2O2 dose (0.5-3.5 g/L). The catalytic performance of nanocomposite was evaluated via adsorption, H_2O_2 oxidation, and HF processes. According to the SEM analysis, α-Fe_2O_3 nanoparticles were well decorated on the hexagonal platelet structure of kaolin. According to the EDX analysis C, O, Al, Si, and Fe were present in the catalyst as 10.36%, 47.62%, 15.90%, 16.64%, and 8.25% by weight, respectively. After the HF process, the Fe ratio reduced to 3.63% by weight, which shows the contribution of iron to the Fenton oxidation reactions. Si-OH, Si-O-Al, Si-O-Si, and Fe-O characteristic bonds were observed via FTIR analysis. The adsorption, H_2O_2, and HF processes were efficient for the decolorization of MG with 67.1%, 70.09%, and 98.00%, respectively, which verifies the catalytic activity of nanocomposite. The optimum operating conditions were determined as pH of 3, catalyst dose of 1.2 g/L, and H_2O_2 dose of 1 g/L. Under optimum conditions, 98.00% MG decolorization was achieved by the HF process. The Kaolin provided a good surface area for doped α-Fe_2O_3 nanoparticles, and α-Fe_2O_3 contributed to HF oxidation with the Fe^{3+}/Fe^{2+} redox cycle. The satisfactory decolorization of MG is possible with α-Fe_2O_3/Kaolin nanocomposite with the HF process.

Keywords: Dye, catalytic activity, heterogenous Fenton oxidation, hematite.

Identification of optimal locations for construction of photovoltaic solar power plants in Iran using the integration of fuzzy DEMATEL and FANP

Khalil Valizadeh kamaran[1*] and **Hesan Shokati**[2]

[1,2]University of Tabriz,Department of Remote sensing and GIS, Iran

Abstract: In parallel with the development and increasing progress in many countries of the world, new technologies are advancing at an astonishing rate and therefore the need for energy is increasing day by day. Iran, as a developing country, to maintain its sustainable development, it is necessary to look for new methods of energy supply. One of these methods is the use of solar energy as one of the sources of renewable energy, which to benefit from this energy, identifying suitable areas for optimal use of solar energy is very important. Therefore, the purpose of this study is to investigate the optimal locations for the construction of photovoltaic solar power plants in Iran with a focus on solar energy. For this purpose, three main groups of climatic criteria including solar radiation, precipitation, and temperature, physical criteria including altitude and slope, economic criteria including land use, distance from roads, and distance from cities have been used. To create the solar radiation layer, the Solar Analyst function was used in the ArcGIS 10.6 software environment. In the next step, the dependence between the criteria was calculated by the fuzzy DEMATEL method and the weight of the criteria and sub-criteria using the fuzzy network analysis process method in MATLAB 2019 software, and a map of all sub-criteria was created according to their weight. Then, in the ArcGIS software environment, by combining all the layers, the final map was drawn as priorities, including highly desirable, desirable, medium, unfavorable, and very unfavorable areas, which are about 15.35% of the areas with highly desirable conditions and about 30.77% of the areas with desirable conditions for the construction and operation of photovoltaic solar power plants were identified throughout country.

A New Bis(NHC)-Pd(II) Complex Supported on Magnetic SBA-15 for The Selective Aerobic Oxidation of Benzyl Alcohols to Benzaldehydes

Somayeh Fekri[1], **Yagoub Mansoori**[1,2*] and **Abolfazl Bezaatpour**[1]

[1]*Department of Applied Chemistry, Faculty of Science, University of Mohaghegh Ardabili, Ardabil, Iran, 56199-11367. Tel: +98 45 31505205. Fax: +98 45 33514024.*

[2]*Nanoscience and Nanotechnology Research Group, University of Mohaghegh Ardabili, Ardabil, Iran, 56199-11367*

Abstract: The present study describes the synthesis, characterization, and use of a new supported magnetic Pd-NHC catalysts based on Pd(II). A composite of magnetite-silica core shells and SBA-15 was successively treated with (3-aminopropyl) triethoxysilane (APTES), cyanuric chloride (CC), imidazole, 2-bromopyridine, and trans-[Pd(Cl)2(SMe2)2] complex. The obtained supported bis(NHC)-Pd(II) complex (Scheme 1), Fe3O4@SiO2@SBA-AP-CC-bis(NHC)-Pd(II), is characterized by FT-IR, CP/MAS 13C-NMR, XRD, TGA, VSM, EDX, and BET. XPS revealed that Pd(II) are present in the prepared catalyst. The palladium content of the supported catalyst (2.83 %wt.; 0.266 mmol/g) was measured by atomic absorption spectroscopy. The catalytic potential of the supported bis(NHC)-Pd(II) complex was explored for the selective preparation of aldehydes from the corresponding benzyl alcohols. Aerobic oxidation reactions of benzyl alcohols (1.0 mmol) with electron-withdrawing and electron-donor substituents were conducted under optimal reaction conditions of solvent (n-hexane 5.0 mL), base (K2CO3 1.5 mmol), and catalyst dosage (Pd 0.27 mol%). Moderate to good yields (53%-86%). The catalyst was removed easily from reaction mixture by magnetic separation, and reused over six runs without significant loss activity, and noticeable stability. The negligible palladium leaching (0.83% in the oxidation of benzyl alcohol) revealed the heterogeneous nature of catalytic reaction and strong bond of supported ligand with palladium.

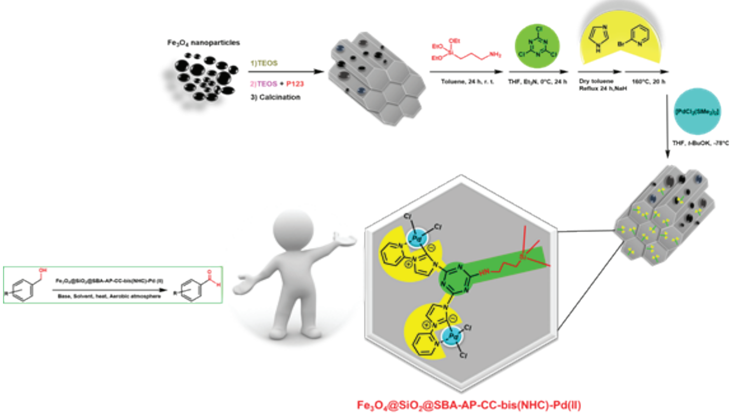

Scheme 1. Synthesis of the magnetically supported NHC-Pd(II) complex.

Smart sol-gel nanocomposite for corrosion protection of AM60B magnesium alloy

D. Seifzadeh and **R. Samadianfard**

Corrosion and Industrial Electrochemistry Research Laboratory, University of Mohaghegh Ardabili, P.O. Box 179, Ardabil, Iran

Abstract: Graphitic carbon nitride (g-C_3N_4) was synthesized by heating dicyandiamide. Next, a corrosion inhibitor compound was grafted on the synthesized g-C_3N_4. The inhibitor-grafted nanomaterial was added to the mixture of silane precursors (TEOS+GPTMS) at appropriate concentration. Afterward, the silane mixture was hydrolysed under acidic condition by stirring, and then applied on the AM60B magnesium alloy using dip-coated instrument. To identify the synthesized and inhibitor-grafted g-C3N4 nanoparticles as well as the conventional and nanocomposite sol-gel coatings, a set of methods including; UV-Vis, BET, DLS, EDS-map, FTIR, FESEM, TEM, AFM, TGA, TGA, and FTIR were used. Corrosion tests were performed by Electrochemical Impedance Spectroscopy (EIS) method in simulated acid rain water solution during 4 days of immersion. The sol-gel nanocomposite showed better corrosion resistance that the conventional sol-gel coating due to smart release of the inhibitor compound from the carbon nitride nano-carriers.

PEG-PCL-based Polymeric Micelles with Reduction Sensitivity for Cancer Drug Delivery: Design, Synthesis and Delivery Investigations

Mohammad Reza Zamanloo[1*], **Sheyda Moradi**[2] and **Zaynab Ahmadian**[2]

[1]*Department of chemistry, Faculty of science, University of mohaghegh ardabili, Iran*
[2]*School of pharmacy, Ardabil university of medical sciences, Iran*

Abstract: In recent years, stimuli-sensitive micelles derived from amphiphilic polymers have been utilized for drug releasing quickly in response to an appropriate stimulus including temperature and pH [1]. The applied copolymers are mostly based on biodegradable polymers such as PEG-PCL copolymers (PUs) [2, 3]. In this research, a biodegradable polymeric micelle with sheddable poly(ethylene glycol) shell was developed based on disulfide-linked poly(3-caprolactone)-b-poly(ethylene glycol)-b-poly(3-caprolactone) (PCL-SS-PEG -SS-PCL) triblock copolymer. The amphiphilic PCL-SS-PEG-SS-PCL polymer with controlled composition was obtained by ring opening polymerization (ROP) of caprolactone monomer with cystamine-modified PEG (2 KDa) in the presence of Sn(oct)2 catalyst, Fig 1. The self-assembled polymeric micelle from amphiphilic triblock copolymer showed sufficient stability in aqueous environment. So, the encapsulation and releasing ability of PCL-SS-PEG-SS-PCL are investigating for DOX as the sample cancer drug inside the cells based on the reduction-responsive, shell-sheddable and biocompatible behavior of its micelle form. The PEG hydrophilic segment equipped with disulfide linkage expect to gain reduction sensitivity to the micelles resulting to cargo releasing in response to glutathione (GSH).

Keywords: Amphiphilic polymer, Polymer micelle, Drug release, Caprolactone.

References:

1. H. Xia, Y. Liang, K. Chen, C. Guo, M. Wang, J. Cao, S. Han, Q. Ma, Y. Sun, B. He, Colloids and Surfaces B: Biointerfaces (2021), 203-111733.
2. C. Yu, X. Tan, Z. Xu, G. Zhu, W. Teng, Q. Zhao, Z. Liang, Z. Wu, D. Xiong. Reactive and Functional Polymers (2020), 148- 104507.
3. Z. Yang, Q. Guo, Y. Cai, X. Zhu, C. Zhu, Y. Li, B. Li. Journal of Orthopaedic Translation (2020), 57-65.

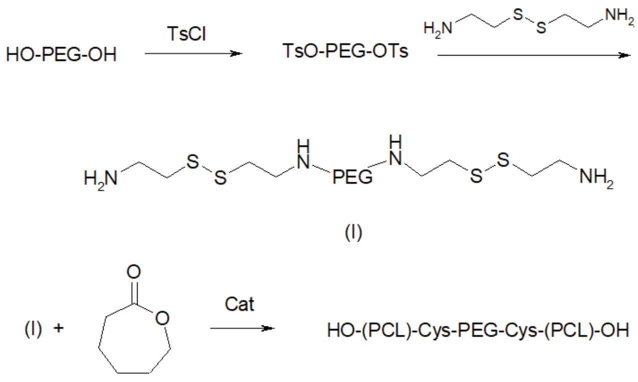

Fig. 1. Synthetic pathway of PCL-SS-PEG-SS-PCL.

Fabrication of Some Novel Visible-Light-Triggered Photocatalysts Based on Colored Titanium Dioxide: Impressive Performances for Degradations of Wastewater Contaminants

Aziz Habibi-Yangjeh*, Nasrin Sedaghati, Arezou Saadati, Zahra Salmanzadeh-Jamadi

Department of Applied Chemistry, Faculty of Science, University of Mohaghegh Ardabili, Ardabil, Iran

With fast increase of the human population and widespread industrialization, a large amounts of harmful compounds are released to the aquatic systems. Amongst various developed strategies to address the resultant environmental pollution, semiconductor-mediated photocatalysis is an effective and promising strategy thanks to its operation at ambient temperatures and pressures under solar energy. Titanium dioxide (TiO_2) is widespread utilized semiconductor in the field of heterogeneous photocatalysis, owing to its fascinating characteristics. Nonetheless, large-scale applications of this semiconductor has bottlenecks of fast recombination of photo-induced charges, poor absorption of visible light, and small specific surface area. Therefore, researchers are attempting to address these shortcomings through oxygen vacancy generation in the structure of TiO2, doping various elements, heterojunction construction with small energy gap semiconductors, and so on.

In these regards, we designed some novel visible-light-triggered photocatalysts based on colored TiO_2 (denoted TiO_{2-x}) through developing heterojunctions with other materials. It was noticed that after anchoring BiOBr and AgBr over TiO_{2-x} to fabricate ternary TiO_{2-x} / BiOBr / AgBr photocatalysts, integration of BiOI and $Ag_6Si_2O_7$ with TiO_{2-x} to synthesis TiO_{2-x} / BiOI / $Ag_6Si_2O_7$ photocatalysts, combination of $Bi_4O_5Br_2$ and TiO_{2-x} to prepare TiO_{2-x} / $Bi_4O_5Br_2$ photocatalysts, deposition of BiOI and Ag_3PO_4 over TiO_{2-x} to synthesize TiO_{2-x} / BiOI / Ag_3PO_4 photocatalysts, the photocatalytic activity of the nanocomposites with the optimum composition was promoted 44.5, 194, 23.2 and 44.3-folds as well as the activity of TiO2 in degradation of RhB under visible-light illumination. Consequently, it was concluded that the fabricated photocatalysts based on TiO_{2-x} could be encouraging materials for utilization in tackling of the environmental pollution and energy shortage.

New Ni(II) complex for the Anticancer application on A549 lung cancer cells: Syntheses, Crystal structures, Theoretical studies

Ghodrat Mahmoudi[1,2*]

[1]Department of Chemistry, Faculty of Science, University of Maragheh, P.O Box 55181-83111, Maragheh, Iran
[2]Advanced Materials for Indistry and Biomedicine Laboratory, Kurgan State University, Sovetskaya Str. 63/4, 640020 Kurgan, Russian Federation
***E-mail:** ghodratmahmoudi@gmail.com*

Abstract: In present work, new Schiff-base ligand, N-2-(6-methylpyridyl)-2-hydroxy-1-naphthaldimine (1) and its Ni(II) complex, bis[N-2-(6-methylpyridyl)-2-oxo-1-naphthaldimnato-k3N^N^O] nickel(II) (2) have been reported and characterized by spectral techniques (IR, 1H NMR, Mass). Solid state structures and non-covalent interactions have great effect on the stability of the final structures. X-ray diffraction study shows zwitter ionic keto-amine tautomer form of planar Schiff base 1 that exists as dimer formed by C13−H13A•••O1i [(i) -x+1, -y, -z+1] hydrogen bonds and distorted octahedral geometry around Ni+2 center in chelate 2 where overall crystal structure stability may be credited to weak C−H•••π, π•••π stacking, van der Waals interactions, and C−H•••O type intermolecular hydrogen bonds. The anticancer activity has been investigated using cytotoxicity measure (MTT assay), apoptosis assay, quantitative polymerase chain reaction (qPCR), and colony formation assays. The Ni(II) metal complex demonstrates dose-dependent cytotoxicity in vitro, killing A549 lung cancer cells via an apoptotic pathway. MTT assay results direct to the fact that at higher concentration, 2 showed toxic effect in Beas-2B cells, while 1 showed almost similar cytotoxic effect (IC50=85.72 μM) as compared to A549 cells. On the A549 lung cancer cell line, the novel Ni(II) complex 2 has a good cytotoxic effect and causes apoptotic cell death. Colony forming assay study reveals that both 1 and 2 affect the proliferation and growth rate of cells at different doses, in fact, 2 inhibited colonization in HUH7 and HCT116 cells more than 1.

Keywords: Schiff base, hydrogen bond, supramolecular architecture, non-covalent interactions, DFT, anticancer.

Using the Magnetic Iron Nanoparticles for Extraction and Determination of Dasatinib- Monohydrate in Real Samples

Eslam Pourbasheer[1*] and **Elahe Javid Germi**[2]

[1]*University of Mohaghegh Ardabili, Iran*
[2]*Payame Noor University, Iran*

Abstract: In this study, the iron oxide magnetic nanoparticles were synthesized by co-precipitation method, then the efficiency of nanoparticles, modified with sodium dodecyl sulfate surfactant (SDS) as an adsorbent for extracting of dasatinib-monohydrate from real samples. The FTIR, and SEM instrumental analyzes are used to confirm and study the structure and morphology of the synthesized nanoparticles. Parameters affecting drug extraction efficiency such as pH, SDS amount, extraction time, detergent type, detergent volume and desorption time were investigated and optimized. Then the drug was quantified using spectrophotometric technique. Under optimal conditions, the calibration curve was linear in the range of 1-12 ppm and the correlation coefficient was 0.99. Based on the obtained results, the proposed method was used to measure the drug in real samples, which yielded satisfactory results.

Ionic Cr(VI) Reduction in Cement and Investigation of its Effects on Cement Properties

Emre AKKEÇİ[1] and **Vahap YÖNTEN**[2]

[1]Fen Bilimleri Enstitüsü, Kimya Mühendisliği A.B.D, Van Yüzüncü Yıl Üniversitesi, Türkiye

Öz: Bu çalışmada, demir sülfat monohidrat (FeSO4.H2O), demir sülfat tetrahidrat (FeSO4.4H2O), demir sülfat heptahidrat (FeSO4.7H2O) gibi indirgen kimyasallar kullanılarak bu kimyasalların çimentodaki Cr(VI)'yı indirgeme etkinlikleri belirlenmiştir. Çimento suyla temas ettiğinde içeriğindeki Cr(VI) suda çözünmekte ve deriye teması sonucunda kontakt dermatite neden olabilmektedir. Çimentodaki Cr(VI) varlığı nedeniyle oluşabilecek sağlık sorunlarını kontrol altına alabilmek ve azaltmak için yasal tedbirler alınmaktadır. Avrupa Parlementosunca hazırlanan 2003/53/EC direktifinde, hidratasyon sonrası çimentoda Cr(VI) içeriği üst limiti 2 ppm olarak belirlenmiş ve bu değerin üzerinde Cr(VI) içeren çimentonun AB satışı 17 Ocak 2005 tarihinden itibaren yasaklanmıştır. Ülkemizde ise elleçleme esas torbalı çimentolarda Kimyasalların Kaydı, Değerlendirilmesi, İzni ve Kısıtlaması yönetmeliği Ek 17, 47. maddesinde çimentoda bulunan çözülebilir kromun 2 ppm'den küçük olması gerektiği belirtilmektedir. Çimentodaki Cr(VI) miktarını yasal sınır olan 2 ppm değeri altına indirgemek için kimyasal indirgen olarak $FeSO_4.H_2O$, $FeSO_4.4H_2O$ ve $FeSO_4.7H_2O$, çimento olarak da 40.26 ppm krom içeriği olan CEM I 42.5 R portland tip çimento kullanılmıştır. İndirgeme sonrasında çimentonun fiziksel ve kimyasal özelliklerine yönelik değişiklikler incelenmiştir. Yapılan çalışmada sonuç olarak kullanılan indirgenlerin hepsinin çimentoda Cr(VI)'yı indirgeme etkinliğinin olduğu görülmüştür ancak kütlece % 0.2 kullanıldığında Cr(VI) miktarının 0.34 ppm değerlerine kadar düşmesi, diğer kimyasallara göre indirgemek için daha az miktarda kullanılması ve çimento özellikleri üzerindeki değişikliklerin makul seviyelerde görülmesi nedeniyle demir sülfat heptahidrat'ın daha etkili indirgen olduğu belirlenmiştir. Bulduğumuz sonucun hem çimento fabrikalarında ki pratik uygulamalarda hem de literatüre kazandırılması konusunda yararlı olacağı kanaatindeyiz.

Anahtar Kelimeler: Çimento, Dermatit, İndirgeme, Krom (VI).

Superhydrophobic Fe/Carbon Composite Coated on Sponge: Preparation, Characterization and Oil-Absorption Properties

Bagher Eftekhari-Sis[1]*, **Maryam Zirak**[2] and **Hossein Rezazad**[1]

[1]*Department of Chemistry, University of Maragheh, Iran*
[2]*Payame Noor University, Iran.*
eftekhari.sis@gmail.com

Abstract: Oil pollution, created during extraction, transportation and storage of oil, is one of the most important biological attacks, which affects the life of marine species and sea grasses. So, in order to prevent the diffusion of oil pollution into a larger area, development of new and cheap aproaches for the fast removal of oil pollution is of interest. Various methods, such as in situ burning, mechanical collection, chemical dispersants, bioremediation and absorption, were reported for oil spill cleanup. In this study, an Fe-carbon (Fe/C) composite coated on polyurethane sponge was developed as a superhydrophobic absorbent for water-oil cleanup. Prepared Fe/C composite is a low cost and easily obtained by hydrothermal carbonization of egg yolk biomass in the presence of different iron precursors. The Fe/C-sponge has been developed by a simple dip-coating method. The prepared Fe/C-sponge exhibited an absorption capacity of 28-87 times its own weight for different organic solvents and oils. It can be also recycled and reused for 6 runs without decreasing in absorption capacity. The results revealed that the Fe/C-sponge is a promising selective material for use in environmental remediation to remove oils from water. So, this strategy is an efficient method to developed inexpensive and recyclable absorbent for oil-water cleanup. Schematic representation of the synthesis of Fe/C composite, and application of Fe/C-sponge in the oil cleanup (for example toluene (a) and DCM (b)) is shown in figure.

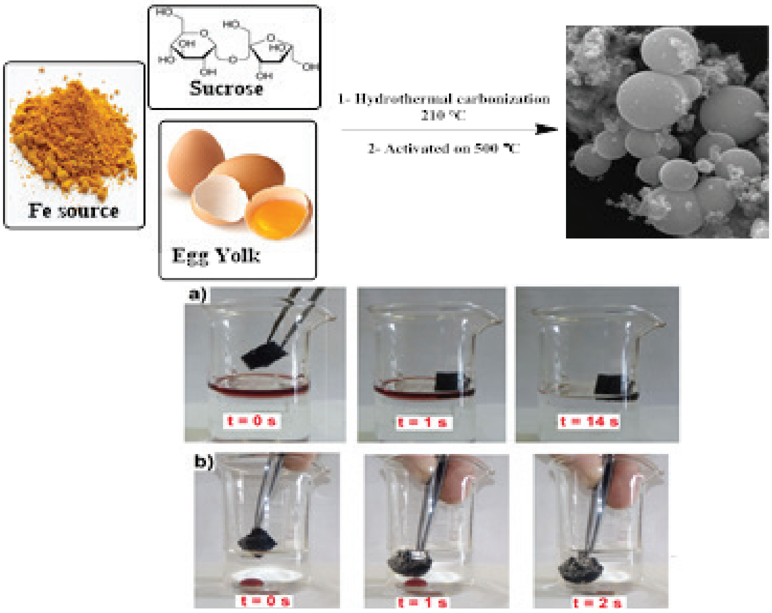

Synthesis and Phase Selective Gelation Properties of N-(4-Hydroxyphenyl) Oleylamide; A Simple Removal of Oil Spills From Top of Water

Maryam Zirak[1*] and **Bagher Eftekhari-Sis**[2]

[1]Payame Noor University, Iran
[2]Department of Chemistry, University of Maragheh, Iran.
m.zirak@pnu.ac.ir

Abstract: An oleylamide based gelator was developed for the removal of oil spills from top of water via formation of organogel by self-assembly. The gelator was synthesized in two steps, by activation of oleic acid with thionyl chloride, followed by amidation with 4-hydroxyaniline. The gelator was able to form organogels in the presence of organic solvent and the xerogel formed by evaporating the solvent from organogel was able to adsorb oil spills on top of the water and remove the pollution. However, most phase selective gelators require a heat–cool cycle or addition of a co-solvent, which is not applicable to oil recovery from open water sources, or could lead to further addition of relatively large volumes of undesirable or toxic solvents into the environment. Reported oleylamide based gelator formed organogels in different organic solvents, such as pentane, hexane, heptane, decane and CCl_4, by self-assembly. Xerogels, obtained by evaporation of organic solvents of organogels under reduced pressure, showed excellent phase-selective gelation properties of organic solvents on top of water at room temperature, by simple mixing, in which neither heating nor addition of a co-solvent was required. The effect of different parameters, including gelator concentration, temperature, salinity and pH on the removing of oil spills were investigated, which revealed that each molecule of gelator captured eight molecules of hexane, as 0.1 g of gelator can gelate 3 mL of hexane. Adsorbing the spill of hexane on top of the water under stationary (a) and shaking (b) conditions is shown below.

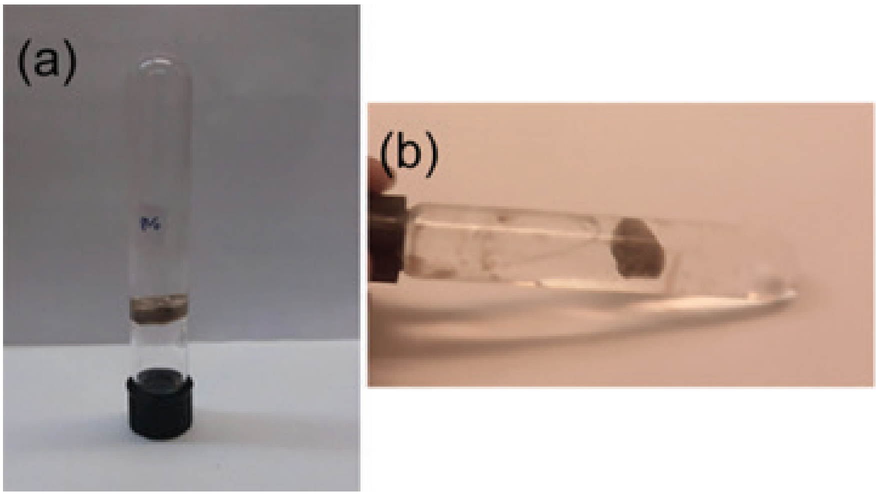

Encapsulation of Polyethylene Glycol (PEG) into Pores of Alumina-Silica Particles as Solid–Liquid Phase Change Material (PCM)

Tuğba Gürmen

Ege University, Faculty of Engineering, Chemical Engineering Department 35100 Bornova-Izmir, Turkey
tugba.gurmen@ege.edu.tr

Abstract: Thermal energy storage is very attractive topic in terms of improvement of energy efficiency. Phase change materials (PCM) are one of the most used materials in thermal energy storage and temperature control of many engineering applications. Encapsulation of PCM is an influential way of preventing possible interaction with the surroundings and leakage during the melting processes and also enhancing thermal conductivity. In this work, the polyethylene glycol/alumina-silica particle composites as shape-stable, solid–liquid PCM was prepared. The polyethylene glycol acts as the latent heat storage material and alumina- silica particles used as the support material, which provides structural strength, high thermal conductivity and prevents the leakage of the melted polyethylene glycol. PEG is enclosed into the alumina-silica particle pores and during the phase change process the leakage of the PEG is prevented. The characterization of the composite PCMs was performed by SEM and DSC analysis. The melting point and heat of fusion were determined as 26.14 oC and 55.17 J/g. The encapsulation ratio was calculated as 49.6%. SEM images showed that the PEG dispersed uniformly into the pores and on the alumina-silica particles surface. There was no leakage and degradation at the composite PCMs after heating and cooling cycles. According to the results, prepared composites showed good thermal energy storage properties, reliability and stability. All results suggested that the presented form-stable composite PCMs has great potential for thermal energy storage applications.

A New Zinc-Based Metal-Organic Framework for Catalytic Synthesis of N-Substituted Pyrroles

Phuong T. K. Nguyen[1,2*] and

Y B. N. Tran[1,2]

[1]*Future Materials & Devices Laboratory Institute of Fundamental and Applied Sciences, Duy Tan University, Ho Chi Minh City 700000, Vietnam;* [2]*Faculty of Natural Sciences,Duy Tan University, Da Nang, 550000, Vietnam*

Abstract: In our work, we synthesized and characterized a new zinc-based metal-organic framework (MOF) $Zn_2(OAB)$ [OAB4-= 4,4′-(oxalylbis(azanediyl))bis(2-oxidobenzoate)],analogous to a well-studied MOF-74 structure, endowed with accessible mesopore channels (24 Å) and high porosity (SBET = 3115 m^2 g^{-1}). Because of the structural features of high density of both Lewis acidic Zn sites and -NH- groups derived from the organic OAB^{4-} unit, $Zn_2(OAB)$ has been demonstrated as a promising candidate for catalysis Paal-Knorr N-substituted pyrroles synthesis. As such, $Zn_2(OAB)$ exhibited excellent catalytic activity in the synthesis of 2,5-dimethyl-1-phenyl-1H-pyrrole (yield of 96%) at 70 °C for 16 min and was able to be reuse up to eight times without noteworthy loss of its activity. Notably, the catalytic activity of $Zn_2(OAB)$ outperformed that of homogeneous, heterogeneous catalysts, and representative Zn-based MOFs (e.g., ZIF-8, MOF-5, Zn-MOF-74).

ZIF-8 Decorated Bimetallic FeMo Nanoparticles: H2 Generation from the Catalytic Hydrolysis of Ammonia-Borane

Can Yılmaz[1], **Hüseyin Ali Yıldırım**[1], **Tuba Top**[2], **Mehmet Zahmakiran**[3] and **Mehmet Yurderi**[1,4*]

[1]Department of Electronics and Automation, Bartın Vocational School, Bartın University, Türkiye;
[2]Department of Mechanical Engineering, Faculty of Engineering, Architecture and Design, Bartın University, Türkiye
[3]Department of Biotechnology, Faculty of Science, Bartın University, Türkiye
[4]Central Research Laboratory, Research & Application Center, Bartın University, Türkiye

Abstract: The development of highly efficient and low-cost catalysts for the hydrolysis of ammonia borane (NH_3BH_3; abbreviation AB) is of great importance for their real applications in hydrogen (H_2) based fuel cells. Here, bimetallic FeMo nanoparticles (NPs) decorated with zeolitic imidazolate framework (ZIF-8) were prepared by a facile impregnation-reduction approach under mild conditions and characterized by advanced analytical techniques. The Fe/Mo ratio in the bimetallic FexMoy/ZIF-8 catalyst was optimized to determine the best catalytic activity in AB hydrolysis. The experimental results showed that $Fe1Mo_2$/ZIF-8 as the catalyst composition had excellent catalytic performance in AB hydrolysis, and the turnover frequency (TOF) was calculated as 775.4 $mol_{H2}.mol_{cat}^{-1}$ min^{-1}, and the activation energy (Ea) as 75.05 kJ mol^{-1}.

Evaluation of world countries and renewable energy sources in terms of electricity generation with cluster analysis

Medine Nur Türkoğlu Elitaş[1*] and
Muharrem Düğenci[2]
Bilecik Şeyh Edebali University, Turkey
Karabük University, Turkey

Abstract: Renewable energy has become an indispensable part of the energy sector for various reasons, especially energy supply security and reduction of greenhouse gas emissions. The most common type of secondary energy used in the world is electrical energy. Thermal power plants, hydraulic power plants, wind power plants and geothermal power plants are used for electricity generation in Turkey. In recent years, the structural arrangements made to encourage the use of renewable energy sources instead of imported sources in electricity generation have continued to show their results. The share of renewable energy sources, which was 30.67% in 2018, increased to 42.10% in 2019. In the study, electricity generation of 45 world countries, including Turkey, between the years 2000-2019 was classified by cluster analysis. As a result of the analysis, the countries were divided into 3 groups. While Canada, Germany, Japan and Korea took place in the second cluster, the USA took place in the third cluster. Turkey, on the other hand, took place in the first group with other countries. It has been observed that the countries in the first and second clusters in electricity production have a larger share compared to other developing countries. In addition, K-Means clustering analysis was carried out in order to see which sources are included in which classifications in the generation made between 2000 and 2019 when the electricity generation from renewable energy sources in the world is classified according to sources. Here the resources are divided into two clusters. Electricity generation from hydraulic energy is included in the first cluster, while all other resources are included in the second cluster.

Keywords: Renewable energy, cluster analysis, electricity generation.

Investigation of analysis of mifepristone Ru-486 molecule using Quantum chemical method

Hanifi KEBİROGLU[1*] and **Sultan ERKAN**[2], **Niyazi BULUT**[1]

[1]*Department of Physics, Faculty of Science, Firat University, 23119 Elazig, Turkey*
[2]*Department of Chemistry, Faculty of Science, Sivas Cumhuriyet University, Sivas 58140, Turkey*

Abstract: The molecule's active sites were identified during the spectroscopic study, and theoretical molecular insertion studies have been used to examine its impacts on breast and ovarian cancer. By using FTIR, UV-VIS spectroscopy, Fukui functions, Molecular Docking, and DOS, the biological evaluation molecule mifepristone (RU-486) was thoroughly examined for its detailed molecular and atomic level characteristics (Destiny of States). We looked at how the structure of an RU-486 molecule affected the absorption peaks of various other compounds, including CH_2CH_3, CH_3, F, FH, KOH, and NO_2. This investigation was carried out via a DFT approach paired with GaussView5 and Gaussian09 for all computations.

New trends in energy storage for implantable medical devices

Filipe Amaral[1,2*] and **Sílvia Soreto**[2]

[1]Polytechnic Institute of Coimbra, Coimbra Health School, Portugal (filipe.amaral@estescoimbra.pt)
[2]i3N and Physics Department, University of Aveiro, Portugal

Abstract: Implantable medical devices (IMDs), used in diagnosis, prognosis and treatment, had a great development in the last decade. These devices can be pointed to help in the monitorization and correction of the physiological mechanisms in a vast sort of organs, like in neural stimulation or cardiac pacing. Now that our populations are achieving a longer average life expectancy, accompanied by all the related chronical diseases, IMDs are becoming even more relevant. In parallel with the demanding of extended operational periods, these IMDs require a higher energy consumption to satisfy new functions and continuous communication of internet of things context, which puts a higher pressure for longer life batteries and higher power energy sources.

Current commercial systems that power implantable electronic devices still use primary batteries (non-rechargeable). Recent research focused on this conventional technology applies nanoengineering techniques to improve energy and power density of cathode technology in non-rechargeable batteries. Meanwhile, new strategies on the harvesting and energy conversion systems, as an alternative to non-rechargeable power sources, use thermoelectric and piezoelectric devices to permanently charge secondary batteries (rechargeable) and supercapacitors. In this work a literature review was completed aiming to explore recent advances in new energy sources for implantable medical devices.

New harvesting technologies, that convert energy from the human body or surroundings into electricity, in parallel with recent developments in rechargeable batteries and supercapacitors, will change the way we manage the energy sources of implantable medical devices.

Optical Properties of Tin Oxide Thin Films

Reşit Özmenteş

Institute of Science, Van Yuzuncu Yil University, Van, Turkey

Abstract: In this study, tin oxide thin film were prepared by spraying technique on glass substrates at 400 oC using tin(IV) chloride aqueous solution. The samples were characterized by UV-Vis spectroscopy and X-ray Diffraction (XRD) techniques at room temperature. The UV-Vis spectrum measurement showed that the films are highly transparent (80%) in the visible light region, the band gap energy was 3.88 eV and this value higher than the pure samples band gap energy of SnO2 (3.6 eV at 300 K). The X-ray diffraction (XRD) analysis of the thin films showed their crystalline nature is amorphous..

High-Entropy Alloys Composite Based on CoCrFeNi System

Kratochvíl P.[1*]and **Průša F.**[1]

[1]*Department of Metals and Corrosion Engineering, University of Chemistry and Technology in Prague,Czech Republic*

Abstract: This study aimed to approach the preparation of high entropy alloys composite in a completely novel manner. A specific combination of mechanical alloying and spark plasma sintering were used to prepare the CoCrFeNiMnTi composite. The material was characterized in terms of chemical and phase composition with X-ray fluorescence spectroscopy and X-ray diffraction spectrometry. Light microscopy and scanning electron microscopy equipped with an energy dispersion spectrometer were used to study the microstructure of prepared materials. The mechanical properties were determined using Vickers hardness testing, compressive stress-strain testing and wear resistance. On top of that, the oxidation resistance of the composite was examined. The composite had a fine-grained microstructure constituted of two FCC solid solutions and the HCP Laves phase. Regarding mechanical properties, the composite reached CYS of 1593 MPa and UCS of 2603 MPa, a superior value compared to the starting ones. This indicates that the chosen path of preparation led to the synergy of mechanical properties maintaining its ductility and being significantly strengthened at the same time.

This research was financially supported by Czech Science Foundation (grant No. 21-11313S).

Mechanical and Tribological Properties of the CoCrFeNiAlX (X=10, 20, 30 at.%) High-Entropy Alloys Prepared by Powder Metallurgy

Angelina Strakosova[1]*, Jan Riedl[1] and **Filip Průša[1]**

[1]*Department of Metals and Corrosion Engineering, University of Chemistry and Technology Prague, Prague, Czech Republic*

Abstract: The study aimed to find out the relationship between the microstructure and mechanical properties as well as the tribological performance of the CoCrFeNiAlx high-entropy alloys. The studied alloys with different Al content (10, 20, 30 at.%) were prepared by two steps powder metallurgy method. The first one was the short-term mechanical alloying (MA) using a planetary ball-milling at 400 rpm for a total of 8 h. The next step was spark plasma sintering (SPS) compaction. In terms of describing the microstructure and phase composition, the scanning electron microscope (SEM) and X-Ray diffraction analysis were used. It was found that with the increasing content of Al, the microstructure becomes finer and materials porosity reduces. The XRD analysis revealed, that the amount of both the solid solutions with BCC and FCC crystallographic lattice changed favouring the existence of a phase with PC lattice. The Vickers hardness, compression tests and tribological tests were made to find out the conjunction between mechanical properties and microstructure of the studied materials. The CoCrFeNiAl10 alloy showed the worst properties. The highest values of HV30, UCS and lowest value of the wear rate and also low ductility were achieved in the CoCrFeNiAl30 alloy. The CoCrFeNiAl20 alloy showed comparable structure and properties with the CoCrFeNiAl30 alloy, but it showed increased ductility. Therefore, the CoCrFeNiAl20 alloy was selected as the best in terms of combining the microstructure with mechanical properties.

The authors wish to thank the Czech Science Foundation for its financial support of this research (project No. 21-11313S).

Synthesis of composite cryosorbents based on polymethacrylic acids-bentonite clay and study of their physico-chemical properties

Baimyrza Perizat*, **Askar Kalen**, **Iminova Rizvangul** and **Kairalapova Gulfairuz**

Al-Farabi Kazakh National University, Faculty of Chemistry and Chemical Technology, department of chemistry and technology of organic matters, natural compounds and polymers, Almaty, Kazakhstan

Abstract: The novelty of the work is to establish the regularities of complexation of organic and inorganic polymers with the formation of chemically crosslinked, stable hybrid sorbents with improved physico-chemical and sorption characteristics with the possibility of their use as sorbents for wastewater treatment from heavy metal ions and surfactants. In this research work, highly cross-linked cryogels based on polymethacrylicacids(PMAA)andcomposite cryogels based on polymethacrylic acids and bentonite clay (PMAA-BC) have been synthesized. Composite cryogels synthesized by radical polymerization in 24 hours at a temperature of 25 °C. According to the physical and chemical studies of PMAA-BC composite cryogels, the density was about 1.5531 g/cm3 and yield was 95%. This shows the economic efficiency of cryogel. The morphological structure of a composite cryogel was studied with an optical microscope, an atomic-force microscope and a scanning electron microscope. Physico-chemical studies have shown that the composition components form a complex that is stabilized due to hydrogen bonds and hydrophobic interactions of the polymer.

The sorption of metal ions, namely Cu2+, Pb2+ ions and surfactants, the cationic cetylpyridinium bromide (CPB) by a cryosorbent was considered.

According to the result, PMAA-BC cryogels had higher sorption values(90%) compared to cryogels based on pure PMAA. Since this BC shows good sorption properties, as its amount increases, the sorption value also increases.

The resulting cryogels are recommended for future use as sorbents in wastewater treatment from heavy metal ions and surfactants.

The using of Bentonite/ Amberlite XAD-7 composite material for the adsorption of Methylen Blue and characterization of adsorbent

Hilal BARAK[1] and **Vahap YÖNTEN**[1]*

[1]Van Yüzüncü Yıl Üniversity/ The Faculty of Engineering, Deparment of Enviromental Engineeering,

Abstract: The human population and the developing of technology are damaging and polluting our natural resources. Protecting our resources has recently become a necessity. Especially the removal and disposal of some toxic, harmful and carcinogenic wastes in drinking water has been an issue that should be emphasized by scientists. Some important techniques and processes are used in this field. In our study, the adsorption process, which is a very preferred method although it is cheap, easy and economical, was used. Methylene Blue (MB), a cationic dyestuff, was selected as the pollutant to be adsorbed and synthetic solutions were prepared. Both calibration and experimental data were calculated quantitatively by measuring the dyestuff at different concentrations in a UV Spectrophotometer. Again in our study, Bentonite/Amberlite XAD-7 composite material was formed by mixing cheap and easily available bentonite as adsorbent material and Amberlite XAD-7, which is a polymeric resin, under certain ambient conditions. Characterization of this material was done with Scanning Electron Microscope (SEM) and Fouirer Transform Infrared Spectrophotometer (FTIR) devices. As a result of the characterization, the structural form of the material was clarified, especially when the structure before and after adsorption was considered, the percentages of the elements and compounds in the dyestuff attached to the material by immobilization changed. These incremental changes proved that the adhesion event was positive. The result show that the composite material' a adsorption capacity was calculate as 14 mgg-1. Langmuir , Freudlich and Temkin isotherms were used to describe the adsorption equilibriums. Temkin models yields a somewhat better than Freudlich and Langmuir models on adsorption of dye on composite material as reflected with correlation coefficients (R2). The data and data obtained as a result of our study have been brought to the literature and practice.

1. Introduction

In connection with the increasing human population, technology and industry, the use of dyes has increased day by day. These materials are used in the textile, paper, plastic, food and cosmetic industries, etc. used. The using of dyes was increased linked with increasing of humans' populations, technology and industry. These materials were used in textile, papers, plastic, food and cosmetic industries etc. Therefore removal of dyes from wastewater is very important. All of them can be toxic, cancer genic, mutagenic and teratogenic (McKay et al. 1985; Gregory et al. 1981). Among these areas, the textile industry in particular is a large one and is considered the largest creator of liquid waste in the form of pollutants. According to the reported study, approximately one thousand tons of textile dye is discharged annually in the form of industrial waste. The wastewater discharged from these industries often contains different types of non-reactive dyes (Kamboh et al., 2011). Some wastewater, especially textile wastewater, has caused some problems in terms of environment and health. Therefore, it is very important to remove dyes from wastewater. All of them can be toxic, carcinogenic, mutagenic and teratogenic (Yonten et al., 2015). Where most countries specify the maximum allowable concentration for some dyes less than 1 ppm in wastewater (Crini, 2006). Dyes are colored substances that color a substrate because they are retained in it by adsorption. Unlike pigments, they dissolve completely or partially in an environment in which they are applied. Dyes must have a specific affinity for the substrate on which they are used. Some dyes are either toxic or carcinogenic. Synthetic dyes have complex aromatic structures that provide them with physicochemical, thermal, biological and optical stability (Seshadri, 1994) and are used as an indicator and biological stain on photographic paper.

Commercial uses of dyes include coloring textile paper, leather, wood, inks, fuels, foodstuffs and metals. This dye can cause respiratory tract, gastrointestinal tract problems, skin irritation and redness of the eyes. Ecoquatic may cause adverse effects on the system (Peng et al., 2009 ; Gessner and Mayer, 2002). Therefore, it is undoubtedly important to treat paint wastewater before it is discharged into a water body (Gore et al., 2014). Among the processes, adsorption was found to be superior to other techniques for water reuse in terms of initial cost, flexibility and simplicity of design, ease of use, and insensitivity to toxicants. It does not cause the formation of harmful substances in the adsorption process (Crini, 2008). Activated carbon, peat, chitin, silica, fly ash, clay and others have been used as sorbent, but the dye absorption capacity of these sorbents is not effective.

Therefore, new sorbents are still being investigated to improve dye absorption performance (Kamboh et al., 2011). Amberlite XAD resins have received much attention as basic matrices for designing new chelating resins. These resins have enormous advantages over others; For example, the structure of these resins provides excellent chemical, physical and thermal stability under various experimental conditions (Li et al., 2001). These advantages include a high degree of selectivity by controlling pH, versatility, durability and enhanced hydrophilicity. Biomass immobilized in a suitable matrix aims to overcome these problems by providing ideal size, mechanical strength, rigidity and porous properties to the biological material (Özdemir et al., 2013).

2. Material and Methods

2.1. Dye and composite material

Bentonite was taken from Mineral Exploration from Van and chemical form of bentonite was given in Table 1. It was chosen as the raw soil material immobilized to the resins to produce composite material.

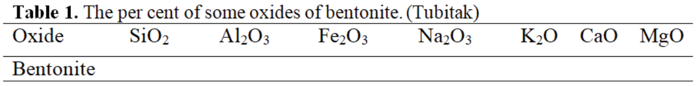

Table 1. The per cent of some oxides of bentonite. (Tubitak)

Oxide	SiO_2	Al_2O_3	Fe_2O_3	Na_2O_3	K_2O	CaO	MgO
Bentonite							

Table 1. The per cent of some oxides of bentonite. (Tubitak)

The resin, Amberlite XAD-7 was purchased from Merck (Germany) and they were taken as ion exchange materials. MB was chosen as the pollutant dye and provided from Acros (USA). The chemical formula of MB is given in Figure 1. The pH adjustments of synthetic dye solutions used in the experiments were made using 1 M NaOH and 0.1 M H2SO4. The pH device was purchased from Isolab Company (Turkey). These chemicals are analytically pure and purchased from Merc (Germany) is provided.

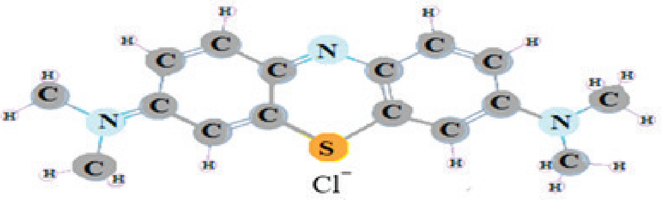

Figure 1. The chemical form and image of MB.

2.2. Preparation of composite material and batch experiment

Bentonite/Amberlite XAD-7 composite material will be used as adorbent and MB dyestuff in aqueous solutions will be removed.To prepare the composite material, 2 g of bentonite will be mixed with 2 g of Amberlite XAD-7. The mixture was soaked three times with 4 mL of ultrapure water to increase the immobilization efficiency and will be thoroughly mixed.The mixture will be heated in an oven at 60°C for 24 hours for drying. The product will then be ground to its original size (120 mesh) and stored in a desiccator as an adsorbent for dye removal. Batch adsorption experiments will be carried out in 50 mL erlenmeyer flasks. The bottles will consist of synthetic solutions containing varying concentrations of adsorbent and MB dye solution according to the batch design. The bottles will then be treated in a water bath with a stirrer. (Yönten et all., 2022)

The experiments were terminated by keeping the composite material in interaction with the MB in a heated water bath in flasks for certain periods. Afterwards, it was centrifuged at 10.000 rpm and the precipitate and filtrate were separated from each other. Analytical calculations were made by taking the supernatants at certain wavelengths to the U.V spectrophotometer (Analytikjena Specord S 600, German).

3. Results

3.1. Characterization of composite material

The FTIR spectra show that various functional groups detected on the surface of MB pre and post adsorption in Figure 2. There are some peaks were shifted, disappeared and new peaks were also detected in the MB dye adsorption on adsorbent. As seen in Figure 2, four significant bands at, 2300-2400, 1300-400 and nm which indicated the bonds -C=C- and C-N, C-O, C-C ve C- group were increased. These four significant bands in the spectrum indicate the possible involvement of the respective functional group on the surface of adsorbent in MB dye adsorption process. Hence, this result suggests that the dye immobilized Bentonite/ Amberlite XAD-7 might induce bulk phase changes.

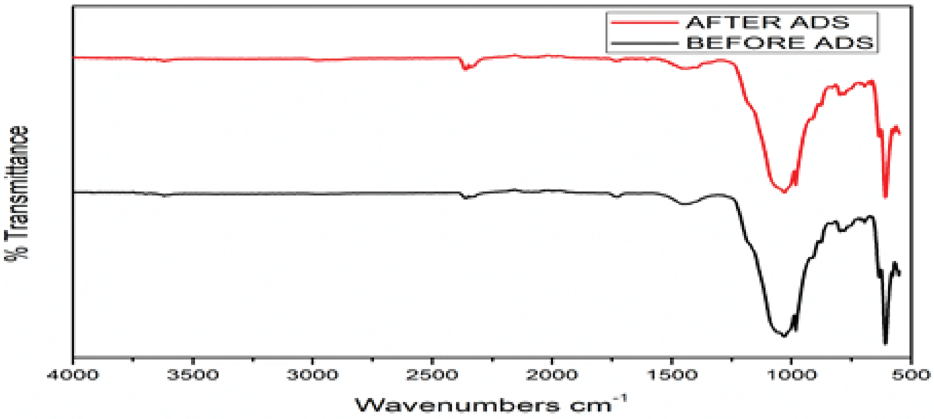

Figure 2. FTIR diagram of pre and post adsorption process.

As seen at Figure 3 and 4, the pre and post adsorption SEM images of adsorbent. Figure 3 pre adsorption images of bentonite/ Amberlite XAD-7 post bonding with MB at 2 μm and 50.00 K X values, and these images are more dense and MB particles hold on to the surface when compared to the post adsorption images shown in Figure 4. The simplicity observed in pre adsorption is apparent in

Post adsorption images, proving the occurrence of adsorption in the current study.

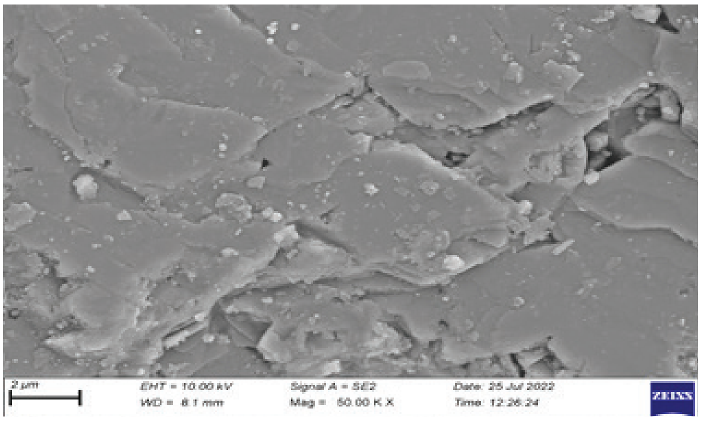

Figure 3. SEM image of pre-adsorption of process.

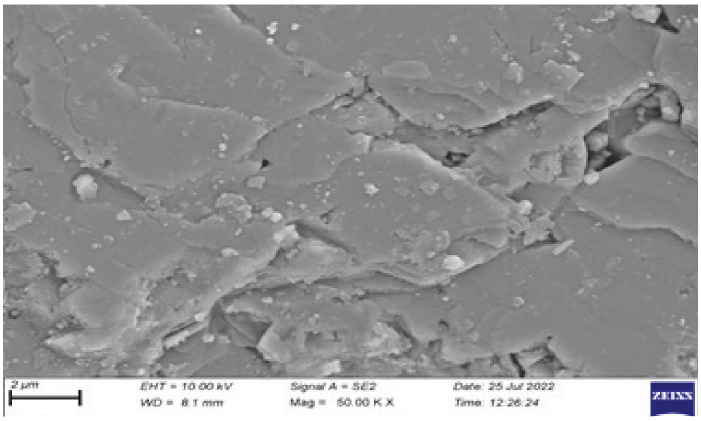

Figure 4. SEM image of post-adsorption of process.

3.2. Adsorption isotherms

Adsorption isotherms were used to explain the interaction between the composite material and the dyes. Some important adsorption isotherms such as Freundlich, Langmuir and Temkin are given in Equations 1, 2 and 3 below to describe the system. (Langmuir, 1918; Freundlich, 1906; Temkin and Pyzhev, 1940) .

$$q_e = K_F C_e^{1/n} \qquad (1)$$

$$\frac{1}{q_e} = \frac{1}{K_L Ce} + \frac{1}{Q_m} \qquad (2)$$

$$q_e = (RT/b_T)\, lnA_T + (RT/b_T) lnCe \qquad (3)$$

in the upper equation; qe is the amount of the dye per unit weight of composite material (mg g^{-1}), Ce the equilibrium concentration of MB (mg L^{-1}), while KF, KL, bT and n are constants that give estimates of the adsorption capacity and intensity respectively in Table 2. KL is measure of the intensity of the biyosorption process (L mg-1), and qm is a adsorption capacity (mg g-1). Qm and KL can be find from slope and intercept from a typical plot of 1/qe versus 1/Ce. In Eq. (1), The slope n-1, ranging between 0 and 1, is a measure for the adsorption intensity or surface heterogeneity. KF is a constant for the system in Eq. (2), KF is adsorption coefficient and it can be defined general capacity of the dye adsorbed on to fungi for a unit equilibrium concentration. The results of isotherms were fitted by using the data of adsorption capacity from the regression of Eq. (3). AT is the isotherm bonding constant (Lg-1). AT and bT can be determined from its slope and intercept from a typical plot of qe versus in Ce. (Kıvanç and Yönten., 2020)

Table 2. The contansts of adsorption ishoterms.

Langmuir			Freudlich			Temkin		
q_m (mg g^{-1})	K_L (Lm g^{-1})	R^2	K_F (mg g^{-1})	n^{-1}	R^2	A_T (Lg^{-1})	b_T	R^2
14	15,01	01	1.5	0.6	4.23	0.27	2.0	97

As shown in Figure 5, the Temkin model yields is a better than other models with correlation coefficients (R2) (Yönten et all., 2022)

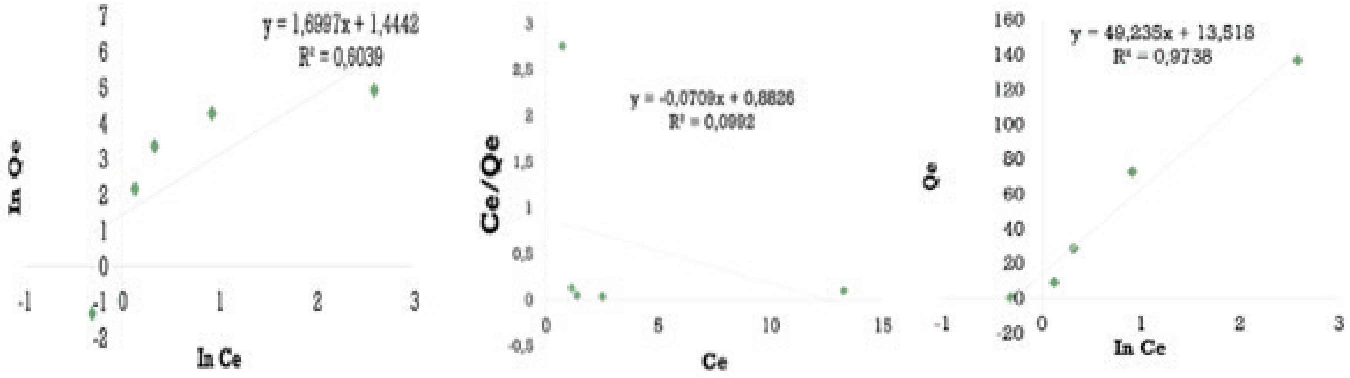

Figure 5. The graphic of adsorption isotherms respectively (Freudlich, Langmuir and Temkin).

4. Discussion and Conclusion

In the study, the prosess mechanism of adsorption can be explain by the following reaction. In the first place, while MB dissolves in water, it gives clorate (R–CH3N-Cl) groups to the environment.

$\text{R-NCH}_3\,\text{Cl} + \text{H}_2\text{O} \rightarrow \text{R–Cl}^- + \text{NCH}_3$

Bentonite/XAD-7 + Cl^{-1} → Adsorption of MB on the composite.

Then, adsorption process was carried out by binding MB anions to the composite material' s surfaces by van der walls and electrostatic interactions (Huang et all., 2017). Here; the removal of MB on bentonite/Amberlite XAD-7 was carried out using adsorption process that cost economical, easy and less time for doing. The equibilirium adsorbent show that our composite material removes the MB dye. Langmuir , Freudlich and Temkin isotherms were used to describe the adsorption equilibriums. Temkin models yields a somewhat better than Freudlich and Langmuir models on adsorption of dye on composite material as reflected with correlation coefficients (R2). The characterizaiton of composite done using SEM and FTIR devices. Because of its sediment-free operation, simplicity and flexibility of design, and complete deletion of dyes even in low concentration solutions, the adsorption process has been demonstrated to be highly effective for dye removal from polluted water. Adsorbent surface modification is very useful in enhancing adsorption capacity and adsorbent selectivity by taking advantage of specific interactions between adsorbents and target molecules in the adsorption technique sector to remove dye from wastewater streams.

References

Ahmad, M.A., Alrozi, R., Optimization of preparation conditions for mangosteenpeel-based activatedcarbonsfor the removal of RemazolBrilliant Blue R using response surface methodology, Chem. Eng. J. 165 (2010) 883–890.

Crini, G., Non-conventionallow-costadsorbentsfordyeremoval: A review, Bioresources Technology, Vol.97, No. 9, pp.1061-1085, (2006).

Crini, G., Kinetic and equilibrium studies on the removal of cationic dyes from aqueous solution by adsorption onto a cyclodextrin polymer, Dyes Pigment. 77 (2008) 415–426.

Gore, M.M., Saharan, V.K., Pinjari D.V, Chavan, P.V., Pandit, A.B., Degradation of reactiveorange 4 dye using hydrodynamic cavitation based hybridtechniques,Ultrason. Sonochem. 21(3) (2014) –1082.

Gessner, T., Mayer, U., Ullmann's Encyclopedia of Industrial Chemistry, Wiley-VCH, Weinheim, Germany, 6th edition, 2002.

Huang R, Liu Q, Huo J, Yang B (2017) Adsorption of methyl orange onto protonated cross-linked chitosan. Arab J Chem 10(1):24–32.

Freundlich,H. M. F. 1906. Over the adsorption in solution. Journal of Physical Chemistry, 57, 385–471.

Kamboh, M.A., Solangi, I.B., Sherazi, S.T., Memon, H.S., A highlyefficientcalyx 4 arenebasedresinfortheremoval of AZO dyes, Desalination 268 (2011) 83–89, https://doi.org/10.1016/j.desal. 2010.10.001.

Kıvanç M.R., Yönten V., A statistical optimization of methylene blue removal from aqueous solutions by Agaricus Campestris using multi-step experimental design with response surface methodology: Isotherm, kinetic and thermodynamic studies., Surfaces and Interfaces Volume 18, March 2020, 100414.

Langmuir, I. 1918.,The adsorption of gases on plane surfaces of glass, mica and platinum. Journal of the American Chemical Society,40, 1361–1403.

Li, A., Zhang, Q., Chen, J., Fei, Z., Long, C., Li, W., Adsorption of phenolic compounds on Amberlite XAD-4 and it sacetylatedderivative MX-4, React. Funct. Polym. 49(3) (2001) 225–233.

Özdemir, K. Cirik, D. Akman, E. Sahinkaya, O. Cinar, Treatment of azodye-containingsynthetictextiledyeeffluentusingsulfidogenicanaerobicbaffledreactor, Bioresour. Technol. 146 (2013) 135–143.

Peng, W., Cotri S. M.L. Han, X., Systemicadministration of an antagonist of the ATP-sensitiver eceptor P2X7 improvesre covery after spinal cordinjury. Proceedings of the National Academy of Sciences of the United States of America, vol. 106, no. 30, pp. 12489–12493, 2009.

Seshadri, S., Bishop, P.L., Agha, A.M., Anaerobic/aerobictreatment of selectedAzodyes in wastewater, Waste Management, vol. 14, no. 2, pp. 127–137, 1994

Temkin, M., and Pyzhev, V.(1940)., Kinetics of Ammonia Synthesis on Promoted Iron Catalysts. Acta Physicochimica URSS, 12, 217-222.

Yonten, V., Tanyol, M., Yildirim, N., Yildirim, N.C., Ince, M., Optimization of Remazol brilliant blue R dye removal by novel biosorbent P. Eryngii immobilized on Amberlite XAD-4 using response surface methodology, Desalin. WaterTreat. 57 (2015) 15592–15602,

Yönten, V., Özgüven A., Ahmed A. A, Akçay M. E., Biosorption of Brilliant Blue G by Amberlite IRA-400 Cl and 4200 Cl Resin/ Agaricus Campestris: the effect of some medium parameters to process. International Journal of Environmental Science and Technology. Arabian Journal for Science and Engineering volume 47, pages441–454 (2022).

IN A CAR AIR CONDITIONING SYSTEM USING R134A THE USE OF R-407C AND R410 A AS ALTERNATIVES AND IN A THERMODYNAMIC PERSPECTIVE PERFORMANCE EVALUATION

Muhammed Taha TOPCU[1*], **Ahmet Tahir KALKIŞIM**[2] and **Kadir BİLEN**[3]

[1]Atatürk University, Faculty of Engineering, Department of Mechanical Engineering;
[2]Gümüşhane University, Faculty of Engineering, Department of Mechanical Engineering
[3]Atatürk University, Faculty of Engineering, Department of Mechanical Engineering

Climate change is increasing in popularity on the world .In this context, various standards have been determined for climate change and global warming issues around the world. In these standards, the limits are determined by the International F-gas regulation. Despite the fact that R 12 gas has been the most used gas in the last 60-70 years, R134a gas with zero ozone depletion effect (ODE) has started to be used as an alternative due to its negative environmental effects. Due to the high global warming effect, the use of r134a gas has been restricted and prohibited. In this context, considering the cooling capacity and cooling effect coefficients of different gases and mixed gases, alternative situations have been started to be investigated. Within the scope of this study, the alternatives of r407c and 410a gases, which are mixed gases, to r134a gas Different condenser temperatures during the study (Tk=40-70 o C) and calculations and applications between different evaporator temperatures (Te=-20-0 o C) has been made. In this study, thermal analyzes were performed using the CoolPack package program.

Short-term mechanical alloying – powerful tool for preparation of high-entropy alloys

Průša F*, **Strakošová A.**, **Kratochvíl P.** and **Thürlová H.**

[1]*Department of Metals and Corrosion Engineering, University of Chemistry and Technology in Prague,Czech Republic*

Abstract: The short-term mechanical alloying nowadays belongs to a powerful tool for swift and thus highly economically viable routes for preparing targeted alloys. Since the preparation is limited to only a few hours, the undesirable contamination of the alloy is suppressed, prolonging the lifetime of the tools. Among modern scientific research, high-entropy alloys are one of the most promising materials usually offering an extraordinary combination of properties. They combine ultra-high strengths while retaining their beneficial ductility and many others as good corrosion resistance. Usually, a variety of methods including induction or arc-melting are used for their preparation, both leading to sort-of coarse-grained microstructures. Thus, the processes like mechanical alloying, which are known to deliver ultrafine-grained or even nanostructured materials, are of interest for the production of these alloys. Refining the microstructure reduces their ductility but tremendously increases remaining mechanical properties like yield strength, ultimate strength and hardness. The already highly promising HEAs might then fully unfold their potential offering yet unseen properties. For this purpose, a variety of HEAs developed from Cantor alloy have been prepared via short-term mechanical alloying and compacted via spark plasma sintering to retain their beneficial microstructure. Their properties underwent a comprehensive characterization to be compared based on the actual chemical composition.

This research was financially supported by Czech Science Foundation (grant No. 21-11313S).

Energy/Exergy Efficiency in Hard Turning Processes: A Case Study

Ali Kemal CAKIR[1]

1Department of Machinery and Metal Technologies, Aydin Vocational School, Adnan Menderes University, PK 09100, Center, Aydin, Turkey. E-mail: ali.kemal.cakir@adu.edu.tr

Abstract: Increasing production demands day by day have led to an increase in energy costs. The increase in turning activities, which has an important place in the manufacturing sector, causes an increase in energy consumption values and therefore increases in costs. For this reason, efficiency studies aimed at reducing the increasing energy costs have gained importance. Efficiency and exergy in turning, which is one of them, are prominent studies in reducing energy costs. This efficiency and cost reduction can be achieved by optimizing the cutting parameters in turning operations. Thus, carbon emission values will also decrease.

In the study, the efficiency calculation was made by subtracting the exergy values of DIN 1.2550 steel material hard turning processes. Within the scope of the study, cutting speeds were focused and optimum conditions were investigated. In this context, there was an increase in efficiency values due to the decrease in exergy losses depending on the cutting speed. Exergy efficiency values of 0.52, 0.56 and 0.59 were obtained, especially at the cutting speeds used in the study, 135, 155 and 175 m/min, respectively. This has shown us that energy efficiency values have increased. In the study, attention was also drawn to the exergy losses in the processing process. The study can be a reference especially for energy and exergy studies in the manufacturing industry.

Keywords: Hard Turning, Energy Efficiency, Exergy, DIN 1.2550

1.Giriş

Doğal kaynakların tüketimi ve endüstriyel süreçlerdeki kirlilik artışları çevresel sorunların artışına sebep olmuştur. Çevre konusundaki endişelerin ele alınması gerekmektedir. Bu endişelerin ele alınması, artan siyasi baskı ve hem üreticiler hem de son kullanıcılar için daha güçlü düzenlemelerin getirilmesini içerir. Sürdürülebilir üretim fikirlerini benimsemek, endüstrinin ekonomik, çevresel ve sosyal performansını iyileştirmenin bir yolunu bizlere sunar [1].

Artan karbon emisyonlarının çoğu endüstri, özellikle imalat sanayi kaynaklıdır. İmalat süreçlerinde büyük miktarda karbon salınımından kaynaklı emisyonların sebepleri şöyle sıralanabilir: İlk olarak, çoğu endüstriyel üretim hala fosil kaynaklarına dayanmaktadır. Bunlar çoğunlukla yüksek enerji üretecek kömür, petrol ve doğal gaz gibi enerji sektöründe kullanılan sera gazı üreticileridir. İkincisi, düşük kullanıma sahip üreticilerdir. Tüm üretim aşamalarında kaynak ve enerji oranı düşük, yani malzeme çıkarma aşaması, üretim aşaması, kullanım aşaması, taşıma aşaması ve kurtarma aşamasında düşük orana sahiptirler. Üçüncüsü, gelişmiş düşük karbonlu teknikler geliştirilmedi ve uygulanmadığında ortaya çıkan sera etkisi. Bu üretimler imalat sanayinde yaygın olarak kullanılmaktadır [2].

Endüstriyel süreçlere olan taleplerin artışı da imalat süreçlerinde artışa sebep olmuştur. Artan imalat süreçleri de hem ekonomik maliyetlerin hem de enerji tüketim değerlerinin artışına sebep olmuştur [3]. İmalat süreçlerindeki bu artışlar sektörün önemli kollarından biri olan Tornalama da etkisini hissettirmiştir. Tornalama süreçleri karmaşık süreçlerdir. Tornalama süreçlerinde iyi yüzey elde etmek kadar onların maliyetlerinin de ekonomik olması gerekmektedir. Bunu enerji tüketiminde yapacağımız verimlik çalışmaları ile elde edebiliriz. Yapılacak enerji verimliliği çalışmaları, tornalama süreçlerinde açığa çıkacak ve çevreye zarar verecek karbon emisyonlarını da azaltacaktır. Dolayısıyla bunlar hem ekonomik hem de çevre dostu çalışmalar olacaktır [4-6].

Tornalamadaki Enerji verimliliği çalışmalarını kesme parametrelerini optimum değerlerde seçerek başlayabiliriz. Çünkü iyi ayarlanmayan kesme parametreleri tornalama süreçlerinde maliyet artışına sebep olmaktadır. Ayrıca, karbon emisyonlarındaki artış nedeniyle çevreye olumsuz etkisi de vardır. Enerji üretiminden kaynaklanan karbon emisyonlarını azaltmak için üretimde kullanılan enerjinin azaltılması gerekir. Literatürde, kesme dışı işlemler için tüketilen enerji, talaşlı imalatta toplam enerji tüketimine hakimdir [7].

Tornalama süreçlerinde kesme parametrelerinin optimizasyonu hakkında birçok çalışma vardır. Ancak, kesme parametrelerindeki optimizasyonun enerji verimliliği ve karbon emisyon değerlerine etkisi hakkında az sayıda çalışma vardır. Ayrıca, tornalama süreçlerindeki işlemlerin belirlenerek, bu süreçlerin ekserji değerlerinin bulunup verimlilik üzerine etkisi hakkında çok daha az çalışma vardır. Bu çalışma ile bu eksilik giderilmeye çalışılmıştır. Çalışmada DIN 1.2550 çelik malzemesinin tornalamasındaki süreçlere ait ekserji değerleri çıkartılarak verimlilik hesabı yapılmıştır. Ayrıca, başka metallerin tornalamasındaki süreçlerin belirlenip, bu süreçlere ait ekserji hesaplamaları ve verimlilik değerleri de çıkartılabilir.

2. Tornalama İşlemlerinin Optimizasyonu

2.1. Minimum Enerji Kriteri

Minimum enerji kriterini belirlemede tornalama sürecinin optimizasyonu kuru tornalama için geliştirilmiştir. Tornalamada kullanılan toplam enerji; kurulum işlemi, kesme işlemleri ve takım değişimi sırasında tezgah tarafından tüketilen enerjiden, bir kesici takım üretmek için harcanan enerjiden ve iş parçası malzemesi üretmek için harcanan enerjiden oluşur. İş parçası malzemesi her ürün için sabitlendiğinden, işleme sürecinden bağımsızdır ve optimizasyon prosedürünü etkilemez. Ayrıca, iş parçası malzemesinin somutlaşmış enerjisini azaltmak her zaman mümkün değildir. Bu nedenle enerji tüketiminin değerlendirilmesinde dikkate alınmaz [8]. Li, C. vd. [9] 2015 yılında yaptıkları çalışmada, tornalama süreçlerinde tüketilen enerji, kayıplar, ekserji verimliliği ve nihayetinde enerji verimliliği denklemlerini formüle etmişlerdir. Bu kapsamda tek geçişli bir tornalama işleminde tüketilen toplam enerji W, aşağıdaki denklem kullanılarak elde edilebilir.

$$W=W_{setup} + W_{machinig} + W_{tool\ change} + E_{tool} \quad (1)$$

W_{setup} kurulum sırasında makine tarafından tüketilen enerjidir ve iş mili kapalıyken makinenin güç tüketiminden ve takım ve iş parçası kurulumu için gereken toplam süreden değerlendirilebilir.

$W_{machining}$ tornalama işlemi sırasında gereken enerjidir ve makine modüllerine güç sağlamak için harcanan enerjiden ve malzeme kaldırma için kullanılacak enerjiden değerlendirilir.

$W_{tool\ change}$ takım değişimi sırasında enerji tüketimi olarak tanımlanır.

Takım genellikle iş mili kapalıyken değiştirildiğinden, takım değiştirme sırasındaki güç, makinenin boş durumdaki güç tüketimine eşittir. E_{tool} kesici takımın enerji ayak izidir ve kesme kenarı başına düşen enerjinin ürününden hesaplanabilir. Ecutting edge işleme geçişini tamamlamak için gereken kesme kenarlarının sayısıdır. Yukarıdaki tartışmaları kullanarak, enerji denklemi aşağıdaki biçimde yazılabilir [9].

$$W = \dot{W}_0 t_{setup} + (\dot{W}_0 + k\dot{V})t_{cutting} + \dot{W}_0 t_{tool\ change}\left(\frac{t_{cutting}}{t}\right) + E_{cutting\ edge}\left(\frac{t_{cutting}}{t}\right) \qquad (2)$$

Burada (W_0) makine modülleri tarafından tüketilen güçtür (yani, kesme olmayan işlemler sırasında makinenin güç tüketimi), k, kesme işlemlerinde spesifik enerji gereksinimi ve *V*, malzeme kaldırma oranıdır.

t_{setup}, $t_{cutting}$ ve $t_{tool\,change}$ sırasıyla makine kurulum süresi, kesme süresi ve takım değiştirme süresidir. t, kesici takımın ömrünü gösterir. Tek geçişli tornalama işlemleri için, takım ömrü Taylor'un [10] uzatılmış takım ömrü denkleminin değiştirilmiş formu kullanılarak elde edilebilir.

$$t = \frac{A}{Vc^{1/\alpha} f^{1/\beta}} \qquad (3)$$

Burada V_c kesme hızı, f ilerleme hızıdır. ☒ ve ☒ ise sırasıyla takım ömrü denklemi için kesme hızı ve ilerleme hızı üsleridir. A, deneysel veriler kullanılarak bulunabilen bir sabittir. Tek geçişli tornalama için kesme süresi aşağıdaki denklemle değerlendirilebilir:

$$t_{cutting} = \frac{\pi D_{avg} l}{f V_c} \qquad (4)$$

$$W = \dot{W}_0 t_{setup} + \frac{\dot{W}_0 \pi D_{avg} l}{f v_c} + \frac{k\pi l}{4} D_i^{\,2} - D_f^{\,2}) + \frac{\dot{W}_0 t_{tool\ change}\, \pi D_{avg} l\, v_c^{\left(\frac{1}{\alpha}\right)-1} f^{\left(\frac{1}{\beta}\right)-1}}{A} + \frac{E_{cutting\ edge}\, \pi D_{avg} l\, v_c^{\left(\frac{1}{\alpha}\right)-1} f^{\left(\frac{1}{\beta}\right)-1}}{A} \qquad (5)$$

Burada l kesme uzunluğu, Davg ise iş parçasının başlangıç ve son çapları olan Dl ve Df'den hesaplanan ortalama iş parçası çapıdır.

Yukarıda belirtilen kesme süresini ve takım ömrünü enerji denklemi ile denklem (5) ile ifade edebiliriz:

Denklem (5)'in kullanılması ile optimum takım ömrünü bularak süreçteki enerji tüketimi en aza indirilebilir. Bu takım ömrü daha sonra minimum enerjiyle işleme için optimum kesme hızı elde etmek için takım ömrü denkleminde kullanılabilir. İşlemin optimizasyonu, denklem (5)'te gösterilen model işlevi için minimum noktayı bularak elde edilebilir. Sunulan model sürekli bir fonksiyon olduğundan, minimum nokta, toplam enerjinin kesme hızına göre türevini elde ederek ve sıfıra eşitleyerek bulunabilir. Bu, aşağıdaki denklemle ifade edilebilir.

$$\frac{\partial W}{\partial v_c} = -\frac{\dot{W}_0 \pi D_{avg} l}{f v_c^{2}} + \left(\frac{1}{\alpha} - 1\right)\left(\frac{\dot{W}_0 t_{tool\ change}\, \pi D_{avg} l v_c^{\left(\frac{1}{\alpha}\right)-2} f^{\left(\frac{1}{\beta}\right)-1}}{A}\right. + \left(\frac{1}{\alpha} - 1\right)\frac{E_{cutting\ edge} \pi D_{avg} l\, v_c^{\left(\frac{1}{\alpha}\right)-2} f^{\left(\frac{1}{\beta}\right)-1}}{A} = 0 \quad (6)$$

Yukarıdaki denklem aşağıdaki gibi basitleştirilebilir:

$$\frac{A}{f^{1/\beta} v_c^{1/\alpha}} = \left(\frac{1}{\alpha} - 1\right)\left(\frac{\dot{W}_0 t_{tool\ change} + E_{cutting\ edge}}{\dot{W}_0}\right) \qquad (7)$$

Taylor'un [10] takım ömrü denklemini kullanarak aşağıdaki denklem (8) elde edilir.

$$t_{opt,En} = \left(\frac{1}{\alpha} - 1\right)\left(\frac{\dot{W}_0 t_{tool\ change} + E_{cutting\ edge}}{\dot{W}_0}\right) \qquad (8)$$

Denklem (8), minimum enerji tüketimini elde etmedeki ana faktörlerin takım ömrü hızı üssü, makine modüllerinin güç tüketimi, takım değiştirme süresi ve kesici takımlar için enerji ayak izi olduğunu göstermektedir. Denklem (8), işleme sırasında minimum enerji kullanımı için optimum takım ömrünü elde etmek için kullanılacaktır.

2.2. Minimum Ekserji Kaybı Kriteri

Kuru tornalama işlemi için ekserji denge denklemi aşağıdaki gibi yazılabilir.

$$Ex_{in} + Ex_{w,in} + Ex_{Q,in} = Ex_{out} + Ex_{w,out} + Ex_{Q,out} + Ex_{loss} \qquad (9)$$

Burada Exin, Exout, giriş ve çıkış kütle ekserjileridir.Çıktıekserjisi,çıktımalzemelerinin çevreleyen ile aynı termodinamik durumda olduğu varsayıldığından sıfır olarak kabul edilir (Ölü hal). Exw,in ve Exw,out, iş exerjilerini temsil eder ve sırasıyla sistemin iş girdisine ve iş çıktısına eşittir. İşleme süreci için iş çıktısının sıfır olduğu açıktır. Kayıp ekserji, ısı ekserjileri olan Exloss , ExQ,in ve Exout ile temsil edilir. İşleme süreci için ısı girdisi ve bununla ilişkili ısı ekserjisi sıfırdır. İşlem için ısı ekserji çıktısı aşağıdaki denklem kullanılarak hesaplanabilir:

$$Ex_{Q,out} = Q_{out}\,(1 - T_0/T) \qquad (10)$$

Qout sistemin ısı çıktısı, T0 çevre sıcaklığı ve T ısı kaynağının sıcaklığıdır. İşleme süreci için iş girdisi, elektrik enerjisi tüketimine eşittir ve aşağıdaki denklem kullanılarak elde edilebilir:

$$W_{elec} = W_{setup} + W_{machining} + W_{tool\ change} \qquad (11)$$

Burada kullanılan, W_{setup} , $W_{machining}$ ve $W_{tool\ change}$ sırasıyla kurulum süresi, kesme süresi ve takım değiştirme süresindeki enerji tüketimidir. Kesme sırasındaki enerji tüketimi Gutowski [11] tarafından önerilen denklem kullanılarak değerlendirilebilir.

$$W_{machining} = (W_0 + kV)\, t_{cutting} \qquad (12)$$

Takım değiştirme süresi sırasındaki elektrik enerjisi tüketimi, makinenin boşta güç tüketimi ve takımı değiştirmek için gereken sürenin ürününden elde edilebilir. Bu nedenle, sürecin girdi işi ekserjisi aşağıdaki denklem ile ifade edilir:

$$Ex_{w,in} = W_{elec} = \dot{W}_o t_{setup} + (\dot{W}_o + k\dot{V})t_{cutting} + \dot{W}_o t_{tool\ change}(\frac{t_{cutting}}{t}) \qquad (13)$$

Kesme süresi ve takım ömrü için yukarıda belirtilen değerleri kullanarak, işlemin iş ekserji girdisi aşağıdaki denklem kullanılarak elde edilecektir:

$$Ex_{w,in} = W_{elec} = \dot{W}_o t_{setup} + \dot{W}_o \frac{\pi D_{avg} l}{f v_c} + \frac{k\pi l(D_i^2 - D_f^2}{4}) + \frac{\dot{W}_0 t_{tool\ change}\, \pi D_{avg} l v_c^{\left(\frac{1}{\alpha}\right)-1} f^{\left(\frac{1}{\beta}\right)-1}}{A} \qquad (14)$$

Kesici takımın elektrik enerjisi ayak izi, işlemin ekserji girdisi olarak kabul edilir. Bu ayak izi, takım malzemesinin somutlaştırılmış enerjisinden, takımın imalatında kullanılan enerjiden ve herhangi bir tamamlayıcı işlemin (kaplama vb.) enerjisinden oluşur. Böylece işleme sürecinin giriş ekserjisi, denklem (15)'deki gibi ifade edilebilir.

$$Ex_{in} = \frac{E_{cutting\ edge} \pi D_{avg} l v_c^{\left(\frac{1}{\alpha}\right)-1} f^{\left(\frac{1}{\beta}\right)-1}}{A} \qquad (15)$$

Takım tezgahının boşta güç tüketimi esas olarak ısı olarak dağıtılır. Bu nedenle, işlemin ısı çıktısının makinenin boşta enerji tüketimine eşit olduğu varsayılabilir.

$$Q = \dot{W}_o(t_{setup} + \frac{\pi D_{avg} l}{f v_c} + \frac{t_{tool\ change}\, \pi D_{avg} l v_c^{\left(\frac{1}{\alpha}\right)-1} f^{\left(\frac{1}{\beta}\right)-1}}{A}) \qquad (16)$$

Yukarıdaki tartışmadan, kuru tornalama işleminde ekserji kaybını hesaplamak için denklem aşağıdaki gibi yazılabilir.

$$Ex_{loss} = \dot{W}_o\left(t_{setup} + \frac{\pi D_{avg} l}{f v_c} + \frac{t_{tool\ change}\, \pi D_{avg} l v_c^{\left(\frac{1}{\alpha}\right)-1} f^{\left(\frac{1}{\beta}\right)-1}}{A}\right)\left(\frac{T_0}{T}\right) + (\frac{k\pi l}{4}(D_i^2 - D_f^2) + \frac{E_{cutting\ edge} \pi D_{avg} l v_c^{\left(\frac{1}{\alpha}\right)-1} f^{\left(\frac{1}{\beta}\right)-1}}{A} \qquad (17)$$

Optimizasyon sürecinin amacı, minimum ekserji kaybı kriterini karşılayan optimum bir takım ömrü elde etmektir. Bu takım ömrü, optimum kesme hızını bulmak için takım ömrü denkleminde kullanılabilir.

Minimum ekserji kaybı için optimum takım ömrü, denklem (17) 'de sunulan model minimize edilerek bulunabilir. Bu, model fonksiyonunun türevini sıfıra eşitleyerek elde edilebilir:

$$\frac{\partial Ex_{loss}}{\partial v_c} = [-\frac{\dot{W}_0 \pi D_{avg} l}{f v_c^{2}} + (\frac{1}{\alpha} - 1)(\frac{\dot{W}_0 t_{tool\ change}\, \pi D_{avg} l v_c^{\left(\frac{1}{\alpha}\right)-2} f^{\left(\frac{1}{\beta}\right)-1}}{A}] + \left(\frac{1}{\alpha} - 1\right) \frac{E_{cutting\ edge} \pi D_{avg} l\, v_c^{\left(\frac{1}{\alpha}\right)-2} f^{\left(\frac{1}{\beta}\right)-1}}{A} = 0 \qquad (18)$$

$$\Rightarrow \frac{A}{v_c^{\left(\frac{1}{\alpha}\right)} f^{\left(\frac{1}{\beta}\right)}} = (\frac{1}{\alpha} - 1)\, \frac{\dot{W}_0 t_{tool\ change}\ + E_{cutting\ edge}\, (\frac{T}{T_0})}{\dot{W}_0} \qquad (19)$$

Denklem (3)’deki Taylor’un takım ömrü denklemini kullanarak;

$$t_{opt,Ex} = (\frac{1}{\alpha} - 1)\, \frac{\dot{W}_0 t_{tool\ change}\ + E_{cutting\ edge}\, (\frac{T}{T_0})}{\dot{W}_0} \qquad (20)$$

Denklem (20), sıcaklık etkisinin eklenmesi dışında minimum enerji tüketimi için optimum takım ömrü için denklem (8) ‘e çok benzer. Bu nedenle, enerji kalitesi kavramının sıcaklık açısından birleştirilmesi yoluyla ekserji analizi, işleme sürecinin çevreye daha uygun bir optimizasyonunu sağlayabilir.

3. Materyal ve Metot

Bu deneysel çalışmada, iş parçası olarak DIN 1.2550 malzemesi kullanılmıştır. Bu malzeme soğuk iş takım çeliği olarak işlenebilirliği ve şekillendirilmesi kolay olduğundan imalatta kullanılan bir malzemedir. Darbeye dayanıklı, tungsten alaşımlı bir iş parçasıdır. Isıl işlem için uygundur. Yüksek sertlik değerlerine kolayca ulaşabilir. Sertleştirme işleminden sonra yüksek mukavemete sahiptir. Korozyona ve sıcaklığa karşı yüksek dirence sahiptir. çalışmada kullanılan DIN 1.2550 soğuk iş takım çeliği Ø44,5x250 mm ölçülerinde imal edilmiş olup kimyasal bileşimi Tablo 1.’de verilmiştir.

C	Si	Mn	Cr	Mo	Ni	V	W	Diğer
0.60	0.85	0.30	1.05	-	-	0.15	1.45	-

Tablo 1. AISI S1 Çeliği Kimyasal Bileşimi [12]

3.1. Kesme Parametreleri

Kesme parametrelerini gösterir detaylar Tablo 2’de verilmiştir.

Çalışmada, Taequtec firmasının 11T04 model DCMT 110408 geometri kesici takımları talaş kaldırma için kullanıldı. Bitirme tornalama işlemi olduğu için bu takım tercih edilmektedir. Şekil 1’de görülebilir.

Kesici Uç	DCMT 11T 308 Cutting Tool
Takım Tutucu	PCLNL2020K12
Kesme Hızı	135, 155, 175 m/dk
İlerleme Oranı	0.045, 0.090, 0.135 mm/rev
Kesme Derinliği	0.10 mm

Tablo 2. Kesme Parametreleri

Şekil 1. DCMT 11T04 Kesici Takım [13]

3.2. Kesici takım için enerji ayak izi

Kesici takımın enerji ayak izi, takım üretimi için gerekli olan enerjidir ve esas olarak takım malzemesinde bulunan enerjiden, sinterleme için gerekli enerjiden (ve bazı aletler için taşlama) ve fiziksel buhar biriktirme (PVD) için gerekli enerjiden veya buhar biriktirme (CVD) kaplama işlemlerinden oluşur.

Ana malzeme olarak tungsten içeren tungsten karbür takımların, 400 MJ / kg enerjiye sahip olduğu tahmin edilmektedir. Takım üretim süreçlerinin her biri, kesici uç başına 1 MJ ila 2 MJ enerji tüketir.

Deneyler için kullanılan kesici takımlar, ortalama kütlesi 9,5 g olan karbür üçgen uçlardır. Bu uçları üretmek için bir sinterleme işlemi kullanıldığından, her kesici uç için enerji ayak izi 5,3 MJ olarak tahmin edilmektedir [9].

3.3. Serbest Yüzey Aşınması ve Takım Ömrü Denklemi

0,3 mm'lik ortalama serbest yüzey aşınma takım ömrü kriteri, tek noktalı tornalama takımlarıyla takım ömrü testi için ISO 3685 standardı tarafından tavsiye edilir. Deneylere dayanarak, 0,3 mm'lik serbest yüzey aşınma takım ömrü kriterine sırasıyla 300, 400 ve 500 m / dakikalık kesme hızlarına 33, 21 ve 9,5 dakika sonra ulaşılmıştır [9].

Takım ömrünün log ölçeği ile kesme hızı arasındaki doğrusal ilişki, kesme hızı üssünü değerlendirmek için kullanılacaktır. Bu ikisi arasındaki doğrusal ilişki denklem (21) ile verilmiştir.

$$l_{ogt} = -2.3968 \log Vc + 5.0033 \qquad (21)$$

Bu nedenle, bu kesme koşulları için kesme hızı üssü 2.3968'dir. Bu değer, optimum takım ömrü denklemlerinde kullanılacaktır.

3.4. Ekserji Kaybı Analizi

Denklem (17) kuru tornalama işleminde ekserji kaybının değerlendirilmesi için kullanılabilir. Bu denklemi kullanmak için gerekli parametreler Tablo 3'te sunulmuştur.

Makine Boşta Çalışma Güç Tüketimi
$3.594x10_3$ W

Makine Boşta Çalışma Güç Tüketimi	$3.594x10_3$ W
Takım Değiştirme Zamanı	120 s
Çevre Sıcaklığı	25 C
Isı Kaynağı Sıcaklığı	36 C

Tablo 3. İşleme Sürecinde Enerji ve Ekserji Hesaplamaları için Gereken Parametreler

Kesme hızındaki değişimin işleme sistemindeki ekserji kaybına etkisi Şekil 2'de gösterilmektedir. Kesme hızındaki bir artışın başlangıçta ekserji kaybında hızlı bir düşüşe neden olabileceği açıktır. Ancak kesme hızı arttıkça ekserji kaybındaki değişim daha az önemli hale gelir.

3.3. Kesme Hızı ve Ekserji kaybı Değişimi

Kesme hızına bağlı olarak tornalama sürecindeki ekserji kaybını gösterir değişim Şekil 2'de gösterilmiştir.

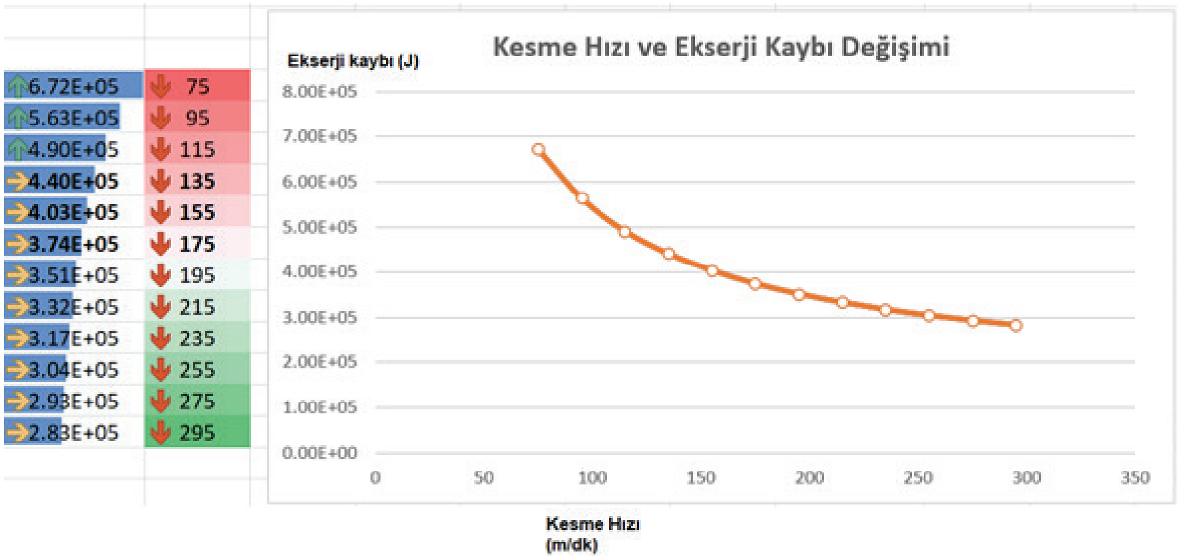

↑6.72E+05	↓ 75
↑5.63E+05	↓ 95
↑4.90E+05	↓ 115
→4.40E+05	↓ 135
→4.03E+05	↓ 155
→3.74E+05	↓ 175
→3.51E+05	↓ 195
→3.32E+05	↓ 215
→3.17E+05	↓ 235
→3.04E+05	↓ 255
→2.93E+05	↓ 275
→2.83E+05	↓ 295

Şekil. 2. Kuru tornalama işlemi sırasında ekserji kaybı pariterilerinin kesme hızı ile değişimi

2.3. Enerji/Ekserji Verimliliği

Sistemin ekserji verimliliğini göstermek için Formül (21) kullanılmıştır.

$$\varphi = 1 - \frac{Ex_{loss}}{Ex_{in}+Ex_{w,in}+Ex_{Q,in}} \quad (21)$$

Şekil 3 kuru tornalama sürecinde kesme işleminde ekserji verimliliği değişimini yansıtmaktadır.

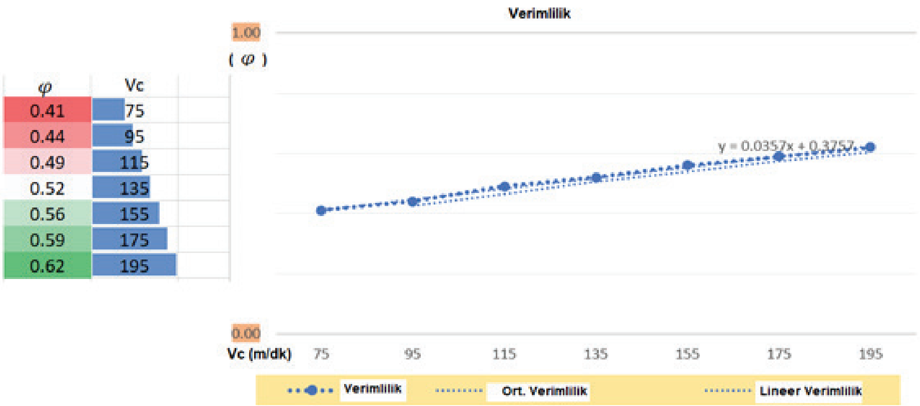

φ	Vc
0.41	75
0.44	95
0.49	115
0.52	135
0.56	155
0.59	175
0.62	195

Şekil 3'e göre, kesme hızındaki artış, verimlilikte gözle görülür bir artışa neden olur. Bu çalışma, Ghandehariun, A. vd. [14]'ün aksine kesme hızındaki artışın ekserji verimliliğinde bir artışa neden olduğunu kanıtlamaktadır. Bu nedenle, kesme hızındaki bir artış, Şekil 2'de gösterildiği gibi işlemdeki ekserji kaybını azaltır ve Şekil 3'te olduğu gibi daha iyi bir verim sağlar.

3. Sonuç ve Öneriler

Minimum maliyet ve minimum enerji tüketimine dayalı işleme operasyonları için optimizasyon yöntemleri halihazırda geliştirilmiştir. Ancak bu yöntemler, makineyle işlemenin sürdürülebilirlik yönleri hakkında kapsamlı bir anlayış sağlamada başarısızdır. Bu makalede, bir işleme sürecinin çevresel etkilerini en aza indirmek için ekserji analizi yöntemi kullanılmıştır. Öncelikle işlemin ekserji kaybı hesaplanmıştır. Çalışma kapsamında kesme hızlarına odaklanılmış ve optimum koşullar araştırılmıştır. Bu kapsamda kesme hızına bağlı olarak ekserji kayıplarında düşüşe bağlı olarak verimlilik değerlerinde artış olmuştur. Özellikle çalışmada kullanılan kesme hızları olan 135, 155 ve 175 m/dk'da sırasıyla, 0.52, 0.56 ve 0.59 ekserji verimlilik değerleri elde edilmiştir. Bu bize enerji verimlilik değerlerinin arttığını göstermiştir. Çalışmada işleme sürecindeki ekserji kayıplarına da dikkat çekildi. Çalışma, özellikle imalat sanayindeki enerji çalışmaları için bir referans olabilir. Çalışma esas olarak şunları yansıtmaktadır:

- Ekserji kaybındaki azalma, kesme hızındaki değişime bağlıdır. Başlangıçta kesme hızındaki bir artış, ekserji kaybında hızlı bir azalmaya yol açmıştır. Ancak kesme hızı arttıkça ekserji kaybındaki düşüş eğilimi azalmıştır. Ancak, kesme hızı optimum bir değere ulaştığında, bu azalma eğilimi daha az önemli hale gelir.
- Kesme hızındaki artış, kesme işlemlerinde optimum değerleri bulmanın önemini yansıtan kuru tornalama işleminde logaritmik bir atışa neden olur.
- Optimum kesim süresi, kesme hızındaki artışa bağlı olarak değişmektedir. Optimum kesim süresi sadece enerji kayıplarını azaltmakla kalmamış, aynı zamanda enerji verimliliğini de olumlu yönde etkilemiştir.
- Bu çalışma gibi enerji ve ekserji verimliliği çalışmaları, sert/kuru tornalama işlemlerinde farklı endüstriyel malzemeler (farklı çelik malzemeler, alüminyum, bronz vb.) kullanılarak da çalışılabilir.

Dizin

l: Kesme uzunluğu (m)

Q: Sistem ve çevre arasında ısı tarnsferi (J)

Ex: Exergy (J)

Exloss: Ekserji kaybı (J)

$Ex_{,Q}$: Isı Ekserjisi (J)

$Ex_{,w}$: İş Ekserjisi (J)

D_{avg}: İş parçasının ortalama çapı(m)

D_f: İş parçasının nihai (son) çapı(m)

D_i: İş parçasının ilk çapı(m)

$E_{cutting\ edge}$: Kesme kenarı başına enerji ayak izi(J)

E_{tool}: Kesici enerji ayak izi(J)

f : İlerleme oranı(mm/rev)

k: Spesifik kesme enerji değeri(J/m3)

t: Takım Ömrü(s)

$t_{cutting}$: Kesme zamanı(s)

$t_{opt, En}$: Minimum enerji tüketiminde optimum takım ömrü(J)

$t_{tool\ change}$: Takım değişim zamanı(s)

T: Isı kaynağı sıcaklığı(oC)

T_o: Çevre Sıcaklığı(oC)

V_c: Kesme Hızı(m/dk)

W_0 : Makine güç tüketimi(W)

V : Malzeme kaldırma oranı(m3/s)

W_{elec}: Elektrik enerji tüketimi(W)

$W_{machinig}$: İşleme sürecindeki enerji tüketimi(J)

W_{setup}: Setup enerji tüketimi(J)

$W_{tool\ change}$: Takım değişimi enerji tüketimi(J)

φ : Verimlilik

Referanslar

1. Pusavec et al., (2010). Pusavec, F., Krajnik, P. and Kopac, J. "Transitioning to sustainable production – Part I: application on machining technologies", Journal of Cleaner Production, Vol. 18, pp.174–184.

2. Lu, Qi, Guanghui Zhou, and Jiakai Zhu. "A calculation method of embodied carbon-energy for low-carbon products." Procedia CIRP 57 (2016): 680-685.

3. Anonymous, a. Karbon Salımı ve Küresel Isınma Arasındaki İlişki Sanıldığı Kadar Karmaşık Değil, https://bilimgenc.tubitak.gov.tr/makale/karbon-salimi-ve-kuresel-isinma-arasindaki-iliski-sanildigi-kadar-karmasik-degil, (in Turkish), (Accessed: 07/09/2022).

4. Gutowski T, Dahmus J, Thiriez A (2006) Electrical energy requirements for manufacturing processes. Proc. of the 13th CIRP on Life cycle engineering. http://web.mit.edu/ebm/www/Publications/CIRP_2006.pdf. (Accessed 10 Aug 2022).

5. Neugebauer, R., Wertheim, R., Harzbecker, C., Energy and resources efficiency in the metal cutting industry, Proceedings of the 8th global conference on sustainable manufacturing, 36, 247–257, 2011.

6. Jiang, Zhipeng, et al. "Electrical energy consumption of CNC machine tools based on empirical modelling." The International Journal of Advanced Manufacturing Technology 100.9 (2019): 2255-2267.

7. Rajemi et al. 2009. Rajemi, M.F., Mativenga, P.T., Jaffery, S.I. "Energy and carbon footprint analysis for machining titanium Ti-6Al-4V Alloy". Journal of Machine Engineering 9 (1), 103–112.

8. Gutowski, T. G., Branham, M. S., Dahmus, J. B., Jones, A. J., Thiriez, A., & Sekulic, D. P. (2009). Thermodynamic analysis of resources used in manufacturing processes. Environmental science & technology, 43(5), 1584-1590.

9. Li, C., Tang, Y., Cui, L., Li, P., A quantitative approach to analyze carbon emissions of CNC-based machining systems, Int. J. Of Advanced Manufacturing Tech., 26 (2015), 911–922.

10. Taylor, J., 1977. "The estimation of tool life equation by extrapolation". Proceeding of the 18th International Machine Tool Design and Research Conference, pp. 379–3385.

11. Gutowski, T. (2010) 'The efficiency and eco-efficiency of manufacturing', International Journal of Nanomanufacturing, Vol. 6, pp.38–45.

12. Anonymous, b. Celik Metal Co., Products, Cold Work Tool Steels, DIN 1.2550 Steel, https://www.celikmetal.com.tr/urunlerimiz/detay/1-2550 (Accessed: 07/09/2022).

13. Cakir, A.K. Analysis of Surface Roughness, Sound Level and Machine Current in the Turning of Hardened AISI S1 Steel. Trans Indian Inst Met (2021). https://doi.org/10.1007/s12666-021-02196-8.

14. Ghandehariun, A., Nazzal, Y., Kishawy, H. and Al-Arifi, N.S.N. (2015) "Investigation of sustainability in machining processes: exergy analysis of turning operations", Int. J. Exergy, Vol. 17, No. 1, pp.1–16.

Comparison of the Treatment Performances of the PbO2 Electrode Prepared by the Thermal Deposition Method with the Commercial PbO2 Electrodes

Dilara ÖZTÜRK[1*], **Umut UYAR**[1] and **Abdurrahman AKYOL**[1]

[1]*Gebze Technical University, Türkiye*

Abstract: The electrooxidation method is a very successful method used in the treatment of wastewater, providing full mineralization and without problems such as waste sludge. The most important part of the electrooxidation system is the anode material. The development of the anode material is one of the most important gaps in this regard. Electrodes known as DSA are commercially available, but the efficiency of these electrodes needs to be improved. Within the scope of this study, it is aimed to compare the coating quality of the electrodes prepared in the laboratory with the commercial ones. Paracetamol (PST) was used as the model contaminant. The plate shaped electrode was produced in the laboratory and the commercially electrode was perforated electrode. Both electrodes have the same composition. The electrode made in the laboratory was produced by thermal oxidation method. Both electrodes have been optimized by varying the pH, current density, conductivity and PST concentration. The removal efficiencies were 52% with the commercial electrode at 5A current, while the TOC removal efficiency was 57% with the lab scale one. In addition, pH was the optimum neutral conditions for the commercial electrode, while basic conditions were for the lab scale. As PST concentration increased, removal efficiencies increased and lab scale electrode offered better removal efficiencies. According to these results, our lab scale production gave good results against the commercial electrode.

Friction Welding of Cu Matrix SiC Reinforced Composite

İhsan KIRIK[1], Ömer BARAÇ[2], Anıl İMAK[3*] and **Serhat ŞAP[4]**

[1]Bingol University, Vocational High School of Technical Sciences, Department of Machinery, Bingol, Turkey, ikirik@bingol.edu.tr
[2]Bingol University, Faculty of Engineering and Architecture, Department of Mechanical Engineering, Bingol, Turkey, omerbarac@hotmail.com
[3]Bingol University, Faculty of Engineering and Architecture, Department of Mechanical Engineering, Bingol, Turkey, aimak@bingol.edu.tr*
4Bingol University, Vocational High School of Technical Sciences, Department of Electricity and Energy, Bingol, Turkey, ssap@bingol.edu.tr

Abstract: In this study, Cu matrix SiC reinforced composite material was produced by the powder metallurgy method. This material produced was combined with pure copper (Cu) rods by friction welding method. During welding, 5 wt. %, 10 wt. % and 15 wt. % SiC reinforced copper matrices composites, moreover different mechanical and microstructural properties were obtained with parameters such as speed and temperature. As a result of the investigations, the effect of the SiC-reinforced copper matrix on the strength of the connection area was determined.

1. Introduction

Advances in technology have led to the need to improve many properties of materials. This contributed greatly to the development of materials science. For this purpose, serious studies are carried out to improve the materials.These required features have revealed the use of different materials together. Composites are named as material groups consisting of two or more components that are visibly combined and do not dissolve in each other, and that have the desired properties of the materials used (Kaw 2014).Ersoy (2001) defined composite materials as a group of materials that are formed by combining at least two different materials for a specific purpose. It usually consists of a composite material, a low-strength resin or matrix, and a small amount of reinforcing elements. The components that combine composite materials are put together at the macro level in a way that keeps their limits. When the composite materials are examined, it is seen that the components are selected and they are at a distinguishable level. Even though these materials show homogeneous properties, they actually have heterogeneous structures. In this context, although the materials combined at the molecular and atomic level appear homogeneous, they do not belong to the composite material class (Şahin 2000).

One of the most common methods used in the production of metal matrix composite materials is the powder metallurgy technique. Powder Metallurgy; sintering, hot pressing, hot isostatic pressing, powder metal injection, nano-particle techniques, mechanical alloying is one of the high technologies that appeal to a constantly growing market (Toptan 2006). This method allows us to obtain durable objects under the melting temperature of metals and alloys with the help of pressure and temperature (Yılmaz 2006).

Friction welding is a solid state joining method. Friction welding, on the other hand, is a welding method in which the parts to be welded rotate at a certain speed and are joined with the help of pressure. Friction welding is seen as a method that can be used for joining metals with different thermal and mechanical properties. Because friction welding works below the melting temperature and the welding time is short, it makes it possible to combine material pairs that cannot be combined with other welding methods with this method (Şahin et al. 1998).

The joining problem in the application area of composite materials has increased the studies on this subject. In this study, the hardness, strength and microstructures of the welding interface formed as a result of the combination of SiC reinforced copper matrix by using the friction welding method, which is one of the joining methods, were investigated.

2. Materials and Method

SiC and Cu powders used in experimental studies and Cu were commercially supplied as Ø12x1000 mm bars. The properties of commercially available SiC and Cu powders are given in Tables 1 and 2.

The first step in the preparation of the samples is the weighing and mixing of the powders forming the matrix and reinforcement phases according to their weight ratios. In the experiments, 99% purity and 325 mesh SiC and 325 mesh Cu powders were used. Here, it is aimed to produce SiC reinforced Cu metal matrix composite.

Four different composites were obtained with the activity, and the ratios of these mixtures are given in Table 3. The powders were weighed on scales with an accuracy of 10-4. The mixing process was carried out in the powder mixing mixer in the Laboratory of the Department of Metal Education, Faculty of Technology, Fırat University (Figure 4.3). With this mixer, it is ensured that the composite mixture becomes homogeneous. This mixing process took 6 hours. 1% by weight of polyethylene glycol (PEG) lubricant was added to prevent the composite from plastering on the inner surfaces of the cylinder and the balls inside the cylinder. The schematic picture showing the pressing steps is shown in Figure 1.

Table 1. *Properties of SiC powder used in the experimental study*

Materials	Material Density (g/cm3)	Melting point (°C)	Thermal expansion coefficient (10-6/°C)	Compression strength (MPa)	Hardness (Hv)	Elasticity module 103 (MPa)
SiC	3.2	2500	5	2000	3000	414

Table 2. *Properties of Cu powders used in the experimental study*

Materials	Density(g/cm3)	Melting point (°C)	Thermal expansion µm/(m·K)	thermal conductivity W/(m·K)	Hardness (Hv)	Ergime Isısı kJ/mol
Cu	8.96	1084	16.5	401	369	66

Sample no	SiC	%SiC (325 mesh)	%Cu (325 mesh)	SiC (g)	Cu (g)
S1	0	0	100	0	100
S2	%5 SiC	5	95	5	95
S3	%10 SiC	10	90	10	90
S4	%15 SiC	15	85	15	85

Table 3. *Sample mixing ratios by weight.*

SiC and Cu powder mixtures were cold pre-pressed at a pressure of 100 MPa. Composite specimens of Ø12x40 mm were produced with this cold pressing process. The inner surface of the mold is lubricated with boron nitride each time to reduce the friction between the mixture and the surface and to easily release the composite parts from the mold. HIP (Hot Isostatic Pressing) was applied to the cold-packed samples to obtain a non-porous structure and good bond strength between the Matrix and the reinforcement material and to obtain a non-porous part. The HIP process was carried out in a hot pressing mold under 50 MPa pressure after the cold-packaged Ø12x40 mm samples were kept in an atmosphere-controlled oven at 550 oC for 20 minutes.

3. Result and Discussion

The samples were etched with nital solution after sanding with sanding papers numbered 400, 600, 800, 1000 and 1200, respectively. Afterwards, images were taken with an optical microscope for microstructure examinations, and the internal structure of the samples was examined, and an idea about the structure was obtained.

Macro pictures obtained by combining Cu matrix composites with SiC reinforcement in different proportions and copper with friction welding are given in figure 1. As can be clearly seen from the figures, the increasing SiC ratio had a negative effect on the joint quality. Consolidation was achieved in all samples except the sample containing 15% SiC.

Figure 1. *Macro images of friction welded samples*

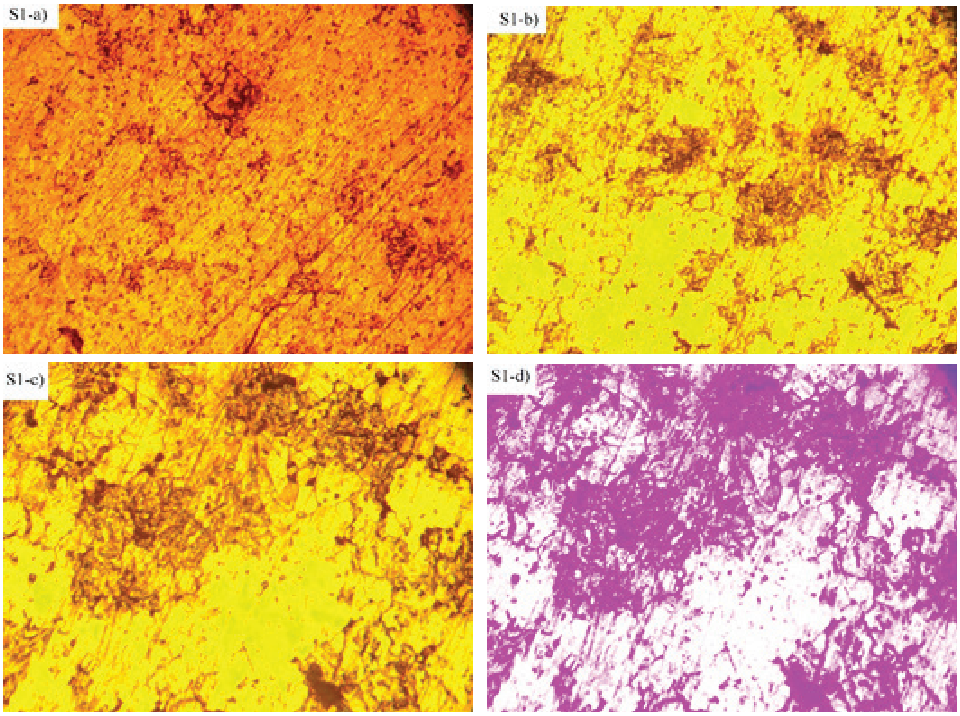

Figure 2. *Optical View of Pure Copper Sample*

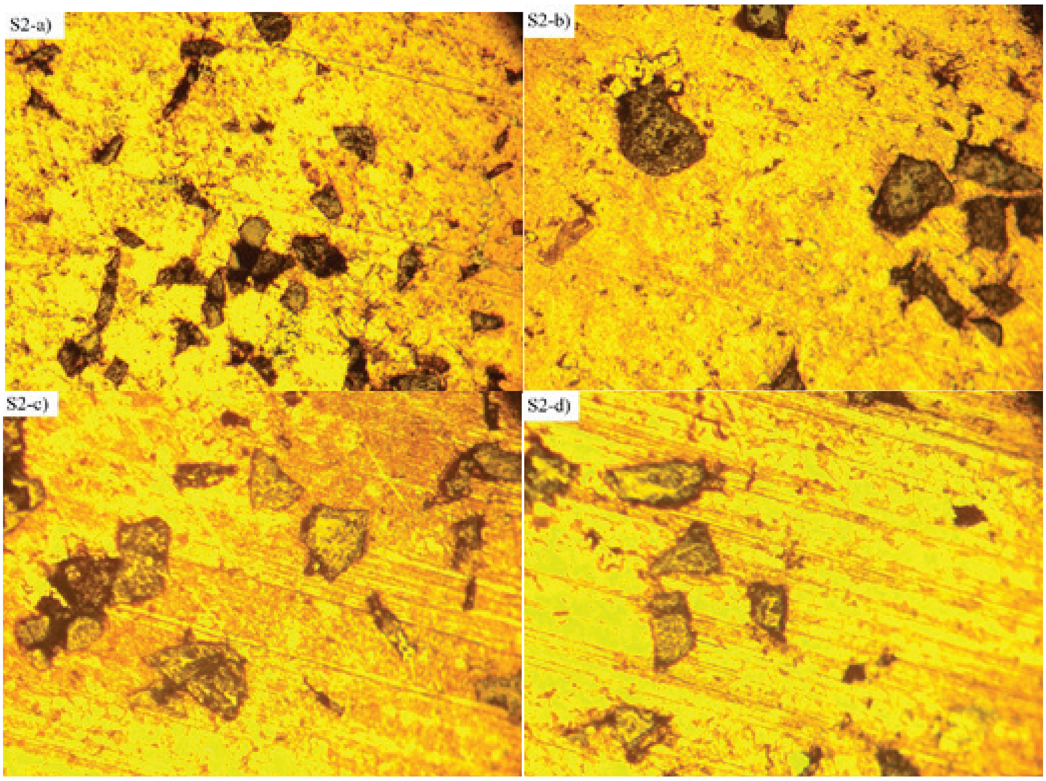

Figure 3. *5% SIC Reinforced Copper Matrix Sample*

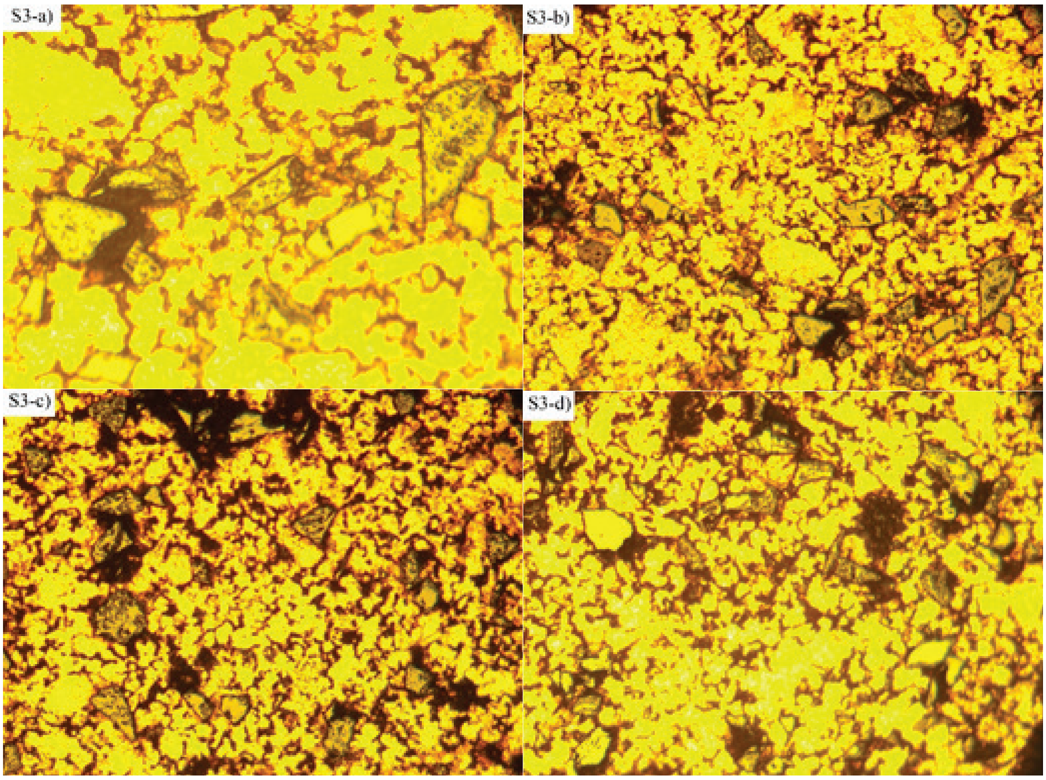

Figure 4. *10% SIC Reinforced Copper Matrix Sample*

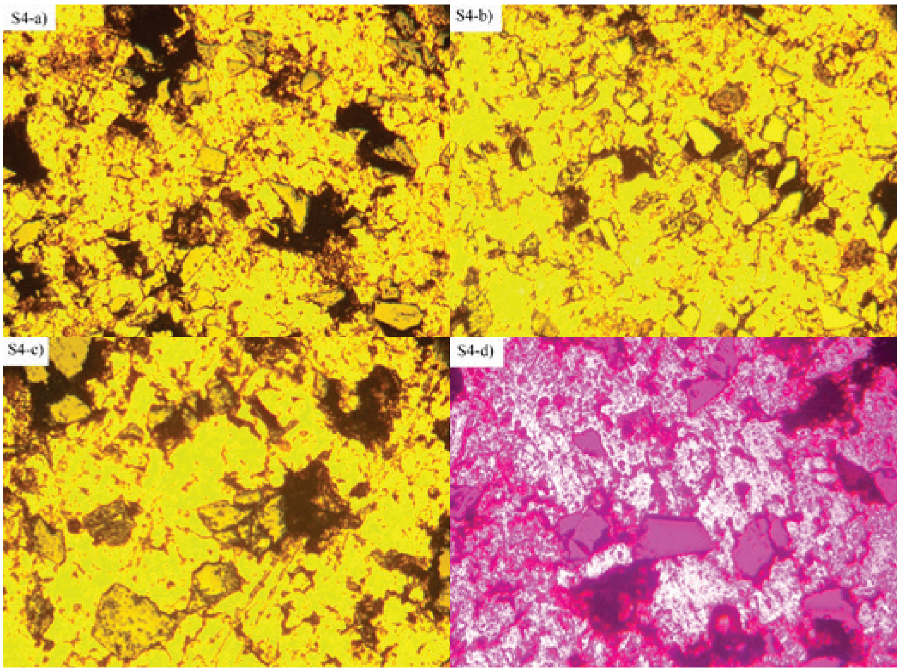

Figure 5. *15% SIC Reinforced Copper Matrix Sample*

While the average hardness value is 50 (HV) in the sample numbered S1 without SIC reinforcement, it is observed in Figure 6 that the hardness of the samples with SiC added increases by around 16-18% in the sample numbered S2, but by around 60-64% in the samples numbered S3 and S4. It is also clearly seen in the given average hardness graph that the average hardness values of copper matrix composites increase with the increasing SiC ratio according to the SIC reinforcement ratio.

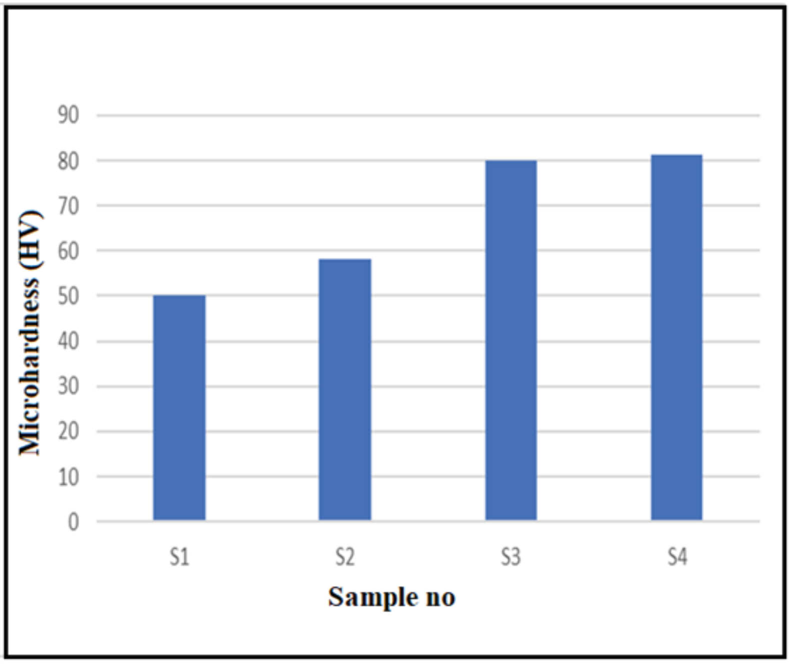

Figure 6. *Microhardnes result of Samples*

The SEM images of the samples are given in Figure 7 when this results examined, it is seen that the SiC particles do not exhibit a homogeneous distribution.

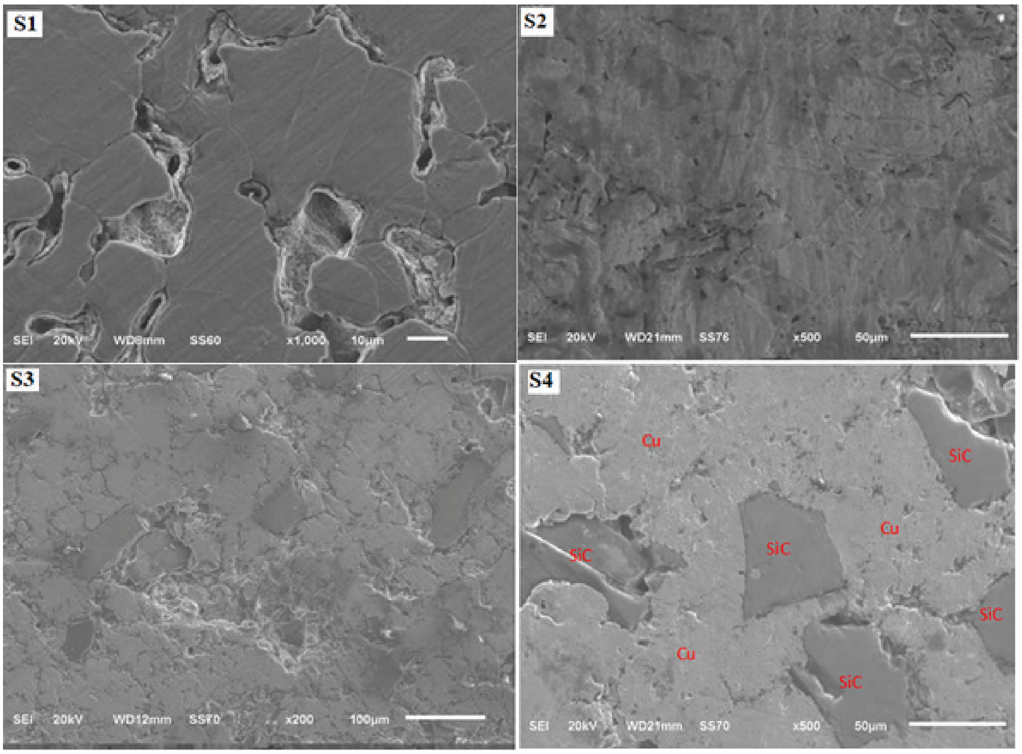

Figure 8. *SEM images of Samples*

4. Conclusion and Recommendations

As a result of the friction welding processes, it was found that the samples produced without the addition of SiC were slightly more suitable for joining with copper material, but there was no union in all of the samples produced by adding SiC, and many trials were inconclusive. As a result, it was concluded that copper matrix SiC added composites produced using pure copper material and powder metallurgy method are difficult and problematic to join with friction welding.

It was observed that the hardness value of the material increased as the percentage of silicon carbide in the samples increased. SiC particles not only reduced the density of the composite material, but also increased the mechanical properties of copper. However, it reduced the weldability of copper.

In our study, the following reasons are listed as the reason why the merger did not take place;

1. Different melting points of the materials (Copper/Melting point 1.085 °C, Silicon carbide/Melting point 2.730 °C)
2. The atomic structures of the materials are different
3. The absence of intermediate structure in the materials, only melting for the material with a low melting point

4. Low weldability of composite materials
5. Different heat conductivity coefficients (Copper/Thermal Conductivity Coefficient 385 W/m.k, Silicon carbide/ Thermal conductivity Coefficient 50-100 W/m.k)
6. Dispersion of the material when friction pressure is applied in friction welding References

References

Ersoy, H.Y. (2001). Kompozit Malzeme, Literatür Yayınları, İstanbul, 44-62.

Kaw, A.K. (2014). Kompozit Malzeme Mekaniği, Efil Yayınları, Ankara, 10- 84.

Kaya, B. (2014). Investigation and Characterization Studies of Mechanical Alloying and Sintering Processes of Al7si-Xb4c and Al7si-Xzrb2 (X= 5%, 10% and 15%) Composites. Master Thesis, Department of Advanced Technologies, Istanbul Technical University, Istanbul, Turkey

Kirik, I. (2012). Investigation of Electrochemical Corrosion Behavior of AISI 1040/AISI 304 L Steel Coupled by Friction Welding. Ph.D. Thesis, Fırat University, Department of Metallurgy Education, Elazig, Turkey

Kirik, I. (2015) Effect of temperature on microstructure and mechanical behavior of diffusion bonded Armor 500 and AISI 1040 steels, Materials Testing, vol. 57, no. 4, pp. 296-300. doi:https://doi.org/10.3139/120.110716.

Kurt, A. (1996). Welding of Bronze Bed Made of Powder Metal to Low Carbon Steel by Diffusion Welding. Ph.D. Thesis, Fırat University, Department of Metallurgy Education, Elazig, Turkey

Ozdemir, N. (2002). Investigation of Compatibility of Grain-Reduced Low Alloy High Carbon Steels by Friction Welding, Ph.D. Thesis, Fırat University, Department of Mechanical Education, Elazig, Turkey

Sarsilmaz, F., Ozdemir, N., & Kirik, I. (2012). Evaluation of microstructure and fatigue properties of dissimilar AA7075/AA6061 joints produced by friction stir welding, Kovove Material, 50, 259–268. doi:10.4149/km.2012.4.259.

Sahin, A. Z., Yılbas, B. S., Ahmed, M., & Nickel, J. (1998). Analysis Of The Friction Welding Process In Relation To The Welding Of Copper And Steel Bars. Journal Of Materials Processing Technology, 82, 127-136.

Toptan, F. (2006). Production of Aluminum Matrix B4C Reinforced Composites by Casting Method. Master Thesis, Yıldız Technical University, Department of Metallurgical Engineering, Istanbul, Turkey

Yilmaz, N. (2006). Machining of Iron Based Powder Metal Materials. PhD Thesis, Süleyman Demirel University, Department of Mechanical Engineering, Isparta, Turkey.

Coating of AISI 1040 steel with Ni-based SiC reinforced ceramic powders by TIG Welding

İhsan KIRIK1, Fadile BULUT2 and
Anıl İMAK3*

1Bingol University, Vocational High School of Technical Sciences, Department of Machinery, Bingol, Turkey, ikirik@bingol.edu.tr
2Bingol University, Faculty of Engineering and Architecture, Department of Mechanical Engineering, Bingol, Turkey,
*3*Bingol University, Faculty of Engineering and Architecture, Department of Mechanical Engineering, Bingol, Turkey, aimak@bingol.edu.tr*

Abstract: In this study, coating of AISI 1040 steel with Ni-based SiC reinforced ceramic powders by TIG Welding Method was investigated. It is aimed to improve the surface properties by coating AISI 1040 steel with TIG Welding Method. Thus, it is aimed to extend the service life of AISI 1040 steel against factors such as abrasion and friction and to reduce maintenance costs. The effects of SiC reinforcing powder ratio and production parameters on the microstructure properties of the formed coating layer were investigated. Transitions and microstructural changes between the coated material and the coating layer were investigated using Optical microscope (OM), Scanning electron microscope (SEM), Energy Dissipative Spectroscopy (EDS) and X-ray diffractometer (XRD) processes.

1. Introduction

With the technological developments, the interest in surface engineering is increasing day by day in order to improve the surface properties of materials and to gain new properties. Surface modification processes are required to prevent or minimize undesirable effects such as wear, corrosion and friction that occur on materials depending on the technical area of use. The created surface layers not only improve the mechanical properties of the surface, but also make them more resistant to the environment in which they will be used, and eliminate undesirable negative effects, moreover give them a decoratively beautiful appearance. In cases where the material surface must be hard and wear resistant, the substrate must be ductile and of sufficient strength; preferably surface hardening or surface coating methods are applied (Buytoz, 2006).

Materials may deteriorate in their environment as a result of environment-surface interaction. Any physical and chemical reaction between the material and the environment can cause damage to the material. Surface treatments have found the most common usage area among iron and iron-based products. It is possible to divide the surface treatments into two classes as coating and surface transformation processes. Plating is the process of forming a shell by depositing an element or compound on the metal surface. In surface transformation processes, the internal structure and/or chemical structure of the surface is changed (Kilic, 2021). Especially in the last few years, the use and development of ceramic reinforced metal matrix composite coatings have attracted the attention of many researchers and industrialists, due to their better wear, corrosion and other mechanical-physical properties. To produce metal matrix composite (MMC) coating; Many methods are used, such as plasma spray, laser coating, tungsten inert gas and surface alloying (Wang, 2016).

TIG coating method is the most practical and does not require much cost among these methods. In addition, TIG coating process stands out as it offers a deeper melting point compared to methods such as laser, plasma and electron beam welding, is much easier to use in atmospheric environment, and moreover, it provides the opportunity to control the thickness, chemical composition and properties of the coating compared to other processes. (Kilic, 2020).

TIG coating or alloying method is seen as an alternative method in ceramic coating to metallic materials, where surface properties are improved by melting the powder mixtures placed on the substrate material surface (Chen, 2009).

In this study, coating of medium carbon steels with nickel-based SiC reinforced powders will be carried out in the light of the literature. In this study, it is aimed to coat silicon carbide powders and improve their surface properties with TIG coating method. At the same time, analysis tests of the coated materials will be carried out and information will be obtained about the materials coated with the different SiC reinforced.

2. Material and Methods

In this study, the surface of AISI 1040 Medium Carbon Steel, whose chemical properties are given in Table 1, was coated with TIG Welding method. It is aimed to improve the surface properties of AISI 1040 steeel. NiAlBCr powder (average particle size 50-150 µm) was used primarily for coating. In the experimental study, a group of coatings were coated at different percentages. The effect of the ratio of Ni-based SiC ceramic-reinforced powders and production variables on the microstructure and mechanical properties of the formed coating surface was investigated.

The chemical composition of the NiAlBCr powder used in the study is given in Table 2. Approximately 25 g of powders were measured from the NiAlBCr powder used as the main powder component. Five different samples were prepared, weighing 25 g. 21.5 gr for Nickel powder, 1 gr for Aluminum powder, 0.5 gr for Boron powder and 2 gr for Chromium powder, which are valid for all of these samples, were added and measured on a precision balance. SiC powders were added in different ratios of 1%-3%-5%-7% to five separate NiAlBCr powder mixing cups and the measurement was made on a sensitive balance. The proportions of the powders are given in Table 3 below. After the samples were dried in the oven, the coating was made on the steel material surface using the TIG welding method and argon gas, using the parameters given in Table 4.

Transitions and microstructural changes between the coated material and the coating layer were investigated using Optical microscope (OM), Scanning electron microscope (SEM), Energy Dissipative X-Ray Spectroscopy (EDS) and X-ray diffractometer (XRD) processes. In order to determine the mechanical properties, microhardness measurements were made and the effects of the test parameters on the results were determined.

Table 1. *AISI 1040 chemical properties of AISI*

C (%)	Mn (%)	Fe (%)	Si (%)	S (%)	P (%)
0.427	1.01	97.82	0.252	0.0205	0.0257

Ni (gr)	Cr(gr)	B (gr)	Al (gr)
21.5	2	0,5	1

Table 2. *Mixing ratios of NiAlBCr powder (gr).*

Samples	Mixture weights (gr)
S1 (NiAlBCr)	25 gr
S2 (NiAlBCr) %1 SiC	25+0.25=25.25 gr
S3 (NiAlBCr) %3 SiC	25+0.75=25.75 gr
S4 (NiAlBCr) %5 SiC	25+1.25=26.25 gr
S5 (NiAlBCr) %7 SiC	25+1.75=26.75 gr

Tablo 3. *Formed powder mixing ratios.*

Shielding gas type	Argon
Shielding gas flow rate (atm)	6
Current type	DC
Torch size (morph) 2.4	2.4
Initial Amps	80
Departure second	1sn
End Amps	80
Transition from 1st Amp to 2nd Amp	4sn

Table 4. *Parameters used for TIG coating*

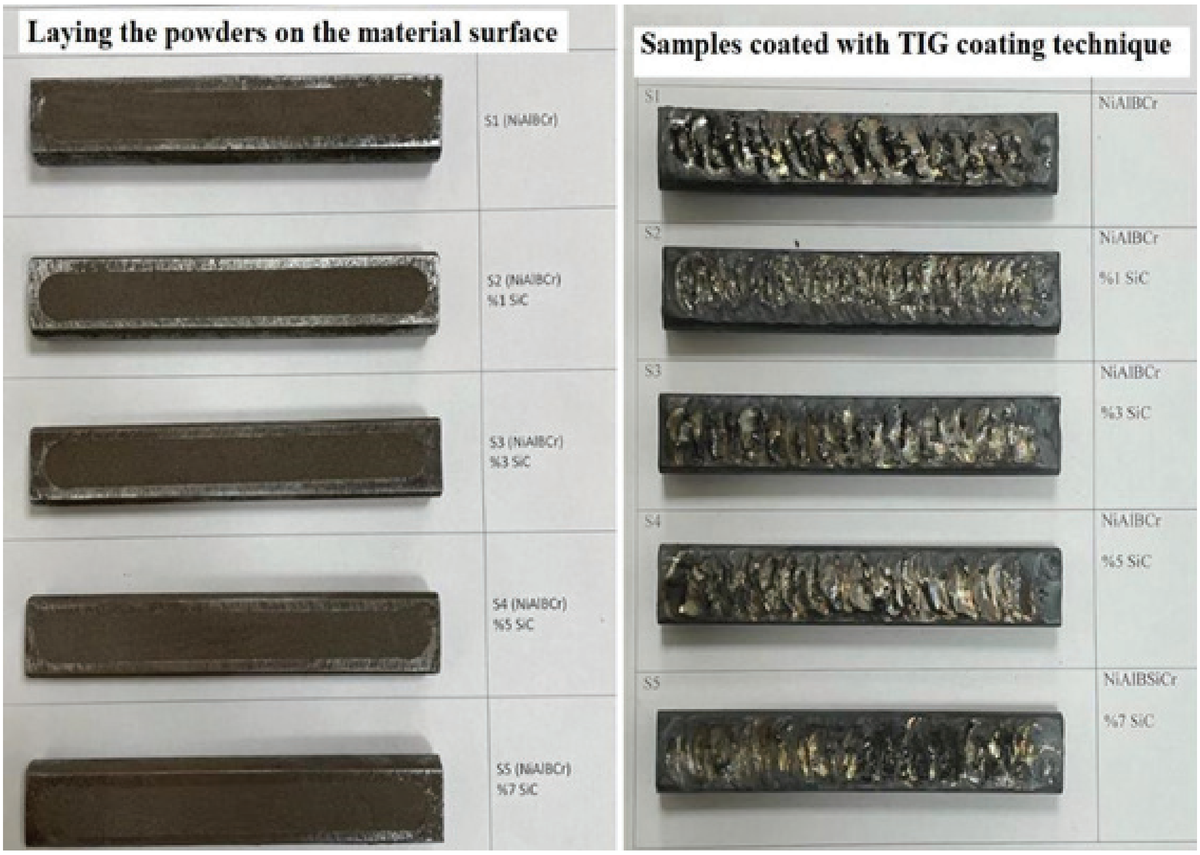

Figure 1. *Macro images of coated samples.*

3. Results and Discussion

3.1. Macro analyses of NiCrBAl-XSiC coated samples.

3.2. Optical examination of NiCrBAl-SiC coated samples.

Optical image of sample S1 coated with NiAlBCr powder on AISI 1040 steel surface with TIG coating method is given in the figure 2. When the optical picture is examined, it is clear that there is a transition zone between the AISI 1040 steel material and the coating zone, and the solidification is in the form of grains extending perpendicular to the transition zone. It can be said that this transition is non-linear and also includes AISI 1040 material. Solidification appears to be from more spherical grains towards the coating surface. No cracked structure was observed between the coating area and the substrate. As seen in the coating layer, it is clear that NiCrBAl used as coating powder dissolves completely and forms an alloy with the substrate and is a completely new structure. In addition, according to Buytoz et al. (2013), the powders were completely dissolved and M7C3 carbides were formed at high powder rates in the study they coated the stainless steel surface with SiC powders with the HVOF coating method. However, according to Serkan et al. (2008), they performed the coating process using NiTi powder on the AISI 304 stainless steel surface using three different plasma arcs. They stated that the coating area consists of four different regions. These regions are named as coating zone (CZ), transition zone (TZ), heat affected region (HAZ) and base material (BM). It was observed that there was a microstructure similar to this study in the coating process.

Optical picture of sample S2 coated by adding 1%SiC powder to NiAlBCr powder is given in the figure 3. As can be clearly seen in the figure, when looking from the substrate to the coating, it is seen that a transition intermediate zone is clearly present at the interface. When going from the transition zone to the coating zone, SiC particles that did not dissolve completely were found. It is seen that SiC particles are spread in the structure due to heat and molten metal, and SiC particles are irregularly dispersed in the microstructure as small particles. The coating process of the steel material with the TIG method is based on the dissolution of coating powders, which have a suitably similar composition, on the substrate surface. Melting occurs simultaneously in both the coating layer and the substrate. During the melting process, solidification occurs rapidly and metallurgically bonds the modified coating material with the base metal (Korkut et al. 2002). Therefore, it is clearly seen that NiAlBCr- 1%SiC powders do not partially melt on the transition zone and coating layer surface. It is clear that the transition zone forms a root-like structure towards the substrate and there is no distinct line. In the coating region, it was observed that the dendritic structure expanded and elongated from the intermediate region to the upper part. In addition, it has been determined

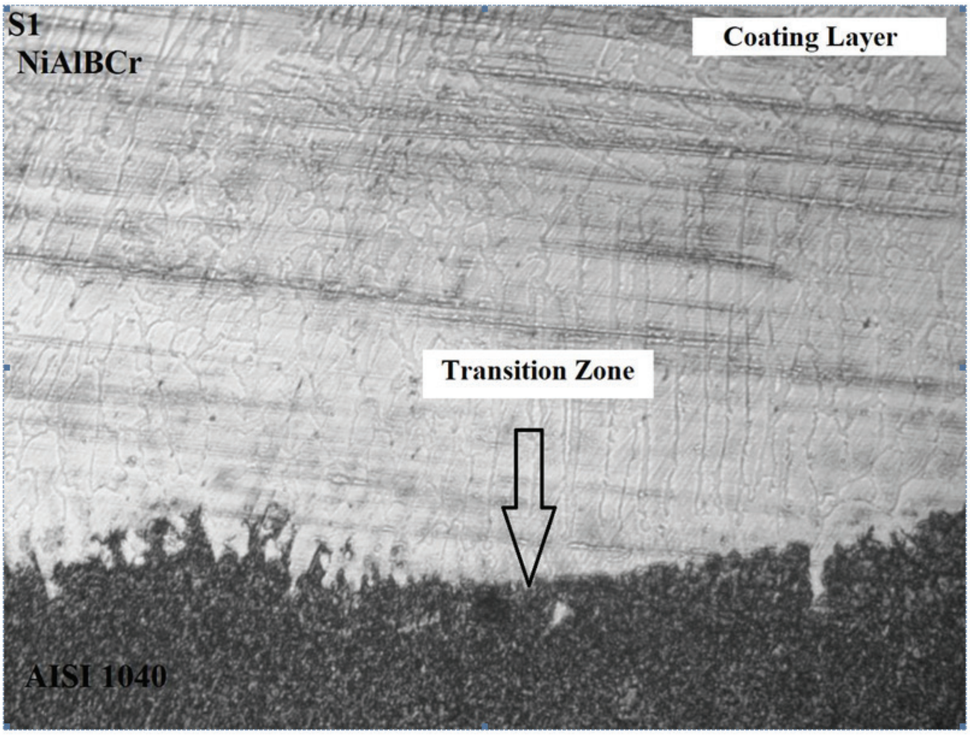

Figure 2. *Optical image of S1 Sample coated with NiCrBAl powder*

that there is an intermediate zone with a different feature between the coating and the substrate in the transition region. Kilic et al. (2020) in their study titled “Coating boron and ekoboron powders on the stainless steel surface with PTA method,” stated that the coating area is dendritic and the powders used are completely dissolved.

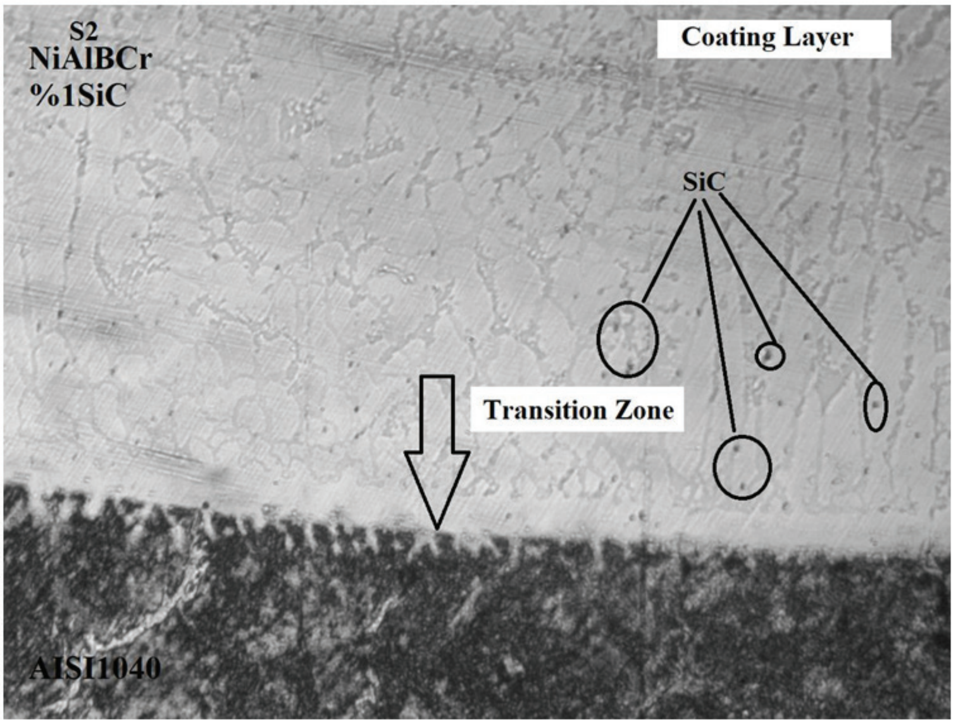

__Figure 3.__ Optical image of S2

The optical image of the sample with NiCrBAl %3 SiC is shown in the Figure 4. When the transition between the AISI 1040 steel material coated with TIG welding method and the coating is examined, it is seen that it consists of three regions: the substrate material, the transition zone and the coating layer. It can be said that there is a regularly progressing transition zone between the backing material and the covering material. In the S3 sample, as in the S2 sample containing 1%SiC, non-melting SiC particles stand out. In coatings made with TIG coating process, it can be said that the powders melting in the appropriate current and environment exhibit a solidification compatible with the microstructure. As a result of the rapid solidification, it was observed that the dendritic solidified upwards from the coating boundary and small-grained microstructures were formed in the structure. Mridha et al., in their study of intermetallic coating produced by TIG surface melting, stated that melting in low energy current (50A) is generally collected in the area of the coated area and there is a thin layer in the melt pool. Pores and voids were found on the coating surface. As a result of this; this is due to the fact that the powder mixture does not completely melt during TIG coating. Since the melting did not occur completely, dust particles were seen on the coating surface. (Mridha et al. 2001)

The optical image of the S4 sample coated with the addition of 5%SiC to NiCrBAl powder is shown in Figure 5. While coating the steel material with the TIG welding method, the dust particles give the heat to the main material and solidify at the moment of contact. An insoluble SiC particle is seen in the coating region. The non-melting SiC particle cooled rapidly on the surface of the coating zone, causing solidification. Therefore, this solidification gradually caused the coating powders to agglomerate and showed itself in the structure. Orhan 2008, in his study of the wear and microstructure properties of the iron-based coating layers produced by the TIG coating process, when the optical pictures of the coatings made with 66% Cr FeCrC powder are examined in general, the melting process of the FeCrC mixture powders with 66% Cr content is as expected. As a result, different current values in the coating process and increased due to the increase in current values, and when the current value is low, there are small and small amounts of certain agglomerations in the cross-sectional areas of the coating samples. The factor that causes this agglomeration is due to the fact that the current values of the coating process and the actual production speed are not very sufficient during the TIG coating method on the material surface. Due to the low welding current, the melting process could not be performed completely at the point where the coating was made. Therefore, FeCrC mixture powders do not dissolve completely and exist in a certain number in the structure, and in this case, the existence of an inhomogeneous agglomeration is striking (Orhan 2008).

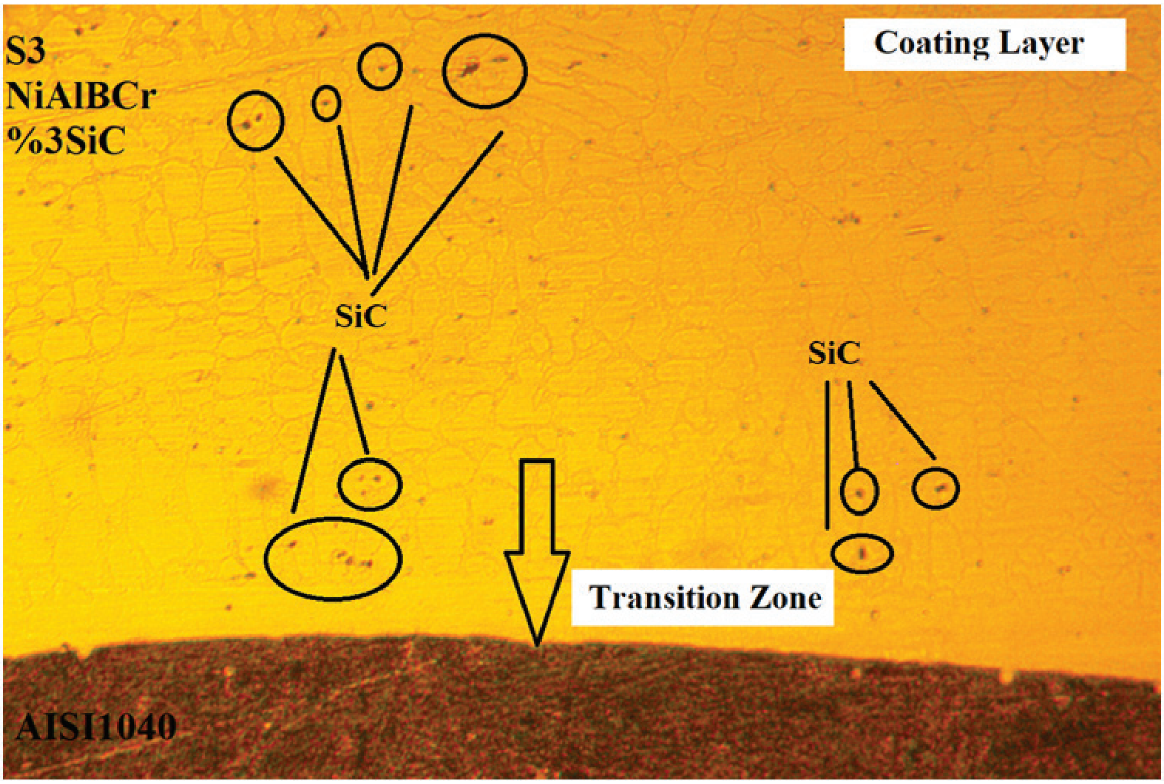

Figure 4. *Optical image of S3*

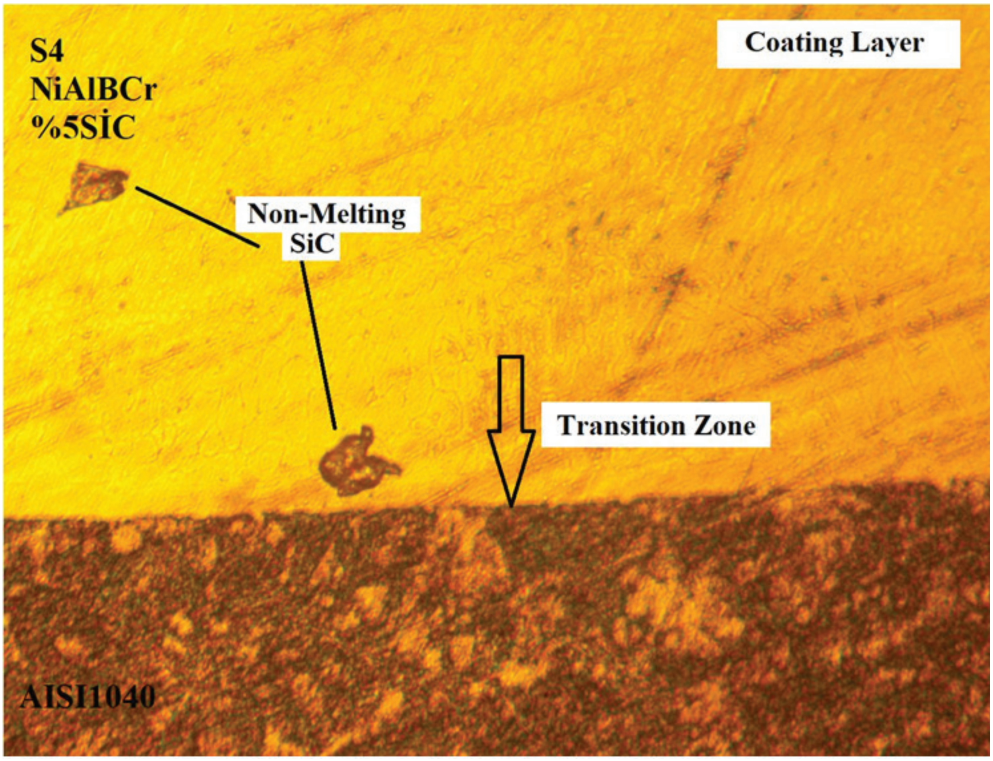

Figure 5. *The optical image of the S4 sample coated with the addition of 5%SiC to NiCrBAl powder*

The optical image of the sample S5 produced by dissolving the powder mixture prepared by adding 7%SiC powder to NiCrBAl powder by TIG coating method is given in Figure 6. As can be seen from the optical image, there is a very distinct transition zone in the interface region formed between the coating region and the substrate. No voids, cracks or undissolved SiC particles were found in the optical image. It can be said that the coating process is close to the desired microstructure and the coating has been done successfully. Dendritic formations and martensite formations seen in the microstructure attract attention. The martensite particles formed in the structure of the steels can occur in two different forms as layers or laths micro-structurally. In Low and Medium Carbon steels, lath type martensite formation is in parallel arrangement or in the form of lath aggregates or lath-shaped grains. Most grains in the form of parallel groups have the same crystallographic orientation (Jha et al. 2003).

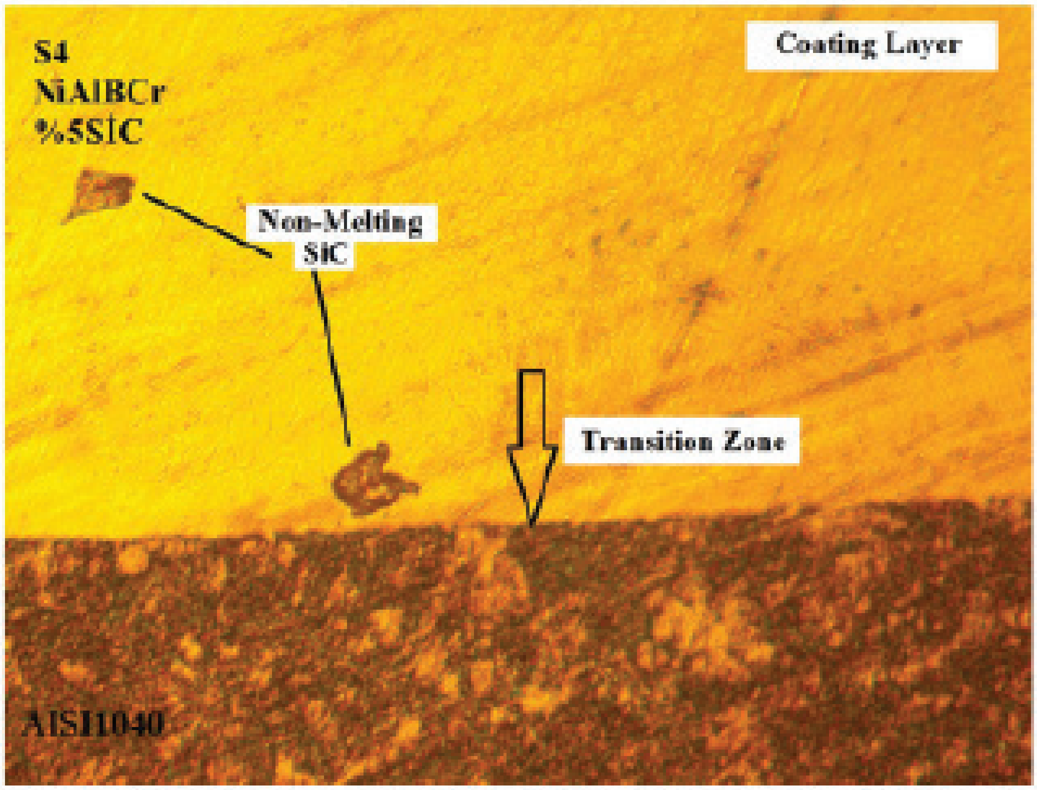

***Figure 6**. Optical image of S5 sample containing with NiCrBAl-SiC (wt.%7)*

3.3. SEM Analysis of samples coated with NiCrBAl and NiCrBAl + XSiC (1, 3, 5 and 7 wt.%) powders

SEM image of samples coated on medium carbon steel surface using NiAlBCr +XSiC powder with TIG welding method is given in Figure 7. It can be said that the micro-voids formed in the substrate material are due to the coating after melting and solidification. It is visibly important that the porous structure is almost absent in the coating material. It is clear that the structure of the coating material is fibrous and interlocking acicular martensitic, as can be clearly seen from the SEM image taken at high magnification.

It is seen that the SiC particles seen in the substrate material, which are seen in the medium carbon steel material coated with the TIG welding process, rapidly cool down and solidify, and exist as small particles and they do not dissolve completely. It can be seen that there is a small amount of micro-void structure in the base material. On the contrary, there is no cracked structure or a defective microstructure. Kırık et al. (2019) in study of coated St.52 steel in different powders with WC reinforcement by TIG welding method. In this study, they predicted that the depth of alloy formation and characteristic structures vary depending on the ratios and types of coating powders. In the SEM images they examined, they deduced that there was no cracking, no matter how many micro-voids on the sample surfaces. On the surface of AISI1040 medium carbon steel, there are rooted structures from the transition zone to the substrate. It is clear that there are a large number of SiC particles seen on the surface. It can be said that SiC particles are partially dissolved in the coating material based on the EDS analyzes taken. Insoluble SiC particle is seen in the coating layer. The unmelted SiC particle formed a solidification by cooling in a way that caused rapid solidification in the coating.

During the coating, it can be said that three basic regions are formed in accordance with the literature (Buytoz et al 2013). The coating layer is in the form of substrate and transition zone. It is said that NiAlBCr %3SiC particles form an alloy within the microstructure of the substrate. It is important that micro-void structure is encountered on the substrate surface, but there is no cracked structure. Special et al. (2008) investigated the microstructures of NiTi powders on the stainless steel surface using the plasma transferred arc method. In this study, four different regions occurred during the coating; They explained that it is in the form of coating layer, interface zone, heat affected zone (HAZ) and substrate. They stated that no cracks or pores were observed in both the coating layer and the interface. In a previous study, it was reported that small pores were detected in the NiTi coating layer produced by the TIG process, and weak bonds caused the formation of pores in the coating layer. It is clear that the SiC powder particles in the coating layer microstructure given in the figure are at the grain boundaries in the austenitic structure and are irregularly distributed. It has been observed that its structure has an appearance resembling a honeycomb.

The SEM image of the mixture of NiCrBAl+%5SiC powders belonging to the S4 sample on the surface of the AISI1040 material coated with TIG Welding process is examined. It is important that there are not too many micro-voids in the coating layer compared to other samples and that no cracked structure is encountered. It can be said that there are very few SiC particles on the coating surface and there is no obvious structure on the surface. The dendritic structure formed in the main material stands out to a great extent. It is assumed that dust particles appearing in the substrate are present and effectively alloy with the coating material. No cracked structure was observed in the base material.

The surface of AISI1040 Medium carbon steel, which is mixed with NiAlBCr %7SiC powder, is coated with TIG welding process. The microstructure SEM image of the S5 sample is analyzed. Sample S5, which consists of three regions, has a clear transition region formed at the substrate, the coating layer and the interface. It is thought that light and dark gray areas are seen in the horse material and they are in different phases. It is said that the matrix forms a Ni-based dendritic structure. There are numerous presences of NiCrBAl+ %7SiC particles in the backing material. It is said that the dust particles formed in the transition zone do not completely melt and solidify and exhibit a dendritic structure. There is a dendritic and ferritic structure on the surface of the 10µm coating layer given in the figure. No cracked structure was observed in the different phases formed on the coating lamellas. It is clear that an effective binder is effective between the backing material and the coating layer. Therefore, it can be said that the coating parameters are suitable.

Figure 8. SEM Analysis of S1, S2, S3, S4 and S5 samples coated with NiCrBAl and NiCrBAl + XSiC (1, 3, 5 and 7 wt.%) powders

3.4. EDS Analysis of Microstructure Samples

EDS results of S1 sample coated with NiCrBAl reinforcement powder are given in Figure 9 and Table 5. When the EDS results are examined, it is seen that Ni, Fe, Mn, Cr, Ti, Al, C elements are dominant in the coating layer. In the EDS diffractogram and analysis, it can be said that Fe and Ni elements are rich in weight. Thus, it is clear that the backing material and the coating material are well covered by the TIG welding process. The presence of Cr element and C elements, which are 5.47% by weight, indicates the presence of inter-metallic compounds in the structure.

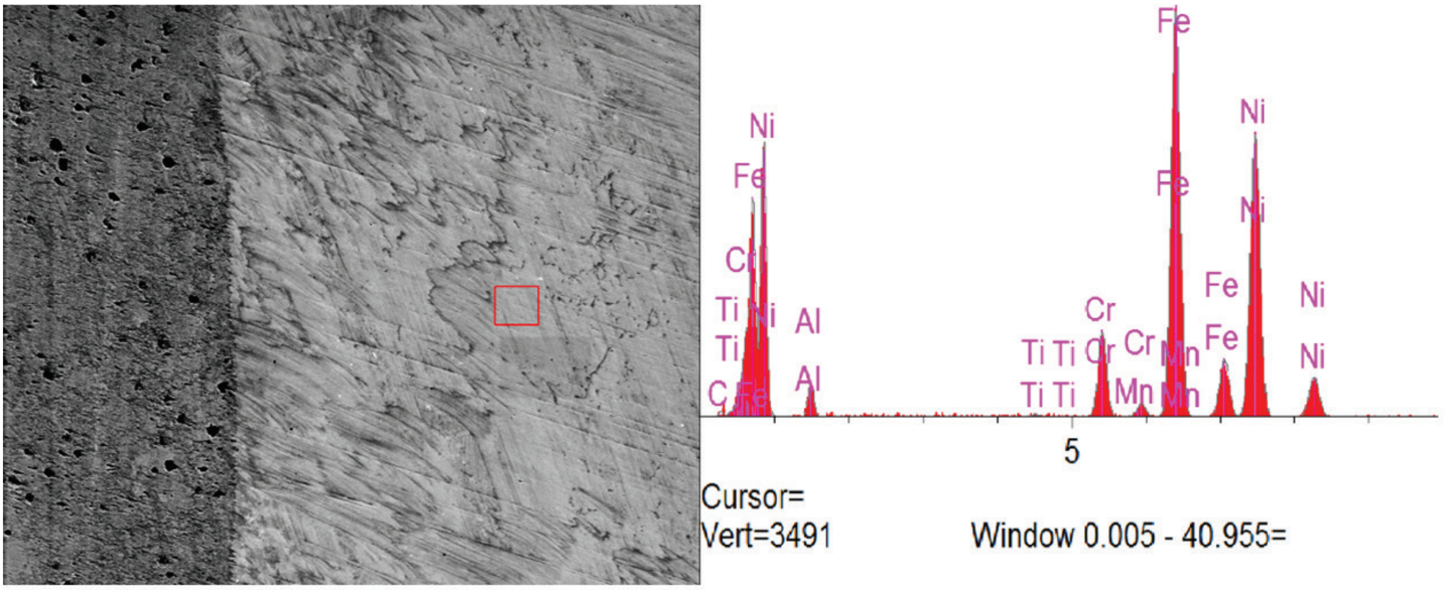

Figure 10. *EDS analysis of S1 sample coated with NiCrBAl*

Elt.	**Line**	**Intensity (c/s)**	**Error 2-sig**	**Conc**	**Units**	
C	Ka	11.88	2.628	1.658	wt.%	
Al	Ka	87.72	5.020	2.418	wt.%	
Ti	Ka	9.73	4.148	0.150	wt.%	
Cr	Ka	331.49	7.662	5.477	wt.%	
Mn	Ka	7.52	3.849	0.162	wt.%	
Fe	Ka	1,710.94	15.521	41.865	wt.%	
Ni	Ka	1,276.22	13.472	48.270	wt.%	
				100.000	wt.%	Total

Table *. EDS result of S1 sample*

DS analysis of the coating layer produced with NiCrBAl+3SiC powder by reinforcing 3% SiC is given in the Figure 11 and Table 6. When the optical pictures and EDS analyzes of the modified upper layer are examined, it has been determined that there are graphite grains containing iron, chromium and silicon, which are located between the dendrites in some regions in the coating layer and are not yet dissolved, and contain a small amount of metal carbide. While a supra-eutectic structure rich in Si element predominates in the intercarbide regions, the carbides were formed rich in C, Si, Fe and Cr contents. Compared to the S2 sample, it was observed that the Si ratio in the matrix/coating layer increased by weight. While not only the Si element has increased, the Cr element is also found to be more in weight than the S2 sample. Looking at the literature; When NiCrBSi–SiC SAE 1030 steel surface is sprayed with Oxygen Fuel (HVOF) on the coating surface, the NiCrBSi and SiC coating powder mixture decomposes due to the high temperature and then resolidifies to form new phases. The main phase of the coating is austenite rich in Ni, Cr, C and Si. They found that the structure. They stated that the probability of this structure being Cr7C3 is quite high. (Buytoz et al. 2013). EDS results support the presence of CrxCy carbides.

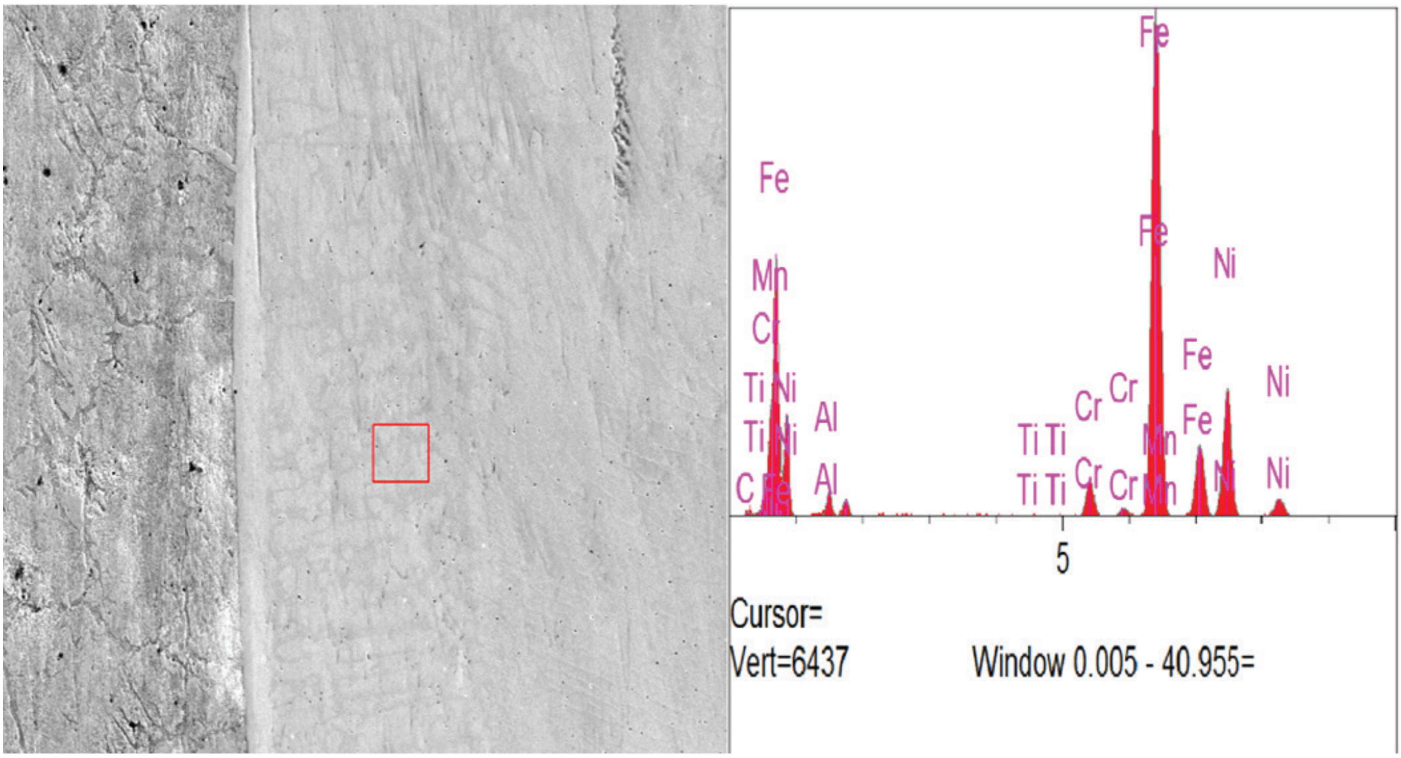

Figure 12. *EDS analysis of the coating layer produced with NiCrBAl+3SiC powder*

3.5. Microhardness Analysis

After the samples were sanded, their hardness was taken in the micro-hardness device on the line given in the Figure 13. Hardness measurements were made from different regions of the surface of all samples and average values were taken. The average coating hardness of the S1 sample (NiCrBAl) has a hardness value of 373.73HV. The mean hardness of the S2 sample, which was coated using NiCrBAl-1%SiC powder, was measured at 359.5 HV. The hardness value of the S3 sample (NiAlBCr-%3SiC) was 320 HV. The hardness value of the S4 sample (NiCrBAl -5%SiC) was measured as 368.4 even though it was the amount of dust. In the measurements made, the S1 sample without SiC reinforcement was higher than the other S2, S3, S4 coded samples. S5 sample with NiCrBAl -7%SiC ratio was measured at 488.1HV and gave the highest average hardness.

Table 6. *EDS results of S3*

Elt.	Line	Intensity (c/s)	Error 2-sig	Conc	Units	
C	Ka	18.91	3.003	1.999	wt.%	
Al	Ka	95.39	5.309	1.986	wt.%	
Si	Ka	72.38	5.235	1.182	wt.%	
Ti	Ka	6.50	4.554	0.075	wt.%	
Cr	Ka	208.76	6.773	2.386	wt.%	
Mn	Ka	26.63	4.498	0.456	wt.%	
Fe	Ka	3,225.66	21.105	65.156	wt.%	
Ni	Ka	870.87	11.400	26.760	wt.%	
				100.000	wt.%	Total

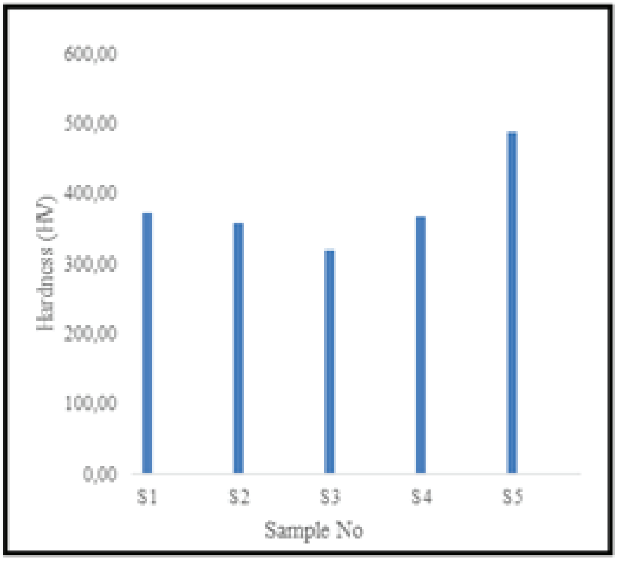

Figure 13. *Hardness measurements*

4. Conclusion

The results obtained by coating AISI 1040 steel with Ni-based SiC reinforced ceramic powders by TIG Welding Method are given below;

When the optical pictures is examined, it is clear that there is a transition zone between the AISI 1040 steel material and the coating zone, and the solidification is in the form of grains extending perpendicular to the transition zone. It can be said that this transition is non-linear and also includes AISI 1040 material. Solidification appears to be from more spherical grains towards the coating surface. No cracked structure was observed between the coating area and the substrate.

Coating area consists of four different regions. These regions are coating zone (CZ), transition zone (TZ), heat affected region (HAZ) and base material (BM). It was observed that there was a microstructure similar to this study in the coating process.

The SEM images show that the material is martensitic with a quality and similar interlocking needles. It is seen that the SiC particles seen in the substrate material, which are seen in the medium carbon steel material coated with the TIG welding process, rapidly cool down and solidify, and exist as small particles and they do not dissolve completely. It can be seen that there is a small amount of micro-void structure in the base material. On the contrary, there is no cracked structure or a defective microstructure.

When the sample S1 is seen, it is seen that Ni, Fe, M, Cr, Ti, Al, C elements are dominant in the coating layer in the EDS appearance. The structural structures of element Cr and element C, which are 5.47% by weight, are indicators of their intermetallic appearance.

In the hardness analysis, the highest average value was measured as 488.1Hv in S5 samples in NiCrBAl -7%SiC.

Acknowledgements

References

Buytoz, S. (2006). Microstructural properties of SiC based hardfacing on low alloy steel. Surface & Coatings Technology, 200 (12-13), 3734–3742.

Buytoz, S., Orhan, A., Gur, A., & Caligulu, U. (2013). Microstructural development of Fe–Cr–C and B4C powder alloy coating on stainless steel by plasma-transferred arc weld surfacing. Arabian Journal for Science and Engineering, 38(8),2197–2204.

Chen, J. H., Chen, P., Lin, C. M, C., Chang, C. M, C., & Chang, Y. (2009). Characterization of multi-element alloy claddings manufactured by the tungsten inert gas process. Surface and Coatings Technology, 203(20-21), 2983-2988.

Jha, A., Prasad, B., Modi, O., Das, S., & Yegneswaran. (2003). Correlating microstructural features and mechanical properties with abrasion resistance of a high strength low alloy steel. Wear, 254 (1-2),120-128.

Kilic, M. (2020). TiC coatings on an alloyed steel produced by thermal diffusion. Materials Testing, 62(9), 909-912.

Kilic, M. (2021). Microstructural characterization of Ni-Based B4C reinforced composite coating produced by tungsten inert gas method. Archives of Metallurgy and Materials, 66(3), 917–924.

Kilic, M., Imak, A., Kirik, I., Okan, C., & Balalan, Z. (2020). Boron and Ekabor III coating of AISI 316 stainless steel by PTA surface alloying. Journal of Materials and Electronic Devices , 3(1),14-19.

Kirik, I., Balalan, Z., Andan, Y., & Yaz, M. (2019). St52 Çeliğinin TIG Kaynak Yöntemi İle WC Takviyeli Tozla Kaplanması. International Journal of Innovative Engineering Applications , 16-20.

Korkut, M., Yilmaz, O., & Buytoz, S. (2002). Effect of aging on the microstructure and tougof the interface zone of a gas tungsten arc (GTA) synthesized Fe–Cr–Si–Mo–C coated low carbon steel. Surface and Coatings Technology, 157(1), 5-13.

Mridha, S., Ong H, S., Poh L, S., & Cheang , P. (2001). Intermetallic coatings produced by TIG surface melting. Journal of Materials Processing Technology, 113(1-3), 516-520.

Orhan, A. (2008). Investigation into microstructural and wear characteristics of Fe-based coating layers produced with gas tungsten arc method. (PhD), Firat University, Institute of Science, Elazığ, Turkey.

Ozel, S., Kurt, B., Somunkıran, I., & Orhan, N. (2008). Microstructural characteristic of NiTi coating on stainless steel by plasma transferred arc process. Surface & Coatings Technology, 202(15),3633-3637.

Wang, J. L., & Tao, W. (2016). Crack initiation and propagation behavior of WC particles reinforced Fe-based metal matrix composite produced by laser melting deposition. Optics & Laser Technology, 82, 170-182.

Photocatalytic Degradation of Basic Blue 41 in Aqueous Suspension of TiO_2/Graphene Nanocomposite

Betül Çiçek Özkan*

Department of Metallurgical and Materials Engineering, Technology Faculty, Fırat University, 23119 Elazığ, Turkey

Abstract: The preparation of TiO_2/Graphene nanocomposite and investigation of its photocatalytic degradation efficiency on basic blue 41was aimed in this study. TiO_2/Graphene nanocomposite has been produced using an ultrasonic mixing route. The properties of produced TiO_2/Graphene nanocomposite were investigated by X-ray diffraction analysis. The prepared composite was employed as a photocatalyst under UVA irradiation using a specially designed glass batch reactor with an external circulation cooling system and a gas tube. The effect of initial solution pH, catalyst concentration, initial basic blue 41 concentration, and process temperature on the decolorization process by TiO_2/Graphene was studied using a UV-Vis spectrophotometer. However, total organic carbon (TOC) analysis has been employed to detect the presence of organic intermediates and the photodegradation performance of the catalyst. The first-order kinetic model was used to determine kinetic parameters. The results demonstrated that the TiO_2/Graphene nanocomposite is a promising candidate for photocatalytic processes.

Analysis of Some Tribological Properties of Canola Oil in Two-Stroke Gasoline Engines

Arzu KEVEN[*1] and **Rabi KARAALI**[2]

[1]*Dep. of Vehicle and Transp. Technol., Golcuk Voc. High School, Kocaeli University, Kocaeli, Turkey.*
[2]*Dep. of Mechanical Engineering, Bayburt University, 69000 Bayburt, Turkey*

Abstract: Vegetable lubricating oil improvement studies are of great interest in the development of alternative oil to polluting fossil-based oils all over the world. In this experimental study, canola oil was used as vegetable lubricating oil in a single-cylinder two-stroke gasoline engine to obtain some tribological properties. For this reason, an experimental engine and a simulation test device were used to investigate some tribological functions of this lubricating oil and the test engine was operated for 100 hours for each selected oil. Mineral oil and canola oil were used as lubricating oil in the test engine. Samples were prepared and SEM analyzes were performed to determine the wear on the cylinder surface. According to the results of the analysis, it has been observed that canola oil increases the wear on the cylinder surface compared to fossil-based mineral oils. Then, the simulation test device was run separately for forty hours for each lubricating oil and cylinder sample. The wear amounts of these samples were determined from the data obtained as a result of the experiments and they were compared.

Keywords: Canola Oil, Cylinder, Wear.

The Synthesis, Characterization, and Catalytic Application of Carbon-Supported Bimetallic NiCo Nanoparticles in the Methanolysis of Ammonia Borane

Tuba TOP[2*], Ahmet BULUT[3], Mehmet YURDERİ[1,4] and **Mehmet ZAHMAKIRAN[3]**

[1]Department of Electronics and Automation, Bartın Vocational School, Bartın University, Türkiye;
[2]Department of Mechanical Engineering, Faculty of Engineering, Architecture and Design, Bartın University, Türkiye
[3]Department of Biotechnology, Faculty of Science, Bartın University, Türkiye
[4]Central Research Laboratory, Research & Application Center, Bartın University, Türkiye

Abstract: Activated carbon supported bimetallic NiCo(0) oleylamine stabilized nanoparticles (NiCo@C) were prepared by colladial method. Identification of the obtained NiCo@C material was carried out using advanced analytical methods such as ICP-OES, P-XRD, XPS, and TEM. The identification results showed that bimetallic NiCo nanoparticles with an average particle size of 5.11 ± 0.54 nm were formed on the activated carbon surface. The catalytic performance of NiCo@C was investigated in the methanolysis reaction of ammonia-borane (NH3BH3) under favorable conditions (25 °C) in terms of activity and stability. We found that Ni0.19Co0.81@C catalyst catalyzes the methanolysis reaction of ammonia borane at high conversion (100%) and with a cycle frequency of 136.65 min-1. Furthermore, activated carbon-supported bimetallic NiCo nanoparticles were found to be highly stable against leaching and sintering, indicating that the NiCo@C catalyst is a reusable heterogeneous catalyst in the ammonia borane methanolysis reaction without losing its effectiveness.

DATA ACQUISITION SYSTEMS (DAQs) IN PHOTOVOLTAIC CELLS

Abdulai Rabiu* and **Prof. Dr. Nuran Doğru**

[1]Gaziantep University, Turkey; 2Gaziantep University, Turkey

Abstract: Solar Energy is one of the most useful resources of renewable energy. The World is committed to increasing the use of renewable energies capable of replacing fossil fuels, diversifying energy sources and reducing carbon dioxide emissions. Technological developments, increased energy demand, reduced fuel supplies, environmental pollution and the highly automated society are factors that have intensified the search for new solutions for energy production. By using data acquisition and applying computer algorithms, it is possible to efficiently and effectively harness this energy system. In order to efficiently analyze the performance of photovoltaic systems, a real-time instrumentation is used whereby the data can be accessible from a personal computer. This paper presents a cost-effective technique necessary for real-time instrumentation of PV panels to enable the measurement and records of various characteristics of panels including the voltage, current, and power using virtual instruments. The system is designed by using a cost-effective Arduino acquisition board to obtain and analyzed values in a Microsoft Excel Streamer via PLX-DAQ data acquisition Excel Macro. This facilitates the exchange of information among the ATMega328 microcontroller of the Arduino UNO board and the UART bus port of the personal computer. Therefore, the characteristics such as I-V and P-V which are in real-time conditions can be acquired and plotted on an Excel spreadsheet without requiring reprogramming of the microcontroller. This work is found to present several beneficial solutions as compared to conventional solutions. One of which is the presentation of real-time data in graphical form.

Keywords: Arduino, PLX-DAQ, PV panel, Instrumentation, Real-time.

Development of A New Liquid-Phase Microextraction Method Based on The Use of Menthol/Decanoic Acid Hydrophobic Eutectic Solvent for Determination of Basic Fuchsin Dye in Water

Funda AYDIN[1] and **Volkan ALKAN**[1]

[1]*Van Yüzüncü Yıl University, Faculty of Pharmacy, Department of Basic Sciences, 65080, Van, Turkey*

Abstract: A new liquid phase microextraction (LPME) method based on the use of hydrophobic eutectic solvent (HES) for spectrophotometric determination (λ_{max} 555 nm) of toxic basic fuchsin (BF) dye in water has been developed as an environmentally friendly, low cost and practical extraction approach. Natural extraction solvent was formed by mixing and heating of biodegradable and nontoxic menthol (Me) and decanoic acid (DeA) components with a molar ratio of 1:2. The formation of hydrogen bonding between Me and DeA was characterized by FT-IR technique. Important analytical parameters affecting the extraction recoveries of analyte such as pH, mole ratio and volume of Me and DeA, type and volume of organic solvent used in dilution, sample volume, vortex and ultrasonic bath times used for ensuring effective mass transfer of the analyte, centrifuge time used for the complete separation of the water and HES phase containing analyte, salt (NaCl) and matrix effects have been examined and optimized. Under the optimized conditions, the developed method showed a good linearity with a regression coefficient (R^2) of 0.9994 in the range of 3.3-167 μg/L. Limit of detection (LOD), limit of quantitation (LOQ), relative standard deviation (RSD) and enrichment factor (EF) values were determined as 2.25 μg/L, 7.42 μg/L, 2.46% and 30, respectively. Addition/recovery test applications in real waters were carried out to verify the accuracy of the succested method. High recoveries (95-105%) demonstrated that the developed Me/DA-based HES-LPME method has been regarded as a promising candidate for monitoring and determining of BF dyestuff in water samples.

Keywords: liquid phase microextraction; hydrophobic eutectic solvent; basic fuchsin; UV-VIS.

Simulation and Analysis of High-performance BaZrS3 Based Perovskite Solar Cells with Theoretical Efficiency Approaching 18%

N. Chawki[1*], **M. Rouchdi**[1] and **B. Fares**[1]

[1]*Group of Semiconductors and Environmental Sensor Technologies-Energy Research Center, Faculty of Science, Mohammed V University, B P 1014, Rabat, Morocco*

Abstract: Chalcogenide perovskites are prototypical absorber materials based solar cells, they could solve both: the stability and toxicity issues existing in conventional perovskites. A device simulation of BaZrS3 as a potential absorbing material (high chemical stability, direct band gap and a strong light absorption coefficient) based chalcogenide perovskite solar cells is performed by using the one dimensional Solar Cell Capacitance Simulator (SCAPS)-1D software. Parameters such as (thickness, doping concentration, defect density of the absorber and interfaces, temperature) are varied in order to inspect their impact on device performance. For this study, a performed architecture has been proposed: FTO (front contact)/TiO_2 (ETL; Electron Transport Layer)/$BaZrS_3$ (Absorber)/Spiro-OMeTAD (HTL; Hole Transport Layer)/Au (metal back contact). To enhance the solar cell efficiency, an optimization of these key parameters is investigated for the absorber, HTL and ETL. Our simulation results after optimization are found to be: PCE (maximum Power Conversion Efficiency) of 16.07%, FF (fill factor) of 88.60%, V_{oc} (Open Circuit Voltage) of 1.08 V and J_{sc} (Short Circuit current density) of 16.80 mA/cm2.

ISBN: 978-975-7616-84-9

Our Contributions To Biomedical Applications of Advanced Hybrid Organic-Inorganic Nanomaterials (Polyhedral Oligomeric Silsesquioxanes)

Ali Akbari*

Solid Tumor Research Center, Cellular and Molecular Medicine Institute, Urmia University of Medical Sciences, Shafa St, Ershad Blvd., P.O. Box 1138, Urmia, 57147, Iran.

Abstract: Recently, hybrid organic-inorganic materials play substantial roles in developing of high-tech materials for various applications. Hybrid materials have gained tremendous attention from both academic and industrial communities due to their unique properties which are not found in pure organic or inorganic materials. Polyhedral oligomeric silsesquioxanes (POSS) are one of the most interesting examples of hybrid nano-building blocks that have nano-size silica core along with surrounding organic functional groups. The typical POSS nano-building possesses a caged-shaped rigid molecular structure represented by the empirical chemical formula (RSiO1.5)n, where n = 4, 6, 8, 10 and the central inorganic core (SinO1.5n) could be functionalized with a range of inert or active organic moieties. For the first time, we have designed and synthesized various POSS-based nanomaterials and used in nanomedicine especially in drug delivery systems.

Effect of Machining Process on Electrochemical Behavior of Ti6Al4V-ELI Dental Implant in PBS Solution

Shaghayegh Alizadeh, Mehrdad Shahbaz*, Majid Kavanlouei

Department of Materials Science and Engineering, Faculty of Engineering, Urmia University, Urmia, Iran.

Abstract: This work discusses the effect of machining process on the corrosion behavior of dental implants made of Ti-6Al-4V alloy. The corrosion behavior of implants in phosphate buffered saline solution (PBS) was investigated by potentiodynamic method and electrochemical impedance spectroscopy (EIS) was used to investigate the electrochemical corrosion properties of the implant. Also, corrosion kinetic parameters were calculated from Tafel extrapolation analysis and AC impedance analysis. An ac circuit model was proposed for a Ti-6Al-4V alloy implant at the corrosion interface in PBS solution, which was based on a simple Randles equivalent circuit. It was found that the machined implants in different machining conditions show a capacitive behavior in PBS solutions. The results obtained for the 3 samples that have been tested showed that by increasing the Q parameter (machining depth, mm) and the S parameter (rpm), the corrosion resistance will be higher and the corrosion current will be lower, as a result, we will have a lower corrosion rate. Finally, experimental results obtained from different electrochemical techniques are compared and discussed.

Evaluation of electrochemical behavior of titanium scaffold produced by selective laser melting (SLM) method in PBS solution with different pH

Mehrdad Shahbaz[b*], Dina Bostanchi[a], Najme Najmedin[a]

[a]*Department of Medical Science and Technologies, Science and Research Branch, Islamic Azad University, Tehran, Iran*
[b]*Department of Materials Science and Engineering, Faculty of Engineering, Urmia University, Urmia, Iran*

Abstract: Selective laser melting (SLM) is a new method in medical applications, which is able to make scaffolds to replace or regenerate bone tissues. In this article, the aim is to investigate the electrochemical behavior of Ti6AL4V scaffold produced by SLM in phosphate buffered saline solution (PBS) with different pH. For this purpose, a cylinder with a height of 12 mm and a diameter of 8 mm with cross-shaped circular holes was designed and built as a scaffold. A scanning electron microscope was used to examine the shape and structure of the produced pores of the scaffold. Electrochemical behavior was evaluated using potentiodynamic polarization curves and electrochemical impedance spectroscopy (EIS) in PBS solution at 25°C. Corrosion kinetic parameters were calculated from Tafel extrapolation analysis and impedance analysis. The results obtained for three different evaluated pH showed that scaffolds made in different pH conditions show different corrosion behavior in PBS solution. Finally, experimental results obtained from different electrochemical techniques were compared and discussed.

Effect of the Vortex Extrusion as a Severe Plastic Deformation Technique on the Precipitations Distribution in Al-Mg-Si Alloy

Sevda Teymorpour[a], Mehrdad Shahbaz[a*], Majid Kavanlouei[a], Maryam Yaldagard[b]

[a]Department of Materials Science and Engineering, Faculty of Engineering, Urmia University, Urmia, Iran
[b]Department of Chemical Engineering, Faculty of Engineering, Urmia University, Urmia, Iran

Abstract: Al-Mg-Si alloy with medium strength, heat treatment capability, good formability, machinability and weldability has a wide application in automotive industries. In this research, the aim is to investigate the effect of vortex extrusion method, as a method of severe plastic deformation, on the distribution of precipitation and as a result, changing the properties of the alloy. For this purpose, the alloy was solution treated and then was subjected to the conventional extrusion (CE) and vortex extrusion (VE), and the effect of the amount of strain and the mechanism of straining on the distribution of precipitations and the change of properties were studied using scanning electron microscope (SEM) images, X-ray diffraction (XRD) and microhardness test. Results showed that, the mechanism of vortex extrusion caused a change in the distribution, shape and size of precipitations and thus resulted in improved properties.

ETKİN BİR KATALİZÖR OLAN AKTİF C DESTEKLİ Rh NANOKÜMELERİNİN N2H4BH3'IN HİDROLİZİNDE KATALİTİK PERFORMANSININ İNCELENMESİ

INVESTIGATION OF CATALYTIC PERFORMANCE IN HYDROLYSIS OF N2H4BH3 OF Rh NANOCLUSTERS SUPPORTED ACTIVE C THAT AN EFFECTİVE CATALYST

Nurgül KAVAK, Mehmet TUNÇ

Van Yüzüncüyıl Üniversitesi Fen Fakültesi Kimya Bölümü, Van

ÖZET: Bu çalışmada, aktif karbon (C) üzerine Rodyum(0) nanokümeleri, sulu fazda rodyum(III) tuzunun katı destek maddesi olan aktif karbon (C) yüzeyine depolanmasıyla uygun indirgeyicilerden sodyum borhidrür (NaBH4) kullanılarak indirgenmesiyle oluşturuldu. Gerçekleştirilen işlemler sonucunda elde edilen katı katalitik malzeme, indüktif olarak çiftleşmiş plazma-optik emisyon spektroskopisi (ICP-OES), toz-X ışınları kırınımı (P-XRD) gibi ileri analitiksel yöntemler kullanılarak tanımlandı. Aktif karbon(C) yapısında kararlaştırılmış Rh(0) nanoparçacıklarının katalitik etkinliği ile Rh/C katalizörü varlığında hidrazin boranın (N2H4BH3) dehidrojenlenmesi tepkimesinin kinetiği; farklı substrat ve katalizör derişimine bağlı olarak incelendi.

ABSTRACT: In this study, Rhodium (0) nanoclusters on the activated carbon (C) were formed by reduction of the rhodium (III) by using sodium borohydride(NaBH4) from suitable reducing agents by storing on the activated carbon(C) surface, which is the solid support material of the rhodium(III) salt in the aqueous phase. Solid catalytic material obtained as a result of the processes carried out was defined by using advanced analytical methods such as inductively coupled plasma-optical emission spectroscopy (ICP-OES), powder-X-ray diffraction (P-XRD). The kinetics of the dehydrogenation reaction of hydrazine-borane (N2H4BH3) in the presence of the Rh@C catalyst with catalytic activity of the Rh (0) nanoparticles stabilited in the structure of the activated carbon (C); depending different substrate and catalyst concentrations were examined.

1.GİRİŞ: Dünya enerji ihtiyacının büyük bir kısmını fosil yakıtlardan karşılamaktadır. Fosil yakıtların yoğun bir şekilde kullanılması sonucu, atmosfere salınan başta CO2 olmak üzere zararlı sera gazları hava kirliliğine ve küresel ısınmaya sebep olmaktadır. Hava kirliliği ve küresel ısınmayı önlemek amacıyla fosil yakıtlara alternatif olarak, rüzgar ve güneş enerjisi başta olmak üzere yenilenebilir enerji kaynakları üzerine çalışılmaktadır. Ancak bu yenilenebilir enerji kaynaklarında en büyük sorun süreksiz olmaları ve kurulum maliyetlerinin yüksek olmasıdır. Bu nedenle yenilenebilir enerji kaynaklarına alternatif olarak, hidrojen enerji taşıyıcı olarak kullanılması avantajlıdır. Katı depolama malzemeleri arasında hidrojen yüksek gravimetrik yoğunluğu ve düşük moleküler ağırlığı ile son derece umut verici bir kimyasaldır (Lu ve ark., 2005). Hidrazin boran 2015'te ağırlıkça % 7 hedefini aşan gravimetrik hidrojen depolama kapasitesine sahip olmuştur (Conti, 2005; Laird, 2014;Stetson, 2013).

2. MATERYAL VE YÖNTEM

2.1. Deneyde kullanılan kimyasal maddeler

Eşitlik (1.1)' e göre hidrolitik dehidrojenasyonu ile uygun katalizörlerin varlığında oda sıcaklığında etkili bir şekilde hidrojen elde edilir.

$$N_2H_4BH_3 \;+\; 2H_2O \xrightarrow{\text{Katalizör}} N_2H_5^{+} \;+\; BO_2^{-} \;+\; 3H_2 \qquad (1.1)$$

Rodyum(III) klorür trihidrat (RhCl3.3H2O, 99%), aktif karbon(C), sodyum-borhidrür(SBH,98%), hidrazin-boran(90%) deneylerde kullanılmıştır. Deneylerde kullanılan kimyasallar, Merck ve Sigma-Aldrich gibi firmalardan satın alındı. Deiyonize su, musluk suyundan cihazla saflaştırılmıştır (Thermo scientific barnsted nanopure system). Tüm cam eşyalar, teflon kaplı manyetik balıklar asetonla temizlenmiş ve saf suyla yıkandıktan sonra 150°C ye ayarlanmış fırında gece boyunca kurutulduktan sonra kullanılmıştır.

2.2 Yöntem

2.2.1. Rh/C nanokatalizörünün hazırlanması

Katalizörün % 2 lik Rh(III) içermesi için RhCl3.3H2O'dan 3.11 mg alınarak 5 mL suda çözülmüştür. Daha sonra 75 mg Aktif karbon tartılarak petri kabına konularak suda çözünmüş olan RhCl33H2O, aktif karbona emdirmek için ağzı kapatılıp karıştırma hızı 700 rpm olan karıştırıcıda 2 saat karıştırılmıştır. Daha sonra 8.61 mg NaBH4 alınıp 1 ml saf suda çözülmüş ve 2 saat karışan çözeltiye eklenilmiştir. Gaz çıkışı sonlanana kadar 40 dakika daha karıştırıldı. Bu süre sonunda karışım sözülmüştür. Sonrasında 3x10 ml saf su ile yıkanan katalizör, vakumlu etüvde 150 0C de 40 dakika kurultulmuştur. Kurutma işleminden sonra hazırlanan katalizör, reaksiyonlarda kullanılmak özere uygun bir yerde muhafaza edilmiştir.

Hazırlanan katalizör, Hidrazin-boranın(HB) dehidrojenlenme tepkimesinde kullanıldı. Elde edilen katalitik malzemenin P-XRD(X-Işınları Kırınımı), ICP-OES (Endüktif Eşleşmiş Plazma Kütle Spektrometresi) gibi ileri analitiksel yöntemler kullanılarak tanımlanmıştır. Bu analitiksel yöntemlerden ICP-OES; katı destek yüzeyine tutturulan kütle metal yüzdesinin belirlenmesi, XRD; metal nanokümelerinin yüzeyde oluşumu sonucu destek malzemesinin kristal yapısının incelenmesi amacıyla kullanılmıştır.

2.2.2. Rh/C nanokatalizörünün hidrazin boranın hidrolizi tepkimesindeki

katalitik etkinliğinin katalizör miktarına bağlı olarak incelenmesi

Katalizör miktarının, HB hidrolizindeki katalitik etkisini anlamak için; HB miktarı 50 mM'da sabit tutularak Rh/C katalizörünün 0.34 mM, 0.68 mM, 1.02 mM, 1.36mM konsantrasyonlarında katalitik etkinlikleri incelenmiştir. 50 mg(0.68mM) Rh/C deney kabı ceketli Schlenk içerisine konulmuş ve üzerine 9 mL saf su eklenmiştir. Schlenk'e mağnet konulup sirkülatör sıcaklığı 25°C'ye ve karıştırma hızı 700 rpm'e ayarlanarak termal dengeye gelmesi için 15 dakika beklenmiştir. Termal dengeye ulaşan karışımın içerisine 1mL saf su içerisinde çözünmüş olan 23 mg HB (50mM) ilave edildi ve Schlenkin ağzı septumla kapatılıp mağnetik karıştırıcı düğmesine basılarak açığa çıkan gazın büret içerisindeki suyu itmesi ile çıkan gaz hacmi zamana karşı gaz çıkışı sonlanana kadar not edilmiştir. Diğer katalizör miktarları için de aynı prosedür uygulanarak katalitik etkinlikleri incelenmiştir.

2.2.3. Rh/C katalizörünün hidrazin boranın hidrolizi tepkimesinde tekrar Kullanılabilirliği

50 mg (0.68 mM) Rh/C deney kabı ceketli Schlenk'e konuldu ve üzerine 9 ml saf su ilave edildi. Schlenk'e mağnet konulup sirkülatör sıcaklığı 25°C'ye ve karıştırma hızı 700 rpm'e ayarlanarak termal dengeye ulaşması için 15 dakika bekletildi. Termal dengeye ulaşan karışımın içerisine 1ml saf su içerisinde çözünmüş olan 23 mg HB ilave edildi ve Schlenk'in ağzı septumla kapatılıp mağnetik karıştırıcının üzerinde karıştırılarak açığa çıkan gazın büret içerisindeki suyu itmesi ile çıkan gaz hacmi zamana karşı gaz çıkışı sonlanana kadar not edilmiştir. Reaksiyon sonlandıktan sonra septum çıkarılarak Schlenk'teki su ve katalizör süzülerek katalizör 3 defa saf su ile yıkandıktan sonra kuruması için 150⌧C'de etüvde 40 dakika bekletildi. Daha sonra katalizör miktarı tartılıp not edildikten sonra deney kabı Schlenk'e konularak daha önce uygulanan prosedürün aynısı, toplam katalitik çevrim sayısı 3 olacak şekilde uygulanmıştır.

3.BULGULAR

3.1. Rodyum Nanopartiküllerinin Sentezi ve Tanımlanması

Aktif karbon üzerine Rodyum(0) nanokümeleri; sulu fazda Rh(III) tuzunun katı yüzeyine depolanması ve daha sonra tepkime sırasında sodyum borhidrür(SBH) çözeltisi kullanılarak indirgenmesiyle oluşturulmuştur. Rodyum(0) nanopartiküllerinin hazırlanmasında izlenen deneysel yöntem, parçacık büyüklüğü ve dağılımı göz önüne alınarak sıcaklık, çözücü ve indirgeyici parametrelerine bağlı olarak optimize edilmiştir. Son olarak elde edilen katalitik malzeme ICP-OES ve XRD gibi analitik yöntemler kullanılarak tanımlanmıştır.

Aktif karbon yüzeyine tutturulan rodyum metali miktarının tayinini yapmak için ICP-OES (İndüktif Eşleşmiş Plazma-Optik Emisyon Spektroskopisi) yöntemi kullanıldı. ICP-OES analizi ile hazırladığımız bu katalitik malzemedeki Rh yoğunluğunun kütlece % 1.40 olduğu tespit edilmiştir.

Metal nanokümelerinin yüzeyde oluşumu sonucu destek malzemesinin kristal yapısının incelenmesi ve metal nanokümelerinin kristalliğinin tespiti için yapılan XRD analizine ait desen Şekil 3.1'te verilmiştir. Desenden de anlaşılacağı üzere rodyum metaline ilişkin sırasıyla 41⌧ ve 70⌧ sinyaller Rh(111) ve Rh(220) yüzeylerine yorumlanabilir (Lin ve ark. 2017). Katı destek malzemesi aktif karbon olduğundan amorf bir malzemedir. Dolayısıyla aktif karbona ilişkin belirgin sinyalleri görmek mümkün olmamıştır.

3.2. Rh/C Katalizörlüğünde Hidrazin-boranın Hidrolizinin Kinetik Çalışmaları

Hidrazin-boranın hidrolizi tepkimesinde

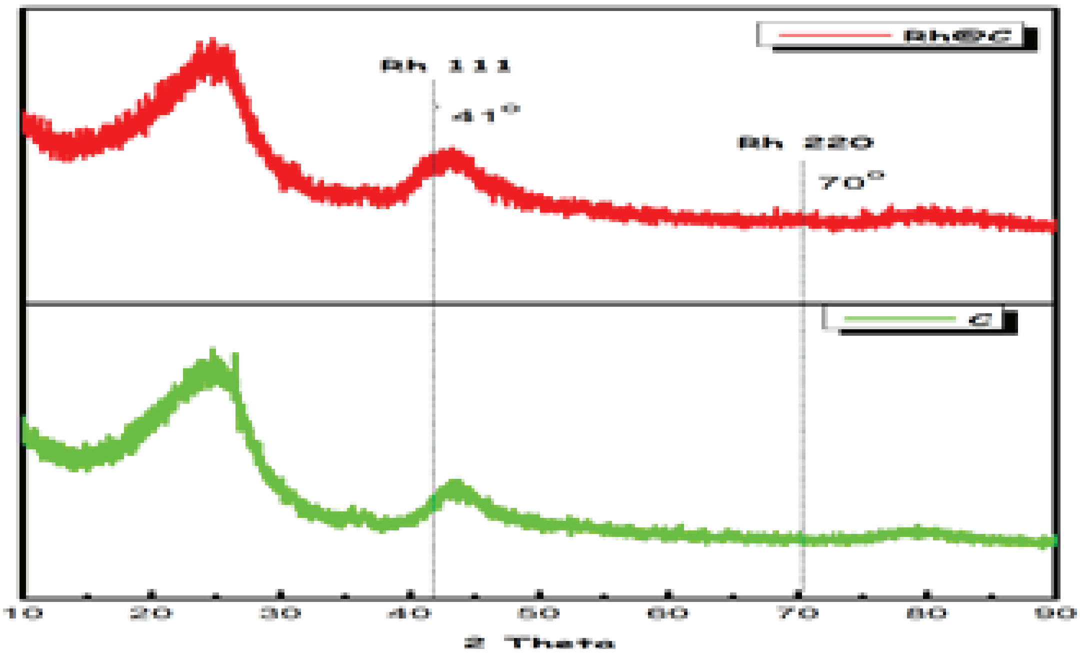

Şekil 3.1. Rh/C nanokatalizörüne ait XRD deseni.

farklı miktarlardaki katalizörün, katalitik tepkimeye etkisini anlamak için farklı derişimlerdeki (0.34 mM, 0.68 mM, 1.02 mM, 1.36mM) Rh/C katalizörleri hazırlanarak her bir parametre için açığa çıkan hidrojen gaz hacminin zamana karşı grafiği Şekil 3.2 (a)’da belirtilmiştir. Şekil 3.2 (b)’deki grafikten her bir Rh/C nanokatalizörünün derişimi için hız sabiti değerleri hesaplandı. Hesaplanan değerlerden ln(k)’ya karşı ln(Rh) eğrisi çizildi. Çizilen doğrusal eğrinin eğimi yaklaşık 1.58 olarak hesaplandı. Bu eğim değeri katalizör derişiminin kaçıncı dereceden ilerlediğini göstermektedir. Eğimden de anlaşılacağı üzere katalizör derişimi açısından 1.58 dereceden ilerlediği görülmektedir.

Rh/C katalizörünün hidrazin-boranın dehidrojenlenme tepkimesindeki katalitik etkinliğinin saptanmasına yönelik yaptığımız

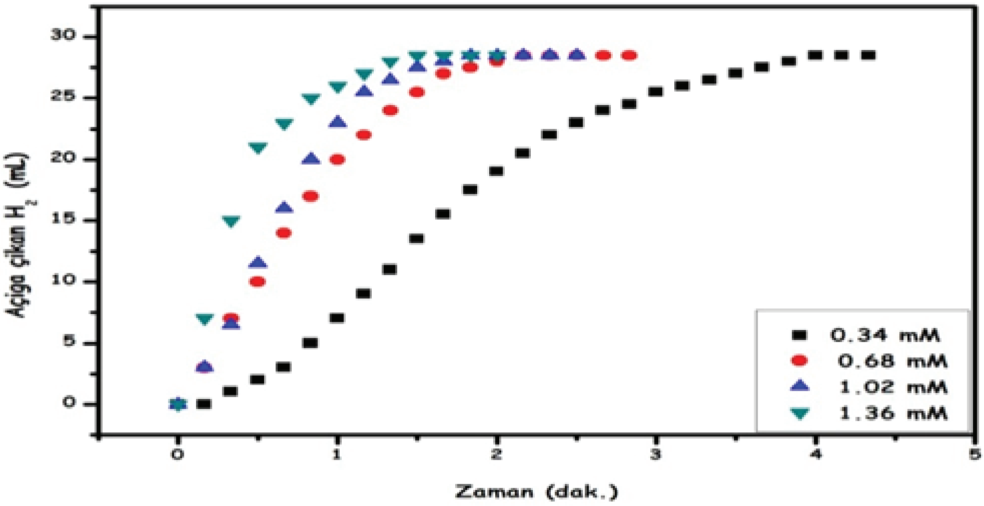

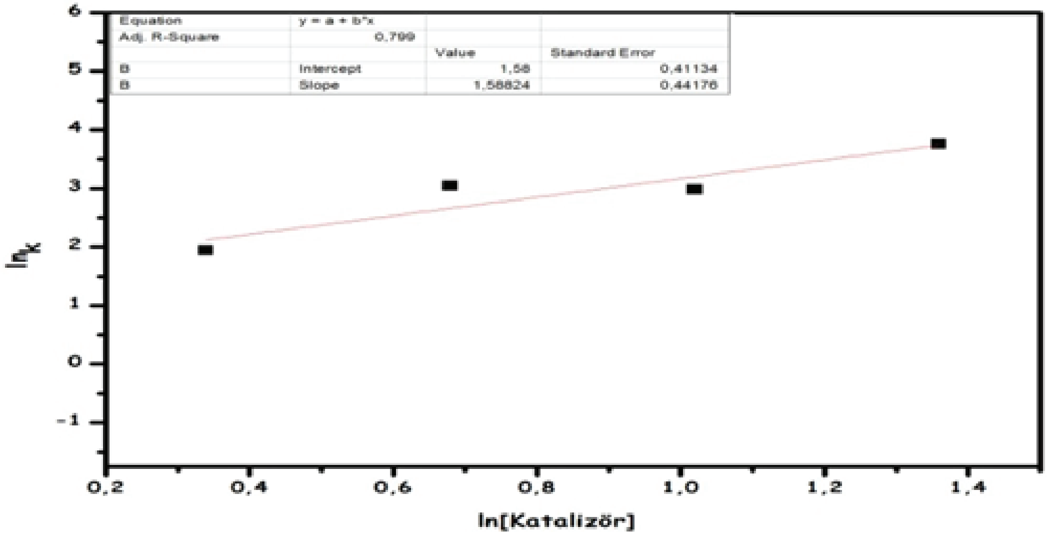

Şekil 3.2. Farklı derişimlerdeki Rh/C ile katalizlenen hidrazin-boranın dehidrojenlenme tepkimesine ait (a) açığa çıkan gaz hacmine karşı zaman grafiği, (b) başlangıç hızlarının katalizör derişimine karşı logaritmik grafiği.

deneylerin dışında bu katalizörün kararlılığını incelemek amacıyla Rh/C katalizörünün hidrazin-boranın dehidrojenlenme tepkimesindeki tekrar kullanılabilirlik performansı da incelendi. Birinci katalitik çevrimden sonra izole edilen Rh/C katalizörü aynı koşullar altında hidrazin-boranın dehidrojenlenmesi tepkimesinde tekrar kullanılmıştır. Şekil 3.5 grafiginde elde ettiğimiz sonuçlara göre Rh/C katalizörünün, hidrazin-boranın dehidrojenlenmesi tepkimesinde tekrar kullanılabilir ve geri dönüştürülebilir bir katalizör olduğunu göstermektedir.

4.TARTIŞMA VE SONUÇ

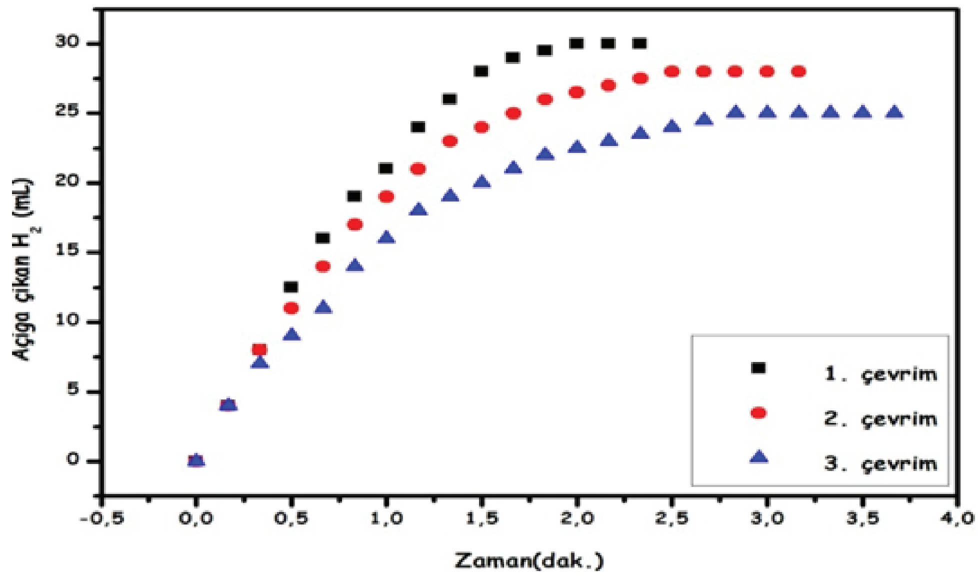

Şekil 3.5. Rh/C ile katalizlenen hidrazin-boranın dehidrojenlenme tepkimesine ait; tekrar kullanılabilirlik (reusability) performansına ilişkin çıkan gaz hacmine (mL) karşı zaman (dak.) grafiği.

Tepkime sonunda kolay izole edilebilme, kolay sentezlenebilme ve düşük maliyete sahip olabilme gibi özellikler dikkate alındığında bu çok önemli tepkime için yeni katalitik sistemlerin geliştirilmesi çok büyük önem arz etmektedir.

Yapılan analitik işlemlerin sonucunda elde edilen deneysel veriler yorumlanarak aşağıdaki gibi sıralanmıştır.

1. RhCl3.3H2O tuzunun sulu fazda çözündüğü ve karbona tutturularak hidrazin boranın hidrolizi ile hidrojen üretimi sağlandığı görülmüştür.
2. Katı destek maddesi üzerine tutturulmuş rodyum(0) nanokümeleri XRD (X Işınları Kırınımı), ICP-OES(Endüktif Eşleşmiş Plazma Spektroskopisi) gibi ileri analitiksel yöntemler kullanılarak tanımlanmıştır.
3. XRD analizi ile metal nanokümelerinin yüzeyde oluşumu sonucu destek malzemesinin kristal yapısı incelenmiştir. XRD deseninden de (Şekil 3.4.) anlaşılacağı üzere rodyum metaline ait sırasıyla 41⊠ ve 70⊠ sinyaller Rh(111) ve Rh(220) yüzeylerine yorumlanabilir (Lin ve ark., 2017).

KAYNAKLAR

Conti j.j., 2005. Annual energy outlook 2005 with projections to 2025, energy information administration, (www.eia.doe.gov). Erişim tarihi: 13.02.2019.

Laird, J., 2014. The future is here! Toyota's hydrogen-powered cars are go for. www.techradar.com. Samsun Erişim tarihi: 29.12.2018.

Lin, C., Wu, G., Li, H., Geng, Y., Xie, G., Yang, J. Liu, B, ve Jin, J., 2017. Rh nanoparticles supported on ultrathin carbonnanosheets for high-performance oxygen reduction reaction and catalytic hydrogenation. Nanoscale, 9: 1834-1839.

Lu Z.H., Yao Q., Zhang Z., Yang Y., Chen X., 2005. Bir kap çekirdek-kabuk Cu @ SiO sentezi 2nanosferler ve amonyak boran ve hidrazin boran hidrolitik dehidrojenasyon için kendi kataliz. J. Nanomater,4: 7597.

Stetson, N., 2013. U.S. Department of Energy, Hydrogen and Fuel Cells Program, Annual Progress Report, Hydrogen Storage Program Overview. www.hydrogen.energy.gov.

MWCNT DESTEKLİ RODYUM NANOKÜMELERİNİN SENTEZİ TANIMLANMASI VE HİDRAZİN BORANIN HİDROLİZİ İÇİN REAKSİYON KİNETİĞİNİN İNCELENMESİ

THE SYNTHESIS OF MWCNT SUPPORTED NANOCLUSTERS AND THE REACTİON KİNETİCS FOR CATALYCTİC HYDROLYSİS OF HİDRAZİNE BORANE

Ömer TANYOL, Mehmet TUNÇ

Van Yüzüncüyıl Üniversitesi Fen Fakültesi Kimya Bölümü, Van

ÖZET: Bu çalışmada, MWCNT yapısında kararlaştırılmış rodyum(0) nanopartiküllerinin hazırlanmasını, tanımlanmasını ve hidrazin-boranın hidroliz tepkimesindeki katalitik etkinliklerinin incelenmesini sunuyoruz. MWCNT yapısında kararlaştırılmış rodyum(0) nanopartikülleri, rodyum (III) klorürün hidrazin-boranın hidrolizi tepkimesinde eş zamanlı (tepkime içi) indirgenmesi ile hazırlandı. Bu şekilde hazırlanan rodyum(0) nanopartikülleri katı olarak izole edildi ve indüktif olarak çiftleşmiş plazma-optik emisyon spektroskopisi (ICP-OES) teknikleri kullanılarak tanımlandı. MWCNT yapısında kararlaştırılmış rodyum(0) nanopartiküllerinin katalitik etkinliği ile bu katalizörün varlığında hidrazin-boranın hidrolizi tepkimesinin kinetiği, farklı katalizör ve substrat konsantrasyonuna bağlı olarak çalışıldı.

ABSTRACT: In this study, we report the preparation, characterization and the investigation of the catalytic activities of MWCNT stabilized rhodium(0) nanoparticles in the hydrolysis of hidrazine-borane. The MWCNT stabilized rhodium(0) nanoparticles were prepared from the in-situ reduction of rhodium(III) chloride in the hydrolysis of hidrazine-borane at room temperature. The prepared rhodium(0) nanoparticles were isolated as solid materials and characterized by using inductively coupled plasma optical emission spectroscopy (ICP-OES). Ransmission electron microscopy (TEM). The catalytic activity of MWCNT stabilized rhodium(0) nanoparticles and the kinetics of hydrogen generation from the hydrolysis of hidrazine-borane were studied depending on catalyst concentration, substrate concentration.

1. GİRİŞ: Uygun hidrojen depolama malzemeleri için hızla artan bir ilgi söz konusudur, çünkü hidrojenin verimli depolanması halen "Hidrojen Ekonomisi" nin ana konularından biridir (U. S. Department of Energy., 2003; Turner ve ark., 2008; van den Berg, 2008) . Bu endişe ile, metal nitrürler ve Hidrojen depolaması için imidler (Chen ve ark., 2002) , karbon nanotüpler (Bacsa ve ark., 2004) , TiO2 nanotüpler (Lim ve ark., 2005) , zeolitler (Dong ve ark., 2007) , organik polimerler (McKeown ve Budd, 2006) , metal organik çerçeveler (Rood ve ark., 2006) ve CBN bileşikleri (Scheideman ve ark., 2008) kullanılmıştır. Bu malzemeler arasında bor bazlı bileşikler, Düşük formül ağırlığına ve yüksek hidrojen yoğunluğuna sahip oldukları için (Hamilton ve ark., 2009) en cazip hidrojen depolama malzemeleridir. Burada, umut verici bir hidrojen depolama malzemesi gibi görünen başka bir bor bazlı bileşik olan hidrazin boranın (N2H4BH3, HB) (A SciFinder literature search with a keyword of "hydrazine borane" yields 62 independent studies and in none of them metal catalyzed hydrolysis of hydrazine borane is reported.) katalitik hidrolizinden hidrojen üretimi ilk kez bildirilmektedir. Hidrazin boran, ABD Enerji Departmanı'nın 2015 hedefinden (pratik olarak uygulanabilir bir malzeme için % 9 wt hidrojen) daha büyük, ağırlıkça % 15.4 bir gravimetrik hidrojen depolama kapasitesine sahiptir (Annual energy Outlook 2005 with Projections to 2025., 2005) . Hidrazin boranın 16 saatte 150°C'ye ısıtıldığında hidrojeni çok yavaş yavaş % 6.5'e kadar çıkardığı gösterilmesine rağmen (Hu¨gle., ve ark., 2009) , metal katalizli hidrolizi ile verimli hidrojen salınımının sağlanabileceğini gösterilmiştir. Oda sıcaklığında;

$$N_2H_4BH_{3(S)} + 2H_2O(I) \xrightarrow[\text{RT}]{\text{Katalizör}} N_2H_5^{+}(aq) + BO_2^{-}(aq) + 3H_2(g)$$

Bu reaksiyonda test edilen katalizör sistemleri arasında, rodyum (III) kloridin en yüksek katalitik etkinliği sağladığı bulunmuştur. Rodyum (III) klorürün mevcudiyetinde, hidrazin boranın tam hidrolizi, sadece sulu çözeltide değil aynı zamanda katı hidrazin borana damla damla su eklendiğinde katı halde de elde edilebilir (Karahan ve ark., 2011).

2. MATERYAL VE YÖNTEM

2.2.1. Rh@MWCNT Katalizörünün Hazırlanması

Katalizörünün %2 lik Rh(III) içermesi için RhCI3.3H2O' dan 3,11 mg alınarak 1mL suda çözüldü. Daha sonra 50 mg MWCNT tartılarak petri kabına konularak suda çözünmüş olan RhCI3.3H2O MWCNT'ye emdirilip petri kabının kapağı kapatılarak 150 0C' deki etüve konularak 50 dakika bekletildi. 50 dakika sonunda petri kabı etüvden çıkartılıp katalizör alınarak reaksiyonlarda kullanılmak üzere stoklandı. Rh(III)@MWCNT reaksiyon ortamında eş zamanlı olarak HB' nin hidrolizinde ilk önce Rh(0)@MWCNT haline geldikten sonra HB' nin hidrolizini sağlayarak hidrojen üretimi sağlandı.

2.2.2. Rh@MWCNT Katalizörünün Hidrazin-Boranın Hidrolizi Tepkimesindeki Katalitik Etkinliğinin Katalizör Miktarına Bağlı Olarak İncelenmesi

Katlizör miktarının HB hidrolizindeki katalitik etkisini anlamak için; HB miktarı sabit tutularak RhNPS@MWCNT katalizörünün 0,48 mM, 0,96 mM, 1,44 mM, 1,92 mM' da katalitik enkinlikleri incelendi. 0,48 mM Rh(III)@MWCNT sistemde ceketli Schlenk içerisine konuldu ve üzerine 8 mL saf su konuldu. Schlenke mağnet konulup sirkülatör sıcaklığı 25 0C'ye ve karıştırma hızı 700 rpm'e ayarlanarak Schlenk içerisine 2 mL saf su içerisinde çözünmüş olan 0,46 mg HB (100Mm) ilave edilerek Schlenkin ağzı septumla kapatılıp mağnetik karıştırıcı düğmesine basılarak açığa çıkan gazın büret içerisindeki suyu itmesi ile çıkan gaz hacmi zamana karşı gaz çıkışı sonlanana kadar not edildi. Diğer katalizör miktarları için aynı prosedür uygulanarak katalitik etkinlikleri incelendi.

4. BULGULAR

MWCNT üzerine rodyum(0) nanokümeleri; sulu fazda rodyum(III) tuzunun katı yüzeyine depolanmasıvedahasonratepkimesırasında sodyum borhirür (SBH) çözeltisi kullanılarak indirgenmesi oluşturuldu. Rodyum(0) nanopartiküllerinin hazırlanmasında izlenen deneysel yöntem, parçacık büyüklüğü ve dağılımı göz önüne alınarak sıcaklık, çözücü ve indirgeyici parametrelerine bağlı olarak optimize edilmiştir. Son olarak elde edilen katalitik malzeme ICP-OES, XRD gibi analitik yöntemler kullanılarak tanımlanmıştır. MWCNT yüzeyine tutturulan rodyum metali miktarının tespitini yapmak amacıyla ICP-OES (İndüktif Eşleşmiş Plazma-Optik Emisyon Spektrometresi) yöntemi kullanıldı. ICP-OES analizi ile hazırladığımız bu katalitik malzemedeki Rh yoğunluğunun kütlece % 1,40 olduğu tespit edilmiştir.

Metal nanokümelerinin yüzeyde oluşumu sonucu destek malzemesinin kristal yapısının incelenmesi ve metal nanokümelerinin kristalliğinin tespiti için yapılan XRD analizine ait desen Şekil 4.1'de verilmiştir.

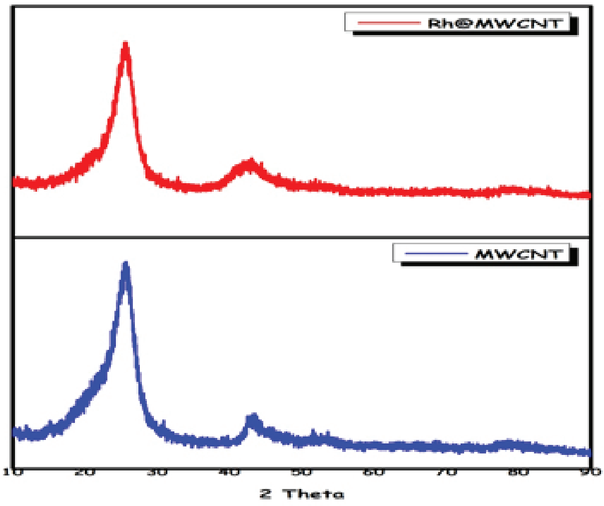

Şekil 4.1. Rh@MWCNT nanokatalizörüne ait XRD deseni.

4.2. Rh@MWCNT Katalizörünün Hidrazin Boranın Hidrolizindeki değişimi

Hidrazln-boranın hidrolizi tepkimesinde farklı miktarlardaki katalizörün, katalitik tepkimeye etkisini anlamak için 0,48 mM, 0,96 mM, 1,44 mM, 1,92 mM derişimlerindeki Rh@MWCNT katalizörleri hazırlanmış ve her bir derişim için açığa çıkan hidrojen gazı hacmi zamana karşı grafiği Şekil 4.2'de verilmiştir.

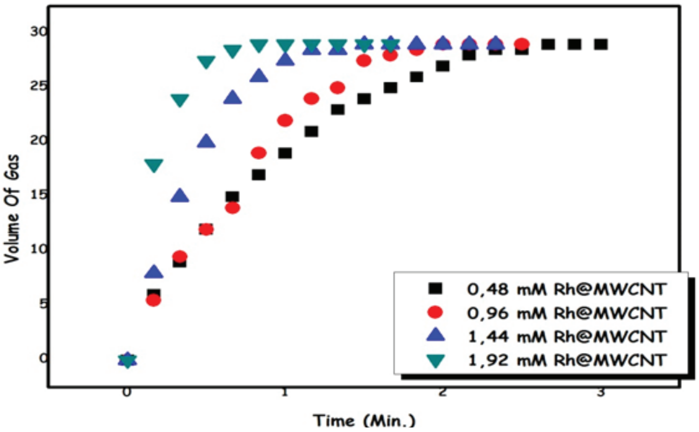

Şekil 4.2. 0,48 mM, 0,95 mM, 1,44 mM ve 1,92 mM Rh ile 20.0± 40.0°C'de katalizlenen 23 mg HB'nin hidrolizinde zamana karşı açığa çıkan H2 gazı miktarı.

5. SONUÇ

Bu çalışmada MWCNT destekli malzemesi üzerine tutturulan Rh(0) nanokümelerinin hidrazin boran katalizörünün derişimine bağlı olarak analitik işlemler yapılmıştır. Yapılan analitik işlemlerin sonucunda elde edilen deneysel verilerden bazıları aşağıdaki gibi sıralanmıştır;

- RhCl3.3H2O tuzunun sulu fazda çözündüğü ve MWCNT'ye tutturularak hidrazin boranın (HB) hidroliziyle hidrojen üretimi sağlandığı görülmüştür.
- Katı destek maddesi üzerine tutturulmuş Rh(0) nanokümeleri XRD (X ışınları kırınımı), ICP-OES gibi ileri analitiksel yöntemler kullanılarak tanımlanmıştır.
- Yapılan bu çalışmalarda Rh(0) nanokatalizörünün etkin olduğu deneysel verilerle tespit edilmiştir.

KAYNAKLAR

Bacsa, R., Laurent, C., Morishima, R., Suzuki , H., & Lelay , M. (2004). Hydrogen storage in high surface area carbon nanotubes produced by catalytic chemical vapor deposition. J Phys Chem B, 108:12718-23.

Chen, P., Xiong , Z., Luo , J., Lin, J., & Tan, K. (2002). Interaction of hydrogen with metal nitrides and imides. Nature, 420: 302,4.

Dong , J., Wang, X., Xu, H., Zhao, Q., & Li, J. (2007). Hydrogen storage in several microporous zeolites. Int J Hydrogen Energ , 32: 4998-5004.

Hu¨ gle , T., hnel, M., & Lentz , D. (2009). Hydrazine borane: a promising hydrogen storage material. J Am Chem Soc, 131:7444-6.

Karahan, S., Zahmakıran, M., & Ozkar, S. (2011). Catalytic hydrolysis of hydrazine borane for chemical hydrogen storage: Highly efficient and fast hydrogen generation system at room temperature. international journal of hydrogen energy 36 , 4958 -4966.

Lim , S., Luo, J., Zhong , Z., Ji, W., & Lin, J. (2005). Room-temperature hydrogen uptake by TiO2 nanotubes. Inorg Chem, 44: 4124-6.

McKeown, N., & Budd, P. (2006). Polymers of intrinsic microporosity (PIMs): organic materials for membrane separations, heterogeneous catalysis and hydrogen storage. Chem Soc Rev , 35:675-83.

Rood , J., Noll , B., & Henderson , K. (2006). Synthesis, structural characterization, gas sorption and guest-exchange studies of the lightweight, porous metal-organic framework alpha- [Mg3(O2CH)6]. Inorg Chem, 45:5521-8.

Scheideman, M., Wang , G., & Vedejs, E. (2008). Amine-directed hydroboration: Scope and limitations. J Am Chem Soc, 130:8669-76.

US Department of Energy. (2003). Basic research needs for the hydrogen economy. Report of the Basic Energy Sciences Workshop on Hydrogen Production, Storage and Use, Office of Science, Washington, DC: /http:// www.sc.doe.gov/ bes/reports/list.htmlS. adresinden alınmıştır.

van den Berg, A. (2008). Arean CO. Materials for hydrogen storage: current research trends and perspectives. Chem Commun, 6:668e81.

Synthesis and Characterization of MXene Stabilized Polymetallic Nanoclusters for the Selective Decomposition of Hydrazine Hydrate*

Yaşar Karataş, Adem Rüzgar, Mehmet Gülcan

Van Yüzüncü Yıl University, Faculty of Science, Chemistry Department, Turkey

Abstract: In the present work, MXene and then MXene stabilized polymetallic nanoclusters were prepared according to the classical impregnation-reduction method. The catalytic performance of the prepared nanocatalysts in hydrogen production from the selective decomposition of hydrazine hydrate was investigated.

Synthesized MXene stabilized heterogeneous nanocatalysts were identified using advanced analytical and spectroscopic methods such as ICP-OES, XRD, XPS, TEM, TEM/EDX, HRTEM, SEM, SEM-Elemental Mapping and FT-IR techniques. After examining the effects of catalyst and substrate concentrations in different compositions on the catalytic reaction, the efficiency of the catalysts was calculated in terms of initial TOF. The efficiency values obtained were higher than many catalytic systems in the literature for the selective decomposition of hydrazine hydrate.

This study was supported by Van YYU Scientific Research Projects Coordination Unit (Project ID: FYD-2022-10146).

The Functionalized Graphene Supported Rh Nanoparticles: Synthesis, Characterization and Investigation of Catalytic Performance of the Ethylenediamine-Bisborane Hydrolysis

Esra Karataş, Lokman Şener, Yaşar Karataş, Mehmet Gülcan

Van Yüzüncü Yıl University, Faculty of Science, Chemistry Department, Turke

Abstract: In this research study, firstly, ethylenediamine-bisborane, a solid hydrogen storage material that has come to the fore in recent years, was synthesized and characterized. Then, amine functionalized graphene supported Rh nanoclusters were prepared and further defined to be used in hydrogen production from the hydrolysis of ethylenediamine-bisborane. The nanocatalyst, whose effectiveness was tested in preliminary studies, was found to be quite effective in ethylenediamine-bisborane hydrolysis compared to its counterparts in the literature. In this framework, kinetic studies based on concentration and temperature in progress.

**This study was supported by Van YYU Scientific Research Projects Coordination Unit (Project ID: FYL-2019-8498).*

Preparation and Detailed Characterization of Hydroxyapatite Decorated Palladium Nanoparticles for The Nitrophenol Reduction*

Yaşar Karataş, Adem Rüzgar, Mehmet Gülcan

Van Yüzüncü Yıl University, Faculty of Science, Chemistry Department, Turkey

Abstract: Nitrophenols and their derivatives constitute a large part of the chemicals, which are quite dangerous and harmful. Due to their toxicity and carcinogenic nature, nitrophenols are considered in the group of compounds that need to be purified primarily [1-2]. However, traditional purification methods do not meet the needs sufficiently due to their long duration, low efficiency, high cost and application difficulties. In this respect, the need to develop highly efficient and applicable new technologies continues. Technological products and methods in micro and nano size, which are becoming widespread worldwide, are candidates to be an alternative to traditional purification methods. In recent years, the reduction of nitrophenols has begun to attract the attention of researchers [3]. Aminophenols, which are reduction products of nitrophenols; they are not listed in the priority pollutants list because they have much lower toxicity than nitrophenols. Due to these properties, aminophenols are widely used as intermediates for the production of pesticides, drugs, dyes, cosmetics, paper and other chemicals.

In this work, Pd nanoparticles decorated on hydroxyapatite were prepared and their catalytic performances in the reduction of nitrophenol compounds such as 2-NP and 4-NP in aqueous medium in the presence of NaBH4 were monitored using UV-vis spectroscopy. The results showed that Pd nanoparticles decorated on hydroxyapatite performed quite well considering parameters such as catalytic efficiency and reusability.

References

1. J.H. Li, D.Z. Kuang, Y. L Feng, F.X. Zhang, Z.F. Xu, M.Q. Liu, A graphene oxide-based electrochemical sensor for sensitive determination of 4-nitrophenol, J. Hazard. Mater., 201–202 (2012) 250-259

2. S. Pandey, S.B. Mishra, Catalytic reduction of p-nitrophenol by using platinum nanoparticles stabilised by guar gum, Carbohydr. Polym. 113 (2014) 525–531.

3. Y. Ma, X. Wu, G. Zhang, Core-shell Ag@ Pt nanoparticles supported on sepiolite nanofibers for the catalytic reduction of nitrophenols in water: enhanced catalytic performance and DFT study, Appl. Catal. B Environ. 205 (2017) 262–270.

---

*This study was supported by Van YYU Scientific Research Projects Coordination Unit (Project ID: FYD-2022-9983).

Synthesis, characterization and application of supported Co-Ni-Cr metal catalysts

Hilal Çelik Kazıcı[1], **Fırat Salman**[2] and **Mehmet Sait İZGİ**[3]

[1]Van Yuzuncu Yil University, Faculty of Science, Department of Chemistry, VAN, Turkey
[2]Van Yuzuncu Yil University, Engineering Faulty, Department of Chemical Engineering, VAN, Turkey
[3]Department of Chemical Engineering, Faculty of Engineering, Siirt University, Siirt, Turkey

Abstract: Nanocatalysts have recently attracted attention due to their particle size and surface electronic properties. Thanks to their high efficiency, their use has become widespread in many areas such as fuel cells, solar cells, sensor applications. In addition, the large size of nanocrystalline structures in some applications also brings some problems. Therefore, adjusting the particle size and the electronic properties of the surface to increase the sensor activity requires nano-engineering experience.

In this study, stable and high catalytic activity nanomaterials were prepared. Thanks to the synergistic effect between the tertiary metals, catalysts with excellent surface electronic structure have been synthesized. Structural characterization of synthesized Co-Ni-Cr/Al_2O_3, Co-Ni-Cr/CNT, Co-Ni-Cr/Eupergit CM catalysts was made and used in hydrogen peroxide sensor applications. The obtained alloys; Surface morphologies and electrochemical parameters were investigated by cyclic voltammetry (CV) technique.

Investigation of the structure and activities of nanocatalysts prepared with Pd-Ru and Co for the direct electrooxidation of NaBH4

Hilal Çelik Kazıcı[1], **Fırat Salman**[2],
Mehmet Sait İZGİ[3] and **Erhan ONAT**[4]

[1]Van Yuzuncu Yil University, Faculty of Science, Department of Chemistry, VAN, Turkey
[2]Van Yuzuncu Yil University, Engineering Faulty, Department of Chemical Engineering, VAN, Turkey
[3]Department of Chemical Engineering, Faculty of Engineering, Siirt University, Siirt, Turkey
[4]Science Institute, Siirt University, Siirt, Turkey

Abstract: In the past few years, borohydrides have gathered a lot of attention as an energy carrier for fuel cell application. Many studies have been done on both hydrogen production and the direct oxidation of NaBH4. However, as is known, only certain catalysts can fully carry out the direct oxidation of NaBH4 at low potentials without hydrogen formation. In this study, nanocatalysts decorated with different supported Pd, Ru and Co nanoparticles were synthesized. The effect of surface modifications of Pd, Ru and Co catalysts on the electrooxidation of sodium borohydride in alkaline medium was evaluated. Physical and electrochemical methods were applied to characterize the structure and surface of the different prepared catalysts. The surface of the electrode was characterized by SEM. The catalytic performance of the modified electrode is evaluated by voltammetry and chronoamperometry. It was investigated in 3.0 mol/L NaOH +0.1 mol/L NaBH4 solution at a potential of -0.8/+0.8 V at a scanning speed of 50 mA/s. Electrochemical measurements reveal that the prepared electrode exhibits good catalytic performance and stability for NaBH4 electrooxidation.

Acknowledgements

This work was supported by Scientific Research Projects Coordination Unit of siirt University. Project No: 2021-SİÜMÜH-05, 2022-SİÜMÜH-010

This work was supported by Scientific Research Projects Coordination Unit of Van YuzuncuYil University. Project No: FYL-2020-9222.

Synthesis of different support nanocatalyzers and hydrogen peroxide sensor applications

Fırat Salman[1], **Hilal Çelik Kazıcı**[2] and **Mehmet Sait İZGi**[3]

[1]Van Yuzuncu Yil University, Engineering Faulty, Department of Chemical Engineering, VAN, Turkey
[2]Van Yuzuncu Yil University, Faculty of Science, Department of Chemistry, VAN, Turkey
[3]Department of Chemical Engineering, Faculty of Engineering, Siirt University, Siirt, Turkey

Abstract: Rapid and accurate determination of hydrogen peroxide (H_2O_2) is of practical importance in various fields such as food, clinical and environmental analyses. Recently, it is of great importance to develop an enzyme-free electrochemical sensor with high sensitivity, fast response time and long-term stability. In particular, metal-supported electrochemically active nanocatalysts have been extensively studied for non-enzymatic electrochemical sensors, as they have large surface-to-volume ratio and increased catalytic activities. To date, H_2O_2 detection has mainly been studied using spectrometry, fluorescence and electrochemistry. Compared with the electrochemical methods all the above mentioned methods are more expensive and time consuming. Beside this, the simplicity, intrinsic sensitivity and high selectivity recommend the electrochemical techniques among the most promising options for H_2O_2 detection. In this study, different supported catalysts showed high catalytic activity and effective sensitivity in the detection of hydrogen peroxide, thanks to its high surface area. The electrochemical behavior of synthesized catalysts during hydrogen peroxide sensor acquisition was investigated by using cyclic voltammetry and chrono amperometric methods.

Preparation and Characterization of Magnetic Rh (0) Nanoparticles Stabilized by Quaternary Hybrid Composite for the Hydrogen Production from Ammonia-Borane*

Arzu Kızıltaş, Lokman Şener, Yaşar Karataş, Mehmet Gülcan

Van Yüzüncü Yıl University, Faculty of Science, Chemistry Department, Turkey

Abstract: Ammonia-borane (AB), a B-N adduct, is considered one of the promising hydrogen storage materials due to its higher hydrogen density compared to the US Department of Energy's 2015 targets. Hydrogen production from the AB can be achieved by high temperature thermolysis, hydrolysis, methanolysis and dehydrogenation/dehydrocoupling reactions. Among these methods, the methanolysis reaction is frequently preferred because it is both cheap and easy to apply. AB is resistant to spontaneous methanolysis and 3 moles of H2 per AB can be obtained by the methanolysis reaction in the presence of a suitable catalyst. In this study, Rh(0) nanoparticles stabilized in a hybrid composite solid support structure were prepared and characterized by wet impregnation and reduction method. Then, the prepared catalytic material was used for the first time as a heterogeneous catalyst in the hydrogen production from the methanolysis of AB and its catalytic performance was tried to be determined. Detailed kinetic studies continue by performing reactions at different concentrations and temperatures with the catalytic material, which has a higher TOF value compared to most catalysts in the literature.

---

*This study was supported by Van YYU Scientific Research Projects Coordination Unit (Project ID: FYL-2022-10163).

Numerical investigation of battery thermal management by using different phase change materials under extreme working conditions

Toygun Dagdevir[1*]

Erciyes University, Department of Mechanical Engineering, Turkey

Abstract: Owing to increasing globally interest on electrical vehicles, battery thermal management (BTM) issue has critically importance in increasing the life time and safety, decreasing the charging time and cost and weight of the electrical vehicles. Li-ion cells are preferred due to high energy density and lo self-discharge rate, long cycle life. BTM by using phase change materials (PCMs) is sensible due to the melting temperature of PCM is in the range of desired temperature of Li-ion cells. This study aims to compare the performance of different PCMs such as paraffin and n-octadecane to cool a Li-ion cell which are used in electrical vehicles. Time dependent numerical analyzes were conducted to show the performance of PCMs on the BTM at cycle time of 20,000. Boundary condition for the numerical analyzes were considered as different discharging time such as 1C, 3C and 5C. As a result, paraffin appears to undergo a phase change longer than n-octadecane. This is because the paraffin has a higher latent heat value compared to n-octadecane. According to the results, it was able to keep cell temperature between 258-313K by using paraffin at a discharge rate of 1C and 3C. However, n-octadecane was not able to keep the temperature of the cell at desired range at discharge rate of 3C. At 5C discharge rate, neither paraffin nor octadecane could provide the desired cell temperatures. On the other hand, both paraffin and n-octadecane ensured that the temperature difference in the cell remained below 2.5K at all discharge rates.

The Use of Surface - Printed Electrodes Modified with Carbon Derivatives in Racemic Drugs Separation

Müge YAYLA[*], Arzu YILDIIRIM[1*], Hilal ÇELİK KAZICI[2], Hilal DEMİR KIVRAK[3] and **Nahit AKTAŞ[4]**

[1,2,4]Van Yüzüncü Yıl University, 3Eskişehir Osmangazi University

Abstract: An electrochemical sensor study was carried out to distinguish the enantiomers of chiral compounds. This electrochemical sensor was implemented using carbon-based electrodes. Carbon material, which has been very popular in sensor studies recently, was synthesized in different derivatives by using chemical reduction method in this study. These derivative is carbon nanotube / β-cyclodextrin (CNT/β-CD). XRD and SEM methods were used for the characterization of the synthesized electrocatalysts. The obtained carbon-based materials were modified on the surface of the surface-printed carbon electrodes (SPCE), carbon nanotube / surface-printed carbon electrode (CNT/SPCE) and surface imprinted carbon electrode / β-cyclodextrin (CNT/ β -CD/SPCE). The efficiencies of the electrocatalysts were characterized by cyclic voltammetry (CV) techniques. Enantioselective chiral differentiation studies were carried out against chiral compounds of electrodes used as enantioselective chiral sensors in electrochemical studies and respectively Fluosectin which is an antidepressant drug active ingredient in racemic form enantiomers were distinguished electrochemically from each other.

Keywords: Carbon, Chirality, Drug, Racemic, Voltammetry

This work was financially supported by Van Yüzüncü Yıl University scientific research projects coordination unit of Turkey (BAP) project (project no: fba-2018-6596).

The Effect of NbB2 Addition at Different Ratios on the Compressive Strength of Aluminium

Hüseyin Demirtaş
Karabuk University, Turkey

Abstract: In this study, the effect of NbB2 particles formed in the aluminium matrix on mechanical properties was investigated. The composites were produced at 850 °C by mixing casting method and poured into a preheated (250 °C) steel mould at 720 °C. 1050 aluminium for the matrix and aluminium matrix master alloys containing 5% B and 3.9% Nb by weight for particle formation were used. The amount of particles formed in the matrix was determined as 2.5% and 3.75 by weight, and by changing the stirring times, it was created with two different production parameters. Microstructural examinations of four different composites produced in this way were conducted using scanning electron microscopy (SEM), and compression tests were performed with a static compression tester. As a result of the tests, it was determined that the particle increase of 1.25% significantly improved the mechanical properties of the composites. Regarding the production parameter, it was determined that increasing stirring time slightly increased the mechanical properties in both particle ratios.

Keywords: Aluminium matrix composite, Stir casting, Mechanical properties, Microstructure.

Effect of electrospun polycarbonate nano fiber on the mechanical properties of glass fiber reinforced composites

Mehmet Safa Bodur*[1] and **Alper Adrian Baysan**[2]

[1]*Yeditepe University, TURKEY*
[2]*Leuven University, BELGIUM*

Abstract: This paper aims to embed thermoplastic nanofibers into glass fibers and see an improvement in the mechanical properties compared to GFRP. Due to the nature of polycarbonate (PC) being able to enhance impact resistance was selected to produce nanofibers via an electrospinning technique. For PC 25 wt% with (60:40) THF to DMF ratio proved to be the best concentration ratios. This study also reveals that mechanical properties of the electrospun nanofiber embedded composites highly depend on the nanofiber type and electrospinning time.

Investigation of the strain inhomogeneity in Cyclic Extrusion Compression in Equal Channel Angular Pressing by FEM and RSM methods for CP-Ti

B. Pasoodeh[1], **V.A. Mirzaloo**[1]*, **M. Shahbaz**[2], **K. Hajizade**[3] and **J.A. Kaklar**[1]

[1]Urmia University, Department of Mechanical Engineering, Faculty of Engineering, Urmia, Iran
[2]Urmia University, Department of Materials Science and Engineering, Faculty of Engineering, Urmia, Iran, m.shahbaz@urmia.ac.ir
[3]Urmia University of Technology, Faculty of Mining and Metallurgical Engineering, Urmia, Iran
**v.alimirzaloo@urmia.ac.ir*

Abstract: In order to study the influences of the input parameters involved in cyclic extrusion compression in equal channel angular pressing (CECAP), on the respond parameters, finite element analysis (FEA) and respond surface method (RSM) were employed. Due to the medical importance of CP-Ti, it was selected as material to be evaluated. To meet this target, ram speed (V), friction coefficient (μ), input extrusion diameter (E) and longitude distance of input extrusion to ECAP region (L) were selected as input parameters, and the strain inhomogeneity was considered as respond variable. To quantify strain inhomogeneity, standard deviation (S.D) was applied. RSM and analysis of variance (ANOVA) were employed to mathematically extract the model for the respond and calculate the effectiveness of the parameters, respectively. Deform 3-D and Design Expert software's were used to numerically simulate the process, and run the RSM experiments, respectively. ANOVA outcomes revealed that ram speed (V), the interaction between ram speed (V) and input extrusion diameter (E), and the interaction between longitude distance of input extrusion to ECAP region (L) and friction coefficient (μ) are the most significant parameters influencing the strain inhomogeneity.

Keywords: CECAP process, strain inhomogeneity, Respond surface Method, Finite Element Analysis, CP-Ti

Novel optimized die geometry to reduce die-roll size in fine-edge blanking process

B. Salehebrahimnejad[1*], **M. Shahbaz**[2] and **M. Moradi**[3]

[1]*Urmia University, Department of Mechanical Engineering, Faculty of Engineering, Urmia, Iran, salehebrahimnejad@gmail.com*
[2]*Urmia University, Department of Materials Science and Engineering, Faculty of Engineering, Urmia, Iran, m.shahbaz@urmia.ac.ir*
[3]*Department of Mechanical Engineering, Isfahan University of Technology, Isfahan, Iran, moradi@cc.iut.ac.ir*

Abstract: In this paper, a new die structure is designed in a fine blanking process due to increase edge quality and reduce the die roll size. To this end, a specified distance was displaced between the two v-ring indenters on the die and blank holder. This fact causes the moment rising between them which consequence in reducing die roll size. An optimization method has been used to improve the newly designed die. For this aim, three parameters consist of v-ring indenters distance, height, and die corner radius have been defined in three levels as input data, which applied in a developed finite element model (FEM) of fine blanking process. Johnson cock fracture criteria and element kill method are used to simulate the process. In order to verify the developed FEM, the results compared with an experimental study. Response to surface method has been used to develop an objective function that correlates the input data and die roll size. In addition, Simplex optimization method has been used to determine the best solution for each parameter in order to minimize the die role size. The findings show that new die decreased the die roll size about 81% in comparison with the fine blanking process in experimental study. Results also show that v-ring indenter's distance has the most significant influence on the reduction of die roll size in the new die design.

Key words: Fine blanking, V ring indenters, Die roll, Response to surface method, Simplex optimization

Nanopatterned and 3D printed Contact Lenses

Haider Butt[*1]

*[1]Asociate Professor, Khalifa University of Science and Technology, Abu Dhabi, UAE,
haider.butt@ku.ac.ae*:

Keywords: Contact lenses, nanostructures, wearable technologies, sensors, healthcare

Abstract

One of the key challenges in producing nanostructures based commercial healthcare applications is the scaling up of the fabrication process. We present the fabrication of dye based nanostructures by using the fast and commercially viable method of holographic laser ablation. In this method we use a single beam of a nanosecond laser, which after reflecting from a mirror self-interferes. This results in an interference pattern which can be used to ablate well-ordered gratings in thin films. The period of the grating is determined by the incident wavelength (⍰) and tilt angle (⍰) of the sample with respect to normal incidence. In this manner we recorded various holographic nanopatterns onto transparent substrates, such as glasses and commercial contact lenses (Fig. 1). Using this quick, scale and economical method we produced several wearable contact lens sensors. These contact lens based holographic sensors can be used for monitoring the eye curvature and pressure of glaucoma patients. The holograms can also be functionalized to sense glucose concentrations in the tears of diabetic patients. The findings have been reported in highly reputable journals and have also received a lot of media attention. The approach was also extended into 3D patterning by ablating 3D assemblies of Ag nanoparticles within polymer media. Through laser ablation, ordered 3D geometries/patterns were written within the polymer layers. These reconfigurable geometries act as holographically recorded optical devices.

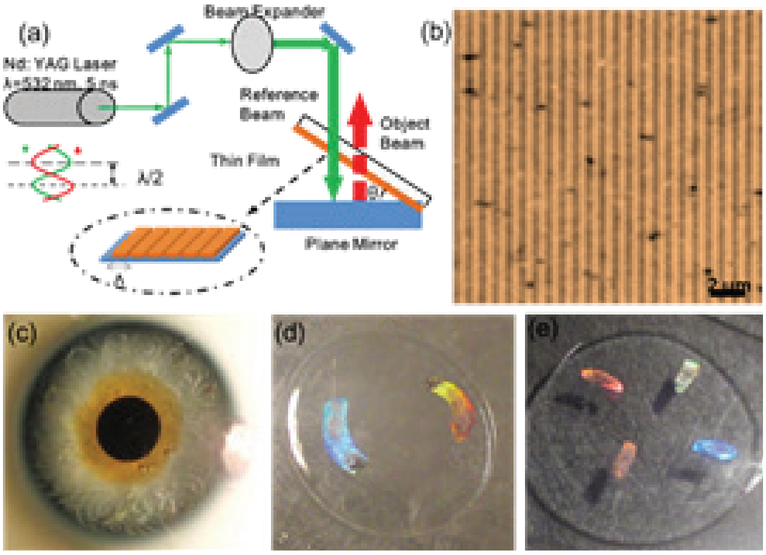

Fig 1: (a) Holographic laser ablation process, (b) the nonpatterns produced, (c-e) holograms printed on commercial contact lenses.

Does decreased antioxidant defense systems cause cancer?

Halit Demir

Van Yüzüncü Yıl University, Faculty of Science, Department of Biochemistry, Van-Turkey.

In most of the studies, antioxidant defense systems are decreased in different cancer types. Cancer is the uncontrolled growth of cells. Changes appear in cells. Antioxidant defense systems may decrease as a result of the increase in free radicals. As a result, lipid peroxidation levels or oxidative stress generally increase. Oxidative stress is known to cause not only cancer but also diseases such as diabetes, aging, cardiovascular diseases, hypertension and rheumatoid arthritis.

In conclusion, antioxidant defense systems or decreased antioxidant activities may play an important role in the etiopathogenesis of cancer diseases.

Key words: Antoxidant enzymes, cancer, oxidative stress.

THE THEORETICAL DESCRIPTION FOR Hg2+ ELECTROCHEMICAL DETERMINATION AND ELIMINATION, ASSISTED BY 2-MERCAPTOBENZIMIDAZOLE

Bohdana Yu. Banul, Tetyana V. Honchar
Bukovinian State Medical University, Ukraine

Mercury determination and demercurization are among the most important desintoxication processes in the world, and the electrochemical methods may be interesting for this purpose.
In this work, 2-mercaptobenzimidazole-assisted mercury ion electrochemical determination is theoretically evaluated. In this case, 2-aminobenzimidazole forms a complex compound with mercury, leading to the simultaneous coordinator and electrochemical polymerization. This process is interesting from both analytical and synthetical point of view (Fig. 1), as yields a highly conducting coating.

The mathematical model for this system confirms the efficiency of this system from both electroanalytical and electrosynthetical point of view.

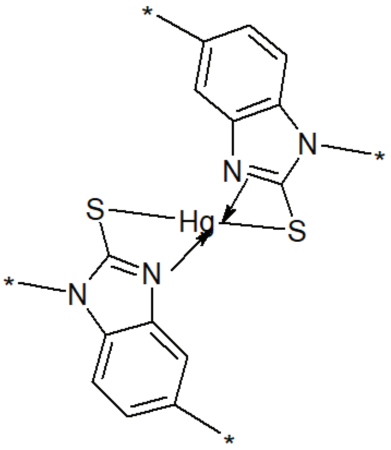

Fig. 1. The (electro)polymerized mercury complex of 2-mercaptobenzimidazole.

THE THEORETICAL DESCRIPTION FOR GALVANOSTATIC COPPER ION DETERMINATION IN WINES

Olga V. Skrypska[1], Valentyna D. Yuzkova*[1], Oksana P. Vitriak[2] and **Yulia M. Andriichuk[1]**

[1]Chernivtsi National University, Ukraine
[2]Kyiv National Trade and Economics University, Ukraine
E-mail: uzkovav@ukr.net

Copper is one of the most used metals. It is one of the first metals known to humanity and it is very important either for the biological functions, or for the industry. For example, hemocyanin, a blue blood pigment of molluscs and some crustacea contains bivalent copper ion in its center. Also, copper is frequently used in motherboard production, reason why the wastewater of computing industry is highly polluted by Cu2+.

In excess, these ions are highly toxic. They may even appear in food and beverages, stored in the copper vessels. Its biological action is dose-related. Therefore, the development of both determination and elimination (recovery) of copper ions from food, beverage and wastewater is really actual.

In the work [1], a spectrophotometric method for copper determination in Brazilian tiquira (cachaça) beverage has been developed. It was based on Cu(II) complexation with Sudan I [2] analog 1-(2-pyridilazo)-2-naphthol (Fig. 1)

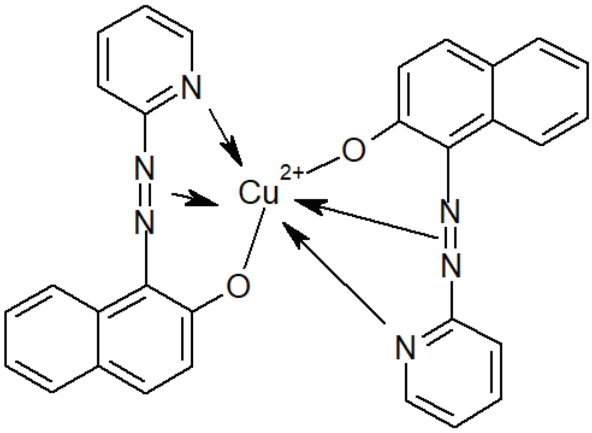

Fig. 1. Copper complex with 1(2-pyridilazo)-2-naphthol

This method may be easily reconfected as electrochemical, as the electrochemical stage would lead to complex compound electropolymerization [3]

The theoretical analysis of the correspondent model, given in this work, confirms the efficiency of the electrochemical reaction for either electroanalytical, or electrosynthetical or eliminative process for copper. As for the oscillatory instability, it will be caused by either chemical or electrochemical influences on the double electric layer.

References:
1. R.W.S. de Oliveira, P.R. Barros Gomes, J. Diniz Ribeiro et al., Rev. Colomb. Cien. Quím. Farm., 49(2020), 353
2. A. Bagheri, B. Hassani Marand, Russ. J. Electrochem., 56(2020), 453
3. V.V. Tkach, M.V. Kushnir, S.C. de Oliveira et al., Lett. Appl. NanoBioSci., 10(2021), 2078

THE THEORETICAL DESCRIPTION FOR COPPER OXIDE NANOPARTICLES ASSISTED THIOPHENE ELECTROPOLYMERIZATION

Zh. O. Kormosh[*1] and **Z.O. Gagolkina**[2]
[1]Lesya Ukrainka Volyn National University, Ukraine
[2]Macromolecular Chemistry Institute of NAN of Ukraine, Kyiv, Ukraine
E-mail: zholt1971@ukr.net

Thiophene is one of the most used monomers for conducting polymers. Polythiophene has been the first CP commercially used by Xerox® in electrostatic brushes.

Polythiophene may be electropolymerized either chemically or electrochemically. In the last case, the electropolymerization becomes more difficult, due to

- High monomer polymerization potential;
- Lower polymer overoxidation potential.

The sum of both of those phenomena is accepted to be named as “the polythiophene paradox”. It occurs during the electropolymerization and, more rarely during the chemically induced polymerization, case it is induced by in situ formed strong oxidant.

This generally occurs if CoO(OH)/CoO2 and CuO/CuO(OH) redox pairs are used. In the last case, when the copper oxide nanoparticles are oxidized or electrooxidized in alkaline media, the aggressive trivalent copper form oxidizes both the monomer and its polymer, leading to the polythiophene paradox, according to the Fig. 1:

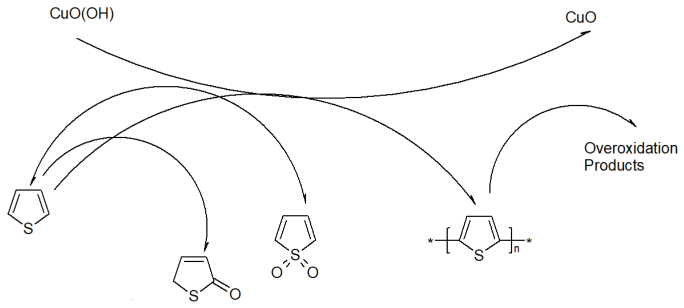

Fig. 1. CuO(OH)-assisted chemical representation for polythiophene paradox

In this work, a mathematical model for trivalent copper-assisted polythiophene paradox. In this case, the oscillatory behavior will be less probable than during the direct electrooxidation of thiophene. Nevertheless, the polythiophene, obtained by this synthesis, remains partially oxidized.

THE THEORETICAL DESCRIPTION FOR VO(OH)-ASSISTED CYANIDE GAS SENSOR

Tetyana V. Morozova, Volodymyr V. Mozgovyi

National Transport University, 02000, M. Omelianovych-Pavlenko Str., 1, Kyiv, Ukraine

Cyanide ion is one of the major pollutants of the environment, including soils, air and natural waters. It is present in the air of the highways either due to the high escape gases concentration, or due to the asphalt components evaporation. Organic nitriles are also present. For this and other reasons, the electrochemical determination of either inorganic or organic cyanides is really actual.

In this work, the possibility of VO(OH)-assisted cyanide determination has been evaluated. In the presence of both cyanides and nitriles, the behavior of this system will be described by the mathematical model (1):

$$\begin{cases} \dfrac{dc}{dt} = \dfrac{2}{\delta}\left(\dfrac{\Delta}{\delta}(c_0 - c) - r_c\right) \\ \dfrac{dn}{dt} = \dfrac{2}{\delta}\left(\dfrac{\Delta}{\delta}(n_0 - n) - r_n\right) \\ \dfrac{dv}{dt} = \dfrac{1}{V}(r_c + r_n - r_v) \end{cases}$$

And the analysis of this model confirms the efficiency of the vanadium oxyhydroxide as cathode modifier for cyanide determination

THE THEORETICAL DESCRIPTION FOR DICLOPHENAC DETERMINATION IN ALKALINE MEDIUM OVER COBALT (III) OXYHYDROXIDE

I.M. Khmeliar, L.O. Kushnir

Rivne State Basic Medical Academy, 33000, M. Karnaukhova Str. 53, Rivne, Ukraine

Diclophenac (Fig. 1) is one of the anti-inflammatory drugs and pain killers, mostly used worldwide. Its mechanism of action is based on alkaline hydrolysis of chlorine atoms (Fig. 1), yielding a polyphenolic compound, scavenging the ROS, yielding in the inflamed tissue during the inflammation process [1].

$X = Na^+, K^+, NH^{4+}$

New radical will be more difficult to recombine, which will thereby detain the inflammation process, providing the pain relief. Diclophenac is applied topically, orally, rectally, intravenously and intramuscularly.

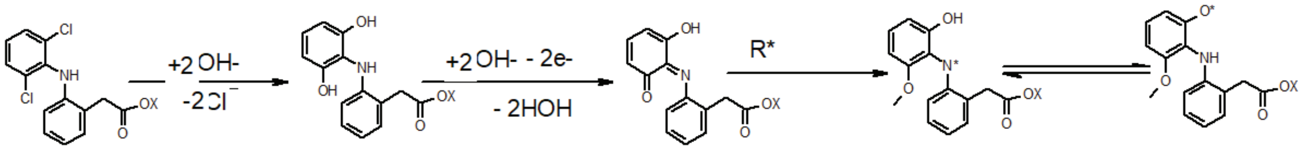

Fig. 1. Diclophenac mechanism of action

On the other hand, in acidic media, it provokes gastritis and gastric ulcers, due to the acidic hydrolysis, yielding a weak acid (Fig. 2).

Also, its excessive concentrations, like also the long-time use may lead to the side effects like tiredness, slumber, nausea and vomit. Therefore, the development of an efficient method for diclophenac quantification is really actual.

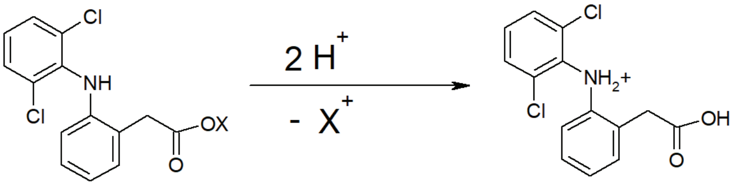

Fig. 2. Acidic hydrolysis of diclophenac

Diclophenac is one of the most popular objects for the electroanalytical processes nowadays. Either direct electrooxidation, or selective membrane development are admitted. In the first case, chemically modified electrodes are widely used, and cobalt (III) oxyhydroxide may be an interesting option for diclophenac electrochemical determination.

The theoretical description for diclophenac electrochemical determination over CoO(OH)-modified electrode. In basic solution, diclophenac is hydrolyzed, generating two parallel oxidation chains. Analyzing the correspondent mathematical model by linear stability theory and bifurcation analysis, we confirm that, despite of the high probability of the oscillatory behavior, the electroanalytical process remains efficient.

THE THEORETICAL DESCRIPTION FOR ECOPIPAM ELECTROCHEMICAL DETERMINATION ON AMAVADIN-ION-MODIFIED CONDUCTING POLYMER ELECTRODE

Fahriddin A. Umarov*

Termez branch of Tashkent Medical Academi,
100109, Termez, Islam Karimov Str. 64, Uzbekistan
e-mail: ufa90@inbox.ru

Ecopipam is a modern selective dopamine receptor antagonist, proposed to be used in the treatment of neurological symptoms like stutter, neural teaks. It is also used in the treatment of pathological gambling, Tourette syndrome, cocaine and morphine dependence. Nevertheless, its dosage isn´t cleared yet, and the development of an electroanalytical method for its determination is really actual [1].

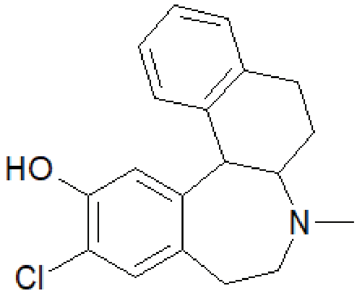

Fig. 1. Ecopipam

Taking into account the ecopipam molecular structure, we may conclude that it is electrochemically active. Moreover, anodic oxidation is preferable and the electropolymerization scenario is not discarded, reason why amavadin-ion, a natural complex from *Amanita muscaria* may be used.

In this work, the theoretical description for ecopipam electrochemical determination over amavadin ion-modified electrode has been given. The correspondent mathematical model analysis confirms the efficiency of amavadin-doped conducting polymer as electrode modifier for ecopipam determination.

References:
1. V.V. Tkach, M.V. Kushnir, I.M. Shevchuk et al., Appl. J. Env. Eng. Sci., 8(2022), 123

THE THEORETICAL DESCRIPTION FOR Co(OH)-ASSISTED RISPERIDONE ELECTROCHEMICAL DETERMINATION

S.M. Lukanova
Chernivtsi National University, Ukraine

Risperidone (Fig.1) is an atypical antipsychotic drug, developed by Johnson&Johnson. It is used for treatment of bipolar syndrome, depressive psychosis, obsessive-compulsive syndrome and even schizophrenia. It is popularly known as mentioned in House M.D. series.

Being the dopamine antagonist, its side effects include movement disorder, dizziness, malign neuroleptic syndroms, weight gain and aument of the suicide risks, reason why the determination of risperidone concentration is really actual, and the electrochemical methods may be efficient method for it.

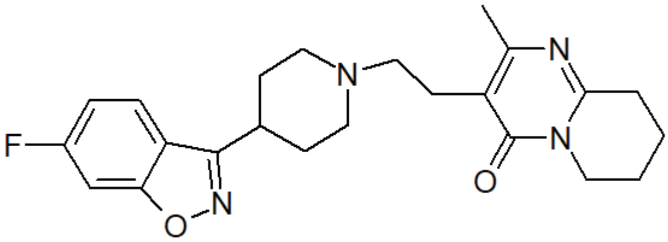

Fig. 1. Risperidone

Either cathodic or anodic routes are possible for risperidone electrochemical determination. In the case of anodic route, cobalt (III) oxyhydroxide may be used. It is an interesting semiconducting electroactive material, capable to be either oxidant or reductant.

Both of the options are applicable for risperidone electrochemical determination. Two correspondent mathematical models were developed and analyzed for this case, and its analysis confirms the efficiency of CoO(OH) for risperidone determination.

THE THEORETICAL DESCRIPTION FOR AMAVADIN-ASSISTED LEDOL ELECTROCHEMICAL DETERMINATION IN HONEYS

Oksana P. Vitriak and **Olena V. Hrabovska**

Kyiv National University of Trade and Economics, 02156, Kyoto Str. 21, Kyiv, Ukraine

Honey is one of the most important food product, known since the Age of Stone. It is produced by honey bees from pollinizing plants nectar.

Generally, the honey is accepted to be secure. Nevertheless, some plants may give a poisonous honey, known as “mad honey”. Its toxic properties are associated with the tertiary alcohol, known as ledol (Fig. 1):

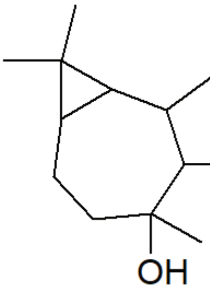

Fig. 1. Ledol

As for now, no electroanalytical processes for ledol electrochemical determination have been developed yet. Nevertheless, it is of high importance, for food security reasons. Therefore, in this work we analyze the possibility for ledol electrochemical determination by amavadin-ion in basic media.

The electroanalytical process is given by cyclopropane ring gradual oxidation by amavadin oxidized form, containing pentavalent vanadium. The model analysis confirms that the electrochemical determination is easily realized and the steady-state stability is easy to obtain and maintain, although the oscillatory behavior is more probable.

THE THEORETICAL DESCRIPTION FOR MAGNESIUM-ION DETERMINATION, BASED ON GALVANOSTATIC ELECTROPOLYMERIZATION OF MAGNEZONE-XC

D. M. Musayeva and **H. Zh. Salomova**
Bukhara State Medical Institute, Uzbekistan

Magnesium chlorate is one of the widely used inorganic pesticides. It is used as secant and defoliant agents in beans, cotton and sunflower. Its structure is described on the Fig. 1:

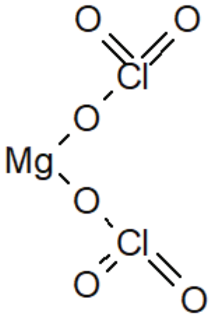

Fig. 1. Magnesium chlorate

Its mechanism of action is based on its hydroscopic properties. As it forms crystallohydrates with the water molecules, it literally "dries" the leaves of the undesirable plant, leading to its degeneration. Nevertheless, while taken in excess, it is may influence not only the weed, but also the cultural plants. Also, it is highly toxic to animals and humans, as the chlorate-ion is a strong oxidant. Therefore, the development of the method for determination of magnesium chlorate is really actual, and the electroanalytical methods, which have already been used for both magnesium and chlorate ions could give an interesting service.

The classical method for the magnesium cation determination consists in its complexation with magnezone azo dye group [11 – 12]. One of these dyes is Magnezone XC, one of Sudan dyes (Fig. 2):

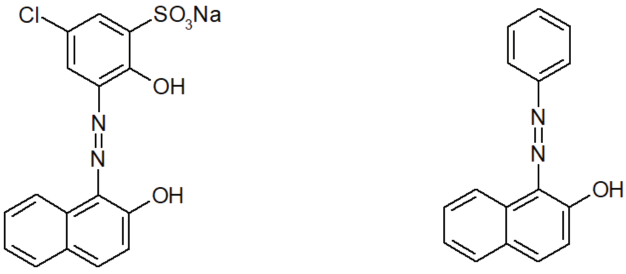

Fig. 2. Magnezone XC (left) and Sudan I (right)

It may be adapted for the electrochemical determination of magnesium cations. Furtherly, the magnezone XC complex may electropolymerize, as in [1], leading to the appearance of a novel material, also capable to assist the electroanalytical processes.

So, the goal of this work is the mechanistic theoretic analysis of the magnesium chlorate electrochemical determination by means of magnesium galvanostatic determination over Magnezone XC. The electroanalytical process will be given as on Fig. 3.

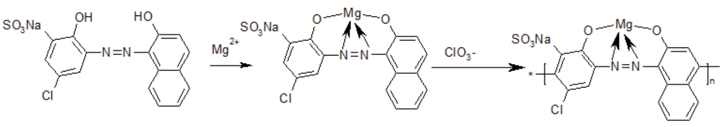

Fig. 3. Scheme of the electroanalytical process

The correspondent mathematical model has been developed and analyzed by means of linear stability theory and bifurcation analysis. It has been shown that from both electroanalytical and electrosynthetical points of view the system is efficient, although the galvanostatic mode is less efficient than the potentiostatic. The linear dependence between the electrochemical parameter and salt concentration is obtained easily, and the material formed during the electroanalytical process is highly conductive and catalytic. On the other hand, the oscillatory behavior in this system will be caused by double electric layer influences on both complexation and electropolymerization stages.

References:

1. V.V. Tkach, M.V. Kushnir, S.C. de Oliveira et al., Orbital Elec. J. Chem., 12(2020), 242

Why Soft,Solution Processing(=Low-EnergyProduction) of Advanced Nano-Materials is Difficult but Necessary for Sustainable Society?

Masahiro YOSHIMURA

Distinguished Chair Professor, Dept of Mater.,Sci. and Eng., National Cheng Kung University, Tainan,Taiwan : yoshimur@mail.ncku.edu.tw
Prof. Emeritus. Tokyo Institute of Technology, Japan : masahiroyoshimura75@gmail.com

Modern our society has been developed with various advanced nano-materials. Most of advanced materials, Metallurgical materials, Semiconductors, Ceramic materials and Plastics have been used in wide area of applications like structural, mechanical, chemical, electrical, electronic, optical, photonic, biological, medical, etc. Most of them except for bio-polymers & bio-minerals have never been produced via biological systems. Thus they have generally been fabricated artificially and/or industrially by so-called high-technology, where high temperature, high pressure, vacuum, molecule, atom, ion, plasma, etc. have been used for their fabrications, then consumed huge amount of resources and energies thus exhausted huge amounts of wastes: materials, heats and entropy. To save this tragedy, we must consider "Cascade use of Heats", and "Low energy Production of advanced nano-materials via water-based industries." Bio-inspired process, which mean that "Learn from Bio-systems then Exceed them" and/or exceed "Green Technology mostly based upon Bio-systems". They should also be necessary for SDGs (Sustainable Developing Goals.)

We have challenged to fabricate those advanced inorganic materials with desired shape/size/location,etc.directlyinlowenergetic routes using aqueous solutions since 1989 when we found a method to fabricate BaTiO3 film on Ti substrate in a Ba(OH)2 solution by Hydrothermal Electrochemical[HEC] method at low temperatures of 60-200 C. We proposed in 1995 an innovative concept and technology, "Soft Processing" or "Soft Solution Processing," which aims low energetic (=environmentally friendly) fabrication of shaped, sized, located, and oriented inorganic materials in/from solutions1,2). It can be regarded as green processing, or eco-processing. When we have activated/stimulated interfacial reactions locally and/or moved the reaction point dynamically, we can get patterned ceramic films directly in solution without any firing, masking nor etching. Direct Patterning of CdS, PbS and CaWO4 on papers by Ink-Jet Reaction method. Furthermore, we have succeeded to fabricate BaTiO3 patterns on Ti by a laser beam scanning3) and carbon patterns on Si by plasma using a needle electrode scanning directly in solutions4). Successes in TiO2 and CeO2 patterns by Ink-Jet Deposition, where nano-particles are nucleated and grown successively on the surface of substrate thus become dense even below 300 C will be presented.Nano-structured films will be also talked. .A recent novel subject, Soft Processing for various nano-carbons including Graphene, functionalized Graphene and Mxene will be introduced. Where we have succeeded to prepare functionalized Graphene Ink via successive processes under ambient temperature and pressure conditions.5-8) In addition we propose Heat cascades for Materials Fabrication to elliminate wastes (Heat and materials =Entropy).

1. MRS Bulletin,25[9],Sept. issue 2000, special issue for Soft Processing of Advanced Inorganic Materials ,Guest Editor:M. Yoshimura and J. Livage.
2. Yoshimura, M., J. Mater. Sci.,41 [5],1299-1306 (2006), 43[7]2085-2103(2008).
3. Watanabe, T.,Yoshimura,M.,et al. Carbon,44,799-802(2006).
4. Watanabe, T.,Yoshimura,M.,et al.,Thin Solid Film, 515,2696-2699(2006)
5. J. Senthilnathan, M.Yoshimura et al., J. Mater Chem A,(2014) 2, 3332-3337 (2015)
6. Sanjeeva Rao, K and Yoshimura, M et al. Adv. Funct. Mater.,25,298-305(2015)
7. E. Satheeshkumar,Y. Gogotsi,M. Yoshimura,et al. Sci, Repts, 6,1-9 (2016)
8. E.Satheeshkumar,J.R. Rombardi,M. Yoshimura,Materials Advances,1,146(2020).

THE THEORETICAL DESCRIPTION FOR PYRROLE DERIVATIVE INDIRECT ELECTROPOLYMERIZATION, ASSISTED BY METAHYPOFERRATE ION

M.C. Nunes[*1], **J. I. Martins**[1] and **P. I. Yagodynets**[´2]

[1]*Faculdade de Engenharia da Universidade do Porto, Portugal*
[2]*Chernivtsi National University, Ukraine*
E-mail: mcnunes@fe.up.pt

The indirect electropolymerization consists is realized, when the monomer does not participate in the electrochemical stage directly. The chain propagation center is thereby created by the reaction between the electrochemical stage product and the monomer, creating the cation(anion)-radical.

One of the methods for the indirect electropolymerization is cathodic electrodeposition. Different redox pairs may be used for this purpose, and one of those pairs is the redox pair FeO_4^{2-} / FeO_3^{2}, like:

$$FeO_4^{2-} + 2H^+ + 2e- \rightarrow FeO_3^{2-} + H_2O \qquad (1)$$

Metahypoferrate becomes, thereby, a pyrrole polymerization initiator

$$FeO_3^{2-} + 6H^+ + Py \rightarrow Fe^{3+} + Py^{*+} + 3H_2O \qquad (2)$$

Iron (III) also begins to initiate the chain:

$$Fe^{3+} + Py \rightarrow Fe^{2+} + Py^{*+} \qquad (3)$$

Analysis of the correspondent model confirms that the electropolymerization is more efficient than on anode in the same conditions. The oscillatory behavior is possible, but it may only be caused by DEL influence on the electrochemical stage.

THE THEORETICAL DESCRIPTION FOR PARACETAMOL AND NAPROXEN ELECTROCHEMICAL DETERMINATION, ASSISTED BY CONDUCTING POLYMER COMPOSITE WITH COBALT (III) OXYHYDROXIDE

Bohdana Yu. Banul

Bukovinian State Medical University, 58001, Teatralna Sq., 9, Chernivtsi, Ukraine

\Paracetamol or acetaminophen (Fig. 1 to the left) is an acylated phenolamine, introduced to the pharmaceutical practice in 1893 by Von Mering as an analgesic drug for adults and children. Its action is based on the prostaglandin synthesis inhibition in central nervous system. Nevertheless, its side effects include the liver intoxication leading even to the death. Therefore, the development of new methods for its determination is really actual [6 – 8].

On the other hand, naproxen] is a non-steroid analgesic drug, based on 2-β-naphthylpropionic acid. Its action is based on the cyclooxidases inhibition. It is used in treatment of muscular pains, convulsions and edemas. Nevertheless, it is contraindicated to babies and children till 2 years old, like also to the people with asthma, gastrointestinal diseases and gastric ulcers. The side effects include sleepiness, fatigue, depression. So, the development of the precise and exact methods for its determination in different conditions is actual.

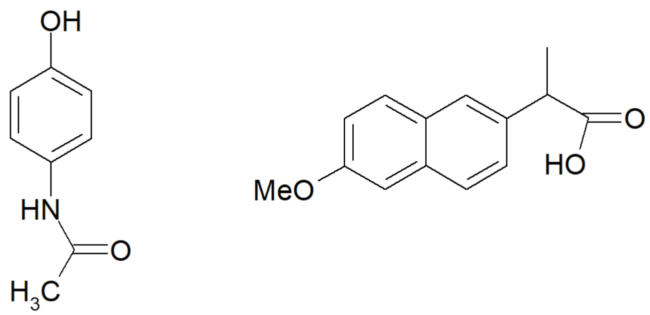

Fig. 1. Paracetamol (left side) and naproxen (right side)

Taking into account the structures of paracetamol and naproxen, it is possible to conclude that both of them are electrochemically active, so the electroanalytical processes are applicable to them. Moreover, in certain conditions, their electropolymerization, yielding a conducting polymer, is also possible, due to the aromatic nature of both of the analytes.

In this work, the possibility for the electrochemical simultaneous determination of naproxen and paracetamol over the electrode, modified by conducting polymer composite with cobalt (III) oxyhydroxide, is analyzed for the first time. The correspondent mathematical model has been developed and analyzed by means of linear stability theory and bifurcation analysis. It has been shown that the electrochemical analysis of both of the substances may be easily conducted and interpreted at moderate electrode potentials. As for the oscillatory behavior, it is more probable than in the simplest cases, due to the ionic forms´ transformations during the naproxen determination and their impact to DEL capacitance.

Novel Topological Thermoelectrics

Oleg A. Tretiakov[1*] and **Y. Achim**[1]

[1]*University of New South Wales, Sydney, Australia*

Abstract: Topological insulators (TI) are novel quantum materials with insulating bulk and topologically protected conducting surfaces with Dirac-like band structure. In this talk I will introduce a proposal on how to enhance thermoelectric transport in TI materials emerging from the topological properties of their band structure. The thermoelectric transport in porous and thin-film three-dimensional TIs will be considered. At high surface to bulk ratio the thermoelectric efficiency, described by the figure of merit ZT, can be large due to the high ratio of perfectly conducting surface states to the bulk and the suppressed phonon thermal conductivity. These large values of ZT, much higher than unity, make this system a very strong candidate for applications in heat management of nanodevices, especially at low temperatures. Our realistic ab-initio calculations show that in thin TI films ZT of order 10 can be reached, hence making it ideal for heat management applications.

THE THEORETICAL DESCRIPTION FOR OMEPRAZOLE CATHODIC DETERMINATION IN ACIDIC MEDIA

T.D. Onyshchuk, A. P. Stibysh and **H.V. Holobosh**

Rivne State Basic Medical Academy, 33000, M. Karnaukhova Str. 53, Rivne, Ukraine

Nowadays, the frequency of verticular and chronic gastritis and gastritic ulcers occurrences has been grown slightly in both urban and rural areas. Gastritis and ulcers may be treated by the H2-blocking molecules, detaining the proton transfer. One of this molecules is omeprazole (Fig. 1):

Its blocking effect is achieved by the formation of its sulphenamide metabolite, forming complex with both H+K+ATPase+ and gastric mucosa carbonic anhydrase[3 - 4], inhibing the proton transfer into the gastric lumen. This effect is possible, due to the presence of both pyrrolic and pyridinic nitrogen atoms, in its composition. Nevertheless, may present various collateral effects, like headache, vertigo, nausea, diarrhea and flatulence, which may cause discomfort. Moreover, the concentration control is also important for successful treatment of patients with liver and kidney insufficiency or older people. Thus, the search of a precise, exact, rapid and sensitive method for its quantification is a really actual problem.

Many electrochemical methods have been proposed for omeprazole electrochemical determination, being generally based on the omeprazole electrochemical oxidation. Nevertheless, the omeprazole electrochemical reduction is also possible, although in specific conditions.

In this work, we describe theoretically the possibility of omeprazole electrochemical determination, assisted by conducting polymer coating in acidic media. In this case, the omeprazole molecule is reduced by sulfoxide group. Therefore, the electroanalytical process will be described by a bivariant equation-set, analysis of which confirms the efficiency of the conducting polymer in acidic media for omeprazole electrochemical determination both in vivo and in vitro.

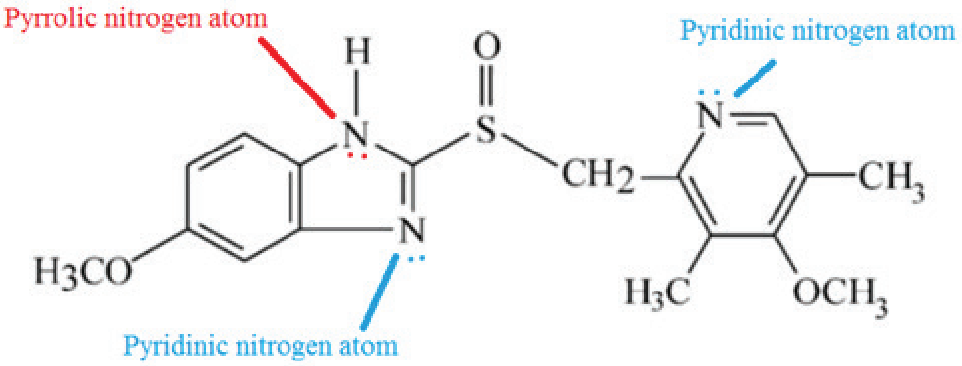

Fig. 1. Omeprazole molecule

ISBN: 978-975-7616-84-9

THE THEORETICAL DESCRIPTION FOR ORELLANIN ELECTROCHEMICAL DETERMINATION AND ELECTROPOLYMERIZATION ON CERIUM DIOXIDE COMPOSITE WITH CHALCONE POLYMERS

Jarem R. Garcia[1], Bárbara C. Fiorin[1], José Inácio Ferrão da Paiva Martins*[2]

[1]Universidade Estadual de Ponta Grossa, Campus de Uvaranas, Av. Gal. Carlos Cavalcanti, 4748, 84030-900, Ponta Grossa, PR, Brazil
[2]Faculdade de Engenharia da Universidade do Porto, Faculdade de Engenharia da Universidade do Porto, 4200-465, Rua Dr. Roberto Frias, s/n, Porto, Portugal
**E-mail: jipm@fe.up.pt*

Orellanin (2-2´ (3,4,3´4´-tetrahydroxy) dipyridyl-N,N-dioxide, Fig. 1) is the main toxin of poisonous mushrooms Orellani (foolish webcaps). The first symptoms of orellanin poisoning are nausea, vomiting, stomach pains, headaches, followed by kidney failure (immense thirst, frequent urination, pain on and around the kidneys). If untreated, death is imminent.

The structure is very similar to that of hydroquinonic compounds, and the human receptor will recognize orellanin as one of those, leading to toxic quinone-like forms, participating in radical oxidation processes in organism, driving it off the normal path. As both the cooked and uncooked mushrooms contain these compounds and as the orellani mushrooms are difficult to be recognized, the orellanin poisonment detection is really actual, and the electrochemical methods, yet used for hydroquinonic compounds, may be used for this purpose.

Possessing electroactive groups (N-oxide, aromatic ring and phenol-like hydroxyls) orellanin is electroactive. Moreover, mimicking the hydroquinonic structure it may be used as a monomer for economical and green (semi)conducting polymer [13 – 19] with interesting catalytic properties. Therefore, the electrochemical (direct or assisted) oxidation of orellanin may serve as the font for both electroanalytical or electrosynthetical purpose.

In this work the Poly(Chalcone)/CeO2 composite function in orellanin and hydroquinone sensing is evaluated. The electrochemical behavior of the sensor is similar to that of cobalt (III) oxyhydroxide. Nevertheless, the electrochemical oscillations are more probable, due to the Ce3+ formation and ionic force impact.

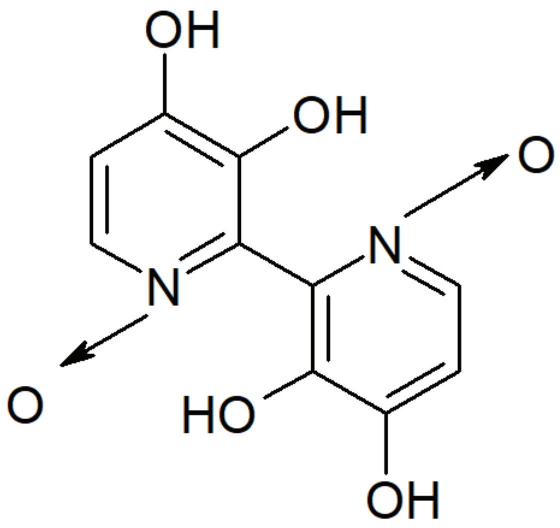

Fig.1. Orellanin structure

Bioengineered Filter Paper Platforms for Efficient Cryopreservation of Cells and 3D Tumor Models

Mohammad A. Qasaimeh, NYU Abu Dhabi

~~*1 Universidade Estadual de Ponta Grossa, Campus*~~

The development of simple and practical cell cryopreservation method is of great interest to many sectors, especially Cell Banks where efficient storage and streamlined transportation of samples are essential. Although the success of such methods has been increased in recent years, there is still need for a unified platform that is highly suitable for efficient logistics of cryogenic storage of cells in addition to their easy-to-manage retrieval and transportation. In the first part of this talk, we will present our technology of paper-based cell cryopreservation as an efficient and simple alternative to conventional methods. The technology is space-saving, cost-effective, simple and easy to manage. Furthermore, the technology supports the formation and cryopreservation of 3D tumor models, which represent physiological conditions of in vivo tumor microenvironment. Hence, 3D tumor models possess big potential in pharmaceutical applications. In the second part of this talk, we will discuss our versatile, robust, and cost-effective method that utilizes a paper platform to create cryopreservable high throughput arrays of 3D tumor models. The paper-based cryopreservation technology offers a low cost, easy, and fast cell cryopreservation, and allows for high-throughput 3D tumor arrays to be generated, cryopreserved, and thawed for on-demand use. The technology could potentially provide unparalleled advantages to the fields of tissue engineering and personalized medicine.

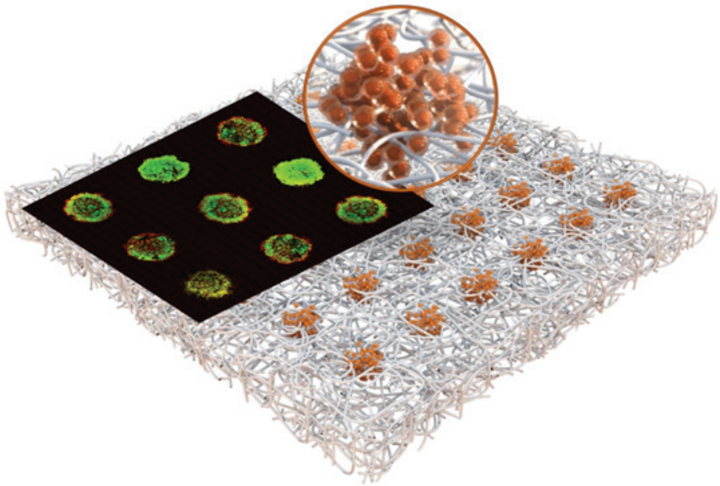

Dr. Qasaimeh is an Associate Professor of Mechanical Engineering and Bioengineering at New York University Abu Dhabi (NYUAD), Abu Dhabi, UAE, and with the Department of Mechanical and Aerospace Engineering and the Department of Biomedical Engineering at New York University (NYU), New York, USA. He established the Advanced Microfluidics and Microdevices Laboratory (AMMLab) in 2014, and his current research interests include developing microfluidic and MEMS devices for point-of-care diagnostics. Recently, Dr. Qasaimeh was awarded the Technology Innovation Pioneers (TIP) Award during the TIP 2020 Summit. Prior to joining NYUAD, he was a Postdoctoral Research Associate at Massachusetts Institute of Technology and a Research Fellow at Harvard Medical School. Dr. Qasaimeh completed his PhD degree in Biomedical Engineering from McGill University, Montreal, where he received several prestigious fellowships and awards including the NSERC Postdoctoral Fellowship and the Alexander Graham Bell Graduate

Scholarship. Dr. Qasaimeh's research has been published in numerous peer-reviewed journals including Nature Communications, Small, Advanced Materials Technologies, and Lab on a Chip, and he delivered more than 40 keynote and invited lectures at national and international conferences. Dr. Qasaimeh is actively involved in organizing several local and international conferences, and currently serving as a Co-Chair at the NYU Biomedical and Biosystems Conference series and the General Chair of the 2023 International Conference on Manipulation, Automation and Robotics at Small Scales (MARSS 2023). Dr. Qasaimeh is serving as an Associate Editor with the Frontiers in Robotics and AI (Nano- and Microrobotics), an Associate Editor with the IEEE Nanotechnology Magazine, a Topic Editor with the journal Biosensors, a Review Editor with the journal Frontiers in Bioengineering and Biotechnology, and an Editorial Board Member of Scientific Reports at the Nature Publishing Group.

THE THEORETICAL MODELING FOR PREGABALIN AND GABAPENTIN VO(OH)-ASSISTED ELECTROCHEMICAL DETERMINATION

Vitalii M. Kishchuk, Oksana D. Matsyuk

Rivne State Basic Medical Academy, 33000, M. Karnaukhova Str. 53, Rivne, Ukraine

Pregabalin is a 3-isobutyl derivative of gamma-amino butyric acid (GABA) with anti-convulsant, anti-epileptic, anxiolytic, and analgesic activities Although the exact mechanism of action is unknown, pregabalin selectively binds to alpha2delta (A2D) subunits of presynaptic voltage-dependent calcium channels (VDCCs) located in the central nervous system (CNS), preventing calcium influx and the subsequent calcium-dependent release of various neurotransmitters. Pregabalin does not bind directly to GABA-A or GABA-B receptors and does not alter GABA uptake or degradation.

Sold under the trade name “Lyrica”, it has been most used most commonly to treat epilepsy, neuropathic pain, fibromyalgia and generalized anxiety disorder, epilepsy. It acts as an add-on therapy for partial seizures with or without secondary generalization in adults. But its action includes side effects like sleepiness, confusion, trouble with memory, poor coordination, dry mouth, problem with vision and weight gain. While potentially serious side effects include angioedema, drug misuse, and an increased suicide risk. So, the development of an efficient and rapid method for its quantification is really actual task.

In this work, the electrochemical determination of pregabalin and gabapentin on vanadium (III) oxyhydroxide-modified cathode is described theoretically. The electroanalytical process will be described by a trivariant equation-set, analysis of which confirms the efficiency of the VO(OH)-assisted selective determination of pregabalin and gabapentin.

THE THEORETICAL DESCRIPTION FOR VO(OH)-ASSISTED PROCARBAZINE CATHODIC ELECTROCHEMICAL DETERMINATION

O.V. Luganska[*1], **M.P. Krasko**[2] and **V.M. Odyntsova**[2]

[1]Zaporizhzhia National University, Zaporizhzhia
[2]Zaporizhzhia State Medical University, Zaporizhzhia.
E-mail: 130805olga@gmail.com

Procarbazine, or, better saying, N-isopropyl-⊠-(2-methylhydrazino)-p-toluamide is one of the drugs commonly used in chemotherapy at different types of cancer.

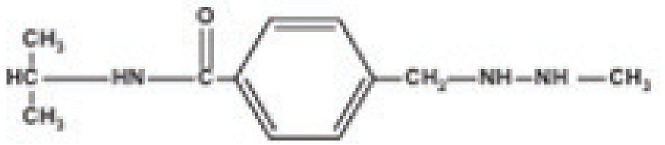

The exact mechanism of its action hasn´t been determined yet. However, it is already known that its interaction with various substances (such as enzymes or compounds of transition metals) in the human organism leads to the formation of toxins (aldehydes, hydrazine and metal complexes). Therefore, search of sensitive, precision and expeditious method for determining the concentration of the compound is a really actual task, and the electrochemical detection, yet used for other substances seems to be an interesting resolution for it.

As procarbazine contains the electroaccepting moieties, the cathodic route is more preferable for its determination, and vanadium (III) oxyhydroxide could be a suitable cathode modifier. In this work, the possibility for the VO(OH)-assisted electrochemical determination of procarbazine is evaluated.

The schematical representation of procarbazine gradual reduction is represented as:

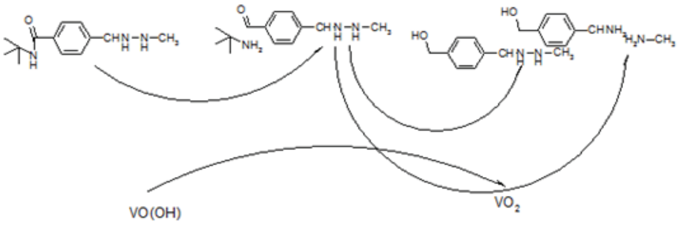

The analysis of the model, correspondent to this system confirms that VO(OH) may be an efficient electrode modifier for procarbazine. As for the linear dependence range, it is relatively wide and may be even wider than for anodic oxidation.

THE ELECTROCHEMICAL OXIDATION OF PROCARBAZINE ON NICKEL(III)OXYHYDROXIDE AND ITS MATHEMATICAL EVALUATION

Mykola P. Krasko[1] and **Vira M. Odyntsova**[*1]

[1]*Zaporizhzhia State Medical University, 69600, Mayakovsky Ave. 24, Zaporizhzhia, Ukraine*
E-mail: *odyntsova1505@gmail.com*

Procarbazine [1], or, better saying, N-isopropyl-⌧-(2-methylhydrazino)-p-toluamide is one of the drugs commonly used in chemotherapy at different types of cancer

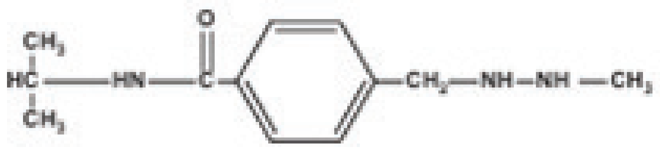

The exact mechanism of its action hasn´t been determined yet. However, it is already known that its interaction with various substances (such as enzymes or compounds of transition metals) in the human organism leads to the formation of toxins (aldehydes, hydrazine and metal complexes). Therefore, search of sensitive, precision and expeditious method for determining the concentration of the compound is a really actual task, and the electrochemical detection, yet used for other substances seems to be an interesting resolution for it.

In this work, the possibility of electrochemical oxidation of procarbazine on nickel (III) oxyhydroxide in slightly alkaline medium, realized for electroanalytical purposes, has been investigated. The corresponding mathematical model has been analyzed by means of linear stability theory and bifurcation analysis. The optimal conditions for electrooxidation and electroanalytical efficiency of the process have been derived. The possibility of oscillatory and monotonic instabilities was also evaluated.

References:

1. V.V. Tkach, S.C. de Oliveira, S.C.B. de Oliveira et al., Anal. Bioanal. Electrochem, 8(2016), 432.

Synthesis and Characterization of Flexible Polydimethylsiloxane Containing Resin for 3D SLA Printers

Emre AKIN1*, Mustafa ÇAKIR1, Boran BERBEROĞLU

1Marmara University, Turkey

Abstract: As well known, epoxy acrylate resins has been widely used in 3D SLA printers applications. Epoxy acrylate system that consisted of bisphenol-A glycerolate diacrylate (epoxy acrylate resin) and 1,6-Hexanediol diacrylate (HDDA, reactive diluent resin) were used in this study. The weight ratio of Bisphenol-A glycerolate diacrylate and HDDA was determined as 1/1. The purpose of this study is to develop a novel epoxy acrylate system for 3D SLA printers and observe its properties. For this reason, a novel polydimethylsiloxane containing urethane acrylate was synthesized as reactive resin and added into epoxy acrylate system with various weight percents. It is also well known that polydimethylsiloxanes increase thermal properties of polymer materials. In order to obtain this novel reactice urethane acrylate resin, hydroxyl terminated polydimethylsiloxane was used as backbone of the chain while isophorone diisocyanate (IPDI) and 2-Hydroxyethyl methacrylate (HEMA) were used for synthesizing urethane acrylate functional groups. The addition of this novel reactive resin was carried out up to 1.5 % into epoxy acrylate system. Mechanical and physical tests were applied to the produced samples such as tensile, Shore-D hardness, abrasive and density tests. Considering of the results, tensile strength and modulus exhibited substantial increases while tensile strain presented large decreases. Taber abrasive resistance showed considerable increases. While Shore-D hardness of the produced novel materials presented slight decreases, the densities showed almost no change.

1. Introduction

In recent years, ultraviolet (UV)-curable products have received great interest due to both technological advances and the increasing environmental pressure to decrease the emission of volatile organic compounds (VOC) [1,2]. In comparison with conventional solvent-based products, UV-curable products present the advantage of low VOC emission, rapid curing at ambient temperature, low energy consumption, high productivity and high degrees of cross-linking (cause to outstanding scratch, chemical resistance). Therefore, these products provide a wide range of economic and ecological benefits. UV-curable coatings usually contain four main components the oligomer, the reactive diluent, the photoinitiator and various additives. Epoxy acrylate (EA) is a common oligomer in UV-curable coatings, which is the most principal component for film formation [3,4]. There have been two kinds of epoxy acrylate oligomers that have been widely used. These are bisphenol diglycidyl ether and epoxy novolac based epoxy acrylate oligomers. As reactive diluents, hexanediol diacrylate (HDDA) and tripropylene glycol diacrylate (TPGDA) have been generally used in epoxy acrylate systems. These reactive diluents dissolve pure epoxy acrylate resin, adjust the viscosity and crosslinking density of epoxy acrylate systems [3,5].

In this study, a novel reactive diluent was used. This reactive diluent was polydimethylsiloxane reactive resin. This polydimethylsiloxane chain was hydroxyl-terminated monomer and was acrylated with the monomer that synthesized from the reaction of isophorone diisocyanate (IPDI) and 2-Hydroxyethyl methacrylate (HEMA). IPDI is diisocyanate having aromatic rings. Therefore, this reactive resin would exhibit higher thermal stability and mechanical properties due to the existing of both siloxane and rigid aromatic groups along this reactive acrylated chain. It was expected that this novel acrylated polybutadien would gain new properties to conventional epoxy acrylate system. In this study, conventional epoxy acrylate system consisted of bisphenol-A glycerolate diacrylate (epoxy acrylate resin) and 1,6-Hexanediol diacrylate (HDDA, reactive diluent resin) was used. The weight ratio of epoxy acrylate and HDDA was determined as 1/1. The synthesized novel polydimethylsiloxane reactive resin was incorporated into this conventional epoxy acrylate system in various ratios. By using this novel reactive resin novel epoxy acrylate systems were obtained. The addition of this novel reactive resin was carried out up to 1.5 %. Mechanical and physical tests were applied to the produced samples such as tensile, shore-D hardness, abrasive and density tests. Considering of the results, substantial increases were observed in terms of tensile strength, modulus and taber abrasive test results. However, Shore-D hardness values presented decreases. Densities did not almost showed no change.

2. Material and Methods

2.1 Materials

Bisphenol A glicerolate diacrylate (Bisphenol A based epoxy acrylate oligomer) and 1,6-Hexanediol diacrylate (HDDA) were purchased from Sigma-Aldrich. Isophorone diisocyanate (IPDI) was used as aromatic diisocyanate that purchased from Covestro. 2-Hydroxymethyl methacrylate (HEMA) was used to acrylate IPDI and this functional monomer terminated hydroxyl-terminated polydimethylsiloxane. This hydroxyl-terminated polydimethylsiloxane purchased from Evonik and its average molecular weight (Mn) was approximately 2250. Irgacure 819 was used as photoinitiator. Dibutyltin dilaurate (T12) was used as catalyst for reactions of isocyanate and hydroxyl functional groups. Tetrahidrofuran (THF) was used as solvent.

2.2. Preparation of conventional epoxy acrylate system

Conventional epoxy acrylate system was prepared by using bisphenol A glicerolate diacrylate and 1,6-Hexanediol diacrylate (HDDA) reactive diluent resin. These components were used as 1/1 by weight. They were mechanically stirred in flask and homogeneous resin was obtained.

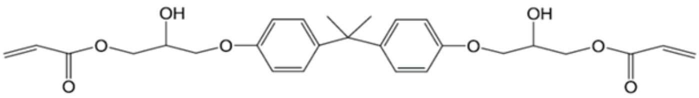

Figure 1. Bisphenol A diglycidyl ether based epoxy acrylate

These components were shown in Figure 1 and Figure 2.

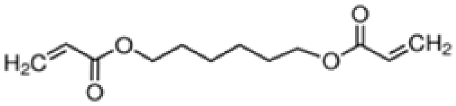

Figure 2. 1,6 Hexanediol diacrylate

2.3. Synthesis of novel polydimethylsiloxane reactive resin

HEMA was added in a flask and THF was poured into the flask. HEMA in THF were magnetically stirred. After disolving, the diisocyanate (IPDI) was added into the flask drop by drop. Then, the tin catalyst (T12) was added and stirred magnetically at 60 oC in a nitrogen atmosphere for two hours. The diisocyanate was reacted with HEMA. The mole ratio was adjusted to 1/1. Therefore one isocyanate molecule of IPDI converted urethane group and a novel monomer was obtained. This novel monomer contained one isocyanate and acrylate functional groups as shown in Figure 3.

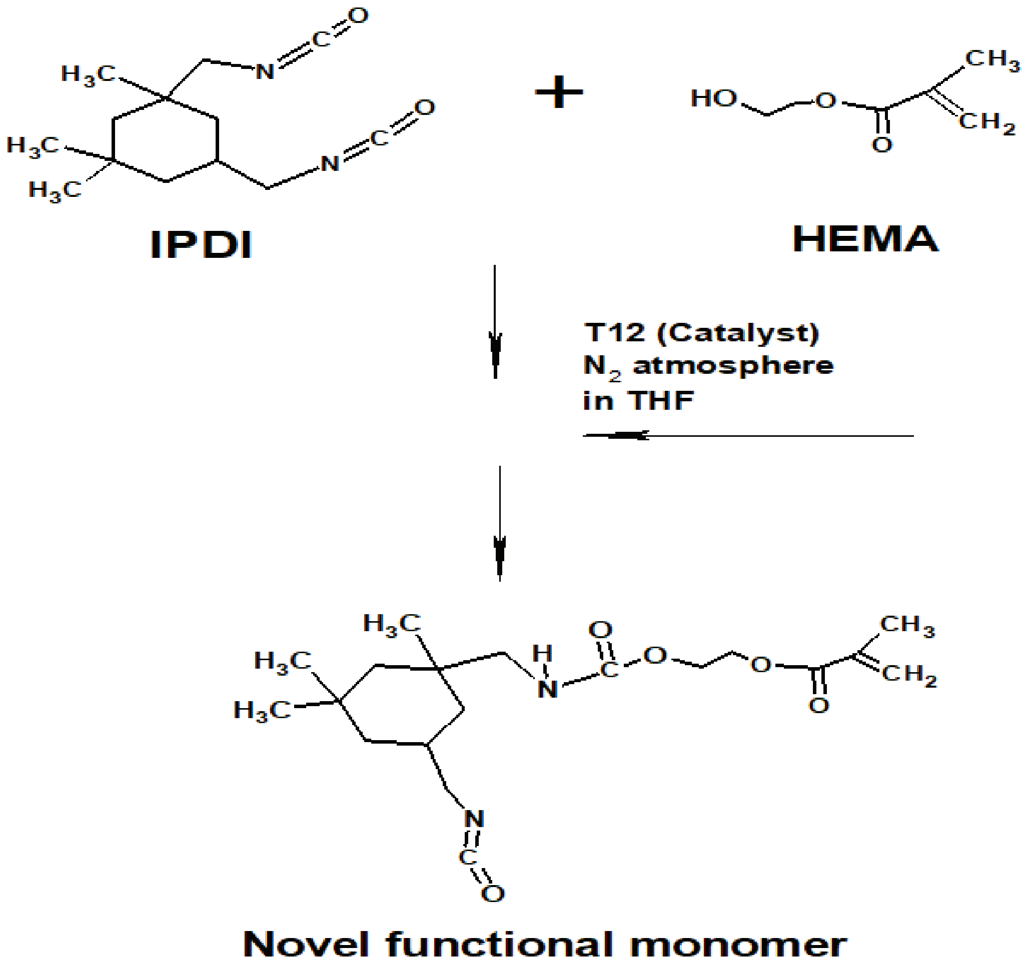

Figure 3. Synthesis of novel functional monomer

Then this novel monomer was reacted with hydroxyl-terminated polydimethylsiloxane in the flask. The mole ratio of the polydimethylsiloxane was half of the synthesized novel monomer in Figure 3. Hence the polydimethylsiloxane was terminated urethane acrylate groups. This structure was shown in Figure 4.

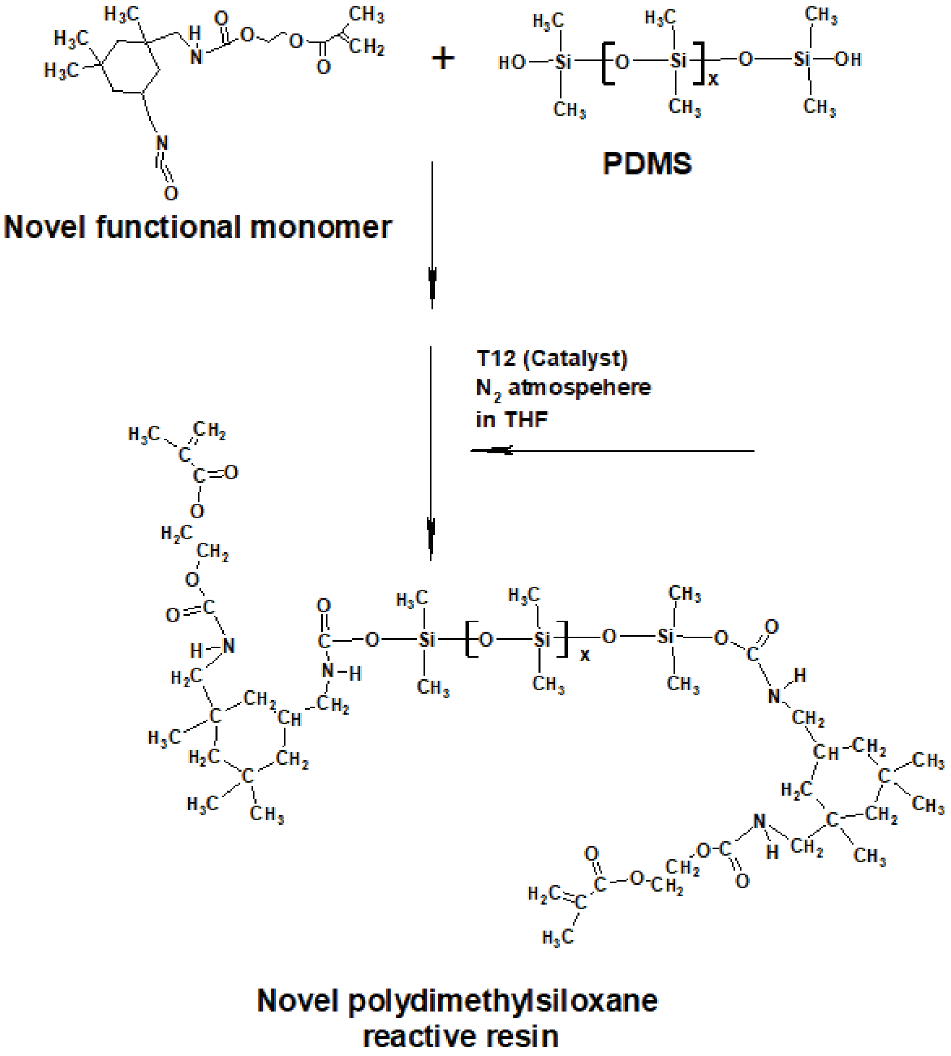

Figure 4. Synthesis of novel polydimethylsiloxane reactive resin

2.4. Preparation of novel epoxy acrylate systems

The synthesized novel polydimethylsiloxane reactive resin in Figure 4 was incorporated into conventional epoxy acrylate system in the range between 0%-1.5%. The novel reactive resin was mechanically stirred into conventional epoxy acrylate system and homogeneous solutions were obtained in various ratios. These resins were cured by SLA 3D printer and the novel products were prepared.

2.5. Measurements

Measurements were carried out for film and coating samples. Coating samples were used to characterize abrasion resistance. Film samples were used for the other tests. Fourier transform infrared spectroscopies (FT-IR) were conducted by Shimadzu 8303 FT-IR Spectrometer. The samples were characterized mechanically by standard tensile test in order to determine in terms of tensile strength, failure strain and young modulus according to ASTM D638. Tensile test was carried out by using a crosshead speed of 5 mm/min. For each product, three replicated sample were prepared and measurements were taken. The average values of these samples was used for the calculations. Hardness of the samples was measured according to Shore D method. Coating samples were also produced for taber abrasion test besides film samples. Taber abrasion test were applied to the produced coating samples and weight loss was calculated. Density was measured according to Archimed principle for film samples.

3. Results

The FT-IR spectras of novel functional monomer and novel urethane acrylate terminated polybutadien reactive resin are given in Figures 5 and Figure 6. The absorption bands were given at around 3350, 1700 and 810 cm-1 relate to –NH stretching, C=O stretching and C=C twisting of acrylate, espectively.

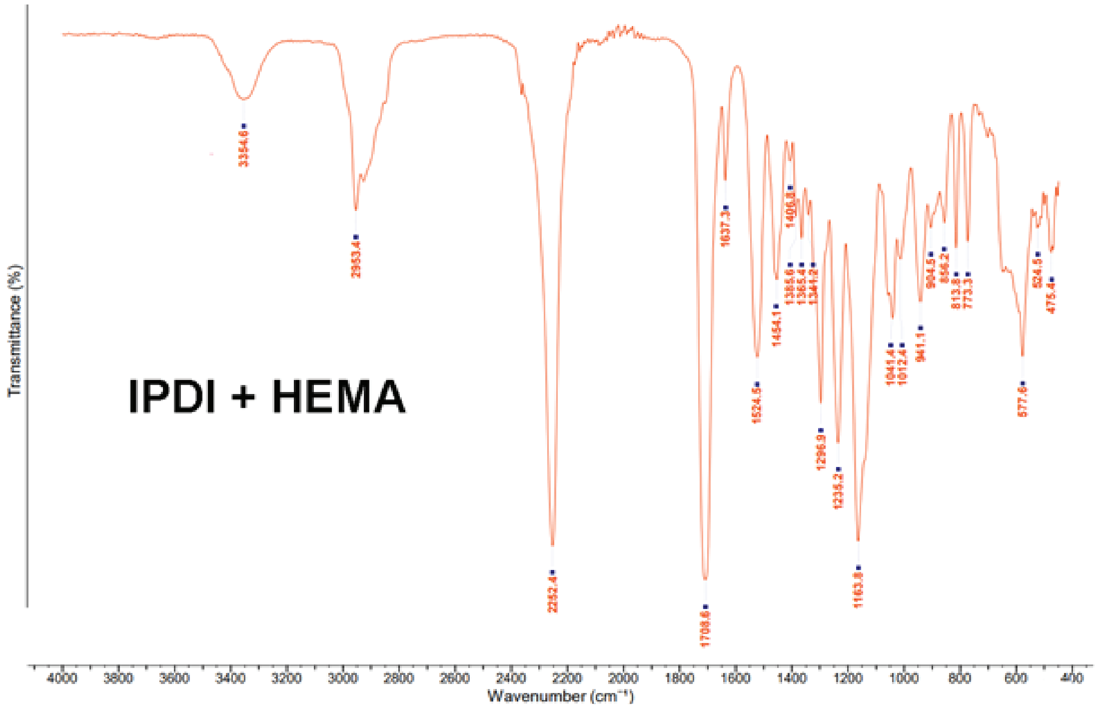

Figure 5. FTIR result of the novel monomer after the reaction of IPDI and HEMA

From the IR spectra in Figure 6, the disappearance of the characteristic absorption band at 2250 cm-1 related to isocyanate group (-NCO) indicates the completion of the reaction. In additon this, the absorption bands at around 2850 and 2900 cm-1 belonging to CH and CH2 bondings in Figure 6 became larger [2]. The shoulder band of siloxane groups was shown in the range between 1100-1010 cm-1 [6]. These results confirmed the synthesizing of novel urethane acrylate terminated polydimethylsiloxane reactive resin.

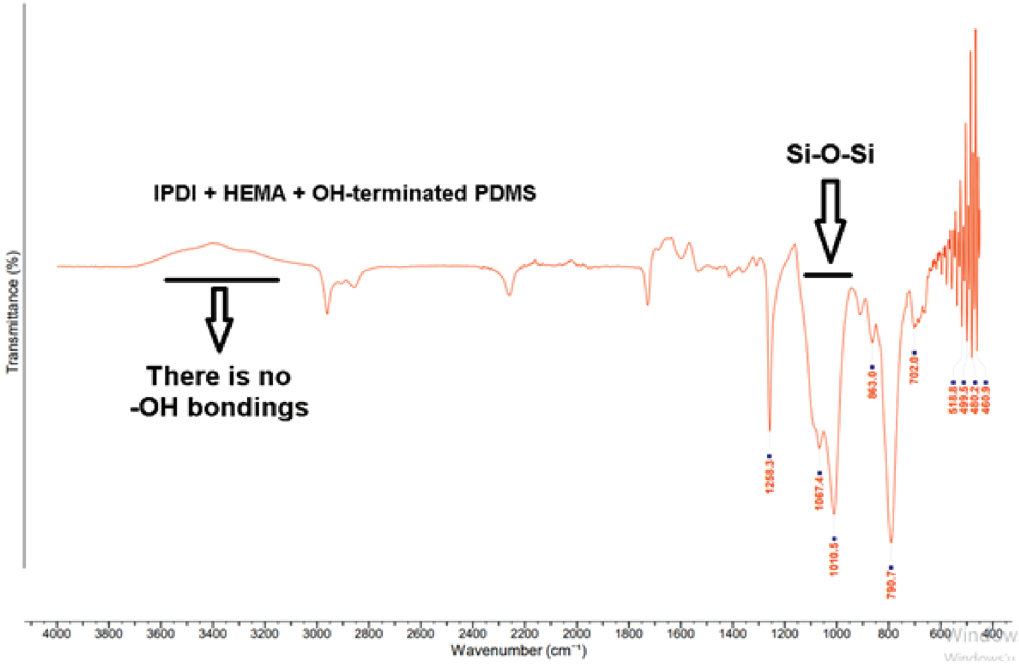

Figure 6. FTIR result of the novel polydimethylsiloxane reactive resin after the reaction of the synthesized monomer (HEMA + IPDI) and polydimethylsiloxane

Mechanical tests were performed to determine the overall effect of the synthesized novel polydimethylsiloxane reactive resin samples on the performance of conventional epoxy acrylate system. This novel polydimethylsiloxane reactive resin was incorporated into conventional epoxy acrylate system up to 1.5% by weight. Mechanical properties of polydimethylsiloxane containing samples showed that ultimate tensile strength and modulus increased up to 67% and 632%, respectively.

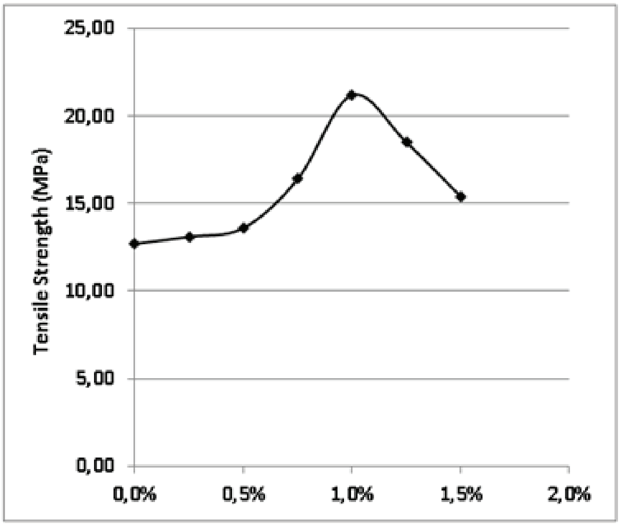

Figure 7. Tensile strength values of the samples

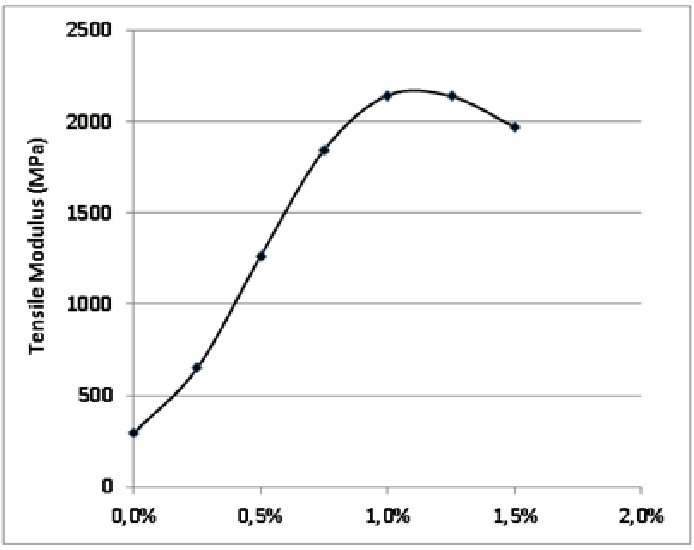

Figure 8. Tensile modulus values of the samples

Novel polydimethylsiloxane reactive resin containing samples exhibited their maximum increase peak at 1.5% wt and slight decrease was observed at higher ratios than 1%. It was thought that this situation could be derived from inhibition of crosslinking between chains due to low mobility of the synthesized reactive resins at high ratios. This situation could be physical entanglement of the reactive chains. Moreover, polydimethylsiloxane is flexible polymer and it was convereted to a novel polymer that terminated urethane acrylate groups having aromatic groups besides its flexible Si-O-Si bondings on the backbone. Therefore it was thought that tensile strength and modulus increased substantially. This situations can be observed in Figure 7 and Figure 8.

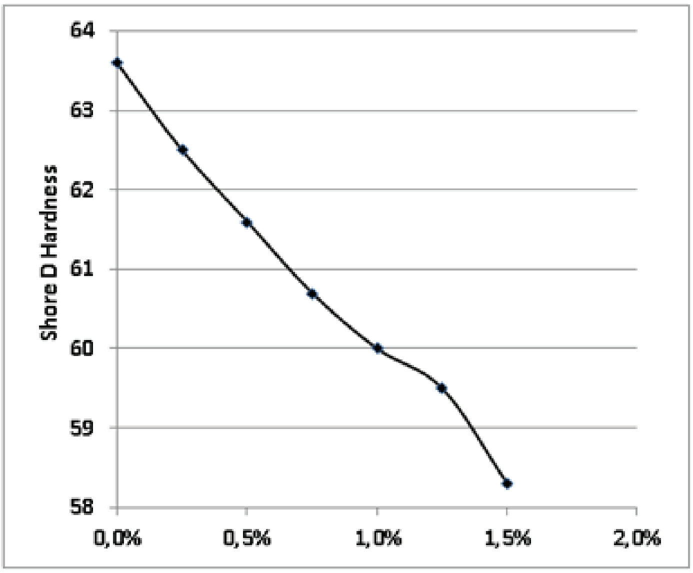

Figure 9. Shore D hardness test results of the samples

However, this situation and changing trend is not available for Figure 9. Hardness values showed a continuous decrease. It was thought that flexible siloxane bondings became dominant compared the crosslinking amount and aromatic groups in terms of hardness of the novel structures. This changing trend of hardness was shown in Figure 9. These results are given in Table 1.

Samples	Tensile Modulus (MPa)	Tensile Strength (MPa)	Density (g/cm^3)	Taber abrasive resistance (weight loss, gr)	Shore D hardness
%0	293	12.70	1.19	0.0011	63.6
%0.25	650	13.1	1.20	0.0011	62.5
%0.5	1256	13.6	1.20	0.0010	61.6
%0.75	1846	16.4	1.20	0.0009	60.7
%1	2145	21.2	1.20	0.0008	60
%1.25	2140	18.5	1.21	0.0011	59.5
%1.5	1972	15.4	1.21	0.0014	58.3

Taber abrasive results were improved by incorporating of the novel reactive resin. Maximum increase of abrasive resistance was observed as 27% in the sample of 1%. At the higher ratios, taber resistance showed a little decrease.

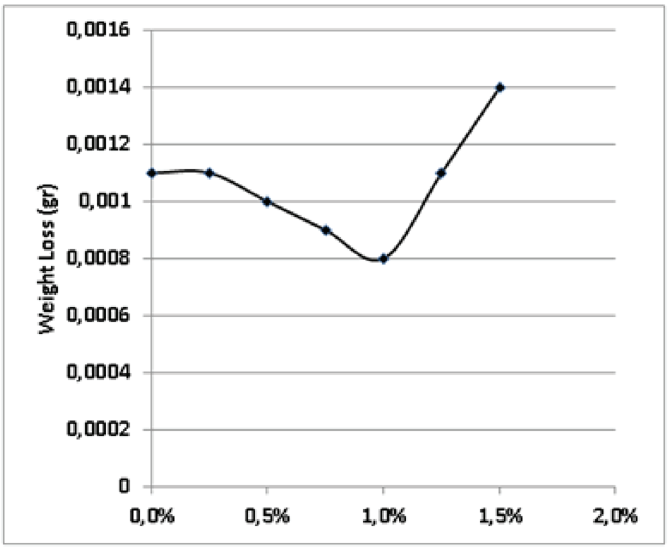

Figure 10. Taber abrasive test results of the samples

Although the hardness of the novel samples decreased, abrasive resistance were increased. It has been well known that polydimethylsiloxane structure on the backbone of the chain decreased the friction coefficient. Therefore polydimethylsiloxane increased the abrasive resistance although it had flexible structure [6].

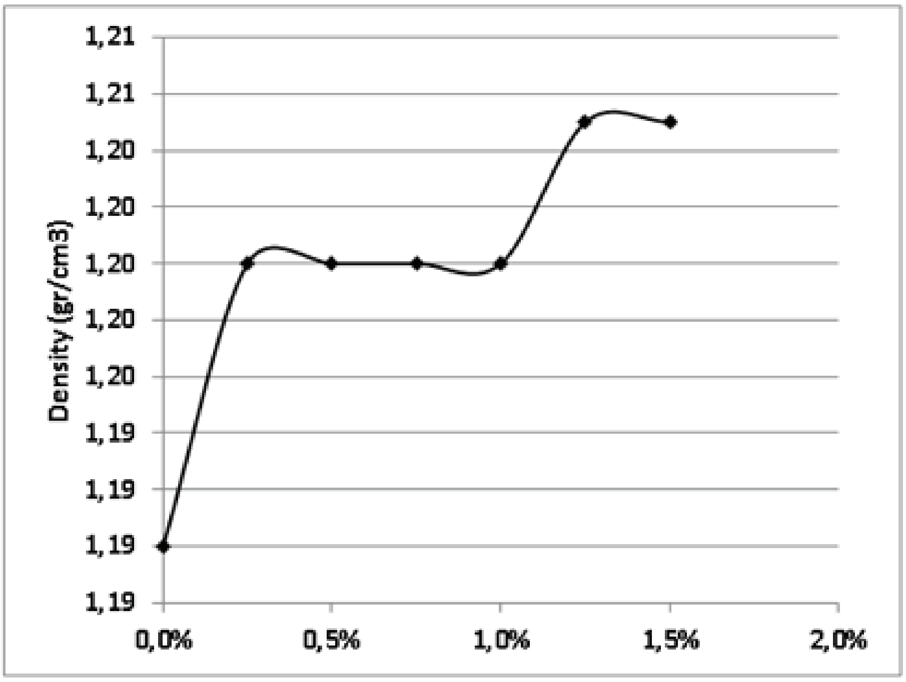

Figure 11. Densities of the samples

These results are also given in Table 1. The changing trend of abrasive test results was shown in Figure 10. On the other hand, densities of the samples presented very close values each other. They showed little increase trend as shown in Figure 11.

4. Discussion and Conclusion

In this study, novel epoxy acrylate systems were developed by synthesizing a novel polydimethylsiloxane reactive resin. This reactive resin was incorporated into conventional epoxy acrylate system in the range between 0%-1.5% by weight. This conventional epoxy acrylate system contained bisphenol A diglycidyl ether based epoxy acrylate and 1,6 hexanediol diacrylate. Tensile, shore-D hardness, taber abrasive and density tests were applied to these produced samples. Considering of the results, novel polydimethylsiloxane reactive resin containing epoxy acrylate systems exhibited much more improved results compared to conventional epoxy acrylate system. It exhibited substantial increases in terms of tensile strength, modulus and taber abrasive ressitance. However, hardness values decreased slightly for novel samples because of flexible structure of polydimethylsiloxane. This synthesized novel polydimethylsiloxane. reactive resin containing epoxy acrylate systems can be used in applications that required higher mechanical and abrasive properties for epoxy acrylate systems of 3D SLA printers.

5. References

1. Aerykssen J.H., Khudyakov I.V. Industrial and Engineering Chemical Research., 9, 50:1523, 2010, DOI: 10.1021/ie101816b.
2. Bayramoglu G., Kahraman M.V, Kayaman-Apohan N., Güngör A. Progress in Organic Coatings, 57:1, 50-55, 2006.
3. Çakir M., Akin E. Journal of Applied Polymer Science, 2019, Doi: 10.1002/APP.47399.
4. Bongiovanni R., Malucelli G., Messori M., Pilati F., Priola A., Tonelli, C. Journal of Applied Polymer Science, 75, 651-659, 2000.
5. Davidson, R.S., Richard, E., Stephen, T. Susan, A.W., Polymer, 33, 14, 3031-3036, 1992.
6. Çakir, M., Akin, E. Journal of Applied Polymer Science, 136(16), 47399, 2019.

Use of medicinal plants as bioactive natural compounds in modern medicine applications

Gül GÖRMEZ

Dr. Öğr. Üyesi, Van Yüzüncü Yıl Üniversitesi, Sağlık Bilimleri Fakültesi Van, Türkiye,

***Mail:** gulgormez@yyu.edu.tr*

For centuries, human beings have used plants as therapeutic as well as food and beverage, cosmetics and chemical industry. Today, modern medicine continues to add plant-based raw materials to many of the medicines it produces. The main reason why the demand for herbal resources has continued to increase in recent years is that synthetically produced drugs cause negative effects that will harm different organs of the body while curing the disease in question. Thanks to the phytochemicals they contain, medicinal plants show therapeutic properties such as antioxidant, antibacterial, anti-cancer, cardioprotective, immune system strengthening, anti-inflammatory, calming and protecting the skin from UV radiation. Atropine, muscarine, reserpine, nicotine, cocaine and resveratrol are some important plant-derived active ingredients used in modern medicine. As a result of detailed studies on plants with each passing day, many plants are used as a disease therapeutic in vivo and in vitro studies after being investigated phytochemically. In this study, it is aimed to evaluate the contents of medicinal plants used as bioactive natural compounds in modern medicine applications.

Keywords: Medicinal plants, bioactive natural compounds, modern medicine applications.

Effects of *Rosa canina L.* extracts on HCT116 cell line

Gül GÖRMEZ

Dr. Öğr. Üyesi, Van Yüzüncü Yıl Üniversitesi, Sağlık Bilimleri Fakültesi Van, Türkiye

Mail: *gulgormez@yyu.edu.tr*

Rosa canina L. is a shrub-shaped tree belonging to the Rosaceae family, widely distributed in North America, Asia, Europe and the Middle East. Its fruits are consumed as food among the people, and because of its high vitamin C content and antioxidant properties, it is used as a common cold, rheumatism, osteoarthritis, obesity, diabetes and antibacterial. In this study, we investigated the effects of extracts of *Rosa canina* fruits prepared with various solvents on a colon cancer cell line (HCT116). *Rosa canina* fruits were extracted with ethanol, methanol and acetone solvents after lyophilized drying. Extracts obtained after removal of toxic with rotary evaporator, substances were dissolved in DMSO (<0.004) at different concentrations (100, 200, 500, 700 and 1200 µg/ml) and applied to cells for 48 hours to determine cell viability. Cell line viability test MTT [3-(4,5-dimethylthiazol-2-yl)-2,5-diphenyltetrazolium bromide] was performed to determine the IC50 concentrations of the extracts after 48 hours. The IC50 value of *rosa canina* fruit extract made with 80% acidic methanol was determined as 625 µg/ml. Other extracts had higher IC50 concentrations. As a result of the study, it was concluded that *Rosa canina* methanol extracts were effective in colon cancer cell line (HCT116). It is thought that the continuation of this study will be repeated in rats and the results will be evaluated.

Keywords: Rosa canina, plant extract, medicinal plant, cancer, HCT116